ACS SYMPOSIUM SERIES 1152

Novel Materials for Catalysis and Fuels Processing

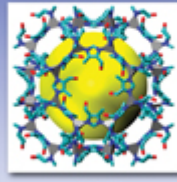

EDITED BY
Juan J. Bravo-Suárez, Michelle K. Kidder, and Viviane Schwartz

Novel Materials for Catalysis and Fuels Processing

In Novel Materials for Catalysis and Fuels Processing; Bravo-Suárez, J., et al.;
ACS Symposium Series; American Chemical Society: Washington, DC, 2013.

In Novel Materials for Catalysis and Fuels Processing; Bravo-Suárez, J., et al.;
ACS Symposium Series; American Chemical Society: Washington, DC, 2013.

ACS SYMPOSIUM SERIES **1132**

Novel Materials for Catalysis and Fuels Processing

Juan J. Bravo-Suárez, Editor
The University of Kansas
Lawrence, Kansas

Michelle K. Kidder, Editor
Oak Ridge National Laboratory
Oak Ridge, Tennessee

Viviane Schwartz, Editor
Oak Ridge National Laboratory
Oak Ridge, Tennessee

Sponsored by the
ACS Division of Energy and Fuels

American Chemical Society, Washington, DC

Distributed in print by Oxford University Press

In Novel Materials for Catalysis and Fuels Processing; Bravo-Suárez, J., et al.;
ACS Symposium Series; American Chemical Society: Washington, DC, 2013.

Library of Congress Cataloging-in-Publication Data

Novel materials for catalysis and fuels processing / Juan J. Bravo-Suárez, editor, Michelle K. Kidder, editor, Viviane Schwartz, editor ; sponsored by the ACS Division of Energy and Fuels.

pages cm. -- (ACS symposium series ; 1132)

Includes bibliographical references and index.

ISBN 978-0-8412-2811-5 (alkaline paper) 1. Catalysis--Research. 2. Catalysts--Research. 3. Fuel--Research. I. Bravo-Suárez, Juan J. II. Kidder, Michelle K. III. Schwartz, Viviane. IV. American Chemical Society. Division of Energy and Fuels.

QD505.N675 2013

660'.2995--dc23

2013016859

The paper used in this publication meets the minimum requirements of American National Standard for Information Sciences—Permanence of Paper for Printed Library Materials, ANSI Z39.48n1984.

Distributed in print by Oxford University Press

PRINTED IN THE UNITED STATES OF AMERICA

In Novel Materials for Catalysis and Fuels Processing; Bravo-Suárez, J., et al.;
ACS Symposium Series; American Chemical Society: Washington, DC, 2013.

Foreword

The ACS Symposium Series was first published in 1974 to provide a mechanism for publishing symposia quickly in book form. The purpose of the series is to publish timely, comprehensive books developed from the ACS sponsored symposia based on current scientific research. Occasionally, books are developed from symposia sponsored by other organizations when the topic is of keen interest to the chemistry audience.

Before agreeing to publish a book, the proposed table of contents is reviewed for appropriate and comprehensive coverage and for interest to the audience. Some papers may be excluded to better focus the book; others may be added to provide comprehensiveness. When appropriate, overview or introductory chapters are added. Drafts of chapters are peer-reviewed prior to final acceptance or rejection, and manuscripts are prepared in camera-ready format.

As a rule, only original research papers and original review papers are included in the volumes. Verbatim reproductions of previous published papers are not accepted.

ACS Books Department

In Novel Materials for Catalysis and Fuels Processing; Bravo-Suárez, J., et al.;
ACS Symposium Series; American Chemical Society: Washington, DC, 2013.

Preface

Catalysis drives the majority of industrial chemical processes and is an essential element for the current fossil fuel based economy. Continual improvement and innovation in catalysis plays a key role in the development of more efficient and effective fuel processing technologies. To achieve this goal, novel catalysts need to be designed for chemical conversions running at much higher yields and with better selectivity, which can improve the economics and sustainability of these processes by reducing the consumption of raw materials, energy, and emissions to the environment.

This book is based on contributions to the symposium "Novel Materials for Catalysis and Fuels Processing" that took place at the 243rd ACS National Meeting in San Diego, California on March, 2012. Many topics concerning the growing area of materials for catalysis and fuel processing were presented in this symposium, and they constitute the main content of this book, including theoretical and experimental advances in the areas of catalyst synthesis, characterization, and kinetics for renewable feedstocks conversion, alternative fuel production, emission control, selective reductive and oxidative processes, and carbon sequestration and transformation.

This book contains 14 peer-reviewed chapters. These chapters have been organized in five sections: (I) general overview (Chapter 1), (II) computer-aided design (Chapters 2 and 3), (III) spectroscopic characterization (Chapter 4), (IV) kinetics-aided design (Chapter 5), and (V) applications of novel catalysts (Chapters 6 to 14).

Part I consists of an introductory chapter (Chapter 1) by Bravo-Suárez, Chaudhari, and Subramaniam, which provides an overview of the recent progress in synthesis, characterization, and kinetics as tools for designing catalysts for targeted applications. The remaining chapters feature a unique overview of synthetic methods, advanced characterization techniques, and computational and kinetic tools to assist in the understanding and development of new catalytic materials as well as compelling applications in fuels and chemicals processing. Topics that address current energy and environmental needs are covered, such as deoxygenation of alternative fuels, production of higher alcohols as fuel additives, hydrocarbon production, hydrodesulfurization, materials for carbon dioxide adsorption, and emission control catalysts for diesel engines. Additionally, topics aimed at a fundamental understanding of catalytic processes such as probing surface interactions via advanced spectroscopic techniques and computational simulations are also discussed.

In Novel Materials for Catalysis and Fuels Processing; Bravo-Suárez, J., et al.;
ACS Symposium Series; American Chemical Society: Washington, DC, 2013.

Current advances in computational power and theoretical methods have tremendously contributed to the understanding of structure–activity and structure–property relationships of catalysts and materials, which can be used to guide the design of novel structures. These topics are covered in Part II of this book. In Chapter 2, Cheng and Curtiss present a review of the theoretical studies covering the nature of supported vanadia clusters for propane oxidative dehydrogenation via Density Functional Theory (DFT) calculations and their implications for the design of improved catalysts. In Chapter 3, Houndonougbo describes important structural factors required for the design of novel Zeolitic Imidazolate Frameworks (ZIFs) for CO_2 adsorption. These factors are established from molecular simulations of CO_2 adsorption at high pressures on ZIFs as carried out by a combination of Grand Canonical Monte Carlo (GCMC) and force fields methods.

The utilization of spectroscopic techniques for the characterization of catalysts is essential for the understanding of the nature of active sites, adsorbed species, and ultimately the reaction mechanism. This fundamental knowledge of the catalyst structure and the catalytic cycle is necessary for the development of improved and new catalysts. This topic is the focus of Part III. In Chapter 4, Formo, Wu, Mahurin, and Dai describe recent developments in the use of Surface Enhanced Raman spectroscopy (SERS) for studying catalyst structure and interface interactions with molecular probes. As detailed in the chapter, the application of SERS for catalyst characterization in various environments at elevated temperatures is made possible by the generation of robust SERS substrates, namely, silver nanowires coated with a protective layer of alumina, which in turn can act as a support for catalyst characterization studies.

Part IV focuses on the use of modern kinetic tools for catalyst and reactor design. In this section, Sharma, Suib, and Mhadeshwar (Chapter 5) describe the challenges associated with the design of sulfur-resistant diesel oxidation catalysts (DOCs), an important component of the exhaust emission control system in diesel engines. In particular, sulfur species interactions with Pt–Pd/Alumina, a typical DOC, are investigated via a microkinetic analysis supported by experimental and computational studies of the reaction mechanism as derived from a critical literature review. Future directions for the design of sulfur resistant materials for efficient and economical DOCs are also discussed.

The final section of this book, Part V, covers applications of novel catalysts for various reactions including hydrodesulfurization, epoxidation, syngas conversion, dehydrogenation, and emerging applications such as renewables conversion. In Chapter 6, Soni, Bhaskar, Kumar, Seetha, Rao, and Dhar describe the development of more active hydrodesulfurization and hydrogenation catalysts based on mesostructured silica (SBA-16) supported Mo, Co–Mo, and Ni–Mo. Detailed and complementary characterizations of catalyst metal coverage are used to establish correlations with catalyst reactivity to explain the observed higher activities of the SBA-16 catalysts in comparison with related 2D and amorphous silica supported materials. Chapter 7 by Pachamuthu, Ramanathan, Santhi, and Maheswari and Chapter 8 by Ramanathan, Maheswari, Thapa, and Subramaniam investigate novel Cu–TUD-1 and Ce–MCM-48 catalysts, respectively, for the epoxidation of alkenes. These catalysts consist of highly dispersed isolated

In Novel Materials for Catalysis and Fuels Processing; Bravo-Suárez, J., et al.;
ACS Symposium Series; American Chemical Society: Washington, DC, 2013.

species of CuO and oligomeric CuO in a 3D amorphous silica matrix and Ce4+ partially incorporated in the MCM-48 framework, whose presence is shown to improve activity and selectivity towards the corresponding epoxide products. In Chapter 9, Chai, Howe, Kidder, Wang, Schwartz, Overbury, Dai, and Jiang report small Rh nanoparticles supported on an ordered mesostructured carbon (OMC) for the conversion of syngas to ethanol. The presence of a carbon support, rhodium, and promoters (Mn, Li, Fe) in the catalyst is shown to be responsible for the increased alcohol selectivities in comparison with similar conventional SiO_2 supported catalysts. In Chapter 10, Schwartz, Overbury, and Liang describe the use of carbon as an alternative material to conventional metal-based catalysts for the oxidative dehydrogenation of alkanes. Challenges and future directions associated with the development of more active and selective carbon catalysts are also discussed in this chapter.

The sustainable production of fuels and chemicals from plant-based biomass is a topic of current and intense research worldwide. Chapters 11 to 14 focus on the catalytic conversion of renewable feedstocks including bioderived ethanol, sugars (e.g., xylitol, sorbitol), and bio-oil components. In Chapter 11, Kandel, Althaus, Pruski, and Slowing report the synthesis of a novel bifunctional enzyme–alkylamine–mesostructured SiO_2 catalyst for C–C coupling reactions of alcohols. The catalyst is able to carry out the condensation of ethanol with high selectivity via a two-step, single pot, low temperature process. In Chapter 12, Jin, Subramaniam, and Chaudhari report the hydrogenolysis of xylitol and sorbitol towards C_2 and C_3 liquid products on admixtures of carbon supported noble metal catalysts and solid base promoters. This work provides mechanistic insights into the reaction network for base-promoted hydrogenolysis and the corresponding effects on activity and selectivity of liquid products. Chapters 13 and 14 cover the upgrading of bio-oil model compounds such as phenols and carboxylic acids, respectively. In Chapter 13, Whiffen and Smith report the application of a Ni_2P catalyst for the hydrodeoxygenation (HDO) of methylphenol. The effect of post-synthesis thermal treatments on the catalyst physicochemical properties and activity in the HDO reaction is discussed. In Chapter 14, He and Wang review the catalytic deoxygenation of carboxylic acids. The authors focus on the properties required for the design of improved catalysts including the presence of metal sites, acid sites, and support oxygen vacancies. Current challenges in the fundamental study of the deoxygenation of acids present in bio-oil are also discussed.

The book will appeal to both basic and applied researchers in academia and industry who would like a comprehensive overview of the most recent studies targeting the development of the next generation of catalysts. The selection of topics presented here touches upon current progress and development of novel materials and catalysts for fuels and chemicals processing. The editors hope that the reader will appreciate the challenges faced in the design and development of catalysts and catalytic technologies and be inspired to contribute to their solution to tackle the increasingly complex environmental and sustainable energy problems of the 21st century.

In Novel Materials for Catalysis and Fuels Processing; Bravo-Suárez, J., et al.;
ACS Symposium Series; American Chemical Society: Washington, DC, 2013.

Acknowledgments

We wish to thank a number of people without whom this book would not have been possible. Special thanks are given to each of the authors who participated in the symposium and contributed chapters to this book and to the reviewers who helped to provide critical comments and suggestions, which improved the quality of the chapters. We thank Nikki Lazenby, Arlene Furman, and Tim Marney from the ACS Books Division for their kind and efficient support to complete this book. We also would like to acknowledge the generous financial support from the ACS Division of Energy & Fuels for the symposium and the colored graphics in the book.

J.J.B.-S. acknowledges the support by the University of Kansas–Center for Environmentally and Beneficial Catalysis (CEBC) as well as the encouragement of Professors Bala Subramaniam and R.V. Chaudhari at CEBC during this project. J.J.B.-S. would like to thank his wife, Samantha, and son, Ian, for their love, support, and patience.

M.K.K. acknowledges the support of Oak Ridge National Laboratory and the Division of Chemical Sciences, Geosciences, and Biosciences, Office of Basic Energy Sciences, U.S. Department of Energy. M.K.K. would like to thank her husband, Mark, and sons, Justin and Nathan, for their unwavering support and affection.

V.S. acknowledges the support of the Center for Nanophase Materials Sciences, which is sponsored at Oak Ridge National Laboratory by the Scientific User Facilities Division, Office of Basic Energy Sciences, U.S. Department of Energy. V.S. would like to thank her family, her husband, Speros, and new born son, Marcus, for their support and inspiration.

Juan J. Bravo-Suárez
Center for Environmentally Beneficial Catalysis
The University of Kansas
1501 Wakarusa Dr., LSRL B133D
Lawrence, KS 66047

Michelle K. Kidder
Chemical Sciences Division
Oak Ridge National Laboratory
Bldg. 4100, MS 6197
1 Bethel Valley Road
Oak Ridge, TN 37381

Viviane Schwartz
Center for Nanophase Materials Science
Oak Ridge National Laboratory
Bldg. 8610, MS 6493
1 Bethel Valley Road
Oak Ridge, TN 37831

In Novel Materials for Catalysis and Fuels Processing; Bravo-Suárez, J., et al.;
ACS Symposium Series; American Chemical Society: Washington, DC, 2013.

Chapter 1

Design of Heterogeneous Catalysts for Fuels and Chemicals Processing: An Overview

Juan J. Bravo-Suárez,[*,1] Raghunath V. Chaudhari,[*,1,2] and Bala Subramaniam[*,1,2]

[1]Center for Environmentally Beneficial Catalysis, University of Kansas, 1501 Wakarusa Dr., LSRL A110, Lawrence, Kansas 66047, USA
[2]Department of Chemical & Petroleum Engineering, University of Kansas, 4158 Learned Hall 1530 W 15th St., Lawrence, Kansas 66045, USA
[*]E-mail: jjbravo@ku.edu, rvc1948@ku.edu, bsubramaniam@ku.edu

A major goal/challenge in catalysis research is to design stable catalysts that selectively form targeted products in high yields. This chapter presents a brief overview of recent progress towards this goal including: (1) fundamental concepts, (2) current approaches to heterogeneous catalyst design and discovery, (3) catalytic materials and synthesis methods, (4) in situ characterization, (5) modern kinetic and computational tools, and (6) emerging catalytic applications for fuels and chemicals from renewable (e.g., biomass) and alternative abundant (e.g., natural gas) feedstocks. In the final section, perspectives and anticipated advances in catalyst synthesis, in situ characterization, and kinetics and computational tools for the design of heterogeneous catalysts are presented. Further, we also briefly highlight concepts that incorporate environmental, health, and safety (EHS), risk, and life cycle assessment (LCA) analyses to guide catalyst design. The literature covering these topics is immense and it would be nearly impossible to include all available references in a single publication such as this. Therefore, only a selected number of references are cited herein to illustrate the most relevant aspects in the design of heterogeneous catalysts for fuels and chemicals processing.

In Novel Materials for Catalysis and Fuels Processing; Bravo-Suárez, J., et al.;
ACS Symposium Series; American Chemical Society: Washington, DC, 2013.

Introduction

Catalysts are materials employed for a variety of chemical conversions of feedstocks to targeted products. The main function of catalysts is to accelerate the formation of desired products, which in the absence of catalysts would either not form or form too slowly and/or unselectively. Catalysts can be of biological (e.g., enzymes) or nonbiological (e.g., organic or inorganic materials) origin. The first route is usually termed enzymatic catalysis, whereas nonbiological routes are usually categorized as either homogeneous or heterogeneous catalysis (Figure 1). In heterogeneous catalysis, several phases are involved consisting of the catalyst (e.g., solid), a solvent (or diluent), and reactants (e.g., liquid and/or gas). It is estimated that over 90% of all the chemical processes currently in use are catalytic (*1*). Among all the catalytic processes used in the industry, heterogeneous catalysts are the most widely used (80%), followed by homogeneous (17%), and enzymatic (3%) catalysts (*2*) (Figure 1).

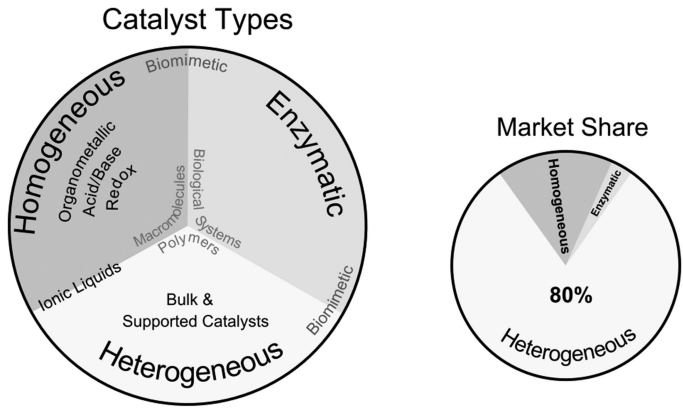

Figure 1. Different types of catalysts and their global market share

The global heterogeneous catalyst demand in 2010 was approximately US$14 billion and it is estimated to grow at an annual rate of 8% in the next few years (Table 1). The main applications of heterogeneous catalysts are roughly equally distributed among petroleum refining, chemical processing, and automotive emission control (Table 1). On a regional basis, approximately one-third of the catalysts were consumed in each of the following regions: North America, the Asia Pacific region, and the rest of the world (Europe, Latin America, Africa, and the Mideast) (*3*). Although the global catalyst market in itself is significant, the biggest impact of catalysts comes from the value created for the chemicals, fuels, and goods they produce. For example, since the cost of catalysts is approximately 0.1% of the cost of the final products (*4*, *5*), it can be estimated that the value of these products in the US alone ($4.5 trillion per annum) represents ~30% of the US gross national income in 2010 (*6*).

In Novel Materials for Catalysis and Fuels Processing; Bravo-Suárez, J., et al.;
ACS Symposium Series; American Chemical Society: Washington, DC, 2013.

Table 1. Global catalyst demand and forecast by application in US$ (billions) per annum[a]

	2010	*2015*	*CAGR (%)[b]*
Petroleum Refining	**4.03**	**4.81**	**4**
Hydroprocessing[c]	2.08	2.62	5
Fluid catalytic cracking[c]	1.23	1.41	3
Alkylation, reforming, and others[c]	0.72	0.78	2
Chemical Processing	**5.20**	**7.02**	**6**
Polyolefins	1.24	1.52	4
Adsorbents	1.30	1.52	3
Chemical catalysts	2.67	3.98	8
Oxidation, ammoxidation, and oxychlorination[d]	1.11	1.61	8
Hydrogen, ammonia, and methanol synthesis[d]	0.81	1.30	10
Hydrogenation[d]	0.17	0.25	7
Dehydrogenation[d]	0.12	0.18	9
Organic synthesis[d]	0.46	0.64	7
Mobile Emission Control	**4.81**	**8.58**	**12**
Heavy-duty diesel	0.72	2.87	32
Motorcycles	0.20	0.42	16
Light-duty	3.90	5.29	6
Total Catalyst Demand	**14.04**	**20.41**	**8**

[a] With data from reference (*7*) (Source: BASF), original data in Euros (1.3 US$ = 1 €). Data excludes precious metal catalysts. [b] Compound annual growth rate. [c] Estimated with data from reference (*8*) (Source: The Fredonia Group, Cleveland). [d] Estimated with data from reference (*9*) (Source: SRI Consulting)

Currently, there is continuing interest in the chemical industry and in academia to develop improved and new catalysts for established and new chemistries motivated by consumer demands of product quality, market forces, external factors such as environmental and energy related legislations, and the availability of cheaper and abundant new feedstocks such as ethanol, glycerol, bio-oil, and shale gas. Undoubtedly, catalysts that are more active, selective, stable over longer periods of operation, and less expensive will be required to develop competitive technologies for targeted applications. The development of such improved and novel catalysts for specific applications is, however, not an easy task. During the last few decades, significant advances have been made in kinetic studies, in situ catalyst probes bridging materials and pressure gaps, computational methods, textural and structural characterization techniques, and

In Novel Materials for Catalysis and Fuels Processing; Bravo-Suárez, J., et al.;
ACS Symposium Series; American Chemical Society: Washington, DC, 2013.

high-throughput synthesis and testing of catalysts. These advances enable a more thorough, though not yet complete, rational design of catalysts. Here, we present a general overview of some of the recent advances and trends in the design of heterogeneous catalysts.

Heterogeneous Catalyst Design

Fundamental Concepts

The main function of a catalyst is to modify the rate of a targeted chemical reaction in such a way that a specific product can be produced preferentially with high space-time yield (*10*). An example of a typical heterogeneous catalyst is that of a highly dispersed metal on a porous and high surface area support. During a catalytic reaction, reactants and products are transferred to and from the catalyst surface where the reaction occurs in an uninterrupted and repeated cycle of elementary steps such that the catalyst is regenerated to its original form in the last step (*11*). These steps are schematically shown in Figure 2 and listed below (*12*, *13*).

1) Diffusion of reactants from the bulk fluid phase to the external surface of the porous catalyst particle.
2) Intraparticle diffusion of the reactants through the catalyst pores to the internal active sites.
3) Adsorption of reactants onto the active sites.
4) Reaction on the surface of the catalyst.
5) Desorption of products from catalyst surface.
6) Intraparticle diffusion of the products through the catalyst pores to the external surface of the catalyst particle.
7) Diffusion of the products from the external particle surface to the bulk of the fluid.

Interphase (steps 1 and 7) and intraparticle (steps 2 and 6) diffusion steps follow well-known physical laws of diffusion (*12*, *14*). These steps can often limit the overall reaction rates and also alter the intrinsic catalytic selectivity. To detect such diffusional intrusions, theoretical and/or experimental protocols are available to ensure whether or not the intrinsic kinetics, activity, and selectivity of a catalytic reaction are being measured (*12*, *15*).

Modern catalysis research focuses on three main interrelated areas, catalyst synthesis, catalyst characterization, and catalytic kinetics. These areas expanded at three different levels of study, micro-, meso-, and macroscales, constitute the basis for fundamental understanding of catalytic phenomena (Figure 3) (*17*, *18*). The microscopic level deals with molecules and active sites, focusing in particular on the elementary reaction steps of reactive species on the catalytic sites, fundamental characterization of catalyst surfaces, theoretical studies of active sites and reaction intermediates, and the synthesis of active sites at the molecular level. The mesoscale level considers the catalyst particle and the catalytic reactor. This is the level most commonly found in catalysis research

In Novel Materials for Catalysis and Fuels Processing; Bravo-Suárez, J., et al.;
ACS Symposium Series; American Chemical Society: Washington, DC, 2013.

laboratories. It concerns catalyst preparation and activation, the measurement of catalytic activities and selectivities in laboratory scale batch and flow reactors, and catalyst characterization ex situ and in situ under working conditions. The macroscopic level mainly involves the preparation of functional catalysts on a larger scale required for pilot/demonstration/commercial scale catalytic reactors (e.g., fluid catalytic cracking catalysts in petroleum refineries) or specific applications such as automotive industry (e.g., as extrudates, monoliths, etc.), catalytic reactor design and control, and the integration of the catalytic reactor in a process. This is the level usually predominant in an industrial setting (*17–19*).

The schematic representation of the different levels in catalysis research, as shown in Figure 3, implies a dynamic process involving an iterative flow of information (related to catalyst synthesis, characterization, and catalytic reaction) between different levels. In this manner, insights and guidance for catalyst discovery can be gained from both top-down and bottom-up research approaches.

Overall, this multilevel approach to catalyst development highlights the cross- and multidisciplinary nature of catalysis research involving disciplines such as solid state and organometallic chemistry, surface science, theoretical and computational chemistry, materials science, analytical instrumentation, biochemistry, chemical kinetics, and reaction/reactor engineering. Additionally, it emphasizes the need for closer collaborations among different disciplines for tackling industrial, environmental, and energy related problems where catalysis is expected to have a significant impact (*11*, *20*, *21*).

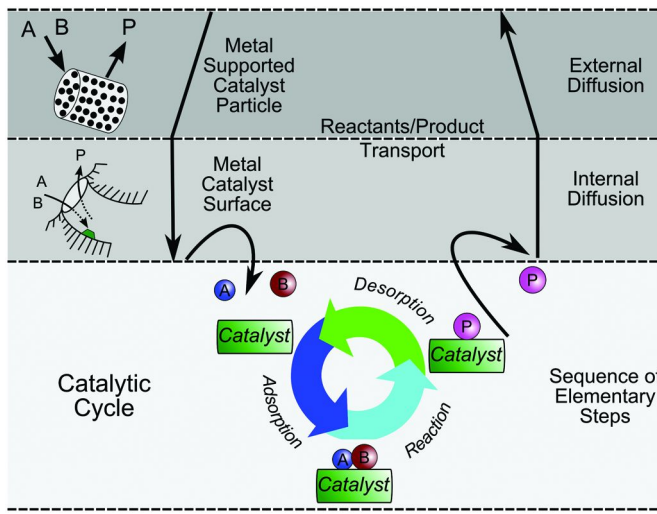

Figure 2. Sequence of steps during reaction on a supported metal catalyst. With data from references (12) and (16).

In Novel Materials for Catalysis and Fuels Processing; Bravo-Suárez, J., et al.;
ACS Symposium Series; American Chemical Society: Washington, DC, 2013.

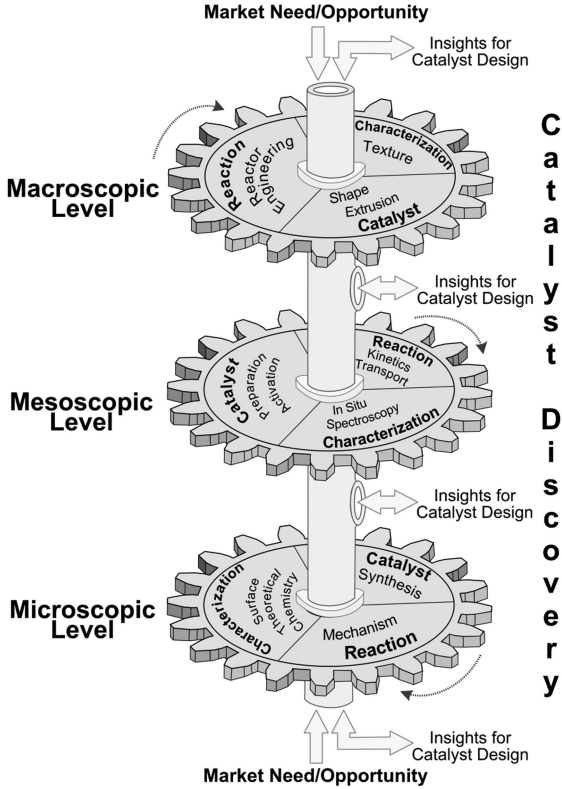

Figure 3. Levels of study and approaches for catalyst discovery in heterogeneous catalysis research. With data from reference (17).

Approaches to Catalyst Design

Classical Approach

Different research approaches for catalyst development have been employed since the early days of industrial catalysis, which have contributed to the discovery of important catalytic processes such as ammonia synthesis and the Fischer-Tropsch process (*19*). The classical approach consists of carrying out a large number of trial and error experimentation in a closed sequential loop of catalyst synthesis, testing, modification, and redesigned synthesis that is continued until the testing step yields a satisfactory catalyst (*4*). With the advent of sophisticated robotic technology and high speed computers, this approach has evolved into the so-called combinatorial high-throughput screening (HTS) methodology where rapid automated synthesis and testing of a large number of catalysts can be carried out (*22*).

Industrial Approach

A step beyond the classical combinatorial approach involves a more scientifically guided preselection of primary and minor components for the catalyst synthesis step, as has been usually employed in industrial research (Figure 4) (*23*, *24*). This preselection takes advantage of the large amount of reactivity data accumulated over the years for many catalyzed reactions by using apparent correlations between activity patterns of different catalysts vs similar class of reactions, catalytic activity vs catalyst bulk properties, geometric considerations, heats of adsorption of different species on catalysts, and qualitative concepts of chemical reactivity, among others (*23*).

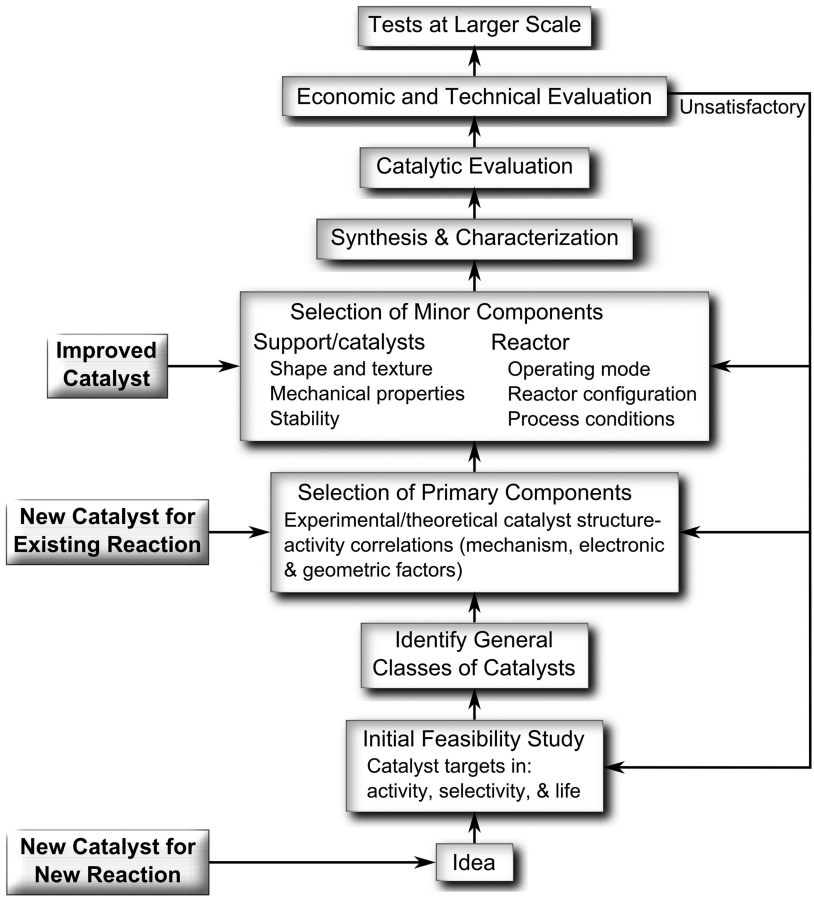

Figure 4. Simplified scheme for planning and development of industrial catalysts. With data from references (25–27).

In Novel Materials for Catalysis and Fuels Processing; Bravo-Suárez, J., et al.;
ACS Symposium Series; American Chemical Society: Washington, DC, 2013.

Virtual Mechanism Based Approach

This strategy may be considered as a variation of the "industrial" approach. As its name implies, this method is based on the assumption of a virtual reaction mechanism for the reaction of interest. This virtual mechanism, however, is not necessarily related to the real catalytic reaction mechanism. In this approach, a set of elementary steps is assumed to be key rate determining steps in the catalytic cycle. Then, catalyst components are selected such that they overcome the chemical restrictions imposed by these key steps (*28*). Further design variables can be included, usually resulting in new components being added to the selected catalysts. For example, in the oxidation of methane to methanol, the key steps in the virtual mechanism and/or design variables were assumed to be: (1) activation of C–H bonds; (2) insertion of oxygen; and (3) the product has to be stable at the reaction conditions and with the selected catalyst. In this way, a catalyst composed of Ga_2O_3 (selected for C–H activation since it is highly active for H–D exchange in a CH_4/D_2 mixture) and MoO_3 (selected for oxygen insertion since it is a known oxidation catalyst and highly active for $^{16}O/^{18}O$ exchange in $^{16}O_2/^{18}O_2$ mixtures) was found to provide relatively high yields of methanol in comparison with the individual components (*28*, *29*).

QSPR/QSAR Descriptor Based Approach

More recently, a refined approach that exploits the vast amount of catalyst reactivity data available in the literature utilizes sophisticated statistical tools such as principal component analysis, partial least squares, genetic algorithms, and artificial neural networks (*30*) to establish quantitative structure–property or structure–activity relationships (QSPR/QSAR) to predict optimal catalyst structures for a particular reaction (*31–33*). This methodology aims at finding solid catalyst attributes or descriptors that correlate with catalytic activity (*34*, *35*). Finding good and general descriptors for heterogeneous catalysts, however, remains the main challenge of this approach since catalytic behavior does not usually correlate with the bulk structural properties of a catalyst, but rather with the nature of the active sites and their environment (e.g., electronic properties, chemical bonding, bond energies) (*36*). To date, the lack of complete databases with experimental information on catalyst structures, adsorbed species, reaction intermediates, and reaction energetics hinders the ability to obtain suitable descriptors (*36*, *37*).

Recent advances in computing are contributing tremendously to a more fundamental understanding of the catalytic phenomena by providing detailed theoretical information on the electronic properties, chemical bonding, and bond energies associated with the reactants, catalysts, and products. Such information, validated by experimental measurements, is expected to greatly facilitate the discovery of reliable descriptors to explain observed catalytic behavior (*36*). These descriptors could then be used to predict new leads for catalytic materials (*32*).

Scientific (Knowledge-Based) Approach

In this approach, a small number of catalysts is usually studied in depth aimed at understanding how mechanistic and material characteristics affect catalytic performance. To this end, rigorous kinetics, characterization, and theoretical studies are carried out (*13*, *16*, *38*). The insights thus obtained are used to guide a synthesis strategy towards new and improved catalysts (*36*).

Multiscale Hierarchical Approach

It will be shown later that utilizing theoretical electronic, chemical, and energetic data (e.g., descriptors) at the microscale in combination with predicted reactivity data at the mesoscale via microkinetic analysis is one of the most powerful and robust approaches to guide the rational design of heterogeneous catalysts (*39–42*). This approach strikes a balance between a completely combinatorial (rapid acquisition with little fundamental knowledge gained from data on numerous catalysts) and scientific (time consuming in-depth understanding of catalytic phenomena from a few catalysts) experimentation (Figure 5) (*36*, *43–45*). The microkinetic analysis relies on a detailed description of the reaction mechanism that involves a comprehensive sequence of elementary reaction steps including adsorption, reaction, and desorption of reactants, intermediates, and products (*46*, *47*). This additional information on the reaction mechanism can be obtained from kinetics data (*13*, *38*), mechanistic studies (*48–50*), catalyst surface characterization (*51*, *52*) and in situ catalyst performance investigations (*43*, *53–55*). Some of these aspects will also be described in later sections.

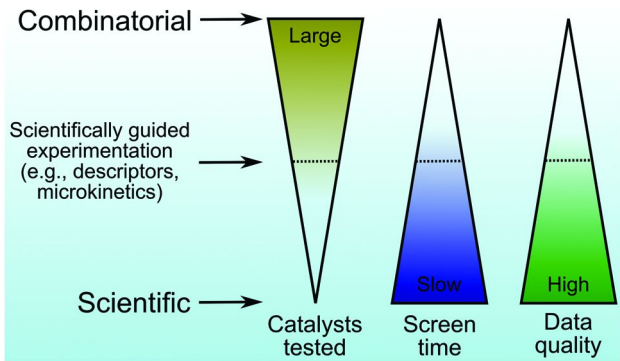

Figure 5. Summary of current approaches to catalyst discovery from a combinatorial to a scientifically guided one. A balance in the number of tested catalysts, speed of screening, and fundamental depth of the data is required for a scientifically guided high-throughput screening of catalysts. With data from references (21) and (36).

Synthesis, Characterization, and Study of Catalytic Reactions

Catalyst Synthesis

Catalyst synthesis is a vital component of catalysis research. Very often, preparing or obtaining catalysts in the laboratory is just the first step towards the preparation of practically viable catalysts for use in an industrial process. As shown in Table 2, industrial catalysts often contain additional components such as modifiers, dopants, selectivity enhancers, and stabilizers that are required to enhance their physical, chemical, and mechanical properties for economical and durable operation in an industrial plant. This section briefly covers various methods for the preparation of bulk and supported catalytic materials. Readers are encouraged to consult the referenced publications for more details about these methods (*2*, *56*–*58*). Detailed information on the preparation of industrial catalysts may also be found elsewhere (*59*–*62*).

Figure 6 presents a summary of the most commonly reported methods for the preparation of bulk and supported catalytic materials, organized by the number of reactant/precursor phases (top) along with examples of materials obtained by each method (bottom) (*56*, *58*, *63*). It is clear that catalyst researchers are equipped with a plethora of methods for the preparation of catalytic materials. Surprisingly, over 80% of the industrial catalysts are prepared by only a few main routes: (co)precipitation and impregnation/coating techniques (*64*). This may be because these methods are simpler, more reproducible, easier to scale-up, and ultimately more economical than others. A literature search on the synthesis/preparation of a range of catalytic materials (Figure 7A) reveals that recent research activity has been mainly focused on carbon-based materials (e.g., activated carbon, carbon nanotubes, graphene), zeolites, mesoporous metal oxides (e.g., silica, aluminosilicate, aluminophosphate), transition metal oxides, and metal phosphides, carbides, and nitrides (metal sulfides were not included, but their results are comparable to those of metal phosphides, carbides, and nitrides combined). As expected, fewer papers have been published on less conventional materials such as those interfacing homogeneous–heterogeneous (e.g., supported ionic liquids) and enzymatic-heterogeneous (e.g., inorganic–organic hybrid materials, supported enzymes) catalysts (Figure 1).

These trends reveal the continuing interest in new methods to produce highly structured catalysts such as carbon-based, zeolitic, and mesoporous materials (*67*). Figure 7B shows that similar trends are also observed on the performance of these materials for applications related to biomass conversion reactions, which will be discussed in a later section.

Carbon-Based Materials

Carbon-based materials have long been recognized as catalyst supports and more recently as catalysts for many reactions. Among all carbons, carbon blacks and activated carbons have been the most widely used (*68*). More

In Novel Materials for Catalysis and Fuels Processing; Bravo-Suárez, J., et al.;
ACS Symposium Series; American Chemical Society: Washington, DC, 2013.

recently, however, interest has grown in carbon nanofibers and cloths (*69*, *70*), nanotubes (*70*), mesostructured carbons (*71*), graphene (*72*), and other graphitic based materials (*73*). These various types of carbons posses different structures and physicochemical properties useful for many applications. They can be prepared in gas, liquid, or solid phase from various carbon precursors (e.g., CO_2, hydrocarbons, polymers, coal, biomass) by any of the following methods: (1) chemical or physical activation or both; (2) catalytic activation of carbon precursors; and (3) carbonization of polymer-based materials (*74*, *75*). Some examples of the preparation methods of carbon materials include:

1) Gas phase conversion. *Carbon black* (soot) can form during pyrolysis of carbon-containing gases by dehydrogenation. Similarly, *pyrolytic carbon* forms at temperatures over 2500 °C by chemical vapor deposition (CVD) of the carbon precursors on a relatively inert substrate, whereas on metallic surfaces (e.g., Fe, Co, Ni) *carbon nanotubes or fibers* are formed (*75*).
2) Liquid phase conversion. In this category thermoplastic polymers (e.g., bituminous coal, PVC: polyvinyl chloride) are treated at high temperatures in a nonreactive medium. *Coke* forms at temperatures below 2000 °C, whereas above this temperature *synthetic graphite* is the resulting product. If the molten phase (formed during carbonization) is subjected to extrusion and orientation, then carbon fibers are obtained (*75*).
3) Solid phase conversion. During the devolatilization of the thermosetting carbon precursor (e.g., low-rank coals, wood, PVDC: polyvinylidene chloride) chars develop porosity. Tuning the conditions to selective gasification can produce *activated carbons or molecular sieves*, whereas *glassy carbon* can also form at high temperatures (*75*).

The aforementioned methods rarely allow for the preparation of carbon materials with uniform pores. To obtain ordered microporous or mesoporous carbon materials, template-based methods are usually employed. In these methods, a carbon precursor/inorganic template composite is prepared (e.g., by introducing the carbon precursor into the pores of the template), then carbonized to produce a carbon/template material from which the carbon material is obtained upon removal of the template (e.g., zeolites, mesoporous silica materials such as MCM-48, SBA-15, etc.) (*74*).

In general, carbons have been recognized to be more resistant to acidic and basic media, aqueous environments, stable at high temperature, relatively inert, and usually cheaper than other supports (*68*). Despite these attractive properties, they have not been used widely as catalysts and/or supports in large-volume industrial processes (Table 2) (*68*). Lately, however, there is a revived interest for using carbon-based materials as catalyst supports in hydrogenation, hydrolysis, hydrogenolysis, and hydrodeoxygenation reactions for the processing of biomass into chemicals and fuels (*76*, *77*).

In Novel Materials for Catalysis and Fuels Processing; Bravo-Suárez, J., et al.;
ACS Symposium Series; American Chemical Society: Washington, DC, 2013.

Table 2. Examples of commercial heterogeneous catalysts (*65*, *66*)

Reactions	*Industrial Catalysts*[a]
Petroleum Refining	
Hydroprocessing *(HDS, HDN, HDO, HDM)*[b]	$CoO(2–5\%)MoO_3(10–20\%)P(0–2\%)/Al_2O_3$; $NiO(2–6\%)MoO_3(6–20\%)P(0–2\%)/Al_2O_3$[c]
Catalytic cracking	Zeolite(30–40%) (e.g., REY, REHY, USY, REUSY)[d] + Matrix(e.g., SiO_2, Al_2O_3, and $SiO_2–Al_2O_3$, clay) + Binder(e.g., aluminum chlorhydrol, peptized alumina, polysilicic acid) + Additives(e.g., P–ZSM-5, Pt, Pd, Sb, Bi, Sn)
Alkylation *Benzene with ethylene*	BF_3/Al_2O_3; MCM-22; Zeolites(10–20%) (e.g., USY, ZSM-5, β-zeolite, dealuminated MOR) + Binders(e.g., halloisite, montmorillonite, or attapulgite)
Catalytic reforming	$Pt(0.30–0.35\%)/\gamma\text{-}Al_2O_3$; balanced $Pt(0.22–0.35\%)–Re(0.22–0.35\%)/\gamma\text{-}Al_2O_3$; skewed $Pt(0.22–0.28\%)–Re(0.42–0.75\%)/\gamma\text{-}Al_2O_3$; $Pt(0.35\%)–Sn(0.30\%)/\gamma\text{-}Al_2O_3$, $Pt(0.3\%)–Ir(0.3\%)/\gamma\text{-}Al_2O_3$
Chemical Processing	
Polymerization *Polyolefin*	$TiCl_4/MgCl_2$; CrO_x(1% Cr)/SiO_2 + Modifiers(TiO_2 (<4% Ti), ZrO_2, or Al_2O_3 co-gelled with SiO_2; fluorides) + Co-catalysts($B/SiO_2\text{-}TiO_2$)
(Amm)oxidation, oxychlorination	
n-Butane to maleic anhydride	10–20% active phase(40% V_2O_5:60%P_2O_5) + Support(e.g., $\alpha\text{-}Al_2O_3$, fused silica)
Ethylene to ethylene oxide	$Ag(10–15\%)/\alpha\text{-}Al_2O_3$ + Promoters(e.g., BaO=1–2%, Cs_2O=0.005–0.05%)
Propene to acrolein/ acrylonitrile	Bi_2MoO_6 + Support(e.g., SiO_2) + Promoters(e.g., $Me(II)_8$=Ni, Co, Mn, or Mg; $Me(III)_3$=Fe, Cr, or Al)
Ethylene to vinyl chloride	$CuCl_2$(10%) + Support(e.g., Al_2O_3, $SiO_2–Al_2O_3$, charcoal) + Additives(e.g., KCl)
Ammonia synthesis	Fe_3O_4 + Promoters(Al_2O_3=2.5–3.0%, K_2O=0.4–0.6%, CaO=2.0–2.5%, MgO<0.5%); $Fe_3O_4–CoO_x$(10–20%) + Promoters(e.g., K_2O); Ru(4%)–Ba(2%)–(K or Cs)(12%) + Support(e.g., carbon, MgO)
Methanol synthesis	$CuO(55\%)–ZnO(25\%)–Al_2O_3(8\%)$
Nitrobenzene reduction	Cu chromite; (CuO, NiO)/Kieselguhr; Raney Cu; NiS_x/Al_2O_3
Phenol hydrogenation	$CuO–ZnO$; $Pd(1\%)/CaO/Al_2O_3$

Continued on next page.

In Novel Materials for Catalysis and Fuels Processing; Bravo-Suárez, J., et al.;
ACS Symposium Series; American Chemical Society: Washington, DC, 2013.

Table 2. (Continued). Examples of commercial heterogeneous catalysts (*65*, *66*)

Reactions	*Industrial Catalysts*[a]
Lower alkanes dehydrogenation	Cr_2O_3/Al_2O_3; $Pt(0.3\%)/Al_2O_3$ + Promoters(e.g., Zn, Cu)
Alcohols dehydrogenation	Cu chromite; CuO/Al_2O_3; ZnO; ZnO/CuO; $Pt(0.05\%)/Al_2O_3$
Mobile Emission Control	
Three-way catalyst	Pt(0.9–3.1 g)–Pd(0–3.1 g)–Rh(0.15-0.5 g)/(Ba, Ca, Mg, Zr, Ce or La oxides)–Al_2O_3/Cordierite($2MgO{\cdot}2Al_2O_3{\cdot}5SiO_2$) monolith

[a] % content in wt %. [b] HDS=hydrodesulfurization, HDN=hydrodenitrogenation, HDO=hydrodeoxygenation, HDM=hydrodemetalization. [c] Impurities of SO_4 (1 wt %), Na_2O (0.06 wt %), and Fe_2O_3 (0.6 wt %). Oxides are converted to sulphides, which are the catalytically active phase . [d] REY=rare-earth metal (e.g., Ce, La, Nd) Y-zeolite, REHY=rare-earth exchanged, hydrogen Y-zeolite, USY=ultra stable Y-zeolite, REUSY=rare-earth exchanged ultra-stable hydrogen Y-zeolite. Rare earth exchanged usually in chloride form.

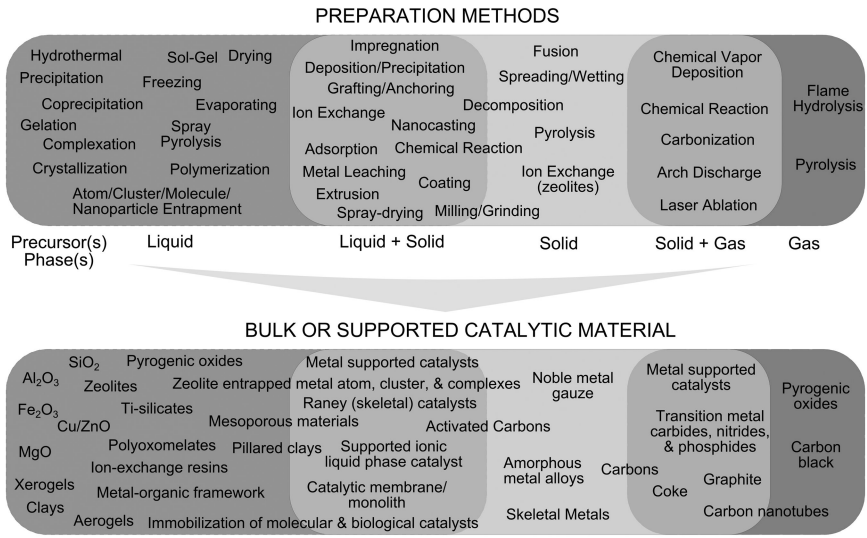

Figure 6. Summary of preparation methods for various catalytic materials.

In Novel Materials for Catalysis and Fuels Processing; Bravo-Suárez, J., et al.;
ACS Symposium Series; American Chemical Society: Washington, DC, 2013.

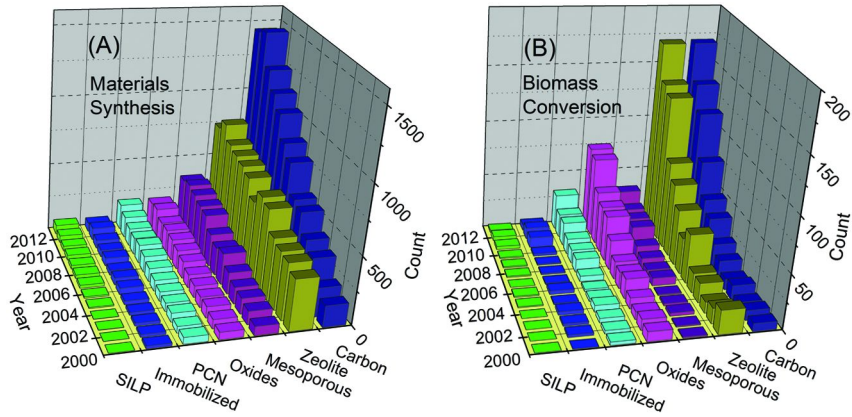

Figure 7. Number of papers published between 2000–2012 related to: (A) synthesis of various catalytic materials; and B) the same materials applied to biomass conversion reactions. Source: Web of Science®, accessed on Feb. 1 2013. SILP: supported ionic liquid phase; PCN: metal phosphides, carbides, and nitrides; Oxides: transition metal oxides.

Zeolitic and Mesoporous Materials

Porous materials are usually classified according to their pore size as microporous (<2 nm), mesoporous (2~50 nm), and macroporous (>50 nm) (*78*). Zeolites are defined as crystalline aluminosilicates with a three-dimensional framework structure containing pores of molecular dimensions (0.3–2 nm). They include, for example, small pore zeolites (0.30–0.45 nm) such as Zeolite A, medium pore zeolites (0.45–0.60 nm) such as ZSM-5, large pore zeolites (0.60–0.8 nm) such as Zeolites X and Y, and extra-large pore zeolites such as UTD-1 (0.7–1 nm) (*79*, *80*). Ordered mesoporous materials such as MCM-41, MCM-48, SBA-15, SBA-16, and KIT-6 also have uniform and ordered pores at the nanometer scale >2 nm, but unlike zeolites they are amorphous and lack order at the atomic level (*2*, *80–83*). Other mesoporous materials with amorphous structure such as TUD-1 have also been reported (*84*, *85*).

Industrial aluminosilicate zeolites are mainly prepared by hydrothermal synthesis. During this synthesis, a mixture of silicon and aluminum compounds, alkali metal cations, water, and organic molecules (i.e., template or structure-directing agent, SDA) converts into a zeolite or zeolite precursor usually at high pH, temperatures of 100–200 °C, and (autogenous) high pressure in a sealed container (or autoclave). In the case where an SDA is employed, the regular channels in zeolite structure are generated upon SDA removal via chemical treatments, extraction, or treatment at high temperature in air. The synthesis of zeolites depends on many variables including the molar composition and nature of reactants, presence of a mineralizing agent (e.g., OH^-, F^-), pressure, and time (*80*, *81*, *86*). In this manner, over a hundred different framework structures of zeolites have been prepared thus far, of which several are produced

In Novel Materials for Catalysis and Fuels Processing; Bravo-Suárez, J., et al.;
ACS Symposium Series; American Chemical Society: Washington, DC, 2013.

at large scale for industrial operations in petroleum refining (Table 2). Other zeolitic and mesoporous materials have been prepared by various methods including variations of the microporous-type preparations. For example, ordered mesoporous materials have been formed by incorporation of ionic or nonionic surfactants (e.g., quaternary alkylammonium ions, polyethylene oxides) as SDAs in microporous-type preparations (*2*, *82*, *83*). Many more variations of the hydrothermal method exist including the use of organic solvents (i.e., solvothermal synthesis) or ionic liquids as the solvent (ionothermal synthesis) (*2*, *81*).

From a fundamental point of view, the continued interest in the synthesis of zeolitic and mesoporous materials is driven by the possibility of preparing materials with controlled surface structure (e.g., crystal shape and size, uniform pore diameter) and chemical reactivity (e.g., nature and number of active sites) at the nanoscale. These can provide new catalytic materials such as novel zeolites (*87*, *88*), mesoporous materials (*87*, *88*), metal organic frameworks (MOFs) (*89*), zeolitic imidazolate frameworks (ZIFs) (*90*), and materials for emerging applications for use as electrode materials, biomaterials, controlled drug delivery devices, and catalysts for fine chemical production (*88*, *91*). From a practical point of view, the rewards are immense if more active, selective, and stable zeolites and mesoporous materials are obtained since they could have a significant impact in the economics of large volume processes such as petroleum refining (Tables 1 and 2), methanol-to-olefins, and methanol-to-gasoline (*92*, *93*).

Bulk and Supported Transition Metal Oxides

Metal oxides are ubiquitous materials which are found in many forms (e.g., single crystal, polycrystalline samples). They cover a wide range of elements in the periodic table ranging from alkali metals (e.g., K) and alkaline earth metals (e.g., Mg) to transition metals (e.g., V, Mo, W, Cu), post-transition metals (e.g. Al), and metalloids (e.g., Si). Oxides of alkaline earth metals, post-transition metals, and metalloids such as MgO, Al_2O_3, SiO_2 are usually employed as high surface area catalyst support materials. Certain properties of transition metal oxides (TMOs) such as crystal and electronic structure, stoichiometry and composition, redox properties, acid–base character, and cation valence make them attractive for use as catalysts as well as supports, additives, or promoters for a variety of chemical reactions (Table 2) (*94–97*). TMOs can be prepared as bulk or supported catalysts and many of their preparation methods are presented in Figure 6.

Bulk TMOs are usually prepared by (co)precipitation, sol–gel formation, complexation, grinding, fusion of a metal oxide mixture, and spray pyrolysis. By far, the most common method of preparation of TMOs is (co)precipitation, in which a precipitating agent (e.g., NaOH) is added to a solution containing the precursor compounds (e.g., metal nitrates) usually at a fixed pH. The resulting precipitate is filtered, washed, and treated at high temperatures to produce (mixed) metal oxides (*2*, *94*, *95*). The sol–gel method, also related to coprecipitation, is also commonly used for the preparation of TMOs. In this method, a colloidal dispersion is formed containing the catalyst metal components, followed by gel

In Novel Materials for Catalysis and Fuels Processing; Bravo-Suárez, J., et al.;
ACS Symposium Series; American Chemical Society: Washington, DC, 2013.

formation induced by changes in pH, cation concentration, or temperature. The gel is treated at high temperatures to form the (mixed) metal oxides (*2*, *94*, *95*, *98*). For the preparation of supported TMOs, impregnation is perhaps the most widely used method for industrial catalysts (*64*, *95*). When a dry support is contacted with the impregnating solution containing the metal precursor whose volume is in slight excess of the total pore volume of the support, the method is called "dry or incipient wetness impregnation" (the solution fills the pores via capillary action). When the pores of the support are filled with the solvent prior to immersing it in the impregnating solution, the method is called "wet impregnation" (the precursor phase transfers to the pores via diffusion processes). The solid is treated at high temperatures, usually in air, to remove the solvent by drying, forming the supported TMO (*2*, *95*, *99*). Other methods for the preparation of supported TMOs include ion-exchange (*99*), grafting (*100*), and deposition–precipitation (*2*).

Transition metal oxides are versatile materials due to the wide range of properties arising from the almost unlimited number of combinations of metals that can be present in a mixed metal oxide. They are widely used as catalysts for numerous applications ranging from fuels to chemical processing to environmental protection (Table 2). Some known catalytic applications of metal oxides include selective oxidation of hydrocarbons (*94–96*, *101*), methane oxidation (*96*, *101*), oxidative dehydrogenation of alkanes (*95*, *96*), metathesis of olefins (*94–96*), combustion of volatile organic compounds (*96*), CO_x hydrogenation (*94–96*), selective catalytic reduction (*94*, *96*, *101*), and base catalysis (*95*, *102*).

Metal Oxide Supported Gold Catalysts

Gold catalysts are perhaps the most remarkable example of how synthetic methods enable precise control of particle size, structure, and composition that can affect catalyst activity and selectivity (*103*, *104*). Since bulk gold is largely unreactive, supported gold catalysts were regarded for a long time as poor catalysts (*105–107*). It was not until the work of Haruta (*108*, *109*) (Figure 8) that gold nanoparticles (2–5 nm) supported on metal oxides were recognized to be active and selective for a variety of reactions. Many more discoveries followed including the development of gold catalysts for liquid-phase reactions (*110*). These advances have spurred a great deal of research in the last decade in novel synthesis, characterization, and applications of gold catalysts (Figure 8) (*104*, *111*, *112*) and in nanotechnology applications to catalysis (*113*, *114*).

Supported gold catalysts have been used for many reactions such as CO oxidation (e.g., Au/Support; support=Fe_2O_3, Co_3O_4, NiO, Al_2O_3) (*108*, *109*), selective oxidation of propylene to propylene oxide (e.g., Au/TiO_2, Au/Ti–SiO_2) (*115*, *116*), propane to propylene (Au/TiO_2) (*117*, *118*), acetone, isopropanol (Au/TS-1) (*117*, *119*), and propylene oxide (Au/TiO_2 + Au/TS-1) (*118*), the water-gas shift (Au/TiO_2) (*120*), hydrogen peroxide synthesis from H_2 and O_2 (Au–Pd/Al_2O_3,) (*121*), and biomass conversion (Au/Support; support=C, Al_2O_3, ZrO_2, TiO_2) (*104*), among others (*103*, *104*, *111*, *112*).

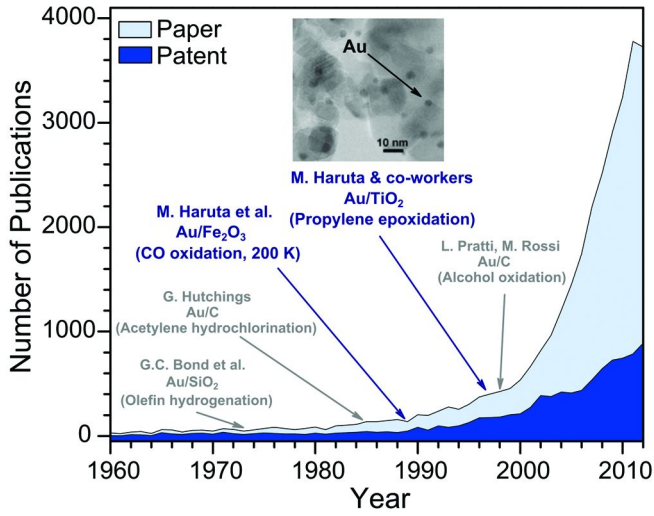

Figure 8. Major breakthroughs in heterogeneous catalysis with supported gold catalysts. Source: SciFinder®, accessed Feb. 20, 2013. Including references (105), (106), (109), (110), and (115).

Immobilized Catalysts

Immobilized catalysts (ICs) can be considered as homogeneous catalysts attached to a solid support. They are also called anchored, hybrid, or heterogenized catalysts. The main objective of preparing ICs is to obtain materials with properties resembling those of heterogeneous catalysts and homogeneous or enzymatic catalysts (heterogenous–homogeneous and heterogenous–enzymatic boundaries in Figure 1). These materials are, in general, composed of well-defined catalytically active phases (e.g., usually a metal with organic ligands) that are molecularly dispersed on the surface of the solid support. These characteristics are required for high activity, high selectivity, good reproducibility (as in homogeneous catalysis), stability, and ease of separation (as in heterogeneous catalysis). Because of the uniformity in structure and high dispersion (i.e., isolation) of the active phase, ICs are also advantageous for precise mechanistic studies aimed at establishing relationships between catalyst structure and performance (*2*, *122–124*). It is envisaged that ICs will follow mechanisms similar to homogeneous catalysts and offer advantages of high activity and selectivity at milder conditions, while being easy to handle like heterogeneous catalysts.

Many solid materials have been used as IC supports. They can be broadly classified as: (1) inorganic oxides (e.g, SiO_2, Al_2O_3, MgO, TiO_2, zeolites, mesostructured metal oxides), (2) carbonaceous materials (e.g., activated carbon, charcoal, carbon nanotubes, graphene), and (3) functionalized organopolymers (e.g., resins, polystyrene, dendrimers). Because of the higher surface area, shape and thermal stability, inorganic oxides are usually the preferred supports for ICs (*123*).

A large number of methods have been developed to prepare ICs (i.e., support–complex(ligand+metal)). The mechanism of immobilization is generally one of the following: (1) weak support–complex interactions (i.e., adsorption via weak dipolar and van der Waals interactions; hydrogen bonding), (2) strong support–complex interactions (i.e., ionic (electrostatic) interactions; covalent binding (σ-bonding); π-bonding interactions), or (3) "soft" immobilization (e.g., entrapment, encapsulation) (*123*, *124*).

Of all the mechanisms of immobilization, (support–ligand) covalent binding based strategies are the most frequently used (*122*, *124*). These strategies include:

1) Grafting methods: by direct linking of the metal complex or the ligand to the solid. In the latter case, the metal is added to the solid–ligand system via complexation.
2) Solid phase synthesis: by synthesis of the ligand onto the support followed by metal complexation.
3) Sol–gel processes: by synthesis of the support using precursors containing the metal complex of the ligand (followed by metal complexation).

Other reported strategies for the preparation of ICs are: (support–ligand) electrostatic interactions such as ion exchange (e.g., anionic metal complexes on layered double hydroxides) and soft immobilization strategies such as entrapment (i.e., building up support cages such as zeolites or a polymer network around a preformed catalytic metal complex) and encapsulation (i.e., opposite to entrapment, building up the complex inside of a preformed support, e.g., Co(salen) complexes inside cages of SBA-16 mesostructured support), among many others (*2*, *122–124*). These strategies can be used to heterogenize not only homogeneous catalysts but also enzymatic catalysts (biocatalysts) (*125*).

Because of the vast number of support–ligands–metals combinations, immobilized catalysts can be applied to almost any type of reaction. They have been mainly studied for synthesis of fine chemicals, but more areas are being explored as novel catalysts with higher activities and selectivities in chemicals and fuel processing emerge. Some examples of ICs applications include: hydrogenation (e.g., selective aldehydes hydrogenation on SiO_2–ferrocene complex), oxidation (e.g., Juliá–Colonna asymmetric epoxidation on SiO_2–polyleucine complex), C–C coupling (e.g., allyl acetates with amines on Polystyrene polymer–$Pd(PPh_3)_4$), hydroformylation (e.g., methanol carbonylation on Polyvinyl pyridine resin–Rh complex), olefin isomerization (e.g., geraniol to citronellal on Polystyrene resin–Rh(I) complex), and biomass conversion (e.g., diesterification of succinic acid on starbon–sulfonic acid) (*122*, *126*).

Metal Phosphides, Carbides, and Nitrides

Transition metal phosphides, carbides, and nitrides (e.g., M_2N, M_2C, MP; M=Mo, W) are a family of interesting compounds combining the chemical properties of metals and the physical properties of ceramics (*127*). The most

In Novel Materials for Catalysis and Fuels Processing; Bravo-Suárez, J., et al.;
ACS Symposium Series; American Chemical Society: Washington, DC, 2013.

salient feature of these materials is, perhaps, the apparent platinum-like properties of metal carbides and nitrides (*127–129*) and excellent catalytic properties of metal phosphides in hydrogen transfer reactions (*127*, *129*, *130*). These materials (e.g., unsupported and supported) can be prepared by different methods, of which the most widely used involves the high temperature reduction of the transition metal oxide(s) (or phosphate in the case of phosphides) with H_2, CH_4/H_2, and NH_3 to produce metal phosphides, carbides, and nitrides, respectively (*127*, *129–131*). The main research work with these materials has been focused on hydrodesulfurization (HDS) and hydrodenitrogenation (HDN) applications for removal of sulfur and nitrogen containing impurities present in crude oil (*127*, *129*, *130*, *132–134*). More recently, there has been a renewed interest in applications of metal carbide, phosphide, and nitride catalysts as electrodes for low-temperature fuel cells (*135*) and biomass conversion reactions of syngas to higher alcohols (*136*) and hydrodeoxygenation (HDO) of bio-oil model compounds (*130*, *137–139*).

Supported Ionic Liquid Phase Materials

Ionic liquids (IL) are salts that melt below 100–150 °C to yield a liquid composed of cations and anions. The cations are generally large, asymmetric, organic ammonium or phosphonium heterocyclic compounds (e.g., 1,3-dialkylimidazolium cations), whereas the anions are usually inorganic halide compounds including tetrafluoroborate (BF_4^-), tetrachloroaluminate ($AlCl_4^-$), and hexafluorophosphate (PF_6^-). Specific properties of the ionic liquids such as acid–base, electrochemical, viscosity, and melting point can be tuned by proper selection of cation–anion combinations (*140–142*). Supported ionic liquid phase (SILP) catalysts are generally composed of: (1) a porous support (e.g., SiO_2, Al_2O_3), (2) the IL (a thin film immobilized on the support surface), and (3) the catalytic component (e.g., metal complexes or nanoparticles dissolved in the non-volatile, inert, free IL). SILP materials are commonly prepared by:

1) Impregnation of the support with the IL phase containing the catalytic component or an IL which is in itself catalytically active (in this case the solid material is usually referred to as supported ionic liquid catalyst (SILC)).
2) Grafting (or anchoring) of an IL fragment, usually the cation, to the support surface, followed by coordination of the catalytic component to the IL anion fragment.
3) Physical pore confinement of the IL/catalytic component mixture by in situ synthesis of the solid support via the sol-gel method (*143–145*).

The literature on SILP catalysts is relatively recent (Figure 7), and more applications are now being increasingly reported based on the several potential advantages as follows: (1) SILPs contain only a fraction of the often expensive ionic phase; (2) in comparison with the unsupported IL-phase complexes, the catalytic phase dispersion in SILPs is higher; (3) the resulting solid material

In Novel Materials for Catalysis and Fuels Processing; Bravo-Suárez, J., et al.;
ACS Symposium Series; American Chemical Society: Washington, DC, 2013.

has all the advantages of heterogeneous catalysts while maintaining the homogeneous-catalyst-like behavior in the active species (i.e., metal complex/IL); and (4) SIPLs are advantageous for use in gas-phase continuous processes in fixed bed reactors (*143*, *144*, *146*). Some recent applications of SILPs catalysts include: (1) hydroformylation (Rh complex/IL/support, support = SiO_2, Al_2O_3, ZrO_2, MCM-41) (*143*, *144*, *146*), hydrogenation (Rh complex/IL/support, support = SiO_2, filter membrane, polymeric material, carbon; Pd nanoparticles/IL/support, support = molecular sieve, sepiolite, SiO_2; Rh nanoparticles/IL/SiO_2) (*143*, *144*, *146*), hydroammination (metal complex/IL/support, metal = Rh, Pd, Cu, Zn; support = chromosorb P) (*143*, *146*), Heck coupling (Pd complex/IL/SiO_2) (*143*), Suzuki cross-coupling (Pd complex/IL/Al–MCM-41) (*143*), methanol carbonylation (Rh complex/IL/SiO_2) (*144*), Mukaiyama-aldol reaction (Cu complex/IL/SiO_2) (*144*), oxidation of alcohols (Ru nanoparticles/IL/MgO) (*144*), and asymmetric epoxidation of olefins (Mn(salen)/IL/MCM-48) (*144*).

Catalyst Characterization

As previously indicated, catalyst characterization is a vital and essential aspect of catalysis research. Its main objectives are:

1) To study the physicochemical properties of a catalyst (e.g., structure, morphology, composition, texture) in the bulk and the surface.
2) To investigate catalyst surface reactivity including (a) adsorption of reactants onto the catalyst surface, (b) formation of reaction intermediates and reaction on the surface of the catalyst, and (c) desorption of products from the catalyst surface (*147*, *148*) (Figure 2).

From a fundamental point of view, catalyst characterization is aimed at understanding the nature of the catalytically active sites and to elucidate the corresponding reaction mechanism (*16*, *37*).

There are many characterization techniques that can be used for the measurement of catalyst properties such as surface area and porosity, particle size and dispersion, structure and morphology, mechanical properties, bulk and surface chemical composition, valence states, and acidity/basicity. They include adsorption, spectroscopic, microscopic, and diffraction/scattering techniques (*58*).

In spite of the large variety of techniques available for catalyst characterization (*149*), conventional (ex situ) spectroscopic measurements usually miss important features of a catalytic cycle (*150*). Capturing information associated with the mechanistic steps during a catalyzed reaction remains a formidable challenge especially when considering the complexity of functional catalysts composed of metal(s) and/or oxide(s) on a support and in the presence of promoters/additives (Table 2). To overcome these difficulties, two main characterization approaches have been used to acquire such information on active sites and associated reaction mechanisms:

In Novel Materials for Catalysis and Fuels Processing; Bravo-Suárez, J., et al.;
ACS Symposium Series; American Chemical Society: Washington, DC, 2013.

1) A surface science approach, which employs well-defined model compounds (e.g., single crystals, particles) (*51*, *151*, *152*).
2) In situ characterization approach, which monitors catalysts as they work under reactions conditions (*37*, *153*, *154*).

Surface Science

Surface science primarily involves the use of well-defined model catalytic surfaces to avoid the complexities of practical catalysts while providing detailed information at the atomic scale on the geometric and electronic structure of these systems (*51*). Surface science techniques are proven to be useful to identify structural and chemical factors that influence catalyst activity and selectivity. On supported metal catalysts, for example, these include (*48*, *51*, *155*, *156*):

1) Metal particle size and surface structure.
2) Presence of promoters.
3) Mobility of metal particles (restructuring) and adsorbates (surface diffusion).
4) Selective site blocking (e.g., poisons, promoters, carbon deposits).
5) Activity of support (bifunctional catalysis).
6) Metal-support interface sites.

As shown in Figure 9, each of these factors can influence any step in the catalytic sequence: reactant(s) adsorption, intermediate(s) reaction, and product(s) desorption.

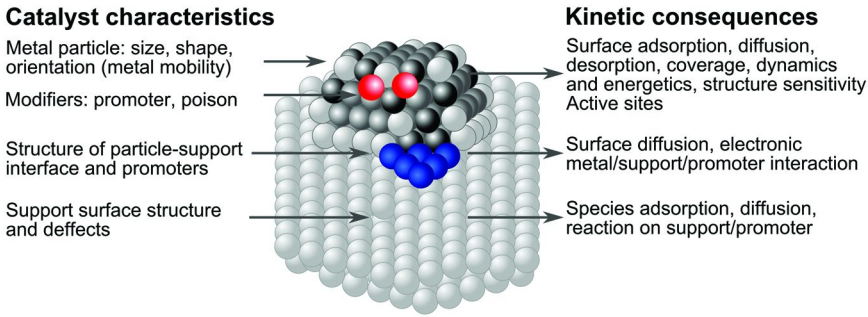

Figure 9. Supported metal catalyst characteristics that affect catalytic activity and selectivity. With data from references (51) and (155).

Although the application of surface science techniques to study model surfaces has provided much needed insight into catalytic reaction mechanisms, this information often cannot be extrapolated to real catalysts under reaction conditions. The reasons for this are inherent to the need to operate most surface

In Novel Materials for Catalysis and Fuels Processing; Bravo-Suárez, J., et al.;
ACS Symposium Series; American Chemical Society: Washington, DC, 2013.

science techniques with model catalysts and ultra-high vacuum conditions, giving rise to the so-called materials and pressure gaps of heterogeneous catalysis.

High Pressure Surface Science Approach

One of the approaches to reduce this materials–pressure gap in traditional surface science characterization has been the development of techniques that can operate at high pressures (> 0.1 Pa) with model surfaces and/or monodispersed metal nanoparticles deposited as a two-dimensional film (*157–162*). These new techniques, such as high pressure scanning tunneling microscopy (HP–STM), have allowed, for example, the observation of how adsorbate molecules (e.g., 20 kPa CO on Pt(111)) arrange themselves in an orderly fashion on the metal surface and induce its reconstruction, something not seen during low pressure (<0.1 Pa) experiments (*163*). Similarly, high pressure sum frequency generation (HP–SFG) vibrational spectroscopy has enabled the study of reaction intermediates. In particular, it has allowed the discrimination of reaction intermediates from spectator species (*164*). For example, by means of HP–SFG and adsorbate isotopic labeling during ethylene hydrogenation to ethane (13 kPa H_2, 4.7 kPa C_2H_4) on Pt(111), it has been shown that π-bonded ethylene is a reaction intermediate for the formation of ethane, whereas adsorbed ethylidyne and di-σ ethylene are spectators, which covered the majority (96%) of the Pt surface sites (*165*).

Interrogative Kinetics Approach

Another strategy to overcome the materials–pressure gap in surface science techniques is the so-called interrogative kinetics approach (*166*, *167*). This methodology consists of a transient response (pulse) technique applied in a temporal analysis of products (TAP) reactor. The TAP reactor mainly consists of two zones, the reaction zone where high-speed pulse valves, a pulse valve manifold, and a microreactor are located and the analysis zone, separated from the microreactor by a slide valve, at high vacuum conditions (10^{-9} mbar) where a quadrupole mass spectrometer is located to monitor the gases exiting the microreactor. The TAP reactor can be operated with pulses of different reactants at sub-millisecond time resolution, on model surfaces and practical catalysts, at pressures of 0.1 Pa and higher. This set of conditions puts the TAP reactor at the boundaries between surface science techniques and traditional steady-state flow techniques, allowing the acquisition of fundamental information of fast kinetic events while operating catalysts at more realistic reaction conditions (*166–169*).

In Situ Characterization

Characterization of catalysts in their working environment, namely, in situ under reaction conditions, can provide long sought information to elucidate

reaction mechanisms, active catalyst surfaces, structure of stable intermediates, and dynamics of reactive species with the catalyst (Figure 2) (*37*, *101*, *153*, *154*, *170*). Some commonly available adsorption, spectroscopic, microscopic, and diffraction/scattering techniques for in situ characterization of catalysts during synthesis and testing are presented in Figure 10. These techniques can be used for characterization of catalysts with reactants in different phases, although the bulk of the literature concentrates on gas-solid catalyzed reactions because they are easier to implement than liquid-solid reactions and the resulting data are relatively simpler to analyze. Only recently has there been a renewed interest for applying spectroscopic characterization techniques to liquid-solid and gas-liquid-solid catalyzed reactions (*171–175*) because of their relevance in fine chemistry and in biomass conversion (*55*).

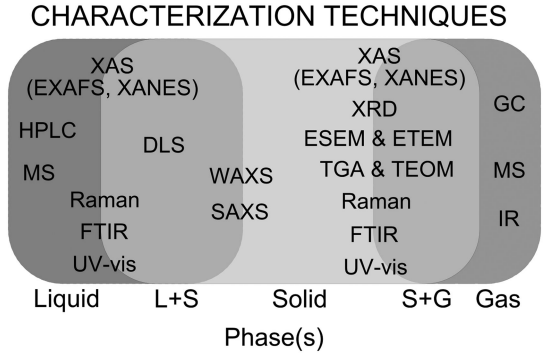

Figure 10. Commonly used in situ characterization techniques during catalyst preparation and testing. XAS: X-ray absorption spectroscopy; EXAFS: extended X-ray absorption fine structure; XANES: X-ray absorption near edge spectroscopy; HPLC: high-performance liquid chromatography; DLS: dynamic light scattering; MS: mass spectrometry; Raman: Raman spectroscopy; FTIR: Fourier transform infrared spectroscopy; UV–vis: ultraviolet visible spectroscopy; WAXS: wide angle X-ray scattering; SAXS: small angle X-ray scattering; XRD: X-ray diffraction; ESEM: environmental scanning electron microscopy; ETEM: environmental transmission electron microscopy; TGA: thermogravimetric analysis; TEOM: tapered element oscillating microbalance; GC: gas chromatography.

These in situ techniques, however, often lack the time and space resolutions of surface science techniques required for monitoring catalytic events (e.g., elementary steps, reaction cycles, surface restructuring), which are usually in the 1×10^{-8}–1×10^{-15} s and 1×10^{-5}–1×10^{-13} m range (*20*, *154*). As shown in Figure 11, a few in situ techniques such as infrared and Raman spectroscopies are used for surface characterization, whereas other techniques such as XRD, EXAFS, and UV–vis characterize mainly the bulk properties of the catalyst. Microscopic techniques, on the other hand, lie at the boundary of surface and bulk characterization methods (Figure 11) (*147*, *148*, *176*).

In Novel Materials for Catalysis and Fuels Processing; Bravo-Suárez, J., et al.;
ACS Symposium Series; American Chemical Society: Washington, DC, 2013.

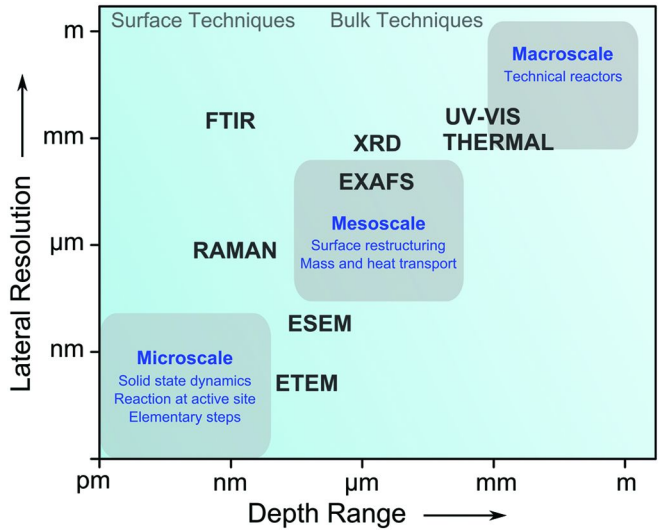

Figure 11. Characteristics of some commonly used in situ characterization techniques. With data from references (147), (148), and (176).

One approach to overcome these time and space resolution limitations is to design clever experiments that can provide information of these catalytic events (*113*). For example, in situ experiments using fluorescence and optical microscopies have demonstrated the possibility of actually seeing and monitoring the overall turnover of a catalytic cycle on a single mixed metal hydroxide catalyst crystallite (*177*), on a ZSM-5 zeolite crystal (*178*), and on a single metal gold nanoparticle (*179*, *180*), and the diffusion dynamics of single molecules in the pores of a mesoporous catalyst structure (*181*). These reports have spurred interest in the development of microscopic, optical, and spectroscopic techniques for imaging catalytic phenomena from the micro-, to meso-, and up to the macroscopic scale (Figure 3) (*182–184*).

A different approach is to combine several in situ characterization techniques that can monitor complementary aspects of the catalyst and reaction intermediates, aimed at acquiring a full picture of the catalyzed reaction by combining complementary pieces of information from different techniques (Figure 12) (*183*, *185*, *186*). Another powerful methodology to investigate catalyst active sites, reaction intermediates, and kinetic parameters of elementary steps is the combination of in situ spectroscopic characterization of catalysts and adsorbed species with rigorous kinetic studies (*187–191*) including steady-state isotopic transient kinetic analysis (SSITKA) (*192*, *193*) and time-resolved methodologies (*194–196*).

In Novel Materials for Catalysis and Fuels Processing; Bravo-Suárez, J., et al.;
ACS Symposium Series; American Chemical Society: Washington, DC, 2013.

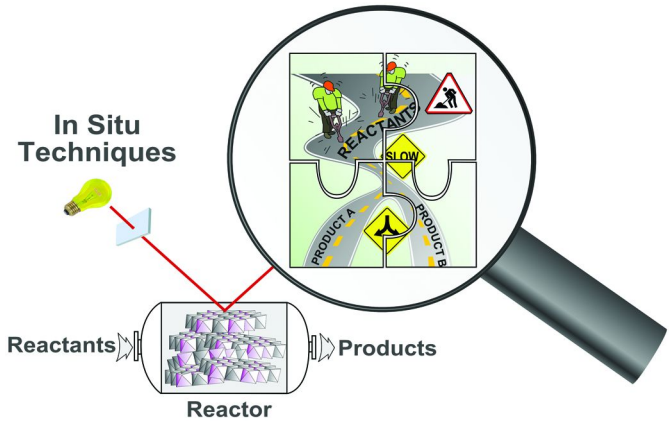

Figure 12. In situ characterization techniques during a catalytic reaction to elucidate catalyst function.

Reaction Kinetics

Empirical and Global Rate Kinetics

Over the past century, the kinetic approach to heterogeneous catalysis has seen a significant evolution from a rate equation-based to a rate constant-based approach. Early work focused on fitting experimental data to empirical rate laws, followed, in the mid-20th century, by fitting to rate equations based on hypothesized mechanisms (e.g., Langmuir–Hinshelwood kinetics, rate determining step assumption, etc.). This approach is still practiced today and provides rate equations that are of practical use for chemical reactor analysis, design, and optimization (*16*, *197*, *198*). The models (and their rate constants) derived in this fitting procedure attempt to explain the data on a fundamental basis (top-bottom approach, Figure 3), but provide little insights into the reaction mechanism, at least in the absence of additional in situ characterization, isotopic labeling, and theoretical studies.

Microkinetics

Within the past two decades, a different approach termed microkinetic modeling has emerged in which rate constants for elementary steps in the catalytic cycle are derived from molecular-level information of the reactants, products, and reactive intermediates on the catalyst surface (bottom-up approach, Figure 3) (*43*, *46*, *47*, *199*). By numerically solving all equations of all the elementary steps in combination with a reactor model (e.g., PFR, CSTR) one can obtain predictions of fractional coverages of surface species, reactant conversion, product yields and selectivities, and relative reaction rates. This methodology has cleverly brought

together the micro- and mesoscopic worlds of heterogeneous catalysis serving as a bridge for surface reactions on model catalysts (e.g., surface science experiments) and reactor performance on functional catalysts (Figure 13) (*40*, *200*). This bottom-up microkinetic approach to kinetic modeling has been by far one of the most recent significant advances in heterogeneous catalysis. From a fundamental point of view, microkinetic models are more useful and robust because most parameters have a physical meaning. Therefore, it is possible to track down relevant aspects of a catalytic reaction to individual steps in the catalytic cycle, all without the need for a priori assumptions of a rate determining step (RDS), most abundant reaction intermediates (MARI), and/or partial equilibrium conditions typically required in classical kinetic analyses (*38*, *201*, *202*). Additionally, from a practical point of view, the microkinetic model is generally superior to global rate equations because it can predict data over a wider range of experimental conditions (*46*, *203*) and be used for reactor optimization (*204*).

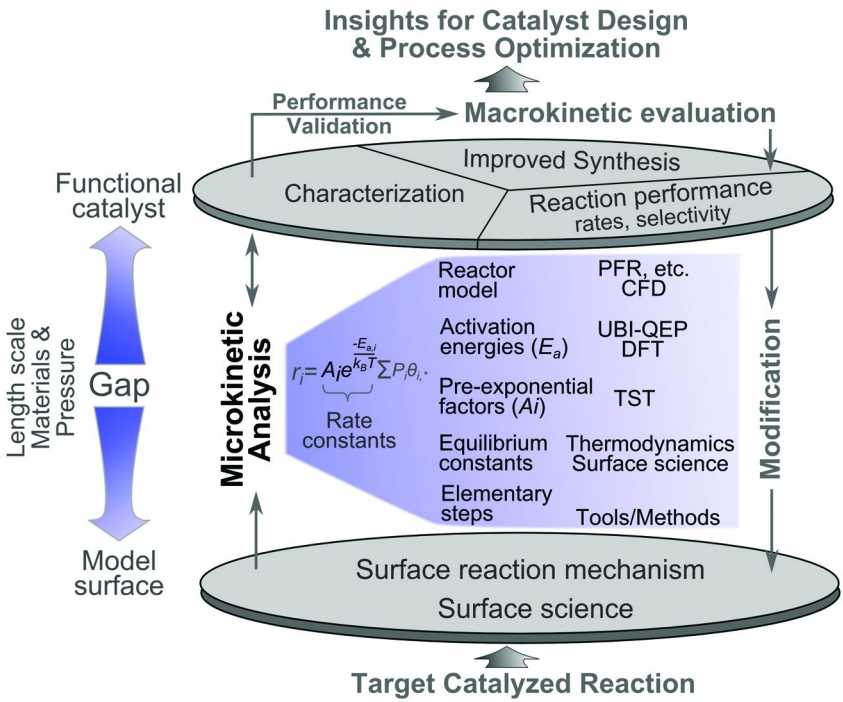

Figure 13. Overview of microkinetic analysis and its role in catalyst and process development. (see color insert)

In Novel Materials for Catalysis and Fuels Processing; Bravo-Suárez, J., et al.;
ACS Symposium Series; American Chemical Society: Washington, DC, 2013.

The formulation of a microkinetic model requires the postulation of a detailed reaction mechanism, including the active site, all potential elementary steps (e.g., adsorption, reaction, and desorption of reactants, intermediates, and products), and associated parameters (e.g., pre-exponential factors, activation energies, sticking coefficients) (Figure 13). Information on active site and elementary steps is often gathered from experimental studies (e.g., surface science, temperature programmed surface reactions) and in situ characterization, whereas equilibrium constants, pre-exponential factors, and activation energies for all elementary steps in the reaction mechanism are estimated from various sources including experimental measurements (e.g., heats of chemisorption), thermodynamics, transition-state theory (TST), bond-order conservation (i.e., unity bond index-quadratic exponential potential, UBI-QEP) method, and density functional theory (DFT) (*40*, *43*, *46*, *47*, *200*, *205*) (Figure 13).

Multiscale Modeling and Microkinetics

The greatest strength of microkinetic models resides in their ability to describe elementary processes occurring in a catalytic cycle; however, this aspect is also its main drawback since estimation of parameters from experimental data for the usually dozens to hundreds of elementary steps is not always available and theoretical DFT calculations, even for a single elementary step, are computationally demanding. During the last decade, microkinetics has seen a renaissance mainly fueled by (1) advances in computational power and theoretical methods that can simulate catalytic phenomena at various time and length scales (Figure 14); and (2) more recently, by the development of methods to estimate parameters of elementary reaction steps in a faster, easier, and computationally less expensive manner without significant loss in accuracy (e.g., group additivity (*206*) and scaling relationships (*206–210*) for adsorption energies and Brønsted–Evans–Polanyi (BEP) type relationships (*211–217*) for activation energies). With these new tools at hand, catalyst researchers have been able to study catalytic reactions in greater detail, combining microkinetics and catalytic descriptors (e.g., binding energies) for high-throughput computational screening of best catalyst candidates in reactions with small molecules (*39*, *216*, *218–221*).

The ability of microkinetics to guide catalysis research has sparked further developments of multiscale methods aimed at understanding catalytic phenomena at all time and length scales (Figure 14) and ultimately to an almost complete computational design of catalysts (*39–41*, *45*, *204*, *205*, *219*, *222*). Despite the advantages offered by microkinetics, current microkinetic models do not incorporate reactor design and operation factors such as heat and mass transport of reactants and products (Figure 2), catalyst deactivation, and reactor stability. For such a purpose, semi-empirical rate expressions (e.g., power-law rate expressions, transport correlations) and/or computational fluid dynamics (CFD) models have been usually employed (Figure 14).

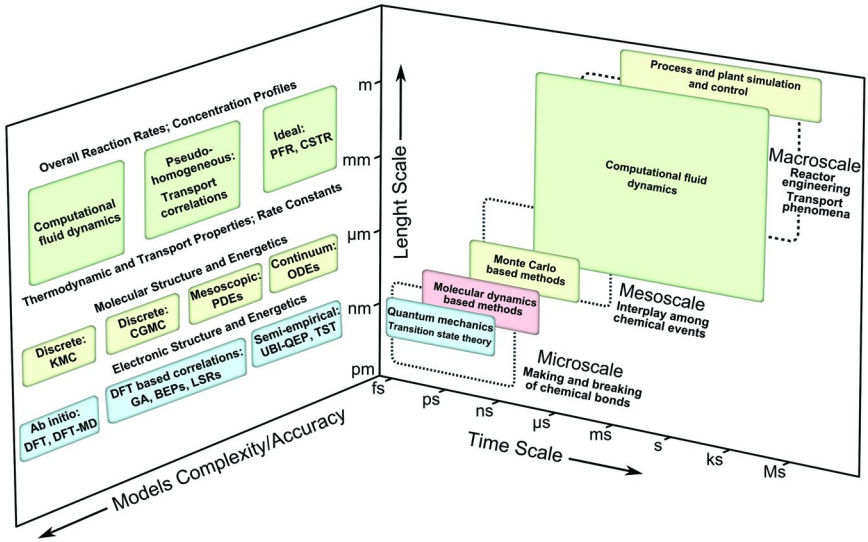

Figure 14. A schematic representation of the time and length scales in heterogeneous catalysis and associated models in order of complexity and accuracy (multiscale modeling). PFR: plug-flow reactor; CSTR: continuous stirred tank reactor; ODE: ordinary differential equation; PDE: partial differential equation; CG-KMC: coarse-grained kinetic Monte Carlo; KMC: kinetic Monte Carlo; UBI-QEP: unity bond index-quadratic exponential potential; TST: transition state theory; DFT: density functional theory; GA: group additivity; BEP:Brønsted–Evans–Polanyi; LSR: linear scaling relationships; MD: molecular dynamics. With data from references (41), (199), and (225).

Since conventional power-law rate expressions can be generated from microkinetic models (e.g., via model reduction), they can be used in combination with CFD (i.e., multiscale approach (Figure 14)) for reactor design, optimization, and control (*200*, *222*, *223*). Simplifying a microkinetic model (with a large number of elementary reaction steps) while still providing sufficient accuracy is, however, not a straightforward process. For example, the reduced model has to capture the dominant reaction steps in the mechanism while still being thermodynamically consistent (*224*). One reported systematic reduction methodology consists of: (1) a sensitivity analysis, followed by (2) a principal component analysis (PCA), and (3) a reaction path analysis (RPA). The PCA provides a simplified model (i.e., reduced number of elementary steps) which accounts for the most significant steps in the reaction mechanism, whereas the RPA identifies partially equilibrated reaction steps, most abundant reaction intermediates, and rate determining steps to finally yield an analytical power-law like rate expression, which can be easily integrated in CFD analyses (*204*, *224*).

Current microkinetic analyses strongly rely on computational calculations; however, the corresponding estimated parameters suffer from uncertainties

In Novel Materials for Catalysis and Fuels Processing; Bravo-Suárez, J., et al.;
ACS Symposium Series; American Chemical Society: Washington, DC, 2013.

associated with the accuracy of the estimation methods (e.g., TST, DFT, UBI-QEP), which in combination with the complex nature of the catalyst structure and/or model inadequacy can result in a microkinetic model with limited predictive capabilities (*203*, *204*). To improve these capabilities, some of the parameters in microkinetic models (e.g., pre-exponential factors) can be refined by fitting the model to macroscopic kinetic data (*46*, *203*). During the parameter refining procedure (i.e., by numerical optimization) many different sets of parameter values (i.e., local minima) are often found that provide good fit to the experimental data. In this case, additional data from temperature-programmed surface reaction (TPSR), isotopic labeling, and in situ characterization experiments would be required to discriminate among these models. For engineering applications, however, any of these parameter sets could be used for reactor design, optimization, and control provided that their values are physically reasonable and within expected ranges (*46*, *203*, *204*).

Emerging Catalytic Applications for Fuels and Chemicals Production

Catalysts are used all across the chemical industry from petroleum refining to chemical processing and to automobile emission control with a demand that is expected to grow at a healthy pace for the next few years (Tables 1 and 2). Besides these well-known applications, there is a current interest in the development of new catalysts (Figure 7B) and catalytic technologies for the production of fuels and chemicals from abundant and cheaper feedstocks (e.g., biomass, shale gas) motivated by energy security concerns and more favorable economics.

Bioderived Feedstocks Conversion to Fuels and Chemicals

Several pieces of legislation have been passed in the US aimed at promoting energy independence. They include the Energy and Policy Act of 2005 (EPACT2005) that mandated the use of biofuels (Renewable Fuel Standard, RFS1), mostly corn ethanol, at a level of 4 billion gallons per year (bgpy) in 2006 increasing to 7.5 bgpy by 2012 (*226*, *227*). EPACT2005 was followed by the Energy Independence and Security Act of 2007 (EISA2007), which expanded EPACT2005's biofuel mandate (RFS2) to require 9 bgpy in 2008 increasing to 36 bgpy by 2022 (Figure 15) (*227*, *228*). EISA2007, however, capped the corn ethanol biofuel amount to 15 bgpy while the remaining increases should be met by advanced biofuels (e.g., cellulosic and non-cellulosic advanced fuel, biodiesel), mostly derived from cellulosic feedstock (Figure 15). As shown in Figure 15, cellulosic advanced biofuels alone have the potential to displace over 10% of current gasoline consumption in the US, a market worth tens of billions of dollars. This has sparked tremendous research efforts in industry and academia for the conversion of cellulosic biomass derived feedstocks into (advanced) fuels (e.g., C_{2+} alcohols, C_5–C_{12} gasoline, C_9–C_{16} jet fuel, and C_{10}–C_{20} diesel range compounds).

In Novel Materials for Catalysis and Fuels Processing; Bravo-Suárez, J., et al.;
ACS Symposium Series; American Chemical Society: Washington, DC, 2013.

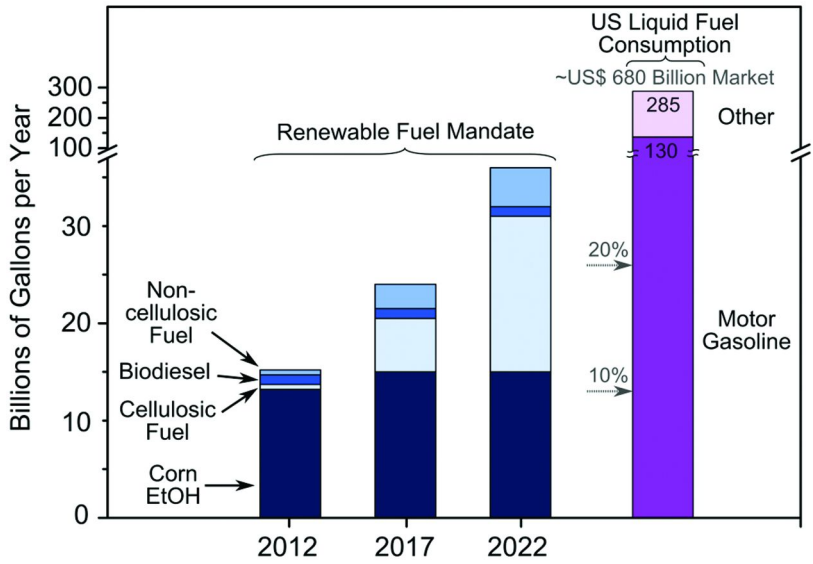

Figure 15. Biofuels production mandated by the Energy Independence Security Act of 2007 (EISA 2007, RFS2) (227, 228). Average US liquid fuel consumption in 2012; Other: jet fuel, distillate and residual fuel oil, naphtha, lubricants, coke, asphalt, petroleum gases (C_1–C_4) (Source: US Energy Information Administration) (241). US liquid fuel consumption in the next 10 years is not expected to significantly change from that in 2012 (Source: US Energy Information Administration (242) and BP (243)). Right side arrows indicate percent levels of total gasoline consumption. Market value based on a US$ 100 per barrel (42 gallons) of crude oil. (see color insert)

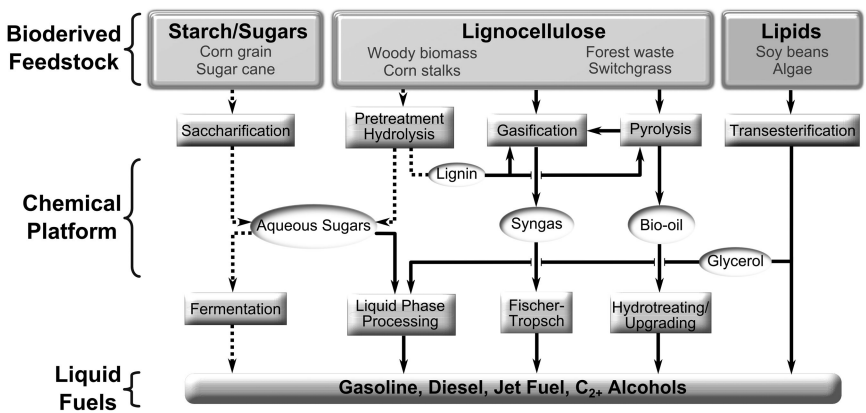

Figure 16. Simplified conversion routes of bioderived feedstocks to hydrocarbon fuels. Dashed and solid lines indicate biological and catalytic routes, respectively. Based on data from references (245) and (246).

Figure 16 presents the main conversion routes of bioderived feedstocks (e.g., starch/sugars, lignocellulose, and lipids) to fuels (e.g., C_{2+} alcohols, gasoline, jet fuel, diesel). Conversion of starch, for example, in corn grain, to aqueous sugars via saccharification (i.e., hydrolysis) and to ethanol via fermentation is a well-established technology which produces the majority of corn ethanol biofuel available in the US (*229–231*). Similarly, the conversion of lipids, for example, from soy beans, to biodiesel via transesterification is also well-known and practiced commercially (*76*, *232–234*). This process coproduces large amounts of glycerol, which is also considered an important building block for the production of fuels and chemicals (*235–239*). It is clear from Figure 16 that catalysis will play a significant role in the development of technologies for the conversion of lignocellulosic sources to so-called chemical platforms (e.g., aqueous sugars, lignin, syngas, bio-oil) and ultimately to liquid fuels and/or chemicals (*235*, *236*, *240*).

Production of Lignocellulosic Chemical Platforms

Lignocellulosic biomass is mainly composed by cellulose (~50 wt %), hemicellulose (~30 wt %), and lignin (~20 wt %). Cellulose is a crystalline glucose polymer (i.e., linear polysaccharide), hemicellulose is a highly substituted (with acetic acid) complex amorphous polymer composed of five different sugars: xylose (predominant component), arabinose, galactose, glucose, and mannose, whereas lignin is a highly branched, substituted, mononuclear aromatic polymer whose main monomeric units are coniferyl, sinapyl, and coumaryl alcohol (Figure 17) (*76*, *244*).

There are three main processes that are used for the conversion of lignocellulosic biomass into intermediate products (i.e., chemical platforms): pretreatment/hydrolysis, gasification, and pyrolysis.

1) *Pretreatment/hydrolysis.* In this process, the biomass is selectively converted into monomeric sugar units. The first step of the pretreatment involves physical (e.g., ball milling), chemical (e.g., cellulose depolymerizing solvents), and/or thermal combination methods (e.g., acid/base, hot water treatments) aimed at increasing biomass surface area, reducing cellulose crystallinity, removing hemicellulose and lignin, and in some cases prehydrolyzing hemicellulose to its sugar monomers. Upon separation of the biomass components, cellulose and hemicellulose are hydrolyzed catalytically in presence of acids or enzymes to glucose and mainly xylose, respectively (*76*, *247*).

2) *Gasification.* During this process, biomass is mainly converted in presence of a limited amount of O_2 or air to a mixture of gases containing predominantly syngas (H_2 + CO) with smaller amounts of CO_2, CH_4, and N_2. This conversion occurs via solid, liquid, and gas reactions involving pyrolysis (e.g., $C_xH_yO_z \rightarrow zCO + 0.5yH_2 + (x-z)C$), partial oxidation (e.g., $C_xH_yO_z + 0.5(x-z)O_2 \rightarrow xCO + 0.5yH_2$), steam reforming (e.g., $C_xH_yO_z + (x-z)H_2O \rightarrow xCO + (0.5y+x-z)H_2$), water-gas shift ($CO + H_2O \rightarrow CO_2 + H_2$), and methanation ($CO + 3H_2 \rightarrow CH_4 + H_2O$). Pyrolysis is favored at lower temperatures (400–650 °C), where a mixture

In Novel Materials for Catalysis and Fuels Processing; Bravo-Suárez, J., et al.;
ACS Symposium Series; American Chemical Society: Washington, DC, 2013.

of liquid, solid, and gaseous products is obtained. Gasification is typically carried out at 700–1000 °C, where syngas along with soot, ash (e.g., CaO, K_2O, P_2O_5, MgO, SiO_2, Na_2O), and tars (e.g., alkyl phenols, heterocyclic ethers, polyaromatic hydrocarbons) are produced. Catalysts (e.g., $Rh/CeO_2/SiO_2$, dolomite) can be used in the gasifiers to help reduce the amount of tars (*76*, *248*, *249*).

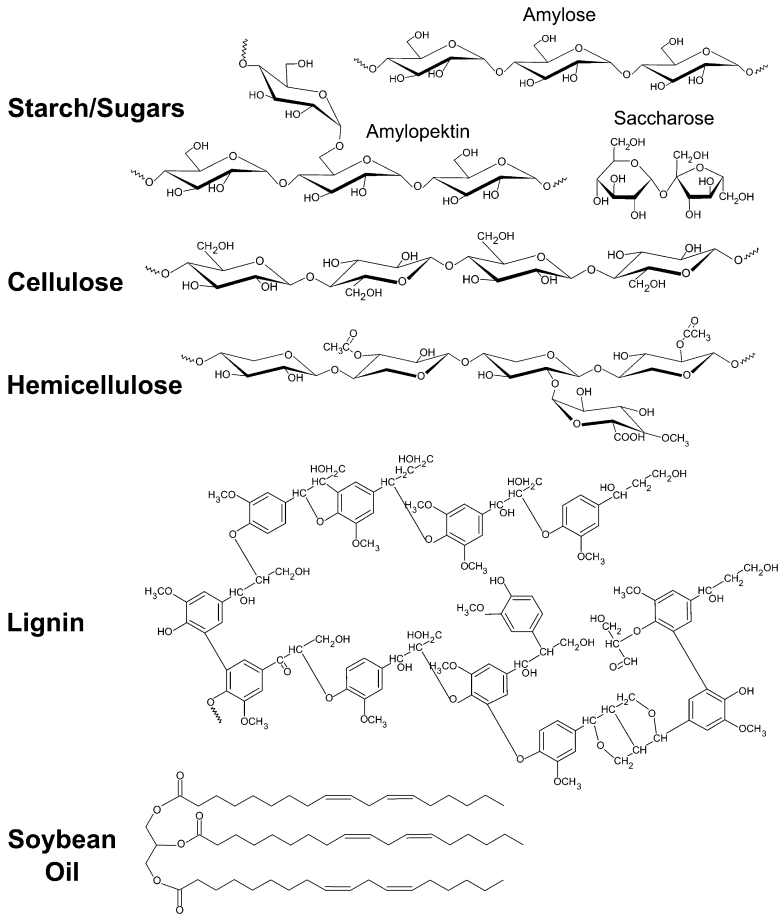

Figure 17. Basic molecular structures of the main constituents of biomass feedstocks. Cellulose: 1,4-β-D-glucopyranose form; (hardwood) hemicellulose: O-acetyl-4-O-methyl-glucoronoxylan; (softwood) lignin. With data from references (250–252).

In Novel Materials for Catalysis and Fuels Processing; Bravo-Suárez, J., et al.;
ACS Symposium Series; American Chemical Society: Washington, DC, 2013.

3) *Pyrolysis.* In this process, biomass is thermally treated under anaerobic conditions, low pressures (1–5 atm), intermediate temperatures (450–550 °C), and short residence times (<1 s, fast pyrolysis), primarily forming pyrolysis vapors. Upon rapid cooling of the vapors, a dark brown, viscous, multicomponent liquid mixture is produced in high yields, containing over 300–400 compounds, which is commonly referred to as bio-oil. The components present in bio-oil are the result of depolymerization (e.g., hydrolysis), fragmentation (e.g., dehydration, dehydrogenation, retro-condensation), and other parallel (e.g., isomerization, aromatization) reactions of cellulose, hemicellulose, and lignin. These products include acids (e.g., acetic, propanoic), aldehydes (e.g., ethanedial), alcohols (e.g., methanol, ethanol, ethylene glycol), sugars (e.g., 1,6-anhydrosugar, acetol), esters (e.g., butyrolactone), ketones (e.g., acetone), furans, and phenolic compounds (e.g., alkyl phenols, guaiacols, syringols). Catalysts (e.g., ZSM-5) have been recently utilized in fast pyrolysis reactors to produce bio-oils rich in aromatic compounds (*76*, *253–257*).

Conversion of Chemical Platforms to Fuels

The *only sustainable option* for producing fuels and chemicals in the long term is *plant-based biomass*. New chemistries and sustainable catalytic technologies are needed to produce chemical intermediates from plant-based feedstocks such as sugars, woody (lignocellulosic) biomass, and vegetable oils. This grand challenge provides fresh opportunities for chemists and chemical engineers to implement biorefineries that coproduce fuels and chemicals. The challenge is not different from what the petroleum industry faced nearly a century ago and has the potential to spur a new manufacturing sector in agro-based economies. In recent years, there has been increased interest to source many megaton chemical intermediates (such as ethylene oxide, linear aldehydes and dicarboxylic acids including terephthalic acid) from biomass-derived feedstocks. Existing technologies for these commodity chemicals are waste generating and energy intensive. Hence, to preserve the "green" potential of renewable feedstocks, new sustainable conversion technologies are needed.

Several strategies have been proposed to convert biomass chemical platforms such as sugars, lignin, syngas, bio-oil, and glycerol to fuels (Figure 16) and/or chemicals via chemical intermediates (e.g., DOE 2010 "Top 10" chemical building blocks in Figure 18). One obvious, short-term alternative is the integration of these chemical platforms with existing infrastructure, for example, with fluid catalytic cracking (FCC) and hydrotreating/hydrocracking units in oil refineries, for the production of fuels (*258*, *259*). This integration, however, is often difficult because of the large incompatibilities between these bioderived compounds such as sugars and bio-oil (e.g., high water content and oxygen content) and crude oil, which can lead, for example, to large amounts of coke under typical FCC conditions (*258*, *259*). A second option is to convert these chemical platforms into fuels (Figure 16) and/or platform chemicals (Figure 18) in dedicated process units in biorefineries (*76*, *239*, *246*, *256*, *260–264*).

In Novel Materials for Catalysis and Fuels Processing; Bravo-Suárez, J., et al.;
ACS Symposium Series; American Chemical Society: Washington, DC, 2013.

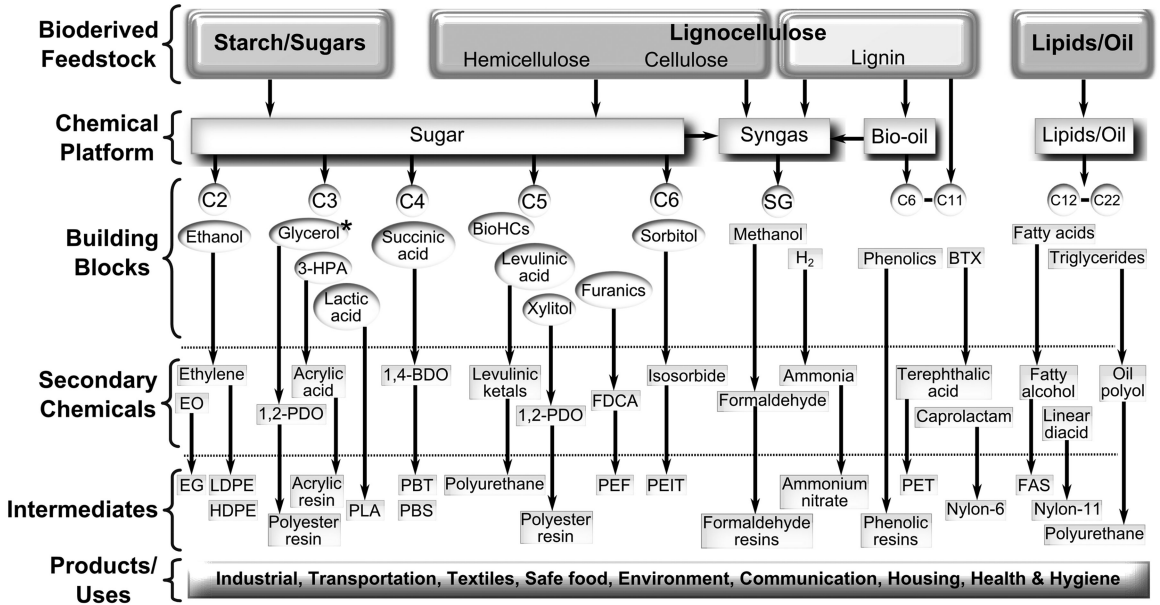

*Figure 18. Overview flow-chart for conversion of bioderived feedstocks to chemicals. With data from references (235), (236), (239), (240), (252) and (282–284). Chemicals in ovals correspond to DOE 2010 "Top 10" promising chemicals from biomass. *Glycerol is mainly formed as a byproduct of lipids/oil transesterification. SG: syngas, 3-HPA: 3-hydroxypropionic acid/aldehyde; Furanics: furfural, 5-hydroxymethlfurfural; BTX: Benzene–Toluene–Xylene; EO: ethylene oxide; 1,2-PDO: 1,2-propanediol; 1,4-BDO: 1,4-butanediol; FDCA:furan-2,5-dicarboxylic acid; EG: ethylene glycol; LDPE & HDPE: low-& high-density polyethylene; PLA: polylactic acid; PBT & PBS: polybutylene terephthalate & succinate; PEF, PEIT, & PET: polyethylene furanoate, isosorbide terephthalate, & terephthalate, respectively; FAS: fatty alcohol sulfate.*

As described above, the majority of research efforts are being dedicated to the production of biofuels given the immediate urgency to fulfill legislation mandating an increasing share of renewable fuels in the fuel pool. It is expected that further advances in novel catalysts, reactor engineering, and separations will contribute to the development of technologies for the conversion of bio-derived feedstocks to fuels via chemical platforms including:

1) Fermentation and chemocatalytic liquid phase processing of aqueous sugars (*246*, *256*, *260*, *265*, *266*).
2) Extraction and dissolution of lignin in solvents (e.g., ionic liquids, CO_2-expanded liquids) followed by catalytic cracking, hydrolysis, reduction, and oxidation (*240*, *263*).
3) Fischer–Tropsch conversions of bioderived syngas (*76*, *267–270*).
4) Catalytic hydrotreating and/or upgrading of bio-oil (*257*, *271–275*).
5) Bioconversion (*276*, *277*) followed by catalytic liquid phase processing and chemoselective reactions of glycerol (*237*, *246*, *278*, *279*).

Conversion of Chemical Platforms to Chemicals

The conversion of chemical platforms to low-volume high-value chemicals along with high-volume low-value fuels is necessary to assure the profitable operation of a biorefinery (*236*, *239*). Production of chemicals, however, from plant feedstocks is a tremendous challenge because of the large number of possible product candidates. Therefore, product identification is a critical step in the development of biorefineries utilizing renewable feedstocks (e.g., lipids/oil) and/or chemical platforms (e.g., syngas, glycerol, sugars, lignin, bio-oil) (Figure 18).

Syngas. Conversion of syngas to chemicals has been studied for a long time and is relatively mature. Additionally, syngas is one of the building blocks in petroleum and chemical industries, and it is used for the industrial production of bulk chemicals (e.g., methanol, ammonia, aldehydes) (*280*, *281*).

Lipids/oil. Conversion of lipids/oil to high-value products has also seen significant advances because they contain a homogeneous distribution of a limited number of simple structure components (e.g., fatty acids, triglycerides). This relative simplicity makes lipids and vegetable oils (e.g., soybean oil in Figure 17) a very interesting feedstock for the production of many high-value industrial chemical intermediates such as fatty alcohols, oil polyols, and long-chain diacids for the production of surfactants, lubricants, and polymers (e.g., polyurethanes, polyamides, polyesters). Heterogeneous catalysis is expected to be of relevance because many of these lipids/oil chemical transformations are catalytic in nature, including oxidations of double bonds and hydroxy groups in fatty acids, epoxidation, C–C bond forming additions to C–C double bonds, and metathesis reactions (*252*, *282–285*).

Glycerol/sugars. Conversion of glycerol (*237*, *238*, *250*) and sugars (*239*, *250*, *260*) to chemicals has seen some remarkable progress in the past years. In the case of sugars, high-value product identification is not straightforward. To facilitate

In Novel Materials for Catalysis and Fuels Processing; Bravo-Suárez, J., et al.;
ACS Symposium Series; American Chemical Society: Washington, DC, 2013.

this process, a methodology analogous to that used in the petroleum industry has been used to identify a small number of most promising chemical building blocks from carbohydrates (*235*). A recently revised list includes the following building blocks: ethanol, furans, glycerol and derivatives, biohydrocarbons (e.g., isoprene), lactic acid, succinic acid, hydroxypropionic acid/aldehyde, levulinic acid, sorbitol, and xylitol. They are also presented in Figure 18 and have been usually referred to as DOE "Top 10" (value-added chemicals from biomass) (*236*, *239*). With the exception of glycerol, which is a byproduct of transesterification of oils, the majority of building blocks are produced from plant feedstocks via biological transformations. Conversion of building blocks to secondary chemicals and intermediates, on the other hand, predominantly proceeds via chemical transformations (e.g., chemical reduction, oxidation, dehydration, bond cleavage, polymerization) (*235*). Figure 18 presents some examples of conversion of DOE "top 10" building blocks to secondary chemicals for the production of high-value polymer and resin chemical intermediates.

Lignin. Among all chemical platforms, lignin and bio-oil conversion to high-value chemicals is, perhaps, the most challenging due to the complex polymeric structure of lignin and large number of components in bio-oil. A recent DOE report has three general categories of products from lignin:

1) *Macromolecules*. In this category of products, the lignin structure is mostly retained to obtain products for high-molecular weight applications. Some examples of products in this category include carbon fiber, binders, polymer modifiers (e.g., fillers, additives), adhesives, and resins (e.g., phenol substitute in phenol-formaldehyde resins).
2) *Aromatics and miscellaneous monomers.* This second category consists of employing thermochemical methods to convert lignin macromolecular structure into lower-molecular weight aromatic components (e.g., depolymerization). Lignin conversion to these intermediate products can be generally achieved by dissolution, reduction (e.g., hydrogenolysis), (hydro)cracking, hydrolysis, oxidation, pyrolysis, and gasification in the presence or absence of solvents, chemical additives, and catalysts. Some of these products include phenol, benzene, toluene, and xylene (BTX), lignin monomers (e.g., eugenol, syringol), oxidized lignin monomers (e.g., vanillin, vanillic acid), aromatic diacids and polyols, and quinones. Products in this category appear to be the most attractive for high volume production because of their higher value including phenol and BTX, which are widely used as building blocks in the petrochemical industry for the production of polymers (e.g., polystyrene, polycarbonate, polyurethane, polyesters), Nylon-6, and phenolic resins (*236*, *240*, *263*, *286*, *287*).
3) *Power, fuel, and syngas*. In this category, lignin is used as a carbon source for direct use as a fuel/heat source (i.e., combustion) or for production of syngas chemical platform via gasification. Syngas can then be converted to chemicals as described above (*240*).

In Novel Materials for Catalysis and Fuels Processing; Bravo-Suárez, J., et al.;
ACS Symposium Series; American Chemical Society: Washington, DC, 2013.

Bio-oil. Fast pyrolysis of lignin also yields bio-oil. As described above, this bio-oil is the result of lignin depolymerization and fragmentation into hundreds of components such as acetic acid, hydroxyacetaldehyde, hydroxyacetone, mono and polysubstituted phenols, among many others. Catalyst development for preconditioning and stabilization of pyrolysis oil remains one of the major issues for integration into petroleum refineries and for conversion to fuels and chemicals (*275*). Phenols, aromatics (e.g., BTX), organic acids, 5-hydroxymethylfurfural (HMF), and levuglucosan have been considered as high-value compounds from bio-oil; however, their production in high yields and cost-effective fractionation are still challenging (*236*, *240*, *286*, *288*).

Natural Gas Conversion

In the last decade, significant advances in horizontal drilling and hydraulic fracturing technologies in combination with higher fuel prices have enabled the economical extraction of shale gas, natural gas trapped in deep underground shale rock formations (*289*, *290*). In the US, this has resulted in a significant share of shale gas in the overall natural gas production from only 2% in 2000 to 34% in 2012, which is expected to reach 50% by 2040 (Figure 19) (*291*). Current projections suggest that the US could become a net natural gas exporter within the next decade (Figure 19). This projected natural gas glut in combination with an estimated recoverable amount of 2203 trillion cubic feet (Tcf) (*292*, *293*) has sparked an increased interest to use this newly abundant and relatively cheap feedstock for synthesis of chemicals and fuels.

Figure 20 shows the typical average composition of shale gas consisting primarily of methane (85%), ethane (6%), propane (2%), nitrogen (3%), and C_4–C_5 hydrocarbons, CO_2, O_2, H_2, and Ar (4%). After extraction, this gas mixture is processed and purified to reach specifications for direct use as a fuel and/or production of methane, ethane, and/or syngas feedstocks (*294*, *295*). The predominance of methane in shale gas underscores its importance as a feedstock for the synthesis of chemicals and fuels (*295–297*). Activation of methane is perhaps one of the foremost grand challenges in catalysis from a fundamental and industrial point of view. For example, methane oxidation to methanol and methane oxidative coupling to C_{2+} hydrocarbons have been investigated for decades, but so far product yields are too low or the process requires corrosive oxidants and expensive separations to be of commercial interest (*298*). Indirect methane conversion routes via syngas ($CO + H_2$) have proven to be more efficient and are practiced commercially worldwide including syngas to methanol, syngas to hydrocarbons (i.e., Fischer–Tropsch process), and the water-gas shift reaction (WGS: $CO + H_2O = CO_2 + H_2$) (*281*, *299*). These indirect routes are, however, energy and capital intensive and significant work has been dedicated towards their process optimization to increase efficiency. Therefore, the development of catalysts that are more active and selective for direct conversion of methane and light paraffins to value added products is highly desirable and of great industrial significance (*300*).

In Novel Materials for Catalysis and Fuels Processing; Bravo-Suárez, J., et al.;
ACS Symposium Series; American Chemical Society: Washington, DC, 2013.

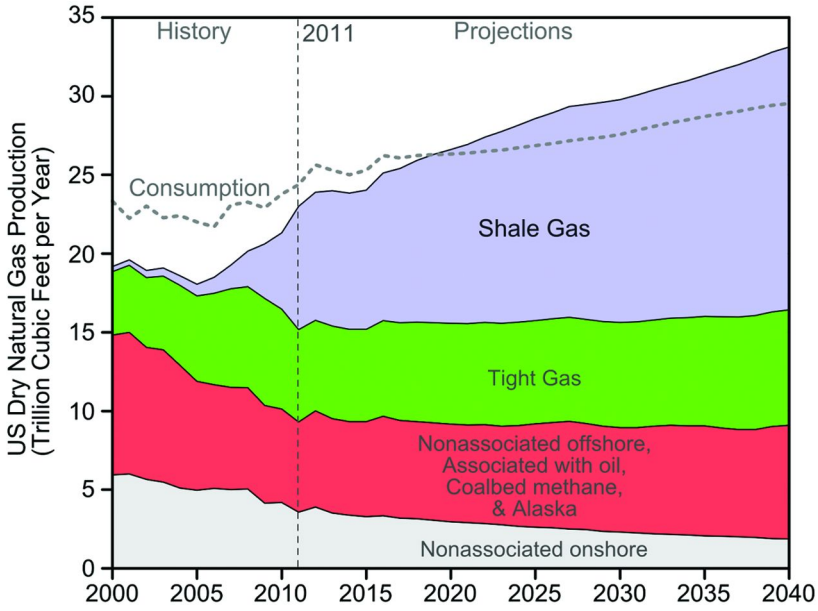

Figure 19. History and projections of US dry natural gas production by source. Source: US Energy Information Administration (291).

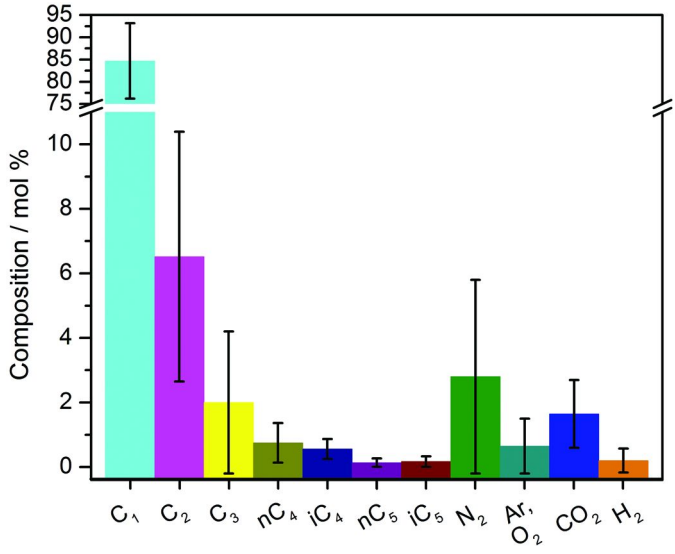

Figure 20. Typical shale gas average composition and standard deviation errors. Data from Texas Barnett shale gas composition in reference (306).

In Novel Materials for Catalysis and Fuels Processing; Bravo-Suárez, J., et al.;
ACS Symposium Series; American Chemical Society: Washington, DC, 2013.

Figure 21 presents a summary of some of the most important direct and indirect routes for methane conversion to chemicals and fuels. Significant fundamental work has been devoted to the development of new catalysts for methane conversion via both routes. For example, recent literature has reviewed direct methane conversion routes including the nonoxidative conversion of methane (e.g., cracking, dehydrogenation) to hydrogen, hydrocarbons, and aromatic compounds (*296*, *297*, *300*, *301*), methane oxidation to methanol and formaldehyde (*296*, *297*, *300*, *302*), oxidative coupling of methane to ethane and ethylene (*297*, *300*, *303*), as well as syngas formation for indirect methane conversion routes via steam reforming (SR: $CH_4 + H_2O = CO + 3H_2$; WGS) (*295*), autothermal reforming ($CH_4 + 1.5O_2 = CO + 2H_2O$; SR; WGS) (*295*), catalytic partial oxidation ($CH_4 + 0.5O_2 = CO + 2H_2$) (*295*, *304*, *305*), and CO_2 reforming ($CH_4 + CO_2 = 2CO + 2H_2$) (*303*, *304*).

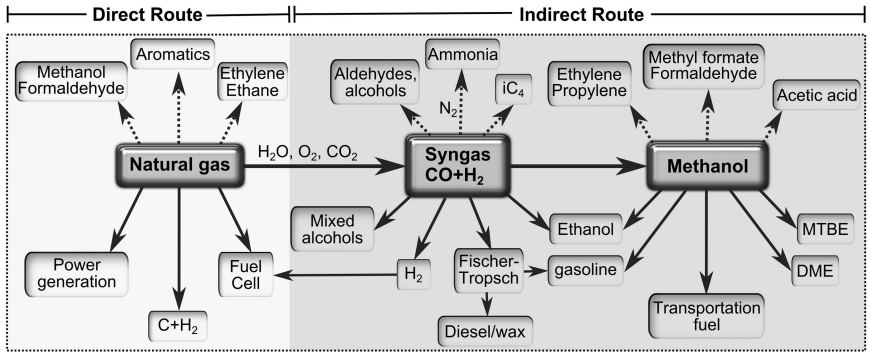

Figure 21. Direct (left panel) and indirect (right panel) routes of production of chemicals (dashed arrows) and fuels(solid arrows) from natural gas. With data from references (280), (281), (303), and (307)

Perspectives in the Development of New and Improved Catalysts

The previous sections have shown a brief overview of the different aspects of catalyst design and their relevance in current industrial and societal challenges of sustainable fuel and chemical production and environmental protection. These views and those from previous reports and perspectives on catalysis (*11*, *67*, *113*, *308–314*) agree on the important role of catalysis in the solution of these problems. More importantly, we are now seeing a dramatic shift in catalysis research towards this direction in academia, national laboratories, and industry. For example, over the next 10–20 years major research efforts in catalysis worldwide will be devoted to deal with environmental sustainability and conversion of renewable resources (sunlight, biomass) and natural gas to fuels and chemicals (*67*).

Today, we are witnessing how industrial (e.g., market forces) and societal (e.g., environmental and energy legislation) needs are driving innovation in catalyst design. This process is aided by parallel advances in theoretical and

In Novel Materials for Catalysis and Fuels Processing; Bravo-Suárez, J., et al.;
ACS Symposium Series; American Chemical Society: Washington, DC, 2013.

experimental tools and methods of catalyst synthesis (e.g., organometallic chemistry, materials science), characterization, and reaction kinetics, which are required for elucidating the relationships among a catalyst's synthesis, its structure and properties, and its activity. This fundamental knowledge can provide insights for the development of improved and new catalysts (Figure 22) and form a basis for further advances in catalytic technologies (*1*, *4*, *21*, *311*, *312*).

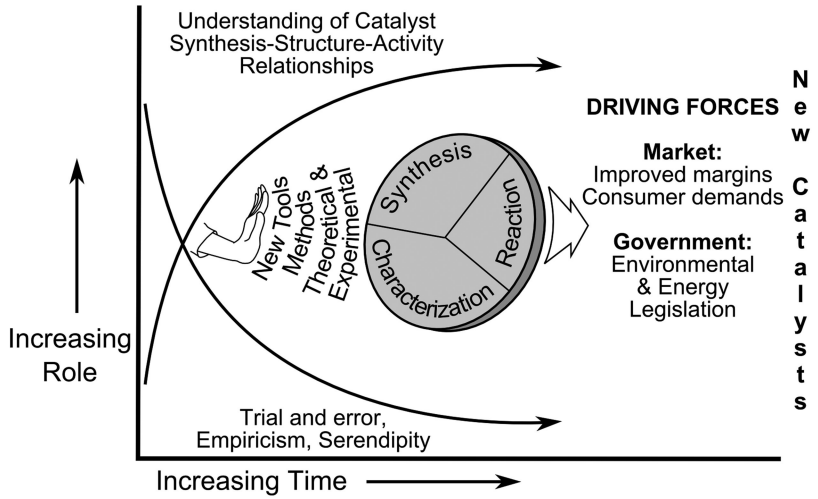

Figure 22. Progress towards a rational design of improved and novel catalysts. Advances in theory and methods of catalyst synthesis, characterization, and kinetics facilitate the understanding of catalytic phenomena and together with societal needs and market forces promote catalyst innovation.

Heterogeneous catalysis is expected to play a significant role in the solution of these environmental and energy issues, judging from its current dominant position in many catalytic applications (Figure 1, Table 1) and its larger share of research funding in comparison with homogeneous catalysis (*313*). Despite significant fundamental advances in heterogeneous catalysis science over the last 20 years, major research areas identified in the past will continue to be of relevance today. They include (*5*, *11*, *67*, *310*, *311*, *313*):

1) New sophisticated methods and tools in order to build tailored catalysts and to create nanoscale materials with superior functional properties (e.g., new synthesis methods, high-throughput synthesis).
2) New experimental techniques to probe reactions of actual catalysts in situ under working conditions (e.g., faster and with atomic resolution) for better fundamental understanding of reaction mechanisms (e.g., intermediate pathways, transition states).
3) Advances in theory and computation, for example, of more powerful computational algorithms for modeling complex molecular systems as well as of models spanning multiple time and length scales.

In Novel Materials for Catalysis and Fuels Processing; Bravo-Suárez, J., et al.;
ACS Symposium Series; American Chemical Society: Washington, DC, 2013.

4) Investigation of novel catalytic approaches for production of chemicals (e.g., with 100% selectivity) and fuels; accelerated rational catalyst design using computational, scientific, and combinatorial tools.

Developments in these areas will not only facilitate the understanding of catalytic processes at atomic/molecular levels required to rationally guide the synthesis of novel catalytic materials, but also provide the tools and recipes to synthesize them. They will bring us closer to meeting the Grand Challenges in catalysis of promoting "*the understanding of the mechanisms and dynamics of catalyzed reactions*" (*311*) and improving "*the design and controlled synthesis of catalyst structures*" (*311*), and ultimately to close the gap towards the "*design and perfect atom- and energy-efficient synthesis of revolutionary new forms of matter with tailored properties*" (*312*).

Some of the specific challenges relevant to the catalytic production of fuels and chemicals include (*5*, *310*, *311*):

1) Alkane functionalization and selective oxidation (e.g., novel pathways and catalysts for the selective conversion of methane and small hydrocarbons to higher molecular-weight products including coupling and alkylation reactions).
2) Conversion of nonpetroleum alternatives (e.g., coal, natural gas) and renewable resources (e.g., biomass) to fuels and chemicals.
3) Environmental applications (e.g., decomposition of nitric oxide to nitrogen and oxygen, and selective deep removal of sulfur and oxygen from fossil and renewable feedstocks).

Other major research areas not discussed in this overview but which are expected to play an important role in the shift towards a more sustainable economy also include: photocatalysis (*311*, *315*, *316*), hydrogen generation and storage (*317–319*), fuel cells, and carbon dioxide storage and utilization (*320–322*).

In what follows, we will present some specific issues that have been identified for further advance towards a more rational design of catalysts. These encompass the areas of catalyst synthesis, in situ characterization, kinetics, and theoretical/ computational descriptions to guide catalysis research.

Catalyst Synthesis

One of the grand challenges in the synthesis of catalysts is to develop synthesis methods with precise control of composition and molecular structure in the 1×10^{-9}–1×10^{-6} m length scale (*67*, *311*, *312*). Using materials with homogeneous composition and structure, it is possible to obtain more detailed information about catalyst structure–activity relationships. Such insights could ultimately guide the preparation of more active, selective, and stable catalysts (*323–325*), as already explored with single-site heterogeneous catalysts (*326–328*). Some examples of recent advances in this direction include: (1) the development of novel methods for synthesis of zeolitic materials with large-pores (e.g., for handling bulky biomass substrates) (*329*) or with improved diffusional

In Novel Materials for Catalysis and Fuels Processing; Bravo-Suárez, J., et al.;
ACS Symposium Series; American Chemical Society: Washington, DC, 2013.

properties by introduction of mesoporosity in their structure (*330–332*), and (2) the synthesis of monodispersed metal (*333*, *334*) and metal oxide (*335*, *336*) nanoparticles with controlled shape and specific surface orientations (*67*, *114*).

In terms of catalyst applications, major challenges exist for the development of new catalytic materials. One example is the replacement of costly and critical components (e.g., platinum-group, rare-earth metals) in industrial catalysts (*39*, *311*, *314*). This offers some unique opportunities for the development of new catalysts that can replace (or at least reduce the content of) noble metals in industrial catalysts for catalytic reforming, dehydrogenation, and emission control (Table 2). Examples include novel catalysts based on metal carbides, which posses noble metal-like properties (*128*, *131*, *337*).

In Situ Catalyst Characterization

During the past decade, materials characterization techniques have in general experienced significant advances in terms of increased resolution with respect to length and time scales, down to atomic and sub-picosecond ranges, respectively (*338*). In characterizing catalytic materials, these techniques have been applied both ex situ and in situ. In situ characterization techniques have become more common in catalysis research because they allow real time monitoring of the dynamics of reaction intermediates and active sites of complex, practical catalysts under actual reaction conditions. Such dynamic measurements in turn have provided more detailed information about the composition and nature of the active sites and reaction mechanisms (*184*, *339*). These insights in combination with microkinetic analyses (Figure 13) are essential to guide the rational development of novel catalyst synthesis methods that allow better control of catalyst structure, morphology, and composition for a given reaction (*170*, *184*, *340*).

Despite the large number of new techniques that have been implemented for catalytic studies, there is a need for improvement in many areas related to in situ characterization of catalysts including (*37*, *153*, *311*, *312*):

1) Elucidation of chemistry during synthesis of catalysts (*11*, *184*).
2) Development of spectrokinetic methodologies that allow discrimination of kinetically relevant adsorbed species (*192*, *196*).
3) Development of label-free imaging techniques, that is, in the absence of (e.g., fluorescent or optical) marker molecules for single molecule and/or single site in situ characterization (*37*, *113*, *183*), particularly those involving liquid phase at high temperature and pressure.
4) New techniques for in situ studies (including design of in situ cells/reactors) of multiphasic reaction systems such as those found in biomass conversion reactions (*37*).
5) Techniques with simultaneous sub-nanometer spatial resolution and picosecond time resolution that enable the study of breaking and making of chemical bonds during a catalyzed reaction (*183*, *184*, *338*). It is worth noting that there have been exciting recent advances in techniques that can provide atomic space resolution. An example of this is the

In Novel Materials for Catalysis and Fuels Processing; Bravo-Suárez, J., et al.;
ACS Symposium Series; American Chemical Society: Washington, DC, 2013.

utilization of aberration-corrected STEM to visualize individual Pt atoms in Pt/γ-Al_2O_3 catalysts (*341*) and Ir atoms in Ir supported on dealuminated HY zeolite (*342*), and of aberration corrected ETEM to visualize adsorbed CO molecules on the {100} facet of a Au nanoparticle (*180*).

6) Development of correlative approaches for multiscale catalyst characterization similar to the multiscale approach for computational modeling of catalysts (Figure 14) (*183*, *338*).

In addition to these topics, a well-recognized grand challenge in materials science as well as in heterogeneous catalysis is the vision of perfect-fidelity material characterization in 4D, that is, time-resolved 3D spatial scanning (*183*, *311*, *338*).

Kinetics and Multiscale Modeling

In the past decades, significant progress in experimental methods in kinetics has been made via the study of reactions dynamically (*196*, *343*) as well as at the fundamental level via microkinetic analyses (*43*, *46*, *47*, *200*). This atomic-scale knowledge of the surface chemistry during catalysis coupled with catalyst performance form the basis to establish relationships for the development of new and improved catalysts and processes (Figure 13) (*311*).

During a catalytic cycle, it is now recognized that the active site structure is very dynamic: it expands and/or contracts, relaxes, and even reconstructs on different time scales (*344*). Consideration of these dynamic structural changes in microkinetic analysis is essential for the development of more realistic kinetic models. For example, the integration of multiscale methods with electronic calculations (Figure 14) has been proposed to determine the chemical properties of these materials (*41*, *199*). Such an approach could also be used to understand catalyst structure sensitivity (*345–348*) via a structure-based microkinetic model, which could then be used to improve activity and selectivity by tuning the catalyst particle size and shape (*41*, *311*).

Today's microkinetic models are able to include to some extent more realistic conditions and effects such as catalyst structure (*41*) and adsorbate coverage effect on activation energies (via DFT) (*41*, *349*). Estimation of adsorbate coverage effects based on DFT calculations, however, is very demanding. Considering the potentially large number of adsorbed species in a surface catalyzed reaction, novel methods that can carry out such calculations in a computationally efficient (e.g., rapid, inexpensive) manner are desirable. Some methodologies have already been reported (*350–352*).

Other aspects that have been identified for improvement of current microkinetic models include: (1) accounting for effects of catalyst nonuniformity (i.e., more realistic catalyst surface), architecture and pore structure (e.g., zeolites, tortuosity), stability (e.g, deactivation by coke formation), support, and presence of promoters (*41*, *199*, *346*, *353*, *354*); and (2) finding strategies to better link models across multiple scales and determining the error propagation in going from micro- to macroscale models (Figure 14) (*41*, *199*).

In Novel Materials for Catalysis and Fuels Processing; Bravo-Suárez, J., et al.;
ACS Symposium Series; American Chemical Society: Washington, DC, 2013.

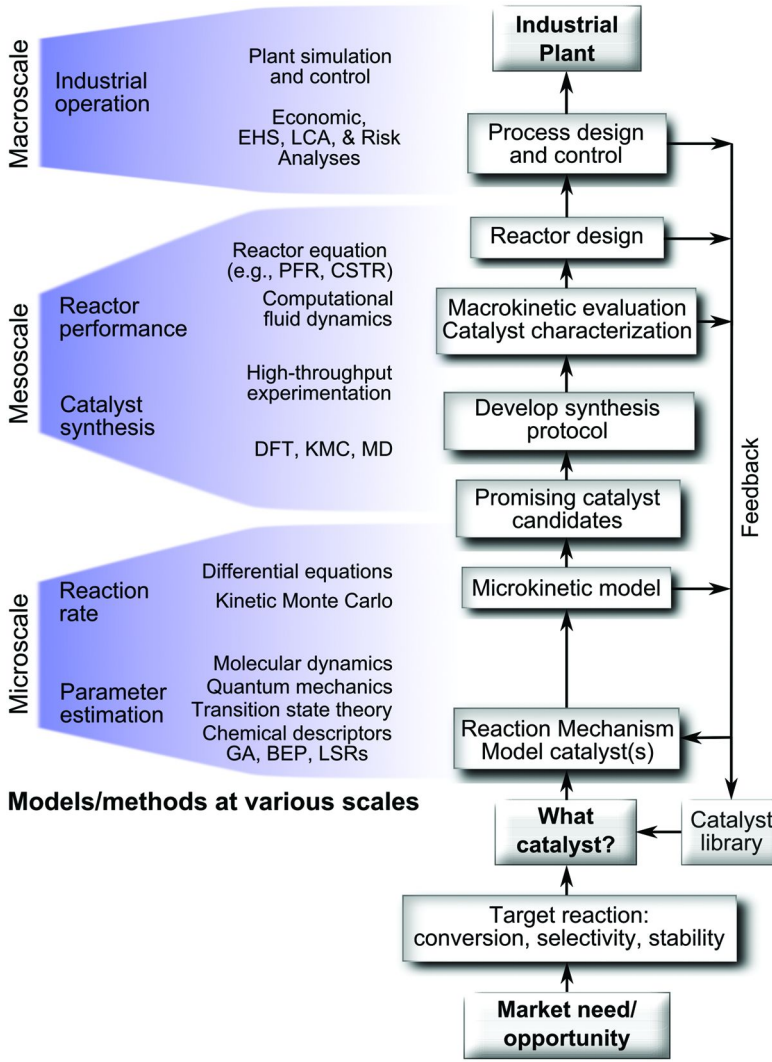

Figure 23. Integrated multiscale hierarchical approach to catalyst design and models/methods utilized at different scales. EHS: environmental, health, and safety; LCA: life cycle assessment; PFR: plug flow reactor; CSTR: continuous stirred-tank reactor; DFT: density functional theory; KMC: kinetic Monte Carlo; MD: molecular dynamics; GA: group additivity; BEP: Brønsted–Evans–Polanyi; LSR: linear scaling relationships.

The computationally-aided multiscale approach to catalyst and process design (*41*, *45*, *204*, *222*) discussed here and summarized in Figure 23 resembles previous molecular design approaches to catalysts and processes (*4*). Here, market needs and technological advances in concepts, methods, materials, and processes provide the driving forces for innovation in catalyst design (Figure

In Novel Materials for Catalysis and Fuels Processing; Bravo-Suárez, J., et al.;
ACS Symposium Series; American Chemical Society: Washington, DC, 2013.

22). Initially, the catalyst and process are simulated with advanced computer modeling techniques providing catalyst candidates that can be prepared by any of the many synthesis methods available in the literature. Catalyst characterization and performance evaluation results can then provide guidance if the process is economical based on target performance goals or if a new synthesis method, catalyst, or process needs to be developed. Such a methodology (although not perfect for a priori design of catalysts) can, in combination with advances in computer design and simulation, novel synthesis methods, in situ characterization techniques, and high-throughput systems, reduce the time and costs for developing new catalytic materials (*1*, *4*, *39*, *41*, *311*, *312*).

Discovering a new catalyst in the laboratory as described above, however, is just the first step towards developing a technical catalyst, a catalytic process, and/or a new catalyst–process combination. Towards this goal, many catalyst variables need to be considered for optimum performance including: high volumetric productivity, high selectivity, site and pore structure stability, mechanical strength, resistance to poisons and inhibitors, efficient use of expensive active components, use of promoters, catalyst resilience to changes in process conditions, catalyst shape/form, catalyst production costs, and reactor design/configuration (*40*, *355*, *356*).

Incorporation of sustainable development criteria in the process design is also indispensable for the overall assessment and evaluation of improved as well as new catalytic processes, and for comparison with existing technologies. These criteria include techno-economic analysis, potential impacts on the environment, worker's health, risk, and safety aspects (EHS) such as hazard and operability study (HAZOP), fault tree analysis (FTA), and life cycle assessment (LCA), among others (*357–360*). These types of analyses should be included in the design of future catalysts for the development of sustainable catalytic technologies for fuels and chemicals production. An example of such economic and environmental (cradle-to-grave LCA, Figure 24) (*361*) assessments was recently reported to guide the design of alternative ethylene epoxidation catalysts that eliminate CO_2 as byproduct (*362*).

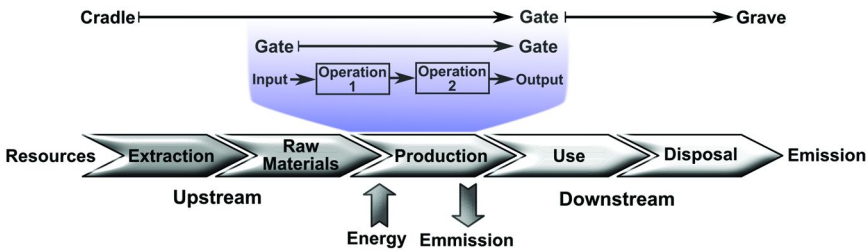

Figure 24. Definitions of system boundaries for product life cycle assessment studies.

In Novel Materials for Catalysis and Fuels Processing; Bravo-Suárez, J., et al.;
ACS Symposium Series; American Chemical Society: Washington, DC, 2013.

Safety and health analyses are well-established and are often part of process design procedures (*358*, *359*). LCA analyses (*361*), on the other hand, are only starting to become more common in catalysis research (*362*, *363*). The reason for this may be because they often require large amounts of information, which are not usually available at the early stages of the catalyst design, where many catalysts and processes may need to be considered. To facilitate and speed up the screening of potential catalysts and processes simpler evaluation methodologies (e.g., indicators), instead of rigorous evaluations (e.g., full LCA), may prove more useful to carry out preliminary decisions at the laboratory stage (*358*, *360*). Such a methodology has been recently proposed (*360*) that employs a series of parameters as proxies for economic feasibility, environmental impact, human health, and risks and opportunities, which include: (1) economic constraint (e.g., price ratio); (2) environmental impact of raw materials (e.g., GHG emissions); (3) process costs and environmental impact (e.g., energy loss index); (4) EHS index; and (5) risk aspects (e.g., feedstock supply risk, market risk).

Computational Chemistry

Today, computational chemistry is commonly used to aid in the interpretation of spectroscopic characterization (e.g., peak assignment) of catalysts, the prediction of the relative stability of different adsorbed species on catalyst surfaces, and the simulation of reaction pathways, useful for cross-validation of proposed reaction mechanisms based on kinetic and spectroscopic measurements (*11*, *67*, *221*, *364*). Computational methods and theory are expected to continue to facilitate the understanding of catalyst reactivity, composition, and structure relationships, necessary for guiding the design of engineered catalytic materials (*311*, *312*). To reach this goal, the following areas have been identified for further advances in computational catalysis:

1) More accurate and precise methods for the analysis of clusters at time and length scales relevant to catalysis (Figure 14) (e.g., current DFT energetic associated errors are in the 10 kJ/mol range). This is needed, for example, to improve predictive capabilities (e.g., for catalyst selectivity) of computational methods (*67*, *199*, *364*, *365*).
2) Methods that can simulate spectra and predict the stability of surface/cluster complexes incorporating solvent effects in the simulations. For example, non-equilibrium structures are difficult to find computationally, surface phase composition can vary under reaction conditions (e.g., at different gas and/or liquid phase composition), and solvents can also affect reactivity (*36*, *113*, *364*).
3) Methods and reactivity/kinetic parameters correlations (e.g., theoretical descriptors of reactivity) for complex systems with extended surfaces such as transition metal oxides, carbides, nitrides, and sulfides, which are not currently available (*364–367*).
4) More efficient methods and associated computer codes for studying complex industrial multicomponent catalysts (e.g., defects, promoters, two- or three-phase systems) (*40*).

In Novel Materials for Catalysis and Fuels Processing; Bravo-Suárez, J., et al.;
ACS Symposium Series; American Chemical Society: Washington, DC, 2013.

5) Predictive catalyst synthesis methods (e.g., incorporating weak forces such as van der Waals interactions) describing reaction intermediates and catalyst precursor transformations during synthesis steps (*36*, *67*, *113*, *364*).

Theory and Experimentation

Computer-aided synthesis of catalytic materials is particularly relevant for catalyst design, but is still in its infancy. Recent advances have been reported, for example, in the computational prediction of crystal structures (*368–371*), computational understanding of the template-based hydrothermal synthesis of zeolites (*372–375*) and metal oxide nanoparticle clusters (*376*). It is also particularly important that these computational advances occur hand-in-hand with the development of experimental synthesis methods that allow control of the catalyst structure and enable more precise knowledge of catalyst structure-activity relationships (*311*, *312*, *366*, *377*). Examples of these methods include the synthesis of well-defined supported metal nanoclusters via organometallic chemistry (*378–382*), single site heterogeneous catalysts (*326–383*), immobilized catalysts (*122–124*), and supported two- and three-dimensional metal nanoparticle structures of controlled size and shape (*157*, *323*, *324*, *384*).

Concluding Remarks

During the past several decades, the field of heterogeneous catalysis has seen tremendous growth globally, fueled by advances in novel synthesis methods that allow more control of the catalyst structure, in situ spectroscopic, microscopic, and diffraction/scattering characterization methods, kinetic modeling, and computational methods, and pulled by current industrial and societal needs of a more sustainable economy (Figure 22). This has resulted in a deeper understanding of catalytic phenomena at various time and length scales, enabling, for example, a systematic computational design of relatively simple reactions on well-defined active sites.

In the coming decades, more advances are expected in these areas of synthesis, in situ characterization, and theoretical and computational studies of more complex catalysts with additional components such as modifiers, dopants, selectivity enhancers, and stabilizers, whose effects on reactivity are still poorly understood. This knowledge will increase our understanding of the relationships among catalyst composition, structure, properties, and reactivity needed for a more rational design and discovery of technical catalysts for targeted reactions. Integrating this methodology with novel process design frameworks incorporating reactor and process design, economic, EHS, risk, and LCA analyses will pave way for the development of novel sustainable catalytic technologies for the resource-efficient conversion (i.e., conserving both feedstock and energy) of biomass-derived and alternative feedstocks into fuels and chemicals, ensuring both economic viability and environmental stewardship.

In Novel Materials for Catalysis and Fuels Processing; Bravo-Suárez, J., et al.;
ACS Symposium Series; American Chemical Society: Washington, DC, 2013.

About This Book

One of the grand challenges in heterogeneous catalysis is to rationally design novel catalysts for a targeted reaction. Thus far, there is no single recipe to reach this goal. As presented in this chapter, there are currently different approaches that can be used in catalysis research, among which a scientifically guided (e.g., computer-aided, descriptor-aided, kinetics-aided) high-throughput experimentation appears to be the most effective for catalyst discovery. Including adequate information on all fundamental aspects, methods, and tools needed to develop new catalysts (e.g., synthesis, characterization, reaction kinetics) for fuels and chemicals processing applications in a publication such as this or in any single book would be nearly impossible, perhaps with the exception of the "Handbook of Heterogeneous Catalysis" (*58*). The first book that provided a general overview of the fundamental aspects of catalyst design was published approximately 25 years ago (*309*). More recent books, however, have only covered individual aspects in depth including: catalyst design based on synthesis, characterization, and computational modeling approaches (*385*), catalyst development via high-throughput experimentation (*22*, *386*), catalyst synthesis (*2*, *57*), characterization (*54*, *149*), kinetics and catalytic reactors (*198*, *387*), computational methods (*213*, *388*, *389*), and applications in fuels and chemicals processing (*390–392*).

The current book is mainly based on contributions from an ACS Symposium titled "Novel Materials for Catalysis and Fuels Processing," organized by M. Kidder, V. Schwartz, and one the authors of this chapter (J.J.B.-S.), which occurred during the 243rd ACS National Meeting held in San Diego, California on March, 2012. The book has been organized in several sections including: (I) General aspects, methods, and tools currently available for catalyst design and some areas of application (this Chapter); (II) Computer-aided design of materials and catalysts (Chapters 2 and 3); (III) Catalyst spectroscopic characterization (Chapter 4); (IV) Kinetics-aided design of catalysts (Chapter 5); and (V) Applications of novel catalysts (Chapters 6 through 14).

The catalysts studied in this book include: unsupported and supported metal (e.g., V, Fe, Ni, Mo, W, Co, Cu, Ce) oxides, phosphides, and sulphides (Chapters 2, 4, 6, 7, 8, 13, and 14), supported noble metals (Chapters 5, 9, 12, and 14), supported enzymes (Chapter 11), amorphous and mesostructured silica materials (Chapters 6, 7, 8, and 11), amorphous and mesostructured carbon materials (Chapters 9, 10, and 12), and zeolitic imidazolate frameworks (ZIFs) (Chapter 3). Specific catalytic applications include propane oxidative dehydrogenation (Chapters 2 and 10), materials for carbon dioxide capture (Chapter 3), mobile emission control (Chapter 5), hydrodesulfurization and hydrogenation (Chapter 6), epoxidation (Chapters 7 and 8), syngas conversion (Chapter 9), and renewables conversion: alcohols (Chapter 11), xylitol and sorbitol (Chapter 12), alkyl phenols (Chapter 13), and carboxylic acids (Chapter 14).

In Novel Materials for Catalysis and Fuels Processing; Bravo-Suárez, J., et al.;
ACS Symposium Series; American Chemical Society: Washington, DC, 2013.

Acknowledgments

The authors acknowledge financial support for this work by the US Department of Agriculture and the National Institute of Food and Agriculture through Grant No. 2011-10006-30362.

References

1. Hegedus, L. L. Introduction. In *Catalyst Design: Progress and Perspectives*; Hegedus, L. L., Rutherford, A., Eds.; Wiley: New York, NY, 1987; pp 1−10.
2. de Jong, K. P., Ed. *Synthesis of Solid Catalysts*; Wiley-VCH: Weinheim, Germany, 2009; pp 1−401.
3. Bewley, L. *Chem. Week* **2008**, *170*, 21–21.
4. Cusumano, J. A. Creating the Future of the Chemical Industry-Catalysts by Molecular Design. In *Perspectives in Catalysis*; Thomas, J. M.; Zamaraev, K. I., Eds.; Blackwell Scientific Publications: London, Great Britain, 1992; pp 1−33.
5. Rabo, J. A. Catalysis: Past, Present and Future. In *New Frontiers in Catalysis (Proceedings of the 10th International Congress on Catalysis)*; Studies in Surface Science and Catalysis 75; Guczi, L., Solymosi, F., Tétényi, P., Eds.; Elsevier: Amsterdam, The Netherlands, 1993; pp 1−30.
6. World Bank - World Development Indicators (GNI, Atlas Method). http://data.worldbank.org/indicator/NY.GNP.ATLS.CD (accessed Nov. 23, 2012).
7. Bozich, F. Group Visit Unicredit - BASF's Catalysts Division: Driving Accelerated Growth. BASF (Investor Relations/News & Publications/Presentations/Functional Solutions); Ludwigshafen, Germany: Aug. 12, 2011; pp 1−51. http://www.basf.com (accessed Nov. 26, 2012).
8. Coons, R.; Valk, V. *Chem. Week* **2011**, *173*, 19–23.
9. Albemarle Corporation (Investors/ Events & Presentations/2011/ Longbow Basic Materials Conference Presentation). Longbow Research Investor Conference; New York, NY: Mar. 10, 2011; pp 1−51. http://www.albemarle.com (accessed Dec. 4, 2012).
10. Boudart, M. Kinetics in Catalysis. In *Perspectives in Catalysis*; Thomas, J. M., Zamaraev, K. I., Eds.; Blackwell Scientific Publications: London, Great Britain, 1992; pp 183−189.
11. Bell, A. T., Ed. *Catalysis Looks to the Future - Panel on New Directions in Catalytic Science and Technology*; The National Academies Press: Washington, DC, 1992; pp 1−86.
12. Fogler, H. S. *Elements of Chemical Reaction Engineering*, 4th ed.; Prentice Hall: Upper Saddle River, NJ, 2005; pp 1−1080.
13. Dumesic, J. A.; Huber, G. W.; Boudart, M. Principles of Heterogeneous Catalysis. In *Handbook of Heterogeneous Catalysis*, 2nd ed.; Ertl, G., Knözinger, H., Schüth, F., Weitkamp, J., Eds.; Wiley-VCH: Weinheim, 2008; pp 1−15.
14. Satterfield, C. N. *Mass Transfer in Heterogeneous Catalysis*; M.I.T. Press: Cambridge, MA, 1970; pp 1−267.
15. Madon, R. J.; Boudart, M. *Ind. Eng. Chem. Fund.* **1982**, *21*, 438–447.

16. Chorkendorff, I.; Niemantsverdriet, J. W. *Concepts of Modern Catalysis and Kinetics*; Wiley-VCH: Weinheim, Germany, 2003; pp 1−452.
17. van Santen, R. A. Concepts in Catalysis. In *Theoretical Heterogeneous Catalysis*; World Scientific Lecture and Course Notes in Chemistry 5; World Scientific: Singapore, 1991; pp 1−13.
18. Moulijn, J. A.; Perez-Ramirez, J.; van Diepen, A.; Kreutzer, M. T.; Kapteijn, F. *Int. J. Chem. React. Eng.* **2003**, *1*, 1–17.
19. van Santen, R. A.; Niemantsverdriet, H. W. The Science of Catalysis. In *Chemical Kinetics and Catalysis*; Fundamental and Applied Catalysis; Springer: New York, NY, 1995; pp 1−19.
20. Schlögl, R. *CATTECH* **2001**, *5*, 146–170.
21. Derouane, E. G. *CATTECH* **2001**, *5*, 214–225.
22. Baerns, M.; Holeňa, M. *Combinatorial Development of Solid Catalytic Materials: Design of High-Throughput Experiments, Data Analysis, Data Mining*; Catalytic Science Series 7; Imperial College Press: London, Great Britain, 2009; pp 1−178.
23. Trimm, D. L. *Design of Industrial Catalysts*; Chemical Engineering Monographs 11; Elsevier Scientific Pub. Co.: Amsterdam, The Netherlands, 1980; pp 1−314.
24. Hagen, J. *Industrial Catalysis: a Practical Approach*, 2nd ed.; Wiley-VCH: Weinheim, Germany, 2006; pp 1−507.
25. Trimm, D. L. The Overall Design of Catalysts. In *Design of Industrial Catalysts*; Chemical Engineering Monographs 11; Elsevier: Amsterdam, The Netherlands, 1980; pp 3−36.
26. Hagen, J. Planning, Development, and Testing of Catalysts. In *Industrial Catalysis: a Practical Approach*, 2nd ed.; Wiley-VCH: Weinheim, Germany, 2006; pp 347−402.
27. Alerasool, S.; Kelkar, C. P.; Farrauto, R. J. Rational Design Strategies for Industrial Catalysts. In *Design of Heterogeneous Catalysts*; Ozkan, U. S., Ed.; Wiley-VCH: Weinheim, Germany, 2009; pp 83−111.
28. Hutchings, G. J. *J. Mater. Chem.* **2009**, *19*, 1222–1235.
29. Hargreaves, J. S. J.; Hutchings, G. J.; Joyner, R. W.; Taylor, S. H. *Chem. Commun. (Cambridge, U. K.)* **1996**, *0*, 523–524.
30. Rothenberg, G. *Catal. Today* **2008**, *137*, 2–10.
31. Le, T.; Epa, V. C.; Burden, F. R.; Winkler, D. A. *Chem. Rev.* **2012**, *112*, 2889–2919.
32. Maldonado, A. G.; Rothenberg, G. *Chem. Eng. Prog.* **2009**, *105*, 26–32.
33. Corma, A.; Serra, J. M. *Catal. Today* **2005**, *107–108*, 3–11.
34. Klanner, C.; Farrusseng, D.; Baumes, L.; Mirodatos, C.; Schüth, F. *QSAR Comb. Sci.* **2003**, *22*, 729–736.
35. Klanner, C.; Farrusseng, D.; Baumes, L.; Lengliz, M.; Mirodatos, C.; Schüth, F. *Angew. Chem., Int. Ed.* **2004**, *43*, 5347–5349.
36. Neurock, M. Theory-Aided Catalyst Design. In *Design of Heterogeneous Catalysts*; Ozkan, U. S., Ed.; Wiley-VCH: Weinheim, Germany, 2009; pp 231−257.
37. Weckhuysen, B. M. *Phys. Chem. Chem. Phys.* **2003**, *5*, 4351–4360.
38. Djéga-Mariadassou, G.; Boudart, M. *J. Catal.* **2003**, *216*, 89–97.

39. Nørskov, J. K.; Bligaard, T.; Rossmeisl, J.; Christensen, C. H. *Nat. Chem.* **2009**, *1*, 37–46.
40. Nørskov, J. K.; Abild-Pedersen, F.; Studt, F.; Bligaard, T. *Proc. Natl. Acad. Sci. U.S.A.* **2011**, *108*, 937–943.
41. Salciccioli, M.; Stamatakis, M.; Caratzoulas, S.; Vlachos, D. G. *Chem. Eng. Sci.* **2011**, *66*, 4319–4355.
42. Guo, N.; Caratzoulas, S.; Doren, D. J.; Sandler, S. I.; Vlachos, D. G. *Energy Environ. Sci.* **2012**, *5*, 6703–6716.
43. Cortright, R. D.; Dumesic, J. A. *Adv. Catal.* **2001**, *46*, 161–264.
44. Kieken, L.; Iglesia, E.; Neurock, M.; Trenkle, J. M. U.S. Patent 6,763,309, 2004.
45. Prasad, V.; Karim, A. M.; Ulissi, Z.; Zagrobelny, M.; Vlachos, D. G. *Chem. Eng. Sci.* **2010**, *65*, 240–246.
46. Dumesic, J. A.; Rudd, D. F.; Aparicio, L. M.; Rekoske, J. E.; Treviño, A. A. *The Microkinetics of Heterogeneous Catalysis*; ACS Professional Reference Book; American Chemical Society: Washington, DC, 1993; pp 1−315.
47. Dumesic, J. A.; Huber, G. W.; Boudart, M. Rates of Catalytic Reactions. In *Handbook of Heterogeneous Catalysis*, 2nd ed.; Ertl, G.; Knözinger, H.; Schüth, F.; Weitkamp, J., Eds.; Wiley-VCH: Weinheim, 2008; pp 1445−1462.
48. Somorjai, G. A. The Building of Catalysts: A Molecular Surface Science Approach. In *Catalyst Design: Progress and Perspectives*; Hegedus, L. L.; Rutherford, A., Eds.; Wiley: New York, 1987; pp 11−69.
49. Zhdanov, V. P. *Surf. Sci.* **2002**, *500*, 966–985.
50. Greeley, J.; Nørskov, J. K.; Mavrikakis, M. *Annu. Rev. Phys. Chem.* **2002**, *53*, 319–348.
51. Libuda, J.; Freund, H. J. *Surf. Sci. Rep.* **2005**, *57*, 157–298.
52. Somorjai, G. A. *Chem. Rev.* **1996**, *96*, 1223–1236.
53. Haw, J. F. *In-Situ Spectroscopy in Heterogeneous Catalysis*; Wiley-VCH: Weinheim, Germany, 2002; pp 1−276.
54. Weckhuysen, B. M., Ed. *In-Situ Spectroscopy of Catalysts*; American Scientific Publishers: Stevenson Ranch, CA, 2004; pp 1−332.
55. Weckhuysen, B. M. *Chem. Soc. Rev.* **2010**, *39*, 4557–4559.
56. Ertl, G.; Knözinger, H.; Weitkamp, J., Eds. *Preparation of Solid Catalysts*; Wiley-VCH: Weinheim, Germany, 1999; pp 1−622.
57. Regalbuto, J., Ed. *Catalyst Preparation: Science and Engineering*; CRC Press: Boca Raton, FL, 2006; pp 1−474.
58. Ertl, G.; Knözinger, H.; Schüth, F.; Weitkamp, J., Eds. *Handbook of Heterogeneous Catalysis*, 2nd ed.; Wiley-VCH: Weinheim, Germany, 2008; pp 1−3865.
59. Satterfield, C. N. Catalyst Preparation and Manufacture. In *Heterogeneous Catalysis in Industrial Practice*, 2nd ed.; McGraw-Hill: New York, NY, 1991; pp 87−130.
60. Stiles, A. B.; Koch, T. A. *Catalyst Manufacture*, 2nd ed.; Chemical Industries 63; Dekker: New York, NY, 1995; pp 1−291.

61. Wijngaarden, R. J.; Kronberg, A.; Westerterp, K. R. *Industrial Catalysis: Optimizing Catalysts and Processes*; Wiley-VCH: Weinheim, Germany, 1998; pp 1−268.
62. Morbidelli, M.; Gavriilidis, A.; Varma, A. *Catalyst Design: Optimal Distribution of Catalyst in Pellets, Reactors, and Membranes*; Cambridge Series in Chemical Engineering; Cambridge University Press: Cambridge, United Kingdom, 2005; pp 1−227.
63. Schwarz, J. A.; Contescu, C.; Contescu, A. *Chem. Rev.* **1995**, *95*, 477–510.
64. Gallei, E. F.; Hesse, M.; Schwab, E. Development of Industrial Catalysts. In *Handbook of Heterogeneous Catalysis*, 2nd ed.; Ertl, G., Knözinger, H., Schüth, F., Weitkamp, J., Eds.; Wiley-VCH: Weinheim, Germany, 2008; pp 57−66.
65. Lloyd, L. *Handbook of Industrial Catalysts*; Springer: New York, 2011; pp 1−490.
66. Rase, H. F. *Handbook of Commercial Catalysts: Heterogeneous Catalysts*; CRC Press: Boca Raton, FL, 2000; pp 1−488.
67. Davis, R., Ed. *International Assessment of Research and Development in Catalysis by Nanostructured Materials*; Imperial College Press: London, Great Britain, 2011; pp 1−302.
68. Rodriguez-Reinoso, F.; Sepulveda-Escribano, A. Carbon as Catalyst Support. In *Carbon Materials for Catalysis*; Serp, P., Figueiredo, J. L., Eds.; Wiley: Hoboken, NJ, 2009; pp 131−155.
69. Figueiredo, J. L.; Pereira, M. F. R. Carbon as Catalyst. In *Carbon Materials for Catalysis*; Serp, P., Figueiredo, J. L., Eds.; Wiley: Hoboken, NJ, 2009; pp 177−217.
70. Serp, P.; Corrias, M.; Kalck, P. *Appl. Catal., A* **2003**, *253*, 337–358.
71. Joo, S. H.; Choi, S. J.; Oh, I.; Kwak, J.; Liu, Z.; Terasaki, O.; Ryoo, R. *Nature* **2001**, *412*, 169–172.
72. Machado, B. F.; Serp, P. *Catal. Sci. Technol.* **2012**, *2*, 54–75.
73. Thomas, A.; Fischer, A.; Goettmann, F.; Antonietti, M.; Muller, J.-O.; Schlogl, R.; Carlsson, J. M. *J. Mater. Chem.* **2008**, *18*, 4893–4908.
74. Lee, J.; Kim, J.; Hyeon, T. *Adv. Mater. (Weinheim, Ger.)* **2006**, *18*, 2073–2094.
75. Radovic, L. R. Physicochemical Properties of Carbon Materials: A Brief Overview. In *Carbon Materials for Catalysis*; Serp, P., Figueiredo, J. L., Eds.; Wiley: Hoboken, NJ, 2009; pp 1−44.
76. Huber, G. W.; Iborra, S.; Corma, A. *Chem. Rev.* **2006**, *106*, 4044–4098.
77. Jin, X.; Dang, L.; Lohrman, J.; Subramaniam, B.; Ren, S.; Chaudhari, R. V. *ACS Nano* **2013**, *7*, 1309–1316.
78. Sing, K. S. W.; Everett, D. H.; Haul, R. A. W.; Moscou, L.; Pierotti, R. A.; Rouquerol, J.; Siemieniewska, T. *Pure Appl. Chem.* **1985**, *57*, 603–619.
79. Flanigen, E. M. Zeolites and Molecular Sieves: An Historical Perspective. In *Introduction to Zeolite Science and Practice*; Studies in Surface Science and Catalysis 137; van Bekkum, H., Flanigen, E. M., Jacobs, P. A., Jansen, J. C., Eds.; Elsevier: Amsterdam, The Netherlands, 2001; pp 11−35.
80. Maschmeyer, T.; van de Water, L. An Overview of Zeolite, Zeotype and Mesoporous Solids Chemistry: Design, Synthesis and Catalytic Properties.

In *Catalysts for Fine Chemical Synthesis: Micro and Mesoporous Solid Catalysts*; Wiley: Chichester, England, 2006; Vol. 4, pp 1−38.
81. Xu, R.; Pang, W.; Yu, J.; Huo, Q.; Chen, J. *Chemistry of Zeolites and Related Porous Materials: Synthesis and Structure*; Wiley: Singapore, 2007; pp 1−679.
82. Kleitz, F. Ordered Mesoporous Materials. In *Handbook of Heterogeneous Catalysis*, 2nd ed.; Ertl, G., Knözinger, H., Schüth, F., Weitkamp, J., Eds.; Wiley-VCH: Weinheim, 2008; pp 178−219.
83. Roth, W. J.; Vartuli, J. C. Synthesis of Mesoporous Molecular Sieves. In *Zeolites and Ordered Mesoporous Materials: Progress and Prospects*; Studies in Surface Science and Catalysis 157; Čejka, J., van Bekkum, H., Eds.; Elsevier: Amsterdam, The Netherlands, 2005; pp 91−110.
84. Angevine Philip, J.; Gaffney Anne, M.; Shan, Z.; Yeh Chuen, Y. Advanced Catalytic Materials for the Refining and Petrochemical Industry: TUD-1. In *Innovations in Industrial and Engineering Chemistry*; ACS Symposium Series 1000; American Chemical Society: Washington, DC, 2008; pp 335−363.
85. Telalovic, S.; Ramanathan, A.; Mul, G.; Hanefeld, U. *J. Mater. Chem.* **2010**, *20*, 642–658.
86. Kirschhock, C. E. A.; Feijen, E. J. P.; Jacobs, P. A.; Martens, J. A. Hydrothermal Zeolite Synthesis. In *Handbook of Heterogeneous Catalysis*, 2nd ed.; Ertl, G., Knözinger, H., Schüth, F., Weitkamp, J., Eds.; Wiley-VCH: Weinheim, 2008; pp 160−178.
87. Corma, A. *Chem. Rev.* **1997**, *97*, 2373–2420.
88. Taguchi, A.; Schüth, F. *Microporous Mesoporous Mater.* **2005**, *77*, 1–45.
89. Farrusseng, D.; Aguado, S.; Pinel, C. *Angew. Chem., Int. Ed.* **2009**, *48*, 7502–7513.
90. Phan, A.; Doonan, C. J.; Uribe-Romo, F. J.; Knobler, C. B.; O'Keeffe, M.; Yaghi, O. M. *Acc. Chem. Res.* **2009**, *43*, 58–67.
91. Davis, M. E. *Nature* **2002**, *417*, 813–821.
92. Haag, W. O.; Chen, N. Y. Catalyst Design with Zeolites. In *Catalyst Design: Progress and Perspectives*; Hegedus, L. L., Rutherford, A., Eds.; Wiley: New York, NY, 1987; pp 163−212.
93. Stöcker, M. *Microporous Mesoporous Mater.* **1999**, *29*, 3–48.
94. Kung, H. H. *Transition Metal Oxides: Surface Chemistry and Catalysis*; Studies in Surface Science and Catalysis 45; Elsevier: Amsterdam, The Netherlands, 1989; pp 1−285.
95. Hutchings, G. J.; Bartley, J. K.; Rhodes, C.; Taylor, S. H.; Wells, R. P. K.; Willock, D. J. Metal Oxides. In *Encyclopedia of Catalysis*; Horvath, I. T., Ed.; Wiley-Interscience: Hoboken, NJ, 2003; pp 602−694.
96. Fierro, J. L. G., Ed. *Metal Oxides: Chemistry and Applications*; Chemical Industries 108; CRC Press: Boca Raton, FL, 2006; pp 1−783.
97. Badlani, M.; Wachs, I. E. *Catal. Lett.* **2001**, *75*, 137–149.
98. Landau, M. V. Sol-Gel Process. In *Handbook of Heterogeneous Catalysis*, 2nd ed.; Ertl, G., Knözinger, H., Schüth, F., Weitkamp, J., Eds.; Wiley-VCH: Weinheim, 2008; pp 119−160.

In Novel Materials for Catalysis and Fuels Processing; Bravo-Suárez, J., et al.;
ACS Symposium Series; American Chemical Society: Washington, DC, 2013.

99. Marceau, E.; Carrier, X.; Che, M.; Clause, O.; Marcilly, C. Ion Exchange and Impregnation. In *Handbook of Heterogeneous Catalysis*, 2nd ed.; Ertl, G., Knözinger, H., Schüth, F., Weitkamp, J., Eds.; Wiley-VCH: Weinheim, 2008; pp 467−484.
100. Averseng, F.; Vennat, M.; Che, M. Grafting and Anchoring of Transition Metal Complexes to Inorganic Oxides. In *Handbook of Heterogeneous Catalysis*, 2nd ed.; Ertl, G., Knözinger, H., Schüth, F., Weitkamp, J., Eds.; Wiley-VCH: Weinheim, 2008; pp 522−539.
101. Banares, M. A.; Wachs, I. E. *J. Raman Spectrosc.* **2002**, *33*, 359–380.
102. AlGhamdi, K.; Hargreaves, J. S. J.; Jackson, S. D. Base Catalysis with Metal Oxides. In *Metal Oxide Catalysis*; Jackson, S. D., Hargreaves, J. S. J., Eds.; Wiley-VCH: Weinheim, Germany, 2009; pp 819−843.
103. Haruta, M. *Catal. Today* **1997**, *36*, 153–166.
104. Takei, T.; Akita, T.; Nakamura, I.; Fujitani, T.; Okumura, M.; Okazaki, K.; Huang, J. H.; Ishida, T.; Haruta, M. *Adv. Catal.* **2012**, *55*, 1–126.
105. Bond, G. C.; Sermon, P. A.; Webb, G.; Buchanan, D. A.; Wells, P. B. *J. Chem. Soc., Chem. Commun.* **1973**, *0*, 444b–445.
106. Hutchings, G. J. *J. Catal.* **1985**, *96*, 292–295.
107. Nkosi, B.; Coville, N. J.; Hutchings, G. J. *J. Chem. Soc., Chem. Commun.* **1988**, *0*, 71–72.
108. Haruta, M.; Kobayashi, T.; Sano, H.; Yamada, N. *Chem. Lett.* **1987**, 405–408.
109. Haruta, M.; Yamada, N.; Kobayashi, T.; Iijima, S. *J. Catal.* **1989**, *115*, 301–309.
110. Prati, L.; Rossi, M. *J. Catal.* **1998**, *176*, 552–560.
111. Bond, G. C.; Louis, C.; Thompson, D. T. *Catalysis by Gold*; Catalytic Science Series 6; Imperial College Press: London, Great Britain, 2006; pp 1−366.
112. Hashmi, A. S. K.; Hutchings, G. J. *Angew. Chem., Int. Ed.* **2006**, *45*, 7896–7936.
113. Hu, E. L.; Davis, S. M.; Davis, R.; Scher, E. Applications: Catalysis by Nanostructures Materials. In *WTEC Panel Report on Nanotechnology Research Directions for Societal Needs in 2020: Retrospective and Outlook*; Science Policy Reports; Roco, M. C., Mirkin, C. A., Hersam, M. C., Eds.; Springer: Boston, MA, 2010; pp 343−362.
114. Cuenya, B. R. *Thin Solid Films* **2010**, *518*, 3127–3150.
115. Hayashi, T.; Tanaka, K.; Haruta, M. *J. Catal.* **1998**, *178*, 566–575.
116. Chowdhury, B.; Bravo-Suárez, J. J.; Date, M.; Tsubota, S.; Haruta, M. *Angew. Chem., Int. Ed.* **2006**, *45*, 412–415.
117. Bravo-Suárez, J. J.; Bando, K. K.; Akita, T.; Fujitani, T.; Fuhrer, T. J.; Oyama, S. T. *Chem. Commun. (Cambridge, U. K.)* **2008**, 3272–3274.
118. Bravo-Suárez, J. J.; Bando, K. K.; Lu, J. Q.; Fujitani, T.; Oyama, S. T. *J. Catal.* **2008**, *255*, 114–126.
119. Bravo-Suárez, J. J.; Bando, K. K.; Fujitani, T.; Oyama, S. T. *J. Catal.* **2008**, *257*, 32–42.
120. Sakurai, H.; Ueda, A.; Kobayashi, T.; Haruta, M. *Chem. Commun. (Cambridge, U. K.)* **1997**, 271–272.

In Novel Materials for Catalysis and Fuels Processing; Bravo-Suárez, J., et al.;
ACS Symposium Series; American Chemical Society: Washington, DC, 2013.

121. Landon, P.; Collier, P. J.; Papworth, A. J.; Kiely, C. J.; Hutchings, G. J. *Chem. Commun. (Cambridge, U. K.)* **2002**, 2058–2059.
122. End, N.; Schöning, K.-U. Immobilized Catalysts in Industrial Research and Application. In *Immobilized Catalysts: Solid Phases, Immobilization and Applications*; Topics in Current Chemistry 242; Kirschning, A., Ed.; Springer-Verlag: Berlin, Germany, 2004; pp 241−271.
123. Anwander, R. Immobilization of Molecular Catalysts. In *Handbook of Heterogeneous Catalysis*, 2nd ed.; Ertl, G., Knözinger, H., Schüth, F., Weitkamp, J., Eds.; Wiley-VCH: Weinheim, 2008; pp 583−614.
124. Fraile, J. M.; García, J. I.; Mayoral, J. A.; Pires, E. Heterogenization on Inorganic Supports: Methods and Applications. In *Heterogenized Homogeneous Catalysts for Fine Chemicals Production: Materials and Processes*; Catalysis by Metal Complexes 33; Barbaro, P., Liguori, F., Eds.; Springer: New York, NY, 2010; pp 65−121.
125. End, N.; Schöning, K.-U. Immobilized Biocatalysts in Industrial Research and Production. In *Immobilized Catalysts: Solid Phases, Immobilization and Applications*; Topics in Current Chemistry 242; Kirschning, A., Ed.; Springer-Verlag: Berlin, Germany, 2004; pp 273−317.
126. Macquarrie, D. Fine Chemicals Synthesis Through Heterogenized Catalysts: Scopes, Challenges and Needs. In *Heterogenized Homogeneous Catalysts for Fine Chemicals Production: Materials and Processes*; Catalysis by Metal Complexes 33; Barbaro, P., Liguori, F., Eds.; Springer: New York, NY, 2010; pp 1−35.
127. Oyama, S. T. Transition Metal Carbides, Nitrides, and Phosphides. In *Handbook of Heterogeneous Catalysis*, 2nd ed.; Ertl, G., Knözinger, H., Schüth, F., Weitkamp, J., Eds.; Wiley-VCH: Weinheim, 2008; pp 342−356.
128. Levy, R. B.; Boudart, M. *Science* **1973**, *181*, 547–549.
129. Oyama, S. T., Ed. *The Chemistry of Transition Metal Carbides and Nitrides*; Blackie Academic and Professional: London, United Kingdom, 1996; pp 1−536.
130. Prins, R.; Bussell, M. *Catal. Lett.* **2012**, *142*, 1413–1436.
131. Alexander, A.-M.; Hargreaves, J. S. J. *Chem. Soc. Rev.* **2010**, *39*, 4388–4401.
132. Furimsky, E. *Appl. Catal., A* **2003**, *240*, 1–28.
133. Oyama, S. T.; Gott, T.; Zhao, H. Y.; Lee, Y. K. *Catal. Today* **2009**, *143*, 94–107.
134. Nagai, M. *Appl. Catal., A* **2007**, *322*, 178–190.
135. Ham, D. J.; Lee, J. S. *Energies* **2009**, *2*, 873–899.
136. Zaman, S.; Smith, K. J. *Catal. Rev.: Sci. Eng.* **2012**, *54*, 41–132.
137. Whiffen, V. M. L.; Smith, K. J. *Energy Fuels* **2010**, *24*, 4728–4737.
138. Zhao, H. Y.; Li, D.; Bui, P.; Oyama, S. T. *Appl. Catal., A* **2011**, *391*, 305–310.
139. Ghampson, I. T.; Sepúlveda, C.; Garcia, R.; Radovic, L. R.; Fierro, J. L. G.; DeSisto, W. J.; Escalona, N. *Appl. Catal., A* **2012**, *439–440*, 111–124.
140. Welton, T. *Coord. Chem. Rev.* **2004**, *248*, 2459–2477.
141. Plechkova, N. V.; Seddon, K. R. *Chem. Soc. Rev.* **2008**, *37*, 123–150.
142. Olivier-Bourbigou, H.; Magna, L.; Morvan, D. *Appl. Catal., A* **2010**, *373*, 1–56.

In Novel Materials for Catalysis and Fuels Processing; Bravo-Suárez, J., et al.;
ACS Symposium Series; American Chemical Society: Washington, DC, 2013.

143. Riisager, A.; Fehrmann, R.; Wasserscheid, P. Supported Liquid Catalysts. In *Handbook of Heterogeneous Catalysis*, 2nd ed.; Ertl, G., Knözinger, H., Schüth, F., Weitkamp, J., Eds.; Wiley-VCH: Weinheim, 2008; pp 631−644.
144. Gu, Y.; Li, G. *Adv. Synth. Catal.* **2009**, *351*, 817–847.
145. Zhang, Q.; Zhang, S.; Deng, Y. *Green Chem.* **2011**, *13*, 2619–2637.
146. Mehnert, C. P. *Chem. − Eur. J.* **2005**, *11*, 50–56.
147. Delannay, F.; Delmon, B. Methods of Catalyst Characterization: An Overview. In *Characterization of Heterogeneous Catalysts*; Chemical Industries 15; Delannay, F., Ed.; Marcel Dekker, Inc.: New York, NY, 1984; pp 1−28.
148. Imelik, B.; Vedrine, J. C. General Introduction. In *Catalyst Characterization: Physical Techniques for Solid Materials*; Fundamental and Applied Catalysis; Imelik, B., Vedrine, J. C., Eds.; Plenum Press: New York, NY, 1994; pp 1−10.
149. Che, M.; Vedrine, J. C., Eds. *Characterization of Solid Materials and Heterogeneous Catalysts*; Wiley-VCH: Weinheim, Germany, 2012; pp 1−1181.
150. Jacoby, M. *Chem. Eng. News* **1998**, *76*, 41–48.
151. Somorjai, G. A. *Introduction to Surface Chemistry and Catalysis*; Wiley: New York, NY, 1994; pp 1−667.
152. Gunter, P. L. J.; Niemantsverdriet, J. W.; Ribeiro, F. H.; Somorjai, G. A. *Catal Rev.: Sci. Eng.* **1997**, *39*, 77–168.
153. Weckhuysen, B. M. *Chem. Commun. (Cambridge, U. K.)* **2002**, 97–110.
154. Niemantsverdriet, J. W. Introduction. In *Spectroscopy in Catalysis: An Introduction*, 3rd ed.; Niemantsverdriet, J. W., Ed.; Wiley-VCH: Weinheim, Germany, 2007; pp 1−10.
155. Grunes, J.; Zhu, J.; Somorjai, G. A. Catalysis and Nanoscience. In *Nanotechnology in Catalysis 1*; Nanostructure Science and Technology; Zhou, B., Hermans, S., Somorjai, G. A., Eds.; Springer: New York, NY, 2003; pp 1−15.
156. Somorjai, G. A.; Yang, M. *Top. Catal.* **2003**, *24*, 61–72.
157. Somorjai, G. A.; Contreras, A. M.; Montano, M.; Rioux, R. M. *Proc. Natl. Acad. Sci. U.S.A.* **2006**, *103*, 10577–10583.
158. Somorjai, G. A.; Park, J. Y. *Phys. Today* **2007**, *60*, 48–53.
159. Somorjai, G. A.; Park, J. Y. *Surf. Sci.* **2009**, *603*, 1293–1300.
160. Somorjai, G. A.; Beaumont, S. K.; Alayoglu, S. *Angew. Chem., Int. Ed.* **2011**, *50*, 10116–10129.
161. Frenken, J.; Hendriksen, B. *MRS Bull.* **2007**, *32*, 1015–1021.
162. Escudero, C.; Salmeron, M. *Surf. Sci.* **2013**, *607*, 2–9.
163. Jensen, J. A.; Rider, K. B.; Salmeron, M.; Somorjai, G. A. *Phys. Rev. Lett.* **1998**, *80*, 1228–1231.
164. Gross, E.; Krier, J.; Heinke, L.; Somorjai, G. *Top. Catal.* **2012**, *55*, 13–23.
165. Cremer, P. S.; Su, X.; Shen, Y. R.; Somorjai, G. A. *J. Am. Chem. Soc.* **1996**, *118*, 2942–2949.
166. Gleaves, J. T.; Yablonskii, G. S.; Phanawadee, P.; Schuurman, Y. *Appl. Catal., A* **1997**, *160*, 55–88.
167. Yablonsky, G. S.; Olea, M.; Marin, G. B. *J. Catal.* **2003**, *216*, 120–134.

In Novel Materials for Catalysis and Fuels Processing; Bravo-Suárez, J., et al.;
ACS Symposium Series; American Chemical Society: Washington, DC, 2013.

168. Pérez-Ramírez, J.; Kondratenko, E. V. *Catal. Today* **2007**, *121*, 160–169.
169. Gleaves, J. T.; Yablonsky, G.; Zheng, X.; Fushimi, R.; Mills, P. L. *J. Mol. Catal. A: Chem.* **2010**, *315*, 108–134.
170. Topsøe, H. *J. Catal.* **2003**, *216*, 155–164.
171. Mul, G.; Hamminga, G. M.; Moulijn, J. A. *Vib. Spectrosc.* **2004**, *34*, 109–121.
172. Bürgi, T.; Baiker, A. *Adv. Catal.* **2006**, *50*, 227–283.
173. Koptyug, I. V.; Lysova, A. A.; Kulikov, A. V.; Kirillov, V. A.; Parmon, V. N.; Sagdeev, R. Z. *Appl. Catal., A* **2004**, *267*, 143–148.
174. Kawai, T.; Chun, W.-J.; Asakura, K.; Koike, Y.; Nomura, M.; Bando, K. K.; Oyama, S. T.; Sumiya, H. *Rev. Sci. Instrum.* **2008**, *79*, 014101/1–014101/6.
175. Kawai, T.; Bando, K. K.; Lee, Y. K.; Oyama, S. T.; Chun, W. J.; Asakura, K. *J. Catal.* **2006**, *241*, 20–24.
176. Myhra, S.; Riviere, J. C. How to Use This Book. In *Handbook of Surface and Interface Analysis: Methods for Problem-Solving*; Riviere, J. C., Myhra, S., Eds.; Marcel Dekker: New York, NY, 1998; pp 23−56.
177. Roeffaers, M. B. J.; Sels, B. F.; Uji-i, H.; De Schryver, F. C.; Jacobs, P. A.; de Vos, D. E.; Hofkens, J. *Nature* **2006**, *439*, 572–575.
178. Roeffaers, M. B. J.; Sels, B. F.; Uji-i, H.; Blanpain, B.; L'Hoëst, P.; Jacobs, P. A.; de Schryver, F. C.; Hofkens, J.; de Vos, D. E. *Angew. Chem., Int. Ed.* **2007**, *46*, 1706–1709.
179. Xu, W.; Kong, J. S.; Yeh, Y.-T. E.; Chen, P. *Nat. Mater.* **2008**, *7*, 992–996.
180. Yoshida, H.; Kuwauchi, Y.; Jinschek, J. R.; Sun, K.; Tanaka, S.; Kohyama, M.; Shimada, S.; Haruta, M.; Takeda, S. *Science* **2012**, *335*, 317–319.
181. Zurner, A.; Kirstein, J.; Doblinger, M.; Brauchle, C.; Bein, T. *Nature* **2007**, *450*, 705–708.
182. Urakawa, A.; Baiker, A. *Top. Catal.* **2009**, *52*, 1312–1322.
183. Weckhuysen, B. M. *Angew. Chem., Int. Ed.* **2009**, *48*, 4910–4943.
184. Buurmans, I. L. C.; Weckhuysen, B. M. *Nat. Chem.* **2012**, *4*, 873–886.
185. Tinnemans, S. J.; Mesu, J. G.; Kervinen, K.; Visser, T.; Nijhuis, T. A.; Beale, A. M.; Keller, D. E.; van der Eerden, A. M. J.; Weckhuysen, B. M. *Catal. Today* **2006**, *113*, 3–15.
186. Bentrup, U. *Chem. Soc. Rev.* **2010**, *39*, 4718–4730.
187. Oyama, S. T.; Li, W. *Top. Catal.* **1999**, *8*, 75–80.
188. Reed, C.; Xi, Y.; Oyama, S. T. *J. Catal.* **2005**, *235*, 378–392.
189. Bensalem, A.; Weckhuysen, B. M.; Schoonheydt, R. A. *J. Phys. Chem. B* **1997**, *101*, 2824–2829.
190. Argyle, M. D.; Chen, K.; Resini, C.; Krebs, C.; Bell, A. T.; Iglesia, E. *J. Phys. Chem. B* **2004**, *108*, 2345–2353.
191. Argyle, M. D.; Chen, K.; Iglesia, E.; Bell, A. T. *J. Phys. Chem. B* **2004**, *109*, 2414–2420.
192. Meunier, F. C. *Catal. Today* **2010**, *155*, 164–171.
193. Kalamaras, C. M.; Americanou, S.; Efstathiou, A. M. *J. Catal.* **2011**, *279*, 287–300.
194. Bravo-Suárez, J. J.; Bando, K. K.; Lu, J. I.; Haruta, M.; Fujitani, T.; Oyama, S. T. *J. Phys. Chem. C* **2008**, *112*, 1115–1123.

195. Gott, T.; Oyama, S. T. *J. Catal.* **2009**, *263*, 359–371.
196. Kondratenko, E. V. *Catal. Today* **2010**, *157*, 16–23.
197. Boudart, M. *Catal. Lett.* **2000**, *65*, 1–3.
198. Froment, G. F.; Bischoff, K. B.; de Wilde, J. *Chemical Reactor Analysis and Design*; Wiley: Hoboken, NJ, 2011; pp 1−860.
199. Broadbelt, L. J.; Snurr, R. Q. *Appl. Catal., A* **2000**, *200*, 23–46.
200. Gokhale, A. A.; Kandoi, S.; Greeley, J. P.; Mavrikakis, M.; Dumesic, J. A. *Chem. Eng. Sci.* **2004**, *59*, 4679–4691.
201. Boudart, M.; Djéga-Mariadassou, G. *Kinetics of Heterogeneous Catalytic Reactions*; Physical Chemistry: Science and Engineering; Princeton University Press: Princeton, NJ, 1984; pp 1−222.
202. Vannice, A. *Kinetics of Catalytic Reactions*; Springer: New York, NY, 2005; pp 1−240.
203. Prasad, V.; Karim, A. M.; Arya, A.; Vlachos, D. G. *Ind. Eng. Chem. Res.* **2009**, *48*, 5255–5265.
204. Vlachos, D. G.; Mhadeshwar, A. B.; Kaisare, N. S. *Comput. Chem. Eng.* **2006**, *30*, 1712–1724.
205. Raimondeau, S.; Vlachos, D. G. *Chem. Eng. J. (Lausanne)* **2002**, *90*, 3–23.
206. Salciccioli, M.; Chen, Y.; Vlachos, D. G. *J. Phys. Chem. C* **2010**, *114*, 20155–20166.
207. Abild-Pedersen, F.; Greeley, J.; Studt, F.; Rossmeisl, J.; Munter, T. R.; Moses, P. G.; Skúlason, E.; Bligaard, T.; Nørskov, J. K. *Phys. Rev. Lett.* **2007**, *99*, 016105/1–016105/4.
208. Jones, G.; Bligaard, T.; Abild-Pedersen, F.; Nørskov, J. K. *J. Phys.: Condens. Matter* **2008**, *20*, 064239/1–064239/6.
209. Fernández, E. M.; Moses, P. G.; Toftelund, A.; Hansen, H. A.; Martínez, J. I.; Abild-Pedersen, F.; Kleis, J.; Hinnemann, B.; Rossmeisl, J.; Bligaard, T.; Nørskov, J. K. *Angew. Chem., Int. Ed.* **2008**, *47*, 4683–4686.
210. Goldsmith, C. F. *Top. Catal.* **2012**, *55*, 366–375.
211. Pallassana, V.; Neurock, M. *J. Catal.* **2000**, *191*, 301–317.
212. Bligaard, T.; Nørskov, J. K.; Dahl, S.; Matthiesen, J.; Christensen, C. H.; Sehested, J. *J. Catal.* **2004**, *224*, 206–217.
213. van Santen, R. A.; Neurock, M. *Molecular Heterogeneous Catalysis - A Conceptual and Computational Approach*; Wiley-VCH: Weinheim, Germany, 2006; pp 1−474.
214. Nørskov, J. K.; Bligaard, T.; Hvolbaek, B.; Abild-Pedersen, F.; Chorkendorff, I.; Christensen, C. H. *Chem. Soc. Rev.* **2008**, *37*, 2163–2171.
215. van Santen, R. A.; Neurock, M.; Shetty, S. G. *Chem. Rev. (Washington, DC, U. S.)* **2009**, *110*, 2005–2048.
216. Salciccioli, M.; Vlachos, D. G. *ACS Catal.* **2011**, *1*, 1246–1256.
217. Sutton, J. E.; Vlachos, D. G. *ACS Catal.* **2012**, *2*, 1624–1634.
218. Greeley, J.; Mavrikakis, M. *Nat. Mater.* **2004**, *3*, 810–815.
219. Andersson, M. P.; Bligaard, T.; Kustov, A.; Larsen, K. E.; Greeley, J.; Johannessen, T.; Christensen, C. H.; Nørskov, J. K. *J. Catal.* **2006**, *239*, 501–506.
220. Greeley, J.; Jaramillo, T. F.; Bonde, J.; Chorkendorff, I.; Nørskov, J. K. *Nat. Mater.* **2006**, *5*, 909–913.

221. Sabbe, M. K.; Reyniers, M.-F.; Reuter, K. *Catal. Sci. Technol.* **2012**, *2*, 2010–2024.
222. Vlachos, D. G. *AIChE J.* **2012**, *58*, 1314–1325.
223. Deshmukh, S. R.; Mhadeshwar, A. B.; Vlachos, D. G. *Ind. Eng. Chem. Res.* **2004**, *43*, 2986–2999.
224. Mhadeshwar, A. B.; Vlachos, D. G. *Catal. Today* **2005**, *105*, 162–172.
225. Maestri, M. Microkinetic Analysis of Complex Chemical Processes at Surfaces. In *New Strategies in Chemical Synthesis and Catalysis*; Pignataro, B., Ed.; Wiley-VCH: Weinheim, Germany, 2012; pp 219−245.
226. Energy Policy Act of 2005. In *Public Law 109-58-Aug. 8, 2005*, 109th Congress: 2005; pp 119 STAT. 594-1143.
227. Ethanol Overview. *Congressional Digest* **2011**, *90*, 226−230.
228. Energy Independence and Security Act of 2007. In *Public Law 110-140-Dec. 19, 2007*, 110th Congress: 2007; pp 121 STAT. 1492-1801.
229. Gulati, M.; Kohlmann, K.; Ladisch, M. R.; Hespell, R.; Bothast, R. J. *Bioresour. Technol.* **1996**, *58*, 253–264.
230. Kirschner, M. Chemical Profile: Ethanol. *Chem. Market Rep.* **2003**, *263*, 27–27.
231. Sánchez, Ó. J.; Cardona, C. A. *Bioresour. Technol.* **2008**, *99*, 5270–5295.
232. Fukuda, H.; Kondo, A.; Noda, H. *J. Biosci. Bioeng.* **2001**, *92*, 405–416.
233. Pinto, A. C.; Guarieiro, L. L. N.; Rezende, M. J. C.; Ribeiro, N. M.; Torres, E. A.; Lopes, W. A.; Pereira, P. A. d. P.; Andrade, J. B. d. *J. Braz. Chem. Soc.* **2005**, *16*, 1313–1330.
234. Sivasamy, A.; Cheah, K. Y.; Fornasiero, P.; Kemausuor, F.; Zinoviev, S.; Miertus, S. *ChemSusChem* **2009**, *2*, 278–300.
235. Werpy, T. A.; Petersen, G. *Top Value Added Chemicals from Biomass: Volume I - Results of Screening for Potential Candidates from Sugars and Synthesis Gas*; Technical Report DOE/GO-102004-1992; Pacific Northwest National Laboratory/National Renewable Energy Laboratory: Oak Ridge, TN, 2004; pp 1−76.
236. de Jong, E.; Higson, A.; Walsh, P.; Wellisch, M. *Bio-based Chemicals: Value Added Products from Biorefineries. International Energy Agency Bioenergy - Task 42 Biorefinery*. pp 1−34. http://www.iea-bioenergy.task42-biorefineries.com/publications/reports/ (accessed Jan. 31, 2013).
237. Zhou, C.-H.; Beltramini, J. N.; Fan, Y.-X.; Lu, G. Q. *Chem. Soc. Rev.* **2008**, *37*, 527–549.
238. Jérôme, F.; Pouilloux, Y.; Barrault, J. *ChemSusChem* **2008**, *1*, 586–613.
239. Bozell, J. J.; Petersen, G. R. *Green Chem.* **2010**, *12*, 539–554.
240. Holladay, J. E.; White, J. F.; Bozell, J. J.; Johnson, D. *Top Value-Added Chemicals from Biomass: Volume II - Results of Screening for Potential Candidates from Biorefinery Lignin*; Technical Report PNNL-16983; Pacific Northwest National Laboratory/National Renewable Energy Laboratory: Richland, WA, 2007; pp 1−79.
241. US Energy Information Administration - Petroleum & Other Liquids (Data/Consumption-Sales/Product Supplied). Monthly Release Date: Dec. 28, 2012. http://www.eia.gov/petroleum/ (accessed Jan. 10, 2013).

In Novel Materials for Catalysis and Fuels Processing; Bravo-Suárez, J., et al.;
ACS Symposium Series; American Chemical Society: Washington, DC, 2013.

242. US Energy Information Administration - Analysis & Projections (Short-Term Energy Outlook (STEO)). Release Date: Jan. 8, 2013. http://www.eia.gov/forecasts/steo/pdf/steo_full.pdf (accessed Jan. 17, 2013).
243. BP Energy Outlook 2030. BP Global (Reports and publications/Statistical Review of World Energy 2012/Energy outlook 2030/Booklet) London, Great Britain: Jan. 2012; pp 1−88. http://www.bp.com (accessed Dec. 17, 2012).
244. Sjöström, E. *Wood Chemistry: Fundamentals and Applications*; Academic Press: New York, NY, 1981; pp 1−223.
245. Regalbuto, J. R. *Science* **2009**, *325*, 822–824.
246. Serrano-Ruiz, J. C.; Dumesic, J. A. *Energy Environ. Sci.* **2011**, *4*, 83–99.
247. Sun, Y.; Cheng, J. *Bioresour. Technol.* **2002**, *83*, 1–11.
248. Han, J.; Kim, H. *Renewable Sustainable Energy Rev.* **2008**, *12*, 397–416.
249. Zinoviev, S.; Müller-Langer, F.; Das, P.; Bertero, N.; Fornasiero, P.; Kaltschmitt, M.; Centi, G.; Miertus, S. *ChemSusChem* **2010**, *3*, 1106–1133.
250. Ruppert, A. M.; Weinberg, K.; Palkovits, R. *Angew. Chem., Int. Ed.* **2012**, *51*, 2564–2601.
251. Pettersen, R. C. The Chemical Composition of Wood. In *The Chemistry of Solid Wood*; Advances in Chemistry 207; Rowell, R., Ed.; American Chemical Society: Washington, DC, 1984; pp 57−126.
252. Xia, Y.; Larock, R. C. *Green Chem.* **2010**, *12*, 1893–1909.
253. Bridgwater, A. V.; Peacocke, G. V. C. *Renewable Sustainable Energy Rev.* **2000**, *4*, 1–73.
254. Carlson, T. R.; Vispute, T. P.; Huber, G. W. *ChemSusChem* **2008**, *1*, 397–400.
255. Elliott, D. C.; Hart, T. R.; Neuenschwander, G. G.; Rotness, L. J.; Zacher, A. H. *Environ. Prog. Sustainable Energy* **2009**, *28*, 441–449.
256. Alonso, D. M.; Bond, J. Q.; Dumesic, J. A. *Green Chem.* **2010**, *12*, 1493–1513.
257. Bridgwater, A. V. *Biomass Bioenergy* **2012**, *38*, 68–94.
258. Huber, G. W.; Corma, A. *Angew. Chem., Int. Ed.* **2007**, *46*, 7184–7201.
259. de Miguel Mercader, F.; Groeneveld, M. J.; Kersten, S. R. A.; Way, N. W. J.; Schaverien, C. J.; Hogendoorn, J. A. *Appl. Catal., B* **2010**, *96*, 57–66.
260. Chheda, J. N.; Huber, G. W.; Dumesic, J. A. *Angew. Chem., Int. Ed.* **2007**, *46*, 7164–7183.
261. Haveren, J. v.; Scott, E. L.; Sanders, J. *Biofuels, Bioprod. Biorefin.* **2008**, *2*, 41–57.
262. Cherubini, F.; Jungmeier, G.; Wellisch, M.; Willke, T.; Skiadas, I.; Van Ree, R.; de Jong, E. *Biofuels, Bioprod. Biorefin.* **2009**, *3*, 534–546.
263. Zakzeski, J.; Bruijnincx, P. C. A.; Jongerius, A. L.; Weckhuysen, B. M. *Chem. Rev.* **2010**, *110*, 3552–3599.
264. Brown, R. C., Ed. *Thermochemical Processing of Biomass: Conversion into Fuels, Chemicals and Power*, 1st ed.; Wiley Series in Renewable Resources; Wiley: Chichester, United Kingdom, 2011; pp 1−330.
265. Huber, G. W.; Dumesic, J. A. *Catal. Today* **2006**, *111*, 119–132.
266. Kunkes, E. L.; Simonetti, D. A.; West, R. M.; Serrano-Ruiz, J. C.; Gartner, C. A.; Dumesic, J. A. *Science* **2008**, *322*, 417–421.
267. Tijmensen, M. J. A.; Faaij, A. P. C.; Hamelinck, C. N.; van Hardeveld, M. R. M. *Biomass Bioenergy* **2002**, *23*, 129–152.

268. Subramani, V.; Gangwal, S. K. *Energy Fuels* **2008**, *22*, 814–839.
269. Swain, P. K.; Das, L. M.; Naik, S. N. *Renewable Sustainable Energy Rev.* **2011**, *15*, 4917–4933.
270. Luque, R.; de la Osa, A. R.; Campelo, J. M.; Romero, A. A.; Valverde, J. L.; Sanchez, P. *Energy Environ. Sci.* **2012**, *5*, 5186–5202.
271. Bridgwater, A. V. *Environ. Prog. Sustainable Energy* **2012**, *31*, 261–268.
272. Mortensen, P. M.; Grunwaldt, J. D.; Jensen, P. A.; Knudsen, K. G.; Jensen, A. D. *Appl. Catal., A* **2011**, *407*, 1–19.
273. Zhao, C.; Kou, Y.; Lemonidou, A. A.; Li, X.; Lercher, J. A. *Angew. Chem., Int. Ed.* **2009**, *48*, 3987–3990.
274. Bulushev, D. A.; Ross, J. R. H. *Catal. Today* **2011**, *171*, 1–13.
275. Vispute, T. P.; Zhang, H. Y.; Sanna, A.; Xiao, R.; Huber, G. W. *Science* **2010**, *330*, 1222–1227.
276. Zorin, V. V.; Petukhova, N. I.; Shakhmaev, R. N. *Russ. J. Gen. Chem.* **2012**, *82*, 1013–1026.
277. Clomburg, J. M.; Gonzalez, R. *Trends Biotechnol.* **2013**, *31*, 20–28.
278. Soares, R. R.; Simonetti, D. A.; Dumesic, J. A. *Angew. Chem., Int. Ed.* **2006**, *45*, 3982–3985.
279. Rahmat, N.; Abdullah, A. Z.; Mohamed, A. R. *Renewable Sustainable Energy Rev.* **2010**, *14*, 987–1000.
280. Spath, P. L.; Dayton, D. C. *Preliminary Screening - Technical and Economic Assessment of Synthesis Gas to Fuels and Chemicals with Emphasis on the Potential for Biomass-Derived Syngas*; Technical Report NREL/TP-510-34929; National Renewable Energy Laboratory: Golden, CO, 2003; pp 1−160.
281. Wender, I. *Fuel Process. Technol.* **1996**, *48*, 189–297.
282. Metzger, J. O.; Bornscheuer, U. *Appl. Microbiol. Biotechnol.* **2006**, *71*, 13–22.
283. Biermann, U.; Bornscheuer, U.; Meier, M. A. R.; Metzger, J. O.; Schäfer, H. J. *Angew. Chem., Int. Ed.* **2011**, *50*, 3854–3871.
284. Foley, P.; Kermanshahi pour, A.; Beach, E. S.; Zimmerman, J. B. *Chem. Soc. Rev.* **2012**, *41*, 1499–1518.
285. Mutlu, H.; Meier, M. A. R. *Eur. J. Lipid Sci. Technol.* **2010**, *112*, 10–30.
286. Pandey, M. P.; Kim, C. S. *Chem. Eng. Technol.* **2011**, *34*, 29–41.
287. Roberts, V. M.; Stein, V.; Reiner, T.; Lemonidou, A.; Li, X. B.; Lercher, J. A. *Chem. − Eur. J.* **2011**, *17*, 5939–5948.
288. Ma, Z. Q.; Troussard, E.; van Bokhoven, J. A. *Appl. Catal., A* **2012**, *423*, 130–136.
289. Modern Shale Gas Development in the United States - A Primer. (NETL: Energy in the Environment-Initiatives 2004-09). April 2009. http://www.netl.doe.gov/technologies/oil-gas/publications/EPreports/Shale_Gas_Primer_2009.pdf (accessed Jan. 5, 2013).
290. Shale Gas: Applying Technology to Solve America's Energy Challenges (NETL/Technologies/Oil and Natural Gas Supply/Publications). March 2011. http://www.netl.doe.gov/technologies/oil-gas/publications/brochures/Shale_Gas_March_2011.pdf (accessed Jan. 5, 2013).

In Novel Materials for Catalysis and Fuels Processing; Bravo-Suárez, J., et al.;
ACS Symposium Series; American Chemical Society: Washington, DC, 2013.

291. US Energy Information Administration - Analysis & Projections (Annual Energy Outlook). Report Number: DOE/EIA-0383ER(2013). Release Date: Dec. 5, 2012. http://www.eia.gov/forecasts/aeo/er/pdf/0383er(2013).pdf (accessed Jan. 5, 2013).
292. US Energy Information Administration - Total Energy (Annual Energy Review 2011). Report Number: DOE/EIA-0384(2011). Release Date: Sep. 27, 2012. http://www.eia.gov/totalenergy/data/annual/pdf/aer.pdf (accessed Jan. 5, 2013).
293. US Energy Information Administration - Analysis & Projections (Annual Energy Outlook). Report Number: DOE/EIA-0383(2012). Release Date: June 25, 2012. http://www.eia.gov/forecasts/aeo/pdf/0383(2012).pdf (accessed Jan. 5, 2013).
294. Bullin, K. A.; Krouskop, P. E. *Oil Gas J.* **2009**, *107*, 50–55.
295. Aasberg-Petersen, K.; Dybkjær, I.; Ovesen, C. V.; Schjødt, N. C.; Sehested, J.; Thomsen, S. G. *J. Nat. Gas Sci. Eng.* **2011**, *3*, 423–459.
296. Lunsford, J. H. *Catal. Today* **2000**, *63*, 165–174.
297. Holmen, A. *Catal. Today* **2009**, *142*, 2–8.
298. Lange, J.-P. *Ind. Eng. Chem. Res.* **1997**, *36*, 4282–4290.
299. Aasberg-Petersen, K.; Bak Hansen, J. H.; Christensen, T. S.; Dybkjaer, I.; Christensen, P. S.; Stub Nielsen, C.; Winter Madsen, S. E. L.; Rostrup-Nielsen, J. R. *Appl. Catal., A* **2001**, *221*, 379–387.
300. Alvarez-Galvan, M. C.; Mota, N.; Ojeda, M.; Rojas, S.; Navarro, R. M.; Fierro, J. L. G. *Catal. Today* **2011**, *171*, 15–23.
301. Abbas, H. F.; Wan Daud, W. M. A. *Int. J. Hydrogen Energy* **2010**, *35*, 1160–1190.
302. Otsuka, K.; Wang, Y. *Appl. Catal., A* **2001**, *222*, 145–161.
303. Takanabe, K. *J. Jpn. Pet. Inst.* **2012**, *55*, 1–12.
304. Hu, Y. H.; Ruckenstein, E. *Adv. Catal.* **2004**, *48*, 297–345.
305. Christian Enger, B.; Lødeng, R.; Holmen, A. *Appl. Catal., A* **2008**, *346*, 1–27.
306. Hill, R. J.; Jarvie, D. M.; Zumberge, J.; Henry, M.; Pollastro, R. M. *AAPG Bull.* **2007**, *91*, 445–473.
307. Ross, J. R. H.; van Keulen, A. N. J.; Hegarty, M. E. S.; Seshan, K. *Catal. Today* **1996**, *30*, 193–199.
308. Thomas, J., Zamaraev, K. I., Eds. *Perspectives in Catalysis*; IUPAC Chemistry for the 21st Century; Blackwell Scientific Publications: Oxford, Great Britain, 1992; pp 1−492.
309. Hegedus, L. L.; Rutherford, A., Eds. *Catalyst Design: Progress and Perspectives*; Wiley: New York, NY, 1987; pp 1−288.
310. Gembicki, S. A., Ed. *Catalytic Process Technology - Committe on Catalytic Process Technology for Manufacturing Applications*; The National Academies Press: Washington, DC, 2000; pp 1−57.
311. Bell, A. T.; Gates, B. C.; Ray, D. *Basic Research Needs: Catalysis for Energy*; Technical Report PNNL-17214; Pacific Northwest National Laboratory: Richland, WA, August 6-8, 2007; pp 1−254.

312. Hemminger, J.; Fleming, G.; Ratner, M. *Directing Matter and Energy: Five Challenges for Science and the Imagination*; Technical Report US Department of Energy - Basic Energy Sciences: Dec. 20, 2007; pp 1−134.
313. Jackson, N. B., Nørskov, J. K., Eds. *Catalysis for Energy: Fundamental Science and Long-Term Impacts of the U.S. Department of Energy Basic Energy Science Catalysis Science Program*; The National Academies Press: Washington, D.C., 2009; pp 1−128.
314. Friedman, D.; Masciangioli, T.; Olson, S. *The Role of the Chemical Sciences in Finding Alternatives to Critical Resources: A Workshop Summary*; The National Academies Press: Washington, D.C., 2012; pp 1−59.
315. Maeda, K.; Domen, K. *J. Phys. Chem. Lett.* **2010**, *1*, 2655–2661.
316. Tong, H.; Ouyang, S.; Bi, Y.; Umezawa, N.; Oshikiri, M.; Ye, J. *Adv. Mater. (Weinheim, Ger.)* **2012**, *24*, 229–251.
317. Holladay, J. D.; Hu, J.; King, D. L.; Wang, Y. *Catal. Today* **2009**, *139*, 244–260.
318. Gupta, R. B., Ed. *Hydrogen Fuel: Production, Transport, and Storage*; CRC Press: Boca Raton, FL, 2009; pp 1−611.
319. Hirscher, M., Ed. *Handbook of Hydrogen Storage - New Materials for Future Energy Storage*; Wiley-VCH: Weinheim, Germany, 2010; pp 1−353.
320. Arakawa, H.; Aresta, M.; Armor, J. N.; Barteau, M. A.; Beckman, E. J.; Bell, A. T.; Bercaw, J. E.; Creutz, C.; Dinjus, E.; Dixon, D. A.; Domen, K.; DuBois, D. L.; Eckert, J.; Fujita, E.; Gibson, D. H.; Goddard, W. A.; Goodman, D. W.; Keller, J.; Kubas, G. J.; Kung, H. H.; Lyons, J. E.; Manzer, L. E.; Marks, T. J.; Morokuma, K.; Nicholas, K. M.; Periana, R.; Que, L.; Rostrup-Nielson, J.; Sachtler, W. M. H.; Schmidt, L. D.; Sen, A.; Somorjai, G. A.; Stair, P. C.; Stults, B. R.; Tumas, W. *Chem. Rev.* **2001**, *101*, 953–996.
321. Aresta, M.; Dibenedetto, A. *Dalton Trans.* **2007**, 2975–2992.
322. Aresta, M., Ed. *Carbon Dioxide as Chemical Feedstock*; Wiley-VCH: Weinheim, Germany, 2010; pp 1−394.
323. Somorjai, G. A.; Park, J. *Top. Catal.* **2008**, *49*, 126–135.
324. Semagina, N.; Kiwi-Minsker, L. *Catal Rev.: Sci. Eng.* **2009**, *51*, 147–217.
325. Zaera, F. *J. Phys. Chem. Lett.* **2010**, *1*, 621–627.
326. Thomas, J.; Raja, R. *Top. Catal.* **2006**, *40*, 3–17.
327. Thomas, J. M. *J. Chem. Phys.* **2008**, *128*, 182502/1–182502/19.
328. Dal Santo, V.; Guidotti, M.; Psaro, R.; Marchese, L.; Carniato, F.; Bisio, C. *Proc. R. Soc. A* **2012**, *468*, 1904–1926.
329. Jiang, J. X.; Yu, J. H.; Corma, A. *Angew. Chem., Int. Ed.* **2010**, *49*, 3120–3145.
330. Perez-Ramirez, J.; Christensen, C. H.; Egeblad, K.; Christensen, C. H.; Groen, J. C. *Chem. Soc. Rev.* **2008**, *37*, 2530–2542.
331. Hua, Z. L.; Zhou, J.; Shi, J. L. *Chem. Commun. (Cambridge, U. K.)* **2011**, *47*, 10536–10547.
332. Moller, K.; Bein, T. *Chem. Soc. Rev.* **2013**, *42*, 3689–3707.
333. Li, Y.; Liu, Q.; Shen, W. *Dalton Trans.* **2011**, *40*, 5811–5826.
334. An, K.; Somorjai, G. A. *ChemCatChem* **2012**, *4*, 1512–1524.
335. van Bokhoven, J. A. *ChemCatChem* **2009**, *1*, 363–364.

In Novel Materials for Catalysis and Fuels Processing; Bravo-Suárez, J., et al.;
ACS Symposium Series; American Chemical Society: Washington, DC, 2013.

336. Zhou, K.; Li, Y. *Angew. Chem., Int. Ed.* **2012**, *51*, 602–613.
337. Villa, A.; Campisi, S.; Giordano, C.; Otte, K.; Prati, L. *ACS Catal.* **2012**, *2*, 1377–1380.
338. Robertson, I. M.; Schuh, C. A.; Vetrano, J. S.; Browning, N. D.; Field, D. P.; Jensen, D. J.; Miller, M. K.; Baker, I.; Dunand, D. C.; Dunin-Borkowski, R.; Kabius, B.; Kelly, T.; Lozano-Perez, S.; Misra, A.; Rohrer, G. S.; Rollett, A. D.; Taheri, M. L.; Thompson, G. B.; Uchic, M.; Wang, X. L.; Was, G. *J. Mater. Res.* **2011**, *26*, 1341–1383.
339. Thomas, J. M. *Angew. Chem., Int. Ed.* **1999**, *38*, 3588–3628.
340. Delmon, B. Catalysts for New Uses: Needed Preparation Advances. In *Catalyst Preparation: Science and Engineering*; Regalbuto, J., Ed.; CRC Press: Boca Raton, FL, 2006; pp 449−463.
341. Pennycook, S. J.; Chisholm, M. F.; Lupini, A. R.; Varela, M.; Borisevich, A. Y.; Oxley, M. P.; Luo, W. D.; van Benthem, K.; Oh, S.-H.; Sales, D. L.; Molina, S. I.; García-Barriocanal, J.; Leon, C.; Santamaría, J.; Rashkeev, S. N.; Pantelides, S. T. *Philos. Trans. R. Soc. A* **2009**, *367*, 3709–3733.
342. Ortalan, V.; Uzun, A.; Gates, B. C.; Browning, N. D. *Nat. Nanotechnol.* **2010**, *5*, 506–510.
343. Berger, R. J.; Kapteijn, F.; Moulijn, J. A.; Marin, G. B.; de Wilde, J.; Olea, M.; Chen, D.; Holmen, A.; Lietti, L.; Tronconi, E.; Schuurman, Y. *Appl. Catal., A* **2008**, *342*, 3–28.
344. Boudart, M. A Catalyst is a Resilient Self-Assembly in Space and Time. In *Combinatorial Catalysis and High Throughput Catalyst Design and Testing*; NATO Science Series C: Mathematical and Physical Sciences 560; Derouane, E. G., Lemos, F., Corma, A., Ribeiro, F. R., Eds.; Kluwer: Dordrecht, The Netherlands, 2000; pp 459−465.
345. van Santen, R. A. *Acc. Chem. Res.* **2009**, *42*, 57–66.
346. Murzin, D. Y. *J. Catal.* **2010**, *276*, 85–91.
347. Murzin, D. Y.; Simakova, I. L. *Catal. Lett.* **2011**, *141*, 982–986.
348. Murzin, D. Y. *Catal. Sci. Technol.* **2011**, *1*, 380–384.
349. Mhadeshwar, A. B.; Kitchin, J. R.; Barteau, M. A.; Vlachos, D. G. *Catal. Lett.* **2004**, *96*, 13–22.
350. İnoğlu, N.; Kitchin, J. R. *Phys. Rev. B* **2010**, *82*, 045414.
351. Maestri, M.; Reuter, K. *Angew. Chem., Int. Ed.* **2011**, *50*, 1194–1197.
352. Wu, C.; Schmidt, D. J.; Wolverton, C.; Schneider, W. F. *J. Catal.* **2012**, *286*, 88–94.
353. Thybaut, J. W.; Sun, J.; Olivier, L.; Van Veen, A. C.; Mirodatos, C.; Marin, G. B. *Catal. Today* **2011**, *159*, 29–36.
354. Murzin, D. Y. *Ind. Eng. Chem. Res.* **2005**, *44*, 1688–1697.
355. Resasco, D.; Miranda, R.; Iglesia, E. *Catal. Today* **1992**, *15*, 339–348.
356. Armor, J. N. *Appl. Catal., A* **2005**, *282*, 1–4.
357. Armor, J. N. *Catal. Today* **2011**, *178*, 8–11.
358. Sugiyama, H.; Fischer, U.; Hungerbühler, K.; Hirao, M. *AIChE J.* **2008**, *54*, 1037–1053.
359. Diwekar, U.; Shastri, Y. *Clean Technol. Environ. Policy* **2011**, *13*, 227–240.
360. Patel, A. D.; Meesters, K.; den Uil, H.; de Jong, E.; Blok, K.; Patel, M. K. *Energy Environ. Sci.* **2012**, *5*, 8430–8444.

In Novel Materials for Catalysis and Fuels Processing; Bravo-Suárez, J., et al.;
ACS Symposium Series; American Chemical Society: Washington, DC, 2013.

361. Jacquemin, L.; Pontalier, P.-Y.; Sablayrolles, C. *Int. J. Life Cycle Assess.* **2012**, *17*, 1028–1041.
362. Ghanta, M.; Ruddy, T.; Fahey, D.; Busch, D.; Subramaniam, B. *Ind. Eng. Chem. Res.* **2013**, *52*, 18–29.
363. Holman, P. A.; Shonnard, D. R.; Holles, J. H. *Ind. Eng. Chem. Res.* **2009**, *48*, 6668–6674.
364. van Santen, R. A.; Sautet, P. Conclusion: Challenges to Computational Catalysis. In *Computational Methods in Catalysis and Materials Science - An Introduction for Scientists and Engineers*; van Santen, R. A.; Sautet, P., Eds.; Wiley-VCH: Weinheim, Germany, 2009; pp 441−446.
365. Bligaard, T.; Nørskov, J. K. Heterogeneous Catalysis. In *Chemical Bonding at Surfaces and Interfaces*; Nilsson, A.; Pettersson, L. G. M.; Nørskov, J. K., Eds.; Elsevier: Amsterdam, The Netherlands, 2008; pp 255−321.
366. Ferguson, G.; Mehmood, F.; Rankin, R.; Greeley, J.; Vajda, S.; Curtiss, L. *Top. Catal.* **2012**, *55*, 353–365.
367. Wachs, I. E.; Routray, K. *ACS Catal.* **2012**, *2*, 1235–1246.
368. M. M. J. Treacy; Foster, M. D.; Rivin, I. Towards a Catalogue of Designer Zeolites. In *Turning Points in Solid-State, Materials and Surface Science*; Harris, K. D. M., Edwards, P. P., Eds.; Royal Society of Chemistry: Cambridge, United Kingdom, 2008; pp 208−220.
369. Almeida-Paz, F. A.; Majda, D.; Bell, R. G.; Klinowski, J. Discovering New Crystal Architectures. In *Turning Points in Solid-State, Materials and Surface Science*; Harris, K. D. M., Edwards, P. P., Eds.; Royal Society of Chemistry: Cambridge, United Kingdom, 2008; pp 221−238.
370. Woodley, S. M.; Catlow, R. *Nat. Mater.* **2008**, *7*, 937–946.
371. Deem, M. W.; Pophale, R.; Cheeseman, P. A.; Earl, D. J. *J. Phys. Chem. C* **2009**, *113*, 21353–21360.
372. Catlow, C. R. A.; Coombes, D. S.; Lewis, D. W.; Pereira, J. C. G. *Chem. Mater.* **1998**, *10*, 3249–3265.
373. Catlow, C. R. A.; Coombes, D. S.; Slater, B.; Lewis, D. W.; Pereira, J. C. G. Modeling Nucleation and Growth in Zeolites (Chapter 4). In *Handbook of Zeolite Science and Technology*; CRC Press: 2003; pp 1−38. DOI: 10.1201/9780203911167.ch4.
374. Auerbach, S. M.; Ford, M. H.; Monson, P. A. *Curr. Opin. Colloid Interface Sci.* **2005**, *10*, 220–225.
375. Verstraelen, T.; Szyja, B.; Lesthaeghe, D.; Declerck, R.; Speybroeck, V.; Waroquier, M.; Jansen, A. J.; Aerts, A.; Follens, L. A.; Martens, J.; Kirschhock, C. A.; van Santen, R. A. *Top. Catal.* **2009**, *52*, 1261–1271.
376. Catlow, C. R. A.; Bromley, S. T.; Hamad, S.; Mora-Fonz, M.; Sokol, A. A.; Woodley, S. M. *Phys. Chem. Chem. Phys.* **2010**, *12*, 786–811.
377. Bell, A. T. *Science* **2003**, *299*, 1688–1691.
378. Basset, J.-M.; Candy, J.-P.; Choplin, A.; Didillon, B.; Quignard, F.; Theolier, A. Surface Organometallic Chemistry on Oxides, on Zeolites and on Metals. In *Perspectives in Catalysis*; Thomas, J. M., Zamaraev, K. I., Eds.; Blackwell Scientific Publications: London, Great Britain, 1992; pp 125−145.
379. Guzman, J.; Gates, B. C. *Dalton Trans.* **2003**, 3303–3318.

380. Basset, J.-M.; Candy, J.-P.; Copéret, C.; Lefebvre, F.; Quadrelli, E. A. Design, Bulding, Charaerization and Performance at the Nanometric Scale of Heterogeneous Catalysts. In *Nanotechnology in Catalysis 2*; Nanostructure Science and Technology; Zhou, B., Hermans, S., Somorjai, G. A., Eds.; Springer: New York, NY, 2004; pp 447−466.
381. Kulkarni, A.; Lobo-Lapidus, R. J.; Gates, B. C. *Chem. Commun. (Cambridge, U. K.)* **2010**, *46*, 5997–6015.
382. Guzman, J. Well-Defined Metallic and Bimetallic Clusters Supported on Oxides and Zeolites. In *Model Systems in Catalysis: Single Crystals to Supported Enzyme Mimics*; Rioux, R. M., Ed.; Springer: New York, NY, 2010; pp 415−439.
383. Raja, R.; Thomas, J. M. Single-Site Heterogeneous Catalysts: Innovations, Advantages, and Future Potential in Green Chemistry and Sustainable Technology. In *Model Systems in Catalysis: Single Crystals to Supported Enzyme Mimics*; Rioux, R. M., Ed.; Springer: New York, NY, 2010; pp 457−474.
384. An, K.; Alayoglu, S.; Ewers, T.; Somorjai, G. A. *J. Colloid Interface Sci.* **2012**, *373*, 1–13.
385. Ozkan, U. S. *Design of Heterogeneous Catalysts: New Approaches based on Synthesis Characterization and Modeling*; Wiley-VCH: Weinheim, Germany, 2009; pp 1−322.
386. Hagemeyer, A.; Strasser, P.; Volpe, A. F., Jr. *High-Throughput Screening in Heterogeneous Catalysis*; Wiley-VCH: Weinheim, Germany, 2004; pp 1−319.
387. Cybulski, A., Moulijn, J. A., Stankiewicz, A., Eds. *Novel Concepts in Catalysis and Chemical Reactors: Improving the Efficiency for the Future*; Wiley-VCH: Weinheim, Germany, 2010; pp 1−372.
388. van Santen, R. A.; Sautet, P. *Computational Methods in Catalysis and Materials Science - An Introduction for Scientists and Engineers*; Wiley-VCH: Weinheim, Germany, 2009; pp 1−455.
389. Nilsson, A.; Pettersson, L. G. M.; Nørskov, J. K., Eds. *Chemical Bonding at Surfaces and Interfaces*; Elsevier: Amsterdam, The Netherlands, 2008; pp 1−520.
390. Centi, G.; van Santen, R. A. *Catalysis for Renewables: From Feedstock to Energy Production*; Wiley-VCH: Weinheim, Germany, 2007; pp 1−423.
391. Barbaro, P.; Bianchini, C., Eds. *Catalysis for Sustainable Energy Production*; Wiley-VCH: Weinheim, Germany, 2009; pp 1−452.
392. Guczi, L. S.; Erdőhelyi, A. *Catalysis for Alternative Energy Generation*; Springer: New York, NY, 2012; pp 1−536.

Chapter 2

Computational Studies of Structure and Catalytic Activity of Vanadia for Propane Oxidative Dehydrogenation

Lei Cheng[1] and Larry A. Curtiss[1,2,*]

[1]Materials Science Division, Argonne National Laboratory, 9700 S. Cass Avenue, Argonne, Illinois 60439, USA
[2]Center for Nanoscale Materials, Argonne National Laboratory, 9700 S. Cass Avenue, Argonne, Illinois 60439, USA
[*]E-mail: curtiss@anl.gov

Understanding catalysis at a molecular level is the key to improving catalytic activity and the rational design of the next generation of catalysts. Despite the development of new surface science research techniques, characterization of surface catalytic sites still remain challenging due to the complexities of catalytic surfaces. Computational chemistry provides reaction studies at the molecular level and has become a very powerful tool for investigating catalysis. In this chapter, we review computational studies of supported vanadium oxide as a catalyst for the propane oxidative dehydrogenation reaction. The determination of the structure of active catalytic sites, elucidation of reaction mechanisms, and structure-activity relationships will be reviewed.

Introduction

The past decade has witnessed increasing numbers of applications of computational chemistry in catalysis research. Computational methods have been widely used for detailed mechanistic understanding of catalytic reactions, and more importantly, for the design of catalysts. One highlight is the computational screening of transition metal catalysts as a function of surface structure and composition. This technique has been successfully implemented and broadly used (*1*, *2*). Besides "bulk" properties such as composition and crystal surfaces,

In Novel Materials for Catalysis and Fuels Processing; Bravo-Suárez, J., et al.;
ACS Symposium Series; American Chemical Society: Washington, DC, 2013.

the local molecular structure of the catalytic site can also play an important role in affecting its activity, especially for catalytic systems that cannot be represented by extended surfaces. To establish such a structure-activity relationship is a very challenging task and has been a long-standing goal of catalysis science. With recent advances in analytical techniques and computer modeling, improved characterization and reactivity studies of catalysts can be achieved. These techniques can provide invaluable insights and guidelines for rational design of more efficient catalysts. Among various computational methods, Density Functional Theory (DFT) is the most commonly used methodology to determine catalyst structure, interpret spectroscopic data, and to investigate reaction networks and mechanisms. The information from such calculations can lead to better understanding of the catalysts, such as the nature of the active center and its catalytic reactivity.

Here, we review the computational studies of supported vanadium oxide (VO_x) clusters for the propane oxidative dehydrogenation (ODH) reaction as an example of how computational chemistry can be a powerful tool for catalyst study and design. Supported vanadium oxide catalysts represent a very important class of oxide-on-oxide catalysts that are very challenging to study. Recently, supported vanadia catalysts have attracted special attention due to their exceptional activity and selectivity for the oxidative dehydrogenation of light alkanes to alkenes, an important class of reaction (*3*, *4*). These catalysts are also very intriguing fundamentally due to the highly dispersed nature of the catalytic sites. Computational chemistry has played an essential role in elucidating the nature of the VO_x catalytic site, as well as its relationship to catalytic activity.

In this review, we first focus on computational studies of the structure determination of supported VO_x clusters. Then, the reaction mechanisms for propane ODH on these catalysts will be reviewed. Finally, the structure-activity relationships and their implications for design of the catalyst will be discussed.

Structures of Supported VO_x

Determining the molecular structure of the catalytic active site is a key step towards understanding of the catalytic working mechanism. For supported oxide catalysts with very low surface coverage, such as highly dispersed VO_x catalysts, the quantity of the active component is too small for measurements by diffraction methods. Thus, experimentally, a combination of spectroscopic techniques is often used to investigate the atomic level structure of the catalytic sites. Computational chemistry can help to derive the molecular structure of a solid catalyst active site in combination with spectroscopic studies by calculating vibrational frequencies of prospective structures and then comparing them with experimental spectral data to assign the bands. Computational chemistry can also be used to calculate formation free energies of different species and comparing their stabilities to determine structures that are most likely to exist on a support surface. A number of plausible structures for supported VO_x clusters have been proposed based on a variety of physical measurements, as well as computational

In Novel Materials for Catalysis and Fuels Processing; Bravo-Suárez, J., et al.;
ACS Symposium Series; American Chemical Society: Washington, DC, 2013.

studies. Here, we review computational studies of low coverage supported vanadia structures on four common support oxides SiO_2, Al_2O_3, TiO_2, as well as the reducible support CeO_2. Note we only discuss structures with V in fully oxidized state because these are the structures that are active for the ODH reaction.

VO_x on SiO_2, Al_2O_3, and TiO_2

Tetrahedral Vanadia Structure

The most commonly accepted supported V_2O_5 structure in the submonolayer regime has vanadium coordinated in a tetrahedral geometry with one terminal vanadyl oxygen (V=O) and three bridging oxygen atoms connecting to cations from either the support (V−O−S) or the neighboring V_2O_5 unit (V−O−V), as the monomeric and dimeric structures in Figure 1 illustrate. Computational studies have played an important role in reaching this conclusion. The vibrational frequencies of vanadia monomers and dimers supported on silica and alumina were calculated by Sauer and co-workers using the density functional theory B-P86 method with cluster models to help interpret experimental IR and Raman spectra (*5*). With the comparative assignment of the vibrational spectra, the band detected from ~1025 to ~1045 cm^{-1} for the alumina-supported VO_x was found to correspond to the vibrations of the vanadyl groups. The vanadyl vibrations are independent from the vibrations of the V−O−Al observed at ~941 cm^{-1}. However, the silica-supported VO_x calculations showed that the vanadyl vibration (1046 cm^{-1}) is coupled to the support. Thus, the band above 1000 cm^{-1} cannot be assigned to vanadyl species exclusively, as had often been done in the literature. The V−O−V vibrations for both systems were found to correspond to a band feature observed at 700 cm^{-1}, instead of 950 cm^{-1} as discussed in previous literature. These results suggest that using the 950 cm^{-1} band as a signature of V−O−V vibrations to assign properties of the "polymeric" vanadia species" may not be correct. A subsequent study of silica supported vanadia using DFT and embedded cluster models again showed significant couplings between bulk phonons and motions of the supported vanadium oxide species (*6*). As a result of the coupling, distinguishing certain structures by vibrational spectroscopy may be difficult.

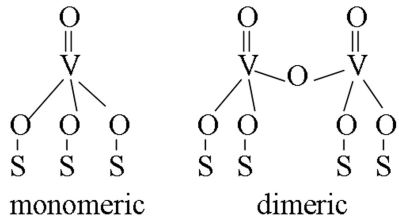

Figure 1. Illustration of the tetrahedral monomeric and dimeric VO_x structures.

In Novel Materials for Catalysis and Fuels Processing; Bravo-Suárez, J., et al.;
ACS Symposium Series; American Chemical Society: Washington, DC, 2013.

The tetrahedral structure of supported V_2O_5 is in accordance with basic chemical intuition and agrees with results of a variety of physical measurements. It was also proven by computational studies to be a feasible structural basis for V_2O_5 supported on other oxides such as Al_2O_3 and TiO_2 (*7–9*).

Partially Hydroxylated Vanadia Structures and Their Coexistence on a Surface

The grafting reaction of the vanadium precursor $OV(OH)_3$ on a hydroxylated support surface $(S{-}OH)_n$ can be envisioned as:

$$OV(OH)_3 + (S{-}OH)_n \rightarrow OV(OH)_{3-n}(O{-}S)_n + nH_2O,$$

where S represents a cation on the support. Depending on the degree of dehydration during this process, the hydroxyl groups can remain on the VO_x structures (n <3) during the preparation process, resulting in partially hydroxylated structures. A partially hydroxylated V_2O_5 structure can also result from the hydrolysis of the bond between the support and the VO_x species (V−O−S) (*10–12*), either under hydration conditions, or during reactions in which water is produced (for example, propane ODH reaction). The V−OH band has been observed by IR and Raman spectroscopies (*10*, *12–22*), under both hydration and dehydration conditions. These are all evidence of partially hydroxylated VO_x structures.

In reality, a catalytic surface can be inhomogeneous. This complicates the structural studies and probably explains why many early attempts to characterize the surface structure of supported VO_x species using "bulk techniques" such as EXAFS, XANES, and ^{51}V MAS NMR led to conflicting results (*23–28*). In a combined experimental and theoretical study of structures of monomeric vanadium oxide on a θ-alumina support (*29*), the B3LYP DFT method was used to calculate relative energies of different monomeric VO_x structures that can form on the surface from the grafting reaction of a vanadium precursor on the hydroxylated support, as discussed above. Using slightly different excitation wavelengths in the preresonance region of Raman spectroscopy, three distinct V=O vibrations were identified, indicating multiple surface species coexisting under reaction conditions. These three Raman frequencies match the V=O stretching frequencies of the three most stable structures calculated by DFT as illustrated in Figures 2a–c. Furthermore, the calculated free energies for the three structures as a function of temperature suggest that all three could exist on the surface and the most stable structure is the tridentate structure (Figure 2a) at the temperature of 823 K, in agreement with experiment. Different monomeric V_2O_5 species were also found to coexist on silica surface by both DFT calculations (*30*) and multiwavelength Raman (*31*). The presence of multiple V_2O_5 structures on TiO_2 anatase was also predicted by computational studies (*32–34*). The vanadia structures predicted on the SiO_2 (*30*) and TiO_2 (*32*) supports are shown in Figures 2d–f and 2g–i, respectively.

In Novel Materials for Catalysis and Fuels Processing; Bravo-Suárez, J., et al.;
ACS Symposium Series; American Chemical Society: Washington, DC, 2013.

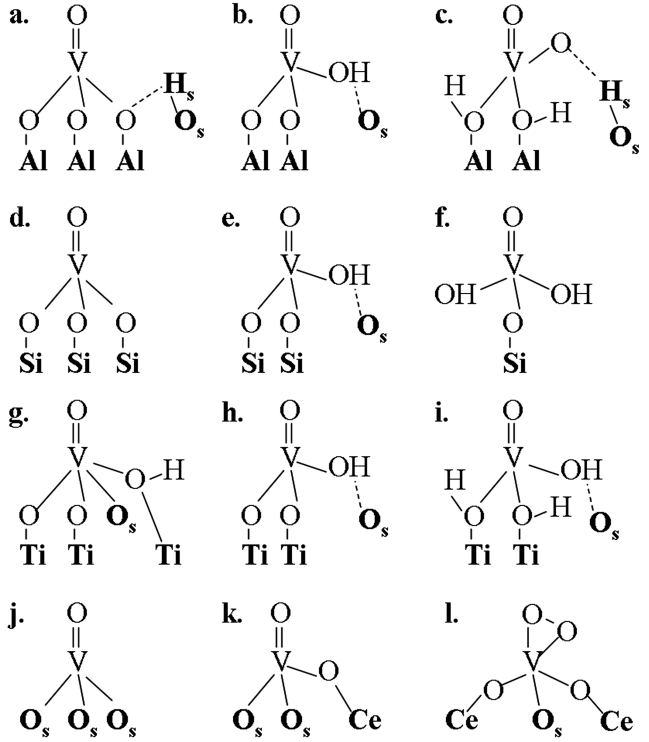

Figure 2. Illustrations of monomeric VO_x structures on different oxide surfaces. a. tridentate, b. bidentate, and c. molecular structures on dehydrated θ-alumina as reported in Ref. (29); d. tri-grafted, e. di-grafted, and f. mono-grafted structures on silica as reported in Ref. (30); g. tridentate, h. bidentate, and i. molecular structures on titania anatase as reported in Ref. (32); j. VO, k. VO_2, and l. VO_4 structures on ceria as reported in Ref. (37). Atoms on the support oxides are shown in bold font. Hydrogen and oxygen atoms on the support are also labeled with subscript "s" for distinction.

Multiple structures can coexist on a support surface if they are all thermodynamically stable under the specific experimental conditions. The relative stability and population of these species are highly sensitive to conditions such as temperature, pressure, and degree of hydration. In a theoretical thermodynamic analysis study of vanadia structures on anatase (001) (*33*), it was shown that the catalyst surface is very complicated with many different structures that can coexist or transform one into another with slight changes of temperature and pressure conditions. The effect of hydration and temperature on vanadia structures on an anatase (001) surface was also investigated by the ab initio molecular dynamics method (*34*). The tetrahedral structure of the VO_x monomer was found to be stable only under severe dehydration conditions, while hydroxylated species are expected to be present even at low water content. More interestingly, through a

In Novel Materials for Catalysis and Fuels Processing; Bravo-Suárez, J., et al.;
ACS Symposium Series; American Chemical Society: Washington, DC, 2013.

quick hydrogen transfer mechanism, different surface species can interconvert very fast (*8*, *34*). Thus, it is very likely that multiple hydroxylated monomeric VO_x species are present on surfaces, with the H distributing dynamically between the vanadia and the support anatase surface instead of remaining on one position. Monomeric and dimeric structures can also interconvert not only as a function of V-coverage (*35*), but also as a result of hydration/dehydration conditions (*34*).

VO_x on CeO_2

CeO_2 is much more easily reduced than SiO_2, Al_2O_3, and TiO_2. Thus, when vanadium oxide (VO_x) is deposited on CeO_2 with stoichiometrically not fully oxidized V (VO or VO_2), vanadium is always in the 5+ state, whereas the support gets reduced. This was first reported in a combined computational and experimental investigation (*36*), where VO monomers, trimers, and oligomers were found on a well defined CeO_2 (111) surface. Photoelectron spectroscopy and the DFT+D calculations showed that all V are in 5+ state and Ce atoms from the support were reduced from the 4+ to the 3+ state to accommodate the extra electron in their 4*f* orbitals. In more systematic theoretical studies of the VO_x monomer structures on CeO_2 (111) (*37*), it was found that under low O_2 pressure and at a large temperature range from 400 to 900 K, the most stable structure has a VO_2 composition, with the VO_2 coordinated to two O atoms of the support, resulting in a tetrahedral geometry (Figure 2k). When the temperature is under 400 K or over 900 K, the most stable VO_x composition changes to VO and VO_4 with structures shown in Figures 2j and 2l, respectively. These results also illustrated the importance of external conditions in controlling the structures of the catalytic sites, and thus the activity of a catalyst.

Reaction Mechanisms of Propane ODH by Supported VO_x

Mechanistic studies of a catalyst can provide a basis for the rational design of more efficient catalytic materials. Experimental and theoretical studies of propane ODH reaction by supported vanadia have generally been based on the Mars-van Krevelen mechanism (*38*).

To capture the basic chemistry of propane ODH reaction on supported vanadia, the reaction mechanism was first investigated computationally on pure vanadium oxide catalyst (*39–41*). Gilardoni et al. investigated the reaction of propane on cluster models of vanadium oxide using DFT (*40*). They found that the first step of the reaction is the hydrogen abstraction from a methylene group by a vanadyl group. The subsequent hydrogen abstraction from a methyl group corresponds to a barrier of 15 kcal/mol and this barrier is the highest on the reaction pathway. Using calculations of cluster and periodic slab models of vanadium oxide, Redfern et al. (*41*) found that the reaction involves large

In Novel Materials for Catalysis and Fuels Processing; Bravo-Suárez, J., et al.;
ACS Symposium Series; American Chemical Society: Washington, DC, 2013.

barriers on a singlet potential energy surface (PES). When a possible crossing to a triplet PES is considered, the barriers are lowered, indicating a potential energy curve crossing in the reaction path. The highest energy on the triplet PES at the B3LYP/6-31G(*) level of theory is 80 kcal/mol above the energy of the reactants, much higher than the 20–30 kcal/mol reported by experimental studies (*4*, *42–44*) and the 15 kcal/mol calculated by Gilardoni et al (*40*). Cheng et al. (*39*) investigated the reaction mechanism using a V_4O_{10} cluster model and the B3LYP method. They found that hydrogen abstraction from the methylene C−H bond by a vanadyl oxygen is rate-limiting for the overall reaction. This step corresponds to a diradical transition state with an open-shell electronic configuration. The barrier was calculated to be 23.9 kcal/mol, in agreement with the experimental value of 20–30 kcal/mol (*4*, *42–44*).

Supported vanadia structures have V–O–S bridging bonds that are not present on a pure vanadia. These bonds were suggested in a study (*45*) to be the active sites for propane ODH. Rozanska et al. (*46*) examined possible reaction mechanisms of propane ODH by SiO_2-supported vanadia using a cubic silsesquioxane cluster model with the B3LYP method. The first step of methylene hydrogen abstraction was calculated to be much more favorable by a vanadyl group than by a bridging V–O–Si group, thus it is most likely to only occur on vanadyl groups without the involvement of a V–O–S bond. As the energy profile in Figure 3 illustrates, the transition state is a diradical species with an open-shell singlet electronic configuration ($TS1_{OS}$). The vanadium at the catalytic site gets reduced and the intermediate diradical C_3H_7•---OH-V^{4+}• has two almost degenerate electronic states: the triplet ($Int1_T$) and the open-shell singlet ($Int1_{OS}$). Under the assumption that the number of propyl radicals in the gas phase is constant and the fraction of active sites that are in the reduced state is small, the expression for the rate equation for propene formation after simplification shows that the first hydrogen abstraction is the rate-determining step. After the first hydrogen abstraction, all reactions that occur at the same active site, as shown in Figure 3, proceed on the triplet potential energy surface because it is lower in energy. The second hydrogen abstraction may occur on either a vanadyl or a bridging oxygen site (V–O–S). However, the site at which this second H abstraction step occurs does not affect the overall kinetics of the reaction because it is not rate-limiting. The apparent activation barrier for the first hydrogen abstraction (rate-limiting) was predicted to be about 29 kcal/mol at 750 K, close to the experimental values reported in literature. The key mechanistic results for VO_x/SiO_2 reported in this work are in good agreement with the results by Cheng et al. (*39*) for pure vanadia. The same reaction mechanism was also reported for titania-supported vanadia by Cheng et al (*32*). In this work, the singlet and triplet minimum energy crossing point was located and the crossing was found to occur in the region of the diradical intermediate (Int1, Figure 3) where the two PESs are largely parallel. The energy of the $TS1_{OS}$ structure with either a triplet or closed-shell singlet configuration is much higher than that of the open-shell singlet, confirming that the first hydrogen abstraction indeed occurs most favorably on the open-shell singlet PES. These detailed mechanistic studies of crystal and supported V_2O_5 provide valuable insight for further activity studies of the catalysts with different structures or support.

In Novel Materials for Catalysis and Fuels Processing; Bravo-Suárez, J., et al.;
ACS Symposium Series; American Chemical Society: Washington, DC, 2013.

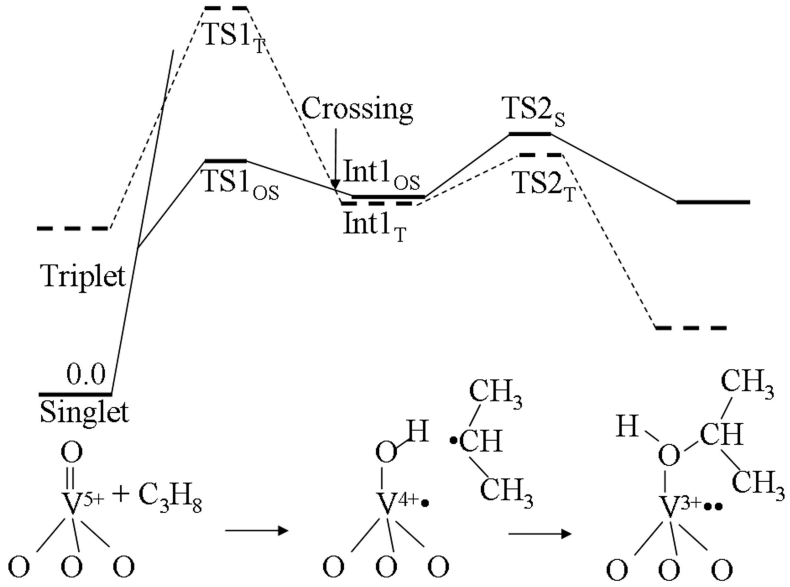

Figure 3. Illustration of the first hydrogen abstraction of a propane molecule and the isopropanol formation on the same vanadyl group of the supported vanadia catalyst. Both the singlet (solid line) and the triplet (dashed line) potential energy surfaces are shown.

Structure-Activity Relationships and Catalyst Design

Based on the conclusion that hydrogen abstraction is rate-limiting for the propane ODH reaction on supported vanadia, the hydrogenation energies of different vanadia surface species were calculated and used as the ODH reactivity descriptor to examine the support effect (*37*, *47*). The hydrogenation energies of the SiO_2-supported vanadia (Figure 2d structure) and the CeO_2-supported VO_2 (Figure 2k structure), the most stable structures at low O_2 pressure and temperature range of 400-900 K, were calculated to be +0.2 and −1.45 eV, respectively, indicating a much lower activity of the former for the ODH reaction. This is in good agreement with the experimental results that vanadia supported on ceria is more active for the ODH than on silica or alumina (*48–50*). CeO_2 is very easily reduced, therefore, upon hydrogenation of the supported VO_2 vanadyl oxygen, V remains in the 5+ oxidation state, whereas the ceria support gets reduced. This explains why the hydrogenation is much more favorable for the CeO_2-supported VO_2 than for the silica-supported vanadia. However, the hydrogenation of the supported VO_2 is 0.24 eV more favorable than that of the uncovered CeO_2 support, indicating an enhanced reactivity of the VO_2 on ceria support as compared to the bare support. Hence, there is a cooperative effect between the supported VO_2 and the CeO_2 support: the support enhances the reactivity of the vanadia by stabilizing the reaction intermediates that have reduced states (such as the C_3H_7•---OH-V^{4+}• that forms after the first hydrogen

In Novel Materials for Catalysis and Fuels Processing; Bravo-Suárez, J., et al.;
ACS Symposium Series; American Chemical Society: Washington, DC, 2013.

abstraction of propane); the vanadia in turn promotes the stabilizing effect of the support. Moreover, these results reveal that an effective stabilization of the reduced states of vanadium is important for improving the ODH activity of supported vanadia.

Kim et al. investigated the reactivities of different θ-alumina-supported vanadia monomer structures (*51*) that were indentified in an earlier study (*29*). The reducibility sequence for the three monomeric species (*29*, *51*) was deduced by following the changes in UV Raman and resonance Raman spectra of vanadia after reduction with H_2. The reaction pathways for H_2 reduction on the three structures were also investigated using DFT. The reduction on all three structures was found to involve the vanadyl bond and the calculated ordering of reactivity is consistent with the experimental ordering of bidentate (Figure 2b) > molecular (Figure 2c) > tridentate (Figure 2a). Calculations showed that the reaction of H_2 on the bidentate and the tridentate structures proceed through the same transition state structure. However, the former is less stable in energy. Therefore, the reaction barrier for the bidentate is lower and the bidentate structure is more active. The H_2 reaction mechanism on the molecular structure was calculated to be different from the bidentate and the tridentate. The calculated barrier is higher than that of the bidentate and lower than that of the tridentate. These combined experimental and theoretical results identified, for the first time, the structure-specific activity of supported vanadia monomers.

The reactivities of different vanadia species on the anatase (001) has been studied by comparing the barriers of the first hydrogen abstraction (rate-limiting) on these structures using DFT (*32*). These different structures show significantly different reactivities for the propane ODH reaction. The supported VO_x structures with a square pyramidal coordination environment (Figure 2g) were found to be much more active for the first hydrogen abstraction. The difference in coordination number of the vanadium atom alone can result in an increase of up to 800 times in the reaction rate of the rate-determining step for the various vanadium oxide species at 600 K. The results demonstrated the remarkable sensitivity of the catalytic site activity to its geometric structure. The coordination number of the vanadium atom is a key structural parameter in predicting the catalytic activity. Furthermore, as discussed earlier, the relative populations of the thermodynamically stable structures depend on temperature, pressure, hydration condition, and coverage. Thus, the varied activities of catalytic structure coexisting on the support suggest that advanced catalyst synthesis techniques to control site specificity could provide greatly improved catalytic efficiency.

Conclusions

Understanding catalysis at a molecular level is the key to improving catalytic activity and the rational design of the next generation of catalysts. Computational studies can provide information of the structures of catalytic sites. In the case of VO_x clusters discussed in this chapter, various structures are possible with different bonding configurations to the support. These multiple structures are likely to coexist on a support surface and interconvert at different conditions. Computations

In Novel Materials for Catalysis and Fuels Processing; Bravo-Suárez, J., et al.;
ACS Symposium Series; American Chemical Society: Washington, DC, 2013.

have also revealed that the reactivity of the catalyst can be affected by the catalytic support and the specific molecular structure of the VO_x active site. Finally, this information can be used to develop structure-function relationships to help in the design of improved catalysts.

Acknowledgments

This research was supported by the U.S. Department of Energy, Office of Basic Energy Sciences, Division of Materials Science and Engineering, Contract No. DE-AC-02-06CH11357.

References

1. Hammer, B.; Norskov, J. K. *Adv. Catal.* **2000**, *45*, 71–129.
2. Norskov, J. K.; Bligaard, T.; Rossmeisl, J.; Christensen, C. H. *Nat. Chem.* **2009**, *1*, 37–46.
3. Cavani, F.; Trifiro, F. *Catal. Today* **1995**, *24*, 307–313.
4. Argyle, M. D.; Chen, K. D.; Bell, A. T.; Iglesia, E. *J. Catal.* **2002**, *208*, 139–149.
5. Magg, N.; Immaraporn, B.; Giorgi, J. B.; Schroeder, T.; Baumer, M.; Dobler, J.; Wu, Z. L.; Kondratenko, E.; Cherian, M.; Baerns, M.; Stair, P. C.; Sauer, J.; Freund, H. J. *J. Catal.* **2004**, *226*, 88–100.
6. Dobler, J.; Pritzsche, M.; Sauer, J. *J. Phys. Chem. C* **2009**, *113*, 12454–12464.
7. Calatayud, M.; Mguig, B.; Minot, C. *Surf. Sci.* **2003**, *526*, 297–308.
8. Calatayud, M.; Mguig, B.; Minot, C. *Theor. Chem. Acc.* **2005**, *114*, 29–37.
9. Calatayud, M.; Minot, C. *Top. Catal.* **2006**, *41*, 17–26.
10. Keller, D. E.; Visser, T.; Soulimani, F.; Koningsberger, D. C.; Weckhuysen, B. M. *Vib. Spectrosc.* **2007**, *43*, 140–151.
11. Launay, H.; Loridant, S.; Pigamo, A.; Dubois, J. L.; Millet, J. M. M. *J. Catal.* **2007**, *246*, 390–398.
12. Lee, E. L.; Wachs, I. E. *J. Phys. Chem. C* **2008**, *112*, 6487–6498.
13. Schramlmarth, M.; Wokaun, A.; Pohl, M.; Krauss, H. L. *J. Chem. Soc., Faraday Trans.* **1991**, *87*, 2635–2646.
14. VanDerVoort, P.; White, M. G.; Mitchell, M. B.; Verberckmoes, A. A.; Vansant, E. F. *Spectrochim. Acta, Part A* **1997**, *53*, 2181–2187.
15. Berndt, H.; Martin, A.; Bruckner, A.; Schreier, E.; Muller, D.; Kosslick, H.; Wolf, G. U.; Lucke, B. *J. Catal.* **2000**, *191*, 384–400.
16. Dzwigaj, S.; El Malki, E. M.; Peltre, M. J.; Massiani, P.; Davidson, A.; Che, M. *Top. Catal.* **2000**, *11*, 379–390.
17. Martra, G.; Arena, F.; Coluccia, S.; Frusteri, F.; Parmaliana, A. *Catal. Today* **2000**, *63*, 197–207.
18. Keller, D. E.; Koningsberger, D. C.; Weckhuysen, B. M. *J. Phys. Chem. B* **2006**, *110*, 14313–14325.
19. Nguyen, L. D.; Loridant, S.; Launay, H.; Pigamo, A.; Dubois, J. L.; Millet, J. M. M. *J. Catal.* **2006**, *237*, 38–48.

20. Topsoe, N. Y.; Anstrom, M.; Dumesic, J. A. *Catal. Lett.* **2001**, *76*, 11–20.
21. Topsoe, N. Y.; Topsoe, H.; Dumesic, J. A. *J. Catal.* **1995**, *151*, 226–240.
22. Busca, G.; Lietti, L.; Ramis, G.; Berti, F. *Appl. Catal., B* **1998**, *18*, 1–36.
23. Weckhuysen, B. M.; Jehng, J. M.; Wachs, I. E. *J. Phys. Chem. B* **2000**, *104*, 7382–7387.
24. Tanaka, T.; Yamashita, H.; Tsuchitani, R.; Funabiki, T.; Yoshida, S. *J. Chem. Soc., Faraday Trans. 1* **1988**, *84*, 2987–2999.
25. Ruitenbeek, M.; van Dillen, A. J.; de Groot, F. M. F.; Wachs, I. E.; Geus, J. W.; Koningsberger, D. C. *Top. Catal.* **2000**, *10*, 241–254.
26. Nielsen, U. G.; Topsoe, N. Y.; Brorson, M.; Skibsted, J.; Jakobsen, H. J. *J. Am. Chem. Soc.* **2004**, *126*, 4926–4933.
27. Kozlowski, R.; Pettifer, R. F.; Thomas, J. M. *J. Phys. Chem.* **1983**, *87*, 5172–5176.
28. Izumi, Y.; Kiyotaki, F.; Yoshitake, H.; Aika, K.; Sugihara, T.; Tatsumi, T.; Tanizawa, Y.; Shido, T.; Iwasawa, Y. *Chem. Commun.* **2002**, 2402–2403.
29. Kim, H.-S.; Zygmunt, S. A.; Stair, P. C.; Zapol, P.; Curtiss, L. A. *J. Phys. Chem. C* **2009**, *113*, 8836–8843.
30. Islam, M. M.; Costa, D.; Calatayud, M.; Tielens, F. *J. Phys. Chem. C* **2009**, *113*, 10740–10746.
31. Wu, Z. L.; Dai, S.; Overbury, S. H. *J. Phys. Chem. C* **2010**, *114*, 412–422.
32. Cheng, L.; Ferguson, G. A.; Zygmunt, S.; Curtiss, L. A. Submitted, 2012.
33. Grybos, R.; Witko, M. *J. Phys. Chem. C* **2007**, *111*, 4216–4225.
34. Lewandowska, A. E.; Calatayud, M.; Tielens, F.; Banares, M. A. *J. Phys. Chem. C* **2011**, *115*, 24133–24142.
35. Vittadini, A.; Selloni, A. *J. Phys. Chem. B* **2004**, *108*, 7337–7343.
36. Baron, M.; Abbott, H.; Bondarchuk, O.; Stacchiola, D.; Uhl, A.; Shaikhutdinov, S.; Freund, H.-J.; Popa, C.; Ganduglia-Pirovano, M. V.; Sauer, J. *Angew. Chem., Int. Ed.* **2009**, *48*, 8006–8009.
37. Popa, C.; Ganduglia-Pirovano, M. V.; Sauer, J. *J. Phys. Chem. C*, *115*, 7399–7410.
38. Mars, P.; van Krevelen, D. W. *Chem. Eng. Sci* **1954**, *3*, 41.
39. Cheng, M. J.; Chenoweth, K.; Oxgaard, J.; van Duin, A.; Goddard, W. A. *J. Phys. Chem. C* **2007**, *111*, 5115–5127.
40. Gilardoni, F.; Bell, A. T.; Chakraborty, A.; Boulet, P. *J. Phys. Chem. B* **2000**, *104*, 12250–12255.
41. Redfern, P. C.; Zapol, P.; Sternberg, M.; Adiga, S. P.; Zygmunt, S. A.; Curtiss, L. A. *J. Phys. Chem. B* **2006**, *110*, 8363–8371.
42. Chen, K. D.; Bell, A. T.; Iglesia, E. *J. Phys. Chem. B* **2000**, *104*, 1292–1299.
43. Chen, K. D.; Iglesia, E.; Bell, A. T. *J. Catal.* **2000**, *192*, 197–203.
44. Chen, K. D.; Khodakov, A.; Yang, J.; Bell, A. T.; Iglesia, E. *J. Catal.* **1999**, *186*, 325–333.
45. Muylaert, I.; Van Der Voort, P. *Phys. Chem. Chem. Phys.* **2009**, *11*, 2826–2832.
46. Rozanska, X.; Fortrie, R.; Sauer, J. *J. Phys. Chem. C* **2007**, *111*, 6041–6050.
47. Ganduglia-Pirovano, M. V.; Popa, C.; Sauer, J.; Abbott, H.; Uhl, A.; Baron, M.; Stacchiola, D.; Bondarchuk, O.; Shaikhutdinov, S.; Freund, H. J. *J. Am. Chem. Soc.* **2010**, *132*, 2345–2349.

48. Wachs, I. E. *Catal. Today* **2005**, *100*, 79–94.
49. Dinse, A.; Frank, B.; Hess, C.; Habel, D.; Schomacker, R. *J. Mol. Catal. A: Chem.* **2008**, *289*, 28–37.
50. Daniell, W.; Ponchel, A.; Kuba, S.; Anderle, F.; Weingand, T.; Gregory, D. H.; Knozinger, H. *Top. Catal.* **2002**, *20*, 65–74.
51. Kim, H.; Ferguson, G. A.; Cheng, L.; Zygmunt, S. A.; Stair, P. C.; Curtiss, L. A. *J. Phys. Chem. C* **2012**, *116*, 2927–2932.

Chapter 3

Molecular Simulation of Carbon Capture in a Series of Isoreticular Zeolitic Imidazolate Materials

Yao Houndonougbo*

Department of Chemistry and Biochemistry, Eastern Washington University, 226 Science Building, Cheney, WA 99004, USA
***E-mail: yhoundonoug@ewu.edu**

The combustion of fossil fuels has led to atmospheric accumulation of greenhouse gases, which continuously increases the threat of global warming. Carbon-capture technologies are promising solutions for reducing the release of greenhouse gases in the atmosphere. The high porosity, high thermal stability, and unusually high chemical stability of Zeolitic Imidazolate Frameworks (ZIFs) make them promising materials and ideal candidates for carbon-capture applications. Here, we present simulation results of CO_2 adsorption up to 80 bar in a series of five isoreticular ZIFs, which allow the direct assessment of the role ZIF functionalization in CO_2 adsorption. The calculated adsorptions agree well with experimental data. The simulation results suggest that electrostatic interactions produced by the ZIF frameworks, the symmetry of their functionalization, and the free volume are controlling factors to consider in the optimization of ZIFs for CO_2 adsorption. The principal CO_2 adsorption sites in the ZIFs are also reported.

Introduction

The majority of the energy needs of the world (about 85%) is currently supplied by fossil fuels (*1*). The successful development of carbon capture and

In Novel Materials for Catalysis and Fuels Processing; Bravo-Suárez, J., et al.;
ACS Symposium Series; American Chemical Society: Washington, DC, 2013.

separation technologies is thus essential for achieving the goal of reducing the release of CO_2 greenhouse gases in the atmosphere while continuing to meet the world's increasing energy demands. Post-combustion carbon capture from flue gas is one of the approaches being actively pursued for controlling greenhouse gas emission because of the potentiality for retrofitting the existing fleet of power plants (*2*).

The common industrial methods used for CO_2 capture from gas mixtures are solvent absorption, cryogenic separation, membrane processes, and solid sorbents adsorption (*3*). Separation by solid–sorbents adsorption, as compared to other methods, offers potential advantages, such as reduced environmental impact and workable pressure (1–300 bar) and temperature (298 K) operating conditions (*4–6*). One of the most used industrial solid sorbent gas separation processes is the pressure swing adsorption (PSA), which is based on high-pressure adsorption and low-pressure desorption (*6–8*). Most studies on the PSA process have focused on zeolites (*7*, *9–13*) and porous carbon (*11*, *12*, *14*, *15*). For the traditional PSA, the regeneration of sorbents is difficult to achieve using zeolites, while using porous carbons improves regeneration, but exhibit lower selectivity relative to zeolites (*9*, *16*).

Recently, metal-organic frameworks (MOFs) have emerged as a new class of porous materials that offer great potentialities for adsorption and separation applications (*17–21*). They are highly crystalline materials formed of metal ions linked by bridging organic ligands. MOFs have received much attention because of their high porosity, very high surface area, and potential of tailoring pore sizes and chemical environment to particular properties (*19*, *22*). However, the chemical, mechanical, and thermal stabilities of many MOFs present a real challenge for industrial applications (*19*, *23*, *24*).

Zeolitic Imidazole Frameworks (ZIFs) are a subclass of MOFs with high porosity that are based on the tetrahedral network of zeolites in which the silicon is replaced by a transition metal and the oxygen by imidazolate. ZIFs have potential for CO_2 capture and separation processes because of their high thermal and unusual chemical stability, varieties of framework pore, and functionalization (*25–28*).

We have recently reported the synthesis of ZIF-25, -71, -93, -96, and -97 using zinc(II) acetate and 4,5 substituted imidazolate links (*29*). The synthetic procedures produced a series of ZIFs with the same zeolite RHO topology that differs only by their imidazole functional groups (Figure 1). In that study, we also combined experimental and computational methods to investigate the enhancement of CO_2 adsorption uptake in the ZIFs at lower pressures up to 1 bar. Since processes for removing CO_2 from flue gases operate at different conditions, both high and low pressures CO_2 capture studies are needed for the selection of optimal capture materials. Herein, we used molecular simulation to investigate the CO_2 adsorption capacity at high pressure up to 80 bar in ZIF-25, -71, -93, -96, and -97. Because the ZIFs structures considered here are different in their chemical functional groups, this work presents an opportunity to study the role of their functionalization on the adsorption capacity of CO_2.

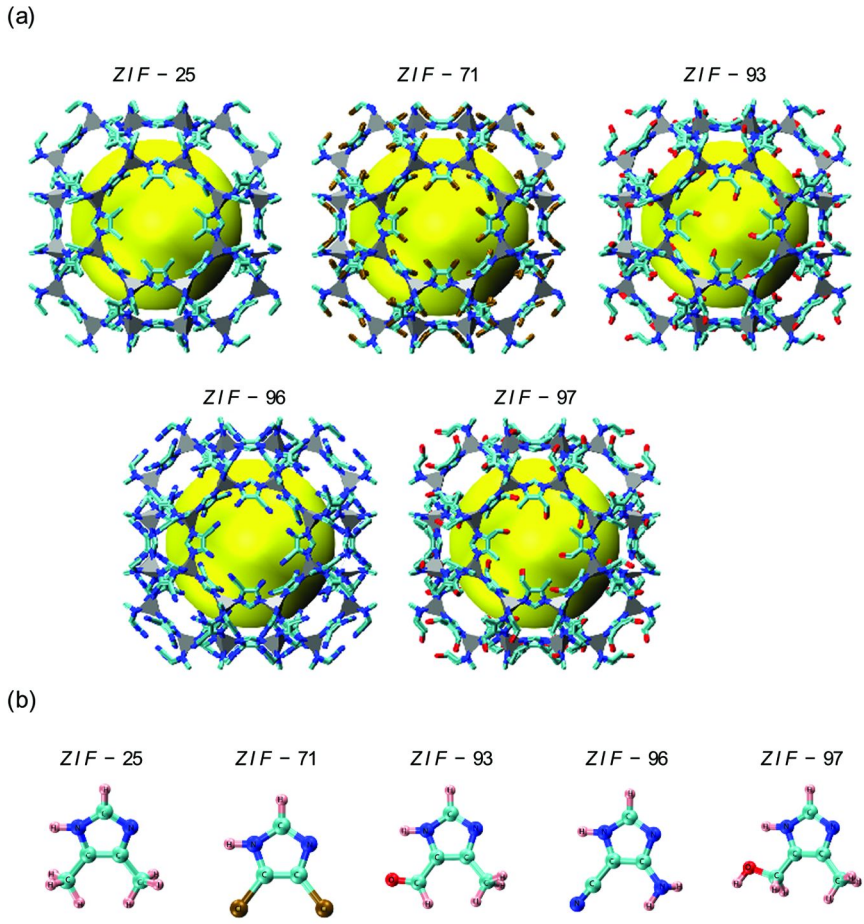

Figure 1. (a) Structures of the LTA cavity in ZIF-25, -71, -93, -96, and -97. A yellow sphere represents the free space within the cavities. The sphere represents the free space within the cavities. Hydrogen atoms are omitted for clarity. (b) Representations of the Imidazolate-type linkers in the ZIFs.Force Fields (see color insert)

Models and Simulation Methods

ZIF Structures

The periodic building unit of the RHO topology ZIFs consists of an α-cavity (also sometimes referred to as an LTA cavity) of 16.8 Å that is composed of twelve four-membered rings, eight six-membered rings, and six eight-membered rings. The α-cavities are connected through double eight-membered rings of 4.8 Å in a body-centered cubic arrangement (*26*). The structural and physical properties of the ZIFs studied in this work are given in Table 1.

In Novel Materials for Catalysis and Fuels Processing; Bravo-Suárez, J., et al.;
ACS Symposium Series; American Chemical Society: Washington, DC, 2013.

Table 1. Structural and physical properties of the RHO topology ZIFs considered in this work

ZIF	*Composition*	*BET surface area* ($m^2\ g^{-1}$)	*Density* ($g\ cm^{-3}$)	*Free volume* ($cm^3\ g^{-1}$) (%)
25	$Zn(dmIm)_2$	1110	0.857	0.532 (45.6)
71	$Zn(dcIm)_2$	652	1.184	0.396 (46.9)
93	$Zn(4me5alIm)_2$	864	0.991	0.414 (41.0)
96	$Zn(4cy5amIm)_2$	960	0.977	0.460 (45.0)
97	$Zn(4mehylIm)_2$	564	0.997	0.369 (36.8)

The intermolecular interactions of all molecules studied in this work are represented by pairwise additive Lennard–Jones (LJ) 12–6 potentials and Coulombic interactions of partial charges:

$$U(r_{ij})=4\varepsilon_{ij}\left[\left(\frac{\sigma_{ij}}{r_{ij}}\right)^{12}-\left(\frac{\sigma_{ij}}{r_{ij}}\right)^{6}\right]+\frac{q_i q_j}{4\pi\varepsilon_0 r_{ij}} \quad (1)$$

where r_{ij}, ε_{ij}, σ_{ij}, q_i, and q_j are the separation, LJ well depth, LJ atomic diameter, and partial charges, respectively, for interacting atoms i and j. The cross-interaction parameters ε_{ij} and σ_{ij} were calculated using the Lorentz–Berthelot combining rules (*30*). The CO_2 molecule was modeled using a rigid three-sites model with the EPM2 potential parameters developed by Harris and Yung (*31*), which was optimized to give good agreement with the experimental vapor–liquid coexistence curve (*31–33*). For the ZIF atoms, LJ interaction parameters from the Universal Force Field (UFF) (*34*) were used. The UFF has been used for similar systems with some success in recent simulations of gas adsorption and separation in other ZIFs (*35*, *36*). Because of the considerable discrepancy between simulation and experiment in ZIF-96, we have also used LJ parameters taken from the Optimized Potentials for Liquid Simulations–All Atom (OPLS–AA) force field (*37*, *38*) for ZIF-96. All the Lennard–Jones parameters are listed in Table 2. The electrostatic interactions between gas molecules and the ZIF framework were modeled using framework charges computed with the REPEAT algorithm (*39*), based on density-functional-theory calculations of electrostatic potentials, following the procedures described in our earlier work (*29*).

The details associated with the calculation of the BET surface area can be found in reference (*29*). Densities are based on the crystal structure. The free volumes were calculated using the PLATON program (*48*) with a probe radius based on the carbon dioxide kinetic diameter (3.3 Å).

In Novel Materials for Catalysis and Fuels Processing; Bravo-Suárez, J., et al.;
ACS Symposium Series; American Chemical Society: Washington, DC, 2013.

Table 2. LJ potential parameters for carbon dioxide and ZIFs

Species	*Atom*	ε/k_b *(K)*	σ*(Å)*
Carbon dioxide	C	28.13	2.76
	O	80.51	3.03
ZIFs(UFF)	C	52.84	3.43
	O	30.19	3.12
	N	34.72	3.26
	Cl	114.23	3.52
	Zn	62.40	2.46
	H	22.14	2.57
ZIF-96 imidazolate ring (OPLS)	C	25.16	2.25
	N	85.55	3.25
	Zn	62.40	2.46
	H	15.10	2.50
ZIF-96 functional groups (OPLS)	$N(NH_2)$	85.55	3.15
	$H(NH_2)$	0.000	0.00
	C(CN)	105.7	3.30
	N(CN)	85.55	2.90

Molecular Modeling

Grand Canonical Monte Carlo simulations (GCMC), as implemented in the program Monte Carlo for Complex Chemical Systems (MCCCS) Towhee (*40*), were employed to calculate the isotherms and adsorption thermodynamics. The initial structures of the ZIFs were constructed from the atomic coordinates given in our previous work (*29*). The 1×1×1 unit cells of the ZIFs (Figure 1a) were adopted in the simulations. The ZIFs used in the simulations were modeled as rigid frameworks and gas-phase fugacities were calculated using the Peng–Robinson equation of state (EOS) (*41*), with parameters taken from the NIST Chemistry WebBook (*42*) and with the standard chemical potential calculated within the model for each temperature studied using NPT simulation at 1.0 bar. We have verified by direct NPT simulation at a few sample pressures that the errors introduced by the use of this EOS are not significant (the maximum deviation is less than 1%). A cutoff radius of 12.8 Å was applied to the nonbonded Lennard–Jones interactions and standard long-range corrections were employed (*43*).

In Novel Materials for Catalysis and Fuels Processing; Bravo-Suárez, J., et al.;
ACS Symposium Series; American Chemical Society: Washington, DC, 2013.

Results and Discussion

CO_2 Adsorption Experimental and Molecular Simulations at Low Pressure

CO_2 adsorption experimental data from reference (*29*) and simulation results at 298 K at pressures up to 1 bar for the five studied ZIFs are plotted in Figure 2. The simulation results using one unit cell for the ZIFs are similar to the results obtained in our previous work where 4 unit cells were employed (*29*). With the exception of ZIF-96, the simulation results based on the UFF force field are in reasonable agreement with the experimental data but slightly overestimate the CO_2 uptakes in ZIF-25, -71, and -97. In the case of ZIF-93, the predictions are in excellent agreement with the experimental results. As was pointed out in our previous work, the notable UFF underestimation of CO_2 adsorption in ZIF-96 is likely due to the use of a fixed single potential for each element, irrespective of bonding, to describe the short-range vdW interactions.

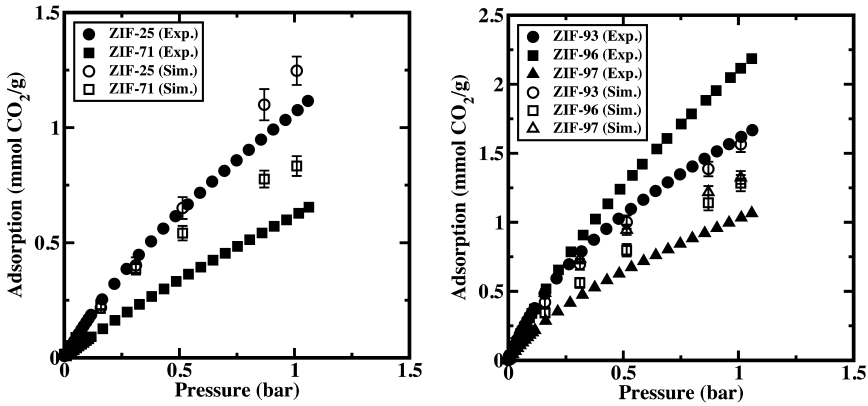

Figure 2. Comparison of experimental (closed symbols) data from reference (29) and calculated (open symbols)low pressure CO_2 adsorption isotherms for the studied ZIFs at 298 K.

Unlike UFF, the OPLS (Optimized Potentials for Liquid Simulations) all atoms (AA) force field (*37*, *38*) was developed by computing thermodynamic and structural properties using Monte Carlo statistical mechanics simulations and distinguishes between atom types. The OPLS interaction parameters were thus used to calculate CO_2 adsorption isotherms of ZIF-96 at 298 K. The results are compared to experimental data in Figure 3. The good agreement between simulation and experiment demonstrates that the OPLS parameters accurately predict CO_2 adsorption in ZIF-96. The OPLS interaction parameters listed in Table 2 were therefore adopted to model ZIF-96 framework atoms.

In Novel Materials for Catalysis and Fuels Processing; Bravo-Suárez, J., et al.;
ACS Symposium Series; American Chemical Society: Washington, DC, 2013.

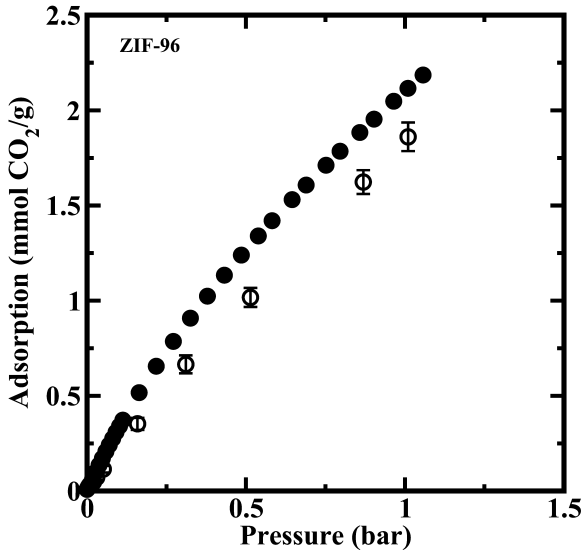

Figure 3. Experimental (closed circles) low-pressure data from reference (29) and calculated (open circles) CO_2 isotherm for ZIF-96 at 298 K. The Lennard–Jones parameter (see Table 2) used in simulations are from the OPLS force field.

The simulated ZIFs CO_2 adsorption values at 1.0 bar are 1.86, 1.57, 1.32, 1.25, and 0.83 mmol g^{-1} for ZIF-96, -93, -97, -25, and -71, respectively. These results show that the highest CO_2 uptake corresponded to ZIF-96, whereas the lowest was for ZIF-71. These adsorption results at low pressure are mainly dependent on the adsorbent–guest interactions (*44*) that include both electrostatic and vdW interactions. The differences in these interactions are exclusively influenced by the functional groups in these ZIFs since the topology is the same for all ZIFs studied here. In addition, the contribution to the adsorption arising from electrostatic interactions is not negligible because CO_2 has a significant quadrupole moment. The effect of framework electrostatic interactions on the ZIFs adsorption will be discussed later in detail below.

CO_2 Adsorption Molecular Simulation Predictions at High Pressure

We performed GCMC simulations at 298 K to examine the adsorption uptake capacity of CO_2 in the ZIFs at pressures up to 80.0 bar. In order to validate the simulation results at high pressure we compared in Figure 4 the simulated CO_2 isotherm in ZIF-93 to the corresponding experimental data from reference (*45*), which is the only published high pressure experimental CO_2 uptake for the ZIFs studied in this work. The results show a good agreement between simulation and the experimental data. These simulations can predict the high-pressure adsorption of CO_2 in ZIF-93 within about 10% of the experimental value. These results further validate the accuracy of the molecular simulation predictions at high pressure in the ZIFs considered in this work.

In Novel Materials for Catalysis and Fuels Processing; Bravo-Suárez, J., et al.;
ACS Symposium Series; American Chemical Society: Washington, DC, 2013.

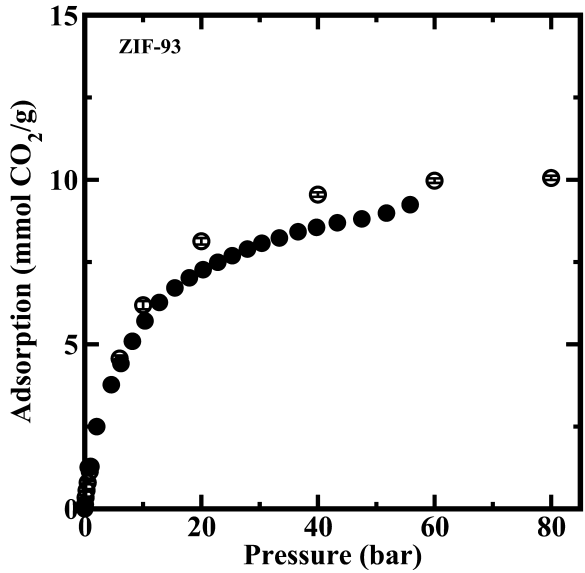

Figure 4. Comparison of high pressure experimental (closed circles) data from reference (45) and calculated (open circles) CO_2 isotherms for ZIF-93 at 298 K.

The calculated ZIFs CO_2 adsorption isotherms up to 80.0 bar are shown in Figure 5. In the high-pressure region above 10.0 bar, the highest observed CO_2 uptake is for ZIF-96, followed by ZIF-25, ZIF-93, ZIF-97, and ZIF-71. We found the CO_2 uptake capacities at 80.0 bar to be 11.60, 10.83, 9.30, 7.96, and 7.85 mmol g^{-1} for ZIF-96, -25, -93, -97, and -71, respectively. These results show a different adsorption order at high pressure than at low pressure (Figure 2). This can be explained by the fact that the amount adsorbed at high pressure is predominantly influenced by surface area and free volume, while the adsorption at low pressure is dominated by framework interactions with CO_2 molecules (*44*). Consequently, ZIF-25 shows the second highest uptake at high pressure while displaying one of the lowest at low pressure. This result reflects the fact that ZIF-25 has the highest free volume.

Effect of Framework Electrostatic Interactions on CO_2 Adsorption

To examine the effect of framework electrostatic interactions on the CO_2 adsorption variations for the different ZIFs, we calculated the adsorptions without considering the framework charges. The percentage deviation between the adsorbed amount with and without framework charges is shown in Figure 6. The adsorption of CO_2 at low pressures is significantly dependent on the electrostatic interactions between the ZIF frameworks and CO_2 molecules. In the current RHO series, the imidazolate is functionalized at the positions 2 and 4 leading

In Novel Materials for Catalysis and Fuels Processing; Bravo-Suárez, J., et al.;
ACS Symposium Series; American Chemical Society: Washington, DC, 2013.

to isoreticular ZIFs with symmetric, ZIF-25 and -71, and asymmetric, ZIF-93, -96, and -97, functionalized frameworks (see Figure 1). As can be seen in Figure 6, the magnitude of the effect of framework charges on CO_2 adsorption is not equivalent for all the ZIFs.

For the frameworks with asymmetric functionalization (ZIF-93, -96, and -97), the insertion of framework charges leads to an increase of up to 60% at low pressure, whereas for symmetric functionalized ZIFs (ZIF-25 and -71) the increase is only about 10%. This can be explained by the cancellation of electrostatic interactions in the symmetrically functionalized ZIFs (ZIF-25 and -71) leading to the negligible effect of framework charges, whereas the non-cancellation of electrostatic interactions in the asymmetric functionalized ZIFs (ZIF-93, -96, and -97) results in an enhanced adsorption (*29*). This effect of electrostatic interactions between the CO_2 and the ZIFs decreases when the pressure increases and the role played by the symmetry of the functionalization becomes nearly negligible at high pressures (Figure 6). This can be related to the importance of CO_2–CO_2 interactions when the pores become nearly filled at high pressures (*46*).

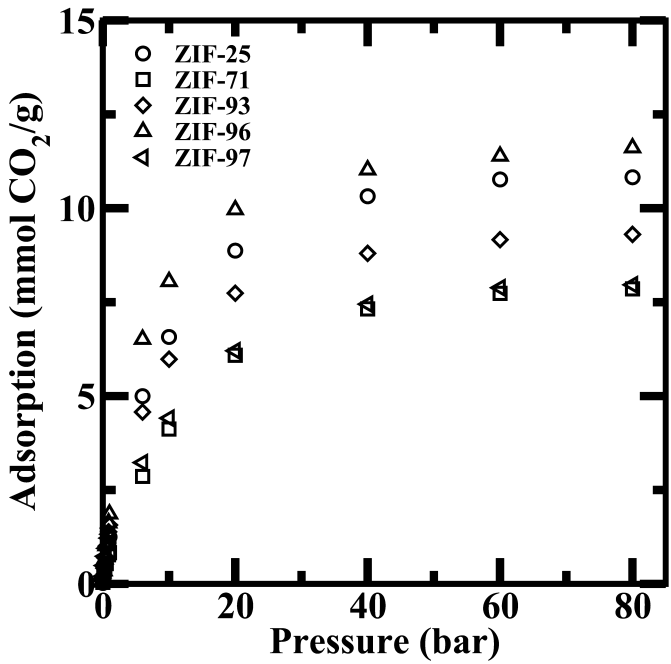

Figure 5. Simulated high-pressure CO_2 adsorption isotherms for ZIFs at 298 K. The error bars have been removed for the sake of clarity.

In Novel Materials for Catalysis and Fuels Processing; Bravo-Suárez, J., et al.;
ACS Symposium Series; American Chemical Society: Washington, DC, 2013.

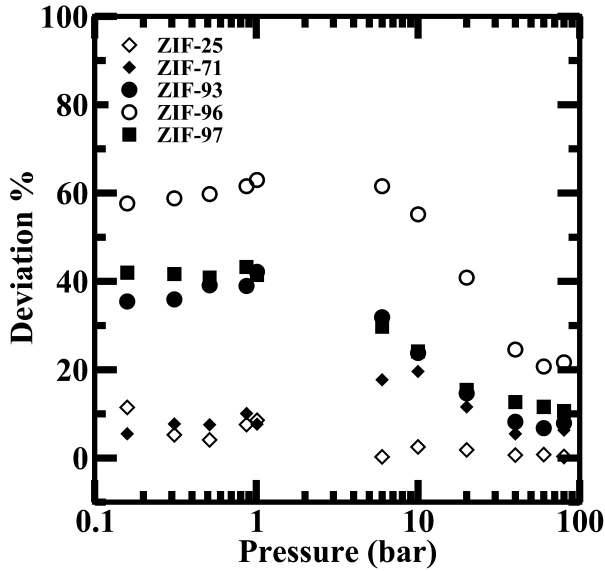

Figure 6. Deviations between the amounts of CO_2 adsorbed in the ZIFs with and without framework charges at 298 K.

Isosteric Heats of Adsorption

The isosteric heat of adsorption can be related to the heat released during the adsorption process. It characterizes the surface energetics of a solid. Thus, the isosteric heat of adsorption is an important thermodynamic property for the design of adsorption processes. To study CO_2-sorbent energetic interactions, we have calculated using GCMC simulations the isosteric heat of adsorption Q_{st} directly from the fluctuations in the total energy of the simulated system using Equation 2 (*47*):

$$Q_{st} = RT - \frac{\langle N\Phi\rangle - \langle N\rangle\langle\Phi\rangle}{\langle N^2\rangle - \langle N\rangle^2} \qquad (2)$$

where Φ, N, T, and R are the potential energy of the adsorbed phase, the number of molecules adsorbed, temperature, and gas constant, respectively, and the angle brackets á..ñdenote averaging. Equation 2 can be computed directly during the GCMC simulation. The calculated isosteric heats of adsorption at 298 K are plotted in Figure 7. The values of Q_{st} decrease to a minimum for all the ZIFs. This behavior is different for all the ZIFs and can be attributed to the degree of energetic heterogeneity in the ZIF adsorption sites. Figure 7 shows that ZIF-97 is highly heterogeneous. Its isosteric heat of adsorption decreases from a very high value of 30.2 kJ mol^{-1} to a minimum value of 17.7 kJ mol^{-1}. ZIF-93 and ZIF-71 also exhibit significant energetic heterogeneities for CO_2 adsorption as their isosteric heat of adsorptions dropped from 26.5 to 19.8 kJ mol^{-1} and from 22.5 to 16.8 kJ mol^{-1}, respectively. The weakly heterogeneous materials are

In Novel Materials for Catalysis and Fuels Processing; Bravo-Suárez, J., et al.;
ACS Symposium Series; American Chemical Society: Washington, DC, 2013.

ZIF-96 and ZIF-25 with Q_{st} values that decrease from 22.5 to 20.3 kJ mol^{-1} and from 19.6 to 18.1 kJ mol^{-1}, respectively. Among the ZIFs, ZIF-97 has the highest Q_{st} at low CO_2 loading. This is because ZIF-97 has the lowest free volume among all the studied ZIFs, which increases the interaction between CO_2 and the framework, thus leading to the highest binding energy. The trends of the isosteric heat of adsorption observed in the studied ZIFs suggest that at low pressure CO_2 adsorbed at a high-energy site and, when the pressure increases, CO_2 molecules preferentially occupy a lower energy site, as will be discussed further in the following section. It is also noticeable from Figure 7 that, after reaching the minimum, Q_{st} gradually increases with coverage. This reverse trend can be attributed to the increasing importance of CO_2–CO_2 interactions when more CO_2 molecules are adsorbed at high pressure.

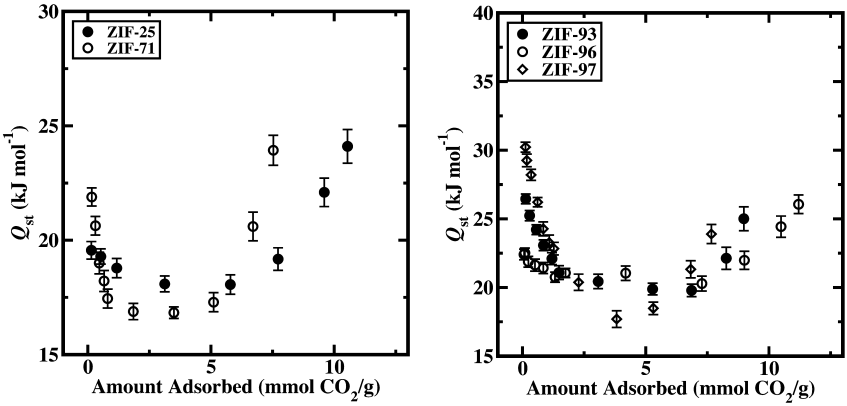

Figure 7. Isosteric heat of CO_2 adsorption at 298 K for the studied ZIFs.

CO_2 Adsorption Sites

Simulations can provide information about the preferred adsorption sites and thus CO_2 adsorption mechanism in the ZIFs frameworks. We have computed the center of mass (COM) of CO_2 probability distribution to gain insights into the nature of these adsorption sites. Two-dimensional distributions at 1.0, 6.0, and 80.0 bar are presented in Figure 8. These figures reveal strong CO_2 densities located near the six-membered ring window of the α-cavities, the connecting double 8-rings, and the inner surface of the α-cavities near to the four-membered ring, consistent with the high-binding-energy sites results of reference (*49*). At low pressure, CO_2 molecules are mainly adsorbed between the ZIFs linkers in the six-membered ring window of the α-cavities making this site the primary adsorption site. A secondary population also appeared in the connecting double 8-rings and at the inner surface of the α-cavities near to the four-membered ring. With increasing pressure, CO_2 begins to populate these two sites and distribute throughout the connecting double 8-rings and the α-cavities.

In Novel Materials for Catalysis and Fuels Processing; Bravo-Suárez, J., et al.;
ACS Symposium Series; American Chemical Society: Washington, DC, 2013.

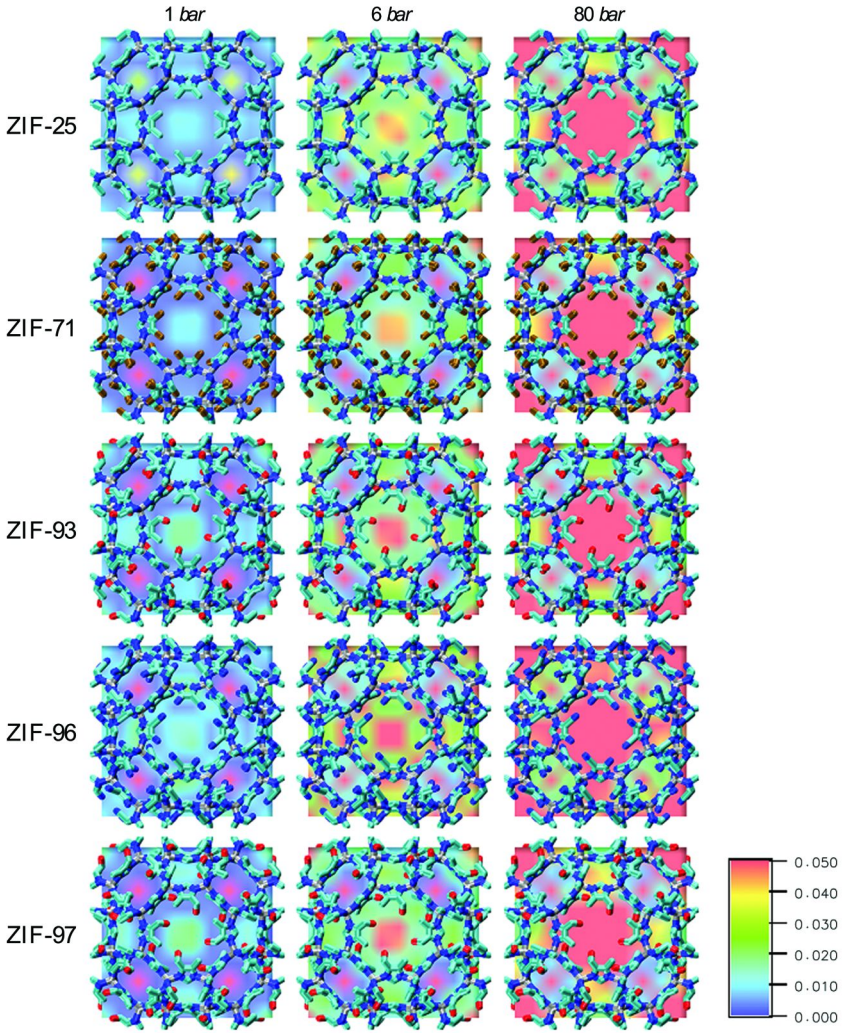

Figure 8. Probability density projected in the XY plane of the center of mass (COM) of CO_2 in each ZIF at 298 K and 1.0, 6.0, and 80.0 bar. The scale bar represents the CO_2 probability density in number of molecules per Å^3. Atom colors: zinc, silver; carbon, cyan; nitrogen, blue; oxygen, red; chlorine, ochre. Hydrogen atoms are omitted for clarity. (see color insert)

The above analyses of CO_2 adsorption sites in the ZIFs explain the trends in the isosteric heat of adsorption (Figure 7). The decrease of Q_{st} with increasing CO_2 coverage can be attributed to the predominant filling of the highest-energy sites in the six-membered rings at lower pressure and, when the pressure increases, the filling of the lower-energy sites in the double 8-rings and at the inner surface

In Novel Materials for Catalysis and Fuels Processing; Bravo-Suárez, J., et al.;
ACS Symposium Series; American Chemical Society: Washington, DC, 2013.

of the α-cavities (Figure 8). The filling of empty space within the pores mainly reverses this trend due to the interaction between CO_2 molecules, emphasizing the importance of the ZIFs free volume for the adsorption at high pressures.

Summary

Zeolitic imidazolate frameworks (ZIFs) are a new class of porous materials that show great promise as a possible alternative to zeolite and other nanoporous materials for gas adsorption. ZIFs are considered suitable candidates for carbon dioxide adsorption. A vast number of different ZIFs can be designed by changing the linker groups. The rational design and computational screening of ZIFs materials are of great importance for CO_2 adsorption applications. In our previous work, experimental measurements supported by computational modeling have been used to study the origins of variations in CO_2 adsorption in a newly synthesized series of isoreticular ZIFs with different functionalities. However, the studies were done at low pressures (up to 1 bar). In this work, Grand Canonical Monte Carlo simulations (GCMC) simulations of CO_2 adsorption in this series of ZIFs were performed up to 80 bar to investigate the factors influencing the uptake capacity in the ZIFs.

The predictive power of molecular simulation depends on the accurate description of the interactions between atoms. Quantum mechanics would be the best method to accurately calculate atomic interactions. However, these calculations are limited because of their high computing time requirements. Therefore, molecular simulations were predominantly performed using force field. First, the performance of the UFF parameters for the ZIFs was evaluated by comparing the calculated adsorption results with the experimental data. The simulations reasonably reproduced the experimental data for all the ZIFs except for ZIF-96. The discrepancy for ZIF-96 was attributed to the failure of the UFF force field to represent the van der Waals (vdW) interactions for the nitrile and amine functional groups on the ZIF-96 imidazolate link because the vdW parameters of the UFF force field are fixed for each element in the periodic table regardless of bonding environment. A good agreement with experimental data was obtained for ZIF-96 by using the optimized potentials for liquid simulations–all atoms (OPLS–AA) force field, which takes into account the atom type and chemical environment. We then compared high-pressure simulation results with the corresponding experimental adsorption for ZIF-93 and the good agreement between the two sets of data validated our simulation models at high pressures. For the computational screening of newly synthesized or hypothetical ZIFs, the transferability of force fields is indispensable for an accurate prediction of their properties. The transferability of force fields available in the literature maybe accessed by comparing simulation results to available experimental data of representative ZIFs structures. In the case where adequate experimental data is not available, more expensive first-principles calculations can be used to develop transferable first-principles-based force fields. Numerous efforts have been made to develop such first-principles-based force fields for the adsorption in the ZIFs (*50–53*).

In Novel Materials for Catalysis and Fuels Processing; Bravo-Suárez, J., et al.;
ACS Symposium Series; American Chemical Society: Washington, DC, 2013.

The results of the GCMC simulations for the RHO ZIFs studied here showed a different order of CO_2 adsorption capacity at high pressures from that observed at low pressures. The analyses of isosteric heat of adsorption and adsorption sites revealed that at high pressures the CO_2 molecules are adsorbed principally in the low-binding-energy sites and occupied the empty space in the pore, highlighting the importance of the ZIFs free volume. The enhancement of CO_2 adsorption at low pressures due to framework charges is significantly dependent on the symmetry of the functionalization as was previously found in reference (*29*), while this dependency is nearly negligible at high pressures. The results of this work suggest that one needs to consider the symmetry of the functionalization and the free volume to obtain high CO_2 uptake in the ZIFs at both low and high pressures, respectively.

Acknowledgments

The author would like to thank Dr. William Morris, Dr. Omar M. Yaghi, Dr. Mark Asta, and Dr. Brian B. Laird for helpful discussions. This material is based upon work supported as part of the Molecularly Engineered Energy Materials, an Energy Frontier Research Center funded by the U.S. Department of Energy, Office of Science, Office of Basic Energy Sciences under Award Number DE-SC0001342. This work made use of the High Performance Computing resources provided by the Eastern Washington University.

References

1. Rao, A. B.; Rubin, E. S. *Environ. Sci. Technol.* **2002**, *36*, 4467–4475.
2. US Department of Energy. http://www.fossil.energy.gov/programs/powersystems/pollutioncontrols/Retrofitting_Existing_Plants.html (accessed Feb 11, 2013).
3. Aaron, D.; Tsouris, C. *Sep. Sci. Technol.* **2005**, *40*, 321–348.
4. Celzard, A.; Fierro, V. *Energy Fuels* **2005**, *19*, 573–583.
5. Mendoza-Cortes, J. L.; Han, S. S.; Furukawa, H.; Yaghi, O. M.; Goddard, W. A., III. *J. Phys. Chem. A* **2010**, *114*, 10824–10833.
6. Ribeiro, A. M.; Santos, J. C.; Rodrigues, A. E.; Rifflart, S. *Energy Fuels* **2012**, *26*, 1246–1253.
7. Liu, Z.; Grande, C. A.; Li, P.; Yu, J.; Rodrigues, A. E. *Sep. Purif. Technol.* **2011**, *81*, 307–317.
8. Dantas, T. L. P.; Luna, F. M. T.; Silva, I. J., Jr.; Torres, A. E. B.; de Azevedo, D. C. S.; Rodrigues, A. E.; Moreira, R. F. P. M. *Chem. Eng. J.* **2011**, *172*, 698–704.
9. Morishige, K. *J. Phys. Chem. C* **2011**, *115*, 9713–9718.
10. Triebe, R.; Tezel, F.; Khulbe, K. *Gas Sep. Purif.* **1996**, *10*, 81–84.
11. Jee, J.; Kim, M.; Lee, C. *Ind. Eng. Chem. Res.* **2001**, *40*, 868–878.
12. Siriwardane, R.; Shen, M.; Fisher, E.; Poston, J. *Energy Fuels* **2001**, *15*, 279–284.
13. Siperstein, F.; Myers, A. *AIChE J.* **2001**, *47*, 1141–1159.

14. Herbst, A.; Harting, P. *Adsorption* **2002**, *8*, 111–123.
15. Dreisbach, F.; Staudt, R.; Keller, J. *Adsorption* **1999**, *5*, 215–227.
16. Sircar, S. *Ind. Eng. Chem. Res.* **2006**, *45*, 5435–5448.
17. Rosi, N.; Eckert, J.; Eddaoudi, M.; Vodak, D.; Kim, J.; O'Keeffe, M.; Yaghi, O. *Science* **2003**, *300*, 1127–1129.
18. Li, J.-R.; Kuppler, R. J.; Zhou, H.-C. *Chem. Soc. Rev.* **2009**, *38*, 1477–1504.
19. Rowsell, J.; Yaghi, O. *Microporous Mesoporous Mater* **2004**, *73*, 3–14.
20. Rowsell, J.; Yaghi, O. *J. Am. Chem. Soc.* **2006**, *128*, 1304–1315.
21. Kaye, S. S.; Dailly, A.; Yaghi, O. M.; Long, J. R. *J. Am. Chem. Soc.* **2007**, *129*, 14176–14177.
22. Furukawa, H.; Ko, N.; Go, Y. B.; Aratani, N.; Choi, S. B.; Choi, E.; Yazaydin, A. O.; Snurr, R. Q.; O'Keeffe, M.; Kim, J.; Yaghi, O. M. *Science* **2010**, *329*, 424–428.
23. Saha, D.; Deng, S. *J. Phys. Chem. Letters* **2010**, *1*, 73–78.
24. Kang, I. J.; Khan, N. A.; Haque, E.; Jhung, S. H. *Chem. Eur. J.* **2011**, *17*, 6437–6442.
25. Park, K. S.; Ni, Z.; Coté, A. P.; Choi, J. Y.; Huang, R.; Uribe-Romo, F. J.; Chae, H. K.; O'Keeffe, M.; Yaghi, O. M. *Proc. Natl. Acad. Sci. U.S.A.* **2006**, *103*, 10186–10191.
26. Banerjee, R.; Phan, A.; Wang, B.; Knobler, C.; Furukawa, H.; O'Keeffe, M.; Yaghi, O. M. *Science* **2008**, *319*, 939–943.
27. Banerjee, R.; Furukawa, H.; Britt, D.; Knobler, C.; O'Keeffe, M.; Yaghi, O. M. *J. Am. Chem. Soc.* **2009**, *131*, 3875–3877.
28. Phan, A.; Doonan, C. J.; Uribe-Romo, F. J.; O'Keefe, C. B. K. M.; Yaghi, O. M. *Acc. Chem. Res.* **2010**, *43*, 58–67.
29. Morris, W.; Leung, B.; Furukawa, H.; Yaghi, O. K.; He, N.; Hayashi, H.; Houndonougbo, Y.; Asta, M.; Laird, B. B.; Yaghi, O. M. *J. Am. Chem. Soc.* **2010**, *132*, 11006–11008.
30. Allen, M.; Tildesley, D. *Computer Simulation of Liquids*; Oxford Science Press: Oxford, 1987.
31. Harris, J.; Yung, K. *J. Phys. Chem.* **1995**, *99*, 12021–12024.
32. Houndonougbo, Y.; Jiu, H.; Rajagopalan, B.; Wong, K.; Kuczera, K.; Subramaniam, B.; Laird, B. *J. Phys. Chem. B* **2006**, *110*, 13195–13202.
33. Houndonougbo, Y.; Guo, J.; Lushington, G.; Laird, B. *Mol. Phys.* **2006**, *104*, 2955–2960.
34. Rappe, A. K.; Casewit, C. J.; Colwell, K. S.; Goddard, W. A. I.; Skiff, W. M. *J. Am. Chem. Soc.* **1992**, *114*, 10024–10035.
35. Pérez-Pellitero, J.; Amrouche, H.; Siperstein, F.; Pirngruber, G.; Nieto-Draghi, C.; Chaplais, G.; Simon-Masseron, A.; Bazer-Bachi, D.; Peralta, D.; Bats, N. *Chem. Eur. J.* **2010**, *16*, 1560–1571.
36. Liu, Y.; Liu, D.; Yang, Q.; Zhong, C.; Mi, J. *Ind. Eng. Chem. Res.* **2010**, *49*, 2902–2906.
37. Kaminski, G. A.; Friesner, R. A.; Tirado-Rives, J.; Jorgensen, W. L. *J. Phys. Chem. B* **2001**, *105*, 6474–6487.
38. Jorgensen, W. L.; Maxwell, D. S.; Tirado-Rives, J. *J. Am. Chem. Soc.* **1996**, *117*, 11225–11236.

39. Campana, C.; Mussard, B.; Woo, T. K. *J. Comput. Chem.* **2009**, *5*, 2866–2878.
40. Martin, M. G.; Chen, B.; Wick, C. D.; Potoff, J. J.; Stubbs, J. M.; Siepmann, J. I. http://towhee.sourceforge.net (accessed Feb 11, 2013).
41. Peng, D.; Robinson, D. *Ind. Eng. Chem. Fundam.* **1976**, *15*, 59–64.
42. The National Institute of Standards and Technology (NIST). Chemistry WebBook: http://webbook.nist.gov/chemistry (accessed Feb 11, 2013).
43. McDonald, I. *Mol. Phys.* **1972**, *23*, 41–58.
44. Frost, H.; Duren, T.; Snurr, R. *J. Phys. Chem. B* **2006**, *110*, 9565–9570.
45. Morris, W.; He, N.; Ray, K. G.; Klonowski, P.; Furukawa, H.; Daniels, I. N.; Houndonougbo, Y. A.; Asta, M.; Yaghi, O. M.; Laird, B. B. *J. Phys. Chem. C* **2012**, *116*, 24084–24090.
46. Amrouche, H.; Aguado, S.; Perez-Pellitero, J.; Chizallet, C.; Siperstein, F.; Farrusseng, D.; Bats, N.; Nieto-Draghi, C. *J. Phys. Chem. C* **2011**, *115*, 16425–16432.
47. Snurr, R. Q.; Bell, A. T.; Theodorou, D. N. *J. Phys. Chem.* **1993**, *97*, 13742–13752.
48. Spek, A. *J. Appl. Crystallogr.* **2003**, *36*, 7–13.
49. Ray, K. G.; Olmsted, D.; He, N.; Houndonougbo, Y.; Laird, B. B.; Asta, M. *Phys. Rev. B* **2012**, *85*, 085410–085418.
50. Han, S. S.; Choi, S.-H.; Goddard, W. A., III. *J. Phys. Chem. C* **2010**, *114*, 12039–12047.
51. Han, S. S.; Kim, D.; Jung, D. H.; Cho, S.; Choi, S.-H.; Jung, Y. *J. Phys. Chem. C* **2012**, *116*, 20254–20261.
52. McDaniel, J. G.; Schmidt, J. R. *J. Phys. Chem. C* **2012**, *116*, 14031–14039.
53. McDaniel, J. G.; Yu, K.; Schmidt, J. R. *J. Phys. Chem. C* **2012**, *116*, 1892–1903.

Chapter 4

Utilizing Surface Enhanced Raman Spectroscopy for the Study of Interfacial Phenomena: Probing Interactions on an Alumina Surface

Eric V. Formo,[1] Zili Wu,[*,1,2] Shannon M. Mahurin,[2] and Sheng Dai[*,1,2]

[1]Center for Nanophase Materials, Oak Ridge National Laboratory, PO BOX 2008 MS6493, Oak Ridge, Tennessee 37831, USA
[2]Chemical Sciences Division, Oak Ridge National Laboratory, PO BOX 2008 MS6493, Oak Ridge, Tennessee 37831, USA
[*]E-mail: dais@ornl.gov; wuz1@ornl.gov

Herein is a discussion of new developments in expanding Surface Enhanced Raman Spectroscopy (SERS) into probing a catalyst's structure and interface interactions. To accomplish this, robust SERS substrates were generated by depositing a protective alumina coating on top of silver nanowires (NWs) via atomic layer deposition (ALD). In situ studies of catalytic systems were conducted by analyzing the effects of heating a solid acid on the alumina surface in various environments at temperatures up to 400 °C. Interestingly, the distance-dependent decay of the SERS effect allowed us to probe with enhanced detail the interfacial region. Further, we monitored adsorbate–interface interactions between the adsorption- desorption of pyridine on the acidic sites of a solid acid.

Introduction

In the study of heterogeneous catalytic systems a number of analytical techniques have been utilized to gain insights into a catalyst's structure or possible reaction pathways (*1*, *2*). In particular, Raman spectroscopy is an especially

In Novel Materials for Catalysis and Fuels Processing; Bravo-Suárez, J., et al.;
ACS Symposium Series; American Chemical Society: Washington, DC, 2013.

powerful technique for catalysis analysis due to its ability to analyze catalytic materials and reaction mechanisms in situ. However, Raman spectroscopy has some shortcomings such as a low detection limit and inability to detect fast reaction pathways (*3*). Further, the intensity of the spectra can be severely reduced when taking measurements at high temperatures caused by a loss of ground state phonons, which may obscure many interesting findings (*4*). One method to overcome these issues is to extend Surface Enhanced Raman Spectroscopy (SERS) into the field of catalysis. Specifically the SERS effect allows us to analyze numerous chemical species at extremely low concentrations, which may unearth new insights into a catalyst's structure and possible reaction mechanisms (*5*, *6*). Moreover, the SERS effect undergoes distance dependent decay, which will cause more data to be gathered at the interface region between the surface of the solid support and the catalytic moiety. This has great significance because the interface bond has been considered as the active site in many metal oxide catalyzed reactions (*7*, *8*).

Silver nanostructures are widely utilized as the SERS active species, owing to their unique plasmonic properties, which gives them a superior enhancement factor of the Raman signal (*9*). However, the enhancement capabilities of silver nanomaterials undergo a steep decline when exposed to harsh conditions such as high temperatures and various atmospheric environments that are common in many catalytic reactions (*10–15*). To expand the utilization of SERS into the field of catalysis, there has been significant interest in the fabrication of extremely robust SERS substrates (*16*). Moreover, as the SERS effect can extend up to 2 nm beyond the nanostructures surface, one can deposit an ultrathin protective film on top of the SERS active moiety to enhance its stability (*17*, *18*). Atomic Layer Deposition (ALD) is an excellent method to produce such films composed of robust materials such as alumina that can range from a single molecular layer to several nanometers thick (*19*). Further, the protective layer can act as a model support for the deposition of catalytic materials for the production of catalytic systems.

Another area in which robust SERS substrates could provide valuable insight is in the study of surface interactions. In particular, those interactions that involve the adsorbate/solid interface and examination of a solid acid are interesting because one can determine the nature of its acidity for acid/base catalysis (*20*). By using a solid acid such as phosphotungstic acid (PTA), one can investigate the adsorbate–interface interactions due to the multiple exposed acid sites. Typically, a base such as pyridine will adsorb via either Lewis acid or Brønsted acid binding. Raman spectroscopy can then be used to determine which type of binding is taking place between the adsorbed pyridine and the solid acid surface with each of these binding possibilities yielding differing spectral bands. However, it must be stated that previous endeavors have noted some limitations in using Raman to study these interfaces, such as the fluorescence of the metal oxide solid support and the detection of the extremely small amounts of adsorbed molecules (*21*). Although more recently the issue of fluorescence has been abated by the utilization of ALD to generate the metal oxide layer; a method to enhance the signal of the adsorbate would be beneficial for more in-depth studies of these interface interactions (*22*).

In Novel Materials for Catalysis and Fuels Processing; Bravo-Suárez, J., et al.;
ACS Symposium Series; American Chemical Society: Washington, DC, 2013.

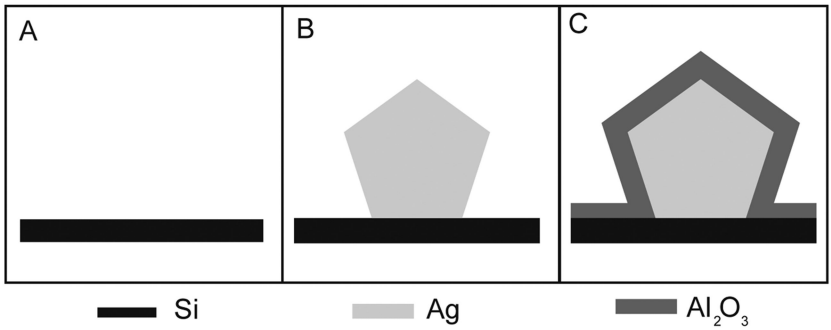

Scheme 1. A schematic diagram illustrating the ALD coating of a Ag nanowire substrate A) is a bare Si or SiO_2 chip; B) nanowires are then deposited onto the substrate; C) the NW covered slide was then coated with a protective Al_2O_3 layer via ALD; as displayed in the cross-sectional diagram, the figure shows a thin layer of ~1.20 nm of Al_2O_3 that encapsulates the NW.

Herein, we discuss methods taken to open SERS for in situ analysis of catalytic systems and interface interactions. Specifically, this capability was unlocked via the utilization of ALD for placing a robust Al_2O_3 overlayer on top of Ag nanowires (NWs) that acted as our SERS active moiety. For the study of the catalyst's structure, we probed PTA placed on top of the protective alumina overlayer by recording the various alterations in the spectra that occurred upon heating in either oxidative or reductive environments. Notably, these SERS substrates had an enhanced capability in analyzing the area closest to the surface of the alumina. Further, these systems allowed us to probe the adsorbate/solid interface interaction between pyridine and the acidic sites on the solid acid PTA, resulting in detection of the base desorption induced by an increase in temperature.

Results and Discussion

Generation of the Stable SERS Substrates

To generate stabile SERS substrates, a bottom-up approach was employed to take advantage of the many novel synthetic techniques used to create nanostructures. Specifically, we chose silver nanowires (NW) to act as our SERS active moiety due to their large recorded enhancement factor (*23*). Illustrated in Scheme 1 is a diagram detailing the fabrication of our SERS active substrates. In the first step, nanowires were deposited via drop-casting onto a glass or silicon chip and allowed to dry in air prior to being placed inside an ALD reaction chamber for overcoating with alumina (Schemes 1A and 1B). A roughly 1.2 nm thick coating of alumina was deposited on top of the nanowires to prevent the presence of pinhole defects in the film (scheme 1C) (*24*).

In Novel Materials for Catalysis and Fuels Processing; Bravo-Suárez, J., et al.;
ACS Symposium Series; American Chemical Society: Washington, DC, 2013.

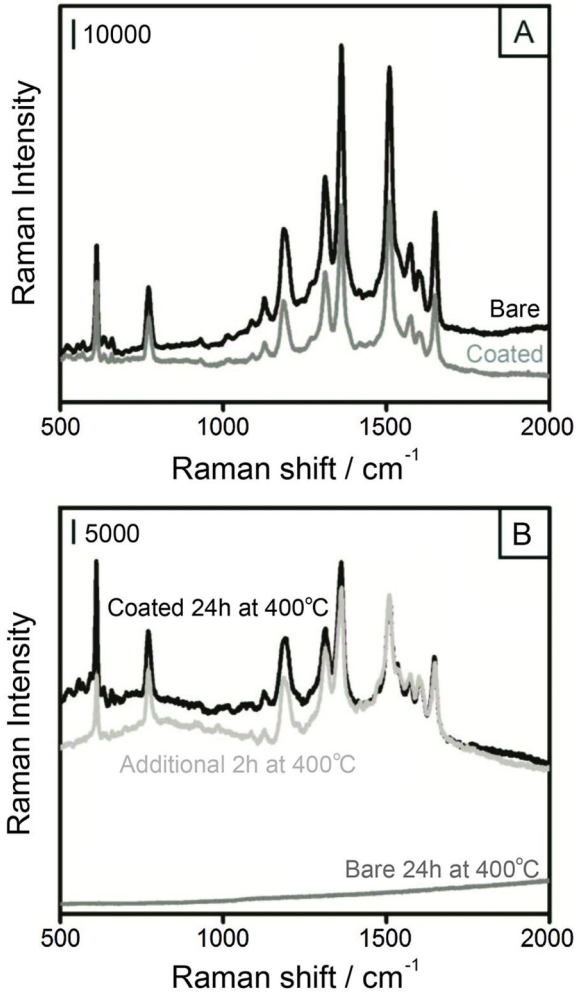

Figure 1. SERS spectra of rhodamine 6G adsorbed onto alumina coated and uncoated Ag NW on glass substrates: A) bare Ag nanowires, and coated with Al_2O_3; B) displays the effects of heating to 400 °C in air for 24 h for both the alumina coated and uncoated, and upon reheating of the alumina coated sample for an additional 2 h. All spectra were taken at room temperature after the reapplication of R6G. The concentration of R6G is 0.1 mM. (Adapted with permission from reference (24). Copyright 2010 American Chemical Society)

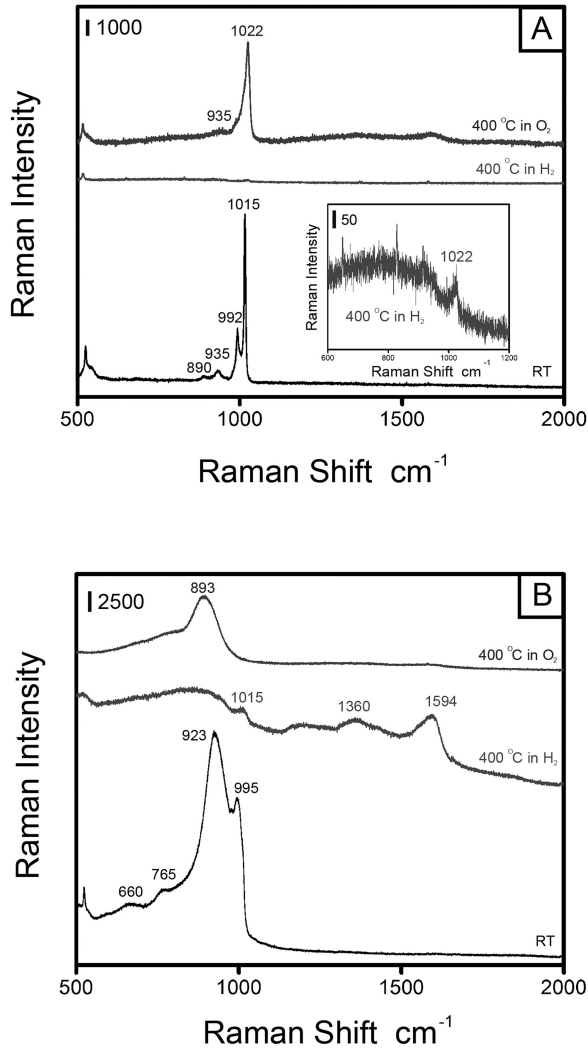

Figure 2. In situ Raman/SERS spectra upon heating of PTA. A) PTA powder on a Si substrate; B) Thin layer of PTA on alumina-coated Ag NWs. SERS substrate at room temperature (bottom traces) and heated to 400 °C in hydrogen or oxygen. (Adapted with permission from reference (25). Copyright 2011 American Chemical Society.)

In Novel Materials for Catalysis and Fuels Processing; Bravo-Suárez, J., et al.;
ACS Symposium Series; American Chemical Society: Washington, DC, 2013.

Subsequently, the Raman signal enhancement of these substrates was elucidated utilizing the equation: *Enhancement Factor (EF)* = $(I_{SERS}/I_{Bulk})(N_{Bulk}/N_{ads})$, for the detection of an organic dye rhodamine 6G (R6G) (*24*). We found that the alumina over-coated sample had a lower EF of 3.0×10^4 in comparison to the EF of 4.4×10^4 for bare Ag NWs, due to the distance dependent decay of the SERS effect (Figure 1A). To determine the robustness of the alumina coated versus the uncoated SERS substrates they were then heated to 400 °C in air for a total time of 24 h, and after cooling to room temperature R6G was reapplied and analyzed. Specifically, the coated sample maintained an EF of 1.08×10^4 whereas the bare substrate was rendered useless for the enhancement of the Raman signal (Figure 1B). Further, after heating of the coated substrate for two more hours at 400 °C, we found the *EF* of the spectrum was nearly unchanged (Figure 1B). These results further substantiate the stabilizing effects of the protective layer and its ability to maintain the enhancing capabilities of the protected NW (*24*).

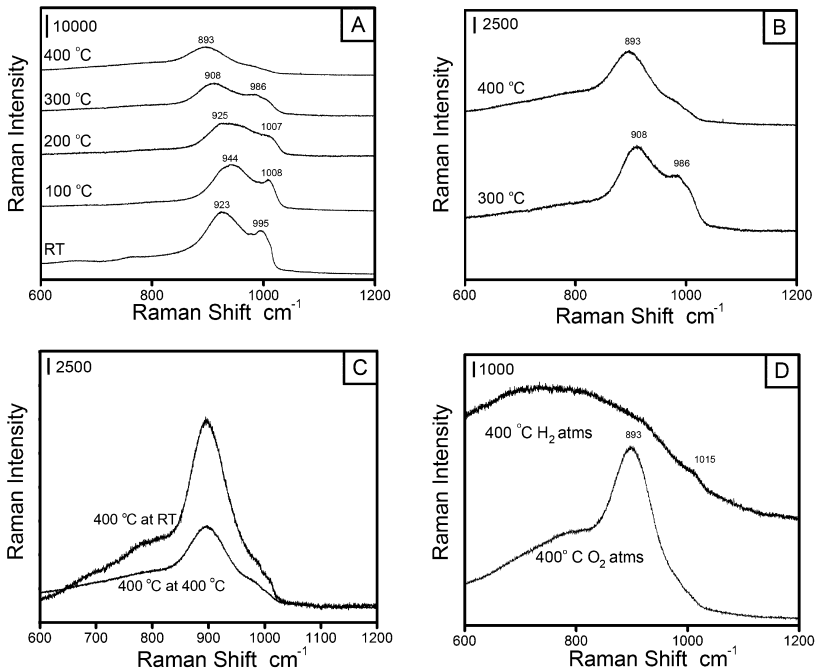

Figure 3. Raman spectra during in situ heating of PTA on Al_2O_3-coated Ag NWs substrate in an oxidative environment. A) In an oxygen atmosphere with SERS spectrum taken at room conditions, 100, 200, 300, and 400 °C; B) close-up of SERS spectra taken at 300 and 400 °C; C) SERS spectra taken at 400 °C and after it had been cooled to RT; D) spectra of PTA on Al_2O_3-coated Ag NWs substrate after reheating to 400 °C in hydrogen, once the substrate had been previously heated to 400 °C in oxygen, then cooled, both spectra taken at 400 °C. (Adapted with permission from reference (25). Copyright 2011 American Chemical Society)

With the generation of these robust SERS substrates, we began to utilize them to probe a catalyst's structure by using the alumina layer as a solid support for the catalytic agent (*25*). In situ Raman spectra of bulk phosphotungstic acid (PTA) on a Si substrate was first collected at room temperature (Figure 2A). The resultant spectrum yielded major peaks at 1015 cm^{-1} corresponding to the ν_s(W=O) mode and at 992 cm^{-1} which is attributed to the ν_{as}(W=O) mode, as well as minor peaks associated with the W–O–W bridging bond at 935 and 890 cm^{-1} (*13*, *14*). Subsequently, the PTA was heated to 400 °C under hydrogen, with a Raman spectra displaying only one discernible feature at 1022 cm^{-1}, which we can assign to the ν_s(W=O) mode. Next, the in situ spectra of the bulk PTA that was heated to 400 °C in an oxidative environment displayed a broad peak at 1022 cm^{-1} that was slightly blue shifted and corresponded to the ν_s(W=O) mode (Figure 2A) (*26–28*).

We then focused on the utilization of the prepared robust SERS substrates to analyze PTA which had been placed on top of the alumina layer (Figure 2B). A number of differences were immediately observed due to the electromagnetic features of the underlying silver NW that caused the parallel ν_s(W=O) band and the perpendicular ν_{as}(W=O) vibrations to invert in signal strength (*25*). The intensity of the spectrum was determined for the peak area between 600 and 1200 cm^{-1}. From the spectrum taken at room temperature, it was determined that the SERS substrate amplified the Raman signal by a factor of 2.4×10^3 (*25*). The SERS substrate enhanced the PTA signal by 9.1×10^2 when heated to 400 °C in a hydrogen environment, displaying a number of interesting features. These included an increase in the relative intensity of the W–O–W signal, the ν_s(W=O) peak, and new features at 1594 and 1360 cm^{-1} corresponding to the formation of some carbonaceous materials (*25*). Subsequently, an in situ SERS spectrum was recorded by heating the PTA/Al_2O_3 substrate under oxygen flow at 400 °C. The spectrum showed a single strong peak at 893 cm^{-1} indicating a dominance of the W–O–W bond with little signal from the W=O component of the structure, resulting in an *EF* of 1.4×10^3 (Figure 2B). These results showcase the robust nature of our SERS substrates to operate under harsh conditions (*25*).

Due to the extreme difference between the spectra of bulk PTA and the PTA/Al_2O_3 SERS substrates when heated in an oxidative environment, a more in-depth study was needed to elucidate the reason for such a disparity. When heated between 100 and 300 °C only slight changes in the spectra occurred which can be attributed to the complete dehydration of PTA, causing initially a blue shift followed by a red shift as a result of a loss of electron density (Figure 3A). Interestingly, at the final step from 300 to 400 °C the two major peaks at 906 and 986 cm^{-1} in the spectra (300 °C) transformed into one single peak at 893 cm^{-1} along with a slight shoulder around 986 cm^{-1} (Figure 3B). This drastic change is caused by the W–O–W bridging bond rotating closer to the alumina overlayer where the signal enhancement is at its most intense from the underlying NWs (*29*, *30*). To determine if these changes were only present at the higher temperatures the sample was cooled to room temperature and the resultant spectrum obtained only showed an increase in intensity (Figure 3C). Since the spectrum did not undergo alteration upon cooling, it can be concluded that the PTA was in a

fixed position on the substrate's surface. As cooling did not seem to alter the arrangement of PTA on the alumina surface, the substrate was then reheated to 400 °C in hydrogen to determine if the PTA would undergo reorientation. This treatment resulted in the re-emergence of the ν_s(W=O) peak which denotes that the PTA rotated again so that some of the W=O species interacted with the alumina surface (Figure 3D).

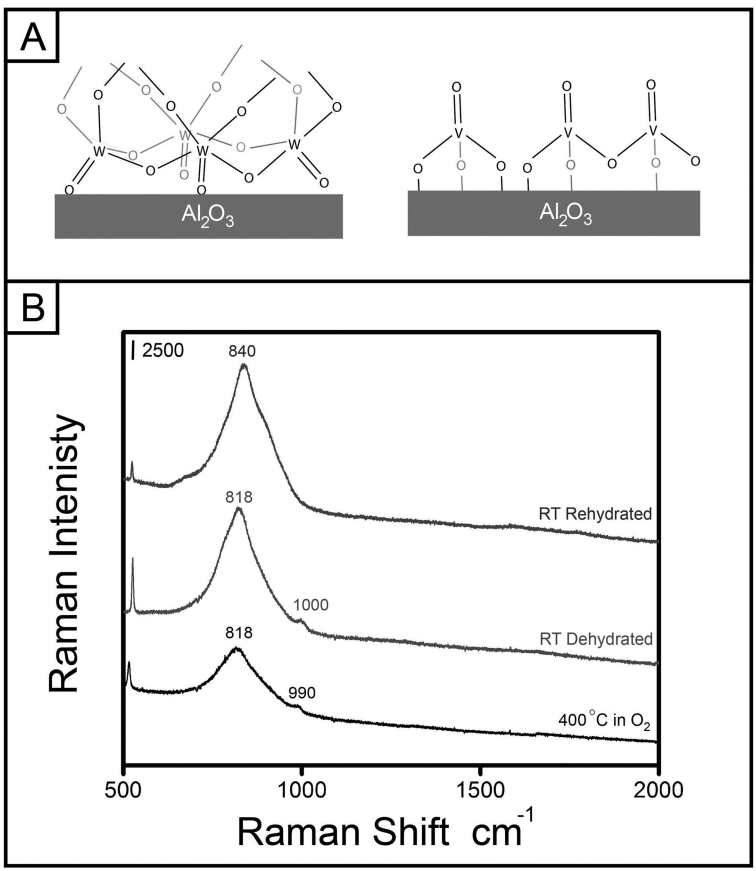

Figure 4. A) Scheme depicting the phosphotungstic acid (PTA) or vanadia closest to the surface of the Al_2O_3-coated SERS substrate. B) Raman spectra of the calcined vanadia-coated sample after it had been heated in oxygen to 400 °C (bottom trace) then cooled to room temperature (middle trace) and once it had been rehydrated (top trace). (Adapted with permission from reference (25). Copyright 2011 American Chemical Society.)

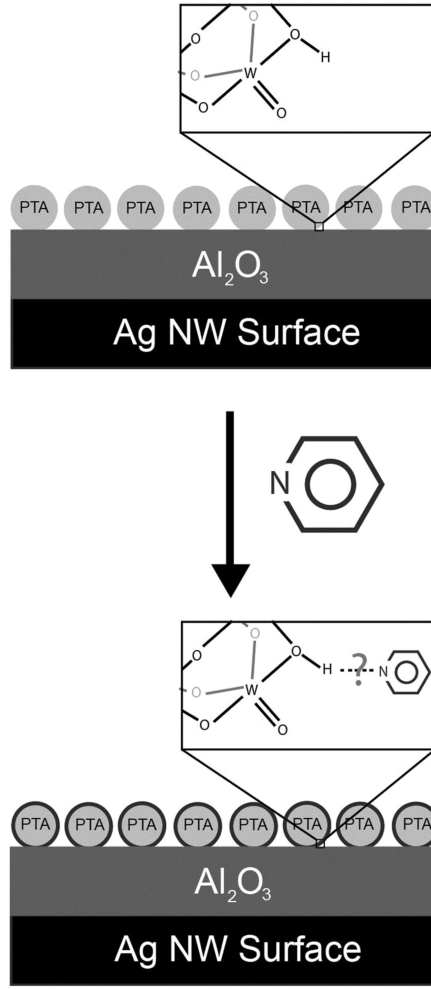

Scheme 2. Scheme depicting steps towards generating the adsorbate/solid interface system. PTA is first assembled onto the preheated alumina surface, which is subsequently exposed to pyridine vapor.

To further prove that the interface region between the catalytic moiety and the solid support is where a predominance of the spectral data is gathered, we deposited vanadia onto the alumina in place of the PTA. Figure 4A illustrates the structural differences between PTA, which can freely associate with the alumina surface, and vanadia, which is directly bound onto the alumina via V–O–Al bonds (*7*, *8*, *31*). Specifically for the vanadia coated Al_2O_3/Ag NWs sample, the interfacial V–O–Al modes should experience a larger enhancement of the Raman signal in comparison to the outer V=O bond. When the vanadia coated Al_2O_3/Ag NWs sample was heated to 400 °C in an oxygen atmosphere, the peak corresponding to the interfacial V–O–Al mode observed at 818 cm^{-1} was much

In Novel Materials for Catalysis and Fuels Processing; Bravo-Suárez, J., et al.;
ACS Symposium Series; American Chemical Society: Washington, DC, 2013.

larger than the peak at 990 cm^{-1} that is attributed to the outer V=O bond (*32*). Subsequently, spectra were taken to study the effect of temperature on the sample. When a spectrum was recorded for the substrate after it had been cooled to room temperature it displayed only a slight change in the position of the V=O peak in relation to the spectra taken at 400 °C (Figure 4B). Finally, the substrate was rehydrated and as expected the Raman spectra displayed no trace of the V=O mode due to facile hydration of the V=O bond (*7*).

Analyzing the Adsorbate/Solid Interface

Scheme 2 depicts the steps in the generation of the adsorbate/solid interface system that we probed. First, a PTA decorated stable SERS substrate was produced using the protocols previously mentioned (Scheme 2A). To generate the adsorbate–interface system, the PTA-coated substrate was suspended above a pyridine solution, allowing pyridine vapor to adsorb directly onto the acid sites on the PTA (Scheme 2B). The signal enhancement imbued by the underlying nanowires allowed us to probe the sites near the alumina surface. In this manner, we could determine whether Brønsted acid, Lewis acid, or H-bonding was taking place at the adsorbate/surface between the pyridine and the acidic sites of the PTA.

Figure 5A displays the SERS spectrum of the adsorbate/surface between the pyridine and the acidic sites of the PTA after removal from the pyridine reaction chamber. Specifically, we observed peak formations between 1007–1015 cm^{-1} and 1025–1035 cm^{-1} corresponding to the symmetric and trigonal ring breathing modes of pyridine under Brønsted acid binding onto the solid acid surface (*21*). Further, we noticed a slight red shift in the spectrum of the structural components of the PTA with the ν_s(W=O) at 985 cm^{-1}, ν_{as}(W=O) at 970 cm^{-1}, and a slight peak at 770 cm^{-1} indicative of the W–O–W bridging bond. Moreover, the ν_s(W=O) peak was more intense than the ν_{as}(W=O), which is different from what is expected for PTA in close proximity of silver nanomaterials where the ν_{as}(W=O) peak will be the most SERS active (see Figures 2B and 3) (*33*). These two variances in the PTA spectrum can be attributed to side effects related to the exposure to pyridine vapor along with oxygen and water vapor in the atmosphere during the adsorption period. Upon heating in an inert environment, we observed a number of changes in the spectra of the adsorbate/surface interactions. When heated to 100 °C, we first noticed a broadening of the PTA ν_s(W=O) peak at 990 cm^{-1}, which engulfed the symmetric ring breathing mode of the pyridine observed as a shoulder in this larger ν_s(W=O) peak area with a strong pyridine peak at 1030 cm^{-1}. These spectral changes are probably caused by the dehydration of any atmospheric water vapor that could have also absorbed on the catalyst surface. At 200 °C, we continued to see a strong pyridine peak at 1030 cm^{-1}; however, in the PTA section of the ν_s(W=O) and ν_{as}(W=O) there was further separation along with an increase in the intensity of the W–O–W bridging bond region. Further heating to 300 °C continued this trend in the PTA component region along with an adsorbed pyridine signal that could still be seen at 1025–1035 cm^{-1} (Figure 5B). After increasing the temperature to 400 °C, the pyridine was completely removed leaving three peaks at 1005, 960, and 924 cm^{-1}, which corresponded to

ν_s(W=O), ν_{as}(W=O), and ν_{as}(W–O–W), respectively (Figure 5C). Upon cooling (to observe if the loss of the bonded pyridine signal was due to the decrease in signal intensity that occurred while operating at higher temperatures), we still did not see any peaks due to pyridine adsorbed on Brønsted acid sites in the spectrum collected at room temperature (Figure 5C). When the region between 950 and 1100 cm^{-1} was explored more closely (Figure 5D), we could clearly see that once heated to 400 °C only the ν_s(W=O) peak at 1005 cm^{-1} was present in comparison to the peaks that were present at 1007–1015 cm^{-1} and 1025–1035 cm^{-1} in the initial spectrum from pyridine adsorption.

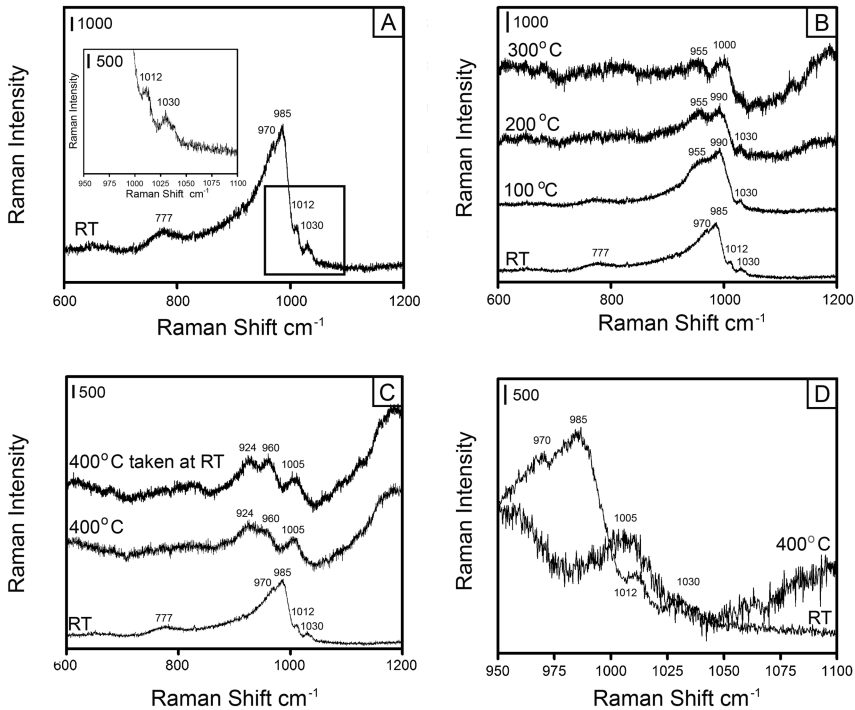

Figure 5. Raman spectra of pyridine adsorbed onto the PTA on Al_2O_3-coated Ag NWs substrate. A) Pyridine adsorbed onto the PTA surface at room conditions; B) after heating to 100, 200, and 300 °C; C) after further heating to 400 °C, taken at 400 °C (middle trace) and once the substrate had cooled back to room temperature (top trace); D) close-up of SERS spectra taken at 400 °C and the initial pyridine/PTA spectrum.

When we compared our SERS data to the Raman spectrum of the bulk PTA that had adsorbed pyridine in a similar manner, a number of discrepancies were observed that highlight the effect of the underlying nanowires enhancing the signal closest to the alumina surface. Bulk PTA showed strong Brønsted acid binding peaks at 1011 and 1062 cm^{-1} along with a shoulder at 1027 cm^{-1} (Figure 6A). When heated, there was a steep reduction in the intensities of the pyridine peaks

In Novel Materials for Catalysis and Fuels Processing; Bravo-Suárez, J., et al.;
ACS Symposium Series; American Chemical Society: Washington, DC, 2013.

particularly after heating to 200 °C, a temperature at which only peaks associated with the PTA W=O bonds had any Raman signals at 1007 and 995 cm^{-1} (Figure 6B). Further, the strong peak at 1007 cm^{-1} also led us to conclude that the large peak at 1011 cm^{-1} in the room temperature spectrum was most likely a combination of the adsorbed pyridine and ν_s(W=O). When we compared the spectra at 300 °C for the SERS case, there was a visible shoulder for the pyridine absorption along with a strong increase in the intensity of the W–O–W bond for PTA on Al_2O_3-coated SERS substrate, whereas only the ν_s(W=O) peak was visible for the bulk case (Figure 6B). This observation indicates that the pyridine is more strongly bound to the surface of the PTA/Al_2O_3 substrate than bulk PTA, likely due to a strong interaction between PTA and alumina. However, in both cases at 400 °C, we only observed data for PTA with the bulk showing W=O and the SERS substrate giving us information about how the PTA has arranged itself on the surface of the alumina after deposition.

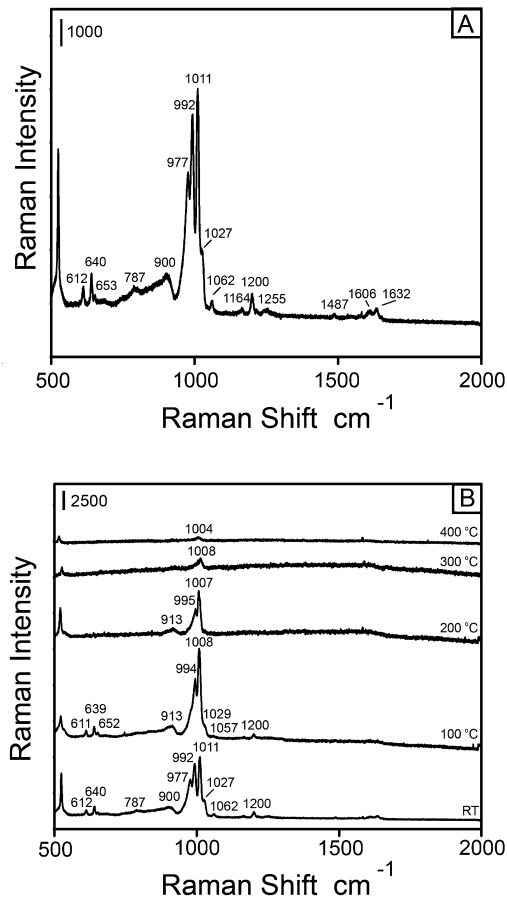

Figure 6. Raman spectra of pyridine adsorbed onto the bulk PTA. A) pyridine adsorbed onto the PTA surface at room conditions; B) after heating to 100, 200, 300, and 400 °C.

Summary

Herein, we have shown a simple method for the generation of stabile SERS substrates, which allowed us to expand the use of Surface Enhanced Raman Spectroscopy (SERS) into probing a catalyst's structure as well as its interface interactions. Specifically, robust SERS substrates were generated via a bottom-up approach in which silver nanowires (NWs) were coated with an ultra-thin protective coating of alumina by the use of atomic layer deposition (ALD). Subsequently, in situ studies were conducted by analyzing the effects of heating a solid acid, phosphotungstic acid (PTA), on the alumina surface in either an oxygen or hydrogen environment at temperatures up to 400 °C. Notably, the distance-dependent decay of the enhancement factor of the SERS signal from the underlying NWs allowed us to probe with enhanced detail the interfacial region between the PTA and the alumina surface. Further, we also monitored adsorbate–interface interactions between the adsorption/desorption of pyridine on the acidic sites of a solid acid at high temperatures.

Acknowledgments

This research was conducted at the Center for Nanophase Materials Sciences, which is sponsored at the Oak Ridge National Laboratory by the Scientific User Facilities Division, Office of Basic Energy Sciences, U.S. Department of Energy. A portion of this research, performed by Shannon M. Mahurin, was conducted through the Division of Chemical Sciences, Geosciences, and Biosciences, Office of Basic Energy Sciences, U.S. Department of Energy. The research was supported in part by the appointment of E. V. Formo to the ORNL Postdoctoral Research Associates Program, administered jointly by ORNL and the Oak Ridge Associated Universities. The Oak Ridge National Laboratory is managed by UT-Battelle, LLC for the U.S. Department of Energy under contract DE-AC05-00OR22725.

References

1. Li, Y.; Somorjai, G. A. *Nano Lett.* **2010**, *10*, 2289–2295.
2. Jones, C. W.; Tao, F.; Garland, M. V. *ACS Catal.* **2012**, *2*, 2444–2445.
3. Weckhuysen, B. M. *Chem. Commun.* **2002**, *2*, 97–110.
4. Xie, S.; Iglesia, E.; Bell, A. T. *J. Phys. Chem. B* **2001**, *105*, 5144–5152.
5. Camden, J. P.; Dieringer, J. A.; Zhao, J.; Van Duyne, R. P. *Acc. Chem. Res.* **2008**, *41*, 1653–1661.
6. Brus, L. *Acc. Chem. Res.* **2008**, *41*, 1742–1749.
7. Bañares, M. A.; Wachs, I. E. *J. Raman Spectrosc.* **2002**, *33*, 359–380.
8. Weckhuysen, B. M.; Keller, D. E. *Catal. Today* **2003**, *78*, 25–44.
9. Camargo, P. H. C.; Cobley, C. M.; Rycenga, M.; Xia, Y. *Nanotechnology* **2009**, *20*, 434020–434028.
10. Heck, K. N.; Janesko, B. G.; Scuseria, G. E.; Halas, N. J.; Wong, M. S. *J. Am. Chem. Soc.* **2008**, *130*, 16592–16600.
11. Fokas, C.; Deckert, V. *Appl. Spectrosc.* **2002**, *56*, 192–199.

12. Beltramo, G. L.; Shubina, T. E.; Koper, M. T. M. *ChemPhysChem* **2005**, *6*, 2597–2606.
13. Lopez, E.; Errazu, A. F.; Borio, D. O.; Bucala, V. *Chem. Eng. Sci.* **2000**, *55*, 2143–2150.
14. Christopher, P.; Linic, S. *J. Am. Chem. Soc.* **2008**, *130*, 11264–11265.
15. Adleman, J. R.; Boyd, D. A.; Goodwin, D. G.; Psaltis, D. *Nano Lett.* **2009**, *9*, 4417–4423.
16. Wachs, I. E.; Roberts, C. A. *Chem. Soc. Rev.* **2010**, *39*, 5002–5017.
17. Bao, L.; Mahurin, S. M.; Dai, S. *Anal. Chem.* **2004**, *76*, 4531–4536.
18. Hao, E.; Schatz, G. C. *J. Chem. Phys.* **2004**, *120*, 357–366.
19. George, S. M. *Chem. Rev.* **2010**, *110*, 111–131.
20. Liu, L.; Quezada, B.; Stair, P. C. *J. Phys. Chem. C* **2010**, *114*, 17105–17111.
21. Takenaka, T. *Adv. Colloid Interface Sci.* **1979**, *11*, 291–313.
22. Lu, J.; Kosuda, K. M.; Van Duyne, R. P.; Stair, P. C. *J. Phys. Chem. C* **2009**, *113*, 12412–12418.
23. Im, S. H.; Lee, Y. T.; Wiley, B. J.; Xia, Y. *Angew. Chem., Int. Ed.* **2005**, *44*, 2154–2157.
24. Formo, E.; Mahurin, S.; Dai, S. *ACS Appl. Mater. Interfaces* **2010**, *2*, 1987–1991.
25. Formo, E.; Wu, Z.; Mahurin, S. M.; Dai, S. *J. Phys. Chem. C* **2011**, *115*, 9068–9073.
26. Rocchiccioli-Deltcheff, C.; Fournier, M.; Franck, R.; Thouvenot, R. *Inorg. Chem.* **1983**, *22*, 207–216.
27. Thouvenot, R.; Fournier, M.; Franck, R.; Rocchiccioli-Deltcheff, C. *Inorg. Chem.* **1984**, *23*, 598–605.
28. Vuurmant, M. A.; Wachs, I. E. *J. Phys. Chem.* **1992**, *96*, 5008–5016.
29. Teague, C. M.; Li, X.; Biggin, M. E.; Lee, L.; Kim, J.; Gewirth, A. A. *J. Phys. Chem. B* **2004**, *108*, 1974–1985.
30. Siiman, O.; Feilchenfeldt, H. *J. Phys. Chem.* **1988**, *92*, 453–464.
31. Brazdova, V.; Ganduglia-Pirovano, M. V.; Sauer, J. *J. Phys. Chem. C* **2010**, *114*, 4983–4994.
32. Kim, H. S.; Zygmunt, S. A.; Stair, P. C.; Zapol, P.; Curtiss, L. A. *J. Phys. Chem. C* **2009**, *113*, 8836–8843.
33. Xie, S.; Iglesia, E.; Bell, A. T. *J. Phys. Chem. B* **2001**, *105*, 5144–5152.

Chapter 5

Interactions of Sulfur Oxides with Diesel Oxidation Catalysts (DOCs)

Hom N. Sharma,[1] Steven L. Suib,[2] and Ashish B. Mhadeshwar*[,1,3]

[1]Department of Chemical, Materials, and Biomolecular Engineering and Center for Clean Energy Engineering, University of Connecticut, 191 Auditorium Rd., Unit 3222, Storrs, Connecticut 06269, USA
[2]Department of Chemistry, University of Connecticut, 55 North Eagleville Rd., Unit 3060, Storrs, Connecticut 06269, USA
***E-mail: ashish.mhadeshwar@gmail.com**
[3]Currently at ExxonMobil Research & Engineering, Annandale, NJ 08801

Sulfur oxides (SO_x) in the diesel engine exhaust are one of the major factors contributing toward deactivation of emissions aftertreatment catalysts. Interactions of SO_x with the catalyst metals and supports can result in sulfate formation. Here, we review various experimental and computational studies regarding SO_x interaction on Pt–Pd/alumina catalysts, which are typically used in Diesel Oxidation Catalysts (DOCs). In addition, we propose a novel microkinetic model for SO_2 oxidation on Pt as a first step toward understanding the DOC-SO_x interactions. The proposed model contains 24 elementary steps (12 reversible) with five surface species. The microkinetic model is validated against experimental data for SO_2 oxidation on Pt. Finally, we discuss the challenges of incorporating sulfur-based deactivation in kinetic modeling, and propose potential directions that could lead to the development of sulfur resistant materials for DOCs.

In Novel Materials for Catalysis and Fuels Processing; Bravo-Suárez, J., et al.;
ACS Symposium Series; American Chemical Society: Washington, DC, 2013.

Introduction

Diesel Engine Emissions

Diesel engines are an essential part of the modern society and backbone of the global economy. Diesel is the predominant source of power used in trucks, railroads, shipping, agriculture, public transportation, airport operations, mining, as well as homeland security and defense (*1*). Diesel provides better fuel economy, greater power density, better performance, unmatched durability, and longer engine life than many other energy sources (*2–6*). However, diesel engines are responsible for producing toxic compounds such as carbon monoxide (CO), carbon dioxide (CO_2), nitrogen oxides (NO_x), hydrocarbons (HC), sulfur oxides (SO_x), volatile organic compounds (VOCs) (*7–9*), poly aromatic hydrocarbons (PAHs) (*10*, *11*), soluble organic fractions (SOF), and particulate matter (PM) (*3*, *12*, *13*). Furthermore, solid emissions such as metals, inorganic compounds, sulfates and solid hydrocarbons (*13*, *14*), nitrogen containing emissions such as hydrogen cyanide (HCN) and ammonia (NH_3) as well as aldehydes such as formaldehyde (CH_2O) and acetaldehyde (CH_3CHO) have also been observed in the diesel engine exhaust (*15–18*). These emissions are known to cause cancer, premature death, acute and chronic respiratory injury, asthma attacks, ground level ozone formation, acid deposition, particulate haze, visibility impairment; and they can damage plants, animals, crops, and water resources (*3*, *19–23*). Major emission components and their ranges from a typical diesel engine exhaust are shown in Table 1.

Exhaust Aftertreatment Components

Due to a higher air to fuel (A/F) ratio (see Figure 1) compared to traditional gasoline engines (A/F = 14.7), the traditional Three Way Catalyst (TWC) for gasoline exhaust is unable to effectively control emissions from diesel engine exhaust; and therefore, the diesel engine exhaust aftertreatment system is quite complex (*21*, *31*). Multiple aftertreatment units are needed to control various components of diesel engine emissions, as shown in Figure 2.

Diesel Particulate Filters (DPF) are the most popular aftertreatment technology to control particulates/soot and to meet the stringent PM emissions standards (*7*, *32*). DPFs are made of porous materials and consist of channels which are alternately blocked (*2*), so the exhaust gas is forced through the channel walls, but the PM is trapped on the filter wall (*33*). Even though DPFs are efficient in removing particulates from the engine exhaust, periodic regeneration of DPFs is necessary to avoid any plugging/backpressure. Oxygen (10–15% of exhaust stream) is the main oxidant to burn off the soot paricles; however, presence of NO_2 in the exhaust stream (from NO oxidation on DOC) can enhance the DPF efficiency significantly along with catalytic coating (in catalytic DPF (cDPF)) (*30*, *34–37*).

In Novel Materials for Catalysis and Fuels Processing; Bravo-Suárez, J., et al.;
ACS Symposium Series; American Chemical Society: Washington, DC, 2013.

Table 1. Typical diesel engine exhaust composition at an equivalence ratio (λ) of 1.1-6 (*3*, *24–30*). λ is 1, when the air to fuel ratio (A/F) is 14.7

Species	*Concentration range*	*Unit*
CO	100–10000	ppm
NO_x	30–1000	ppm
HC	50–500	ppm C_1
SO_x	Proportional to fuel sulfur (*3*), 10–100[a] (*24*), ~1.0[b]	ppm
CO_2	2–12	%
PM	20–200	mg/m^3
O_2	5–15	%
H_2O	1.4–7	%
NH_3	2	mg/mile
Cyanides	1	mg/mile
Benzene	6	mg/mile
Toluene	2	mg/mile
PAH	0.3	mg/mile
Aldehydes	0.0131–0.1244	mg/km

[a] Based on the information that fuel with 500 ppm of sulfur produces ~20 ppm SO_x.
[b] Based on current EPA regulations for fuel sulfur level (15 ppm maximum).

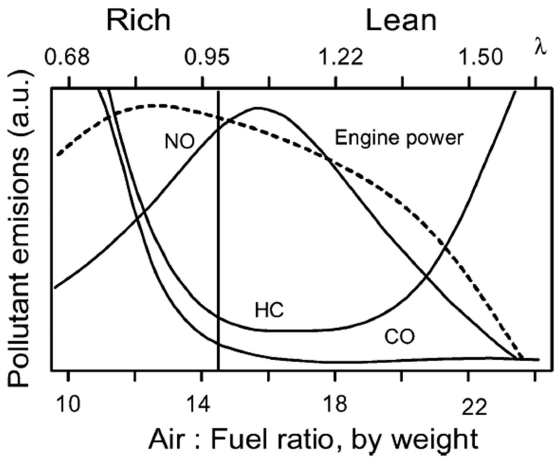

Figure 1. Effect of air to fuel ratio on engine emissions and engine power. Reproduced with permission from reference (24). Copyright 2003 Elsevier.

In Novel Materials for Catalysis and Fuels Processing; Bravo-Suárez, J., et al.;
ACS Symposium Series; American Chemical Society: Washington, DC, 2013.

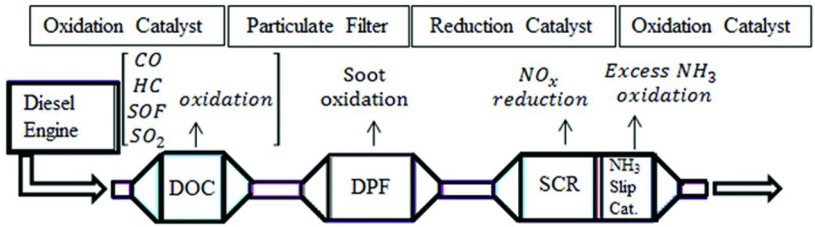

Figure 2. Schematic of DOC, DPF, DeNO$_x$, and Ammonia Slip Catalyst (ASC) components in a typical diesel engine exhaust aftertreatment system. Position of the aftertreatment component units can vary according to the manufacturer, type of DeNO$_x$ unit used, and the regulations.

It is extremely difficult to reduce NO_x from the diesel engine exhaust under excess oxygen conditions (*38*). To reduce/remove NO_x from the diesel engine exhaust, two common strategies are considered, namely, Selective Catalytic Reduction (SCR) and NO_x Storage and Reduction (NSR). SCR selectively reduces the nitrogen oxides (NO and NO_2) to N_2 using either NH_3/Urea (typically V_2O_5–WO_3/TiO_2 catalyst and more recent Fe-/Cu- zeolite based monolithic catalysts) or hydrocarbons (Ag/Al_2O_3 based catalyst) (*21*, *39–46*). On the other hand, NSR catalysts (also known as Lean NO_x Traps (LNT)) first remove NO_x from a lean gas stream by reversible chemical adsorption onto a catalyst (typically $Pt/BaO/Al_2O_3$) in the form of nitrates/nitrites, followed by reduction under stoichiometric or rich conditions (*47–49*).

Urea/NH_3-SCR is a popular technology for NO_x reduction. However, it is also associated with excess/unreacted NH_3 in the downstream, typically ~10 ppm (*50*). A Pt/Al_2O_3 coated oxidation catalyst—Ammonia Slip Catalyst (ASC) —is often installed after the NH_3/Urea-SCR to control the excess NH_3 (*51–55*). ASC oxidizes NH_3 to N_2 with high selectivity, allows high NH_3/urea dosing without increasing NH_3 emissions, and avoids undesirable products such as NO_x and N_2O (*55*, *56*). Recent commercial ASC involves the implementation of bifunctional dual-layer catalysts, where the lower layer contains a Pt/Al_2O_3 catalyst to oxidize ammonia, while the upper layer consists of an SCR catalyst (*54*).

Finally, Diesel Oxidation Catalysts (DOCs) represent the most predominant technology to oxidize the toxic emissions/byproducts from diesel engine exhaust (*31*, *57–63*). Typical DOCs are Platinum (Pt)/Palladium (Pd)/Pt–Pd alloy coated honeycomb like structures, as shown in Figure 3. Pd is essential to prevent the sintering of Pt particles at high temperature, which improves the overall DOC lifetime and thermal stability (*64*). Pd also reduces the DOC cost, which is a very expensive component of diesel exhaust aftertreatment. In the next section, we elaborate on the role of DOC in diesel engine exhaust aftertreatment.

In Novel Materials for Catalysis and Fuels Processing; Bravo-Suárez, J., et al.;
ACS Symposium Series; American Chemical Society: Washington, DC, 2013.

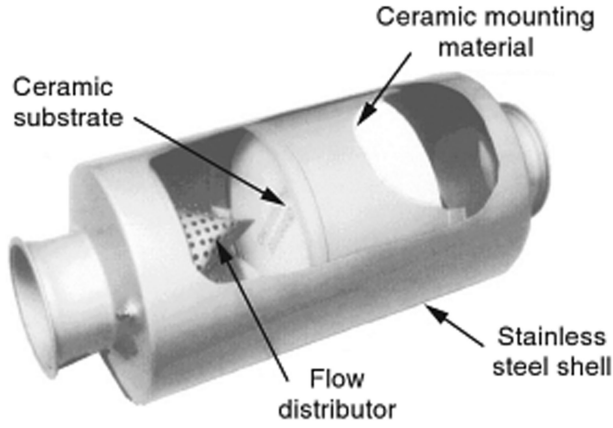

Figure 3. Schematic of a typical Diesel Oxidation Catalyst (DOC). Reproduced with permission from reference (29).Copyright 2009 John Wiley & Sons.

Role of DOC in Exhaust Aftertreatment

The primary function of the DOC is to oxidize hydrocarbons (HC), NO, CO, and byproducts from upstream components to less/nontoxic compounds. Furthermore, DOC also provides NO_2 for a downstream urea-SCR, which operates efficiently at an equimolar ratio of NO and NO_2 (*31*, *65*, *66*). NO_2 produced from DOC can also be used to oxidize soot in the DPF at lower temperature than with O_2 alone (*20*, *31*, *67*, *68*). Finally, DOC may be needed downstream of a hydrocarbon (HC)-SCR to oxidize the SCR byproducts (or unreacted species), such as CO, HC, NO, NH_3, HCN, CH_2O, N_2O, acetonitrile (CH_3CN), and CH_3CHO (*15*, *16*, *69–71*). Major catalytic reactions on the DOC can be summarized as follows (*61*, *62*, *72*, *73*)

$$CO + ½\ O_2 \rightarrow CO_2 \quad (1)$$

$$[HC] + O_2 \rightarrow CO_2 + H_2O \quad (2)$$

$$NO + ½\ O_2 \rightarrow NO_2 \quad (3)$$

$$NH_3 + O_2 \rightarrow N_2 + NO_x + H_2O \quad (4)$$

$$HCN + O_2 \rightarrow NO_x + CO_2 + H_2O \quad (5)$$

$$[Aldehydes] + O_2 \rightarrow CO_2 + H_2O \quad (6)$$

$$[SOF] + O_2 \rightarrow CO_2 + H_2O \quad (7)$$

$$SO_2 + \tfrac{1}{2}\, O_2 \rightarrow SO_3 \quad (8)$$

Despite the versatile nature and utility of DOC, its deactivation due to sulfur is a major challenge in diesel engine exhaust aftertreatment, which is the primary focus of the sections to follow.

Impact of Sulfur on DOC Sulfation and Deactivation

Most catalysts deactivate over time, as reflected by decreased conversion/selectivity, thereby requiring catalyst regeneration/replacement and/or process shutdown. Typical catalyst deactivation mechanisms include (i) poisoning, (ii) fouling, (iii) thermal degradation, (iv) vapor formation, (v) vapor-solid and/or solid-solid reactions, and (vi) attrition/crushing (*74*, *75*). Here, we focus on the deactivation of DOC due to sulfur (poisoning).

Sulfur is present in the diesel fuel and it also comes from the lubricants used (*14*, *49*, *61*). Due to the United States Environmental Protection Agency (USEPA) regulations, the currently used ultra low sulfur diesel (USLD) contains up to 15 ppm sulfur (*49*, *76–78*). In typical diesel engine exhausts, this results into ~1 ppm of sulfur in oxide form (*8*), which can deactivate the DOC after long term exposure as well as increase the PM emissions (*8*, *14*, *79*, *80*). An example of DOC deactivation due to sulfur in the fuel is shown in Figure 4, where the NO oxidation performance decreased significantly in a few hours in the presence of sulfur (*8*). Lubricant oil can also adversely impact the sulfur level in exhaust leading to catalyst deactivation (*81*).

Sulfur in the diesel fuel and lubricants is oxidized to sulfur dioxide (SO_2) in the engine (*61*). Due to the excess oxygen in the exhaust, SO_2 can be further oxidized to sulfur trioxide (SO_3) on the DOC or cDPF above 300 °C (*14*, *61*, *82–84*). SO_3 has been reported to be stable up to 700 °C (*31*, *85*). Both sulfur oxides interact with the DOC, resulting in its deactivation. In general, catalyst deactivation due to sulfur is a complex phenomena, associated with changes in structural, morphological, and electronic properties (*86*). For simplicity, DOC deactivation due to sulfur can be divided into three major categories, namely, metal oxide sulfation, support sulfation, and SO_x interactions with water and ammonia in the exhaust, as described next.

In Novel Materials for Catalysis and Fuels Processing; Bravo-Suárez, J., et al.;
ACS Symposium Series; American Chemical Society: Washington, DC, 2013.

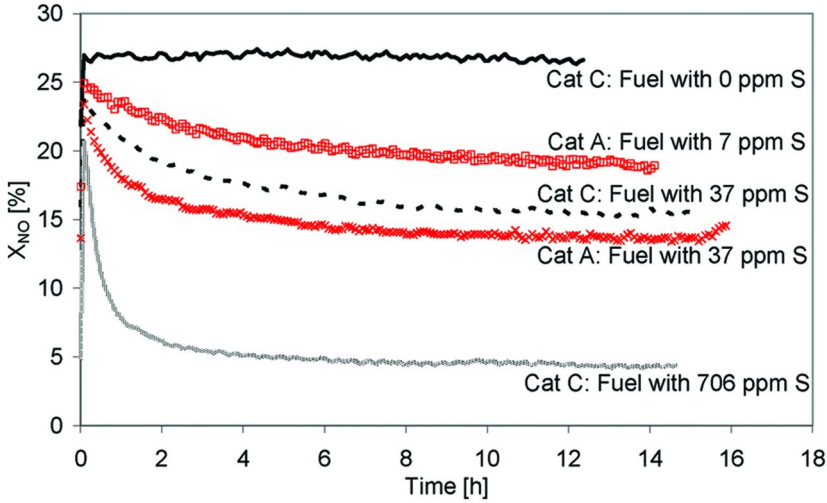

Figure 4. Effect of fuel sulfur level on NO conversion on commercial DOCs. Reproduced with permission from reference (8). Copyright 2009 American Chemical Society (ACS).

Metal Oxide Sulfation

The sensitivity order of sulfation of oxidation catalysts used in diesel engine exhaust aftertreatment is Pd > Pt > Rh (*87*), that is, Pd is more likely to be sulfated compared to Pt DOCs. Pd is typically converted to PdO due to the high oxygen content in the diesel engine exhaust, whereas Pt remains in the metallic form (*64*). Pt is highly active for SO_2 oxidation (*82*, *88*, *89*), but platinum sulfate ($PtSO_4$) formation is not favored (*14*). On the other hand, palladium sulfate ($PdSO_4$) formation is widely reported in the literature (*81*, *90*). Under lean-burn Natural Gas Vehicles (NGV) operating conditions (in the presence of SO_2), deactivation of Pd catalysts due to formation of inactive $PdSO_4$ has also been observed (*84*, *90*). The overall reaction for the metal oxide sulfation can be written as follows (*61*, *91*).

$$PdO + SO_3 \rightarrow PdSO_4 \quad (9)$$

Support Sulfation

In Pt–Pd based DOCs, the precious metal catalysts are dispersed on a support (washcoat) to increase the catalyst surface area which in turn provides higher catalytic activity. Supports can also provide thermal/mechanical stability (*24*, *61*). Typically, γ–Al_2O_3, SiO_2, or ZrO_2 are used as support materials, as they are highly porous inorganic oxides and ideal for gas diffusion; among these, γ–Al_2O_3 is the most common support for DOCs (*14*, *31*, *61*, *72*). However, presence of sulfur oxides in the diesel engine exhaust can be detrimental to the Al_2O_3 support, which ultimately deteriorates the DOC activity (*61*, *81*, *82*, *92*, *93*). Studies

show that SO_3 strongly interacts with the Al_2O_3 support in DOC (*94*). Once SO_3 is formed on the catalyst, there is a reaction with Al_2O_3 to form aluminum sulfate ($Al_2(SO_4)_3$) (*94–96*), which blocks the alumina pores or covers its surface, resulting in decreased surface area (*31*, *57*, *97*) and decreased catalytic activity (*95*). Even though the support sulfation reaction is reversible, that is, $Al_2(SO_4)_3$ forms Al_2O_3 and SO_3 upon heating (*87*), this decomposition reaction requires a very high temperature (~727 °C) (*98*). The overall reaction of Al_2O_3 support sulfation can be written as follows (*72*).

$$Al_2O_3 + 3\ SO_3 \rightarrow Al_2(SO_4)_3 \quad (10)$$

SO_x Interactions with Water and Ammonia

Diesel engine exhaust contains significant water vapor (1.4–7%, see Table 1); therefore, SO_3 can also react with the water vapor to form sulfuric acid (H_2SO_4), thus creating tremendous challenges for emissions aftertreatment (*8*, *61*). H_2SO_4 contributes to the increase in particulates formation; ultrafine particles in diesel exhaust are considered especially hazardous because of their ability to penetrate deeply into the lungs (*14*, *99*, *100*). H_2SO_4 can desorb at 350–400 °C or decompose back to SO_3 and H_2O at >250 °C (*8*). The overall reaction of sulfuric acid formation from SO_3 and water vapor can be written as follows.

$$SO_3 + H_2O \rightarrow H_2SO_4 \quad (11)$$

Presence of NH_3, for example, through byproduct formation in HC-based SCR of NO_x, could also result in ammonium (bi)sulfate ($(NH_4)_2SO_4$) formation, which increases the catalyst deactivation rate (*101–103*). The overall reaction of $(NH_4)_2SO_4$ formation can be written as follows.

$$2NH_3 + SO_3 + H_2O \rightarrow (NH_4)_2SO_4 \quad (12)$$

Literature Review of DOC–SO_x Interactions

More than 98% of the sulfur in diesel is oxidized to SO_2 during combustion (*74*, *75*, *104*). H_2S has been reported during fuel rich conditions (*104*); but in fuel lean conditions for diesel engines, H_2S (if any) would be further oxidized to SO_2 and SO_3 above 300 °C in the presence of a Pt–Pd catalyst (*14*, *31*, *61*). SO_2 and SO_3 subsequently interact with the DOC components–metal oxide and support. DOC sulfation has been widely studied and discussed in the literature (*8*, *13*, *14*, *57*, *61*, *87*, *89*, *90*, *92*). In this section, we present a brief review of the experimental and computational investigations regarding the interactions of sulfur with DOC, that is, metal, metal oxides, as well as the alumina support.

Experimental Studies

Interaction of SO_x with Pt Metal

Compared to other noble metals, Pt remains in metallic form in the typical oxidizing environment (*64*). Pt is very active towards SO_2 oxidation (*61*, *82*); and various techniques such as Temperature Programmed Desorption (TPD), X-ray Photoelectron Spectroscopy (XPS), Ultraviolet Photoelectron Spectroscopy (UPS), High Resolution Electron Energy Loss Spectroscopy (HREELS), Near Edge X-ray Absorption Fine Structure (NEXAFS) spectroscopy, and Low Energy Electron Diffraction (LEED), have been used to study the interaction of SO_2 with Pt metal (*105–112*).

Ultra High Vacuum (UHV) studies show that SO_2 binds strongly (molecular adsorption with a sticking coefficient of ~0.5) on the Pt surface with S and O atoms in η^2-SO_2 configuration (where η^2 represents the number of atoms of adsorbate coordinated to the surface) (*106*, *109*). Astegger and Bechtold (*109*) reported that SO_2 desorbs at 400, 480, and 580 K (multiple peaks) in their TPD experiments on Pt(111); however, the peaks at 480 and 580 K were due to molecularly adsorbed SO_2, whereas the peak at 400 K was due to saturated SO_2 surface. The peak at 400 K appeared only at higher initial coverages suggesting that the peak is from multilayered SO_2 adsorption. In the case of co-adsorbed SO_2 and O_2 on Pt(111), a SO_3 desorption peak was observed at 580 K (*109*). The SO_2 desorption peak at 480 K decreased and the SO_3 peak at 580 K increased while increasing the oxygen surface coverage. From XPS and HREELS studies, Sun et al. (*106*) observed that SO_2 also forms sulfur monoxide (SO) and sulfate (SO_4) on Pt at 300 K.

Streber et al. (*113*) studied the adsorption and reaction of SO_2 on clean and oxygen precovered Pt(111) surfaces by in situ high resolution XPS and suggested that SO_2 reacts with oxygen to form SO_3 at 130 K, and subsequently to SO_4, which is stable up to 500 K. The sulfate ions impact the metal sites by deteriorating the chemisorption ability (*114*). Many studies suggest that Pt metal is not converted to $PtSO_4$; however, it helps migrating the sulfur species to the support, which subsequently gets sulfated (*31*, *115*, *116*). Based on these studies, the generalized sulfur chemistry on Pt can be summarized as follows.

$$SO_{2(g)} \rightarrow SO_2^* \quad (13)$$

$$SO_2^* \rightarrow SO^* + O^* \quad (14)$$

$$SO^* \rightarrow S^* + O^* \quad (15)$$

$$SO_2^* + O^* \rightarrow SO_3^* \quad (16)$$

$$SO_3^* + O^* \rightarrow SO_4 \quad (17)$$

In Novel Materials for Catalysis and Fuels Processing; Bravo-Suárez, J., et al.;
ACS Symposium Series; American Chemical Society: Washington, DC, 2013.

Here, the subscript (g) and superscript * represent the gas phase and the surface species, respectively.

Interaction of SO_x with PdO

Unlike Pt, in a typical oxidizing environment, Pd is converted to more active oxidized form of PdO (*61*, *64*, *117*). Studies using Scanning Tunneling Microscopy (STM), LEED, Auger Electron Spectroscopy (AES), and TPD suggest a three-step mechanism of PdO formation, that is, chemisorption of oxygen on Pd, diffusion of chemisorbed oxygen into the Pd metal, and formation of the stochimetric PdO structure (*117*). In atmospheric conditions, PdO phase is stable up to ~800 °C, whereas metallic Pd is stable above ~800 °C (*61*, *117–121*)

Based on Fourier Transform Infrared (FT-IR) spectroscopy, Mowrey and McCormick (*90*) suggested that PdO is active in converting SO_2 to SO_3, which further reacts with PdO to form $PdSO_4$. This is also consistent with the findings of Lampert et al. (*84*) based on fixed bed and monolith scale experiments. According to Lampert et al. (*84*), Pd on a sulfating (γ–Al_2O_3) support deactivates more slowly than a non-sulfating (SiO_2) support. The slower deactivation is due to a reservoir type of action of the sulfating support to take SO_2/SO_3. On the other hand, PdO deactivation is faster on a non-sulfating support due to the inability of the support to take SO_2/SO_3 leaving PdO as the only target. Furthermore, they suggested the formation of PdO–SO_3 complex for the decreased activity of the catalyst. Mowrey and McCormick (*90*) studied PdO sulfation with and without support and suggested that the sulfation was faster in the absence of a support. Their XPS and FTIR studies showed sulfation of the PdO surface layer and activity loss for methane oxidation. They suggested the following mechanism for PdO sulfation, which is also shown in Figure 5.

$$Pd^o + \tfrac{1}{2}\, O_2 \rightarrow PdO \quad (18)$$

$$PdO + SO_2 \rightarrow Pd^o(\text{surface}) + SO_3 \quad (19)$$

$$PdO_{(\text{interior})} + Pd^o{}_{(\text{surface})} \rightarrow Pd^o{}_{(\text{interior})} + PdO_{(\text{surface})} \quad (20)$$

$$PdO + SO_3 \rightarrow PdSO_4 \quad (21)$$

Here, Pd^o represents the metallic form of palladium.

In Novel Materials for Catalysis and Fuels Processing; Bravo-Suárez, J., et al.;
ACS Symposium Series; American Chemical Society: Washington, DC, 2013.

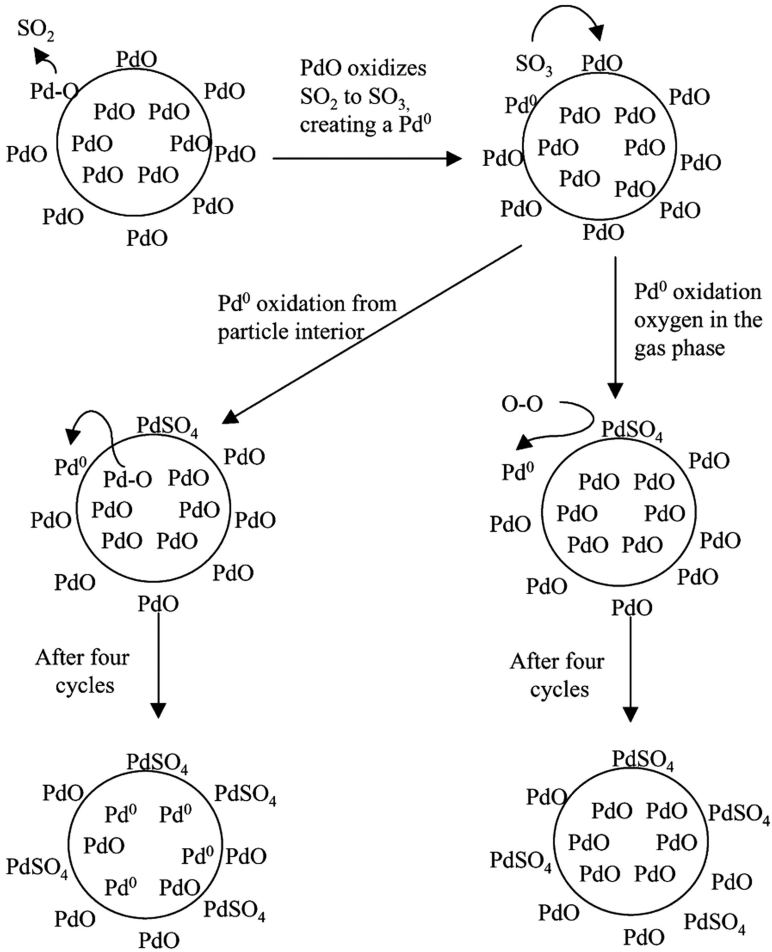

Figure 5. Proposed mechanism of PdO sulfation without support. Reproduced with permission from reference (90). Copyright 2001 Elsevier.

Interaction of SO_x with Al_2O_3 Support

Common support materials in DOC, such as Al_2O_3, are prone to sulfur poisoning, which results in partial blocking of pores, decrease in pore size, and increase in diffusional limitations (*29*, *81*). Due to such limitations, activation energies of the overall emissions oxidation reactions are affected, thus shifting the conversion to higher temperature (*29*).

In Novel Materials for Catalysis and Fuels Processing; Bravo-Suárez, J., et al.;
ACS Symposium Series; American Chemical Society: Washington, DC, 2013.

During Temperature Programmed Oxidation (TPO) experiments with SO_2 and O_2 on γ–Al_2O_3, Corro et al. (*91*) observed that SO_2 oxidation to SO_3 starts at 400 °C, which subsequently forms $Al_2(SO_4)_3$. In XPS, TPR, and IR studies of SO_2 and H_2S effects on Ru/Al_2O_3 and Pt/Al_2O_3 catalysts, Wakita et al. (*122*) observed the presence of SO_4^{-2} species in the support as well as bulk Al_2O_3. In situ FTIR study of SO_2 oxidation on Pt/Al_2O_3 catalyst showed peaks due to adsorbed surface sulfur species on Al_2O_3 at 1382 cm^{-1} ($Al_2(SO_4)_3$), 1188 cm^{-1} (bulk adsorbed $Al_2(SO_4)_3$ or surface adsorbed SO_2), 1120 cm^{-1} (surface $Al_2(SO_4)_3$), and 977 cm^{-1} (sulfite over Al_2O_3) (*90*, *123–125*).

Two types of mechanisms have been suggested for the sulfation of Pd/Al_2O_3 in the presence and absence of water (see Figure 6) (*90*). When water is present, there is inhibition of SO_2 adsorption on Al_2O_3; and therefore, the SO_2 adsorbed on PdO cannot spill over to the Al_2O_3 support. However, SO_2 is oxidized to SO_3 and the rate of $PdSO_4$ formation becomes faster (*90*). Once SO_3 is formed, formation of $Al_2(SO_4)_3$ is still favored due to SO_3 migration to the Al_2O_3 support. This observation is consistent with a previous study which suggests that SO_2 (Lewis base) and SO_3 (Lewis acid) are adsorbed on different types of sites on Al_2O_3 and the adsorption is independent of each other (*126*) Furthermore, H_2O inhibition of SO_2 adsorption on Al_2O_3 has been reported previously (*116*, *126*, *127*), which is also consistent with the mechanism suggested by Mowrey and McCormick (*90*).

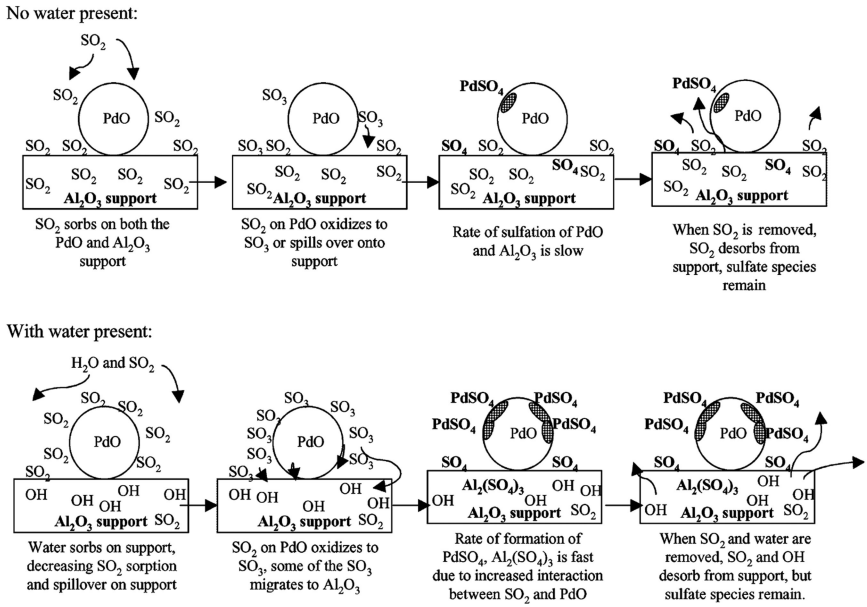

Figure 6. Pd/Al_2O_3 sulfation mechanism with or without water. Reproduced with permission from reference (90). Copyright 2001 Elsevier.

Studies have suggested that other supports, such as zirconia (ZrO_2), titania (TiO_2), and silica (SiO_2), show non-sulfating behavior (*14*, *29*, *128*, *129*); however, the use of such non-sulfating supports can be responsible for faster sulfation of metal/metal oxide (e.g., PdO) due to the absence of a sulfur reservoir (support) for SO_3 spillover (*29*).

Impact of SO_x on Emissions Oxidation Reactions on DOC

Many experimental investigations have been carried out to understand the effects of SO_x on the primary DOC chemistry of oxidation of emissions such as CO, NO_x, and HC (*57*, *81*, *82*, *84*, *114*, *122–124*, *130–135*). Some of these are reviewed in the next subsections.

CO Oxidation

Multiple studies have reported the negative impact of sulfur on the CO oxidation activity on Pd and Pt catalysts (*81*, *122*, *130*, *136*, *137*). Figure 7 shows the results from the work of Kim et al., who investigated the effect of SO_2 and H_2O on CO oxidation using Pt/Al_2O_3 and Pd/Al_2O_3 (*130*). First, Pd/Al_2O_3 showed higher CO oxidation activity compared to Pt/Al_2O_3 in the absence of SO_2 and H_2O. Second, in the presence of H_2O, CO oxidation activity of the Pd/Al_2O_3 catalyst is affected, but Pt/Al_2O_3 is not. Kim et al. (*130*) suggested that such decrease in the activity of Pd/Al_2O_3 with addition of H_2O is due to the formation of less active $Pd(OH)_2$ on the surface, consistent with the results reported by Roth et al. (*138*). Third, presence of SO_2, unlike H_2O, adversely impacts the catalytic activity of both Pt/Al_2O_3 and Pd/Al_2O_3 catalysts. Finally, in the presence of both SO_2 and H_2O, Pd/Al_2O_3 catalyst was more adversely affected than Pt/Al_2O_3, suggesting the higher sensitivity of Pd/Al_2O_3 towards sulfation (*130*). Formation of a less active Pd–SO_x complex, consistent with the mechanism proposed by Mowrey and McCormick (*90*), is responsible for the reduced activity of Pd/Al_2O_3 (*130*). Results of Kim et al. are consistent with the studies of Mowrey et al. (*139*), who reported decreased SO_2 spillover from PdO to Al_2O_3 in the presence of water, and also with the studies of Yao et al. (*115*), who reported the non-sulfating behavior of Pt.

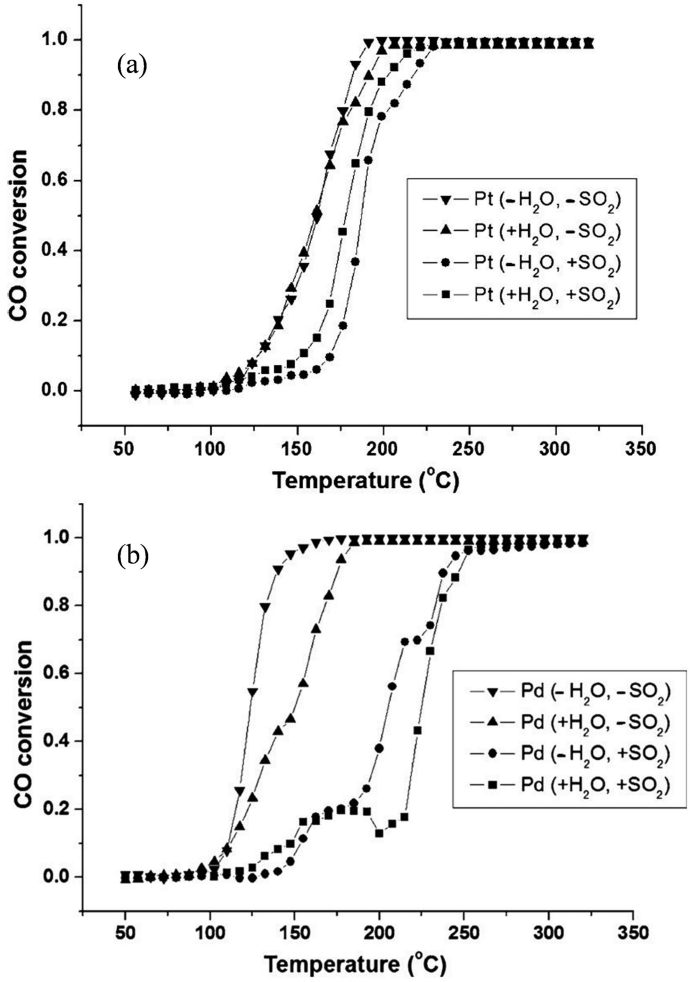

Figure 7. Effect of SO_2 and H_2O on CO conversion using: (a) Pt/Al_2O_3 and (b) Pd/Al_2O_3. Reproduced with permission from reference (130). Copyright 2011 Springer.

NO Oxidation

The effect of sulfur species—especially SO_2 in the diesel engine exhaust—on NO oxidation has been reported in the literature (*8*, *82*, *88*, *92*, *123*, *132–134*, *140–143*). Using commercial DOCs, Krocher et al. (*8*) reported that sulfur in the fuel is detrimental to the DOC's NO oxidation performance, as shown earlier in Figure 4. Suppression of NO conversion due to SO_2 is reported on various Pt–support combinations, for example, Pt/TiO_2 (*134*), Pt/SiO_2 (*88*), and Pt/Al_2O_3 (*132*). Xue et al. (*82*) compared multiple Pt–support combinations for NO oxidation in the presence of SO_2. Their results show that Pt/SiO_2 is more active

In Novel Materials for Catalysis and Fuels Processing; Bravo-Suárez, J., et al.;
ACS Symposium Series; American Chemical Society: Washington, DC, 2013.

than Pt/Al_2O_3 and Pt/ZrO_2, which could be due to the non-sulfating behavior of SiO_2 (*8*). In the presence of SO_2 and H_2O, Pd catalysts (Pd/TiO_2) showed a sharp drop in NO conversion (*144*).

HC Oxidation

The effect of SO_2 on the oxidation of HCs, such as C_3H_8 and C_3H_6, has been studied on oxidation catalysts (*111*, *112*, *129*, *135*, *137*, *145–147*). The presence of SO_2 promotes the oxidation of alkanes on Pt, but hinders the oxidation of alkenes, as shown in Figure 8 (*112*, *128*). The improvement in the C_3H_8 oxidation activity on Pt/Al_2O_3 in the presence of SO_2 is consistent with other studies as well (*129*, *146*, *148*, *149*). The formation of surface sulfates on $Pt/\gamma–Al_2O_3$ promotes the dissociative adsorption of C_3H_8 (*128*). Along these lines, Yao et al. also suggested that the increase in C_3H_8 oxidation activity in the presence of SO_2 is due to dissociative chemisorption, which is not present in other molecules like CO (*115*). Surface sulfates could decrease the adsorption of C_3H_6 on Pt/Al_2O_3 and suppress the oxidation activity (*115*).

Compared to Pt, which is active for CO, NO, HC, and SO_2 oxidation, Pd is found to be better for HC oxidation in lean conditions (*84*). Lampert et al. (*84*) suggested that the deactivation of Pd catalysts is due to the formation of less active $Pd–SO_x$ sites (not formed on Pt) from PdO. Furthermore, Pd with a sulfating support shows slow deactivation compared to a non-sulfating support, which is attributed to the scavenging of SO_3 by the sulfating support.

Computational Studies on DOC-SO_x Interactions

To develop a fundamental understanding of sulfur interactions with Pt and Pd, a few researchers have focused on quantum mechanical studies using first principles density functional theory (DFT) (*150–156*). Electronic and geometrical structures, adsorbate configurations, species binding energetics, and surface reaction energetics are generally studied using DFT (*157–161*). Such information can be subsequently implemented in kinetic and reactor modeling.

SO_x Adsorption and Stability

Since the DOC sulfation process starts with the SO_2 molecule, it is essential to understand the interaction of SO_2 with the catalyst surface and other adsorbed molecules present in the diesel engine exhaust. Lin et al. (*152*) investigated the possible and energetically stable configurations of SO_2 on Pt(111) at multiple surface coverages using DFT-GGA calculations. Based on the calculated binding energies, they categorized 20 different stable configurations of the SO_2 molecule on Pt(111) surface into three groups, namely, strong, intermediate, and weak binding. Consistent with previous experimental studies (*105*, *106*), the most stable configurations had the SO_2 molecular plane either perpendicular or parallel to the metal surface. The fcc $\eta^2–S_b,O_a$ (SO_2 molecular plane perpendicular to the

In Novel Materials for Catalysis and Fuels Processing; Bravo-Suárez, J., et al.;
ACS Symposium Series; American Chemical Society: Washington, DC, 2013.

metal surface) and η^3–S_b,O_a,O_a (SO_2 molecular plane parallel to the metal surface) configurations (where η^2 and η^3 represents the number of atoms of adsorbate coordinated to surface atom, that is, 2 and 3, respectively, and the subscripts a and b represent the atom on top and bridge sites, respectively) were the two most stable configurations. The fcc η^2–S_b,O_a (SO_2 molecular plane perpendicular to the metal surface) configuration was the most stable one with a binding energy of 129.6 kJ/mol at zero coverage. The configuration of SO_2 adsorption on Pd(111) is also consistent on Pt surface as observed by Terada et al. (*162*) using surface X-ray absorption molecular plane normal to the surface. Based on Infrared Reflection Absorption Spectroscopy (IRAS) and DFT, Hapel et al. (*154*) also confirmed the perpendicular or parallel adsorption of SO_2 on Pt(111). Lin et al. reported that the presence of the metal-sulfur bond (89–98 kJ/mol) is the key feature in SO_2 stability on Pt compared to the weak metal-oxygen bond (−30.7 to −11.7 kJ/mol) (*152*). In a DFT study of SO_2 adsorption on Pt–Pd, Ohashi et al. (*163*) suggested that the order for SO_2 binding energy is on-top > bridge > hollow sites. Pd shows stronger affinity for SO_2 adsorption and is prone to sulfur deactivation compared to Pt. Based on X-ray photoelectron spectroscopy and DFT studies, Luckas et al. (*156*) suggested two different SO_2 configurations, namely, upright standing and flat lying, on Pd (100) surface. The upright standing structure is more stable compared to the flat lying structure resulting in an energy difference of 13 kJ/mol. The calculated binding energy of SO_2 on Pd(100) was in the range of 134–149 kJ/mol (*156*).

The fcc η^3–S_a,O_a,O_a and fcc η^3–O_a,O_a,O_a configurations are energetically most favorable for SO_3 and SO_4 on Pt(111) respectively (*150*). The most stable configuration for SO_3 on Pt(111) has a binding energy of 150.7 kJ/mol. In the case of SO_4 adsorption on Pt(111) surface, the most stable configuration has a binding energy of 356.5 kJ/mol. DFT as well as experimental observations suggest that the reactions forming SO_4 species are favorable and SO_4 is a very stable surface species on Pt(111) (*112*, *147*, *150*, *154*). In the case of Pd(100), the binding energy of SO_3 and SO_4 were reported to be 157 and 415 kJ/mol, respectively (*156*).

Coverage Effects in SO_x Adsorption

Lateral adsorbate interactions on the catalyst surface can have significant impact on the adsorption/desorption and reaction kinetics. DFT results (*150*) for SO_2 adsorption on Pt(111) showed that SO_2 binding energy decreased by 14–19 kJ/mol as the SO_2 coverage increased from 1/9 to 1/4 ML. Similarly, the decrease in binding energy while increasing the coverages from 1/9 to 1/4 ML were about 31, 26, 25, and 43 kJ/mol for S, SO, SO_3, and SO_4, respectively.

The relative stability of SO_x species changes with coverage (*150*). Under high coverage conditions, stability follows the order: $SO_4 > SO_3 + O > SO_2 + 2O > S + 4O > S + 3O$. Therefore, SO_4, SO_3, and SO_2 are stable to dissociation in the high coverage limit. In the presence of oxygen, thermodynamics favors the formation of the most oxidized species possible (*150*), suggesting that SO_2 dissociation to SO or atomic S is not favored. The energetics of adsorption in the low coverage limit shows the order $S + 4O > SO + 3O > SO_4 > SO_2 + 2O > SO_3 + O$, which is different

In Novel Materials for Catalysis and Fuels Processing; Bravo-Suárez, J., et al.;
ACS Symposium Series; American Chemical Society: Washington, DC, 2013.

from the high coverage limit. The authors suggested that all the sulfur oxides are energetically favorable to dissociation to the elements in the low coverage limit.

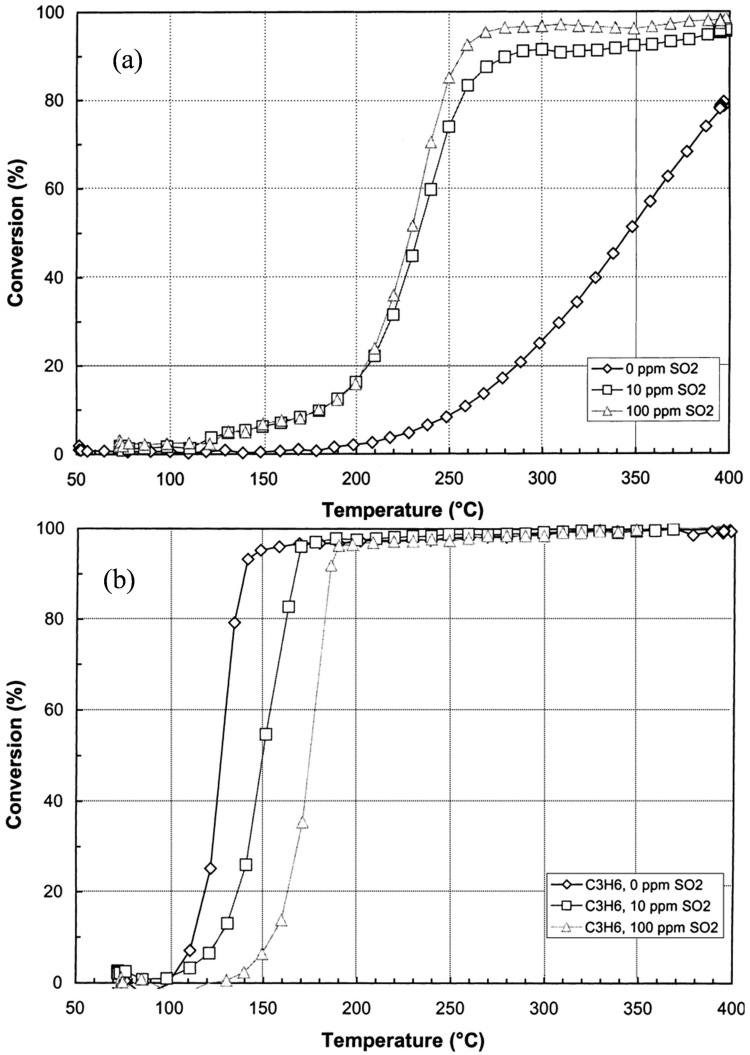

Figure 8. Conversion of 500 ppm of (a) C_3H_8 and (b) C_3H_6 with 20% O_2 on Pt/γ–Al_2O_3 in the presence of 0, 10, and 100 ppm of SO_2. Reproduced with permission from reference (128). Copyright 2001 Elsevier.

SO_2 Oxidation

Gas phase SO_2 oxidation to SO_3 is exothermic but slow in the absence of a catalyst (*164*). The presence of oxygen greatly increases the driving force towards oxidation and the energetic order of $SO_4 > SO_3 > SO_2 > SO > S$ is observed in that case (*150*). Using DFT and IRAS, Hepel et al. (*154*) reported that SO_2 desorption from Pt(111) is favored in the absence of oxygen; however, the formation of SO_3 and SO_4 is observed in the presence of oxygen, even at low temperature. Lin et al. (*151*) studied the SO_2 oxidation chemistry on Pt(111) using DFT, particularly to compare the energetics of Langmuir-Hinshelwood (surface reaction between adsorbed SO_2 and O atoms) and Eley–Rideal (reaction between a gas phase SO_2 molecule and an absorbed O atom) mechanisms. As shown in Figure 9, the activation barrier for the Eley–Rideal reaction is significantly less than that for the Langmuir-Hinshelwood reaction (25 vs. 46 kJ/mol, respectively). This is mainly because the Langmuir–Hinshelwood surface reaction step involves a more constrained transition state (*151*).

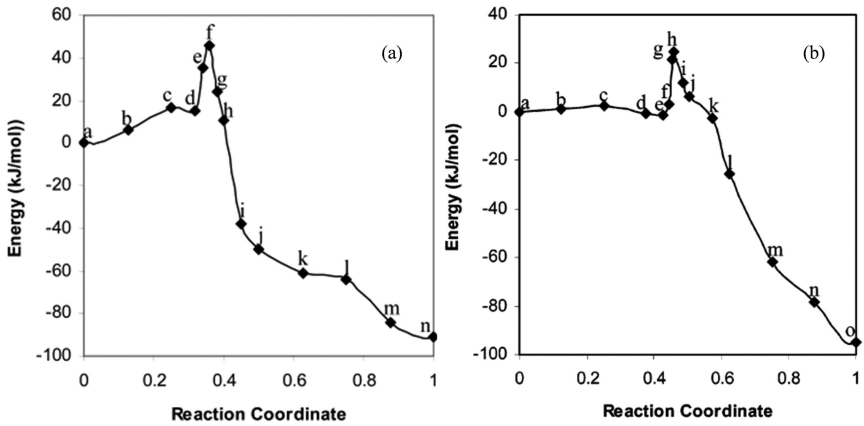

Figure 9. Minimum energy path of the oxidation of SO_2 on Pt(111) : Panel a is Langmuir-Hinshelwood mechanism and panel b is Eley–Rideal mechanism. Reproduced with permission from reference (151). Copyright 2004 American Chemical Society (ACS).

In a DFT study, Luckas et al. (*156*) suggested the oxidation of SO_2 to SO_3 in the presence of oxygen on the Pd(100) surface. The study suggested that the SO_3 formation reaction mechanism is Eley–Rideal type. At higher temperature, formation of SO_4 was observed, which is also consistent with their HR-XPS study. Furthermore, two types of SO_4 (proximity or remote to oxygen adatoms) molecules are reported in the study. The same authors reported that the SO_3 formation is endothermic (~23 kJ/mol), however the sulfate formation is reported to be an exothermic process on Pd(100) (*156*).

In Novel Materials for Catalysis and Fuels Processing; Bravo-Suárez, J., et al.;
ACS Symposium Series; American Chemical Society: Washington, DC, 2013.

Kinetic Modeling for SO_2-Based Deactivation

Kinetic modeling of sulfur interactions with Pt has received increased attention over the last decade or so (*150–153*, *164–166*), mostly for Pt-based LNT/NSR applications (*165*, *166*). Nonetheless, the findings specific to Pt could be relevant for understanding the DOC-SO_x interactions. Olsson et al. (*165*) developed a global kinetic model for LNT deactivation due to sulfur, which consists of interaction of SO_2 (poisoning and regeneration) on two types of sites, namely, Barium (Ba) and Al_2O_3. For both types of sites, the kinetic model contained two steps, namely, adsorption/binding of SO_2 and subsequent oxidation. Furthermore, the model also contained steps for the formation of sulfates on both types of sites during the lean phase and regeneration in the presence of hydrogen. The authors suggested that sulfur poisoning occurs on both types of sites (Ba and Al_2O_3), consistent with the observations by Matsumoto et al. (*167*). As all alumina sites are not covered by NO_x, SO_2 adsorption is possible. Similarly, Dowdy et al. (*166*) developed a global mean field kinetic model for SO_2 interaction with NSR (Pt/BaO/Al_2O_3 and BaO/Al_2O_3), which consists of SO_2 storage on NO_x storage sites, SO_2 storage on bulk sites, SO_2 oxidation, SO_2 interaction with Pt in the presence of H_2, and oxidation of accumulated sulfur compounds on Pt by NO_2. The model is able to predict the decrease in NO_x storage performance due to sulfur accumulation and accumulation of bulk sulfates in Pt/BaO/Al_2O_3 after exposure of SO_2 and oxygen. Except for a few studies of sulfur interactions with NO_x reduction/storage catalyst discussed above, details of sulfation kinetics are not available; and therefore, there is an urgent need to understand the complex nature of sulfation kinetics. Along these lines, next we briefly mention the main gaps and challenges in the understanding of DOC-SO_x interactions.

Gaps and Challenges in the Understanding of DOC-SO_x Interactions

Kinetic Modeling for SO_2 Oxidation

Predicting DOC performance over time will require a novel kinetic and reactor modeling framework to incorporate the extent of metal and support sulfation coupled with the oxidation kinetics of emissions. Previous studies deal with global kinetic models on catalysts relevant to NO_x reduction/SCR (*165*, *166*), but not for DOC-SO_x interactions. Detailed and robust kinetic models for SO_2 oxidation on DOC are needed to capture the chemistry under dilute concentration conditions (~1 ppm SO_2).

Bimetallic Nature of DOC

Modern DOCs contain both Pt and Pd, and Pd is essential to prevent the sintering of Pt particles at high temperature, which improves the overall DOC lifetime and thermal stability (*64*). Pd also helps in reducing the DOC cost. Despite

In Novel Materials for Catalysis and Fuels Processing; Bravo-Suárez, J., et al.;
ACS Symposium Series; American Chemical Society: Washington, DC, 2013.

the strong interaction of Pt and Pd in a DOC, kinetics (parameters) for emissions-oxidation reactions is not well understood on these bimetallic catalysts.

Kinetics for Metal Oxide Sulfation

Pd is converted to PdO due to the high oxygen content in diesel engine exhaust, whereas Pt remains in the metallic form (*64*). Based on in situ IR experiments, $PdSO_4$ is formed when PdO supported on alumina is exposed to SO_2 (*90*). Under lean-burn Natural Gas Vehicles (NGV) operating conditions (in the presence of SO_2), deactivation of Pd catalysts due to formation of inactive $PdSO_4$ has been observed (*84*, *90*). Given these findings, it is important to include the kinetics of PdO sulfation in the emissions-oxidation modeling to correctly simulate DOC deactivation. However, kinetics of PdO sulfation has been typically ignored in DOC models.

Kinetics for Support Sulfation

Given the important role of SO_x-support interactions, the kinetics of alumina support sulfation must be included in the emissions-oxidation modeling to correctly simulate DOC deactivation. However, estimating the kinetics of support sulfation using first-principles techniques is nontrivial, and has been typically ignored in previous DOC models (*63*, *168–173*).

Impact of Sulfation on Emissions Oxidation Kinetics

Many experimental investigations reveal that sulfur has a strong effect on emissions oxidation kinetics on DOC, as discussed earlier. However, computational studies that investigate such effects are rare. The experimental investigations are generally limited to the effect of SO_2 and sulfur aged catalysts on emission components without considering cumulative effects and interactions. Sulfation is a dynamic phenomena, and the details of the interaction and impact of sulfation on emissions oxidation need to be understood.

Reactor Modeling with Sulfation

Even if the sulfation kinetics parameters were estimated, predicting DOC performance over time will require a novel kinetic and reactor modeling framework to incorporate the extent of metal and support sulfation coupled with the emissions-oxidation kinetics. As sulfation is typically slower than the emissions oxidation reactions on DOC, multiscale modeling of the two chemistries is essential to predict the time dependent DOC deactivation.

In Novel Materials for Catalysis and Fuels Processing; Bravo-Suárez, J., et al.;
ACS Symposium Series; American Chemical Society: Washington, DC, 2013.

As Pt–Pd based DOCs deactivate in the presence of sulfur oxides, it is critical to identify novel material compositions that are more resistant to sulfation and deactivation. Sulfur-resistant catalysts could be explored based on catalyst screening, but a potentially faster computational approach for sulfur-resistant catalyst design has not been developed due to the lack of reliable kinetic and reactor models.

Microkinetic Modeling for Emissions and SO_2 Oxidation on Pt

In this section, we present a new microkinetic model for SO_2 oxidation on Pt to address the first challenge mentioned in the previous section. We start with a brief summary of the emissions oxidation reaction mechanism that we developed earlier on Pt, followed by the development, validation, and analysis of the microkinetic model for SO_2 oxidation on Pt.

Emissions Oxidation Reaction Mechanism on Pt: Background

We recently developed a comprehensive microkinetic model for the oxidation of five major emissions, namely, CO, NO, CH_2O, NH_3, and HCN, in the diesel engine exhaust aftertreatment (*174*). The Pt-based model consists of 124 irreversible (62 reversible) catalytic reactions and 21 surface species. Most of the kinetic parameters for the species and reactions were first estimated from literature UHV TPD/R experiments or taken from literature DFT calculations. The microkinetic model was then rigorously validated against monolith and fixed bed experimental data at practically more relevant operating conditions, such as atmospheric pressure, high O_2 concentration, dilute emissions concentration, and high space velocity. Based on reaction path analysis, preliminary model reduction was carried out, which further decreased the mechanism size to 94 irreversible (47 reversible) catalytic reactions and 20 surface species. Important reactions and intermediate species in the microkinetic model along with the stable reactants and products are shown in Figure 10. The emissions oxidation mechanism on Pt is expanded in this work to include the SO_2 oxidation chemistry on Pt.

SO_2 Oxidation Reaction Mechanism on Pt

Approach for Kinetic Model Development

The overall approach for kinetic model development of SO_2 oxidation on Pt-DOC consists of three major steps, namely, (i) estimation/extraction of kinetic parameters in the surface reaction mechanism, (ii) performance and analysis of the microkinetic model, and (iii) additional validation. In a typical diesel engine exhaust with high O_2 concentration, the primary reaction for SO_2 is its oxidation to SO_3; however, some additional reactions between S and SO_x species are also considered in the reaction mechanism. Based on the information for possible

In Novel Materials for Catalysis and Fuels Processing; Bravo-Suárez, J., et al.;
ACS Symposium Series; American Chemical Society: Washington, DC, 2013.

reaction intermediates, pathways, and final products, we have considered 24 irreversible (12 reversible) catalytic reactions (see Table 2) and five surface (adsorbed) species (O*, S*, SO*, SO_2*, and SO_3*). The overall approach used in microkinetic modeling has some limitations associated with the reaction mechanism, uncertainty in the kinetic parameters, as well as catalyst and reactor modeling, which have been discussed in our earlier work (*174*).

Kinetic Parameters for SO_2 Oxidation Mechanism

Kinetic parameters such as species binding energies (Q) are taken from literature experimental and/or DFT data (*109*, *150–152*, *175*), whereas the reaction activation energies are calculated using the semi-empirical Unity Bond Index-Quadratic Exponential Potential (UBI-QEP) method (*176*, *177*). Binding energies are coverage and temperature dependent (*178*) as shown in Equation 22.

$$Q(T) = Q(T_o) - \alpha\,\theta - \gamma\,R\,(T - To) \qquad (22)$$

Here, α is the coverage dependence coefficient (kcal/mol/ML), θ is the coverage of species (ML), γ is the temperature dependence coefficient for binding energies (unitless), R is the universal gas constant (kcal/mol/K), and T is the temperature (K). ML stands for monolayer. To is taken as 300 K.

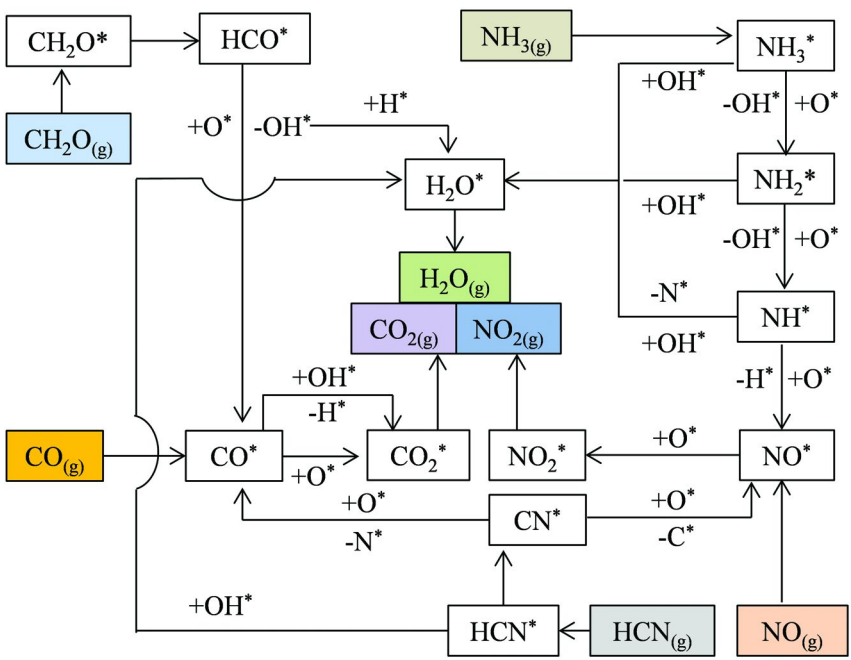

Figure 10. Schematic of the important reaction pathways, intermediates, reactants, and products from the microkinetic model for oxidation of emissions on Pt (174). The reactants and products in gas phase are shown in shaded boxes.

In Novel Materials for Catalysis and Fuels Processing; Bravo-Suárez, J., et al.;
ACS Symposium Series; American Chemical Society: Washington, DC, 2013.

Coverage dependent parameters (adsorbate interactions) are taken from the literature (*179*). The temperature dependence is derived from the statistical mechanics based calculations for degrees of freedom lost/gained upon adsorption on the catalyst surface (*178*). Coverage and temperature dependent activation energies are calculated on-the-fly using the UBI-QEP method. Sticking coefficients for O_2 and SO_2 are taken from the literature (*109*, *175*, *180*), whereas those for the other species are assumed to be unity. Initial values of pre-exponential factors (A) are taken from Transition State Theory (TST) estimates, which include 10^{13} s^{-1} and 10^{11} s^{-1} for desorption and the Langmuir-Hinshelwood (L–H) type surface reactions, respectively (*181*). For SO_2 desorption, a pre-exponential factor of 1×10^{16} s^{-1} is used in this mechanism, which is based on the typically reported high values (*164*, *166*). A site density of 1.5×10^{15} sites/cm^2 (2.5×10^{-9} mol/cm^2) corresponding to the Pt(111) surface (*182*) is used in the simulations.

Table 2. Surface reaction mechanism for SO_2 oxidation on Pt. * indicates an empty (vacant) site, whereas superscript * indicates an adsorbed species. Activation energies in the last column are reported at 300 K; the functional dependence on coverage and temperature originates from Equation 22 in the text. ΔT = T − To, where To is taken as 300 K. Activation energies are computed on-the-fly using the UBI-QEP formalism, as the surface coverages changes in the simulations. Bond index represents the position of the transition state along the reaction coordinate. It ranges between 0 (transition state similar to reactants) to 1 (transition state similar to products). Bond index is also used to compute the activation energies according to the UBI-QEP formalism. Additional calculation details are presented in the supplementary material of our earlier work on emissions oxidation on Pt (*174*). Shaded reactions in the second column are the least important ones for typical DOC conditions, and can be ignored during the reactor simulations

No.	*Reactions*	*Bond index (BI) (unitless)*	*Sticking coefficient (unitless) or Pre-exponential factor (s^{-1})*	*Activation energy at 300 K (kcal/mol)*
	Oxygen adsorption/desorption (174)			
R_1	$O + * \rightarrow O^*$	0.5	1	0
R_2	$O^* \rightarrow O + *$	0.5	1×10^{13}	$86 - 13.3\theta_o - 1.5R\Delta T$ (179)
R_3	$O_2 + 2* \rightarrow 2O*$	0.5	0.05 (175, 180)	0
R_4	$2O^* \rightarrow O_2 + 2*$	0.5	1×10^{13}	$52.9 - 26.6\theta_o$ + f(T)
	SO_x adsorption/desorption			
R_5	$S + * \rightarrow S^*$	0.5	1	0
R_6	$S^* \rightarrow S + *$	0.5	1×10^{13}	$119.53 - 1.5R\Delta T$ (150)
R_7	$SO + * \rightarrow SO^*$	0.5	1	0
R_8	$SO^* \rightarrow SO + *$	0.5	1×10^{13}	$70.99 - 2R\Delta T$ (150)
R_9	$SO_2 + * \rightarrow SO_2^*$	0.5	0.5 (109)	0
R_{10}	$SO_2^* \rightarrow SO_2 + *$	0.5	1×10^{16}	$30.98 - 2.5R\Delta T$ (150)
R_{11}	$SO_3 + * \rightarrow SO_3^*$	0.5	1	0
R_{12}	$SO_3^* \rightarrow SO_3 + *$	0.5	1×10^{13}	$36.01 - 2.5R\Delta T$ (150)

Continued on next page.

In Novel Materials for Catalysis and Fuels Processing; Bravo-Suárez, J., et al.;
ACS Symposium Series; American Chemical Society: Washington, DC, 2013.

Table 2. (Continued). Surface reaction mechanism for SO_2 oxidation on Pt. * indicates an empty (vacant) site, whereas superscript * indicates an adsorbed species. Activation energies in the last column are reported at 300 K; the functional dependence on coverage and temperature originates from Equation 22 in the text. ΔT = T − To, where To is taken as 300 K. Activation energies are computed on-the-fly using the UBI-QEP formalism, as the surface coverages changes in the simulations. Bond index represents the position of the transition state along the reaction coordinate. It ranges between 0 (transition state similar to reactants) to 1 (transition state similar to products). Bond index is also used to compute the activation energies according to the UBI-QEP formalism. Additional calculation details are presented in the supplementary material of our earlier work on emissions oxidation on Pt (*174*). Shaded reactions in the second column are the least important ones for typical DOC conditions, and can be ignored during the reactor simulations

No.	*Reactions*	*Bond index (BI) (unitless)*	*Sticking coefficient (unitless) or Pre-exponential factor (s^{-1})*	*Activation energy at 300 K (kcal/mol)*
	SO_x oxidation/reduction			
R_{13}	$SO_3^* + * \rightarrow SO_2^* + O^*$	0.95 [a]	1×10^{11}	$23.7 + f(\theta_O,T)$
R_{14}	$SO_2^* + O^* \rightarrow SO_3^* + *$	0.95 [a]	2×10^{12} [b]	$21.5 + f(\theta_O,T)$
R_{15}	$SO_2^* + * \rightarrow SO^* + O^*$	0.5	1×10^{11}	$22.3 + f(\theta_O,T)$
R_{16}	$SO^* + O^* \rightarrow SO_2^* + *$	0.5	1×10^{11}	$16.6 + f(\theta_O,T)$
R_{17}	$SO^* + * \rightarrow S^* + O^*$	0.5	1×10^{11}	$20.0 + f(\theta_O,T)$
R_{18}	$S^* + O^* \rightarrow SO^* + *$	0.5	1×10^{11}	$30.0 + f(\theta_O,T)$
R_{19}	$2SO_2^* \rightarrow SO^* + SO_3^*$	0.5	1×10^{11}	$13.7 + f(T)$
R_{20}	$SO^* + SO_3^* \rightarrow 2SO_2^*$	0.5	1×10^{11}	$10.2 + f(T)$
R_{21}	$S^* + SO_2^* \rightarrow 2SO^*$	0.5	1×10^{11}	$25.6 + f(T)$
R_{22}	$2SO^* \rightarrow S^* + SO_2^*$	0.5	1×10^{11}	$9.9 + f(T)$
R_{23}	$SO^* + SO_2^* \rightarrow S^* + SO_3^*$	0.5	1×10^{11}	$7.7 + f(T)$
R_{24}	$S^* + SO_3^* \rightarrow SO^* + SO_2^*$	0.5	1×10^{11}	$19.9 + f(T)$

[a] Modified from the initial value of 0.5 to improve the agreement with experimental data.
[b] Modified from the initial value of 10^{11} s^{-1} to improve the agreement with experimental data.

Mechanism Performance and Analysis

Steady state isothermal PFR simulations were carried out using the SO_2 oxidation mechanism to compare its SO_2 conversion performance against experiments conducted with Pt/SiO_2 coated monolith catalysts. The GRI Mech 3.0 gas phase reaction mechanism (*183*) was used to account for the gas phase chemistry. Transient simulations were performed at the reactor inlet to get the initial surface species coverages. The resulting set of differential and algebraic (DAE) equations were solved using the DDASPK solver (*184*).

Figure 11 shows that the SO_2 oxidation reaction mechanism captures the experimental data fairly well over the entire temperature range. At high temperatures, the experimental data are limited by SO_2 oxidation equilibrium, which is well captured by our simulations. Only two parameters were adjusted to capture the experimental results. These include (i) pre-exponential of reaction

In Novel Materials for Catalysis and Fuels Processing; Bravo-Suárez, J., et al.;
ACS Symposium Series; American Chemical Society: Washington, DC, 2013.

R_{14} (SO_2* + O* → SO_3* + *), which was modified to 2×10^{12} s^{-1} (starting from 1×10^{11} s^{-1}), and (ii) bond index of reaction pair R_{13}-R_{14} (SO_3* + * ↔ SO_2* + O*), which was modified to 0.95 (starting from 0.5). The bond index modification implemented here is similar to previous work for CO oxidation reaction (*185*).

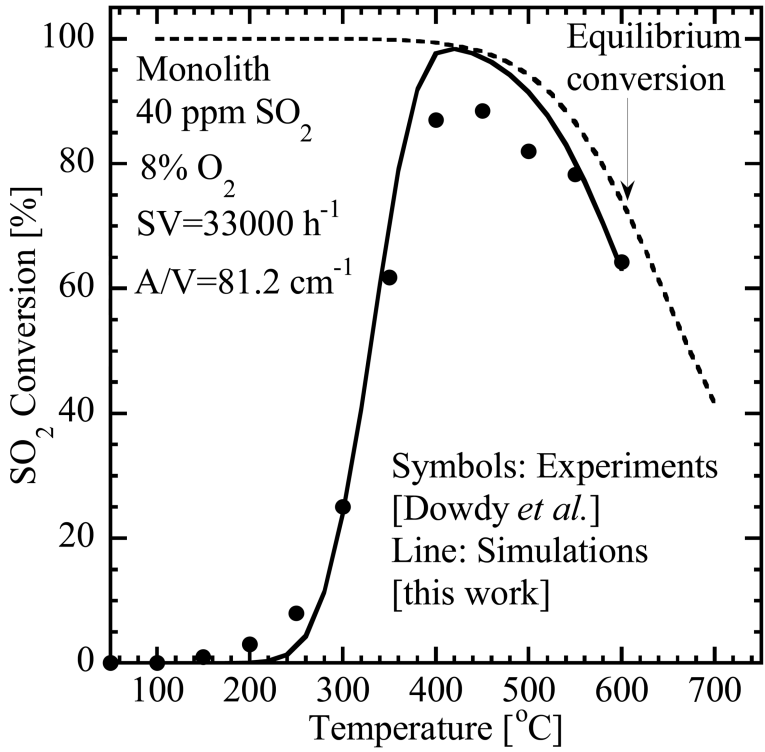

Figure 11. Performance of the microkinetic model for SO_2 oxidation on Pt. Symbols represent experimental data; solid lines represent our simulations; and dashed lines represent the equilibrium calculations using GASEQ software (186) Operating conditions (133): Pt/SiO_2 monolith; feed of 40 ppm SO_2, 8% O_2, and ~92% N_2; space velocity of 33,000 h^{-1}; and catalyst area per unit reactor volume of 81.2 cm^{-1}. Simulations are in close agreement with the experimental data.

The reaction pair R_{13}–R_{14} (SO_3* + * ↔ SO_2* + O*) was identified as the most important reaction based on sensitivity analysis. The normalized sensitivity coefficient is defined as $d\ln R/d\ln P$ (i.e., $(dR/dP)\times(P/R)$), where dP is the change in parameter P (pre-exponential factors) and dR is the change in model response R (conversion). Surface reactions with the highest normalized sensitivity coefficients are shown in Figure 12. At low temperature (250 °C), SO_3 adsorption/desorption pair R_{11}–R_{12} showed the largest sensitivity, but the conversion was very low at this temperature. At 350 °C, SO_2 oxidation step R_{13}–R_{14} showed the highest sensitivity. As moderate levels of SO_2 conversion were observed around 350 °C, kinetic parameters for the reaction pair R_{13}–R_{14}

were adjusted to capture the experimental data in Figure 11. At even higher temperatures (e.g., 450 °C), as the data become equilibrium limited, none of the the reaction pre-exponentials were sensitive as expected.

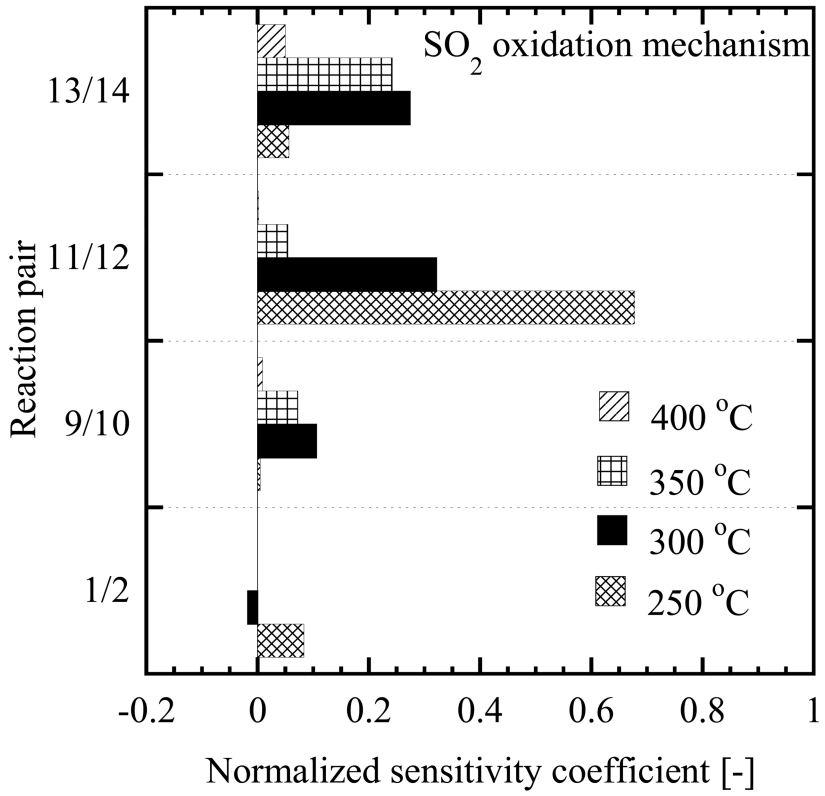

Figure 12. Sensitivity analysis for SO_2 oxidation model responses with respect to the pre-exponential factor pairs in the surface reaction mechanism. Pre-exponentials are modified pairwise without perturbing the equilibrium constant. Only those reaction pairs with the highest normalized sensitivity coefficients (dlnR/dlnP, i.e., (dR/dP)×(P/R)) are shown here. The sensitivity coefficients above 400 °C are negligible (not shown here). Operating conditions are the same as in Figure 11.

Simulated surface coverages at the reactor exit (which are also very close to the average coverage over the reactor length) are shown in Figure 13a, whereas Figures 13b and 13c show the axial coverage profiles of dominant surface species at two representative temperatures: low (350 °C) and high (550 °C), respectively. At most of the conditions (> 300 °C), O* is the most abundant reaction intermediate (MARI), which is expected given its high concentration in the feed (and also in a typical diesel engine exhaust). The high coverage of O* also justifies the inclusion of repulsive adsorbate–adsorbate (O*–O*) interactions

In Novel Materials for Catalysis and Fuels Processing; Bravo-Suárez, J., et al.;
ACS Symposium Series; American Chemical Society: Washington, DC, 2013.

(coverage effects) in our reaction mechanism. At low temperature, the simulations predict some SO_3* coverage, but negligible coverage of SO_2*, SO*, and S*. This is because SO_2* is oxidized to SO_3* even at low temperature, but it is difficult to desorb SO_3*. At high temperature, SO_3* desorption becomes easier, resulting in more vacancies and less SO_3* coverage. Finally, above 500 °C, even oxygen also starts to desorb resulting in an increase in vacancies.

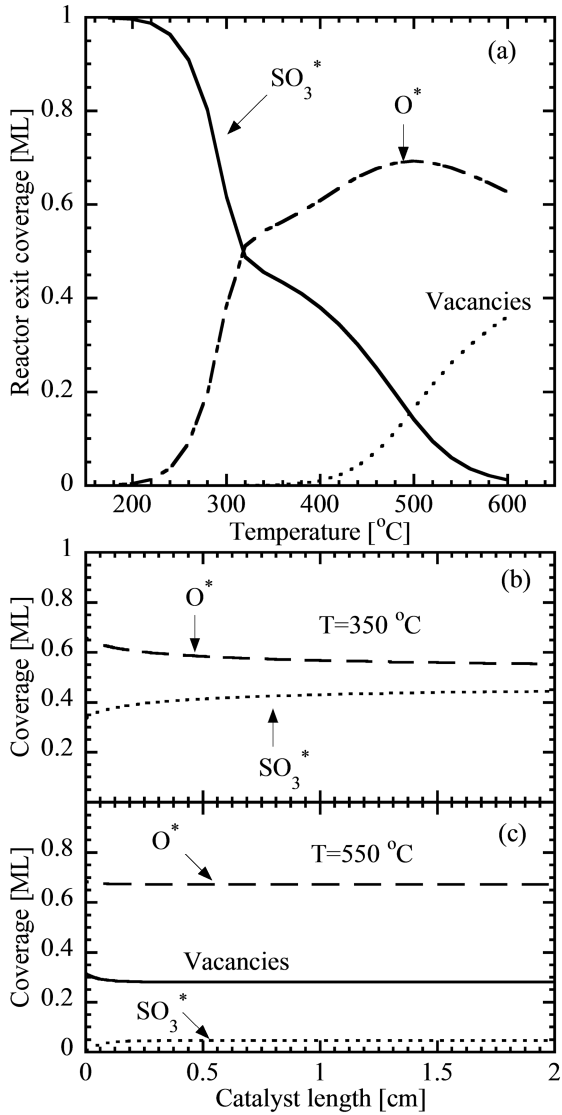

Figure 13. (a) Simulated steady state coverage profiles at reactor exit, (b) simulated axial coverage profiles at 350 °C, and (c) simulated axial coverage profiles at 550 °C. Operating conditions are the same as in Figure 11.

In Novel Materials for Catalysis and Fuels Processing; Bravo-Suárez, J., et al.;
ACS Symposium Series; American Chemical Society: Washington, DC, 2013.

The reaction path analysis (RPA) is shown in Figure 14 at two representative temperatures: low (350 °C, Figure 14a) and high (450 °C, Figure 14b). At low temperature, SO_2* reacts with oxygen via reaction R_{14}: $SO_2* + O* \rightarrow SO_3* + *$ to form SO_3*, which subsequently desorbs, resulting in SO_2 conversion (oxidation). This RPA also aligns with the sensitivity analysis in Figure 12 and the coverage profiles in Figure 13. This observation, albeit on Pt, is also consistent with the experimental results reported by Luckas et al. (*156*) in their HR-XPS studies of SO_2 oxidation on Pd(100) surface. At high temperature, SO_3 readsorbs on the surface, and decomposes via the reverse reaction R_{13}: $SO_3* + * \rightarrow SO_2* + O*$, which is consistent with the equilibrium limitations. SO_2* on the surface then follows two separate reaction pathways. The primary pathway (~94%) is desorption to gas phase SO_2 via reaction R_{10}, whereas the secondary pathway (~6%) is decomposition to SO* and O* via reaction R_{15}. However, instead of desorbing, SO* further reacts with SO_3* to regenerate SO_2* via reaction R_{20}: $SO* + SO_3* \rightarrow 2SO_2*$. Thus, the secondary minor pathway is not important in terms of the overall reaction of SO_3 decomposition at high temperature.

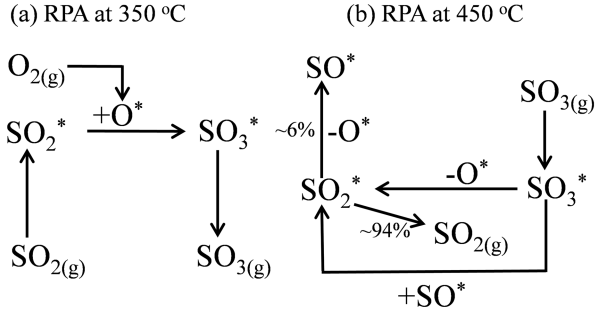

Figure 14. Reaction path analysis at 350 °C (panel a) and 450 °C (panel b) using our microkinetic model for SO_2 oxidation on Pt. Operating conditions are the same as Figure 11.

Mechanism Validation

Despite showing good agreement with the monolith experiments, two kinetic parameters in the surface reaction mechanism had to be adjusted to improve the agreement with the experimental data. Therefore, to assess the fidelity of the surface reaction mechanism, we carried out further validation against additional SO_2 oxidation experimental data on Pt/TiO_2 fixed bed (*89*), without any further modification of kinetic parameters. Predictions using the microkinetic model are shown in Figure 15, along with the experimental data. This set of experimental data is not very relevant to the DOC operating conditions, as the feed contained an extremely high SO_2 concentration (11%) instead of a few ppm, along with an extremely high space velocity. Nonetheless, a fair agreement with experimental

In Novel Materials for Catalysis and Fuels Processing; Bravo-Suárez, J., et al.;
ACS Symposium Series; American Chemical Society: Washington, DC, 2013.

data demonstrates the robustness of our SO_2 oxidation surface reaction mechanism on Pt, even under extreme operating conditions.

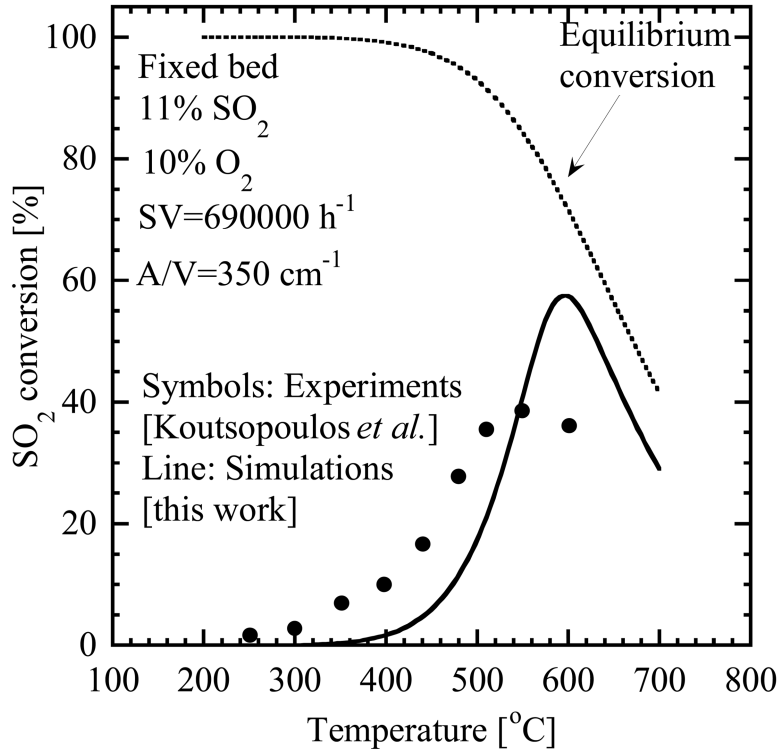

Figure 15. Validation of the microkinetic model for SO_2 oxidation on Pt/TiO_2 fixed bed. Operating conditions (89): Pt/TiO_2 fixed bed, feed of 11% SO_2, 10% O_2, and 79% N_2, space velocity 690,000 h^{-1}, and catalyst area per unit reactor volume of 350 cm^{-1}.

Mechanism Reduction

Based on the sensitivity analysis, coverage profiles, and RPA, a preliminary mechanism reduction is carried out. Adsorption/desorption of some radicals (O*, S*, SO*) and some surface reactions involving SO* are not important (shaded reactions in Table 2); hence, they can be removed from the mechanism without affecting the simulation results. Finally, a 12-step SO_2 oxidation model is proposed after the mechanism reduction.

Future Directions to Model DOC-SO_x Interactions

In this work, we addressed the first challenge of developing and validating a surface reaction mechanism for SO_2 oxidation on Pt. However, as discussed earlier in the 'Gaps and Challenges in the Understanding of DOC-SOx Interactions' section, multiple issues need to be addressed to model the DOC-SO_x interactions. Here, we briefly discuss our outlook on addressing such challenges.

Bimetallic Nature of DOC

As Pt and Pd form bimetallic particles when heated (*64*), extension of the emissions (CO, NO, CH_2O, NH_3, HCN, and SO_2) oxidation model on Pt from our work to a Pt–Pd bimetallic catalyst is needed to correctly capture the DOC chemistry. Kinetic parameter estimation for bimetallics will be challenging due to the lack of surface science experimental data, but a combination of first principles DFT and semi-empirical UBI-QEP could be used to estimate the species binding energies and reactions activation energies on Pt–Pd bimetallic catalysts. Model validation could be carried out against literature experimental data for Pt–Pd based DOCs under simulated and real exhaust conditions.

Kinetics for Metal Oxide Sulfation

$PdSO_4$ is formed when PdO is exposed to SO_2. Therefore, PdO sulfation should be included as another important mechanism contributing to DOC deactivation. DFT and TST calculations should be conducted to compute the theoretical estimate for the kinetic rate constant for PdO sulfation.

Kinetics for Support Sulfation

Kinetics of alumina support sulfation to $Al_2(SO_4)_3$ needs to be included in the emissions oxidation model to correctly simulate DOC deactivation. Similar to the PdO sulfation, DFT and TST calculations should be conducted to compute the theoretical estimates for the kinetic rate constant for alumina support sulfation.

Kinetics for SO_x Interactions with Water and Ammonia

To develop a complete understanding of SO_x chemistry and DOC deactivation due to sulfur, interactions of SO_x with H_2O and NH_3 need to be included in the emissions oxidation model. These should include estimation of binding energies for H_2SO_4 and $(NH_4)_2SO_4$ on the Pt–Pd bimetallic system and activation energies for the formation of these sulfates.

Reactor Modeling Including Sulfation

Once the emissions oxidation model is augmented with kinetic parameters for catalyst sulfation, reactor modeling can be used to predict the DOC activity/performance over time. However, incorporation of catalyst sulfation in reactor

In Novel Materials for Catalysis and Fuels Processing; Bravo-Suárez, J., et al.;
ACS Symposium Series; American Chemical Society: Washington, DC, 2013.

modeling is a challenging task, as the extent of metal and support sulfation needs to be coupled with the emissions oxidation kinetics. The emissions oxidation reactions are typically faster than the DOC sulfation reactions, so the disparity in reaction time scales needs to be accounted for in the catalytic reactor simulations.

Materials Design for Sulfur-Resistant Catalysts

A critical objective in kinetic modeling is to provide new directions for computational design of improved catalysts. To identify sulfur-resistant catalysts, one ideally needs to generate (and validate) multiple kinetic models on different catalysts, compare the kinetic parameters, analyze the dominant reaction pathways, and explore why a particular catalyst shows improved/deteriorated performance. An alternate and more elegant option for computational catalyst design is identification of the most important parameters (descriptor) and its screening on a series of catalysts. Such a descriptor is currently unknown for DOC sulfation, but the descriptor could be one or more of the binding energies for S-containing species, activation energies for support or metal sulfation, or adsorbate-adsorbate interactions. Relative timescales and importance of the two sulfation mechanisms vs the primary emissions oxidation chemistry in the presence of SO_x need to be investigated using time-dependent reaction path analysis. This should yield information about the important chemistries of the augmented emissions oxidation model. Screening of DOC sulfation descriptors and kinetic parameters for SO_x interaction with the catalyst should provide insights regarding the SO_x binding strength and the catalyst sulfation rates on different surfaces, which may result in identification of S-resistant catalytic materials for emissions oxidation.

Summary

Despite the widespread use and importance of diesel engines, toxic emissions from the diesel engine exhaust create a huge challenge for human health and environment. Some of the important emissions present in the diesel engine exhaust are CO, NO, CO_2, NO_2, SO_2, NH_3, HCN, CH_2O, CH_3CHO, PAHs, SOF, and PM. Many aftertreatment units, such as DOC, DPF, and $DeNO_x$ systems, are being used to control these emissions. Due to increasing stringent regulations to control emissions, the aftertreatment units need to be robust and efficient.

DOC is mainly responsible for oxidation of emissions from the engine as well as toxic byproducts. However, the deactivation of DOC due to sulfur present in the diesel fuel and lubricants creates a tremendous challenge, as DOC is a very expensive unit. Sulfur present in the fuel and lubricants is converted to SO_2 in the diesel engine. This SO_2 is converted to SO_3 due to high oxygen concentration in the engine exhaust. Formation of SO_3 triggers many interactions with metal oxides and supports which leads to the formation of sulfates and subsequent deactivation of the DOC. In addition to the metal and support sulfation, the presence of H_2O and NH_3 also leads to the production of sulfuric acid and ammonium sulfate, respectively, to hasten the DOC deactivation.

In Novel Materials for Catalysis and Fuels Processing; Bravo-Suárez, J., et al.;
ACS Symposium Series; American Chemical Society: Washington, DC, 2013.

Many experimental and computational studies have focused on understanding the sulfation mechanism and its impacts on the emissions oxidation chemistries. Pt is more active in SO_2 oxidation than Pd; and no sulfate formation is observed on Pt. Unlike Pt, Pd metal remains in oxidized form (PdO) in the presence of oxygen and forms sulfate on the surface. γ–Al_2O_3, a common support materials for DOC, is also prone to sulfate formation in the presence of SO_3. The presence of sulfur also impacts the emissions oxidation chemistry of DOC. Studies show that CO and NO oxidation activities on Pt–Pd are severely impacted due to sulfur.

Sulfation of DOC is a challenging and complex phenomena. Very limited information of this complex chemistry is available in the literature. Details of the SO_x interaction mechanism and kinetics on bimetallic DOC are not available. Similarly, SO_x interaction with supports adds more challenges to the chemistry and kinetics. Therefore, a complete understanding of the sulfation mechanism and kinetics is necessary to predict the DOC deactivation and design sulfur resistant materials, thereby ultimately reducing the cost of operation.

Here, we have extended the recently developed microkinetic model for five major emissions oxidation chemistries on Pt to include the SO_2 oxidation chemistry on Pt. The developed mechanism correctly captures experimental data for SO_2 oxidation relevant to DOC operating conditions. This is the first step towards understanding SO_x interactions with Pt–Pd/alumina DOCs. In the future, understanding the sulfation mechanism using various approaches discussed here can be crucial to design sulfur resistant catalysts and to make the DOC an efficient and economical component of the diesel engine aftertreatment system.

Acknowledgments

HNS acknowledges Department of Education GAANN Fellowship and the United States EPA STAR graduate fellowship for funding support. This publication (article) was made possible by EPA fellowship number FP917501. Its contents are solely the responsibility of the fellow and do not necessarily represent the official views of the EPA. Furthermore, the EPA does not endorse the purchase of any commercial products or services mentioned in the publication. SLS acknowledges support of the U. S. Department of Energy, Office of Basic Energy Sciences, Division of Chemical, Biological, and Geochemical Sciences under contract DE-FG02-86ER13622.A000.

References

1. Diesel-Powered Machines and Equipment: Essential Uses, Economic Importance and Environmental Performance. http://www.dieselforum.org/files/dmfile/Diesel-PoweredMachinesandEquipment.pdf (accessed July 17, 2012).
2. Bensaid, S.; Caroca, C. J.; Russo, N.; Fino, D. *Can. J. Chem. Eng.* **2011**, *89*, 401–407.
3. Prasad, R.; Bella, V. R. *Bull. Chem. React. Eng. Catal.* **2010**, *5*, 69–86.
4. Fino, D. *Sci. Technol. Adv. Mater.* **2007**, *8*, 93–100.

5. Xi, J.; Zhong, B. J. *Chem. Eng. Technol.* **2006**, *29*, 665–673.
6. Diesel fuel explained- use of diesel. http://www.eia.gov/energyexplained/index.cfm?page=diesel_use (accessed Feb 5, 2012).
7. Bera, P.; Hegde, M. S. *J. Indian Inst. Sci.* **2010**, *90*, 299–325.
8. Kröcher, O.; Widmer, M.; Elsener, M.; Rothe, D. *Ind. Eng. Chem. Res.* **2009**, *48*, 9847–9857.
9. Magara- Gomez, K. T.; Olson, M. R.; Okuda, T.; Walz, K. A.; Schauer, J. J. *Atmos. Environ.* **2012**, *50*, 307–313.
10. Lim, M. C. H.; Ayoko, G. A.; Morawska, L.; Ristovski, Z. D.; Rohan Jayaratne, E. *Atmos. Environ.* **2005**, *39*, 7836–7848.
11. Chiang, H.; Lai, Y.; Chang, S. *Atmos. Environ.* **2012**, *47*, 399–406.
12. Jung, J.; Lee, J.; Song, S.; Chun, K. *Int. J. Automot. Technol.* **2008**, *9*, 423–428.
13. Zhao, H.; Ge, Y.; Wang, X.; Tan, J.; Wang, A.; You, K. *Energy Fuels* **2010**, *24*, 985–991.
14. Corro, G. *React. Kinet. Catal. Lett.* **2002**, *75*, 89–106.
15. Zhao, H.; Tonkyn, R. G.; Barlow, S. E.; Koel, B. E.; Peden, C. H. F. *Appl. Catal., B* **2006**, *65*, 282–290.
16. Kröcher, O.; Elsener, M. *Appl. Catal., B* **2009**, *92*, 75–89.
17. Macor, A.; Avella, F.; Faedo, D. *Appl. Energy* **2011**, *88*, 4989–5001.
18. Tan, P.; Hu, Z.; Lou, D. *Fuel* **2009**, *88*, 1086–1091.
19. Rodriguez-Fernandez, J.; Oliva, F.; Vazquez, R. A. *Energy Fuels* **2011**, *25*, 2039–2048.
20. Shrivastava, M.; Nguyen, A.; Zheng, Z.; Wu, H.; Jung, H. S. *Environ. Sci. Technol.* **2010**, *44*, 4796–4801.
21. Liu, G.; Gao, P. *Catal. Sci. Technol.* **2011**, *1*, 552–568.
22. Ghzaoui, E.; Lindheimer, M.; Lindheimer, A.; Lagerge, S.; Partyka, S. *Colloids Surf. Physicochem. Eng. Aspects* **2004**, *233*, 79–86.
23. Lin, C.; Huang, J. *Ocean Eng.* **2003**, *30*, 1699–1715.
24. Kašpar, J.; Fornasiero, P.; Hickey, N. *Catal. Today* **2003**, *77*, 419–449.
25. Salomons, S. Ph.D. thesis, University of Alberta, Alberta, 2008.
26. Jelles, S. J. Ph.D. thesis, Delft Technical University, Delft, NL, 1999.
27. Kumar, S.; Nayek, M.; Kumar, A.; Tandon, A.; Mondal, P.; Vijay, P.; Bhangale, U. D.; Tyagi, D. *Am. Chem. Sci. J.* **2011**, *1*, 1–27.
28. Zheng, M.; Reader, G. T.; Hawley, J. G. *Energy Convers. Manage.* **2004**, *45*, 883–900.
29. Heck, R. M.; Farrauto, R. J.; Gulati, S. T. *Catalytic air pollution control: Commercial technology*, 3rd ed.; John Wiley & Sons: 2009; p 522.
30. Neeft, J. P. A.; Makkee, M.; Moulijn, J. A. *Fuel Process. Technol.* **1996**, *47*, 1–69.
31. Russell, A.; Epling, W. S. *Catal. Rev. Sci. Eng.* **2011**, *53*, 337–423.
32. Williams, S. Ph.D. thesis, University of Toronto, Ontario, 2008.
33. Martyn, V. T. *Catal. Today* **2011**, *163*, 33–41.
34. Yezerets, A.; Currier, N. W.; Kim, D. H.; Eadler, H. A.; Epling, W. S.; Peden, C. H. F. *Appl. Catal., B* **2005**, *61*, 120–129.
35. Azambre, B.; Collura, S.; Darcy, P.; Trichard, J. M.; Da Costa, P.; García-García, A.; Bueno-López, A. *Fuel Process. Technol.* **2011**, *92*, 363–371.

36. Stanmore, B. R.; Tschamber, V.; Brilhac, J. *Fuel* **2008**, *87*, 131–146.
37. Jacquot, F.; Brilhac, J.; Noirot, R. *SAE Technical Paper* **2004**, *2004-01-1943*.
38. Basile, F.; Fornasari, G.; Grimandi, A.; Livi, M.; Vaccari, A. *Appl. Catal., B* **2006**, *69*, 58–64.
39. Kelly, J. F.; Stanciulescu, M.; Charland, J. *Fuel* **2006**, *85*, 1772–1780.
40. Houel, V.; Millington, P.; Rajaram, R.; Tsolakis, A. *Appl. Catal., B* **2007**, *73*, 203–207.
41. Grossale, A.; Nova, I.; Tronconi, E. *Catal. Today* **2008**, *136*, 18–27.
42. Tronconi, E.; Nova, I.; Ciardelli, C.; Chatterjee, D.; Bandl-Konrad, B.; Burkhardt, T. *Catal. Today* **2005**, *105*, 529–536.
43. Hernandez Carucci, J. R.; Arve, K.; Bartova, S.; Eranen, K.; Salmi, T.; Murzin, D. Y. *Catal. Sci. Technol.* **2011**, *1*, 1456–1465.
44. Arve, K.; Backman, H.; Klingstedt, F.; Eränen, K.; Murzin, D. Y. *Appl. Catal., A* **2006**, *303*, 96–102.
45. Metkar, P. S.; Balakotaiah, V.; Harold, M. P. *Catal. Today* **2012**, *184*, 115–128.
46. Metkar, P. S.; Harold, M. P.; Balakotaiah, V. *Appl. Catal., B* **2012**, *111–112*, 67–80.
47. Choi, J.; Partridge, W. P.; Daw, C. S. *Appl. Catal., A* **2005**, *293*, 24–40.
48. Mulla, S. S.; Chen, N.; Delgass, W. N.; Epling, W. S.; Ribeiro, F. H. *Catal. Lett.* **2005**, *100*, 267–270.
49. Epling, W. S.; Campbell, L. E.; Yezerets, A.; Currier, N. W.; Parks, J. E. *Catal. Rev. Sci. Eng.* **2004**, *46*, 163–245.
50. Colombo, M.; Nova, I.; Tronconi, E. *Chem. Eng. Sci.* **2012**, *75*, 75–83.
51. Scheuer, A.; Hauptmann, W.; Drochner, A.; Gieshoff, J.; Vogel, H.; Votsmeier, M. *Appl. Catal., B* **2012**, *111–112*, 445–455.
52. Scheuer, A.; Hirsch, O.; Hayes, R.; Vogel, H.; Votsmeier, M. *Catal. Today* **2011**, *175*, 141–146.
53. Scheuer, A.; Votsmeier, M.; Schuler, A.; Gieshoff, J.; Drochner, A.; Vogel, H. *Top. Catal.* **2009**, *52*, 1847–1851.
54. Scheuer, A.; Drochner, A.; Gieshoff, J.; Vogel, H.; Votsmeier, M. *Catal. Today* **2012**, *188*, 70–79.
55. Votsmeier, M.; Scheuer, A.; Drochner, A.; Vogel, H.; Gieshoff, J. *Catal. Today* **2010**, *151*, 271–277.
56. Kamasamudram, K.; Yezerets, A.; Chen, X.; Currier, N.; Castagnola, M.; Chen, H. *SAE Technical Paper* **2011**, *2011-01-1314*.
57. Luo, J.; Kisinger, D.; Abedi, A.; Epling, W. S. *Appl. Catal., A* **2010**, *383*, 182–191.
58. Wallington, T. J.; Lambert, C. K.; Ruona, W. C. *Energy Policy* **2011**, *54*, 47–53.
59. Oh, H.; Luo, J.; Epling, W. *Catal. Lett.* **2011**, *141*, 1746–1751.
60. Morlang, A.; Neuhausen, U.; Klementiev, K. V.; Schütze, F. W.; Miehe, G.; Fuess, H.; Lox, E. S. *Appl. Catal., B* **2005**, *60*, 191–199.
61. Neyestanaki, A. K.; Klingstedt, F.; Salmi, T.; Murzin, D. Y. *Fuel* **2004**, *83*, 395–408.
62. Majewski, W.; Khair, M. *Diesel Emissions and Their Control*; SAE International: Warrendale, PA, 2006; pp 121−143.

63. Hauff, K.; Tuttlies, U.; Eigenberger, G.; Nieken, U. *Appl. Catal., B* **2010**, *100*, 10–18.
64. Johnson Matthey. *Platinum*; 2009; pp 39−41.
65. Koebel, M.; Madia, G.; Elsener, M. *Catal. Today* **2002**, *73*, 239–247.
66. Ciardelli, C.; Nova, I.; Tronconi, E.; Chatterjee, D.; Bandl-Konrad, B.; Weibel, M.; Krutzsch, B. *Appl. Catal., B* **2007**, *70*, 80–90.
67. Setiabudi, A.; Makkee, M.; Moulijn, J. A. *Appl. Catal., B* **2004**, *50*, 185–194.
68. Tighe, C. J.; Twigg, M. V.; Hayhurst, A. N.; Dennis, J. S. *Combust. Flame* **2012**, *159*, 77–90.
69. Miessner, H.; Francke, K.; Rudolph, R. *Appl. Catal., B* **2002**, *36*, 53–62.
70. Centi, G.; Perathoner, S. Selective catalytic reduction(SCR) processes on metal oxides. In *Metal Oxides: Chemistry And Applications*; Fierro, J. L. G., Ed.; Taylor & Francis: Boca Raton, FL, USA, 2006; pp 661−682.
71. Liu, I.; Cant, N.; Kögel, M.; Turek, T. *Catal. Lett.* **1999**, *63*, 214–244.
72. Sampara, C. S. Ph.D. thesis, University of Michigan, MI, 08.
73. Heck, R. M.; Farrauto, R. J. *Appl. Catal., A* **2001**, *221*, 443–457.
74. Bartholomew, C. H.; Farrauto, R. J., In *Fundamentals of Industrial Catalytic Processes;* John Wiley & Sons: Hoboken, NJ, 2006; Vol. 2, pp 996.
75. Bartholomew, C. H. *Appl. Catal., A* **2001**, *212*, 17–60.
76. Fuels and Fuel Additives: Diesel Fuel. http://www.epa.gov/oms/fuels/dieselfuels/index.htm (accessed July 21, 2012).
77. Clean Diesel Fuel Alliance. http://www.ct.gov/dep/lib/dep/air/ultra_low_sulfur_diesel/ulsdfs.pdf (accessed July 20, 2012).
78. Environmental Protection Agency. *Fed. Regist.* **2006**, *71* (83), Air Docket No. EPA-HQ-OAR-2006-0224.
79. Lemmetty, M.; Rönkkö, T.; Virtanen, A.; Keskinen, J.; Pirjola, L. *Aerosol Sci. Technol.* **2008**, *42*, 916–929.
80. Bielaczyc, P.; Keskinen, J.; Dzida, J.; Sala, R.; Ronkko, T.; Kinnunen, T.; Matilainen, P.; Karjalainen, P.; Happonen, M. J. *SAE Technical Paper* **2012**, *2012-01-0366*.
81. Kolli, T.; Huuhtanen, M.; Hallikainen, A.; Kallinen, K.; Keiski, R. *Catal. Lett.* **2009**, *127*, 49–54.
82. Xue, E.; Seshan, K.; Ross, J. R. H. *Appl. Catal., B* **1996**, *11*, 65–79.
83. Stratakis, G. A. Ph.D. thesis, University of Thessaly, Thessaly, Greece, 2004.
84. Lampert, J. K.; Kazi, M. S.; Farrauto, R. J. *Appl. Catal., B* **1997**, *14*, 211–223.
85. Russell, A.; Henry, C.; Currier, N. W.; Yezerets, A.; Epling, W. S. *Appl. Catal., A* **2011**, *397*, 272–284.
86. Rodriguez, J. A.; Hrbek, J. *Acc. Chem. Res.* **1999**, *32*, 719–728.
87. Truex, T. *SAE Technical Paper* **1999**, *1999-01-1543*.
88. Xue, E.; Seshan, K.; van Ommen, J. G.; Ross, J. R. H. *Appl. Catal., B* **1993**, *2*, 183–197.
89. Koutsopoulos, S.; Rasmussen, S. B.; Eriksen, K. M.; Fehrmann, R. *Appl. Catal., A* **2006**, *306*, 142–148.
90. Mowery, D. L.; McCormick, R. L. *Appl. Catal., B* **2001**, *34*, 287–297.
91. Corro, G.; Velasco, A.; Montiel, R. *Catal. Commun.* **2001**, *2*, 369–374.
92. Pazmiño, J. H.; Miller, J. T.; Mulla, S. S.; Nicholas Delgass, W.; Ribeiro, F. H. *J. Catal.* **2011**, *282*, 13–24.

93. Mathieu, M.; Primet, M. *Appl. Catal.* **1984**, *9*, 361–370.
94. Hammerle, R. H.; Truex, T. J. *Am. Chem. Soc.* **1976**, *21*, 769–783.
95. Matsumoto, S. *Catal. Today* **2004**, *90*, 183–190.
96. Corro, G.; Cano, C.; Fierro, J. L. G. *J. Mol. Catal. A: Chem.* **2010**, *315*, 35–42.
97. Kolli, T.; Kanerva, T.; Huuhtanen, M.; Vippola, M.; Kallinen, K.; Kinnunen, T.; Lepistö, T.; Lahtinen, J.; Keiski, R. L. *Catal. Today* **2010**, *154*, 303–307.
98. Breen, J. P.; Burch, R.; Hardacre, C.; Hill, C. J.; Krutzsch, B.; Bandl-Konrad, B.; Jobson, E.; Cider, L.; Blakeman, P. G.; Peace, L. J.; Twigg, M. V.; Preis, M.; Gottschling, M. *Appl. Catal., B* **2007**, *70*, 36–44.
99. Zelenka, P.; Cartellieri, W.; Herzog, P. *Appl. Catal., B* **1996**, *10*, 3–28.
100. Farrauto, R. J.; Voss, K. E. *Appl. Catal., B* **1996**, *10*, 29–51.
101. Gieshoff, J.; Pfeifer, M.; Schäfer-Sindlinger, A.; Spurk, P.; Garr, G.; Leprince, T. *SAE Technical Paper* **2001**, *2001-01-0514*.
102. Herner, J. D.; Hu, S.; Robertson, W. H.; Huai, T.; Chang, M. -. O.; Rieger, P.; Ayala, A. *Environ. Sci. Technol.* **2011**, *45*, 2413–2419.
103. Ramachandran, B.; Herman, R. G.; Choi, S.; Stenger, H. G.; Lyman, C. E.; Sale, J. W. *Catal. Today* **2000**, *55*, 281–290.
104. Kozak, M.; Merkisz, J. *TEKA Kom. Mot. Energ. Roln.* **2005**, *5*, 96–106.
105. Polčik, M.; Wilde, L.; Haase, J.; Brena, B.; Comelli, G.; Paolucci, G. *Surf. Sci.* **1997**, *381*, L568–L572.
106. Sun, Y. -.; Sloan, D.; Alberas, D. J.; Kovar, M.; Sun, Z.; White, J. M. *Surf. Sci.* **1994**, *319*, 34–44.
107. Köhler, U.; Wassmuth, H. *Surf. Sci.* **1983**, *126*, 448–454.
108. Köhler, U.; Wassmuth, H. *Surf. Sci.* **1982**, *117*, 668–675.
109. Astegger, S.; Bechtold, E. *Surf. Sci.* **1982**, *122*, 491–504.
110. Höfer, M.; Hillig, S.; Wassmuth, H. *Vacuum* **1990**, *41*, 102–104.
111. Lee, A. F.; Wilson, K.; Goldoni, A.; Larciprete, R.; Lizzit, S. *Surf. Sci.* **2002**, *513*, 140–148.
112. Wilson, K.; Hardacre, C.; Baddeley, C. J.; Lüdecke, J.; Woodruff, D. P.; Lambert, R. M. *Surf. Sci.* **1997**, *372*, 279–288.
113. Streber, R.; Papp, C.; Lorenz, M. P. A.; Höfert, O.; Darlatt, E.; Bayer, A.; Denecke, R.; Steinrück, H. *Chem. Phys. Lett.* **2010**, *494*, 188–192.
114. Cabello Galisteo, F.; Mariscal, R.; López Granados, M.; Zafra Poves, M. D.; Fierro, J. L. G.; Kröger, V.; Keiski, R. L. *Appl. Catal., B* **2007**, *72*, 272–281.
115. Yao, H. C.; Stepien, H. K.; Gandhi, H. S. *J. Catal.* **1981**, *67*, 231–236.
116. Chang, C. C. *J. Catal.* **1978**, *53*, 374–385.
117. Han, J. Ph.D. thesis, Worcester Polytechnic Institute, Worcester, MA, 2004.
118. Bayer, G.; Wiedemann, H. G. *Thermochim. Acta* **1975**, *11*, 79–88.
119. Bell, W. E.; Inyard, R. E.; Tagami, M. *J. Phys. Chem.* **1966**, *70*, 3735–3736.
120. Lyubovsky, M.; Pfefferle, L. *Appl. Catal., A* **1998**, *173*, 107–119.
121. Mallika, C.; Sreedharan, O. M.; Gnanamoorthy, J. B. *J. Less-Common Met.* **1983**, *95*, 213–220.
122. Wakita, H.; Kani, Y.; Ukai, K.; Tomizawa, T.; Takeguchi, T.; Ueda, W. *Appl. Catal., A* **2005**, *283*, 53–61.

123. Abdulhamid, H.; Fridell, E.; Dawody, J.; Skoglundh, M. *J. Catal.* **2006**, *241*, 200–210.
124. Gracia, F. J.; Guerrero, S.; Wolf, E. E.; Miller, J. T.; Kropf, A. J. *J. Catal.* **2005**, *233*, 372–387.
125. Uy, D.; Wiegand, K. A.; O'Neill, A. E.; Dearth, M. A.; Weber, W. H. *J. Phys. Chem. B* **2002**, *106*, 387–394.
126. Summers, J. C. *Environ. Sci. Technol.* **1979**, *13*, 321–325.
127. Karge, H. G.; Dalla Lana, I. G. *J. Phys. Chem.* **1984**, *88*, 1538–1543.
128. Skoglundh, M.; Ljungqvist, A.; Petersson, M.; Fridell, E.; Cruise, N.; Augustsson, O.; Jobson, E. *Appl. Catal., B* **2001**, *30*, 315–328.
129. Hubbard, C. P.; Otto, K.; Gandhi, H. S.; Ng, K. Y. S. *J. Catal.* **1993**, *144*, 484–494.
130. Kim, Y.; Lim, S.; Kim, Y.; Lee, J.; Lee, H. *Res. Chem. Intermed.* **2012**, *38*, 947–955.
131. Cabello Galisteo, F.; Larese, C.; Mariscal, R.; López Granados, M.; Fierro, J.; Fernández-Ruiz, R.; Furió, M. *Top. Catal.* **2004**, *30-31*, 451–456.
132. Dawody, J.; Skoglundh, M.; Fridell, E. *J. Mol. Catal. A: Chem.* **2004**, *209*, 215–225.
133. Dawody, J.; Skoglundh, M.; Olsson, L.; Fridell, E. *J. Catal.* **2005**, *234*, 206–218.
134. Irfan, M.; Goo, J.; Kim, S. *The Environmentalist* **2011**, *31*, 4–10.
135. Corro, G.; Montiel, R.; Vázquez, L. C. *Catal. Commun.* **2002**, *3*, 533–539.
136. Matyshak, V. A.; Bondareva, N. K.; Panchishnyi, V. I. *Kinet. Catal.* **1998**, *39*, 720–727.
137. Ruth, K.; Hayes, M.; Burch, R.; Tsubota, S.; Haruta, M. *Appl. Catal., B* **2000**, *24*, L133–L138.
138. Roth, D.; Gélin, P.; Primet, M.; Tena, E. *Appl. Catal., A* **2000**, *203*, 37–45.
139. Mowery, D. L.; Graboski, M. S.; Ohno, T. R.; McCormick, R. L. *Appl. Catal., B* **1999**, *21*, 157–169.
140. Amberntsson, A.; Skoglundh, M.; Ljungström, S.; Fridell, E. *J. Catal.* **2003**, *217*, 253–263.
141. Amberntsson, A.; Fridell, E.; Skoglundh, M. *Appl. Catal., B* **2003**, *46*, 429–439.
142. Olsson, L.; Karlsson, H. *Catal. Today* **2009**, *147* (Supplement), S290–S294.
143. Dagaut, P.; Lecomte, F.; Mieritz, J.; Glarborg, P. *Int. J. Chem. Kinet.* **2003**, *35*, 564–575.
144. Mitome, J.; Aceves, E.; Ozkan, U. S. *Catal. Today* **1999**, *53*, 597–606.
145. Orlik, S.; Shashkova, T. *Theor. Exp. Chem.* **2008**, *44*, 178–182.
146. Burch, R.; Halpin, E.; Hayes, M.; Ruth, K.; Sullivan, J. A. *Appl. Catal., B* **1998**, *19*, 199–207.
147. Lee, A. F.; Wilson, K.; Lambert, R. M.; Hubbard, C. P.; Hurley, R. G.; McCabe, R. W.; Gandhi, H. S. *J. Catal.* **1999**, *184*, 491–498.
148. Hubbard, C. P.; Otto, K.; Gandhi, H. S.; Ng, K. Y. S. *Catal. Lett.* **1994**, *30*, 41–51.
149. Wilson, K.; Hardacre, C.; Lambert, R. M. *J. Phys. Chem.* **1995**, *99*, 13755–13758.
150. Lin, X.; Schneider, W. F.; Trout, B. L. *J. Phys. Chem. B* **2004**, *108*, 250–264.

151. Lin, X.; Schneider, W. F.; Trot, B. L. *J. Phys. Chem. B* **2004**, *108*, 13329–13340.
152. Lin, X.; Hass, K. C.; Schneider, W. F.; Trout, B. L. *J. Phys. Chem. B* **2002**, *106*, 12575–12583.
153. Lin, X.; Ramer, N. J.; Rappe, A. M.; Hass, K. C.; Schneider, W. F.; Trout, B. L. *J. Phys. Chem. B* **2001**, *105*, 7739–7747.
154. Happel, M.; Luckas, N.; Viñes, F.; Sobota, M.; Laurin, M.; Görling, A.; Libuda, J. *J. Phys. Chem. C* **2011**, *115*, 479–491.
155. Luckas, N.; Viñes, F.; Happel, M.; Desikusumastuti, A.; Libuda, J.; Görling, A. *J. Phys. Chem. C* **2010**, *114*, 13813–13824.
156. Luckas, N.; Gotterbarm, K.; Streber, R.; Lorenz, M. P. A.; Hofert, O.; Vines, F.; Papp, C.; Gorling, A.; Steinruck, H. *Phys. Chem. Chem. Phys.* **2011**, *13*, 16227–16235.
157. Truhlar, D. G.; Garrett, B. C.; Klippenstein, S. J. *J. Phys. Chem.* **1996**, *100*, 12771–12800.
158. Sommer, A.; Ku, M.; Roati, G.; Zwierlein, M. W. *Nature* **2011**, *472*, 201–204.
159. Marques, M. A.; Troiani, H. E.; Miki-Yoshida, M.; Jose-Yacaman, M.; Rubio, A. *Nano Lett.* **2004**, *4*, 811–815.
160. Ma, P. N.; Pilati, S.; Troyer, M.; Dai, X. *Nat. Phys.* **2012**, *8*, 601–605.
161. Kohn, W.; Becke, A. D.; Parr, R. G. *J. Phys. Chem.* **1996**, *100*, 12974–12980.
162. Terada, S.; Yokoyama, T.; Sakano, M.; Kiguchi, M.; Kitajima, Y.; Ohta, T. *Chem. Phys. Lett.* **1999**, *300*, 645–650.
163. Ohashi, N.; Yoshizawa, K.; Endou, A.; Takami, S.; Kubo, M.; Miyamoto, A. *Appl. Surf. Sci.* **2001**, *177*, 180–188.
164. Benzinger, W.; Wenka, A.; Dittmeyer, R. *Appl. Catal., A* **2011**, *397*, 209–217.
165. Olsson, L.; Fredriksson, M.; Blint, R. J. *Appl. Catal., B* **2010**, *100*, 31–41.
166. Dawody, J.; Skoglundh, M.; Olsson, L.; Fridell, E. *Appl. Catal., B* **2007**, *70*, 179–188.
167. Matsumoto, S.; Ikeda, Y.; Suzuki, H.; Ogai, M.; Miyoshi, N. *Appl. Catal., B* **2000**, *25*, 115–124.
168. Hauptmann, W.; Votsmeier, M.; Gieshoff, J.; Drochner, A.; Vogel, H. *Appl. Catal., B* **2009**, *93*, 22–29.
169. Hauptmann, W.; Votsmeier, M.; Gieshoff, J.; Vlachos, D.; Drochner, A.; Vogel, H. *Top. Catal.* **2009**, *52*, 1925–1928.
170. Sampara, C. S.; Bissett, E. J.; Chmielewski, M. *Ind. Eng. Chem. Res.* **2008**, *47*, 311–322.
171. Kim, Y.; Kim, W. *Ind. Eng. Chem. Res.* **2009**, *48*, 6579–6590.
172. Wang, T. J.; Baek, S. W.; Lee, J. *Ind. Eng. Chem. Res.* **2008**, *47*, 2528–2537.
173. Chakravarthy, K.; Daw, C.; Conklin, J. *SAE Technical Paper* **2001**, *2002-01-1879*.
174. Sharma, H. N.; Mhadeshwar, A. B. *Appl. Catal., B* **2012**, *127*, 190–204.
175. Campbell, C. T.; Ertl, G.; Kuipers, H.; Segner, J. *Surf. Sci.* **1981**, *107*, 220–236.
176. Shustorovich, E.; Sellers, H. *Surf. Sci. Rep.* **1998**, *31*, 1–119.
177. Shustorovich, E. *Adv. Catal.* **1990**, *37*, 101–164.

178. Mhadeshwar, A. B.; Wang, H.; Vlachos, D. G. *J. Phys. Chem. B* **2003**, *107*, 12721–12733.
179. Grabow, L. C.; Gokhale, A. A.; Evans, S. T.; Dumesic, J. A.; Mavrikakis, M. *J. Phys. Chem. C* **2008**, *112*, 4608–4617.
180. Yeo, Y. Y.; Vattuone, L.; King, D. A. *J. Chem. Phys.* **1997**, *106*, 392–401.
181. Dumesic, J. A.; Rudd , D. F.; Aparicio, L. M.; Rekoske, J. E.; Trevino, A. A. *The Microkinetics of Heterogeneous Catalysis*; American Chemical Society: 1993; p 315.
182. Gorte, R. J.; Schmidt, L. D.; Gland, J. L. *Surf. Sci.* **1981**, *109*, 367–380.
183. Smith, G. P.; Golden, D. M.; Frenklach, M.; Moriarty, N. W.; Eiteneer, B.; Goldenberg, M.; Bowman, C. T.; Hanson, R. K.; Song, S.; Gardiner, W. C.; Lissianski, V. V.; Qin, Z. *GRI-Mech 3.0*; 1999. http://www.me.berkeley.edu/gri_mech/.
184. Li, S.; Petzold, L. *Design of new DASPK for Sensitivity Analysis*; Technical report; Los Alamos National Laboratory: 1999.
185. Mhadeshwar, A. B.; Vlachos, D. G. *Combust. Flame* **2005**, *142*, 289–298.
186. Morley, C. Gaseq: A chemical equilibrium program for windows. http://www.c.morley.dsl.pipex.com (accessed Aug 24, 2012).

Chapter 6

Hydrodesulfurization Studies on SBA-16 Supported Molybdenum Hydrotreating Catalysts

Kapil Soni,[1] Thallada Bhaskar,[1] Manoj Kumar,[1] Kamaraju Seetha Rama Rao,[2] and Gudimella Murali Dhar*[,3]

[1]CSIR-Indian Institute of Petroleum (IIP), Haridwar Road, Dehradun 248005, India
[2]CSIR-Indian Institute of Chemical Technology (IICT), Tarnaka, Hyderabad 500007, India
[3]Gayatri Vidya Parishad (GVP) College of Engineering, Visakapatnam-530041, India
***E-mail: dhargm@gmail.com**

Well ordered SBA-16 mesoporous silica with characteristic pore structure and spherical cavities was synthesized by established procedures. Mo, Co–Mo, and Ni–Mo catalysts were supported on SBA-16 mesoporous silica. The support and catalysts were characterized by low angle as well as wide angle X-ray diffraction (XRD), transmission electron microscopy (TEM), and pore size distribution measurements. The XRD, TEM, and pore size distribution indicated that an ordered mesopore structure with spherical cavities was obtained in the support and the same structure is retained after addition of Mo and Co or Ni. The wide angle XRD measurements indicated that molybdenum is well dispersed up to 8 wt % Mo loading in the oxide precursors. Surface area analysis indicated that Mo is dispersed as a monolayer both in the oxide and sulfided states, whereas oxygen chemisorption measurements confirmed these high dispersions. The temperature programmed reduction (TPR) profiles displayed a two peak pattern and indicated that MoO_3 is not completely reduced at all the Mo loadings studies. However, the promoter increased the reducibility of molybdenum oxide. Thiophene hydrodesulfurization and cyclohexene

In Novel Materials for Catalysis and Fuels Processing; Bravo-Suárez, J., et al.;
ACS Symposium Series; American Chemical Society: Washington, DC, 2013.

hydrogenation activities showed a maximum at 8 wt % Mo and 3 wt % Co or Ni loading. The oxygen chemisorption correlated well with the two catalytic functionalities. SBA-16 supported Mo and Co–Mo catalysts showed superior activities compared to SBA-15 and γ–Al_2O_3 supported analogues of comparable composition.

Introduction

Mesoporous silicas have been investigated as catalyst supports because of their high surface area, chemical inertness, and well-controlled pore architectures. The family of mesoporous structures is expanding continuously. Following the earlier reports on M41S mesoporous materials (*1*, *2*), many new types of materials have been developed, such as FSM-16 (*3*), various MSU (*4*), KIT (*5*), and many SBA materials (*6*, *7*). These mesoporous materials find application in a variety of fields including adsorption and catalysis. To be applicable as a superior catalyst support, these materials should meet a number of important requirements, such as good stability, a fairly inexpensive, simple, and ecologically friendly synthesis method, and unambiguous criteria to evaluate the quality of the final material. A secondary, but also a very important requirement is good accessibility of the pores to the reactants and a combined and controllable micro- and mesoporosity. The combined micro- and mesoporosity can greatly enhance the activity and selectivity of the catalyst. The accessibility of the pores is best achieved by a three-dimensional porous structure (*8*). SBA-15 and SBA-16 materials meet most of these criteria. They are synthesized using the environmentally friendly triblock copolymers, which can, if desired, be regenerated and reused (*6*, *9*). They have intrinsically both micro- and mesopores in their structure and possess relatively thick walls (3–4 nm compared to typical values of 1 nm for MCM-41, MCM-48, and FSM). Their thermal, hydrothermal, and mechanical stabilities are better than those of the more often used MCM-41 and MCM-48.

Materials in the SBA-16 family comprise of close-packed spherical empty cages (*10*, *11*, *13*) with a body-centered cubic symmetry (*Im3m*). Each cage, with a spherical cavity diameter of 9.5 nm, is connected to eight neighboring cages by narrow openings of 2.3 nm along the (111) direction. The dimensions of the cages and the openings can be adjusted by the synthesis conditions (*12*). For supporting metal nanoparticles, the SBA-16 is considered to be superior to 2D hexagonally structured mesoporous silica because it stabilizes the nanoparticles by "locking" them inside the interconnected cages. One example is that presented by Li et al. (*13*) who reported the confinement of a Ni–Cu alloy in the SBA-16 cages for the adsorptive removal of sulfur impurities in warm syngas. In addition, compared to other mesoporous silica materials, SBA-16 has better thermal stability, which is a prerequisite for applications involving high temperature operations such as those used in catalytic processes (*14*).

The optimization of the synthesis of hexagonal SBA-15 (*15*, *16*), its catalytic activation (*17*, *18*), surface modification, and subsequent use as a selective adsorbent (*19–21*) has received a lot of attention in the past few years. In

In Novel Materials for Catalysis and Fuels Processing; Bravo-Suárez, J., et al.;
ACS Symposium Series; American Chemical Society: Washington, DC, 2013.

mesoporous materials such as MCM-41 and SBA-15, migration and sintering of metal catalyst particles is a common problem, when used as metal supports, due to their straight channel pore structure (*22–24*). Moreover, the mesopores can be blocked by the metal particles if they grow to dimensions similar to the pore diameter. The cubic counterpart, SBA-16, which in principle can overcome this deficiency, has not been extensively studied. This is probably due to the difficulties encountered in the synthesis and especially in the characterization of this material. For instance, only until recently a clear model of SBA-16 structure (*25*), its wall thickness, pore size, and relative and absolute amounts of micro and mesopores have been reported (*26*).

In general, mesoporous materials are studied with great interest for a number of catalytic applications including hydrotreating reactions (*27*). In recent years, many approaches such as (i) different preparation method, (ii) support modification, and (iii) altering the active component have been followed in order to improve the activity of hydrotreating catalysts. Among these approaches, variation of the support is an important one (*28*). Different materials such as zeolites (*29*, *30*), metal oxides (*31–36*), carbon (*37*, *38*), mixed metal oxides (*39–44*), and mesoporous materials such as hexagonal mesoporous silica (HMS) (*45–47*), MCM-41 (*48–52*), SBA-15 (*53–57*), KIT-6 (*58*), and FSM-16 (*59*) have been studied as supports for hydrotreating catalysts. Among these catalysts, MCM-41 supported Co–Mo and Ni–Mo are reported to exhibit superior activities for hydrodenitridation (HDN) and hydrodesulfurization (HDS) of model compounds (*49*, *51*, *60*). MCM-41 type materials, however, have poor hydrothermal stability (*61*, *62*), which represents a serious limitation to their practical applications. Reddy et al. (*63*) have applied the Co–Mo/Al-MCM-41 catalyst for the upgrading of a petroleum residue. In this case, the Co–Mo/Al-MCM-41 catalyst was not as active as the commercial Co–Mo/γ-Al_2O_3 possibly because the pore size of MCM-41 is not large enough to convert the heavy molecules (e.g., asphaltenes) present in this feed. The hydrotreating activity of thiophene (*53*) and dibenzothiophene (*54*) on siliceous SBA-15 supported Ni–W (*53*), Co–Mo, and Ni–Mo (*54*) catalysts, on the other hand, was superior to that of the conventional γ-Al_2O_3 supported catalysts. FSM-16 and KIT-6 supported Co–Mo and Ni–Mo catalysts (*58*, *59*, *64–66*) were also reported to exhibit outstanding activities compared to conventional γ-Al_2O_3 supported catalysts. Despite all these previous reports, there have been only a few publications on the application of SBA-16 as catalyst supports (*67–69*). For example, Fierro and co-workers (*69*) found that Co–Mo–W supported on SBA-16 (with and without P additive) based catalysts are more active than Al_2O_3 supported catalysts. The same group also found that Al–SBA-16 supported Co–Mo–W were, however, less active than the corresponding Al–HMS supported catalysts. For the hydrogenolysis of anisole, used as a model reaction for pyrolysis gasoline upgrading, Loricera et al. (*69*, *70*) found that Co–Mo–W/SBA-16 with a phosphorous additive yielded superior activities compared to the SBA-15 supported catalysts. For the HDS of refractory sulfur compounds (e.g., 4,6-dimethyldibenzothiophene (4,6-DMDBT)), other metal supported SBA-16 catalysts have been also investigated including (1% P)–Ni–Mo–W/SBA-16 (*71*), Ni–Mo supported on Ti chemically grafted SBA-16, Ni–Mo/Ti–SBA-16, and Ni–Mo/Al–SBA-16 (*72*, *73*). The Al or Ti substitution in

In Novel Materials for Catalysis and Fuels Processing; Bravo-Suárez, J., et al.;
ACS Symposium Series; American Chemical Society: Washington, DC, 2013.

SBA-16 significantly increased 4,6-DMDBT conversion in comparison to SBA-16 supported catalysts. However, hydrogenation (HYD)/direct desulfurization (DDS) ratios are higher in the case of the SBA-16 supported catalysts, except for the chemically grafted Ti. Dominguez and co-workers (*74*) reported that Mo carbides and nitrides supported on SBA-16 predominantly favor direct desulfurization pathways during the HDS of dibenzothiophene.

In this investigation, in order to get further insight into the structural features of SBA-16 and their influence on dispersion, reducibility of molybdenum and cobalt phases and catalytic activities, a systematic investigation of hydrodesulfurization and hydrogenation functionalities as a function of molybdenum and cobalt loading was carried out together with catalyst structural characterizations obtained by oxygen chemisorption, temperature programmed reduction (TPR), and X-ray diffraction techniques. The above mentioned objectives together with a comparison of SBA-16 supported Mo catalysts with SBA-15 supported catalysts form the content of this chapter.

Experimental

Synthesis of SBA-16 and SBA-15 Supports

SBA-16 was prepared by using a triblock copolymer surfactant ($EO_{106}PO_{70}EO_{106}$, F127) as a structure directing agent, tetraethyl orthosilicate (TEOS) as silica source at low acid concentration (*75*). In a typical synthesis batch, 3.72 g of F127 was dissolved in 139 cm^3 of 0.5 M HCl at 40 °C. After 2–3 h stirring, 18 cm^3 TEOS was added dropwise. The resulting mixture with the following molar composition 1 TEOS: 0.00367 F127: 0.864 HCl: 100.2 H_2O was stirred for 20 h at 40 °C, and subsequently transferred to a Teflon bottle and aged at autogenous pressure for 24 h at 100 °C. The material was filtered, washed with water, and dried at 80 °C, and then calcined at 550 °C for 4 h with a heating rate of 3 °C/min and characterized. All the chemicals are obtained from Aldrich (research grade).

In a typical SBA-15 synthesis, 4 g of tri-block copolymer, Pluronic P123 (Sigma-Aldrich, CAS 9003-11-6) is dissolved in 30 g of distilled water and 120 g of 2 M HCl solution with stirring at 35 °C. Then, 8.5 g of tetraethyl orthosilicate (TEOS) (Sigma-Aldrich, CAS 78-10-4, Reagent Plus >99%) is added with constant stirring at 35 °C and the stirring is further continued for 20 h at the same temperature. The resultant gel mixture is aged at 100 °C for 24 h without stirring. The solid product obtained was filtered off, washed with distilled water, and then dried at room temperature followed by treatment in air at 550 °C for 6 h to remove the polymer template. The typical molar ratio of reactants is as follows: 1.0 SiO_2: 0.017 P123: 5.88 HCl: 163 H_2O.

Preparation of Molybdenum and Co or Ni Promoted Catalysts

The molybdenum supported catalysts were prepared by incipient wetness impregnation method using a calcined siliceous SBA-16 as the support and an appropriate amount of ammonium heptamolybdate tetrahydrate

In Novel Materials for Catalysis and Fuels Processing; Bravo-Suárez, J., et al.;
ACS Symposium Series; American Chemical Society: Washington, DC, 2013.

($(NH_4)_6Mo_7O_{24}\cdot 4H_2O$, Fluka, A. R. Grade, CAS 12054-85-2, >99%). The Co and Ni promoted catalysts were prepared by impregnating the corresponding nitrate salts (cobalt nitrate hexahydrate, $Co(NO_3)_2\cdot 6H_2O$, Sigma-Aldrich, CAS 10026-22-9, >99%; nickel nitrate hexahydrate, $Ni(NO_3)_2\cdot 6H_2O$, Sigma-Aldrich, CAS 13478-00-7, >98.5%) over the Mo impregnated catalysts (sequential impregnation). The impregnated catalysts were dried in an oven at 100 °C overnight followed by a treatment in air (static muffle furnace) at 550 °C for 6 h. For comparison, γ-Al_2O_3, SBA-15, and other mesoporous supports were prepared in a similar manner. The concentrations of the metals are nominal (the calculated amount).

Characterization

The catalysts and supports were characterized by low angle as well as wide angle X-ray diffraction (XRD), transmission electron microscopy (TEM), low temperature oxygen chemisorption (LTOC) and temperature programmed reduction (TPR).

X-ray Diffraction

The XRD patterns were obtained with Cu K_α radiation (40 kv and 40 mA) using a Rigaku model D/Max IIIB instrument in reflection geometry equipped with a NaI scintillation counter, a curved graphite crystal monochromator, and a Nickel filter.

Surface Area and Pore Size Distribution

The surface area and pore size distributions of supports as well as catalysts were obtained at liquid N_2 temperature (77 K) using an ASAP 2010 Micromeritics (USA) instrument and a typical standard procedure (ASTM).

Low Temperature Oxygen Chemisorption

The oxygen chemisorptions were carried out at −78 °C in a conventional volumetric high vacuum system, on a catalyst sulfided at 400 °C for 2 h using a CS_2/H_2 mixture at a flow rate of 40 cm^3/min. The detailed procedure is described elsewhere (*31*, *32*, *42*, *44*, *45*). Briefly, a conventional static volumetric high vacuum (up to 10^{-6} torr) system was used for the low temperature oxygen chemisorption (LTOC) measurement. Suitable modifications were made to sulfide the catalyst in situ prior to chemisorption. The standard procedure employed for sulfidation of the catalyst sample (around 0.2 g) consisted of passing a stream of H_2 saturated with CS_2 vapor at ambient temperature (25 °C) through the catalyst bed while raising the temperature from ambient to 400 °C at a rate of 4 °C/min. The process was continued for 2 h at 400 °C and the system was evacuated at the same temperature for 3 h at 10^{-6} torr. The catalyst tube was cooled to −78 °C using a bath containing a mixture of liquid nitrogen and isopropanol, followed by

In Novel Materials for Catalysis and Fuels Processing; Bravo-Suárez, J., et al.;
ACS Symposium Series; American Chemical Society: Washington, DC, 2013.

evacuation at this temperature for 1 h. Oxygen chemisorption on this catalyst was carried out as follows: purified oxygen from a storage bulb, connected to the high vacuum manifold, was allowed to enter in the catalyst chamber of a known dead space. After an initial quick fall, the pressure leveled off within about 15−20 min and the equilibrium pressure was noted. This process was repeated at different equilibrium pressures (between 100 and 300 torr) resulting in an adsorption isotherm that represents both the chemisorbed and physically adsorbed oxygen. After the catalyst was evacuated at −78 °C for 1 h at 10^{-6} torr, to remove the physisorbed oxygen, a second isotherm was acquired that represents only the physisorbed oxygen on the catalysts. From the difference of these two linear and parallel isotherms, the chemisorption isotherm is obtained, which is used to determine the amount of chemisorbed oxygen.

Temperature Programmed Reduction

The TPR profiles were obtained using a TPD/TPR 2720 Micromeritics (USA) instrument for analyzing the nature of reducible oxide species present in the sample. The TPR profiles were taken from ambient temperature to 1000 °C (10 °C/min) and then the temperature was kept isothermal for 30 min. A 10% H_2/Ar mixture at a flow rate of 25 cm^3/min was used as the reducing gas. The H_2 consumption corresponding to the reduction of the metal oxide at various stages of reduction was computed from the peak areas calibrated with a standard Ag_2O sample.

Catalytic Activity

The hydrodesulfurization (HDS) of thiophene (Sigma-Aldrich, CAS 110-02-1, >99%) and hydrogenation (HYD) of cyclohexene (Sigma-Aldrich, CAS 110-83-8, >99.5%) were chosen as model reactions for testing the catalytic activities of Mo, Co–Mo, and Ni–Mo supported catalysts. Briefly, about 0.2 g of catalyst sample was secured between two plugs of quartz wool inside a microreactor (Pyrex glass tube, 0.8 cm I.D.). Prior to activity measurements, catalysts were sulfided at 400 °C for 2 h with CS_2 (43.6 mol%)/H_2 (40 cm^3/min). After sulfidation, thiophene HDS or cyclohexene HYD was conducted at 400 °C with about 40 cm^3/min of hydrogen previously saturated in a saturator containing the corresponding reactant feed at room temperature, that is, 10.7 mol % of thiophene or 11.7 mol % of cyclohexene, respectively. The products were analyzed online with a gas chromatograph (Agilent) equipped with a packed column (2 m, s.s., 10% OV-17) and an FID detector. The reaction products of thiophene HDS are butane, 1-butene, 2-butene and its isomer, and small amounts of 1,3,-butadiene, whereas for cyclohexene hydrogenation, cyclohexane is the predominant product along with small amounts of methyl cyclopentene, a skeletal isomerized product, specially on acidic supported catalysts.

The first order rates were calculated using $r = (F/W) \cdot x$ where r is rate in mol/h/g-cat., x is the fractional conversion, W is the catalyst weight in grams, and F is the flow rate of the reactant in mol/h. The reaction rate constants have been calculated assuming a first order reaction. Catalysts of 20–40 mesh particle size

In Novel Materials for Catalysis and Fuels Processing; Bravo-Suárez, J., et al.;
ACS Symposium Series; American Chemical Society: Washington, DC, 2013.

and conversions below 12% were used to operate in the differential regime and to avoid mass diffusion limitations (*32*, *42*, *45*).

Results and Discussion

Characterization of the Support

In order to confirm the formation of the SBA-16 structure and symmetry of the material low as well as wide angle XRD patterns were analyzed.

Low Angle XRD

The XRD pattern of the calcined SBA-16 is given in Figure 1, which shows a sharp peak of the (110) reflection (0.85°) of the cubic *Im3m* structure, confirming that the synthetic procedure yielded the SBA-16 structure. This reflection gave a unit cell parameter a_o of 146.8 Å, by using the equation $a_o = \sqrt{2}d_{110}$, indeed confirming that the measured structure was the *Im3m* (*36*). The pore wall thickness (W) of SBA-16 can be calculated by using a simple equation $W = \sqrt{3}a_o/(2D_P)$, where D_P and a_o are the mesopore diameter and cubic unit cell parameter, respectively.

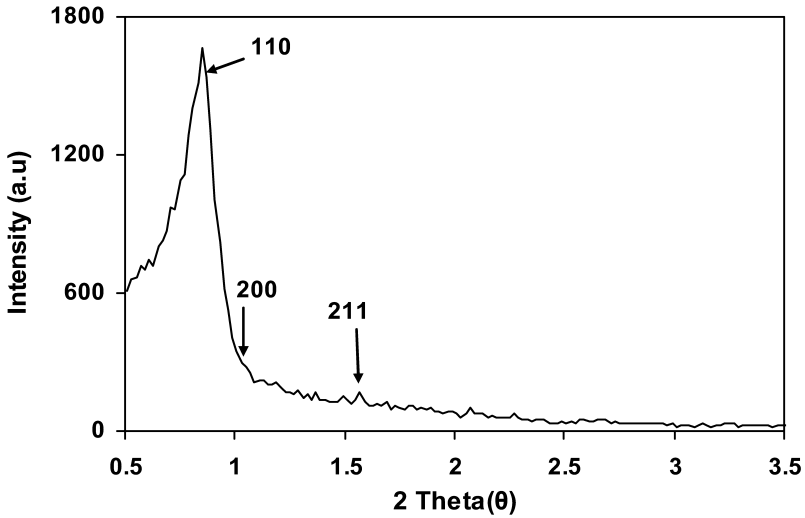

Figure 1. Low angle XRD pattern of SBA-16 material.

The wall thickness of SBA-16 calculated using the a_o (146 Å) value from the X-ray diffractograms is 67.4 Å. This means that the average wall thickness is greater than the pore diameter. It can be seen that the wall of SBA-16 is therefore many times thicker than that of its counterparts (hexagonal MCM-41 and cubic MCM-48), which would suggest a higher stability compared to MCM-41 type materials.

In Novel Materials for Catalysis and Fuels Processing; Bravo-Suárez, J., et al.;
ACS Symposium Series; American Chemical Society: Washington, DC, 2013.

N_2 Adsorption–Desorption Isotherms

N_2 adsorption–desorption isotherms and pore size distribution of SBA-16 are presented in Figure 2. The hysteresis loop characteristic of the ink-bottle pores in the SBA-16 material can be seen in this figure. The pore size distribution for the SBA-16, calculated from the desorption branch of the isotherm using the BJH method, presents a narrow distribution of mesopores, around an average pore diameter of 60 Å.

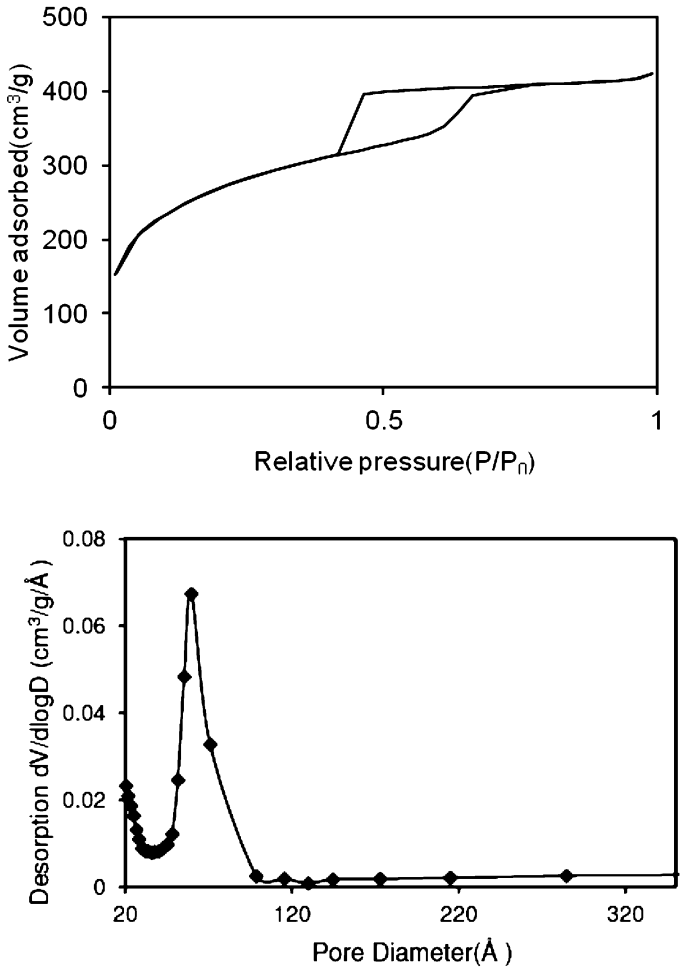

Figure 2. N_2 adsorption–desorption isotherm (top figure) and pore size distribution (bottom figure) of SBA-16.

The total surface area as calculated by the BET method was 950 m^2/g. The SBA-16 material shows a type-IV isotherm with H2 hysteresis loop according to the IUPAC classification. The shape of the N_2 adsorption–desorption isotherm

In Novel Materials for Catalysis and Fuels Processing; Bravo-Suárez, J., et al.;
ACS Symposium Series; American Chemical Society: Washington, DC, 2013.

is characteristic of a well-formed SBA-16 material. The smooth increase in the adsorption branch has been traditionally assigned to the pore size distribution of conventional mesoporous materials and the steep desorption branch has often been ascribed to the pore blocking effect due to the ink-bottle shape of pores.

Transmission Electron Microscopy (TEM)

Figure 3 shows the TEM micrograph of the SBA-16 support with [111] projections of the cubic arrangement in the pore structure. The TEM images confirmed the *Im3m* symmetry with large domains of ordered pores. Well ordered cubic mesopores can be seen from the micrograph when the electron beam is perpendicular to the main axis. The adjacent pores are about 135 Å and the pore diameter is about 60 Å, which correlates well with the pore diameter calculated by the BJH method.

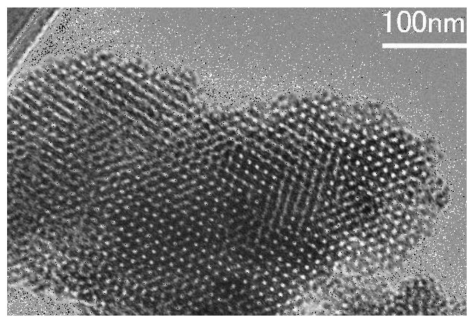

Figure 3. TEM image of the SBA-16 support.

Characterization of Catalysts

With the aim to know more about the structure, pore size, surface area, dispersion, and reducibility of molybdenum supported catalysts and cobalt and Ni promoted catalysts, low and wide angle XRD, N_2 adsorption–desorption, LTOC, and TPR measurements were carried out. The results of these experiments will be discussed next.

Low Angle XRD Pattern

The low angle XRD patterns of 8 wt % Mo/SBA-16 and Co and Ni promoted catalysts are given in Figure 4. For comparison purposes, the XRD pattern of SBA-16 is also given. In all the cases, the position of the (110) reflection was the same as in the parent purely siliceous SBA-16, giving an a_o value of 146.8 Å (Table 1). The existence of this characteristic peak shows that the primary SBA-16 structure remains intact even after the Co and Mo impregnation. However, the intensity of the peak due to the (110) reflection decreases with the increase of Mo concentration possibly due to the strong absorption of X-rays by Mo or partial loss of the highly ordered mesostructure (*76*). The SBA-16 structure does not undergo

In Novel Materials for Catalysis and Fuels Processing; Bravo-Suárez, J., et al.;
ACS Symposium Series; American Chemical Society: Washington, DC, 2013.

any major changes after the deposition of Mo and Co, which is in close agreement with the N_2 adsorption–desorption data.

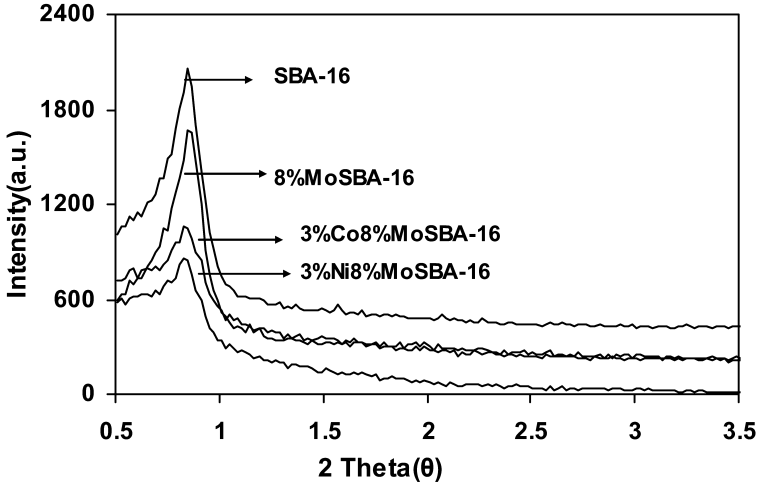

Figure 4. Low angle XRD pattern of the SBA-16 supported catalysts. For simplicity, % is used to indicate wt % of metal.

Wide Angle XRD

Various catalysts containing different amounts of Mo supported on SBA-16 were examined in their oxidic state by X-ray diffraction in the region where MoO_3 peaks appear ($2\theta = 10–40°$). The diffractograms of the catalysts with different Mo loading are shown in Figure 5. It can be noted that all catalysts with Mo in its oxidized state show diffraction patterns, with a single, very broad hump at around 24° characteristic of siliceous materials. The signals due to Mo start appearing at Mo loadings over 8 wt %. It is important to note that there is no indication for the presence of large crystallites of molybdenum oxide for Mo contents up to 8 wt %, suggesting that MoO_3 is well dispersed on the SBA-16, whereas at higher Mo loadings the XRD results indicate the possible presence of crystalline MoO_3. The absence of XRD signals indicates that the particle size of MoO_3 is smaller than ~40 Å up to 8 wt % Mo, whereas beyond this loading the crystallite size is larger. The X-ray results therefore suggest that MoO_3 is well dispersed up to 8 wt % Mo loading and probably present as a monolayer, whereas beyond this loading MoO_3 dispersion is poor. These results are well supported by surface area analysis to be discussed in the following sections.

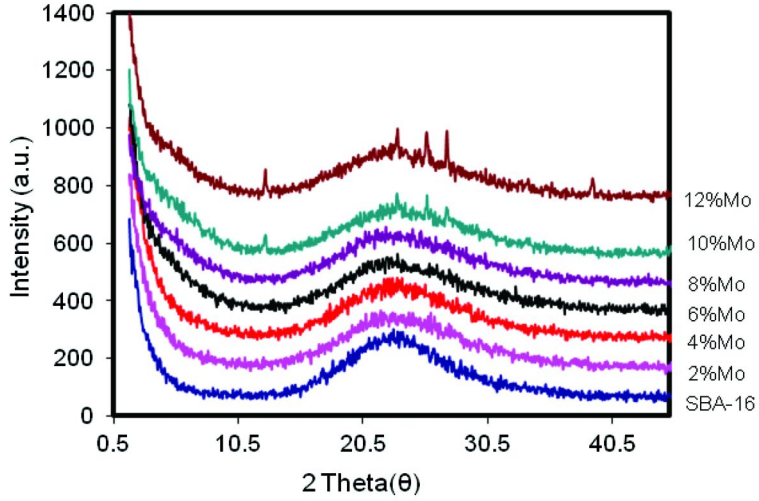

Figure 5. XRD patterns of SBA-16 supported Mo catalysts. For simplicity, % is used to indicate wt % of metal.

The XRD patterns of Co and Ni promoted Mo/SBA-16 catalysts is shown in Figure 6. In the case of Co promoted catalysts the diffraction lines corresponding to the reflection of a segregated orthorhombic $CoMoO_4$ phase appear from 3 wt % onwards at around 26.5° on the background of the amorphous silica support. The intensity of this peak increases as the metal content increases, whereas in the case of the Ni promoted catalysts, the Ni is well dispersed up to 3 wt % and only a low intensity peak due to $NiMoO_4$ and/or NiO appears at higher Ni loadings.

N_2 Adsorption–Desorption Isotherms

N_2 adsorption–desorption experiments give useful information about textural properties like pore shape, size, and distribution. Figure 7 displays N_2 adsorption–desorption isotherms (at 77 K) of SBA-16, 8 wt % Mo/SBA-16 and 12 wt % Mo/SBA-16 samples. The BET surface area, pore volume, and pore size data for SBA-16 and various Mo, Co–Mo, Ni–Mo catalysts are listed in Tables 1 and 2. For all the materials, a Type IV isotherm was observed, with a hysteresis loop typical of SBA-16, indicating that incorporation of Mo species did not change the structure of mesoporous SBA-16. The pore sizes were calculated from the desorption branch of the isotherm using the BJH model, whereas the specific surface areas were calculated with the BET equation.

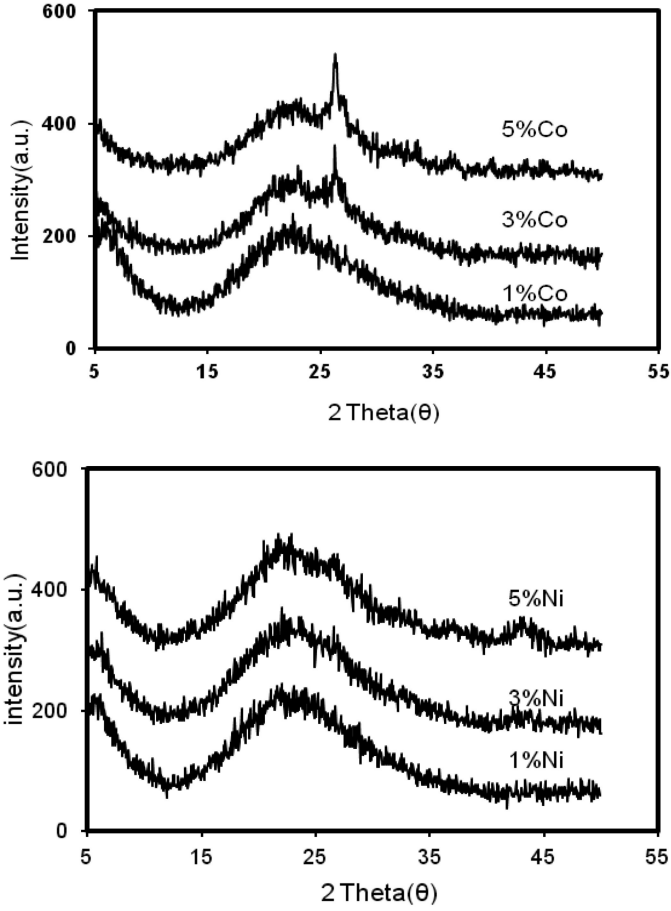

Figure 6. XRD profiles of Co (top figure) and Ni (bottom figure) promoted catalysts supported over 8 wt % Mo/SBA-16. For simplicity, % is used to indicate wt % of metal.

The height of the hysteresis loop is slightly reduced on the 8 wt % Mo catalyst and it is further reduced with increasing Mo contents up to 12 wt % indicating the corresponding decrease in pore volumes (Figure 7). The total pore volume decreases from 0.65 cm^3/g for SBA-16 to 0.35 cm^3/g for 12 wt % Mo/SBA-16. From these isotherms, it can be concluded that the ordered mesoporosity of the support is preserved even after incorporation of MoO_3 onto SBA-16 materials.

The N_2 adsorption–desorption isotherms of Co and Ni promoted catalysts with characteristic SBA-16 hysteresis loops are shown in Figure 8, indicating that Co and Ni promoter addition to the 8 wt % Mo/SBA-16 did not alter the pore structure and size significantly.

In Novel Materials for Catalysis and Fuels Processing; Bravo-Suárez, J., et al.;
ACS Symposium Series; American Chemical Society: Washington, DC, 2013.

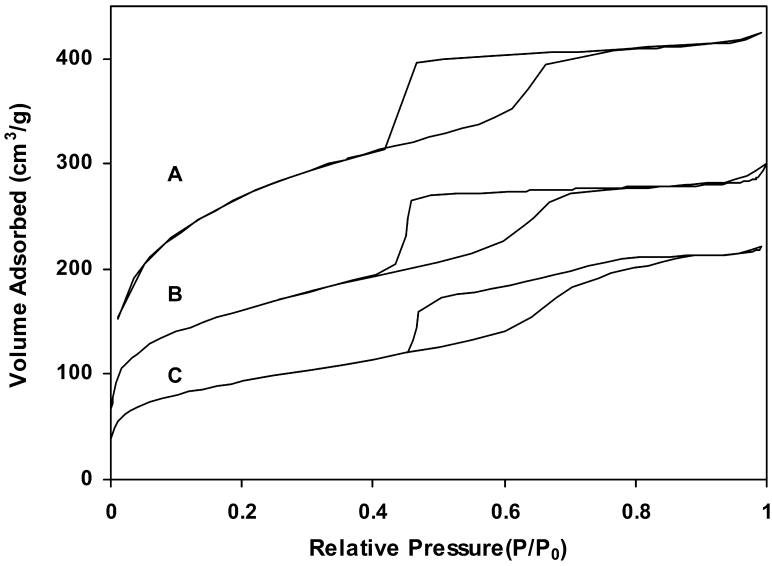

Figure 7. N_2 adsorption–desorption isotherms of SBA-16 supported catalysts (A) SBA-16, (B) 8 wt % Mo/SBA-16, and (C) 12 wt % Mo/SBA-16.

Surface Area Analysis

The SBA-16 mesoporous material and its Mo supported analogues containing 2–12 wt % Mo were examined by BET surface area measurements. The BET surface area of all the catalysts is shown in Table 3. From the surface area per gram of catalysts, the surface area per gram of support was also calculated and the results were plotted in Figure 9 as a function of the Mo loading both for Mo catalysts in oxidic and sulfided states. It can be noted that the surface area per gram of catalyst decreases with Mo loading while the surface area per gram of support remains more or less constant both for oxide precursors and sulfided catalysts. Both these parameters decreased for Mo loadings higher than 8 wt %. Massoth (*76*) suggested that from these observed trends it is possible to extract information about the completion of the monolayer of the supported Mo species. Massoth's surface area analysis in the case of Mo supported on γ-Al_2O_3 catalysts also resulted in constant surface areas per gram of support for Mo loadings up to 8 wt %. The invariance of surface area per gram of support is attributed to the formation of monolayer of Mo species on γ-Al_2O_3. The fact that similar behavior is also noted for Mo/SBA-16 up to 8 wt % Mo suggests that on these catalysts Mo is highly dispersed and probably in the form of a monolayer up to this loading. The XRD results discussed earlier are also in agreement with this observation. Similar observations were also noted on Mo and W supported on other supports (*77*, *78*). The fact that there is no difference of surface area per gram of support up to 8 wt % loading is noted both in the case of the oxide precursors and the sulfided catalysts indicating that the high dispersion of Mo in the oxide state is carried on to the sulfided state.

In Novel Materials for Catalysis and Fuels Processing; Bravo-Suárez, J., et al.;
ACS Symposium Series; American Chemical Society: Washington, DC, 2013.

Table 1. Textural characteristics of SBA-16 supported Mo catalysts

Sample[a]	S_{BET} (m^2/g)	S_{EXT} (m^2/g)	V_T (cm^3/g)	V_{MESO} (cm^3/g)	*Mean Pore Diam. (Å)*	a_o (Å)
SBA-16	950	505	0.65	0.44	59.7	146.8
2%Mo/SBA-16	572	266	0.46	0.26	38.3	143.4
8%Mo/SBA-16	502	232	0.37	0.27	44.4	146.8
12%Mo/SBA-16	377	226	0.35	0.24	38.6	146.8

[a] For simplicity, % is used to indicate wt % of metal.

Table 2. Textural characterization of Co and Ni promoted Mo/SBA-16 catalysts

Sample[a]	S_{BET} (m^2/g)	S_{EXT} (m^2/g)	V_T (cm^3/g)	V_{MESO} (cm^3/g)	*Mean Pore Diam. (Å)*
SBA-16	950	505	0.65	0.44	59.7
8%Mo/SBA-16	502	232	0.37	0.27	44.4
3%Co8%Mo/SBA-16	267	205	0.34	0.26	42.2
3%Ni8%Mo/SBA-16	230	58	0.15	0.10	40.4

[a] For simplicity, % is used to indicate wt % of metal.

Table 3. BET surface area and oxygen chemisorption data of SBA-16 supported molybdenum catalysts

Mo (wt %)	S_{BET} (m^2/g)	O_2 *uptake* ($\mu mol/g$)	*O/Mo ×100*	*EMSA*[a] (m^2/g)	*% surface coverage*[b]	*Crystallite size (Å)*[c]
0	950					
2	582(593)[d]	18	34.6	10.1	1.7	20.6
4	561(584)	39	37.4	22.1	4.1	18.9
6	531(565)	52	33.2	29.4	5.8	21.2
8	471(512)	71	34.0	40.2	8.3	23.4
10	434(482)	53	10.1	30.0	7.4	34.7
12	377(428)	39	6.2	22.1	6.1	56.8

[a] EMSA = O_2 uptake × 0.566616 (this constant value is obtained from pure MoS_2 BET surface area divided by oxygen uptake). [b] Surface coverage =100 × (EMSA/surface area). [c] Crystallite size = 5×10^4/(F x *M*), where F is density of MoS_2 (4.8 g/cm³) and *M* is the EMSA/(g of MoS_2). [d] The value in the parenthesis indicates the BET surface area per gram of support.

In Novel Materials for Catalysis and Fuels Processing; Bravo-Suárez, J., et al.;
ACS Symposium Series; American Chemical Society: Washington, DC, 2013.

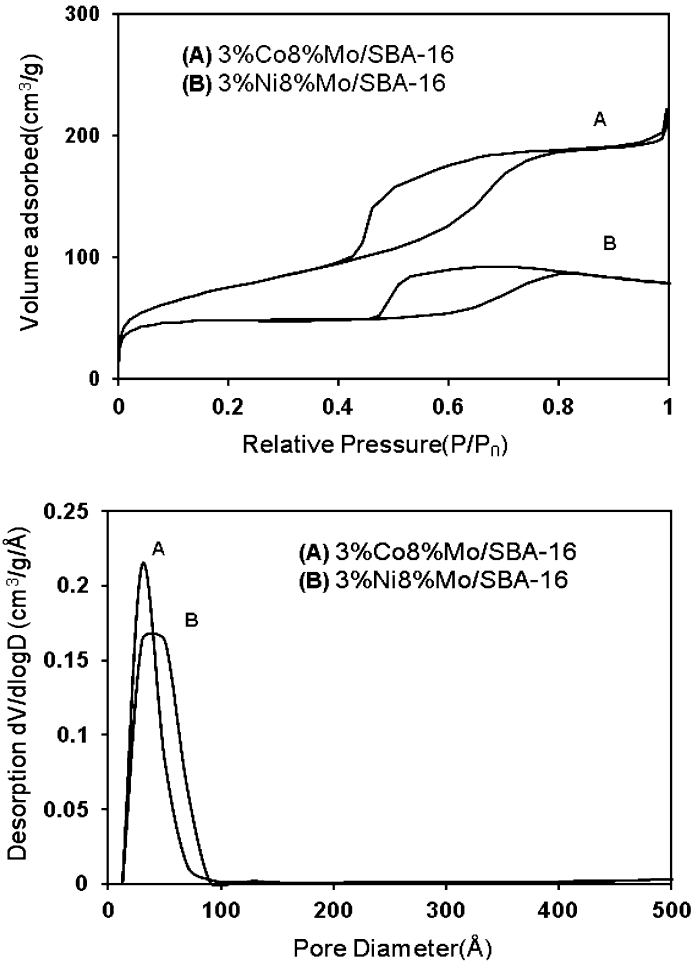

Figure 8. N_2 adsorption–desorption isotherms (top figure) and pore size distributions (bottom figure) of 3 wt % Co and 3 wt % Ni promoted 8 wt % Mo/SBA-16 catalysts. For simplicity, % is used to indicate wt % of metal.

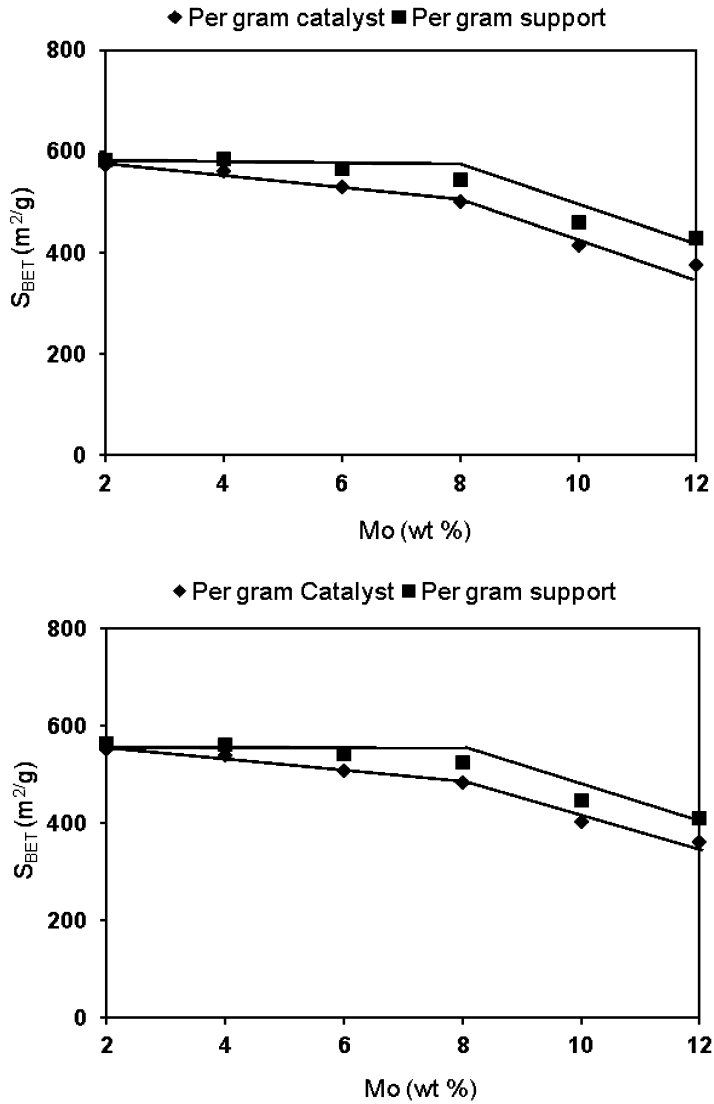

Figure 9. BET surface area analysis of SBA-16 supported Mo catalysts (top figure) before sulfidation (bottom figure) after sulfidation. For simplicity, % is used to indicate wt % of metal.

Temperature Programmed Reduction

The TPR patterns give useful information about the reducibility of various phases that are present in the molybdenum catalysts. The TPR patterns of oxide catalysts obtained as a function of molybdenum loadings of 2–12 wt % are shown in Figure 10. It can be seen that at 2 wt % a large peak is observed in the higher temperature region centered around 875 °C. At 4 wt % Mo a two peak pattern is developed with a peak in the low temperature region at around 502 °C and in the high temperature region around 855 °C. At 6 wt % Mo the two peak pattern is continued with a peak in the low temperature region at around 510 °C and a high temperature peak around 825 °C. The two peak pattern continued up to the highest loading studied. However, the intensity of the high temperature peak decreased considerably as the loading is increased. The low temperature peak intensity is increased with the increase of Mo loading. It can also be seen that a new peak centered at around 680 °C develops from 10 wt % Mo and increases in intensity with increasing Mo loading. It is well known that Mo interacts with the support surface strongly at low loadings, therefore, the high temperature peak can be attributed to this strongly interacted species. It is also known that at low loading Mo is present predominantly as tetrahedral species, which are known to be difficult to reduce (*78*, *79*). Octahedral species and polyhedral Mo species, which are reduced easily are formed at higher loadings. Therefore the peak in the lower temperature region can be considered as due to the reduction of these octahedral and polyhedral species. Further, at loadings above 8 wt % crystalline MoO_3 is also present as can be noted from the wide angle XRD patterns. The peak at around 680 °C may be due to the reduction of these MoO_3 species; the intensity of this peak increases from 8 to 12 wt % Mo loading similar to that observed for the XRD Patterns. Therefore, the peak may be assigned as due to reduction of crystalline MoO_3 at high loading.

Data for hydrogen consumption per gram of catalyst and the corresponding calculated H_2/Mo ratio are useful to get more insights about the extent of reduction of the supported phase and its promoted analogues. The peak positions and quantitative H_2 consumption data are shown in Table 4. It can be seen that hydrogen consumption per gram of catalyst as well as per gram of Mo increase with Mo loading. The H_2/Mo molar ratio is less than the theoretical value of 3, indicating that Mo is not reduced completely at all the loadings, although the reducibility increases with Mo loading.

Since catalytic activities are evaluated at 400 °C, it is reasonable to assume that reducibility represented by low temperature peak is more relevant to the catalytic activities. In order to view the data in this manner, the ratio of the area of the low temperature peak (A) divided by the total area of the reduction profile is plotted as a function of Mo loading in Figure 11. It can be seen that the ratio increases with loadings up to 8 wt % Mo and at higher loadings it remains more or less at the same level, suggesting that the effective reducibility increases up to a Mo loading of 8 wt %. The increase in reduction results in an increase of anion vacancies, which are known to be part of active sites for HDS and HYD.

In Novel Materials for Catalysis and Fuels Processing; Bravo-Suárez, J., et al.;
ACS Symposium Series; American Chemical Society: Washington, DC, 2013.

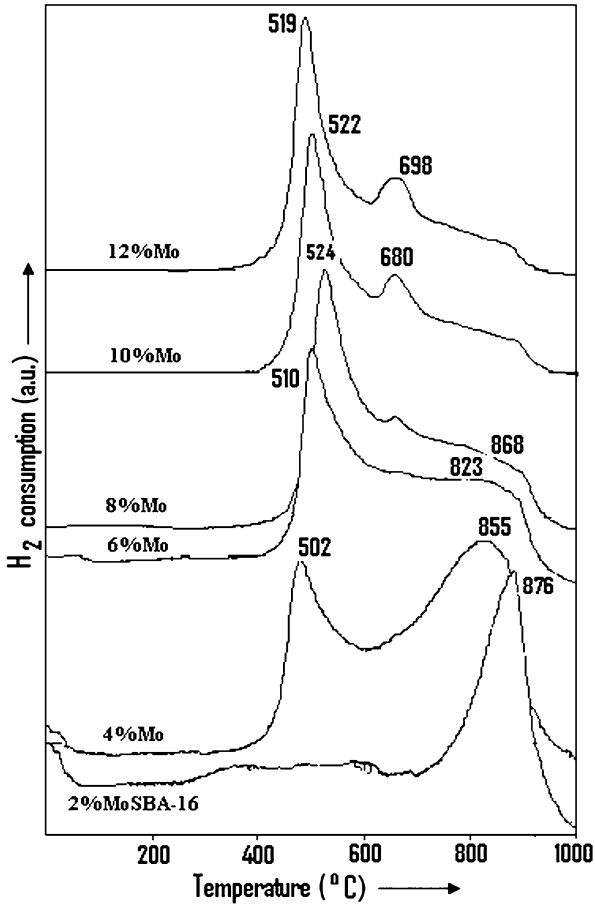

Figure 10. TPR profiles of SBA-16 supported molybdenum catalysts. For simplicity, % is used to indicate wt % of metal.

TPR Patterns of Promoted Catalysts

To understand the role of promoters in altering the reducibility of SBA-16 supported Mo catalysts TPR experiments on Co and Ni promoted catalysts were conducted and the results are shown in Figure 12. The hydrogen consumption data of the reduction profiles and peak positions of the TPR peaks are given in Tables 5 and 6. In all cases, the addition of metal promoters causes the low temperature peak to shift to lower values. However, the shift was more prominent in the case of Ni promoted catalysts (as high as 125 °C). It is clear that the promoter atoms increase the reducibility of Mo phase and Ni appears to be more effective in this respect. In the case of 3 and 5 wt % Co, there is an additional peak around 700 °C, which increases with Co loading. In the XRD patterns a peak attributed $CoMoO_4$ also exhibited similar behavior. Therefore, this peak could be due to the reduction of the $CoMoO_4$ phase. In the TPR patterns of Ni promoted catalysts, the peak

In Novel Materials for Catalysis and Fuels Processing; Bravo-Suárez, J., et al.;
ACS Symposium Series; American Chemical Society: Washington, DC, 2013.

broadens with an increase in Ni content indicating a distribution of reducibility of the metal species. This may be due to differences of interaction between the molybdenum species and the SBA-16 support.

Table 4. TPR data of SBA-16 supported molybdenum catalysts

Mo wt %	*Reduction Temp. (°C)*		*Hydrogen consumption (cm³), STP[a]*		
	T_1max	*T_2max*	*per g catalyst*	*per g Mo*	*H_2/Mo[b]*
0	-	-	-	-	-
2	-	876	-	-	-
4	502	855	3.8	95	0.8
6	510	823	11.1	185	1.6
8	524	-	21.0	262	2.3
10	522	679	34.2	342	2.9
12	518	698	35.4	295	2.5

[a] Corresponding to first peak. [b] Molar ratio.

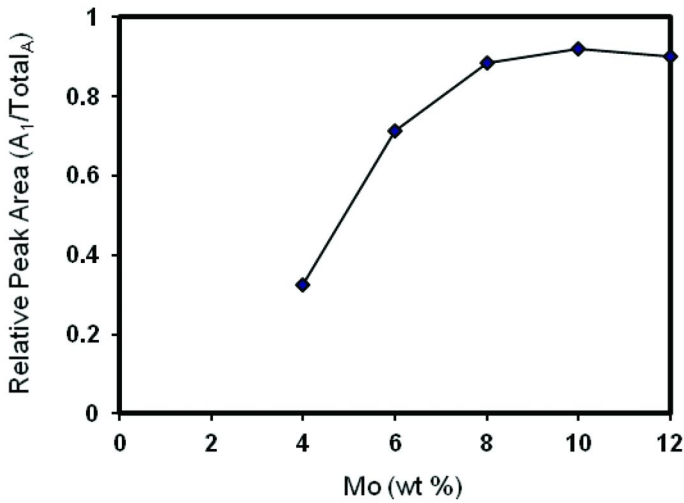

Figure 11. Variation of the fraction of low temperature peak area relative to total TPR profile with Mo loading (A1: area of peak 1 and A: total peak area of reduction profile).

In Novel Materials for Catalysis and Fuels Processing; Bravo-Suárez, J., et al.;
ACS Symposium Series; American Chemical Society: Washington, DC, 2013.

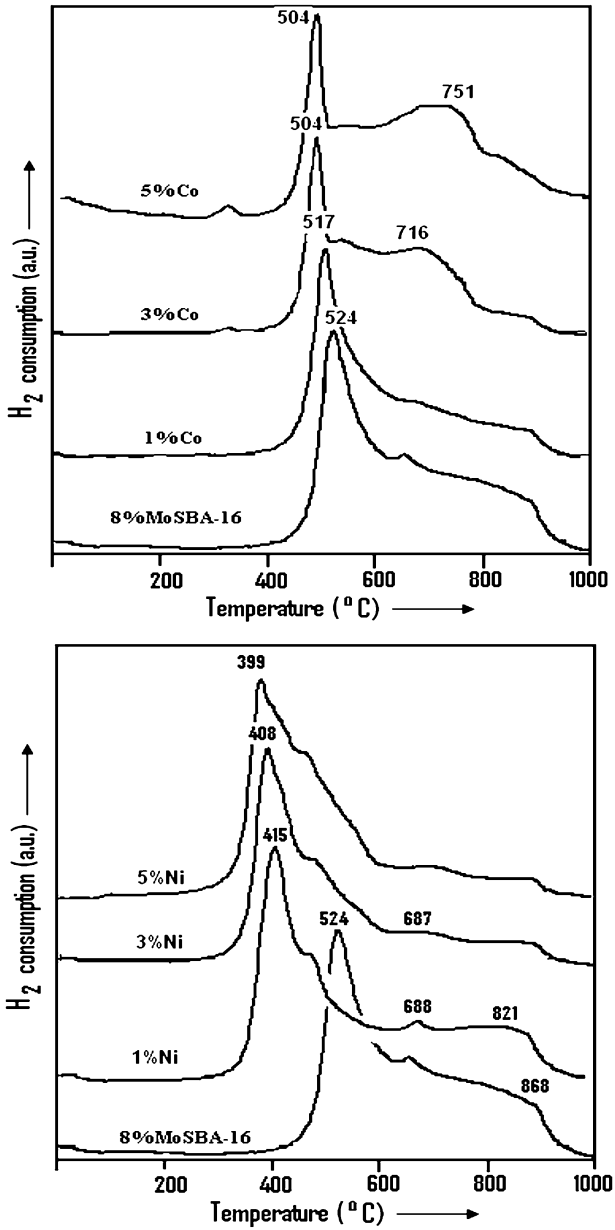

Figure 12. TPR patterns of Co (top figure) and Ni (bottom figure) promoted Mo/SBA-16 supported catalysts. For simplicity, % is used to indicate wt % of metal.

In Novel Materials for Catalysis and Fuels Processing; Bravo-Suárez, J., et al.;
ACS Symposium Series; American Chemical Society: Washington, DC, 2013.

Table 5. TPR data of Co promoted 8 wt % Mo/SBA-16 catalysts

Co(wt %)	*Reduction Temperature(°C)*	*Hydrogen consumption (cm³)*	
		per g catalyst	*H_2/Mo[a]*
0	524, 867	21.0	2.3
1	517	29.6	3.2
3	503, 716	29.1	3.1
5	504, 751	33.5	3.6

[a] Assuming that only MoO_3 is undergoing reduction

Table 6. TPR data of Ni promoted 8 wt % Mo/SBA-16 catalysts

Co(wt %)	*Reduction Temperature(°C)*	*Hydrogen consumption (cm³)*	
		per g catalyst	*H_2/Mo[a]*
0	524, 867	21.0	2.3
1	415, 688, 821	17.4	1.9
3	408, 688, 874	25.7	2.8
5	399, 870	42.6	4.6

[a] Assuming that only MoO_3 is undergoing reduction

The H_2 consumption per gram of catalyst and H_2/Mo ratios for Co and Ni promoted molybdenum catalysts are shown in Tables 5 and 6, respectively. It can be seen that the H_2 consumption increases with Co and Ni promoter content. This result together with an increase in the H_2/Mo ratios suggest that in both cases the promoters significantly increase the reducibility of the catalysts. The fact that H_2/Mo value is more than the theoretical reducibility ratio of *3* indicates that other reducible species are also contributing to the observed total reducibility. The wide angle XRD patterns provided evidence for the presence of $CoMoO_4$ in cobalt promoted catalysts and $NiMoO_4$ in Ni promoted catalysts at metal loadings above 3 wt % Co or Ni. Therefore, additional contribution due to these species and Co or Ni oxide species that may be present at higher loadings may be responsible for the observed higher H_2/Mo ratios.

Low Temperature Oxygen Chemisorptions (LTOC)

LTOC is a useful technique to study the dispersion and concentration of anion vacancies in supported MoS_2 and WS_2 catalysts. LTOC studies were carried out on the sulfided Mo and promoted catalysts. Table 7 presents the results of oxygen chemisorption carried out at low temperature (–78 °C) on various catalysts sulfided at 400 °C. The oxygen uptake variation as a function of molybdenum loading on sulfided catalysts is shown in Figure 13 (right Y axis). It can be seen that the oxygen uptake increases with molybdenum loading up to 8 wt %, after which it

In Novel Materials for Catalysis and Fuels Processing; Bravo-Suárez, J., et al.;
ACS Symposium Series; American Chemical Society: Washington, DC, 2013.

decreases. Oxygen is known to chemisorb on anion vacancies present in sulfided Mo and W systems (*79*). Therefore, such variation suggests that anion vacancies also increase up to 8 wt % Mo and decrease at higher loadings. It was suggested by Zmierczak et al. (*79*) that oxygen uptake represents the general state of dispersion of MoS_2 on supported catalysts. Therefore, the observed variation also indicates that MoS_2 dispersion is passing through maximum at 8 wt % Mo loading.

Table 7. Characterization and HDS and HYD catalytic activity of SBA-16 supported Mo, Co–Mo, Ni–Mo catalysts

Catalyst[a]	*SBET* (m^2/g)	*O_2 Uptake* ($\mu mol/g$)	*Reaction rate* ($mol/h/g\text{-}cat \times 10^{-3}$)		k_{HYD}/k_{HDS}
			HDS	*HYD*	
8%Mo/SBA-16	471	71.2	46.0	52.1	1.13
1%Co8%Mo/SBA-16	283	73.3	51.1	47.6	0.93
3%Co8%Mo/SBA-16	267	77.6	57.7	53.6	0.81
5%Co8%Mo/SBA-16	260	68.0	47.2	44.1	0.94
1%Ni8%Mo/SBA-16	271	65.5	47.8	52.6	1.10
3%Ni8%Mo/SBA-16	230	72.2	53.0	58.0	1.34
5%Ni8%Mo/SBA-16	221	67.2	39.4	57.9	1.46

[a] For simplicity, % is used to indicate wt % of metal.

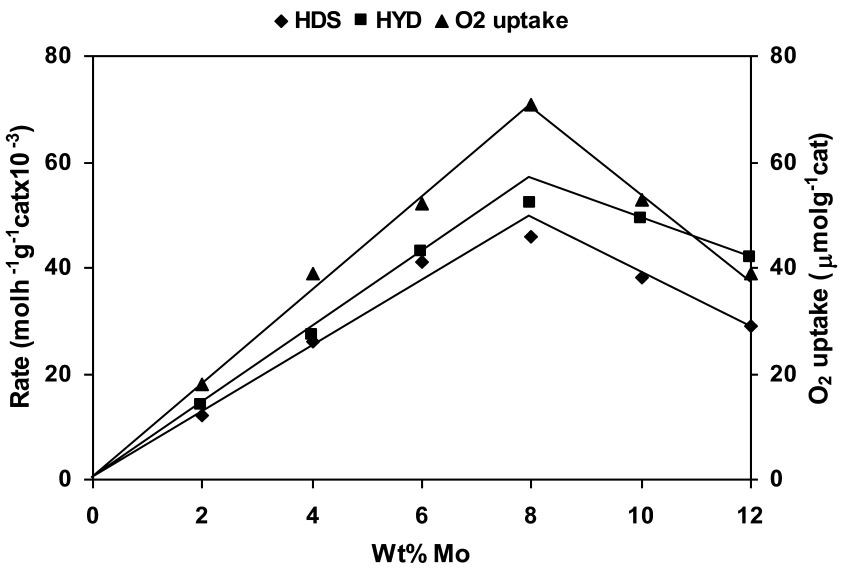

Figure 13. Variation of HDS and HYD catalytic activity and O_2 uptake with molybdenum loading on SBA-16 support.

In Novel Materials for Catalysis and Fuels Processing; Bravo-Suárez, J., et al.;
ACS Symposium Series; American Chemical Society: Washington, DC, 2013.

It is possible to calculate parameters like % dispersion, equivalent molybdenum sulfide area (EMSA), % surface coverage, and crystallite size of MoS_2 from oxygen uptake. The results of such calculations are shown in Table 3. The dispersion is constant up to 8 wt % Mo and then decreases at higher loadings. The equivalent molybdenum sulfide area (EMSA) increases up to 8 wt % Mo and then decreases beyond this loading. The crystallite size is more or less constant at ~21Å up to 8 wt % Mo and then onward increases rapidly at higher loadings. It is important to mention at this point that peaks due to the presence of MoO_3 are noticed in the XRD patterns at 10 and 12 wt % Mo loadings. The surface coverage by MoS_2 is only 8.3%, indicating that molybdenum is selectively attached to certain preferred portions of the SBA-16 support surface.

It is well known that oxide surfaces terminate with hydroxyl groups and some of such hydroxyl groups of suitable strength and energy are involved in the fixing of molybdenum (*80*) onto the support surface. These hydroxyl groups with requisite energy are expected to be distributed randomly as small monolayer patches of Mo moieties. The average crystallite size as calculated from oxygen chemisorption is 21 Å. These crystallite size data is also in agreement with XRD data, indicating that MoS_2 is well dispersed up to a loading of 8 wt % Mo with crystallite sizes lower than ~40 Å.

Hydrotreating Catalytic Functionalities

The thiophene hydrodesulfurization (HDS) and cyclohexene hydrogenation (HYD) are taken as model reactions to represent hydrogenolysis and hydrogenation functionalities, respectively. Catalytic activities for thiophene HDS and cyclohexene HYD were carried out in a fixed bed reactor on a sulfided catalyst, at 400 °C temperature, and atmospheric pressure.

The catalyst was sulfided prior to the reaction at 400 °C for 2 h in a flow of a CS_2/H_2 mixture in the same reactor. The HDS and HYD catalytic activities and corresponding rate parameters are presented in Figure 13 and Table 8, respectively. It can be seen that both reaction rates (HDS and HYD) increase with Mo loading up to 8 wt % Mo and then start decreasing at higher loadings. The O_2 uptakes plotted in the same figure varies in a manner similar to that of the catalytic activities. It is well known that oxygen uptakes are related to the anion vacancies. It is also known that the active sites of hydrotreating catalysts consist of anion vacancies. Therefore, it is not a surprise that there appears to be a strong correlation between these parameters.

Effect of the Promoters on Catalytic Functionalities

The promotional effects of Co(Ni) for HDS of thiophene and HYD of cyclohexene on 8 wt % Mo catalysts supported on SBA-16 are shown in Table 7 and Figure 14. It can be seen that the addition of Co or Ni promoters to 8 wt % Mo/SBA-16 increases both HDS and HYD catalytic activities. The activities increase up to 3 wt % Co or Ni and then decrease with increasing of both promoter loadings. It is interesting to note that oxygen uptakes on both promoted catalysts also vary in a similar manner, since oxygen uptakes are related

In Novel Materials for Catalysis and Fuels Processing; Bravo-Suárez, J., et al.;
ACS Symposium Series; American Chemical Society: Washington, DC, 2013.

to dispersion of the Mo phase and anion vacancies. Topsøe and co-workers based on STM studies and density functional theory calculations proposed that the promoter atoms preferentially substitute at sulfur edges of Mo nanoclusters (*81*). Therefore, it appears that an increase of anion vacancies results from an increase in edge dispersion and the accommodation of more promoter atoms at the edges is responsible for an increase in HDS and HYD activities.

The HYD/HDS rate constant ratios are useful to understand the suitability of the catalysts for applications where the hydrogenation function and hydrogenolysis ability are important such as in ultra-deep desulfurization of diesel, hydrodenitrogenation, etc. The HYD/HDS rate constant ratios, in the case of promoted catalysts, are shown in Table 7. The HYD/HDS rate constant ratio is 1.13 for the unpromoted catalyst. This value decreases with cobalt addition at all the three loadings studied. However, 5 wt % Co shows a slight increase compared to 3 wt % cobalt catalyst. This observation suggests that cobalt catalysts preferentially promote the HDS functionality. In the case of Ni promoted catalysts, the rate constant ratios increase with increasing Ni loading, indicating that Ni promoted catalysts are more selective for hydrogenation compared to unpromoted or Co promoted Mo/SBA-16 supported catalysts. The results are in agreement with the well-known fact that on Al_2O_3 supported catalysts, Co is a better promoter for hydrodesulfurization and Ni is a better promoter for hydrogenation (*80*).

Table 8. HDS and HYD reaction rates and selectivity of SBA-16 supported molybdenum catalysts

Mo (wt %)	*Reaction rate (mol/h/g-cat ×10^{-3})*		k_{HYD}/K_{HDS}
	HDS	*HYD*	
2	12	14	1.16
4	26	27	1.04
6	41	43	1.05
8	46	52	1.13
10	38	49	1.28
12	29	42	1.44

In Novel Materials for Catalysis and Fuels Processing; Bravo-Suárez, J., et al.;
ACS Symposium Series; American Chemical Society: Washington, DC, 2013.

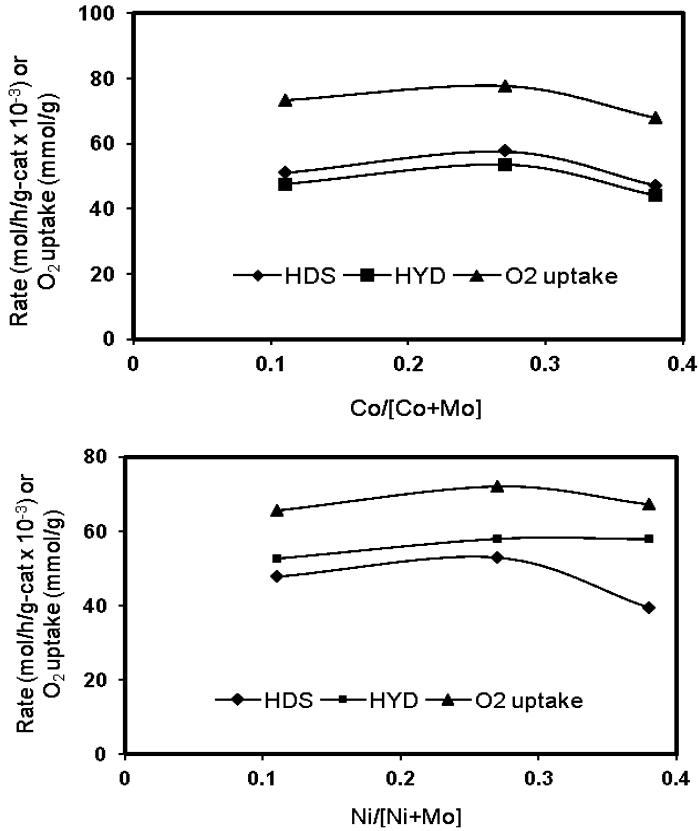

Figure 14. Effect of Co (top figure) and Ni (bottom figure) promoters on HDS and HYD catalytic functionalities of SBA-16 supported molybdenum catalysts.

Comparison of Mo Catalysts Supported on SBA-16, SBA-15, and γ-Al_2O_3

In order to assess the efficacy of the SBA-16 supported systems for the hydrotreating functionalities, it is necessary to compare them with standard γ-Al_2O_3 supported catalysts of similar composition. Towards this end, we have evaluated the catalytic activities of γ-Al_2O_3 supported Mo catalysts with 3 wt % Co (or Ni) and 8 wt % Mo compositions under the same reaction conditions. A comparison of γ-Al_2O_3 supported catalysts with SBA-16 supported catalysts is shown in Table 9. It can be seen from the data presented that SBA-16 supported catalysts are 2 to 2.5 times more active than γ-Al_2O_3 supported catalysts for both HDS and HYD functionalities.

Table 9. Characterization and HDS and HYD catalytic activity of Mo, Co–Mo and Ni–Mo supported on SBA-16, SBA-15, and γ-Al_2O_3 catalysts

Catalyst[a]	S_{BET} (m^2/g)	O_2 uptake (μmol/g)	*Rate (mol/h/g-cat × 10-3)*	
			HDS	*HYD*
8% Mo/SBA-16	471	71.2	46.1	52.3
3%Co8%Mo/SBA-16	267	77.6	57.7	53.6
3%Ni8%Mo/SBA-16	230	72.2	43.0	58.0
8% Mo/SBA-15	322	62.2	24.0	25.7
3%Co8%Mo/SBA-15	222	68.4	49.1	41.2
3%Ni8%Mo/SBA-15	212	72.6	39.6	32.5
8%Mo/γ-Al_2O_3	204	22.1	11.2	25.4
3%Co8%Mo/γ-Al_2O_3	138	31.8	26.8	24.7
3%Ni8%Mo/γ-Al_2O_3	141	29.0	19.1	29.1

[a] For simplicity, % is used to indicate wt % of metal.

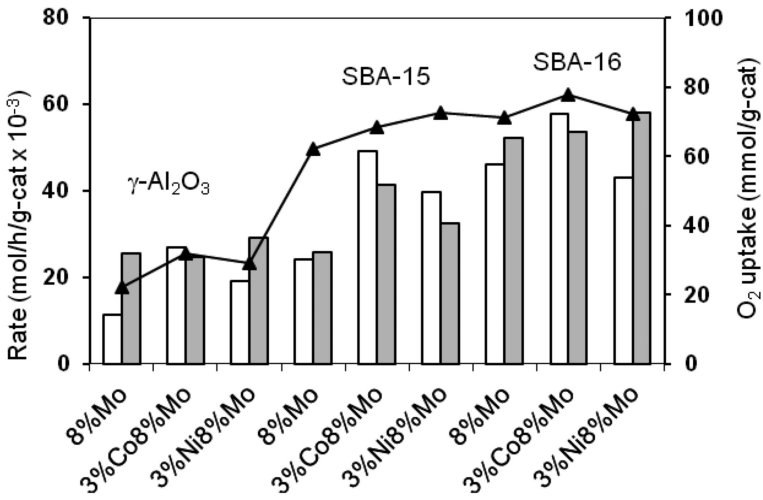

Figure 15. Correlation between the HDS (grey bar), HYD activities (empty bar), and O_2 uptake (triangle) of Mo, Co–Mo and Ni–Mo supported catalysts. For simplicity, % is used to indicate wt % of metal.

In Novel Materials for Catalysis and Fuels Processing; Bravo-Suárez, J., et al.;
ACS Symposium Series; American Chemical Society: Washington, DC, 2013.

In the mesoporous material family of catalysts, there are members with two dimensional pore structures such as SBA-15, MCM-41, and HMS and three dimensional structures such as KIT-6, MCM-48, and SBA-16. Among these materials, SBA-15 and SBA-16 are synthesized by similar procedures and are similar in all respects except the pore structure with interconnected spherical cavities. Literature reports suggest that such structural differences may lead to improvement in catalytic activities and long life of the catalysts (*13*). In order to probe these inferences, SBA-15 catalysts with the same Co–Mo composition as SBA-16 supported catalysts were also prepared and tested under similar reaction conditions. The results of such measurements are also presented in Figure 15 and Table 9. It can be noticed that SBA-16 supported catalysts are 1 to 1.5 times more active than their SBA-15 counterparts. These results suggest that SBA-16 supported catalysts display higher activities for the HDS and HYD functionalities compared to γ-Al_2O_3 and SBA-15 supported catalysts. The oxygen uptakes are also plotted in Figure 15. This data suggested that the observed increases in activities are due to an increase in dispersion of MoS_2 and consequent increase in the anion vacancies in these catalysts. Therefore, the SBA-16 support helps to better disperse molybdenum in comparison to γ-Al_2O_3 or SBA-15, which results in a superior performance.

Conclusions and Summary

In this investigation, SBA-16 mesoporous silica with characteristic spherical cavity pore structure was synthesized and used to prepare Mo, Co–Mo, and Ni–Mo catalysts. The Mo concentration was varied between 2 and 12 wt % Mo, whereas the promoter concentration was varied between 1 and 3 wt %. Both, supports and catalysts were characterized by low angle XRD, wide angle XRD, pore size distribution (PSD), surface area analysis, temperature programmed reduction (TPR), and oxygen chemisorption. The low angle XRD of the support and catalysts indicated that the SBA-16 structure obtained during synthesis is retained even after Mo and promoter addition. The BJH pore size distribution and hysteresis loops of the supports and catalysts suggested that the mesopore structure with spherical cavities is retained even after Mo and promoter addition. The wide angle XRD results indicated that Mo is highly dispersed up to 8 wt % Mo with crystallite sizes smaller than ~40 Å, beyond this loading bigger crystallite are obtained. The wide angle XRD results of promoted catalysts gave evidence for the presence of $CoMoO_4$ and $NiMoO_4$ in the promoted catalysts at the 5 wt % loading. The surface area analysis in both oxidic as well as sulfided states suggested the presence of a monolayer-like dispersion up to 8 wt % Mo, both in the oxide as well as sulfided catalysts. Oxygen chemisorption at −78 °C increased with Mo loading up to 8 wt % Mo and decreased beyond this loading. The crystallite size calculated from oxygen uptakes is small (~20 Å) and remained more or less the same up to 8 wt % Mo and increased at higher loading. These results suggested that MoS_2 is well dispersed on all these catalysts up to 8 wt % Mo loading, indicating that high dispersion in the oxide state (as suggested by XRD) is carried into the sulfided state. The low Mo surface coverage derived

In Novel Materials for Catalysis and Fuels Processing; Bravo-Suárez, J., et al.;
ACS Symposium Series; American Chemical Society: Washington, DC, 2013.

from oxygen uptakes indicated that MoS_2 is attached to selected portions of the SBA-16 support surface as monolayer patches with an average size around ~20 Å.

The TPR profiles displayed a two peak pattern with a low temperature peak and a high temperature peak. The relative area of the low temperature peak varied in a similar manner to oxygen uptakes up to 8 wt % Mo loading. In this range, the reduction process creates anion vacancies and these anion vacancies are the sites where oxygen chemisorbs and hence the similarity. The quantitative TPR measurements indicated that Mo is not completely reduced at all the Mo loadings studied. The TPR measurements on promoted catalysts suggested that the promoter increases the reducibility of molybdenum oxide.

The catalytic activities for both the functionalities HDS and HYD increases with Mo loading up to 8 wt %, similar to that of oxygen chemisorption and TPR relative peak area. Since oxygen chemisorption correlates well with HDS as well as HYD functionalities, it is clear that oxygen chemisorption is not specific to any one of the functionalities but rather measures a general state of dispersion of MoS_2. In the promoted catalysts, the catalytic activities increases with Co or Ni loading with a maximum at 3 wt % of promoter loading.

It is well known that oxide surfaces terminate with hydroxyl groups and also that the molybdenum is fixed on the support through these hydroxyl groups on γ-Al_2O_3. Along the same lines, hydroxyl groups of suitable energy in SBA-16 can fix Mo in an oxidic state in the form of monolayer patches. These hydroxyl groups of suitable energy are expected to be distributed randomly, therefore, Mo monolayer patches are also distributed in a similar way on the surface. It appears that the MoO_3 monolayer is converted to MoS_2 monolayer patches with an average size of ~20 Å because of the high observed metal dispersions. These patches formed in the reductive sulfiding atmosphere possess anion vacancies that are measured by oxygen uptake. Since these anion vacancies are also involved in the active site structure, a correlation between oxygen uptakes and catalytic activities is obtained. The monolayer like MoS_2 dispersion exists up to 8 wt % Mo, bigger crystallite formation takes place in the post monolayer region, reducing the number of anion vacancies reflected in lower oxygen uptakes. In the promoted catalysts the promoter ions substitute Mo on the molybdenum edges. This edge is more likely to be the sulfur edge as proposed by the Topsøe group studies.

We carried out comparisons between SBA-16 and SBA-15 supported HDS and HYD catalysts because they are both prepared by similar procedures but only differ in pore structure. Such comparison, discussed earlier, showed that Co and Ni promoted SBA-16 molybdenum supported catalysts are 1 to 1.5 times more active than the SBA-15 supported analogues. Since the only apparent difference is the spherical cavity pore structure of the support, it is tempting to attribute the improvement in activities in the SBA-16 catalyst to this pore structure; however, more detailed studies are needed to confirm this observation.

References

1. Kresge, C. T.; Leonowicz, M. E.; Roth, W. J.; Vartuli, J. C.; Beck, J. S. *Nature* **1992**, *359*, 710–712.

2. Beck, J. S.; Vartuli, J. C.; Roth, W. J.; Leonowicz, M. E.; Kresge, C. T.; Schmitt, T.; Chu, C. T. W.; Olson, D. H.; Sheppard, E. W. *J. Am. Chem. Soc.* **1992**, *114*, 10834–10843.
3. Inagaki, S.; Fukushima, Y.; Kuroda, K. *Chem. Commun.* **1993**, 680–682.
4. Bagshaw, S. A.; Prouzet, E.; Pinnavaia, T. J. *Science* **1995**, *269*, 1242–1244.
5. Ryoo, R.; Kim, J. M.; Ko, C. H.; Shin, C. H. *J. Phys. Chem.* **1996**, *100*, 17718–17721.
6. Zhao, D.; Feng, J.; Huo, Q.; Melosh, N.; Fredrickson, G. H.; Chmelka, B.; Stucky, G. D. *Science* **1998**, *279*, 548–552.
7. Zhao, D.; Huo, Q.; Feng, J.; Chmelka, B.; Stucky, G. D. *J. Am. Chem. Soc.* **1998**, *120*, 6024–6036.
8. Voort, P. V. D.; Benjelloun, M.; Vansant, E. F. *J. Phys. Chem. B* **2002**, *106*, 9027–9032.
9. Margolese, D.; Melero, J. A.; Christiansen, S. C.; Chmelka, B. F.; Stucky, G. D. *Chem. Mater.* **2000**, *12*, 2448–2459.
10. Christiansen, S. C.; Zhao, D.; Janicke, M. T.; Landry, C. C.; Stucky, G. D.; Chmelka, B. F. *J. Am. Chem. Soc.* **2001**, *123*, 4519–4529.
11. Sakamoto, Y.; Kaneda, M.; Terasaki, O.; Zhao, D. Y.; Kim, J. M.; Stucky, G. D.; Shin, H. J.; Ryoo, R. *Nature* **2000**, *408*, 449–453.
12. Kim, T. W.; Ryoo, R.; Kruk, M.; Gierszal, K. P.; Jaroniec, M.; Kamiya, S.; Terasaki, O. *J. Phys. Chem. B* **2004**, *108*, 11480–11489.
13. Liyu, L.; King, D. L.; Liu, J.; Huo, Q.; Zhu, K.; Wang, C.; Gerber, M.; Stevens, D.; Wang, Y. *Chem. Mater.* **2009**, *21*, 5358–5364.
14. Kruk, M.; Hui, C. M. *J. Am. Chem. Soc.* **2008**, *130*, 1528–1529.
15. Ryoo, R.; Ko, C. H. *J. Phys. Chem. B* **2000**, *104*, 11465–11471.
16. Imperor-Clerc, M.; Davidson, A.; Davidson, P. *J. Am. Chem. Soc.* **2000**, *122*, 11925–11933.
17. Luan, Z.; Maes, E. M.; van der Heide, P. A. W.; Zhao, D.; Czernuszewicz, R. S.; Keven, L. *Chem. Mater.* **1999**, *11*, 3680–3686.
18. Yue, Y.; Gedeon, A.; Bonardet, J. L.; Espinose, J. B. D.; Fraissard, J.; Melosh, N. *Chem. Commun.* **1999**, 1967–1968.
19. Liu, A. M.; Hidajat, K.; Kawi, S.; Zhao, D. *Chem. Commun.* **2000**, 1145–1146.
20. Marcowitz, M. A.; Klaehn, J.; Hendel, R. A.; Qadriq, S. L.; Golledge, D. G.; Castner, D. G.; Gaber, B. P. *J. Phys. Chem. B* **2000**, *104*, 10820–10826.
21. Yiu, H. H. P.; Botting, C. H.; Botting, N. P.; Wright, P. A. *Phys. Chem. Chem. Phys.* **2001**, *3*, 1144–1152.
22. Sietsma, J. R. A.; Meeldijk, J. D.; Versluijs-Helder, M.; Broersma, A.; van Dillen, A. J.; de Jongh, P. E.; de Jong, K. P. *Chem. Mater.* **2008**, *20*, 2921–2931.
23. Sietsma, J. R. A.; Friedrich, H.; Broersma, A.; Versluijs-Helder, M.; van Dillen, A. J.; de Jongh, P. E.; de Jong, K. P. *J. Catal.* **2008**, *260*, 227–235.
24. Yang, C. M.; Kalwei, M.; Schuth, F.; Chao, K. J. *Appl. Catal., A* **2003**, *254*, 289–296.
25. Sakamoto, Y.; Kaneda, M.; Terasaki, O.; Zhao, D. Y.; Kim, J. M.; Stucky, G. D.; Shin, H. Y.; Ryoo, R. *Nature* **2000**, *408*, 449–453.
26. Ravikovitch, P. I.; Neimark, A. V. *Langmuir* **2002**, *18*, 911–916.

27. Trong On, D.; Desplantier-Giscard, D.; Danumah, C.; Kaliaguine, S. *Appl. Catal., A* **2003**, *253*, 545–602.
28. Murali Dhar, G.; Srinivas, B. N.; Rana, M. S.; Kumar, M.; Maity, S. K. *Catal. Today* **2003**, *86*, 45–60.
29. Kunisada, N.; Choi, K.; Korai, Y.; Mochida, I.; Nakano, K. *Appl. Catal., A* **2004**, *269*, 43–51.
30. Ding, L.; Zheng, Y.; Zhang, Z.; Ring, Z.; Chen, J. *J. Catal.* **2006**, *241*, 435–445.
31. Yermakov, Y. I.; Startsev, A. N.; Burmistrov, V. A. *Appl. Catal.* **1984**, *11*, 1–13.
32. Shimada, H.; Sato, T.; Yoshimura, Y.; Hiraishi, J.; Nishijima, A. *J. Catal.* **1988**, *110*, 275–284.
33. Maity, S. K.; Rana, M. S.; Srinivas, B. N.; Murali Dhar, G.; Bej, S. K.; Prasada Rao, T. S. R. *J. Mol. Catal. A: Chem.* **2000**, *153*, 121–127.
34. Maity, S. K.; Rana, M. S.; Bej, S. K.; Ancheyta-Juarez, J.; Murali Dhar, G.; Prasada Rao, T. S. R. *Appl. Catal., A* . **2001**, *205*, 215–225.
35. Zdrazil, M. *Catal. Today* **2003**, *86*, 151–171.
36. Shimada, H. *Catal. Today* **2003**, *86*, 17–29.
37. Prins, R.; De Beer, V. H. J.; Somorjai, G. A. *Catal. Rev. Sci. Eng.* **1989**, *31*, 1–41.
38. Lee, J. J.; Han, S.; Kim, H.; Koh, J. H.; Hyeon, T.; Moon, S. H. *Catal. Today* **2003**, *86*, 141–149.
39. Massoth, F. E.; Murali Dhar, G.; Shabtai, J. *J. Catal.* **1984**, *85*, 53–62.
40. Daly, F. P.; Ando, H.; Schmitt, J. L.; Sturm, E. A. *J. Catal.* **1987**, *108*, 401–408.
41. Zhaobin, W.; Qin, X.; Xiexian, G.; Sham, E. L.; Grange, P.; Delmon, B. *Appl. Catal.* **1990**, *63*, 305–317.
42. Zhaobin, W.; Qin, X.; Xiexian, G.; Sham, E. L.; Grange, P.; Delmon, B. *Appl. Catal.* **1991**, *75*, 179–191.
43. Pophal, C.; Kameda, F.; Hoshino, K.; Yoshinaka, S.; Segawa, K. *Catal. Today* **1997**, *39*, 21–32.
44. Rana, M. S.; Srinivas, B. N.; Maity, S. K.; Murali Dhar, G.; Prasada Rao, T. S. R. *J. Catal.* **2000**, *195*, 31–37.
45. Halachev, T.; Nava, R.; Dimitrov, L. *Appl. Catal., A* **1998**, *169*, 111–117.
46. Chiranjeevi, T.; Kumar, P.; Maity, S. K.; Rana, M. S.; Murali Dhar, G.; Prasad Rao, T. S. R. *Microporous Mesoporous Mater.* **2001**, *44*, 547–556.
47. Chiranjeevi, T.; Kumar, P.; Rana, M. S.; Murali Dhar, G.; Prasad Rao, T. S. R. *J. Mol. Catal. A: Chem.* **2002**, *181*, 109–117.
48. Wang, A.; Wang, Y.; Kabe, T.; Chen, Y.; Ishihara, A.; Qian, W. *J. Catal.* **2001**, *199*, 19–29.
49. Turaga, U. T.; Song, C. *Catal. Today* **2003**, *86*, 129–140.
50. Silva-Rodrigo, R.; Calderon-Salas, C.; Melo-Banda, J. A.; Dominguez, J. M.; Vazquez-Rodrıguez, A. *Catal. Today* **2004**, *98*, 123–129.
51. Herrera, J. M.; Reyes, J.; Roquero, P.; Klimova, T. *Micropororous Mesoporous Mater.* **2005**, *83*, 283–291.
52. Souza, M. J. B.; Marinkovic, B. A.; Jardim, P. M.; Araujo, A. S.; Pedrosa, A. M. G.; Souza, R. R. *Appl. Catal., A* **2007**, *316*, 212–218.

53. Murali Dhar, G.; Muthu Kumaran, G.; Kumar, M.; Rawat, K. S.; Sharma, L. D.; Raju, B. D.; Rama Rao, K. S. *Catal. Today* **2005**, *99*, 309–314.
54. Vradman, L.; Landau, M. V.; Herskowitz, M.; Ezersky, V.; Talianker, M.; Nikitenko, S.; Koltypin, Y.; Gedanken, A. *J. Catal.* **2003**, *213*, 163–175.
55. Sampieri, A.; Pronier, S.; Blanchard, J.; Breysse, M.; Brunet, S.; Fajerwerg, K.; Louis, C.; Perot, G. *Catal. Today* **2005**, *107*, 537–544.
56. Muthu Kumaran, G.; Garg, S.; Soni, K.; Kumar, M.; Sharma, L. D.; Murali Dhar, G.; Rama Rao, K. S. *Appl. Catal., A* **2006**, *305*, 123–129.
57. Gutierrez, O. Y.; Fuentes, G. A.; Salcedo, C.; Klimova, T. *Catal. Today* **2006**, *116*, 485–497.
58. Soni, K.; Rana, B. S.; Sinha, A. K.; Bhaumik, A.; Nandi, M.; Kumar, M.; Dhar, G. M. *Appl. Catal., B* **2009**, *90*, 55–63.
59. Garg, S.; Soni, K.; Kumar, M.; Bhaskar, T.; Gupta, J. K.; Rama Rao, K. S.; Murali Dhar, G. *Catal. Today* **2012**, *198*, 263–269.
60. Song, C.; Reddy, K. M. *Prepr. Am. Chem. Soc., Div. Pet. Chem.* **1996**, *41*, 567–570.
61. Li, Z.; Gao, L.; Zheng, S. *Appl. Catal., A* **2002**, *236*, 163–171.
62. Kooyman, P. J.; Waller, P.; van Langeveld, A. D.; Song, C.; Reddy, K. M.; van Veen, J. A. R. *Catal. Lett.* **2003**, *90*, 131–135.
63. Reddy, K. M.; Wei, B.; Song, C. *Catal. Today* **1998**, *43*, 261–272.
64. Muthu Kumaran, G; Garg, S.; Soni, K.; Kumar, M.; Gupta, J. K.; Sharma, L. D.; Murali Dhar, G. *Microporous Mesoporous Mater.* **2008**, *114*, 103–109.
65. Garg, S.; Soni, K.; Muthu Kumaran, G.; Kumar, M.; Gupta, J. K.; Sharma, L. D.; Murali Dhar, G. *Catal. Today* **2008**, *130*, 302–308.
66. Garg, S.; Bhaskar, T.; Soni, K.; Muthu Kumaran, G.; Muto, A.; Sakata, Y.; Murali Dhar, G. *Chem. Commun.* **2008**, 5310–5311.
67. Huirache-Acuña, R.; Pawelec, B.; Loricera, C. V.; Rivera-Muñoz, E. M.; Nava, R.; Torres, B.; Fierro, J. L. G. *Appl. Catal., B* **2012**, *125*, 473–485.
68. Huirache-Acuña, R.; Pawelec, B.; Rivera-Muñoz, E.; Nava, R.; Espino, J.; Fierro, J. L. G. *Appl. Catal., B* **2009**, *92*, 168–184.
69. Loricera, C. V.; Pawelec, B.; Infantes-Molina, A.; Álvarez-Galván, M. C.; Huirache-Acuña, R.; Nava, R.; Fierro, J. L. G. *Catal. Today* **2011**, *172*, 103–110.
70. Nava, R.; Pawlec, B.; Castano, P.; Alvarex-Galvan, M. C.; Loricera, C. V.; Fierro, J. L. G. *Appl. Catal., B* **2009**, *92*, 154–167.
71. Guzmán, M. A.; Huirache-Acuña, R.; Loricera, C. V.; Hernández, J. R.; Díaz de León, J. N.; de los Reyes, J. A.; Pawelec, B. *Fuel* **2013**, *103*, 321–333.
72. Amezcua, J. C.; Lizama, L.; Salcedo, C.; Puente, I.; Domínguez, J. M.; Klimova, T. *Catal. Today* **2005**, *107-108*, 578–588.
73. Klimova, T.; Lizama, L.; Amezcua, J. C.; Roquero, P.; Terrés, E.; Navarrete, J.; Domínguez, J. M. *Catal. Today* **2004**, *98*, 141–150.
74. Aguillón-Martínez, E. C.; Melo-Banda, J. A.; Guevara, L. A.; Reyes, T. A.; Ramos Galván, C. E.; Silva, R. R.; Domínquez, J. M. *Adv. Mater. Res.* **2010**, *132*, 111–125.
75. Grudzien, R. M.; Graicka, B. E.; Jaroniec, M. *J. Mater. Chem.* **2006**, *16*, 819–823.
76. Massoth, F. E. *J. Catal.* **1977**, *50*, 190–195.

In Novel Materials for Catalysis and Fuels Processing; Bravo-Suárez, J., et al.;
ACS Symposium Series; American Chemical Society: Washington, DC, 2013.

77. Chiranjeevi, T.; Kumar, P.; Rana, M. S.; Murali Dhar, G.; Prasada Rao, T. S. R. *J. Mol. Catal. A: Chem.* **2002**, *181*, 109–117.
78. Saiprasad Rao, K.; Murali Dhar, G. *J. Catal.* **1989**, *115*, 277–281.
79. Zmierczak, W.; Muralidhar, G.; Massoth, F. E. *J. Catal.* **1982**, *77*, 432–438.
80. Murali Dhar, G.; Massoth, F. E.; Shabtai, J. *J. Catal.* **1984**, *85*, 44–52.
81. Lauritsen, J. V.; Kibsgaard, J.; Olesen, G. H.; Moses, P. G.; Hinnemann, B.; Helveg, S.; Nørskov, J. K.; Clausen, B. J.; Topsøe, H.; Lægsgaard, E.; Besenbacher, F. *J. Catal.* **2007**, *249*, 220–233.

Chapter 7

Characterization and Catalytic activity of Cu–TUD-1 for Styrene Epoxidation

Muthusamy Poomalai Pachamuthu,[1] Anand Ramanathan,[2] Kannan Santhi,[1] and Rajamanickam Maheswari*,[1,2]

[1]Department of Chemistry, Anna University, Sardar Patel Road Guindy, Chennai, 600025, India
[2]Center for Environmentally Beneficial Catalysis, The University of Kansas, 1501 Wakarusa Dr., Lawrence, KS 66047, USA
***E-mail: rmmahes@ku.edu**

Cu–TUD-1 has been synthesized hydrothermally by a sol-gel method employing triethanolamine (TEA) as a mesopore structure directing agent. Cu(II) species were found to be grafted and highly dispersed in the 3D mesoporous silica framework. Isolated Cu^{2+}, oligonuclear CuO, and bulk CuO are the main species present in the foam-like disordered silica (TUD-1). The nature of the copper species and its coordination with silica were evaluated by means of diffuse reflectance UV-Vis, EPR, FT-Raman, and TPR studies. Cu–TUD-1 catalyzed the epoxidation of styrene with *tert*-butyl hydroperoxide (TBHP) in liquid phase under mild reaction conditions. Important factors associated with the catalytic activity and selectivity such as reaction time, temperature, $n_{TBHP}/n_{Styrene}$ molar ratio and copper loading were also investigated.

Introduction

Epoxidation is an important reaction in organic synthesis since the formed epoxides can be readily converted into a variety of industrially significant chemicals (*1*). The direct epoxidation of alkenes is generally carried out using expensive peracids as oxidants. In general, these processes are energy intensive and generate an excessive amount of effluents. Alternatively, a process involving

In Novel Materials for Catalysis and Fuels Processing; Bravo-Suárez, J., et al.;
ACS Symposium Series; American Chemical Society: Washington, DC, 2013.

an environmentally friendly heterogeneous catalyst enables an easy separation of products with reduction of toxic wastes. Transition-metal complexes (*2*), hydrotalcites (*3*), mesoporous molecular sieves containing transition metals such as Mn, Co, Fe, Ti, Zr, and V (*4–15*), and tethered / grafted / encapsulated metal complexes (*16–18*) in a silica matrix have been screened as catalysts for styrene epoxidation by employing different oxidants such as O_2, H_2O_2, TBHP, and iodosylbenzene.

Copper ions and complexes are known to catalyze the selective oxidation of organic compounds (*19*). In addition, the higher reduction potential of copper with respect to other transition metals such as Fe(II), Mn(II), Ni(II), and Co(II) plays an important role in its catalytic activity. Cu(II)−complexes unsupported and immobilized on solid supports have been reported for the styrene epoxidation (*20–24*). Recently, the immobilization of a salicylaldimine Cu(II) complex on mesoporous silica nanoparticles was found to be active in styrene epoxidation (99% styrene conversion and 80% epoxide selectivity) using TBHP as the oxidant (*15*). However, the disadvantages of such heterogenized metal complexes are their complicated synthesis procedure and poor stability under reaction conditions. Lu and Yuan synthesized Cu–HMS and reported that well-dispersed copper active sites were responsible for the observed higher styrene conversion (99%) (*13*).

TUD-1 is a 3D amorphous mesoporous material with wormhole-like structure, which can be easily synthesized by hydrothermal methods employing low-cost triethanolamine (TEA) as a bifunctional template. This novel synthesis route leads to the incorporation in the silica structure of various active metals such as Co, Fe, Cr, Al, Zr, Cu, Mn, and Ti (*25*). Ramanathan et al. reported the synthesis of a Mn containing TUD-1 and its evaluation as an epoxidation catalyst for styrene and trans-stilbene (*10*). The epoxidation of bulky substrates such as trans-stilbene was also reported over Co–TUD-1 (*26*). Silylated Ti–TUD-1 was found to be active in epoxidation of oct-1-ene (*27*). Mandal et al. also studied Ga–TUD-1 for styrene epoxidation reaction and showed that these catalysts were active up to 48 h without loss of their catalytic activity (*28*). Recently, we have reported copper containing TUD-1 materials as an effective catalyst for the oxidation of ethylbenzene with TBHP (*29*). However, the styrene epoxidation over Cu containing TUD-1 with aqueous TBHP has not been reported thus far. In this work, the styrene epoxidation with aqueous TBHP is studied on Cu–TUD-1 with different Cu contents. Additionally, the nature of the copper species present in Cu–TUD-1 is studied in detail by means of different characterization techniques. It will be shown that the catalytic activity of Cu–TUD-1 for styrene epoxidation with TBHP depends on the nature of the copper sites present in the catalyst. The influence of various reaction parameters on the styrene conversion and the selectivity of styrene oxide were also determined.

Experimental

Synthesis of Cu–TUD-1

The detailed synthesis of Cu–TUD-1 was outlined in our previous work (*29*). In a typical synthesis of Cu–TUD-1, a mixture containing 14 g of triethanolamine

In Novel Materials for Catalysis and Fuels Processing; Bravo-Suárez, J., et al.;
ACS Symposium Series; American Chemical Society: Washington, DC, 2013.

(TEA, 97%, SISCO-India) and 2 g deionized water (0.5 μS cm^{-1}) was added dropwise into the mixture of 19.8 g tetraethyl orthosilicate (TEOS, 98%, Sigma Aldrich) and an appropriate amount of copper nitrate ($Cu(NO_3)_2.3H_20$, 99.5%, Merck) in 4 g water solution. After stirring for 1 h at room temperature, 20 g of tetraethylammonium hydroxide (TEAOH, 35%, Sigma Aldrich) was added to the above solution and vigorously stirred for another 3 h. The final gel composition of the synthesis mixture was $1SiO_2$: 1TEA: (0.01-0.1) CuO: 0.5 TEAOH: 11 H_2O. The mixture was aged at room temperature for 24 h, dried at 98 °C for 24 h, and then hydrothermally treated in a Teflon-lined autoclave at 180 °C for 8 h. Finally, the wet solid (as-synthesized) samples (obtained without filtration or washing) were calcined in a tubular furnace at 600 °C for 10 h, ramp rate of 1 °C min^{-1} and 50 cm^3 min^{-1} flow of air. The calcined Cu–TUD-1 catalyst is hereafter referred as Cu–TUD-1(*m*), where '*m*' is the Si/Cu atomic ratio (104, 53, 21 and 10) evaluated by ICP-OES.

Catalyst Characterization

The surface area, pore volume, and pore size distribution of Cu–TUD-1 samples were evaluated by nitrogen physisorption carried out at −196 °C using a surface area analyzer (ASAP-2020, Micromeritics). Diffuse reflectance (DR) UV–Vis spectra were recorded in the range of 200–800 nm on a Thermo Scientific UV–vis spectrometer (Evolution 600) with a diffuse reflectance sphere accessory using $BaSO_4$ as the reference material. High-resolution transmission electron microscopy (HRTEM) imaging was performed using a HRTEM JEOL 3010 with a UHR pole piece operating at an accelerating voltage of 300 kV. Elemental analysis was carried out with a Perkin Elmer ICP-OES Optima 5300 DV spectrometer. Temperature programmed reduction (TPR, 5% H_2 in Ar) of Cu–TUD-1 samples (ca. 100 mg) were analyzed with a Micromeritics TPR/TPD 2900 instrument. Prior to TPR analysis, the samples were pretreated in Ar flow at 500 °C for 2 h. Then, the gas was switched to 5% H_2 in Ar gas at a flow rate of 20 std cm^3 min^{-1} while the temperature was raised from ambient to 500 °C at a rate of 20 °C min^{-1}. Thermal analysis of the as-synthesized Cu–TUD-1 was performed on a TGA SDT Q600 (TA Instruments, Inc.) thermal analyzer. The measurements were carried out with 4.5 mg of the as-synthesised sample by flowing nitrogen at 100 STP cm^3 min^{-1} and a heating rate of 10 °C min^{-1}.

FT-Raman spectra of Cu–TUD-1 samples (ca. 10 mg) were acquired on a BRUKER RFS 27 instrument with a resolution of 2 cm^{-1}. The Nd:YAG laser source (1064 nm) was used for excitation in liquid nitrogen cooled condition. For SEM-EDAX imaging a FEI Quanta FEG 200 high-resolution scanning electron microscope was used. Electron paramagnetic resonance (EPR) spectra were recorded on a Bruker ER 200D EPR spectrometer at room temperature with a microwave frequency of 9.45 GHz.

Cu–TUD-1 as Catalyst for Styrene Epoxidation

In a typical styrene epoxidation reaction, 200 mg of Cu–TUD-1 catalyst (pretreated at 200 °C in a muffle furnace for 4 h) was added to a two-neck

In Novel Materials for Catalysis and Fuels Processing; Bravo-Suárez, J., et al.;
ACS Symposium Series; American Chemical Society: Washington, DC, 2013.

round-bottomed flask containing 10 mmol of styrene (99%, Sigma Aldrich), 3 mmol of chlorobenzene (internal standard, 99.5%, SISCO), and 15 g of acetonitrile. The flask is then immersed in a thermostated oil bath set at the reaction temperature, after which 10 mmol of TBHP (70 wt % aqueous solution, Sigma Aldrich) were added, which is considered as the start of the reaction. The reactant mixture was stirred vigorously (650 rpm) and samples were periodically withdrawn and analyzed on a gas chromatograph equipped with a DB-624 capillary column and a flame ionization detector (FID, 280 °C, N_2 as carrier gas, and injector temperature of 250 °C). The products were identified on a GC–MS (Agilent Technologies 6850 N series with an HP-5 capillary column).

Results and Discussion

Characterization of Cu–TUD-1

The mesoporosity of the Cu–TUD-1 materials was verified by nitrogen physisorption which showed type IV isotherms with H_2 type hysteresis loop characteristic of mesoporous materials with wormhole-like disordered structure (*30*). A representative N_2 adsorption–desorption isotherm and BJH pore size distribution of the Cu–TUD-1(104) sample is shown in Figure 1. Surface areas of Cu–TUD-1 samples were observed in the range of 483–531 $m^2\ g^{-1}$ with pore volumes of 0.69–0.76 $cm^3\ g^{-1}$ (*29*). These materials exhibit an average adsorption pore size distribution of around 5 nm that is not affected by the copper loading, as observed in other similar disordered-type materials (*31*). The mesostructured nature of Cu–TUD-1 samples was confirmed by means of low-angle XRD patterns (not shown) (*29*).

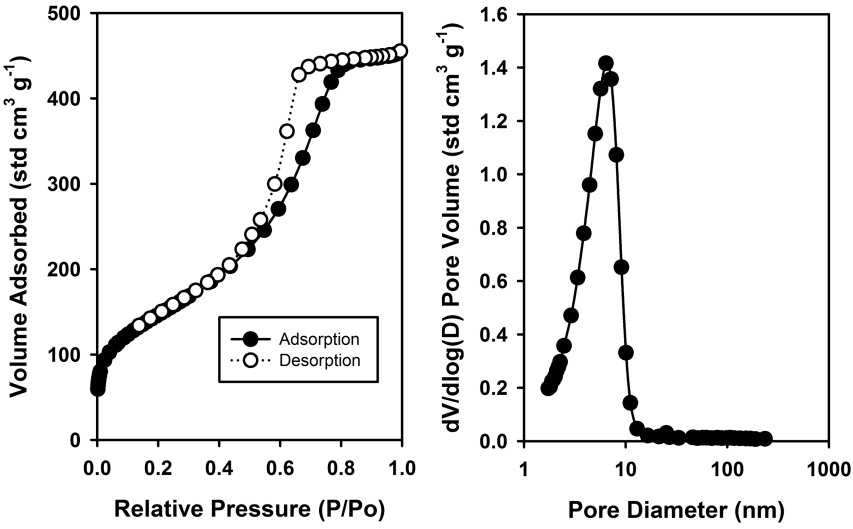

Figure 1. N_2 adsorption–desorption isotherm and pore size distribution profile of Cu–TUD-1(104)

In Novel Materials for Catalysis and Fuels Processing; Bravo-Suárez, J., et al.;
ACS Symposium Series; American Chemical Society: Washington, DC, 2013.

A decrease in the Si/Cu atomic ratio from 104 to 10 (i.e., as the copper amount is increased) results in the formation of CuO phase, which is observed with increasing peak intensity in the wide-angle XRD (Figure 2). CuO tenorite phase was noted at high loadings of copper for Cu–TUD-1(21) and Cu–TUD-1(10) at 2θ values of 35.5 and 38.6°, respectively (*29*). The CuO crystallite sizes estimated with the Debye–Scherrer equation were in the 2–5 nm range. A SEM image of the Cu–TUD-1(104) catalyst (Figure 3) showed uneven size and shape of individual silica particles. The disordered worm-hole like arrangement of pores was further evident for the Cu-TUD-1(104) sample from HR-TEM results (Figure 3). The copper atomic percentage evaluated from the corresponding energy-dispersive spectroscopy (EDAX) analysis is 1%, which is close to the Si/Cu atomic ratio of 104 estimated from ICP-OES.

The thermogravimetric analysis (TG-DTG) of the as-synthesized Cu–TUD-1(104) sample (Figure 4) revealed that three processes took place during the temperature ramp up to 800 °C. Initially, a weight loss of 15% below 100 °C is attributable to the removal of physisorbed water and ethanol. The 40% weight loss observed between 110 and 280 °C is due to the decomposition and desorption of organic moieties (TEA and TEAOH). Finally, the 6% weight loss at temperatures over 280 °C is attributed to the removal of water from surface O–H groups and some of the undesorbed organic species. Overall, a total weight loss of 61% was observed for the as-synthesized Cu–TUD-1(104) sample during the thermal analysis.

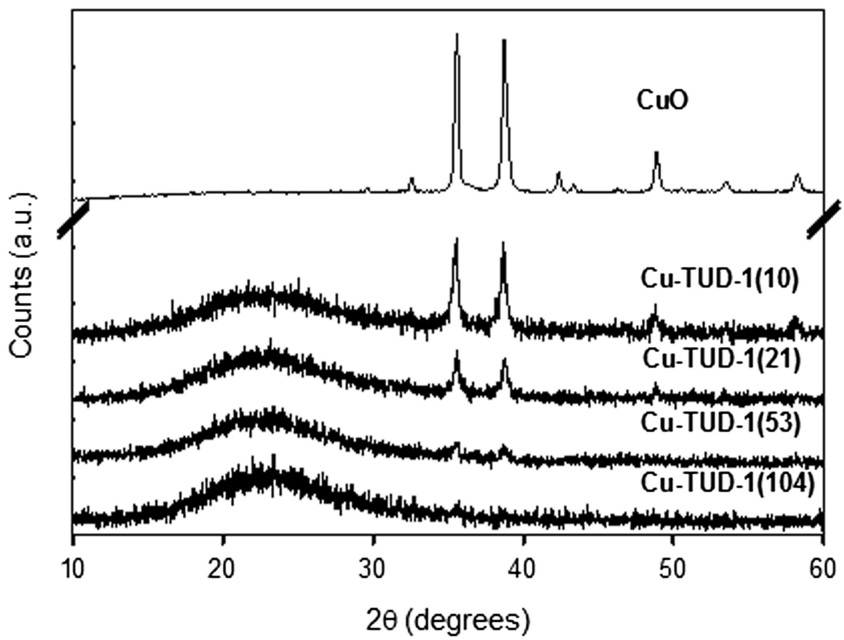

Figure 2. XRD patterns of Cu–TUD-1 samples. CuO pattern included for comparison

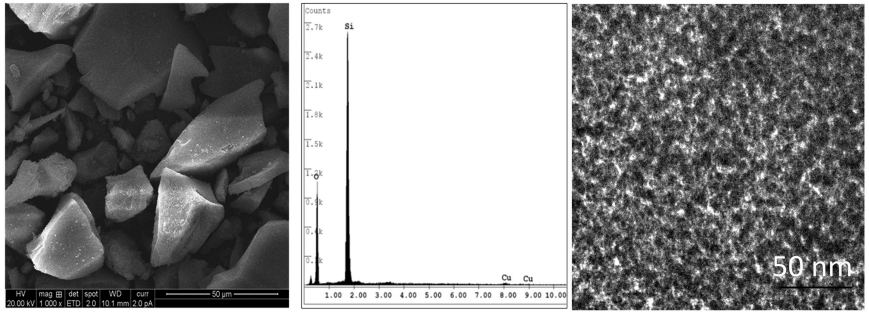

Figure 3. SEM image (left), EDAX analysis (middle), and TEM image of Cu–TUD-1(104)

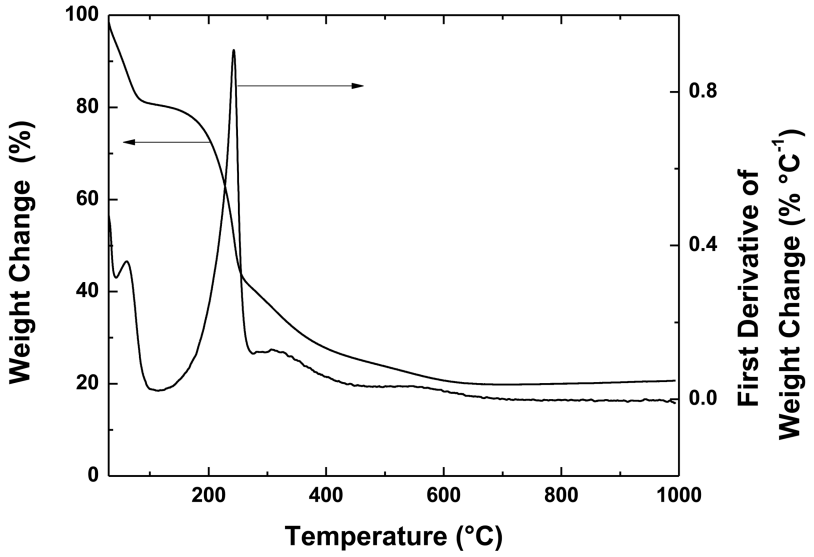

Figure 4. TG-DTG of as-synthesized Cu–TUD-1(104). TGA conditions: catalyst weight = 4.5 mg, ramp rate = 10 °C min^{-1}, flow of nitrogen = 100 std cm^3 min^{-1}.

To investigate the presence of CuO species, all the Cu−TUD-1 samples were characterized by FT-Raman spectroscopy and the results are shown in Figure 5. Cu–TUD-1 samples showed two bands centered at 295 and 345 cm^{-1}. These bands are assigned to the A_g and $2B_g$ Raman active modes of CuO (*32*). With these results, we cannot ascertain the presence of smaller amounts of highly dispersed oligonuclear CuO apart from the isolated Cu^{2+} species even at lower Si/Cu atomic ratios (104 and 53) because of their little infuence on the peaks size and broadness with the present laser source (1064 nm). The presence of isolated and oligonuclear CuO, however, has been verified by EPR and UV–vis spectroscopies, as discussed next.

In Novel Materials for Catalysis and Fuels Processing; Bravo-Suárez, J., et al.;
ACS Symposium Series; American Chemical Society: Washington, DC, 2013.

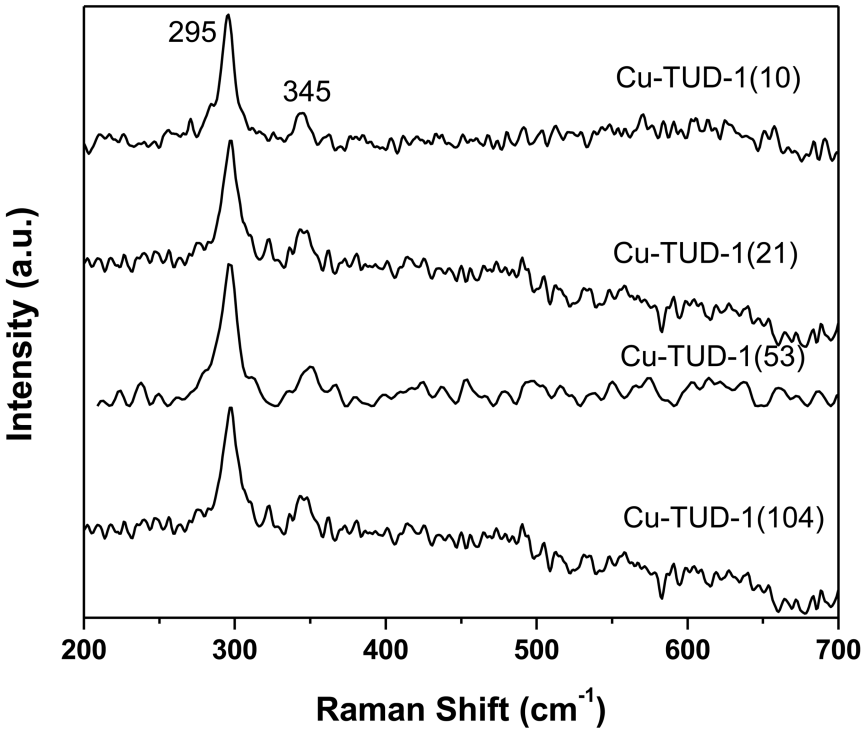

Figure 5. FT-Raman spectra of Cu–TUD-1 samples with different Si/Cu atomic ratios

The X-band EPR spectra of Cu−TUD-1(104) and Cu−TUD-1(10) samples recorded at room temperature is presented in Figure 6. The EPR signal shape and intensity of these samples confirm the presence of isolated Cu^{2+} ions and small clusters of $[-Cu-O-Cu-O-]_n$ species, since bulk CuO does not show EPR lines due to the strong interactions of the copper ions in the crystal lattice. Kucherov et al. reported that the isolated copper ions coordination and quantitative dispersion on M-MCM-41 support mainly affects the EPR signals shape and normalized double integral intensities (*33*). No significant changes in the EPR signal were observed for the Cu−TUD-1(10) and Cu−TUD-1(104) samples. These results reveal the existence of highly dispersed isolated Cu^{2+} sites and oligonuclear CuO species on TUD-1 even at higher copper loadings (Si/Cu = 10). Although the resolution of the hyperfine splitting is poor in the EPR spectra, the g and the hyperfine coupling constant ($A_\parallel$) values of Cu–TUD-1(104) samples can be calculated from the parallel and perpendicular lines as $g_\parallel = 2.37$, $g_\perp = 2.08$, $A_\parallel = 142$ G. These values are due to the distorted octahedral geometry of Cu sites, which are coordinated with water molecules and surface silica present in the pore channels of TUD-1. However, evacuation and heat treatment of the catalyst may lead to geometrical variations from octahedral to square pyramidal and square planar (*34*). Hence, the coordinated water molecules can also influence the Cu sites geometry.

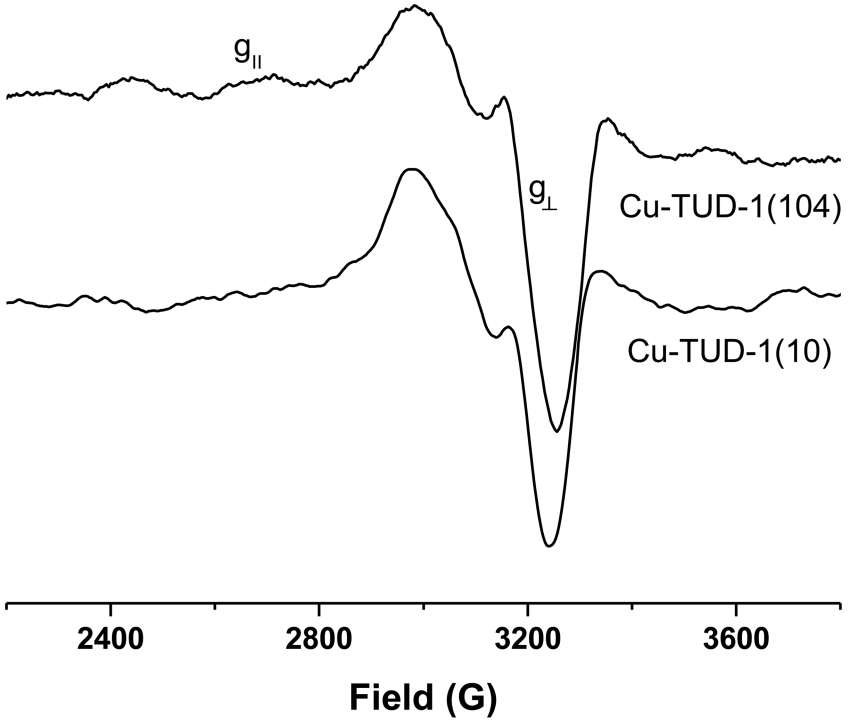

Figure 6. EPR spectra of the calcined Cu–TUD-1(104) and Cu–TUD-1(10) samples recorded at room temperature

H_2-TPR profiles of Cu–TUD-1 samples (Figure 7) showed two peaks in the temperature range of 160–450 °C. These peaks are associated with the reduction of isolated Cu^{2+}, finely dispersed, and bulk CuO to copper metal in the channels of TUD-1. It has been reported that the lower temperature reduction peak corresponds to the one step reduction of isolated CuO_x clusters to Cu^0 and the partial reduction of isolated Cu^{2+} ions to Cu^+ (*35*).

Two low temperature peaks were observed for Cu–TUD-1(104) at 185 and 225 °C. These peaks are attributed to the reduction of Cu^{2+} and finely dispersed CuO, respectively. It is reported that the reduction of CuO diluted with SiO_2 occurs at 220 °C. For Cu–TUD-1(53) and Cu–TUD-1(21), two peaks observed at 280 and 340 °C can be temptatively assigned to the presence of highly dispersed CuO nanoparticles and larger CuO clusters, respectively (*36*). The low temperature reduction peak with high intensity in Cu–TUD-1(10) suggests the possible presence of a uniform dispersion of CuO in the surface of TUD-1. Hartman *et al.* correlated the effect of reduction temperature with pore diameter of the support and copper loadings (*37*). The formation of larger CuO aggregates was not favored in small pore channels and as a consequence, the peak maximum of the reduction profile varied with different supports. This could also be true for Cu–TUD-1, as these materials possessed broad distribution of pore sizes. Variable particle sizes of CuO species could be formed in the mesopores of TUD-1 that could also affect the broadness of observed TPR profiles. In summary, the

In Novel Materials for Catalysis and Fuels Processing; Bravo-Suárez, J., et al.;
ACS Symposium Series; American Chemical Society: Washington, DC, 2013.

observed features in the TPR profiles suggest the presence of isolated, highly dispersed, and large CuO particles. A conclusive peak assigment, however, is not possible because of the reasons discussed above and beacuse of the possibility of experimental artifacts at the studied conditions (TPR characeristic number $P > 20$ K).

The catalysts were further probed by UV–vis spectroscopy. Samples of Cu–TUD-1(104) and Cu–TUD-1(10) were reduced in flowing H_2 (40 std cm^3 min^{-1}) at 400 °C for 6 h and designated as Cu–R-1 and Cu–R-4, respectively. The DR UV–Vis spectra of the calcined samples of Cu–TUD-1(104) and Cu–TUD-1(10) along with their corresponding reduced samples, Cu–R-1 and Cu–R-4, are shown in Figure 8. According to Bravo-Suárez et al., the absorption range between 200 and 500 nm corresponds to the isolated Cu^{2+} and oligomeric CuO, whereas absorption bands noticed at around 600–800 nm are due to d–d transition of Cu in distorted octahedral coordination, respectively (*38*, *39*). The drastic reduction in the absorbance intensities between 350 and 800 nm for Cu–R-1 and Cu–R-4 samples indicate the reduction of both CuO species (oligomeric and bulk CuO). In addition, the intensity of isolated Cu^{2+} species region (250–400 nm) is also diminished for Cu–R-1 due to the reduction of grafted Cu^{2+} species in the pores surface. These observed results are in good agreement with the TPR measurements.

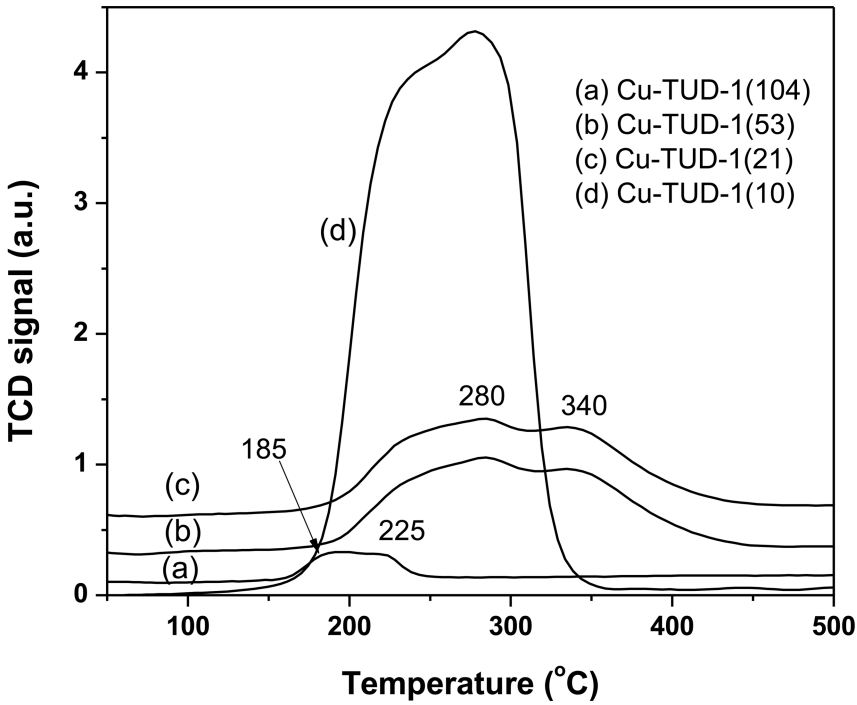

Figure 7. H_2-TPR profiles of the Cu–TUD-1 catalysts with different Si/Cu atomic ratios. Samples pretreated at 500 °C for 1 h in flowing of argon. Condition: Sample weight = 50–100 mg, heating rate = 20 °C min^{-1}, 5% H_2 in Ar flow rate = 20 std cm^3 min^{-1}. (characteristic number P range > 100)

In Novel Materials for Catalysis and Fuels Processing; Bravo-Suárez, J., et al.;
ACS Symposium Series; American Chemical Society: Washington, DC, 2013.

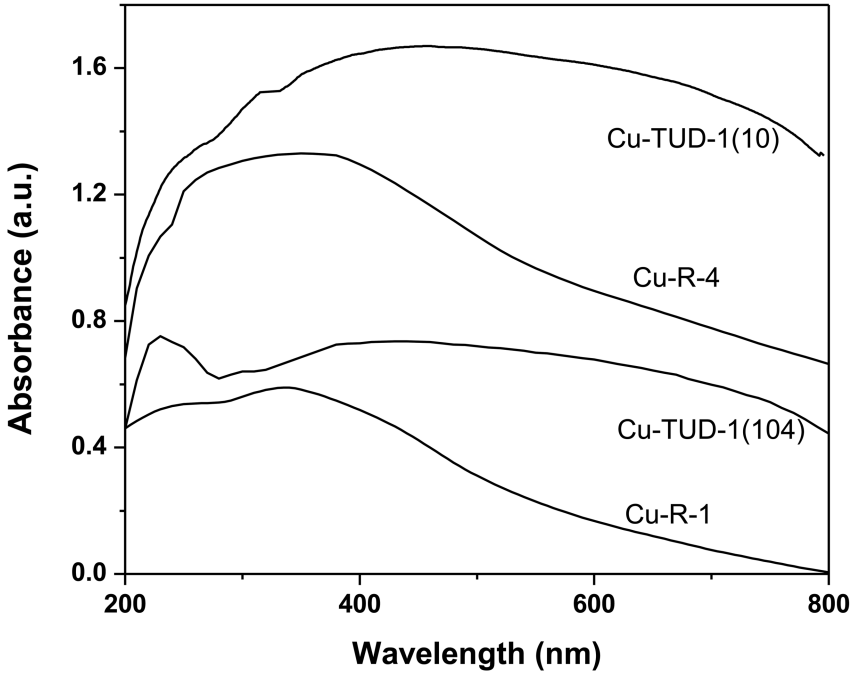

Figure 8. DR UV–vis spectra of Cu–TUD-1 (104), Cu–TUD-1 (10), and the corresponding reduced samples, Cu–R-1 and Cu–R-4, respectively

From all of the structural characterizations of Cu–TUD-1 samples discussed above, it can be concluded that it is difficult to incorporate all the Cu species into TUD-1 framework even at lower loadings of Cu (as in Cu–TUD-1(104)). Copper exists as isolated Cu^{2+} species and as highly dispersed oligonuclear CuO at lower loadings of Cu, whereas higher loadings of copper lead to the formation of bulk CuO species (Scheme 1).

Catalytic Activity of Cu–TUD-1 in the Epoxidation of Styrene

The catalytic properties of the Cu–TUD-1 were tested in the epoxidation of styrene with TBHP (70% in H_2O) at 80 °C. The major products of styrene (S) epoxidation were styrene oxide (SO), benzaldehyde (PhCHO), and phenylacetaldehyde (PA). Benzoic acid (PhCOOH) was also observed as a minor product (Scheme 2). Further small amounts of unidentified products (grouped as others in Tables 1 and 2) were observed in all the runs. From literature reports, these unidentified products are likely to be diols and phenylacetic acid. A blank reaction without catalyst resulted in about 8% styrene conversion with 49 and 38% selectivities to SO and PhCHO, respectively. The reaction with a Cu-free TUD-1 sample resulted in 10% styrene conversion with 55 and 25% selectivities towards SO and PhCHO, respectively (Table 1). The styrene conversion tremendously increased when Cu–TUD-1 was employed as the catalyst.

In Novel Materials for Catalysis and Fuels Processing; Bravo-Suárez, J., et al.;
ACS Symposium Series; American Chemical Society: Washington, DC, 2013.

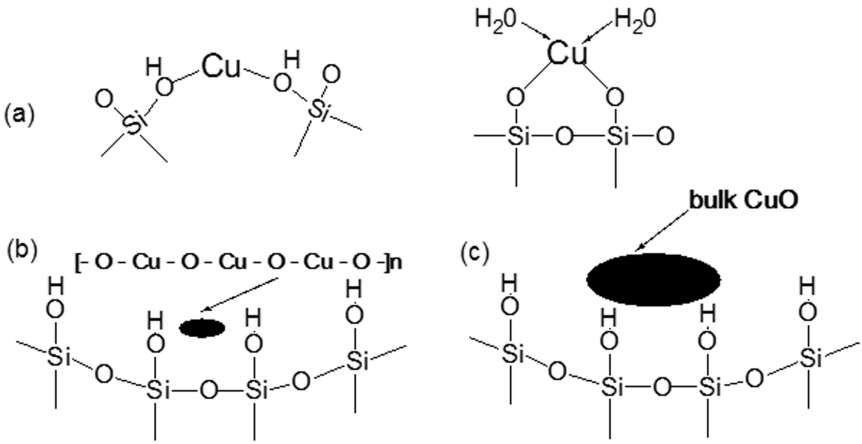

Scheme 1. Possible copper species present in the TUD-1 matrix (a) Isolated/grafted CuO, (b) Oligonuclear CuO, and (c) Bulk CuO.

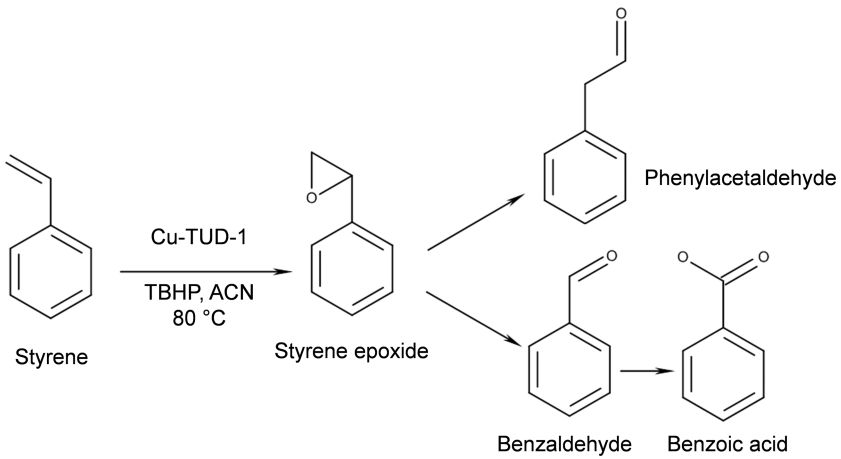

Scheme 2. Styrene epoxidation reaction over Cu–TUD-1 catalyst with possible reaction products

In Novel Materials for Catalysis and Fuels Processing; Bravo-Suárez, J., et al.;
ACS Symposium Series; American Chemical Society: Washington, DC, 2013.

Table 1. Influence of Si/Cu atomic ratio in the epoxidation of styrene[a]

Catalyst	*Cu content (wt %)*	*Conv. TBHP (%)*	*Conv. Styrene (%)*	*Selectivity (%)*					*Conversion Rate* $mol_{styrene}\ mol_{Cu}^{-1}\ h^{-1}$
				PhCHO[b]	*SO*[c]	*PA*[d]	*PhCOOH*[e]	*Others*[f]	
Blank[g]			8.2	39.1	49.9	8.3	0.0	2.7	
Si–TUD-1[g]			10.2	25.3	55.2	9.2	6.5	3.9	
Cu–TUD-1(104)	0.95	86.0	74.8	28.9	57.1	3.4	4.2	6.4	292
Cu–TUD-1(53)	1.85	94.2	80.7	31.5	52.5	3.7	4.3	8.0	160
Cu–TUD-1(21)	4.5	95.0	84.6	32.7	47.1	3.0	4.4	12.8	67
Cu–TUD-1(10)	9.1	72.1	56.1	27.1	54.6	2.8	3.0	12.5	21

[a] Reaction conditions: $n_{Styrene}/n_{TBHP}/n_{PhCl}$ = 1/1/0.3, $n_{Styrene}$ = 10 mmol, m_{cat} = 200 mg, $m_{acetonitrile}$= 15 g, t = 8 h, T = 80 °C. [b] PhCHO = Benzaldehyde. [c] SO = Styrene oxide. [d] PA = Phenylacetaldehyde. [e] PhCOOH = Benzoic acid. [f] Mainly diols, phenylacetic acid, and high boiling polymers. [g] Reaction carried out for 24 h.

The effect of reaction time on styrene and TBHP conversion over Cu–TUD-1(104) was investigated and depicted in Figure 9. A steep increase in both the conversion of styrene and TBHP was observed with time, whereas the SO selectivity passed through a maximum. The selectivity for PhCHO decreased with time and remained relatively constant after 16 h. A maximum selectivity of SO (57%) and PhCHO (29%) were observed at a reaction time of 8 h. For further studies, a reaction time of 8 h was considered as the optimum duration because undesirable side products were kept to a minimum at this reaction time.

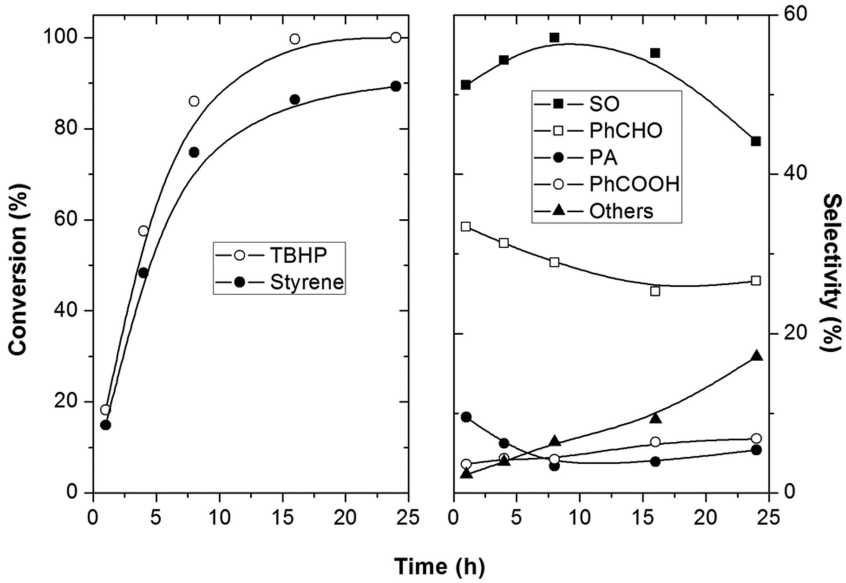

Figure 9. Influence of reaction time on the epoxidation of styrene with TBHP over Cu–TUD-1(104). Reaction conditions: $n_{Styrene}/n_{TBHP}/n_{PhCl}$ = 1/1/0.3, $n_{Styrene}$ = 10 mmol, m_{cat} = 200 mg, $m_{acetonitrile}$ = 15 g, t = 8 h, T = 80 °C.

The influence of reaction temperature on styrene conversion and selectivity in the temperature range of 60–90 °C is shown in Figure 10. As expected, styrene conversion increased with temperature and reached 88.2% at 90 °C. Despite the higher styrene conversion, this higher temperature was not explored further because of the lower selectivity towards SO product (40.7%) and the higher formation of undesirable high boiling products (15.4%). A maximum and almost similar SO selectivity was observed at both 70 and 80 °C. Nevertheless, an overall highest SO yield of around 42% was achieved at 80 °C.

In Novel Materials for Catalysis and Fuels Processing; Bravo-Suárez, J., et al.;
ACS Symposium Series; American Chemical Society: Washington, DC, 2013.

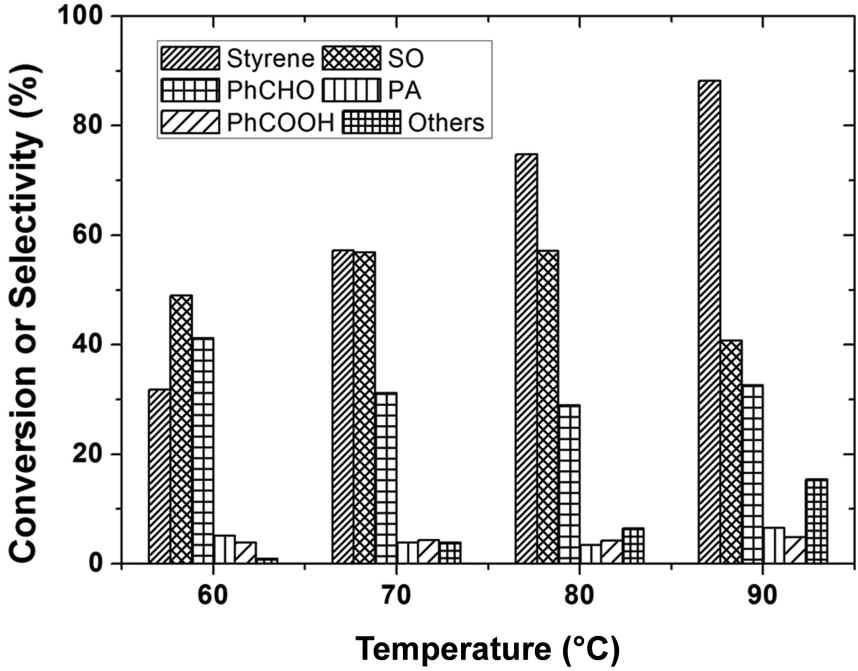

Figure 10. Influence of reaction temperature on conversion of styrene and product selectivies over Cu–TUD-1(104). Reaction conditions: $n_{Styrene}/n_{TBHP}/n_{PhCl}$ = 1/1/0.3, $n_{Styrene}$ = 10 mmol, m_{cat} = 200 mg, $m_{acetonitrile}$ = 15 g, t = 8 h, T = 80 °C.

Table 1 summarizes the results of styrene epoxidation over Cu–TUD-1 with different Si/Cu atomic ratios at 80 °C. With the exception of Cu–TUD-1(10), all other Cu–TUD-1 catalysts showed styrene conversions above 74%, which is attributed to the efficiency of the catalyst in the conversion of TBHP. A maximum TBHP conversion of 95% was observed for Cu–TUD-1(21) suggesting that both isolated CuO sites and oligonuclear CuO species are highly active in the decomposition of TBHP in comparison with bulk CuO. The styrene conversion and SO selectivity may be altered depending on the relative amount of the CuO species present in the TUD-1 matrix.

A comparison of styrene conversion per Cu atom present in the Cu–TUD-1 samples revealed that the reaction rate normalized per Cu atom decreased with a decrease in the Si/Cu atomic ratio. The higher conversion rate achieved with the Cu–TUD-1(104) is mainly due to the highly dispersed isolated CuO sites and, therefore, it is believed to be the most active species for styrene epoxidation. Nevertheless, a higher styrene conversion of 84.6% was achieved over Cu–TUD-1(21). These results indicate that oligonuclear CuO species present in Cu–TUD-1 promote styrene epoxidation as well. On the other hand, supported CuO systems have also been reported to catalyze the styrene epoxidation reaction with reasonable selectivity (*40*). The presence of large-size CuO crystallites in Cu–TUD-1(10) reduces the number of surface active sites (due to lower CuO

In Novel Materials for Catalysis and Fuels Processing; Bravo-Suárez, J., et al.;
ACS Symposium Series; American Chemical Society: Washington, DC, 2013.

dispersion) and thus leads to the low observed styrene conversion (see Table 1). This reduction in CuO dispersion explains the lower activity of bulk CuO in Cu–TUD-1(10) in comparison with that of nanocrystalline CuO present in other Cu–TUD-1 samples. Further optimization studies were carried out with the Cu–TUD-1(104) catalyst.

The $n_{TBHP}/n_{Styrene}$ molar ratio was varied from 0.5 to 3 and the results of styrene epoxidation at 80 °C for 8 h are presented in Table 2. The styrene conversion sharply increased from 39.3 to 74.8% when the $n_{TBHP}/n_{Styrene}$ molar ratio increased from 0.5 to 1. Thereafter, at higher $n_{TBHP}/n_{Styrene}$ molar ratios, the increase in styrene conversion was slow. Instead, a drastic decrease in the selectivity of the desired SO product was noticed along with a concomitant increase of unknown (polymeric) products. This is attributed to the uncontrollable free radical reaction when excess TBHP is present in the reaction mixture. Hence, a $n_{TBHP}/n_{Styrene}$ molar ratio of 1 is suggested as optimal for this catalytic system. Also, the heterogeneity of the reaction was tested by hot-filtering the reaction mixture and the filtrate was analyzed by atomic absorption spectroscopy (AAS), which revealed only about 1−1.25 ppm of Cu leaching for the Cu−TUD-1(104) catalyst.

Table 2. Influence of TBHP to styrene ratio in the epoxidation of styrene over Cu–TUD-1(104)[a]

n_{TBHP} / $n_{Styrene}$	Conv. Styrene (%)	Selectivity (%)				
		PhCHO[b]	SO[c]	PA[d]	PhCOOH[e]	Others[f]
0.5	39.3	22.3	66.4	5.9	2.1	3.3
1.0	74.8	28.9	57.1	3.4	4.2	6.4
2.0	88.4	36.3	42.5	4.7	6.7	9.8
3.0	94.7	32.5	36.5	5.4	8.2	17.4

[a] Reaction conditions: $n_{Styrene}/n_{TBHP}/n_{PhCl}$ = 1/0.5–3/0.3, $n_{Styrene}$ = 10 mmol, m_{cat} = 200 mg, $m_{acetonitrile}$ = 15 g, t = 8 h, and T = 80 °C. [b] PhCHO = Benzaldehyde. [c] SO = Styrene oxide. [d] PA = Phenylacetaldehyde. [e] PhCOOH = Benzoic acid. [f] Mainly diols, phenylacetic acid, and high boiling polymers.

Conclusions

In summary, a series of copper containing mesoporous material TUD-1 were hydrothermally synthesized by a sol-gel method with a bifunctional-molecule templating pathway under basic conditions. The disordered pore morphology and uneven shapes of the particles were confirmed by N_2 physisorption and SEM, respectively. FT-Raman, TPR, and DR UV–Vis studies evidenced the presence of three types of copper species: isolated Cu^{2+}, oligonuclear CuO, and bulk CuO. Although these materials do not present a well-defined ordered porous structure, they showed a remarkably high activity and selectivity for the styrene epoxidation reaction in the presence of TBHP as the oxidant. Highly dispersed isolated

In Novel Materials for Catalysis and Fuels Processing; Bravo-Suárez, J., et al.;
ACS Symposium Series; American Chemical Society: Washington, DC, 2013.

CuO and oligonuclear CuO are shown to be active sites for styrene epoxidation. Optimum reaction parameters, which achieve the best catalytic results, were found to be 80 °C, a $n_{TBHP}/n_{Styrene}$ ratio of 1, a reaction time of 8 h, and acetonitrile as the solvent.

Acknowledgments

The author M.P is thankful for JRF support from "UGC - Research Fellowship in Sciences for Meritorious Students" scheme. The authors are thankful to Prof. B. Viswanathan, NCCR, IIT-Madras for providing laboratory and characterization facilities to carry out this work.

References

1. Mandelli, D.; van Vliet, M. C. A.; Sheldon, R. A.; Schuchardt, U. *Appl. Catal., A* **2001**, *219*, 209–213.
2. Jorgensen, K. A. *Chem. Rev.* **1989**, *89*, 431–458.
3. Kirm, I.; Medina, F.; Rodriguez, X.; Cesteros, Y.; Salagre, P.; Sueiras, J. *Appl. Catal., A* **2004**, *272*, 175–185.
4. Zhang, Q.; Wang, Y.; Itsuki, S.; Shishido, T.; Takehira, K. *J. Mol. Catal. A: Chem.* **2002**, *188*, 189–200.
5. Tang, Q.; Zhang, Q.; Wu, H.; Wang, Y. *J. Catal.* **2005**, *230*, 384–397.
6. Zhang, Q.; Wang, Y.; Itsuki, S.; Shishido, T.; Takehira, K. *Chem. Lett.* **2001**, 946–947.
7. Zhang, W.; Fröba, M.; Wang, J.; Tanev, P. T.; Wong, J.; Pinnavaia, T. J. *J. Am. Chem. Soc.* **1996**, *118*, 9164–9171.
8. Wang, Y.; Guo, Y.; Wang, G.; Liu, Y.; Wang, F. *J. Sol-Gel Sci. Technol.* **2010**, *57*, 185–192.
9. Anand, R.; Shevade, S. S.; Ahedi, R. K.; Mirajkar, S. P.; Rao, B. S. *Catal. Lett.* **1999**, *62*, 209–213.
10. Ramanathan, A.; Archipov, T.; Maheswari, R.; Hanefeld, U.; Roduner, E.; Glaser, R. *J. Phys. Chem. C* **2008**, *112*, 7468–7476.
11. Cui, H. T.; Zhang, Y.; Zhao, L. F.; Zhu, Y. L. *Catal. Commun.* **2011**, *12*, 417–420.
12. Jinka, K. M.; Bajaj, H. C.; Jasra, R. V.; Prasetyanto, E. A.; Park, S. E. *Top. Catal.* **2010**, *53*, 238–246.
13. Lu, X. N.; Yuan, Y. Z. *Appl. Catal., A* **2009**, *365*, 180–186.
14. Selvaraj, M.; Song, S. W.; Kawi, S. *Microporous Mesoporous Mater.* **2008**, *110*, 472–479.
15. Tang, D. H.; Zhang, W. T.; Zhang, Y. L.; Qiao, Z. A.; Liu, Y. L.; Huo, Q. S. *J. Colloid Interface Sci.* **2011**, *356*, 262–266.
16. Yu, K.; Lou, L. L.; Ding, F.; Wang, S. J.; Wang, Z. L.; Liu, S. X. *Catal. Commun.* **2006**, *7*, 170–172.
17. Sujandi; Park, S. E. *Res. Chem. Intermed.* **2008**, *34*, 871–880.
18. Rahiman, A. K.; Bharathi, K. S.; Sreedaran, S.; Narayanan, V. *Catal. Lett.* **2009**, *127*, 175–182.

19. Punniyamurthy, T.; Rout, L. *Coord. Chem. Rev.* **2008**, *252*, 134–154.
20. Zolezzi, S.; Spodine, E.; Decinti, A. *Polyhedron* **2003**, *22*, 1653–1658.
21. Diaz-Requejo, M. M.; Belderrain, T. R.; Perez, P. J. *Chem. Commun. (Cambridge, U. K.)* **2000**, 1853–1854.
22. Ghadiri, M.; Farzaneh, F.; Ghandi, A.; Alizadeh, M. *J. Mol. Catal. A: Chem.* **2005**, *233*, 127–131.
23. Yang, Y.; Guan, J. Q.; Qiu, P. P.; Kan, Q. B. *Appl. Surf. Sci.* **2010**, *256*, 3346–3351.
24. Jana, S.; Dutta, B.; Bera, R.; Koner, S. *Langmuir* **2007**, *23*, 2492–2496.
25. Telalovic, S.; Ramanathan, A.; Mul, G.; Hanefeld, U. *J. Mater. Chem.* **2010**, *20*, 642–658.
26. Quek, X. Y.; Tang, Q. H.; Hu, S. Q.; Yang, Y. H. *Appl. Catal., A* **2009**, *361*, 130–136.
27. Prasad, M. R.; Hamdy, M. S.; Mul, G.; Bouwman, E.; Drent, E. *J. Catal.* **2008**, *260*, 288–294.
28. Mandal, S.; SinhaMahapatra, A.; Rakesh, B.; Kumar, R.; Panda, A.; Chowdhury, B. *Catal. Commun.* **2011**, *12*, 734–738.
29. Maheswari, R.; Pachamuthu, M. P.; Anand, R. *J. Porous Mater.* **2012**, *19*, 103–110.
30. Sing, K. S. W. *Pure Appl. Chem.* **1985**, *57*, 603–619.
31. Hamdy, M. S.; Mul, G.; Wei, W.; Anand, R.; Hanefeld, U.; Jansen, J. C.; Moulijn, J. A. *Catal. Today* **2005**, *110*, 264–271.
32. Xu, J. F.; Ji, W.; Shen, Z. X.; Li, W. S.; Tang, S. H.; Ye, X. R.; Jia, D. Z.; Xin, X. Q. *J. Raman Spectrosc.* **1999**, *30*, 413–415.
33. Kucherov, A. V.; Shigapov, A. N.; Ivanov, A. V.; Kucherova, T. N.; Kustov, L. M. *Catal. Today* **2005**, *110*, 330–338.
34. Jana, S.; Bhunia, S.; Dutta, B.; Koner, S. *Appl. Catal., A* **2011**, *392*, 225–232.
35. Wang, Y.; Chu, H.; Zhu, W. M.; Zhang, Q. H. *Catal. Today* **2008**, *131*, 496–504.
36. Zhu, W.; Wang, L.; Liu, S.; Wang, Z. *React. Kinet. Catal. Lett.* **2008**, *93*, 93–99.
37. Hartmann, M.; Racouchot, S.; Bischof, C. *Microporous Mesoporous Mater.* **1999**, *27*, 309–320.
38. Balsamo, N. F.; Chanquia, C. M.; Herrero, E. R.; Casuscelli, S. G.; Crivello, M. E.; Eimer, G. A. *Ind. Eng. Chem. Res.* **2010**, *49*, 12365–12370.
39. Bravo-Suárez, J. J.; Subramaniam, B.; Chaudhari, R. V. *J. Phys. Chem. C* **2012**, *116*, 18207–18221.
40. Choudhary, V. R.; Jha, R.; Chaudhari, N. K.; Jana, P. *Catal. Commun.* **2007**, *8*, 1556–1560.

Chapter 8

Rapid Room Temperature Synthesis of Ce–MCM-48: An Active Catalyst for *trans*-Stilbene Epoxidation with *tert*-Butyl Hydroperoxide

Anand Ramanathan,[1] Rajamanickam Maheswari,[1] Prem S. Thapa,[3] and Bala Subramaniam[*,1,2]

[1]Center for Environmentally Beneficial Catalysis, The University of Kansas, 1501 Wakarusa Dr, Lawrence, KS 66047, USA
[2]Department of Chemical and Petroleum Engineering, The University of Kansas, 1501 Wakarusa Dr, Lawrence, KS 66045, USA
[3]Microscopy and Imaging Laboratory, University of Kansas, 1501 Wakarusa Dr, Lawrence, KS 66045, USA
[*]E-mail: bsubramaniam@ku.edu

A rapid, facile, room temperature synthesis procedure was employed for preparing cerium containing MCM-48 (Ce–MCM-48) samples with different Si/Ce ratios. These materials were characterized by powder XRD, N_2 physisorption, TEM, diffuse-reflectance UV–Vis, and Raman spectroscopy. The Ce–MCM-48 materials catalyze the epoxidation of *trans*-stilbene (a bulky substituted alkene) with *tert*-butyl hydroperoxide. The framework incorporated Ce^{4+} ions are found to favor epoxide formation. A plausible mechanism is provided.

Introduction

Since the discovery of periodic ordered mesoporous silicas (designated as M41S) by Mobil researchers (*1*), most of the subsequent studies have focused on the hexagonal MCM-41 because its synthesis process is highly facile and reproducible (*2*). Within the M41S family, the hexagonal MCM-41 and lamellar

In Novel Materials for Catalysis and Fuels Processing; Bravo-Suárez, J., et al.;
ACS Symposium Series; American Chemical Society: Washington, DC, 2013.

MCM-50 are energetically more stable than cubic MCM-48 (*3*). However, MCM-48 materials possess unique interwoven three-dimensional pore network and are particularly advantageous as a catalyst and/or catalyst support due to decreased diffusion resistances. The silicate network of MCM-48 is catalytically inactive. Hence, various metal ions such as Al (*4*), Fe (*5*), Cr (*6*), Co (*7*), Mn (*8*), Ce (*9*), and Zr (*10*) have been incorporated into the mesoporous silicate framework to create active sites. Recently, a procedure for the rapid, facile and room temperature synthesis of siliceous MCM-48 was reported (*11*). Metals such as Ti (*12*), W (*13*), and Fe (*14*) were incorporated following this procedure and are shown to be catalytically active for various transformations.

Cerium containing materials have been shown to be powerful one-electron oxidation catalysts (*15*). In particular, cerium incorporation into mesoporous silica materials yields both acidic and redox properties (*16–20*). Several reports describe cerium incorporation into various well-known mesoporous silicates such as MCM-41 (*17*), MCM-48 (*9*, *21*, *22*), SBA-15 (*23*, *24*), TUD-1 (*25*), and KIT-6 (*20*). These studies employ conventional synthesis methods. In the present investigation, we synthesized Ce–MCM-48 with different amounts of cerium by employing a gel composition similar to that reported for the rapid, room temperature synthesis of siliceous MCM-48. The prepared materials were characterized using powder XRD, N_2 physisorption, diffuse reflectance UV–Vis, TEM, and Raman spectroscopy. The resulting Ce–MCM-48 materials are shown to be catalytically active for epoxidation of *trans*-stilbene (TS) with *tert*-butyl hydroperoxide (TBHP).

Experimental

Synthesis of Ce–MCM-48

Ce–MCM-48 materials with different n_{Si}/n_{Ce} atomic ratio were synthesized by using cetyltrimethylammonium bromide (CTAB) as a structure-directing agent and ethanol as a cosolvent/additive in the presence of ammonia solution. Tetraethyl orthosilicate (TEOS, 98% Acros organics) and ceric ammonium nitrate (CAN, 98.5% Sigma-Aldrich) were used as the silica and cerium sources, respectively. In a typical synthesis, 2.4 g of CTAB (Aldrich) were dissolved in 100 cm^3 deionized water. Then, 55 g of absolute ethanol were added and the mixture was stirred for 30 min. Following this step, 13.5 g of ammonium hydroxide solution in water (25%, Fisher) were added and the stirring was continued for another 30 min. Finally, 3.7 g of TEOS (Acros organics) and appropriate amounts of CAN were added and the stirring continued for 5–6 h. The resulting precipitate was filtered, washed with deionized water, dried, and calcined at 550 °C for 5 h in a muffle furnace under flowing air (300 std cm^3 min^{-1}). The samples prepared were denoted as Ce–MCM-48(*x*), where *x* represents the n_{Si}/n_{Ce} atomic ratio in the synthesis gel.

In Novel Materials for Catalysis and Fuels Processing; Bravo-Suárez, J., et al.;
ACS Symposium Series; American Chemical Society: Washington, DC, 2013.

Characterization

Low angle XRD (2θ range of 1.5–5°) measurements were carried out on a Bruker D8 instrument. High angle XRD patterns were obtained with a Bruker SMART APEX single-crystal diffractometer equipped with a Mo sealed tube X-ray source, a graphite monochromator, MonoCap collimator and a SMART APEX charge-coupled device (CCD) area detector. The nitrogen adsorption and desorption isotherms were obtained on a Quantachrome NOVA 2200e instrument. The textural properties (surface area, pore volume, and pore size distribution) were evaluated from nitrogen physisorption isotherms at −196 °C. Transmission electron micrographs were captured using a 2K x 2K CCD, each mounted on a 200 kV FEI Tecnai F20 G2 X-Twin Field Emission Scanning/Transmission Electron Microscope operating at 200 kV. Diffuse reflectance UV–Vis spectra were collected in the 200–800 nm range at room temperature with a PerkinElmer LAMBDA 850 UV–Vis spectrophotometer equipped with a 60 mm integrating sphere, using Spectralon as the reference material. Raman spectra were acquired on a SENTERRA (Bruker) dispersive Raman microscope equipped with a thermoelectrically cooled CCD detector and an argon laser (785 nm) operated at 50 mW.

The reducibility of the CeO_2 species in Ce–MCM-48 samples were analyzed by temperature programmed reduction (TPR) using 10% H_2/Ar (30 std cm^3 min^{-1}) on a Micromeritics Autochem 2910 instrument equipped with a thermal conductivity detector (TCD). About 100–150 mg of Ce–MCM-48 samples were calcined in situ at 550 °C in a flow of helium for 1 h and subsequently cooled to ambient temperature. The samples were then heated to 800 °C at a heating rate of 10 °C min^{-1}. The TPR characteristic number *P*, calculated as reported elsewhere (*26*), is in the range of 24−160. The H_2 consumption was monitored by a thermal conductivity detector (TCD).

Epoxidation of *trans*-Stilbene

Into a 50 cm^3 two-necked round-bottomed flask equipped with a condenser, *trans*-stilbene (TS, 96%, Acros Organics, 1 mmol), *tert*-butyl hydroperoxide (TBHP, 70% in water, Aldrich, 3 mmol) and 30 cm^3 of acetonitrile solvent were added. About 150 mg of catalyst were charged and the reaction flask was immersed in an oil bath maintained at 70 °C. The reaction mixture was stirred vigorously and samples were withdrawn periodically and analyzed by an Agilent Technologies 7890A gas chromatograph equipped with a DB-FFAP column and an FID detector. The carbon balance was >99+% based on TS consumed and the products (*trans*-stilbene oxide, benzaldehyde, benzoic acid) detected.

Results and Discussion

Low angle XRD patterns of calcined Ce–MCM-48 samples with different n_{Si}/n_{Ce} atomic ratios are shown in Figure 1. An intense peak corresponding to the d_{211} reflection and a weak d_{220} shoulder were observed corresponding to the *Ia3d* cubic phase typical for the MCM-48 material (*27*). A distinct shoulder peak seen

In Novel Materials for Catalysis and Fuels Processing; Bravo-Suárez, J., et al.;
ACS Symposium Series; American Chemical Society: Washington, DC, 2013.

clearly in samples with lower Ce contents was not resolved in samples with higher Ce contents [Ce–MCM-48(10)], suggesting that higher amounts of the heteroatom lead to a relative disordering of the pore structure. The cubic unit cell parameter (a_0) estimated from the diffraction peak (d_{211}), using the correlation $a_0 = d_{211} \times \sqrt{6}$, is listed in Table 1. The a_0 values for the Ce–MCM-48 samples increase slightly with an increase in the Ce content. Due to the larger ionic radius of Ce compared to Si, the incorporation of Ce ions in the framework might increase the unit cell parameter (*9*).

It is well known that extraframework metal oxide (i.e., CeO_2) species form with higher amounts of Ce loading. Powder XRD patterns of Ce–MCM-48 in the high angle region (10–80°) are shown in Figure 2. The diffraction peaks observed at 2θ values of 27.8, 47, and 56° are attributed to the (111), (220), and (311) planes of CeO_2 (*28*). These peaks are observed for all Ce–MCM-48 samples, except the Ce–MCM-48(100) sample. The intensity of these characteristic peaks increased gradually with Ce content suggesting that the CeO_2 species in the channel or in the extra-framework of the MCM-48 increase with Ce loading. Based on the XRD results, it is clear that Ce is only partially incorporated as ions into the MCM-48 framework. Elemental (Si and Ce) analyses of the samples performed by ICP–OES reveal that the n_{Si}/n_{Ce} atomic ratios in the final calcined Ce–MCM-48 samples are lower than the corresponding ratios used in the synthesis solution (see Table 1), which is also observed for other elements incorporated by this procedure (*13*, *14*).

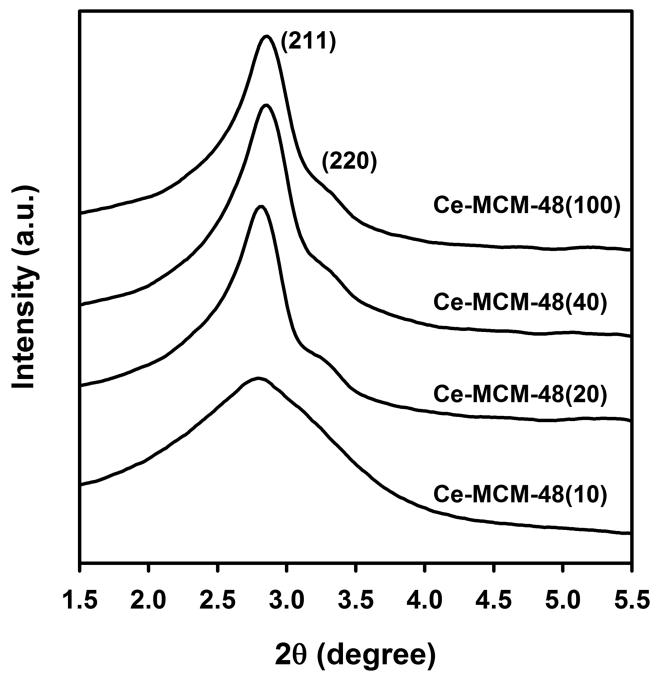

Figure 1. Low angle XRD of Ce–MCM-48 (Si/Ce) samples in the 2θ range of 1.5–5.5°

In Novel Materials for Catalysis and Fuels Processing; Bravo-Suárez, J., et al.;
ACS Symposium Series; American Chemical Society: Washington, DC, 2013.

Table 1. Physicochemical characteristics of calcined Ce–MCM-48 samples with different cerium content

Ce–MCM-48 (Si/Ce)[a]	*Si/Ce*[b]	a_0 [c] *nm*	S_{BET} [d] $m^2\ g^{-1}$	V_p [e] $cm^3\ g^{-1}$	$d_{P,\ BJH}$ [f] *nm*
Ce–MCM-48(100)	142	7.6	1251	0.72	2.12
Ce–MCM-48(50)	58	7.6	1225	0.70	2.15
Ce–MCM-48(25)	28	7.7	1108	0.68	2.22
Ce–MCM-48(10)	14	7.7	1077	0.62	2.71

[a] Molar ratio in the synthesis gel [b] Molar ratio determined from ICP–OES [c] $a_0 = d_{211} \times \sqrt{6}$ [d] S_{BET} = specific surface area determined using Brunauer–Emmett–Teller (BET) equation from adsorption isotherm at P/P_0 between 0.05 and 0.30 [e] $V_{P,BJH}$ = total pore volume at 0.99 P/P_0 [f] $d_{P,BJH}$ = desorption pore diameter

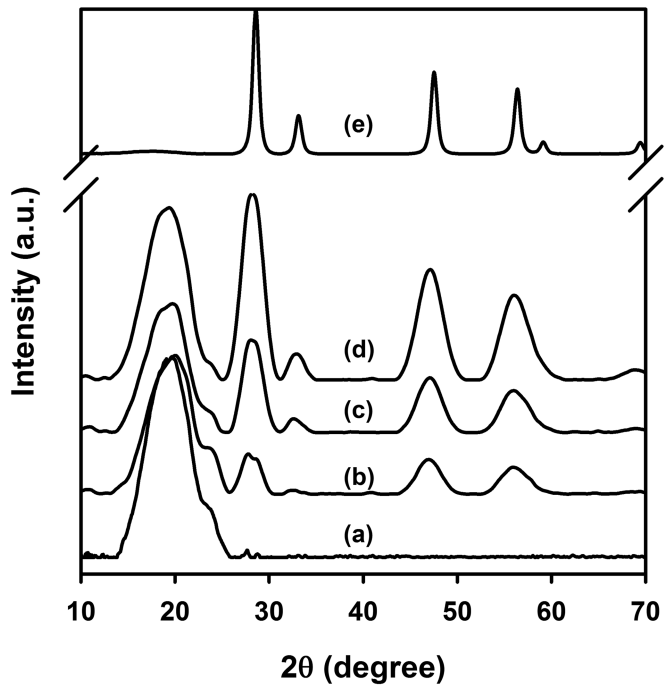

Figure 2. The XRD patterns of the calcined Ce–MCM-48 samples with different Si/Ce atomic ratio of (a) 100, (b) 40, (c) 20, and (d) 10 compared with (e) CeO_2.

Nitrogen physisorption isotherms and the corresponding pore size distribution of the Ce–MCM-48 samples are shown in Figure 3a. All the samples show a Type IV isotherm typical of mesoporous solids (*29*). A sharp inflection exhibited by Ce–MCM-48 samples around P/P_0 = 0.2–0.4 is characteristic of capillary

In Novel Materials for Catalysis and Fuels Processing; Bravo-Suárez, J., et al.;
ACS Symposium Series; American Chemical Society: Washington, DC, 2013.

condensation within the mesoporous. Additionally, these isotherms are typical of highly ordered mesoporous solids with uniform pore sizes as also inferred from low angle XRD and further confirmed by the uniform pore size distribution (Figure 3b). The Ce–MCM-48(10) sample exhibits two H1 hysteresis loops, in the 0.2–0.4 and 0.7–1.0 P/P_0 ranges. This behavior is attributed to framework confined and textural confined mesoporosity (*16*). The hysteresis loop in the 0.7–1.0 P/P_0 range is consistent with the observed mesoporosity hump around 10 nm from pore size distribution measurements (Figure 3b). The larger area of the hysteresis loop observed in the 0.2–0.4 P/P_0 range indicates that the size of the pore channels in Ce–MCM-48(10) is not as uniform as in the other Ce–MCM-48 samples. This feature is also noticed as peak broadening in the low angle XRD analysis of the Ce–MCM-48(10) (see Figure 1).

The textural properties of the Ce–MCM-48 materials derived from nitrogen physisorption analysis are listed in Table 1. In general, the surface area and the pore volume of the Ce–MCM-48 samples are in the range of 1050–1250 $m^2\ g^{-1}$ and 0.62–0.72 $cm^3\ g^{-1}$, respectively. Both the surface area and pore volume decrease with an increase in Ce content. The pore diameter estimated from the desorption isotherms using the Barrett–Joyner–Halenda (BJH) equation increases with an increase in cerium content from 2.12 (for $n_{Si}/n_{Ce} = 100$) to 2.71 nm (for $n_{Si}/n_{Ce} = 10$). Interestingly, the Ce–MCM-48(10) sample shows an abrupt increase (rather than a gradual increase up to that point) in absorption at relative pressure (P/P_0) values between 0.9 and 1.0, suggesting the existence of some macropores in this sample. The wall thickness calculated using the correlation [$w_t = (a_0/3.0919) - (d_p/2)$] is 1.4 nm.

The MCM-48 type structure with uniform pore channel was further evidenced from a representative TEM image of the Ce–MCM-48(20) sample (Figure 4). In addition, at a higher resolution, ceria nanoparticles of about 2–3 nm could be observed.

The nature of Ce coordination in the mesoporous structure was investigated using diffuse reflectance UV–Vis spectroscopy, a sensitive tool to probe for the presence of framework and extraframework transition metal species. The diffuse reflectance UV–Vis spectra of the Ce–MCM-48 samples compared with bulk CeO_2 is displayed in Figure 5. An intense absorption peak centered around 300 nm, characteristic of ligand to metal charge transfer (LMCT) between O^{2-} and framework Ce^{4+} in tetrahedral coordination (*16*) was noticed for all the Ce–MCM-48 samples. The intensity of this peak increases with an increase in Ce content. However, Ce–MCM-48(10) showed a considerable decrease in intensity of this peak. This is attributed to a decrease in the amount of framework incorporated Ce^{4+} ions in this sample compared to Ce–MCM-48(20) sample. In reported mesoporous silicas containing similar amounts of Ce, two distinct peaks corresponding to tetra- and hexa-coordinated species (around 300 and 400 nm, respectively) have been reported (*22*, *23*). The peak observed around 400 nm is attributed to the presence of bulk CeO_2 species. Interestingly, bulk CeO_2 (micron powder, Aldrich) exhibits a spectrum with two distinct maxima at around 269 and 342 nm. While high angle XRD results suggest the existence of CeO_2 species in Ce–MCM-48(40 and 20) samples, the diffuse reflectance UV–Vis peaks corresponding to bulk CeO_2 species could not be resolved due to the broadness of

In Novel Materials for Catalysis and Fuels Processing; Bravo-Suárez, J., et al.;
ACS Symposium Series; American Chemical Society: Washington, DC, 2013.

the 300 nm absorption peak. We therefore conclude that the amount of bulk CeO_2 species in these Ce–MCM-48 samples is too small for its peaks to be resolved in the diffuse reflectance UV–Vis spectra.

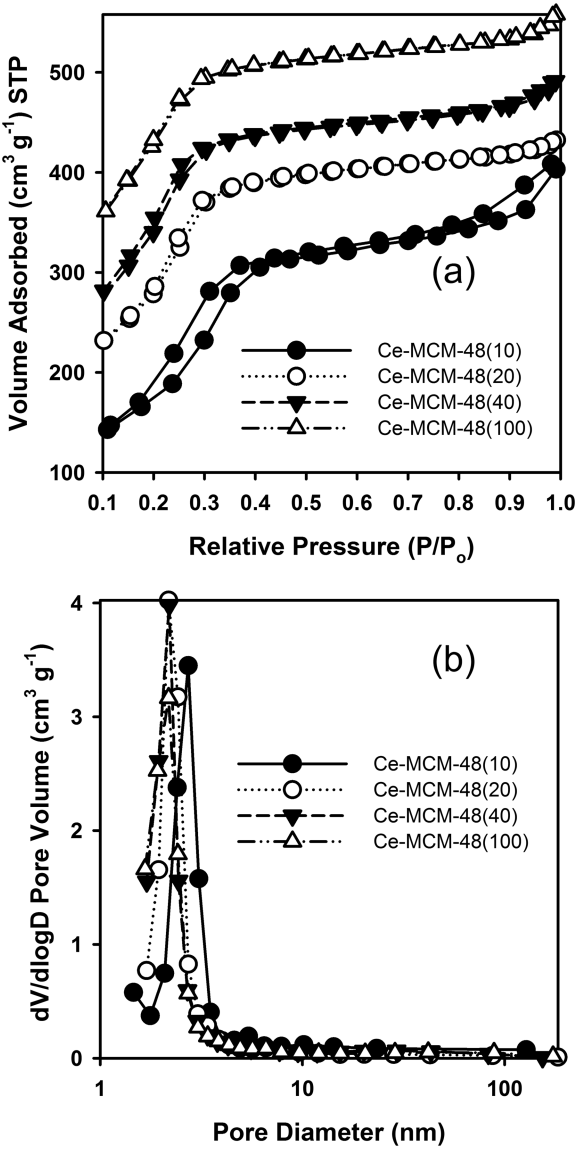

Figure 3. N_2 physisorption isotherms (a) and BJH desorption pore-size distributions (b) of calcined Ce–MCM-48 with different Si/Ce atomic ratios

In Novel Materials for Catalysis and Fuels Processing; Bravo-Suárez, J., et al.;
ACS Symposium Series; American Chemical Society: Washington, DC, 2013.

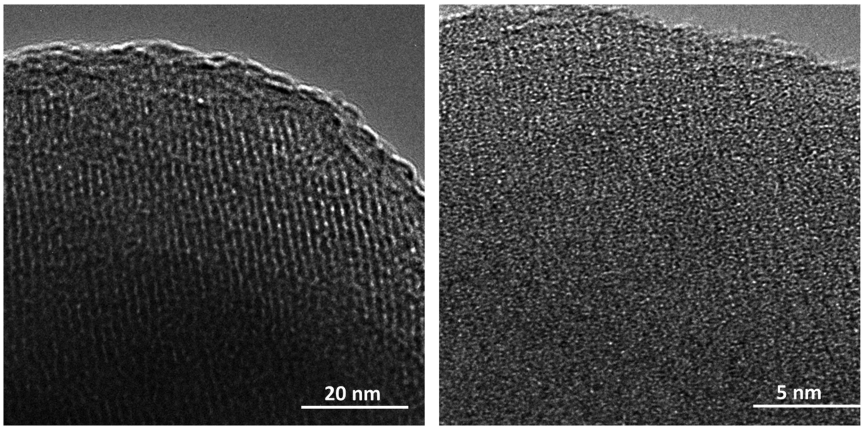

Figure 4. High resolution TEM image of Ce–MCM-48(20) at magnification of 20 and 5 nm

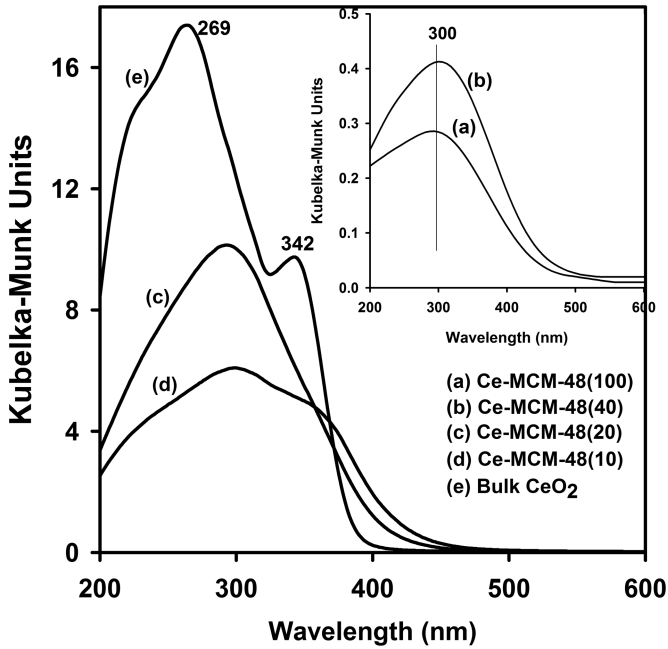

Figure 5. Diffuse reflectance UV–Vis spectra of calcined Ce–MCM-48 samples with different n_{Si}/n_{Ce} atomic ratio of (a) 100, (b) 40, (c) 20, and (d) 10 compared with (e) bulk CeO_2.

To identify metal oxide species, Raman spectroscopy was also employed. Figure 6 shows the results of Raman spectra of Ce–MCM-48 samples with different n_{Si}/n_{Ce} atomic ratios. The Raman bands observed at around 490, 600, and 800 cm^{-1} are assigned to silica (*30*). A prominent peak centered around 453

cm^{-1} was observed for all except the Ce–MCM-48(100) sample. In addition, the intensity of this peak increases with Ce loading. CeO_2 exhibits a strong and sharp peak centered at 465 cm^{-1} in the Raman spectra and this peak is red shifted with a decrease in CeO_2 particle size (*31*, *32*). Thus, the observed Raman results also provide evidence for the presence of CeO_2 species in the Ce–MCM-48 samples and are consistent with the XRD and diffuse reflectance UV–Vis results.

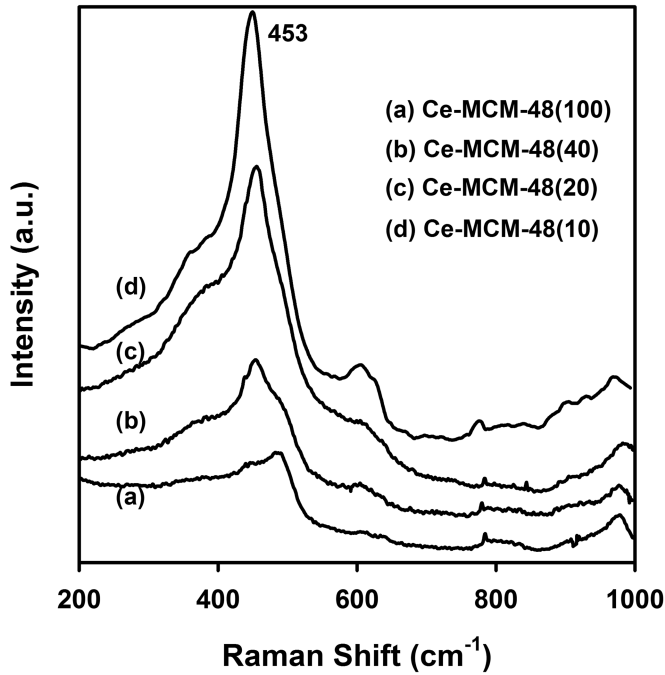

Figure 6. Raman spectra of calcined Ce–MCM-48 samples with different Ce content.

The TPR profile of Ce–MCM-48(100) showed a broad H_2 consumption with a peak centered at around 550 °C (Figure 7). This peak center shifted to a lower temperature (~530 °C) for the Ce–MCM-48(40) sample having approximately 2.5 times more Ce content. However, for higher Ce content samples, Ce–MCM-48(20 and 10), two peaks were noticed. The first peak, observed around 490 °C, was approximately 60 °C lower than for the Ce–MCM-48(100) sample. The second peak was observed around 608 °C for the Ce–MCM-48(20) and shifted to a higher temperature (625 °C) for the Ce–MCM-48(10) sample. The TPR profile of bulk CeO_2 has two reduction peaks (*33*). The low temperature reduction peak observed by Yao et.al. around 500 °C, is attributed to the reduction of the most easily reducible surface-capping oxygen of CeO_2 and the bulk reduction of CeO_2 was observed at a higher temperature (~820 °C) (*33*). The shifting of high temperature reduction peak to lower values has also been reported with a decrease in CeO_2 particle size (*34*). The absence of high temperature reduction peaks in all the Ce–MCM-48 samples suggests that the CeO_2 is present as highly dispersed small

particles. In the case of the Ce–MCM-48 (100 and 40), only peaks centered around 530 and 550 °C are evident. In the case of Ce–MCM-48(10 and 20) samples, the presence of twin peaks around 500 and 600 °C may indicate an experimental artifact. The TPR characteristic number *P* is in the range of 22–42 for Ce–MCM-48(100 and 40). However, the *P* values are significantly higher (80–160) for the Ce–MCM-48(20 and 10) samples indicating the possible presence of anomalies due to the experimental conditions at these higher CeO_2 loadings.

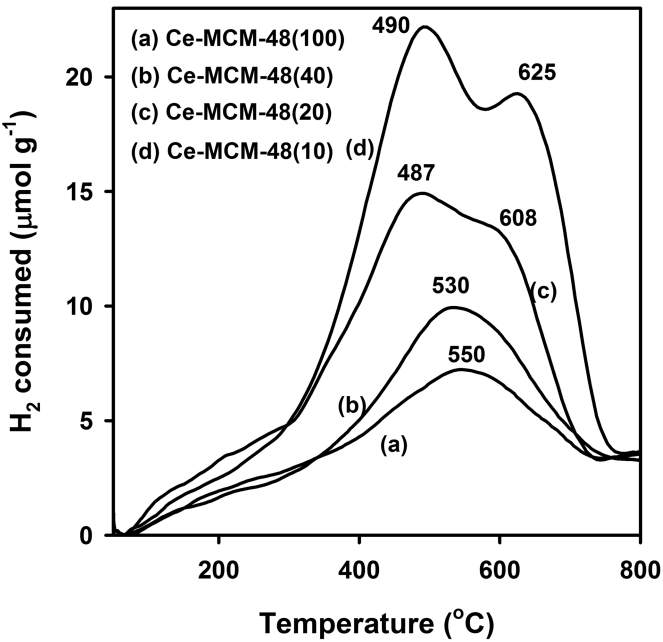

Figure 7. H_2-TPR profile of Ce–MCM-48 samples with different Ce content.

The catalytic activity of the Ce–MCM-48 samples was tested by oxidizing *trans*-stilbene (TS) with *tert*-butyl hydroperoxide (TBHP). In general, TS oxidation over Ce–MCM-48 with TBHP results in *trans*-stilbene oxide (TSO) as the main product with benzaldehyde (PhCHO) and benzoic acid as side products (Scheme 1). We varied the n_{TBHP}/n_{TS} molar ratio from 3 to 10 to investigate TS conversion and product selectivity. The reactions were performed at 70 °C and ambient pressure in 12 h batch runs over the Ce–MCM-48(20) catalyst. The pore diffusion resistance was calculated following methods described on recently published literature (*35*), whose value is less than 0.2. This means that the pore diffusion resistance can be considered to be insignificant under our reaction conditions.

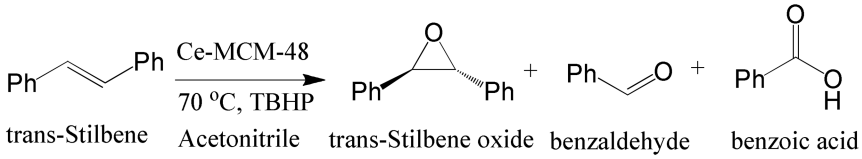

Scheme 1. Products for trans-stilbene epoxidation.

As shown in Figure 8, the TS conversion proportionally increased with the amount of TBHP oxidant. However, TSO selectivity drastically decreased at higher oxidant concentrations. This is attributed to the reaction of the epoxide with excess water present at higher TBHP concentrations. Whereas most literature reports suggest that an optimum n_{TBHP}/n_{TS} molar ratio of 10 is needed to achieve higher TS conversion and TSO selectivity (*36–39*), our studies indicate that the TBHP efficiency is higher when the n_{TBHP}/n_{TS} molar ratio is much lower. Similar results were reported for manganese oxide containing SBA-15 catalyst (*37*). Hence an optimum n_{TBHP}/n_{TS} molar ratio of 3 was chosen for subsequent studies.

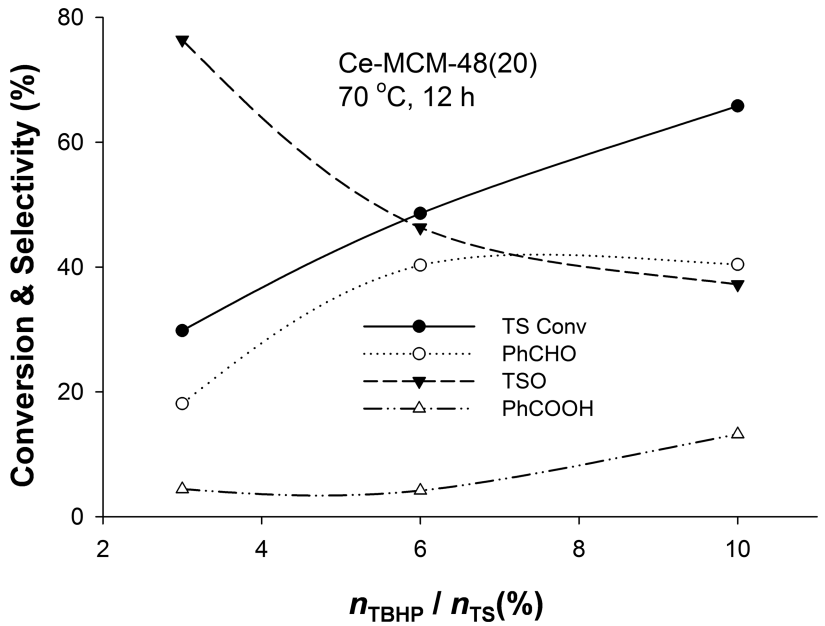

Figure 8. Effect of n_{TBHP}/n_{TS} molar ratio on TS conversion and product selectivies over Ce–MCM-48(20). Reaction conditions: n_{TBHP} / n_{TS} = 3–10, n_{TS} = 1 mmol, m_{cat}= 150 mg, $V_{acetonitrile}$= 30 cm³, t = 24 h, T = 70 °C.

At a n_{TBHP}/n_{TS} molar ratio of 3, we tested the cerium containing MCM-48 samples for TS conversion and TSO selectivity. All samples showed higher TS conversion compared to the control reaction without catalyst (Table 2) with an increase in TSO selectivity with Ce loading (Figure 9). For 24 h runs, the TS conversion was 16% with the Ce–MCM-48(100) sample and increased linearly with cerium loading, reaching 44% with the Ce–MCM-48(10) sample. At low TS conversions, approximately 38% selectivity towards PhCHO was observed indicating that in addition to the epoxidation product, the cleavage of carbon–carbon double bond is also favored. This trend is reversed at longer reaction times when more *tert*-butanol forms as a result of increased TBHP conversion. The *tert*-butanol may interact with the silanol groups of the catalyst via hydrogen bonding. This deactivation of silanol groups is believed to increase the selectivity toward TSO (*38*).

Table 2. TS conversion and product selectivites over Ce–MCM-48(40) compared with Ce/SiO_2 and without catalyst[a]

Catalyst	X_{TS} (%)	S_{PhCHO} (%)	S_{TSO} (%)	S_{PhCOOH} (%)	S_{Others} (%)
None	6	26	71	2	1
Ce/SiO_2	19.8	23.3	58.1	7.2	11.4
CeO_2	22.3	32.0	48.8	13.2	5.9
Ce–MCM-41(40)[b]	18.8	20.6	66.6	6.7	6.1
Ce–MCM-48(40)	23.4	17.6	77.1	4.2	1.2

[a] Reaction conditions: $n_{TBHP} / n_{TS} = 3$, $n_{TS} = 1$ mmol, $m_{cat} = 150$ mg, $V_{acetonitrile} = 30$ cm^3, $t =$ 24 h, T = 70 °C. [b] Prepared according to reference (*16*).

We compared the catalytic oxidation activitities of the ordered Ce–MCM-48 catalysts to several controls: (i) no catalyst, (ii) a cerium-containing amorphous silica sample (Ce/SiO_2), and (iii) commercial CeO_2. With no catalyst present, the TS conversion is 6% with 71% selectivity to TSO and 26% selectivity to PhCHO (Table 2). The amorphous silica sample (Ce/SiO_2), with a n_{Si}/n_{Ce} atomic ratio of 40, was synthesized by a wet impregnation method. It showed an appreciable TS conversion of 19.8% with a TSO selectivity of 58%. However, about 11.4% of unknown side products were also noted. All these reaction mixtures were filtered hot after after the reaction and an ICP analysis of the filtrate showed 2–8% Ce-leaching after 24 h.

Interestingly, Ce–MCM-41 showed relatively lower conversion (attributed to pore diffusion limitations) compared to Ce–MCM-48 and other Ce based catalysts studied. Guo et. al. studied TS epoxidation with TBHP over V–MCM-41, V–SBA-15 and V–TUD-1 catalysts and estimated the activation energies of these catalysts as 24.0, 28.1 and 43.9 kJ mol^{-1}, respectively. The low activation energy observed for MCM-41 and even SBA-15 type materials suggest that the reaction is likely pore diffusion controlled (*38*).

In Novel Materials for Catalysis and Fuels Processing; Bravo-Suárez, J., et al.;
ACS Symposium Series; American Chemical Society: Washington, DC, 2013.

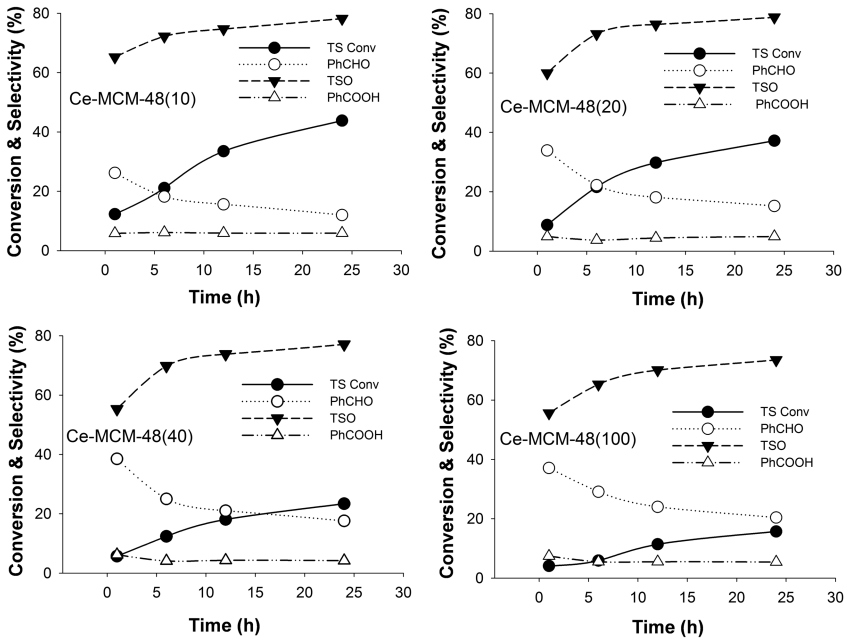

Figure 9. Epoxidation of trans-stilbene with tert-butyl hydroperoxide over Ce–MCM-48 catalysts with different Si/Ce atomic ratio. Reaction conditions: n_{TBHP} / n_{TS} = 3, n_{TS} = 1 mmol, m_{cat}= 150 mg, $V_{acetonitrile}$= 30 cm³, T = 70 °C.

To probe further, commercial CeO_2 (25 mg, 0.04 mmol Ce) was also tested. The amount of Ce present in CeO_2 and Ce–MCM-48(40) is nearly the same. Interestingly, about 22% TS conversion (similar to Ce–MCM-48(40) sample) with 49% TSO selectivity and 32% PhCHO selectivity were observed. However, secondary reactions such as the formation of PhCOOH (about 13%) and unidentified high boiling point compounds (6%) indicate that CeO_2 is active but not selective. The higher selectivity for epoxide formation can be explained as follows: TBHP is chemisorbed on active Ce^{4+} sites resulting in the activation of the proximal oxygen of the peroxo species which is then inserted across the C–C double bond of TS yielding TSO (Scheme 2) (*39*). Based on the foregoing observations, it is surmised that framework-incorporated Ce is both active and selective for epoxide formation. Nevertheless, small amounts of CeO_2 nanoclusters present at high Ce loadings in Ce–MCM-48 samples might also promote the reaction albeit in a non-selective manner.

In Novel Materials for Catalysis and Fuels Processing; Bravo-Suárez, J., et al.;
ACS Symposium Series; American Chemical Society: Washington, DC, 2013.

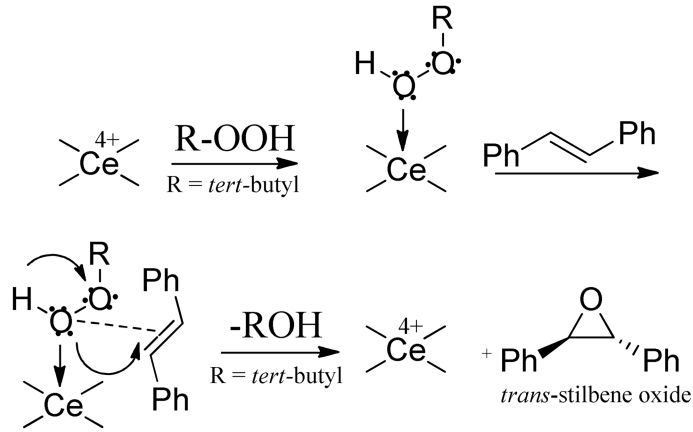

Scheme 2. Possible mechanistic pathway of TSO formation at Ce^{4+} active centers.

Conclusion

Ce-containing MCM-48 samples were successfully prepared by a rapid and facile synthesis procedure at room temperature conditions. The cubic phase of the Ce–MCM-48 and the partial incorporation of Ce are verified by XRD results. The Ce coordination as Ce^{4+} is further confirmed by diffuse reflectance UV–Vis. XRD and Raman spectroscopy results confirm the presence of small amounts of hexa-coordinated CeO_2 at higher cerium loadings. Ce–MCM-48 materials are shown to be active for *trans*-stilbene conversion and framework incorporated Ce^{4+} ions are shown to be particularly selective as active sites for *trans*-stilbene oxide formation.

Acknowledgments

This research was partially supported with funds from the National Science Foundation Accelerating Innovation Research Grant (IIP-1127765).

References

1. Kresge, C. T.; Leonowicz, M. E.; Roth, W. J.; Vartuli, J. C.; Beck, J. S. *Nature* **1992**, *359*, 710–712.
2. Wang, K.; Lin, Y.; Morris, M. A.; Holmes, J. D. *J. Mater. Chem.* **2006**, *16*, 4051.
3. Diaz, I.; Perez-Pariente, J.; Terasaki, O. *J. Mater. Chem.* **2004**, *14*, 48–53.
4. Campelo, J. M.; Luna, D.; Luque, R.; Marinas, J. M.; Romero, A. A.; Calvino, J. J.; Rodriguez-Luque, M. P. *J. Catal.* **2005**, *230*, 327–338.
5. Zhao, W.; Luo, Y. F.; Deng, P.; Li, Q. *Z. Catal. Lett.* **2001**, *73*, 199–202.
6. Dapurkar, S. E.; Sakthivel, A.; Selvam, P. *New J. Chem.* **2003**, *27*, 1184–1190.
7. Vralstad, T.; Oye, G.; Stocker, M.; Sjoblom, J. *Microporous Mesoporous Mater.* **2007**, *104*, 10–17.

8. Zhao, D.; Goldfarb, D. *J. Chem. Soc., Chem. Commun.* **1995**, 875–876.
9. Shao, Y. F.; Wang, L. Z.; Zhang, J. L.; Anpo, M. *J. Phys. Chem. B* **2005**, *109*, 20835–20841.
10. Chen, L. F.; Zhou, X. L.; Norena, L. E.; Wang, J. A.; Navarrete, J.; Salas, P.; Montoya, A.; Del Angel, P.; Llanos, M. E. *Appl. Surf. Sci.* **2006**, *253*, 2443–2451.
11. Boote, B.; Subramanian, H.; Ranjit, K. T. *Chem. Commun. (Cambridge, U. K.)* **2007**, 4543–4545.
12. Peng, R.; Zhao, D.; Dimitrijevic, N. M.; Rajh, T.; Koodali, R. T. *J. Phys. Chem. C* **2011**, *116*, 1605–1613.
13. Zhao, D.; Rodriguez, A.; Dimitrijevic, N. M.; Rajh, T.; Koodali, R. T. *J. Phys. Chem. C* **2010**, *114*, 15728–15734.
14. Subramanian, H.; Nettleton, E. G.; Budhi, S.; Koodali, R. T. *J. Mol. Catal. A: Chem.* **2010**, *330*, 66–72.
15. Molander, G. A. *Chem. Rev. (Washington, DC, U. S.)* **1992**, *92*, 29–68.
16. Laha, S. C.; Mukherjee, P.; Sainkar, S. R.; Kumar, R. *J. Catal.* **2002**, *207*, 213–223.
17. Kadgaonkar, M. D.; Laha, S. C.; Pandey, R. K.; Kumar, P.; Mirajkar, S. P.; Kumar, R. *Catal. Today* **2004**, *97*, 225–231.
18. Araujo, A. S.; Aquino, J. M. F. B.; Souza, M. J. B.; Silva, A. O. S. *J. Solid State Chem.* **2003**, *171*, 371–374.
19. Yao, W. H.; Chen, Y. J.; Min, L.; Fang, H.; Yan, Z. Y.; Wang, H. L.; Wang, J. Q. *J. Mol. Catal. A: Chem.* **2006**, *246*, 162–166.
20. Prabhu, A.; Kumaresan, L.; Palanichamy, M.; Murugesan, V. *Appl. Catal., A* **2010**, *374*, 11–17.
21. Longloilert, R.; Chaisuwan, T.; Luengnaruemitchai, A.; Wongkasemjit, S. *J. Sol-Gel Sci. Technol.* **2012**, *61*, 133–143.
22. Zhan, W.; Lu, G.; Guo, Y.; Guo, Y.; Wang, Y.; Wang, Y.; Zhang, Z.; Liu, X. *J. Rare Earth* **2008**, *26*, 515–522.
23. Selvaraj, M.; Park, D. W.; Ha, C. S. *Microporous Mesoporous Mater.* **2011**, *138*, 94–101.
24. Timofeeva, M. N.; Jhung, S. H.; Hwang, Y. K.; Kim, D. K.; Panchenko, V. N.; Melgunov, M. S.; Chesalov, Y. A.; Chang, J. S. *Appl. Catal., A* **2007**, *317*, 1–10.
25. van de Water, L. G. A.; Bulcock, S.; Masters, A. F.; Maschmeyer, T. *Ind. Eng. Chem. Res.* **2007**, *46*, 4221–4225.
26. Bravo-Suárez, J. J.; Subramaniam, B.; Chaudhari, R. V. *J. Phys. Chem. C* **2012**, *116*, 18207–18221.
27. Vartuli, J. C.; Kresge, C. T.; Leonowicz, M. E.; Chu, A. S.; McCullen, S. B.; Johnson, I. D.; Sheppard, E. W. *Chem. Mater.* **1994**, *6*, 2070–2077.
28. Li, J.; Hao, Y.; Li, H.; Xia, M.; Sun, X.; Wang, L. *Microporous Mesoporous Mater.* **2009**, *120*, 421–425.
29. Sing, K. S. W. *Pure Appl. Chem.* **1985**, *57*, 603–619.
30. Strunk, J.; Vining, W. C.; Bell, A. T. *J. Phys. Chem. C* **2011**, *115*, 4114–4126.
31. Yang, C. C.; Li, S. *J. Phys. Chem. B* **2008**, *112*, 14193–14197.
32. Scholes, F. H.; Hughes, A. E.; Hardin, S. G.; Lynch, P.; Miller, P. R. *Chem. Mater.* **2007**, *19*, 2321–2328.

In Novel Materials for Catalysis and Fuels Processing; Bravo-Suárez, J., et al.;
ACS Symposium Series; American Chemical Society: Washington, DC, 2013.

33. Yao, H. C.; Yao, Y. F. Y. *J. Catal.* **1984**, *86*, 254–265.
34. Giordano, F.; Trovarelli, A.; de Leitenburg, C.; Giona, M. *J. Catal.* **2000**, *193*, 273–282.
35. Wan, H.; Chaudhari, R.; Subramaniam, B. *Top. Catal.* **2012**, *55*, 129–139.
36. Zhang, Q.; Wang, Y.; Itsuki, S.; Shishido, T.; Takehira, K. *J. Mol. Catal. A: Chem.* **2002**, *188*, 189–200.
37. Tang, Q.; Hu, S.; Chen, Y.; Guo, Z.; Hu, Y.; Chen, Y.; Yang, Y. *Microporous Mesoporous Mater.* **2010**, *132*, 501–509.
38. Guo, Z.; Zhou, C.; Hu, S.; Chen, Y.; Jia, X.; Lau, R.; Yang, Y. *Appl. Catal., A* **2012**, *419–420*, 194–202.
39. Hu, S. Q.; Liu, D. P.; Wang, C. A.; Chen, Y. T.; Guo, Z.; Borgna, A.; Yang, Y. H. *Appl. Catal., A* **2010**, *386*, 74–82.

In Novel Materials for Catalysis and Fuels Processing; Bravo-Suárez, J., et al.;
ACS Symposium Series; American Chemical Society: Washington, DC, 2013.

Chapter 9

Rhodium Nanoparticles Confined in Ordered Mesoporous Carbon: Microscopic Characterization and Catalytic Application for Synthesis Gas Conversion to Ethanol

Song-Hai Chai,[*,1] Jane Y. Howe,[2] Michelle Kidder,[1] Xiqing Wang,[1] Viviane Schwartz,[3] Steven H. Overbury,[1,3] Sheng Dai,[1,3,4] and De-en Jiang[*,1]

[1]Chemical Sciences Division, Oak Ridge National Laboratory, 1 Bethel Valley Road, Oak Ridge, Tennessee 37831, USA
[2]Materials Science and Technology Division, Oak Ridge National Laboratory, 1 Bethel Valley Road, Oak Ridge, Tennessee 37831, USA
[3]Center for Nanophase Materials Sciences, Oak Ridge National Laboratory, 1 Bethel Valley Road, Oak Ridge, Tennessee 37831, USA
[4]Department of Chemistry, University of Tennessee, 1331 Circle Park Drive, Knoxville, Tennessee 37966, USA
[*]E-mail: chais@ornl.gov; jiangd@ornl.gov

Rh nanoparticles (2−4 nm) confined in the nanopores (6.5 nm) of ordered mesoporous carbon (OMC) were characterized by scanning transmission electron microscopy imaging on the cross-section of OMC grains generated using state-of-the-art focused ion beam lift-out technique. The catalytic activity (turnover frequency) and ethanol selectivity of Rh/OMC for synthesis gas conversion to ethanol are enhanced greatly when triply promoted with Mn, Li, and Fe oxides. Compared with traditional mesoporous silica having similar pore size, OMC as the support of promoted Rh catalyst increases the ethanol selectivity along with suppressing the formation of undesired hydrocarbons, although its overall activity is lowered to some extent.

In Novel Materials for Catalysis and Fuels Processing; Bravo-Suárez, J., et al.;
ACS Symposium Series; American Chemical Society: Washington, DC, 2013.

Introduction

Catalytic conversion of synthesis gas to ethanol ($2CO + 4H_2 \rightarrow C_2H_5OH + H_2O$), as an alternative fuel or fuel additive to petroleum-derived fuels, has been extensively studied in an effort to improve air quality and increase energy security by using renewable energy sources such as biomass (*1*, *2*). Hydrocarbons and CO_2 are often formed simultaneously by Fischer-Tropsch reaction, water-gas-shift (WGS) reaction, and Boudouard reaction.

$$nCO + (2n+1)H_2 \rightarrow C_nH_{2n+2} + nH_2O \ (n = 1, 2, 3, \ldots) \text{ (Fischer-Tropsch reaction)}$$

$$CO + H_2O \rightarrow CO_2 + H_2 \text{ (WGS reaction)}$$

$$2CO \rightarrow C + CO_2 \text{ (Boudouard reaction)}$$

Supported rhodium (Rh) catalysts promoted by transition metal oxides (e.g., Mn, Fe, V) and alkali oxides (e.g., Li, Cs) have been known among the most selective catalysts for the ethanol production from CO hydrogenation (*3*). The major challenge for Rh-based catalysts is their low ethanol selectivity relative to undesired light hydrocarbons (C_1−C_4) that are thermodynamically favored. Support materials, other than the promoters, influence the catalytic activity and ethanol selectivity greatly by means of their textural properties (porosity and surface area) as well as unique interaction with active components. Much attention has been given to inorganic metal oxides (e.g., SiO_2, Al_2O_3, and TiO_2) (*4*, *5*), but very few researchers have focused on carbon materials, especially ordered mesoporous carbon (OMC) as the supports of Rh-based catalysts. Pan et al. (*6*) reported that confining Rh nanoparticles inside multi-wall carbon nanotubes (MWCNTs) led to more than a two-fold enhancement in the yield of C_2^+-oxygenates in comparison to unconfined metal particles located on the external surface of MWCNTs. Such a confined environment can also be provided by the OMC supports because of their comparable pore size (4−10 nm). In addition, the OMC can be prepared facilely by a soft-template method in a variety of morphologies such as powder, fiber, membrane, and monolithic column (*7*–*9*), thereby conferring more flexibility to the support than MWCNTs.

The size and morphology of metal nanoparticles supported on porous solids are often characterized by using electron microscopy such as transmission electron microscope (TEM). However, direct observations of metal nanoparticles in the interior of a porous solid grain have been seldom reported, due to the difficulty in preparing cross-sectional samples. Focused ion beam (FIB) lift-out is a promising technique developed in the past decade for site-specific preparation of ultra-thin (e.g., < 200 nm) lamellar, cross-sectional TEM specimens detached from their bulk materials including semiconductors, metal, ceramics, polymers, and biological materials (*10*–*13*). This technique makes it possible for direct observation and characterization on the interior of solid grains. Using a TEM capable of imaging in transmission electron (TE) and secondary electron (SE) modes, the surface (SE) and bulk (TE) features of supported metal catalysts can be well studied.

This work aims to develop a reliable protocol to load Rh nanoparticles into the nanopores of OMC and characterize the metal particles by scanning transmission

In Novel Materials for Catalysis and Fuels Processing; Bravo-Suárez, J., et al.;
ACS Symposium Series; American Chemical Society: Washington, DC, 2013.

electron microscopy (STEM) in combination with the FIB lift-out technique. The catalytic activity and ethanol selectivity of Rh/OMC for CO hydrogenation are shown to be enhanced greatly when promoted triply with Mn, Li, and Fe oxides. For comparison, a traditional mesoporous silica (SBA-15) is examined to study the support effect on the catalytic performance of promoted Rh catalysts.

Experimental

Chemicals

All chemicals were used as received without further purification unless specified otherwise. Resorcinol (> 99.0 wt %), triblock copolymer Pluronic® F127 ($EO_{106}PO_{70}EO_{106}$), formaldehyde (37 wt % aqueous solution), and hydrochloric acid (37 wt %) were purchased from Sigma-Aldrich. Anhydrous ethanol (absolute 200 proof) was purchased from Fisher Scientific, and high purity deionized water (resistance of ~18.2 MΩ) was produced by water purification systems (ZRQS6005Y, Millipore). Hydrogen (H_2, 99.999%) and carbon monoxide (CO, 99.5%) were purchased from Air Liquide, and CO was purified using 13X molecular sieves and active charcoal.

Catalyst Preparation

OMC was synthesized by carbonization of nanostructured polymeric composites, which were obtained by self-assembly of block copolymer (Pluronic F127) and phenolic resin (resorcinol-formaldehyde) under acidic conditions via the soft-template method (*14*). In a typical synthesis, 1.1 g of resorcinol and 1.1 g of Pluronic block copolymers (F127) were dissolved in 4.5 mL of C_2H_5OH and 4.5 mL of 3.0 M HCl aqueous solution. To this solution, 1.3 g of HCHO (37%) was then added. After stirring for about 11 min at room temperature, the clear mixture turned turbid, indicating the formation of resorcinol-HCHO-F127 nanocomposite, and a phase separation. The polymer-rich gel phase was obtained by centrifugation at 9500 rpm for 4 min after the mixture was stirred for 40 min. The gel was then loaded on a large Petri dish, dried at room temperature overnight, and subsequently cured at 353 and 393 K for 24 h each. Carbonization was carried out under N_2 atmosphere at 673 K for 2 h with a heating rate of 1 K min^{-1}, which was followed by further treatment at 1123 K for 3 h with a heating rate of 5 K min^{-1}.

Rh/OMC was prepared by impregnation of an OMC (dried at 473 K for 2 days before use) with the desired amount of $Rh(NO_3)_3$ in isopropanol solution at room temperature, followed by sonication for 2 h and removing the solvent slowly by stirring in air. The resulting solid was further dried in a tubular furnace in air flow at 393 K for 10 h (ramping at 1 K min^{-1}) and subsequently calcined in He flow at 673 K for 3 h (ramp at 4 K min^{-1}) to decompose the $Rh(NO_3)_3$. The same protocols were followed to prepare Mn, Li, and Fe triply promoted Rh/OMC catalyst (Rh-Mn-Li-Fe/OMC). $Mn(NO_3)_3$, $LiNO_3$, and $Fe(NO_3)_3$ were used as the precursors of Mn, Li, and Fe, respectively. For comparison with the OMC support, a traditional mesoporous silica (SBA-15), synthesized according to the

In Novel Materials for Catalysis and Fuels Processing; Bravo-Suárez, J., et al.;
ACS Symposium Series; American Chemical Society: Washington, DC, 2013.

method reported by Zhao et al. (*15*), was used to prepare supported Rh-Mn-Li-Fe catalyst by the same protocols. Table 1 lists the elemental composition and metal dispersion of the as-prepared catalysts.

Table 1. Composition and metal dispersion of supported Rh catalysts

Catalyst	*Elemental composition (wt %)*[a]				*Atomic ratio*				*H_2 chemisorption*	
	Rh	*Mn*	*Li*	*Fe*	*Rh*	*Mn*	*Li*	*Fe*	*D (%)*[b]	*d (nm)*[c]
Rh/OMC	3.1	-	-	-	1	-	-	-	46	2.4
Rh-Mn-Li-Fe/OMC	1.6	0.6	0.06	0.04	1	0.66	0.55	0.05	33	3.3
Rh-Mn-Li-Fe/SBA-15	1.5	0.5	0.05	0.05	1	0.62	0.49	0.06	41	2.7

[a] Measured by ICP-AES. [b] Dispersion of metallic Rh is defined as the percentage of surface Rh atoms per total Rh atoms assuming a 1: 1 stoichiometry of chemisorbed H to surface Rh atoms). [c] Metal particle size determined by H_2 chemisorption.

Catalyst Characterization

Nitrogen physisorption was performed on a Micromeritics Tristar analyzer at 77 K. Prior to measurement, the sample was purged with flowing N_2 at 423 K for 2 h. Specific surface area was calculated using the Brunauer–Emmett–Teller (BET) method (*16*) from the nitrogen adsorption data in the relative range (P/P_0) of 0.06–0.20. The total pore volume was determined from the amount of N_2 uptake at a relative pressure of $P/P_0 = 0.95$. The pore size distribution plot was derived from the adsorption branch of the isotherm based on the Barrett–Joyner–Halenda (BJH) model (*17*).

Electron microscopy was performed on a Hitachi HF-3300 field emission scanning transmission electron microscope (STEM) operating at 300 kV under SE, high-angle annular dark-field (Z-contrast), and bright-field high-resolution modes. Cross-sectional STEM specimen of Rh/OMC catalyst was prepared using FIB lift-out technique on a Hitachi NB-5000 Duet FIB-SEM System.

Elemental composition was measured by inductively coupled plasma atomic emission spectroscopy (ICP-AES).

Powder X-ray diffraction (XRD) patterns were recorded on a Siemens D5005 diffractometer with Ni-filtered Cu Kα (λ = 1.54 Å) radiation operating at 40 kV and 40 mA.

Dispersion of metallic Rh, defined as the percentage of surface Rh atoms per total Rh atoms, was measured by hydrogen (H_2) chemisorption at 298 K on a Micromeritics AutoChem II 2920. Approximately 100 mg of sample was placed in a U-type quartz reactor and reduced in flowing 4 vol% H_2/Ar (30 cm^3 (STP) min^{-1}) at 623 K for 2 h with a heating rate of 6 K min^{-1}. The sample was then purged with Ar (30 cm^3 (STP) min^{-1}) at 623 K for 10 min before cooling down to

In Novel Materials for Catalysis and Fuels Processing; Bravo-Suárez, J., et al.;
ACS Symposium Series; American Chemical Society: Washington, DC, 2013.

ambient temperature (298 K) in the same flow. Pulses of 4 vol % H_2/Ar (0.01455 cm^3-H_2 (STP) per pulse) were injected into the Ar carrier gas (30 cm^3 (STP) min^{-1}) flowing through the sample, until the saturation of H_2-chemisorption was attained. A thermal conductivity detector was used to monitor the volume of H_2 leaving the reactor after the addition of each pulse. The saturation point was determined when the integrated areas from successive eluted peaks were equal. The stoichiometry number of chemisorbed H atom per surface Rh atom is assumed to be unity. The average particle diameter (d_{Rh}, nm) of metallic Rh was calculated using equation 1:

$$d_{\mathrm{Rh}}(nm) = \frac{6 \times V_{\mathrm{Rh}}}{SA_{\mathrm{Rh}}} = \frac{6 \times (\frac{w_{\mathrm{Rh}}}{100 \times \rho_{\mathrm{Rh}}})}{6.023 \times 10^{23} \times (\frac{2 \times V_{\mathrm{STP}}}{22414}) \times A_{\mathrm{Rh}}} \quad [1]$$

Where V_{Rh} (nm^3 g_{Rh}^{-1}) is the volume per gram of Rh metal, SA_{Rh} (nm^2 g_{Rh}^{-1}) is the surface area per gram of Rh metal, w_{Rh} (wt %) is the weight percentage of Rh, D_{Rh} is the density of Rh metal (12.4×10^{21} nm^3 g_{Rh}^{-1}), V_{STP} (cm^3-H_2 (STP) g_{cat}^{-1}) is the measured volume of chemisorbed H_2 molecules at standard conditions per gram of catalyst, and A_{Rh} is the cross-sectional area of Rh atom (0.0752 nm^2).

Catalytic CO Hydrogenation

CO hydrogenation was carried out in a catalytic microreactor consisting of a single-pass tubular reactor (9.4 mm i.d. × 56 cm length, silica-lined 316 stainless steel tube) with an axisymmetric thermowell in contact with the catalyst bed. For each run, the catalyst (0.1 g), diluted with quartz sand (1.0 g), was reduced in situ in flowing H_2 (Air Liquide, 99.999%, 40 cm^3 (STP) min^{-1}) at 623 K and ambient pressure for 2 h. The catalytic experiments were performed at 593 K, 2.0 MPa total pressure, volumetric H_2/CO ratio of 2, and gas hourly space velocity (GHSV) of 36000 cm^3 (STP) $(h\ g_{cat})^{-1}$. The reactor effluent was analyzed on-line at regular intervals using a gas chromatograph (Agilent 7890) equipped with a thermal conductivity detector (TCD) and a flame ionization detector (FID). Reactants and products were separated using two capillary columns in series: HP-Plot-Q (0.32 mm o.d. × 20 μm film thickness × 30 m length) followed by HP-5 (0.32 mm o.d. × 1 μm film thickness × 30 m length). CO and major products (CO_2, CH_4, methanol, ethanol, acetaldehyde, ethyl acetate, and 1-propanol) were identified and calibrated by using their individual chemicals (> 99% in purity) purchased from Air Liquide and Sigma-Aldrich. The conversion of CO (X_{CO}) was reported as the fraction of CO that formed carbon-containing products according to equation 2, and the selectivity to carbon-containing product i (S_i) was reported on a carbon basis according to equation 3:

$$X_{\mathrm{CO}}\ (\%) = 100 \cdot \sum n_i \cdot C_i / (\sum n_i \cdot C_i + C_{\mathrm{CO}}) \quad [2]$$

$$S_i\ (\text{mol-C}\%) = 100 \cdot n_i \cdot C_i / \sum n_i \cdot C_i \quad [3]$$

In Novel Materials for Catalysis and Fuels Processing; Bravo-Suárez, J., et al.;
ACS Symposium Series; American Chemical Society: Washington, DC, 2013.

where n_i is the number of carbon atoms in product i, and C_i and C_{CO} are the molar concentrations of product i and unreacted CO in the reactor effluent. Turnover frequency (TOF, s^{-1}) was reported as CO molecules converted per second and per surface Rh site. The measured carbon balance for all the tests was 95±10%.

Results and Discussion

Characterization of OMC Support

The mesoporous structure of the as-synthesized OMC was characterized by N_2 physisorption and low-angle XRD. Figure 1A shows the physisorption isotherm and pore size distribution of the OMC. A Type IV isotherm is observed along with a Type II hysteresis loop between the relative pressures (P/P_0) of 0.5 to 0.8 (*18*). The pore size distribution (inset of Figure 1A), determined from the adsorption branch data using the BJH model, indicates the maximum pore diameter of OMC at 6.5 nm with a full width at half maximum (FWHM) of 2.0 nm. The BET surface area and pore volume of the OMC are 645 $m^2\ g^{-1}$ and 0.65 $cm^3\ g^{-1}$, respectively. Figure 1B shows the low-angle XRD pattern of the OMC. An obvious diffraction peak appears at 2θ = 0.81° with two broad and weak peaks between 2θ = 1−2°, suggesting the ordered mesoporous structure of OMC. The physisorption and XRD data generally agree with our previously reported work (*14*).

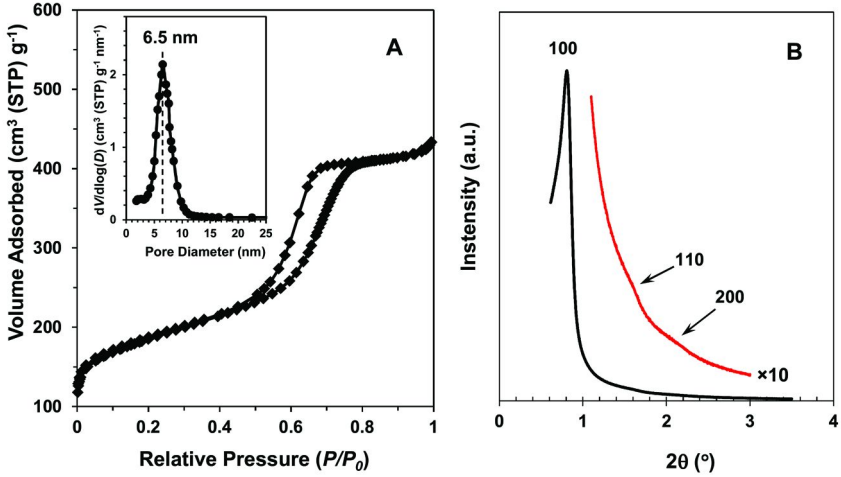

Figure 1. (A) N_2-physisorption isotherm and pore size distribution (inset) and (B) low-angle XRD pattern of the OMC support.

Preparation and Microscopic Characterization of Rh/OMC

We loaded Rh nanoparticles into the nanopores of the OMC by using a wetness impregnation method. The key point is to use isopropanol, less polar than most often used water, as the solvent of Rh-precursor in order to improve the penetration of Rh solution into the pores of OMC (having a very hydrophobic surface). The

In Novel Materials for Catalysis and Fuels Processing; Bravo-Suárez, J., et al.;
ACS Symposium Series; American Chemical Society: Washington, DC, 2013.

other important aspect is to control the drying process and make a slow removal of the solvent, in order to prevent Rh from being "wicked" back out of the pores by capillary action when the solvent is vaporized too fast. The isopropanol solvent was removed at ambient temperature and under air flow, followed by further drying at 393 K with a slow ramping rate of 1 K min^{-1}. The dried sample was thermally treated at 673 K in flowing He, followed by reduction at 623 K in flowing H_2 to obtain the Rh/OMC catalyst. The BET surface area and pore diameter (not shown here) of the as-prepared Rh/OMC showed little changes when compared to the OMC support.

The OMC support used in the present work was a fine powder, comprising of small carbon grains at the micrometer scale. In order to observe the Rh nanoparticles confined in the mesopores that are within the grains, the FIB technique was applied to "slice" a representative carbon grain as shown in Figure 2A (with a carbon and tungsten capping layer for protection). The obtained lamellar specimen (~150 nm in thickness) was then lifted out and placed on a TEM half-grid, exposing the grain cross-section for direct observation. Figure 2B shows the SE image of the as-prepared Rh/OMC cross-section at low magnification. One typical cross-sectional area was then selected for further analysis at higher magnification under SE and Z-contrast modes to determine the channel width, and the location and size of the Rh nanoparticles; the representative images are shown in Figure 3. The parallel pore channels can be discernible in Figure 3A, indicative of a long-range hexagonal arrangement of the OMC porous structure along the [110] direction (*14*). Rh nanoparticles (bright dots shown in Figure 3B) are well dispersed over the imaged cross-section with a diameter of 2−4 nm, consistent with the size measured by high-resolution STEM (see dark dots circled out in Figure 4). The average metal particle size of Rh/OMC is also estimated by H_2 chemisorption to be 2.3 nm (Table 1), in agreement with that measured by STEM. From the STEM and chemisorption results, the Rh particle size is smaller than the pore diameter (6.5 nm) of the OMC support, suggesting that Rh nanoparticles are successfully loaded into the nanopores of the OMC.

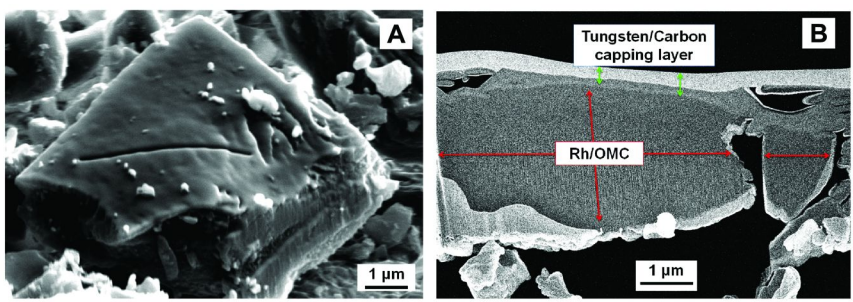

Figure 2. Secondary-electron images of (A) a representative grain of the Rh/OMC catalyst and (B) the Rh/OMC grain cross-section prepared by focused ion beam lift-out technique.

In Novel Materials for Catalysis and Fuels Processing; Bravo-Suárez, J., et al.;
ACS Symposium Series; American Chemical Society: Washington, DC, 2013.

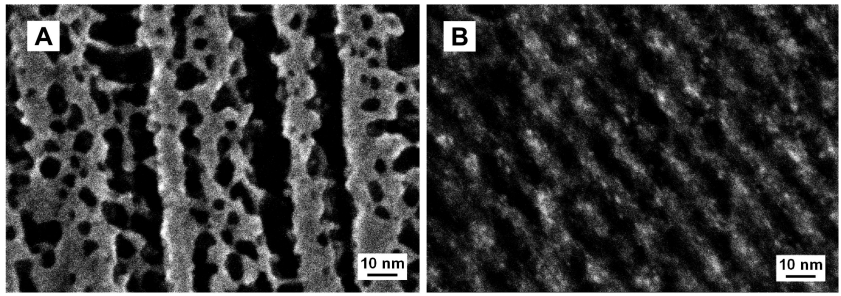

Figure 3. (A) Secondary-electron and (B) dark-field STEM images of the Rh/OMC grain cross-section prepared by focused ion beam lift-out technique.

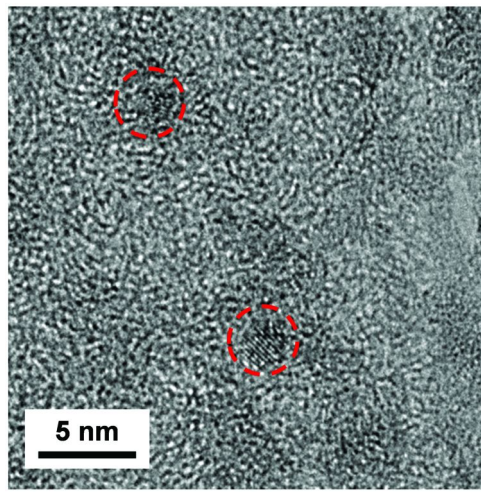

Figure 4. High-resolution STEM images of the Rh/OMC grain cross-section prepared by focused ion beam lift-out technique.

Catalytic Properties for CO Hydrogenation

CO hydrogenation over OMC-supported Rh catalysts was conducted at 593 K, 2.0 MPa, $H_2/CO = 2$, and GHSV = 36000 cm^3 (STP) $(h\ g_{cat})^{-1}$. The conversion of CO increases a little over the first ~16 h and then reaches steady state. The same induction period is required to get stable product selectivities. The steady-state catalytic data of the supported Rh catalysts were measured at the reaction time-on-stream of 20−24 h and are shown in Table 2. Turnover frequency (TOF, s^{-1}), defined as CO molecules converted per second and per surface Rh site, is listed in Table 2 and used for evaluation of the catalyst activity. As expected, Rh/OMC exhibits a poor catalytic activity in terms of CO conversion (0.2%) and TOF (0.0018 s^{-1}) as well as a low C_2H_5OH selectivity of ~6 mol-C% on a CO_2-free basis. A large amount of CH_4 and higher hydrocarbons (mainly C_2−C_4) is produced with a selectivity of ~59 mol-C%, leading to a low selectivity ratio of C_2H_5OH to total hydrocarbons (S_{C2H5OH}/S_{HC}) of only 0.11. CO_2 (13 mol-C% selectivity) forms presumably via either water-gas shift reaction ($CO + H_2O \rightarrow H_2 + CO_2$) or Boudouard reaction ($2CO \rightarrow C + CO_2$) (*1*).

For Rh-based catalysts, transition metal oxides (e.g., MnO_x, FeO_x) and alkali oxides (e.g., LiO) are often added as promoters in order to obtain decent catalytic activity and C_2H_5OH selectivity for CO hydrogenation (*19*). Therefore, we also prepared and tested Mn, Li, and Fe triply promoted Rh/OMC catalyst (Rh-Mn-Li-Fe/OMC) with 1.6 wt % Rh and molar ratio of Rh: Mn: Li: Fe = 1: 0.66: 0.55: 0.05 that is close to the optimized composition reported for Rh-based catalysts (*19*). The metal particle size (3.3 nm) of the Rh-Mn-Li-Fe/OMC, estimated from H_2 chemisorption (Table 1), increases to a small extent in relation to the Rh/OMC, but still falls within the pore diameter of the OMC. This suggests that the metal particles are confined in the OMC mesopores even after the promoter addition. As shown in Table 2, Rh-Mn-Li-Fe/OMC exhibits a much enhanced catalytic activity (TOF = 0.060 s^{-1}), more than 30 times higher than that of the Rh/OMC; C_2H_5OH selectivity increases up to ~34 mol-C% (CO_2-free basis). Moreover, the formation of unfavorable CH_4 over Rh-Mn-Li-Fe/OMC is suppressed considerably, resulting in a S_{C2H5OH}/S_{HC} ratio higher than unity. Compared with the MWCNTs-supported Rh-Mn-Li-Fe catalyst reported in the literature (*6*), Rh-Mn-Li-Fe/OMC shows comparable TOF but higher ethanol selectivity (33.8 vs. ~25 mol-C%) and S_{C2H5OH}/S_{HC} ratio (1.07 vs. ~0.70), although the reported catalyst composition (1 wt % Rh and Rh: Mn: Li: Fe = 1: 1.9: 1.1: 0.1) and reaction conditions (603 K, 3.0 MPa, $H_2/CO = 2$, and GHSV = 12000 h^{-1}) are somewhat different.

In Novel Materials for Catalysis and Fuels Processing; Bravo-Suárez, J., et al.;
ACS Symposium Series; American Chemical Society: Washington, DC, 2013.

Table 2. Steady-state catalytic properties of Rh-based catalysts for CO hydrogenation at 593 K, 2.0 MPa, $H_2/CO = 2$, and 36000 cm^3 (STP) $(h\ g_{cat})^{-1}$

Catalyst	*X_{CO} (%)*	*TOF[a] (s^{-1})*	*S_{CO2}[b] (mol-C%)*	*Carbon Selectivity (mol-C%, CO_2-free)*						*S_{C2H5OH}/S_{HC} [e]*
				CH_4	*C_{2+}-HC [c]*	*CH_3OH*	*C_2H_5OH*	*CH_3CHO*	*Other C_{2+}-oxy.[d]*	
Rh/OMC	0.2	0.0018	13.0	48.7	9.9	28.6	6.2	6.6	–	0.11
Rh-Mn-Li-Fe/OMC	2.2	0.060	34.0	20.0	11.7	15.6	33.8	7.1	11.8	1.07
Rh-Mn-Li-Fe/SiO_2 [f]	1.8	0.103	3.2	34.3	6.2	2.8	28.6	24.0	4.1	0.71
Rh-Mn-Li-Fe/ MWCNTs [Pan et al. (*6*)][g]	~8.3	~0.056[h]	~23	~21	~15	~2	~25	~25	~4	~0.70

[a] Turnover frequency defined as CO molecules converted per second and per surface metal site. [b] CO_2 selectivity. [c] Hydrocarbons with two or more carbons. [d] Oxygenates with two or more carbons other than C_2H_5OH and CHM_3CHO, including ethyl acetate, 1-propanol, 2-propanol, and acetone. [e] The selectivity ratio of C_2H_5OH to total hydrocarbons (i.e., CH_4 and C_{2+}-HC). [f] 593 K, 2.0 MPa, $H_2/CO = 2$, and GHSV = 90000 cm^3 (STP) $(h\ g_{cat})^{-1}$. [g] The reaction conditions were 603 K, 3.0 MPa, $H_2/CO = 2$, and GHSV = 12000 h^{-1}. [h] The TOF data was normalized to total Rh atoms.

For comparison with the OMC support, a traditional mesoporous silica (SBA-15) with a pore diameter of 6.8 nm (see Figure 5 for N_2-physisorption isotherm and pore size distribution) and BET surface area of 750 m^2 g^{-1} was also used to support the Rh-Mn-Li-Fe catalyst (Rh-Mn-Li-Fe/SBA-15) for the reaction of CO hydrogenation to ethanol. Table 1 shows that the Rh-Mn-Li-Fe/SBA-15 has a similar elemental composition, metal dispersion, and particle size to the Rh-Mn-Li-Fe/OMC. In order to compare both catalysts under a similar conversion level, the Rh-Mn-Li-Fe/SBA-15 catalyst was tested under the same reaction conditions but at a higher GHSV (90000 cm^3 (STP) $(h\ g_{cat})^{-1}$), and the catalytic data is included in Table 2. The Rh-Mn-Li-Fe/SBA-15 shows a lower ethanol selectivity (28.6 vs. 33.8 mol-C%) but a higher hydrocarbon selectivity (40.5 vs. 31.7 mol-C%), in spite of its enhanced catalytic activity in terms of TOF (0.103 vs. 0.060 s^{-1}). As a result, the S_{C2H5OH}/S_{HC} ratio over Rh-Mn-Li-Fe/SBA-15 decreases to 0.71, lower than that over the Rh-Mn-Li-Fe/OMC. Furthermore, both catalysts have a major difference in the product distribution. The use of the OMC support tends to promote the formation of CO_2 and other C_{2+}-oxygenates (including 1-propanol, 2-propanol, ethyl acetate, and acetone), but decrease CH_3CHO selectivity. Given their similar metal particle size, support pore diameter, and CO conversion, the performance differences between Rh-Mn-Li-Fe/OMC and Rh-Mn-Li-Fe/SBA-15 most likely arise from metal-support and metal-promoter interactions. The surface properties of supports including chemical composition and structure would not only influence the electronic structure of active metals (*20–22*), but also the metal-promoter interfaces where the catalytically active sites are located (*23*). The reaction of CO hydrogenation over multi-component promoted Rh catalysts proceeds via a complex mechanism involving a sequence of elementary steps and surface intermediates (*24*). A slight variation of the metal-promoter interfaces due to the change of supports may considerably vary the reaction routes and intermediates, thus affecting the overall activity and product distribution. A thorough investigation on the metal-promoter interfaces over different supports is deserved in the future.

Conclusions

Ordered mesoporous carbon (OMC) prepared via a soft-template route was used as the support for Rh-based catalysts for ethanol production from synthesis gas. Direct microscopic observation on the cross-section of Rh/OMC catalyst grains was obtained by applying a state-of-the-art focused ion beam lift-out technique, revealing that Rh nanoparticles (2−4 nm in diameter) are successfully confined in the nanopores (6.5 nm) of the OMC. The catalytic activity (in terms of turnover frequency) and ethanol selectivity of the Rh/OMC are enhanced greatly with the addition of Mn, Li, and Fe promoters. Compared with a traditional mesoporous silica (SBA-15), OMC as the support of promoted Rh catalyst leads to higher ethanol selectivity along with suppressing to some extent the formation of undesired hydrocarbons, although the overall activity of the OMC-supported catalyst is lower. The metal-support and metal-promoter interactions are presumably responsible for the difference between the catalytic

In Novel Materials for Catalysis and Fuels Processing; Bravo-Suárez, J., et al.;
ACS Symposium Series; American Chemical Society: Washington, DC, 2013.

performances of OMC- and SBA-15-supported catalysts, given that both have comparable metal particle sizes and support pore diameters.

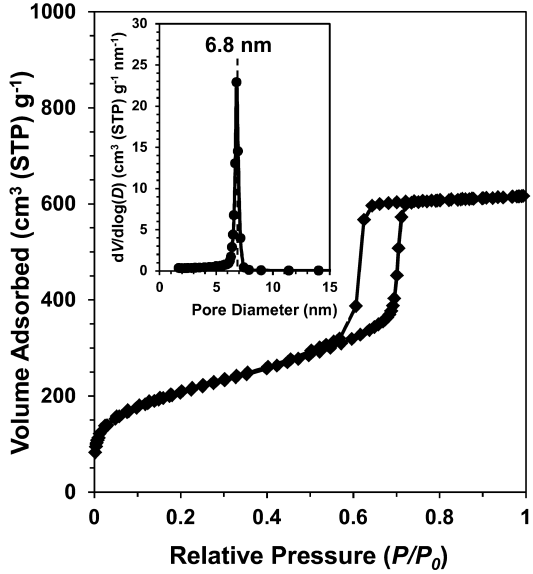

Figure 5. N_2-physisorption isotherm and pore size distribution (inset) of the mesoporous silica (SBA-15) support.

Acknowledgments

This work was supported by the laboratory-directed research and development (LDRD) program of Oak Ridge National Laboratory, managed and operated by UT-Battelle, LLC. A portion of this research was conducted at the Center for Nanophase Materials Sciences, which is sponsored at Oak Ridge National Laboratory by the Division of Scientific User Facilities, U.S. Department of Energy. The microscopy work was carried out using ORNL's Shared Research Equipment (ShaRE) User Facility that sponsored by the Office of Basic Energy Sciences, U.S. Department of Energy.

References

1. Spivey, J. J.; Egbebi, A. *Chem. Soc. Rev.* **2007**, *36*, 1514–1528.
2. Surisetty, V. R.; Dalai, A. K.; Kozinski, J. *Appl. Catal., A* **2011**, *404*, 1–11.
3. Subramani, V.; Gangwal, S. K. *Energy Fuels* **2008**, *22*, 814–839.
4. Solymosi, F.; Tombácz, I.; Kocsis, M. *J. Catal.* **1982**, *75*, 78–93.
5. Gronchi, P.; Tempesti, E.; Mazzocchia, C. *Appl. Catal., A* **1994**, *120*, 115–126.
6. Pan, X.; Fan, Z.; Chen, W.; Ding, Y.; Luo, H.; Bao, X. *Nat. Mater.* **2007**, *6*, 507–511.

7. Liang, C.; Dai, S. *J. Am. Chem. Soc.* **2006**, *128*, 5316–5317.
8. Liang, C.; Li, Z.; Dai, S. *Angew. Chem., Ind. Ed.* **2008**, *47*, 3696–3717.
9. Hou, C.-H.; Wang, X.; Liang, C.; Yiacoumi, S.; Tsouris, C.; Dai, S. *J. Phys. Chem. B* **2008**, *112*, 8563–8570.
10. Giannuzzi, L. A.; Stevie, F. A. *Micron* **1999**, *30*, 197–204.
11. Stokes, D. J.; Wilhelmi, O.; Reyntjens, S.; Jiao, C.; Roussel, L. *J. Nanosci. Nanotechnol.* **2009**, *9*, 1268–1271.
12. Evans, R.D.; Nixon, H.P.; Darragh, C.V.; Howe, J.Y.; Coffey, D.W. *Tribol. Int.* **2007**, *40*, 1649–1654.
13. Yu, M.; Howe, J.; Jeong, K.; Shim, I.; Kim, W.; Kim, C.; Ahn, J.; Lee, J.; Urban, M. W. *J. Mater. Chem.* **2010**, *20*, 5748–5755.
14. Wang, X.; Liang, C.; Dai, S. *Langmuir* **2008**, *24*, 7500–7505.
15. Zhao, D.; Huo, Q.; Feng, J.; Chmelka, B. F.; Stucky, G. D. *J. Am. Chem. Soc.* **1998**, *120*, 6024–6036.
16. Brunauer, S.; Emmett, P. H.; Teller, E. *J. Am. Chem. Soc.* **1938**, *60*, 309–319.
17. Barrett, E. P.; Joyner, L. G.; Halenda, P. P. *J. Am. Chem. Soc.* **1951**, *73*, 373–380.
18. Sing, K. S. W.; Everett, D. H.; Haul, R. A. W.; Moscou, L.; Pierotti, R. A.; Rouquerol, J.; Siemieniewska, T. *Pure Appl. Chem.* **1985**, *57*, 603–619.
19. Yin, H.; Ding, Y.; Luo, H.; Zhu, H.; He, D.; Xiong, J.; Lin, L. *Appl. Catal., A* **2003**, *243*, 155–164.
20. Trautmann, S.; Baerns, M. *J. Catal.* **1994**, *150*, 335–344.
21. Ponec, V.; Nonneman, L. E. Y. *Stud. Surf. Sci. Catal.* **1991**, *61*, 225–234.
22. Mochida, I.; Ikeyama, N.; Ishibashi, H.; Fujitsu, H. *J. Catal.* **1988**, *110*, 159–170.
23. Ponec, V. *Catal. Today* **1992**, *12*, 227–254.
24. Chuang, S. S. C.; Stevens, R. W., Jr.; Khatri, R. *Top. Catal.* **2005**, *32*, 225–232.

Chapter 10

Carbon-Mediated Catalysis: Oxidative Dehydrogenation on Graphitic Carbon

Viviane Schwartz,[*,1] Steven H. Overbury,[1,2] and Chengdu Liang[1]

[1]Center for Nanophase Materials Sciences, Oak Ridge National Laboratory, PO Box 2008 MS6493, Oak Ridge, TN 37831, USA
[2]Chemical Science Division, Oak Ridge National Laboratory, PO Box 2008 MS6493, Oak Ridge, TN 37831, USA
[*]E-mail: schwartzv@ornl.gov

Although carbon has been widely used in catalytic processes as a support material, very little is known about its function as an active catalyst. The scientific challenge is to achieve a detailed mechanistic understanding of the structural or chemical sites of the carbon that are catalytically active especially because of the very heterogeneous nature of carbon surfaces. This problem is complicated by the fact that there are limited tools to characterize the surface chemical and structural properties of carbon materials. This review highlights recent efforts from our group in utilizing well-defined synthetic nanostructure carbons in which surface properties can be controlled and systematically varied in order to identify their function for oxidative dehydrogenation reactions. Manipulation of exposed edge sites and oxygen functionalities are some of the aspects studied for controlling activity and selectivity on carbon catalysis.

Introduction

In catalysis, carbon has been traditionally used as a support to anchor transition metal catalysts for a number of different reactions, such as oxidation of alcohols and hydrogenation of alkenes (*1*). The high efficiency of carbon as a support material is the result of several different reasons, such as their extremely large porosity, their surface inertness and high resistance to corrosion,

In Novel Materials for Catalysis and Fuels Processing; Bravo-Suárez, J., et al.;
ACS Symposium Series; American Chemical Society: Washington, DC, 2013.

and their electronic properties, which are largely dependent on its hybridization state. The adsorption properties of a carbon material are closely determined by its surface chemistry and presence of heteroatoms. The unparalleled flexibility of the carbon-based catalysts is mainly due to the controllability of their surface acidity/basicity and π-electron density through surface functionalization rendering the unique quality of this class of materials (*2–4*). Actually, they have the appropriate electronic and morphological characteristics required for a heterogeneous catalyst: existence of surface termination defects for electron localization or for anchoring of active sites; and high surface area for catalysis. The same properties are determinants in their use as catalytic materials in its own. However, their widespread use is hindered by the lack of fundamental understanding of their physical and chemical properties that impact their catalytic performance. One of the reasons for this is the fact that there are almost no appropriate research tools to characterize the surface chemical and structural properties in carbon materials. Additionally, carbon materials for catalysts or catalyst supports have largely relied upon activated carbons produced commercially from natural feedstocks. These materials are difficult to characterize and there is little control over the structure, ash content, and chemical functionality.

The main application of activated carbons in catalysis lies in the field of pollution control as they are efficient oxidants for the removal of H_2S, SO_2, and NO_x (*5*, *6*). The first reports of carbon as a catalytically active material in the oxidative dehydrogenation (ODH) reaction of ethylbenzene came in the 1980s (*7*, *8*). However, the growing utilization of carbon-based materials for catalysis, both as a support or as an active phase parallels the development of well-defined synthetic nanostructured carbons (*9*). Different allotropic forms of carbon, such as carbon nanotubes (*9*), fullerene-like carbons (*10*), carbon nanofibers (*11*), onion-like carbon (*12*), and nano diamonds (*10*, *13*), have exhibited catalytic activity in heterogeneous oxidative reactions. Most recently, two dimensional graphene materials have become an exciting topic of research (*14*) and there are already few reports dealing with the application of this material in catalysis (*2*, *15*, *16*).

This review highlights recent efforts from our group in investigating metal-free carbon-based catalysts for the ODH reaction (*17–19*). Traditionally, ODH reactions have been catalyzed using metal oxides such as Mg–V–Sb–oxide, vanadium oxide, and manganese molybdate and lattice oxygen is assumed to play a role in the redox process (*20*). Our approach was to use synthetic carbons in an effort to understand the structural sites that control activity and selectivity. High selectivity is a crucial factor for these reactions and the development of a milder oxidant catalyst is needed to fulfill one of the major challenges, that is, to minimize the combustion side reactions leading to the undesired CO and CO_2 products while increasing the limited alkene yield. The utilization of synthetic carbons brings the advantage of introducing surface chemical functionalities in a controlled fashion either during the synthesis of the carbon or by post-processing of an existing carbon. By controlled functionalization of the carbon, their roles could be systematically varied to study their effect on the catalytic activity and selectivity of graphitic carbons for ODH reactions. Our results suggest that

In Novel Materials for Catalysis and Fuels Processing; Bravo-Suárez, J., et al.;
ACS Symposium Series; American Chemical Society: Washington, DC, 2013.

the generally accepted importance of oxygenate sites for the ODH reactions on carbon surfaces might have been overestimated, while the existence of edge sites are of fundamental importance.

ODH and Carbon Surface

Oxidative dehydrogenation (ODH) provides an alternate route for the conversion of alkanes to alkenes as limitations by the chemical equilibrium are removed by coupling dehydrogenation and hydrogen oxidation (*21*). The first reports of carbon as active catalysts dealt with the observation of deposited coke as an active species for ODH of ethylbenzene (*7*, *8*, *22*). ODH of ethylbenzene is a less demanding process as the activation of the ethyl group is favored by the aromatic ring as opposed to the ODH of linear alkanes. That is most likely the reason why the first systematic studies of carbon catalysts were focused on the ethylbenzene process (*9*, *13*, *23–27*). These studies emphasized the effect of oxygen groups at the surface of the carbon and their role as active sites for the formation of styrene. To provide an idea of the generic type of surface bond these oxygen groups represent, a schematic representation of different surface functional groups is shown in Figure 1. The abundance of the different oxygen functionalities on a given reaction condition will depend on several factors, such as, the type and origin of the graphitic carbon, post-treatments applied, and the temperature and reactive gas under which the graphitic carbon is being catalytically tested. The hypothesis generally accepted (*9*, *23*) is that, for ODH reactions on carbons, surface quinone-type oxygen functional groups are the active sites and the reaction has been assumed to proceed via a redox mechanism.

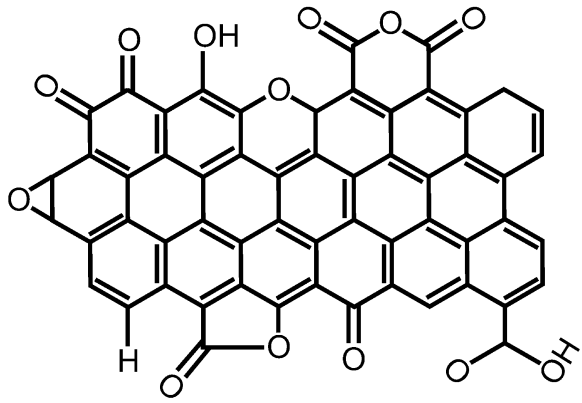

Figure 1. Surface groups on carbon.

In Novel Materials for Catalysis and Fuels Processing; Bravo-Suárez, J., et al.;
ACS Symposium Series; American Chemical Society: Washington, DC, 2013.

The promising results from the ODH of ethylbenzene prompted the study of unfunctionalized alkanes (*10*, *12*, *28–31*) on carbon surfaces. Activation of low molecular weight alkanes is still a challenging task due to their low intrinsic chemical reactivity that demands a high energy input to activate them. Vanadium and molybdenum oxide are usually the main components in the catalysts developed for ODH reactions (*32*). Despite several decades of optimization, vanadia and molybdena systems still show limited selectivity for alkenes. Indeed, high selectivities to alkenes are only obtained at low alkane conversions, and the selectivity decreases dramatically when the total conversion increases. That happens because the starting compound, alkane, is much less active than the alkene and the reaction appears to occur via a combination of parallel and sequential oxidation (*19*, *33*), as shown in Scheme 1 for the ODH of isobutane.

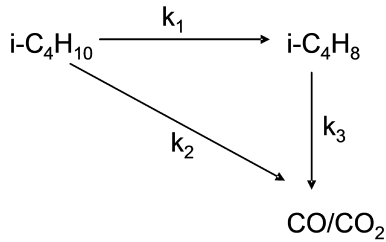

Scheme 1. Reaction network in oxidative dehydrogenation of isobutane.

In order to verify that the same reaction network occurs on carbon surfaces, we have applied a simple method when studying ODH of isobutane on graphitized mesoporous carbon (GMC) (*19*). Primary products of a reaction can be discriminated from secondary or even higher-order products by checking the zero-conversion intercept of their selectivities. In this method, products with nonzero intercepts are from primary reactions. Indeed, we found that selectivity to isobutene increased when isobutane conversion decreased but did not reach 100% when extrapolated to zero conversion. Likewise, selectivity analyses of CO and CO_2 confirmed that both species were also primary products of ODH of isobutene, since nonzero intercepts were found for the selectivities at zero conversion. Therefore, our studies confirmed that the ODH reaction of isobutane on carbon catalysts is a parallel-consecutive pathway with partial oxidative dehydrogenation for the formation of isobutene and deep oxidation pathway for the direct formation of CO and CO_2 from isobutane (*19*).

Effect of Open Edges

In our previous work (*17*), we have explored the fullerene-like cavities of mesoporous glassy carbon using heating treatments and oxidation. Our approach was based on using the "soft-template synthesis" for the synthesis of uniform

mesoporous carbon materials with controlled pore sizes and periodicity (*34*). The resulting mesoporous carbon possesses a graphitic structure and the mesoporosity can survive treatment at temperatures as high as 2600 °C. The openness and oxygen content of the fullerene-like cavities were varied systematically through deliberate variation of synthesis conditions. The ultimate goal was to correlate the nanostructure features and presence of oxygen functionalities created by this method with the catalytic performance.

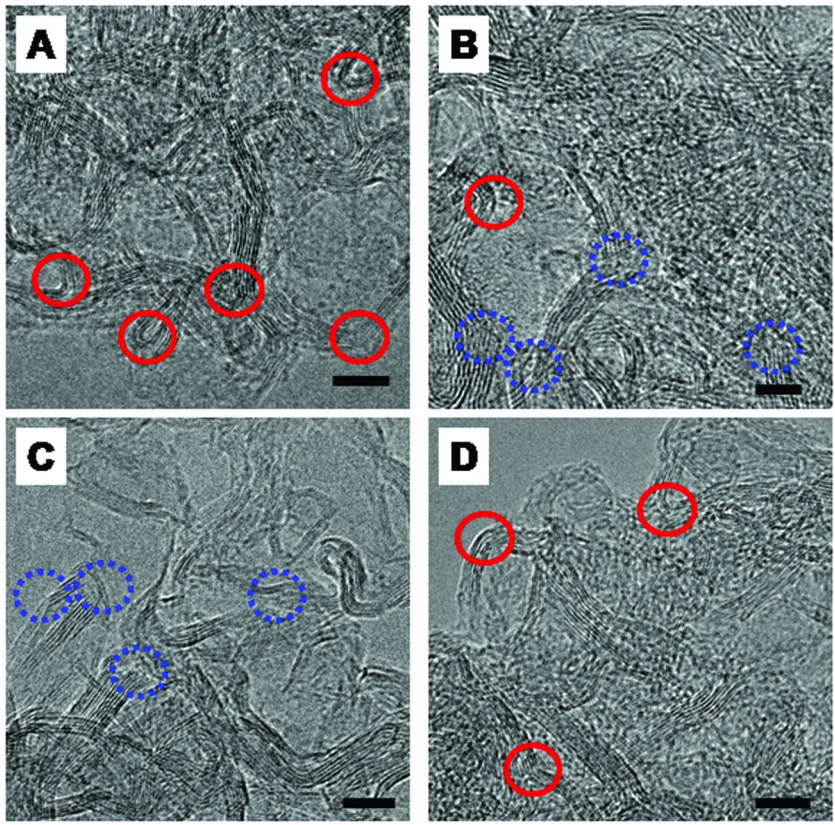

Figure 2. HR-TEM images of samples: a) as-prepared GMC; b) after oxidation in air of sample (a) at 500 °C for 15 h; c) after heat treatment of sample (b) in He for 1 h at 1600 °C; and, d) after heat treatment of sample (c) in He at 2600 °C. The red circles indicate the 'loop back structures' (closed edges) whereas the blue dotted circles indicate the open edge sites of the graphitic carbon. The scale bars represent 5 nm. (Reproduced with permission from reference (17). Copyright 2009 ACS.)

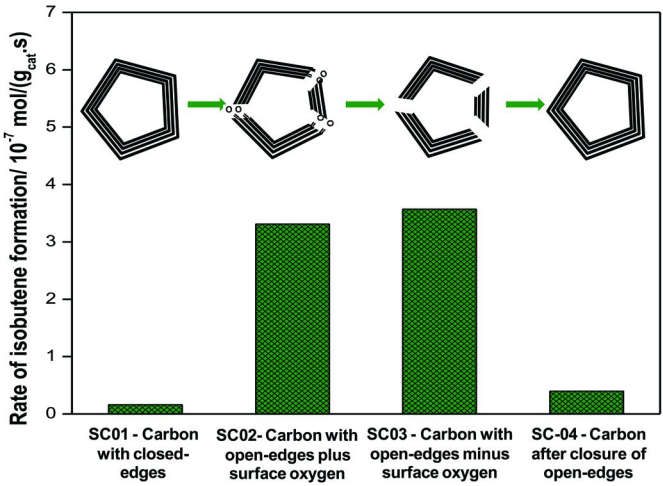

Figure 3. Isobutene evolution during ODH of i-C_4H_{10} after 20 h of time on stream for the GMC materials. Reaction conditions: T = 400 °C, 0.2 g of catalyst, feed composition of 4% i-C_4H_{10} and 2% O_2, and balance N_2, and total gas hourly space velocity (GHSV) of 5100 std cm^3/(h.g$_{cat}$).

The TEM images in Figure 2 (*17*) show the consecutive treatments applied: a) the pristine carbon structure of the as prepared GMC (treated at 2600 °C in helium for 1 h); b) result from oxidation of GMC (sample a) in air at 500 °C for 15 h; c) further heat treatment of sample (b) in helium for 1 h at 1600 °C; d) final heat treatment of sample (c) to 2600 °C in helium. The red circles in Figures 2a and 2b are the sharp turns or loop back structures of the defective graphitic structures. These turns are most likely due to amorphous and reactive carbon that gasifies upon oxidation in air leading to the formation of open fullerene-like carbon cavities of 2–3 nm diameter that are functionalized by oxygen (Figure 2b). The blue dotted circles in Figures 2b and 2c indicate the open edge sites of the graphitic carbon that were preserved after further heating the oxygenated GMC to 1600 °C in He. The presence (Figure 2b) and removal (Figure 2c) of the oxygenated functionalities were confirmed by temperature programmed desorption methods (*17*) which follow the release of CO and CO_2 under an inert atmosphere while ramping the temperature (not shown). Final heat treatment to 2600 °C in He closed both the open edges and the fullerene-like cavities as well, showing a microstructure in Figure 2d similar to that of the initial GMC.

The resulting model carbons were structurally characterized and tested for their activity and selectivity in the isobutane ODH reaction. Catalytic activities of the carbon catalysts were calculated based on the reaction rate of isobutane and selectivity to isobutene (Figure 3). The GMCs showed catalytic activity in the ODH reaction when the fullerene-like cavities were open, regardless of the existence of the surface oxygenated functionalities and they were deactivated after the fullerene-like cavities were closed by thermal treatment. The results give insights to the active sites of carbon catalysts and reveal that the open cavities

In Novel Materials for Catalysis and Fuels Processing; Bravo-Suárez, J., et al.;
ACS Symposium Series; American Chemical Society: Washington, DC, 2013.

of the fullerene-like structures are the most active sites for the selective ODH of isobutane to isobutene. These open cavities have accessible graphitic planes with open edges, which should function as active sites in the ODH reactions.

Effect of Oxygen Functionalities

Two distinct approaches were used to correlate the amount and type of oxygen functionality on graphitic carbon with the catalytic activity for ODH of isobutane. In one case, oxygen functionalities were progressively added to the surface of GMC materials by post air oxidation treatment and, in the other case, we started with graphite oxide and applied different thermal and chemical treatments to systematically remove oxygen groups present on the surface.

In the first approach, the concentration of the oxygenated functional groups on the surface of the GMCs was varied in a continuous manner through a simple control of the burn-off level, defined as the weight change after the oxygen treatment (*19*). Oxygen treatment (oxidation in air) at 500 °C and variable time (24, 30, 36, and 48 h) resulted in a continuous increase of burn-off level and, consequently, higher oxygen surface density. N_2 physisorption measurements confirmed that the structural integrity of the GMC was conserved with a burn-off level up to 70%. However, the burn-off did cause a significant and steady increase of the pore volume and surface area, therefore altering the edge/basal plane ratio throughout the oxidative treatment. Oxygen functionalities were characterized by a temperature programmed desorption method, a method typically used for carbon materials. In this method, the carbon–oxygen groups of acid character (carboxylic, lactonic) evolve as CO_2 upon thermal desorption whereas the non-acidic (carbonyl, ether, quinone) and phenol groups give rise to CO. Anhydride evolve as both CO and CO_2 (*35*). The similar desorption profiles of CO and CO_2 during temperature programmed heating in He of the samples prepared using different burn-offs indicated that the nature of the surface oxygen (type of functionality) was generated homogenously (*19*). Additionally, the functional groups, independently of the burn-off level of the GMC, were composed mostly of quinone-type functionalities.

The progressive changes in the ratio of edge to basal planes and the amount of surface oxygen groups deposited on the surface due to the systematic burn-off process clearly caused changes in activity and selectivity. The effect of burn-off on the surface chemistry of the carbons and, consequently, their catalytic performance are summarized in Figure 4 (*19*). The calculated reaction rate constants were plotted as a function of surface oxygen, that is, total amount of oxygen desorbed as CO and CO_2 (Figure 4). The two reaction pathways show different dependence on the quinone-type oxygen sites: the rate constant leading to the desired partial oxidation product does not show a strong correlation to the density of oxygen sites, whereas the rate constant leading to the unselective CO_x products increases continuously with the density of oxygen sites. The rate constant analyses suggest that two different active sites appear to be responsible for partial oxidative dehydrogenation and deep oxidation processes separately.

In Novel Materials for Catalysis and Fuels Processing; Bravo-Suárez, J., et al.;
ACS Symposium Series; American Chemical Society: Washington, DC, 2013.

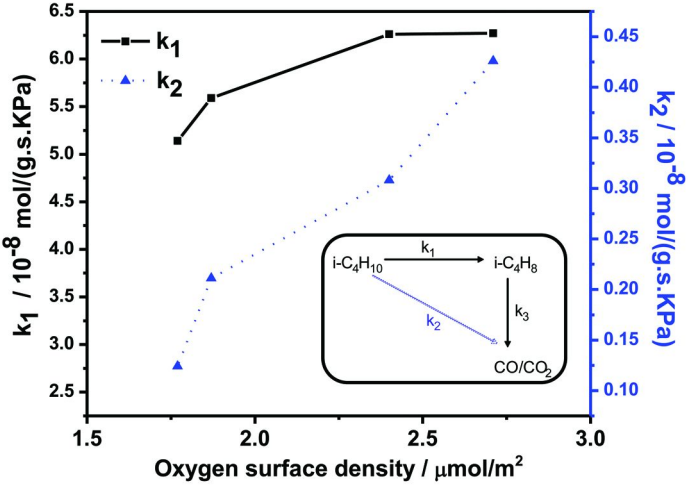

Figure 4. Dependence of the calculated rate constants of k_1 and k_2, assuming a first-order analysis, on the density of surface oxygen (total oxygen desorbed as measured by TPD) for different GMC carbons. Data taken from reference (19).

Our second approach was based on the investigation of oxygen-functionalized few layered graphene as a more simplified model system for the catalytic activity of graphitic carbon (*36*). Graphene, a two-dimensional material consisting ideally of a single layer of carbon atoms arranged in six-membered rings, offers an excellent opportunity to elucidate the catalytic properties of carbon-based materials and has been the subject of a few catalytic studies, such as the catalytic oxidation of various alcohols and *cis*-stilbene and the hydration of various alkynes (*15*, *16*). In an attempt to circumvent the issue of modifying the edge/basal plane ratio and focus solely on the effect of oxygen content, we removed oxygen from graphene oxide (GO) instead of trying to incorporate oxygen groups into reduced graphene. In our studies (*36*), the precursor, GO material, was prepared by the modified Hummers method (*37*). Oxygen functionalized graphene samples containing lesser amounts of oxygen groups were created by utilizing further thermal and/or chemical treatments (*2*), such as vacuum drying, microwave exfoliation, hydrogen reduction, and chemical reduction with hydrazine. The resulting oxygen functionalized graphene materials showed a large range of oxygen content (more than an order of magnitude variation of oxygen content amongst the samples). Despite that, no clear correlation (Figure 5) was found between isobutane consumption rate and the total amount of oxygen groups (as measured by TPD experiments). The results would be similar whether the oxygen content was normalized by surface area or mass. Additionally, the selectivity to isobutene was fairly constant which should be indicative of lack of variation in the kinetics of competing reaction pathways with increasing oxygen content. $^{18}O/^{16}O$ switch experiments revealed that re-oxidation of the graphene surface occurred at the same rate as the ODH reaction suggesting that the oxygen groups on the carbon edges should mimic the Mars-van Krevelen mechanism that occurs

In Novel Materials for Catalysis and Fuels Processing; Bravo-Suárez, J., et al.;
ACS Symposium Series; American Chemical Society: Washington, DC, 2013.

on oxide surfaces with the difference that no lattice oxygen takes part on the mechanism (*5*, *38*). Although these model catalysts have a simpler surface structure compared to other carbon materials, there is still a large degree of complexity involved on the carbon surface. Therefore, we have not been able to identify a specific oxygen functionality that is the active center for the selective ODH of isobutane on the functionalized graphene materials.

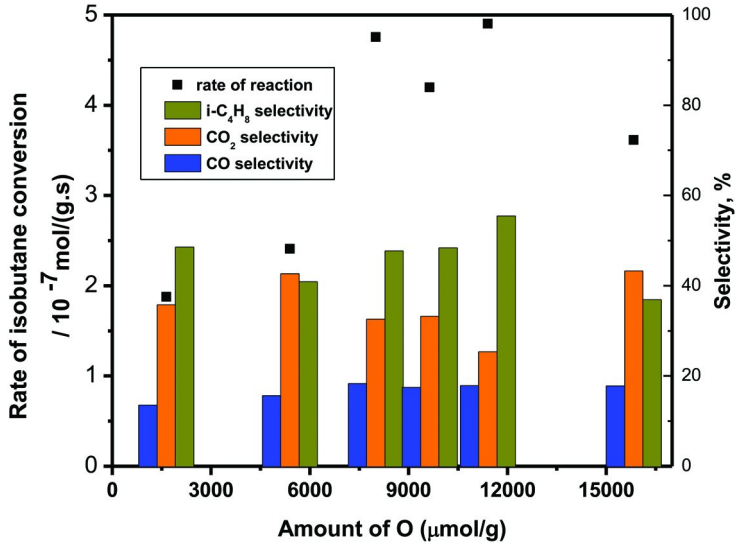

Figure 5. Rate of isobutane conversion for a single residence time versus total amount of oxygen on the surface of the functionalized graphene samples and product selectivity at similar conversions (3.4 to 3.6%) obtained from data at variable residence time (W/F varied from 0.02 to 0.12 (g_{cat}.s)/(std cm^3 isobutane)).

Outlook

Nanostructured carbon materials have proven to be attractive alternatives to conventional metal-based catalysts for several important reactions involving pollution control, aromatic hydrocarbons, and alkanes (*1–3*, *6*). They are also environmentally benign since metal-free carbon-based catalysts can be easily disposed by combustion after reaching their life-time. The continuing scientific challenge is to achieve a detailed mechanistic understanding of the structural or chemical sites of the carbon that are catalytically active and to be able to explore how catalytic reactions proceed on carbon surfaces. This is special challenging in the case of carbon materials due to the limited array of spectroscopy and operando tools that are suitable for these materials.

A very important point that should not be overlooked when searching for alternative metal-free catalysts is their stability under reaction conditions. Highly

In Novel Materials for Catalysis and Fuels Processing; Bravo-Suárez, J., et al.;
ACS Symposium Series; American Chemical Society: Washington, DC, 2013.

reactive carbon surfaces are known to have limited thermal stability in reactive gas atmospheres. On the other hand, highly stable carbon materials provide little activity. Therefore, a balance between stable versus reactive sites must be achieved when designing new carbon nanostructures for catalytic applications. This can be achieved by controlling their nanostructure (such as degree of crystallinity of graphitic carbons), presence of defects, and types of functional groups during synthesis. For instance, both, the GMC and the functionalized few-layered graphene materials, showed to be fairly robust under reaction conditions. It was found out that the selectivity and activity measurements were hardly affected by carbon burn-off (*19*, *36*). Indeed, the burn-off after reactivity tests was estimated to be less than 4 wt % (*36*). This fact was confirmed by the close carbon balance (within ± 0.5%) and their high performance stability (reaction studies were run for more than 24 h and the conversion rate dropped by less than 5%).

In the case of graphitic carbons and oxidative dehydrogenation reaction, the function of oxygen atoms and defects and edges can be hard to decouple since oxygen sites can be removed and regenerated during the reaction leaving behind open sites that can be also catalytically active. It has been reported (*9*, *12*, *30*, *31*, *39*, *40*) that the nature of the oxygen species (nucleophilic or electrophilic) governs the activity and selectivity in ODH reactions. For instance, the electron-deficient oxygen species would attack the C=C bonds in alkenes which would lead to the unselective path of total combustion. Our studies (*36*) and others (*9*, *12*, *39*) have shown that, similar to metal oxides, carbon surfaces may switch between a reduced and oxidized phase by reoxidation with gas-phase oxygen during their reaction. However, the bulk of the graphite catalyst does not serve as a reservoir for oxygen atoms as opposed to metal oxides.

Another important aspect of carbon catalysis is the manipulation of their nanostructure and carbon hybridization state. We (*36*) and others (*10*) have shown that graphitic surfaces that contain carbon atoms with a certain degree of sp3 hybridization can provide active sites for the selective pathway for the formation of alkenes. Manipulation of exposed edge sites (*18*, *30*) is another tool used for balancing activity and selectivity by suppressing undesirable products.

In summary, the development of novel synthesis methods in the preparation of nanostructure carbons shifted the study of carbon catalysis, which was hindered before by the formation of carbonaceous overlayers on the traditional activated carbons and the presence of variable porosity, functionality, and ash content. Therefore, an opportunity exists by continuing the development of synthetic approaches that will lead to a better understanding of the factors which control the condensation and functionalization of synthetic carbon nanomaterials. In the case of ODH reactions, novel synthetic methods should be exploited towards the manipulation of the curvature and defect sites on graphitic materials, introducing a higher degree of sp^3 hybridization character and defects, as well as controlling the number of exposed edges and the type and number of functional groups. As a result, it may be possible to further refine the structure–reactivity relationships in carbon catalysis by construction of model carbon materials that have the potential to unravel mechanistic aspects that govern their catalytic function.

In Novel Materials for Catalysis and Fuels Processing; Bravo-Suárez, J., et al.;
ACS Symposium Series; American Chemical Society: Washington, DC, 2013.

Acknowledgments

This work was conducted at the Center for Nanophase Materials Sciences, which is sponsored at Oak Ridge National Laboratory by the Scientific User Facilities Division, Office of Basic Energy Sciences, U. S. Department of Energy.

References

1. Rodriguez-Reinoso, F. *Carbon* **1998**, *36*, 159–175.
2. Machado, B. F.; Serp, P. *Catal. Sci. Technol.* **2012**, *2*, 54–75.
3. Resasco, D. E. *Nat. Nanotechnol.* **2009**, *4*, 148–148.
4. Su, D. S.; Zhang, J.; Frank, B.; Thomas, A.; Wang, X. C.; Paraknowitsch, J.; Schlogl, R. *ChemSusChem* **2010**, *3*, 169–180.
5. Bashkova, S.; Armstrong, T. R.; Schwartz, V. *Energy Fuels* **2009**, *23*, 1674–1682.
6. Juntgen, H.; Richter, E.; Kuhl, H. *Fuel* **1988**, *67*, 775–780.
7. Cadus, L. E.; Arrua, L. A.; Gorriz, O. F.; Rivarola, J. B. *Ind. Eng. Chem. Res.* **1988**, *27*, 2241–2246.
8. Schraut, A.; Emig, G.; Sockel, H. G. *Appl. Catal.* **1987**, *29*, 311–326.
9. Zhang, J.; Su, D. S.; Zhang, A. H.; Wang, D.; Schlogl, R.; Hebert, C. *Angew. Chem., Int. Ed.* **2007**, *46*, 7319–7323.
10. Liu, X.; Frank, B.; Zhang, W.; Cotter, T. P.; Schlogl, R.; Su, D. S. *Angew. Chem., Int. Ed.* **2011**, *50*, 3318–3322.
11. Zhao, T. J.; Sun, W. Z.; Gu, X. Y.; Ronning, M.; Chen, D.; Dai, Y. C.; Yuan, W. K.; Holmen, A. *Appl. Catal., A* **2007**, *323*, 135–146.
12. Zhang, J.; Liu, X.; Blume, R.; Zhang, A. H.; Schlogl, R.; Su, D. S. *Science* **2008**, *322*, 73–77.
13. Su, D. S.; Maksimova, N. I.; Mestl, G.; Kuznetsov, V. L.; Keller, V.; Schlogl, R.; Keller, N. *Carbon* **2007**, *45*, 2145–2151.
14. Park, S.; Ruoff, R. S. *Nat. Nanotechnol.* **2009**, *4*, 217–224.
15. Dreyer, D. R.; Jia, H. P.; Bielawski, C. W. *Angew. Chem., Int. Ed.* **2010**, *49*, 6813–6816.
16. Jia, H. P.; Dreyer, D. R.; Bielawski, C. W. *Tetrahedron* **2011**, *67*, 4431–4434.
17. Liang, C. D.; Xie, H.; Schwartz, V.; Howe, J.; Dai, S.; Overbury, S. H. *J. Am. Chem. Soc.* **2009**, *131*, 7735–7741.
18. Schwartz, V.; Xie, H.; Meyer, H. M.; Overbury, S. H.; Liang, C. D. *Carbon* **2011**, *49*, 659–668.
19. Xie, H.; Wu, Z. L.; Overbury, S. H.; Liang, C. D.; Schwartz, V. *J. Catal.* **2009**, *267*, 158–166.
20. Michaels, J. N.; Stern, D. L.; Grasselli, R. K. *Catal. Lett.* **1996**, *42*, 135–137.
21. Corberan, V. C. *Catal. Today* **2005**, *99*, 33–41.
22. Whitehurst, D. D. *Abstr. Pap. Am. Chem. Soc.* **1997**, *213*, 77-FUEL.
23. Pereira, M. F. R.; Orfao, J. J. M.; Figueiredo, J. L. *Appl. Catal., A* **1999**, *184*, 153–160.
24. Pereira, M. F. R.; Orfao, J. J. M.; Figueiredo, J. L. *Appl. Catal., A* **2000**, *196*, 43–54.

25. Pereira, M. F. R.; Orfao, J. J. M.; Figueiredo, J. L. *Appl. Catal., A* **2001**, *218*, 307–318.
26. Delgado, J. J.; Chen, X. W.; Su, D. S.; Hamid, S. B. A.; Schlogl, R. *J. Nanosci. Nanotechnol.* **2007**, *7*, 3495–3501.
27. Delgado, J. J.; Chen, X.; Tessonnier, J. P.; Schuster, M. E.; Del Rio, E.; Schlogl, R.; Su, D. S. *Catal. Today* **2010**, *150*, 49–54.
28. Velasquez, J. D. D.; Suarez, L. A. C.; Figueiredo, J. L. *Appl. Catal., A* **2006**, *311*, 51–57.
29. Gniot, I.; Kirszensztejn, P.; Kozlowski, M. *Appl. Catal., A* **2009**, *362*, 67–74.
30. Frank, B.; Zhang, J.; Blume, R.; Schlogl, R.; Su, D. S. *Angew. Chem., Int. Ed.* **2009**, *48*, 6913–6917.
31. Frank, B.; Morassutto, M.; Schomacker, R.; Schlogl, R.; Su, D. S. *ChemCatChem* **2010**, *2*, 644–648.
32. Zboray, M.; Bell, A. T.; Iglesia, E. *J. Phys. Chem. C* **2009**, *113*, 12380–12386.
33. Albonetti, S.; Cavani, F.; Trifiro, F. *Catal. Rev.: Sci. Eng.* **1996**, *38*, 413–438.
34. Liang, C. D.; Li, Z. J.; Dai, S. *Angew. Chem., Int. Ed.* **2008**, *47*, 3696–3717.
35. Figueiredo, J. L.; Pereira, M. F. R.; Freitas, M. M. A.; Orfao, J. J. M. *Carbon* **1999**, *37*, 1379–1389.
36. Schwartz, V.; Fu, W.; Tsai, Y. T.; Meyer, H. M., III; Rondinone, A. J.; Wu, Z.; Overbury, S. H.; Liang, C. D. **2013**, in preparation.
37. Hummers, W. S.; Offeman, R. E. *J. Am. Chem. Soc.* **1958**, *80*, 1339–1339.
38. Vannice, M. A. *Catal. Today* **2007**, *123*, 18–22.
39. Frank, B.; Blume, R.; Rinaldi, A.; Trunschke, A.; Schlogl, R. *Angew. Chem., Int. Ed.* **2011**, *50*, 10226–10230.
40. Frank, B.; Rinaldi, A.; Blume, R.; Schlogl, R.; Su, D. S. *Chem. Mater.* **2010**, *22*, 4462–4470.

Chapter 11

Supported Hybrid Enzyme-Organocatalysts for Upgrading the Carbon Content of Alcohols

Kapil Kandel, Stacey M. Althaus, Marek Pruski, and Igor I. Slowing*

U.S. Department of Energy Ames Laboratory, Ames, Iowa 50011, USA, and Department of Chemistry, Iowa State University, 1605 Gilman Hall, Ames, Iowa 50011, USA
***E-mail: islowing@iastate.edu**

A bicatalytic system was prepared by the immobilization of alcohol oxidase enzyme and an alkylamine organocatalyst in distinct locations of mesoporous nanoparticles. The resulting nanocomposites were able to perform a sequence of oxidation and aldol coupling reactions, which transformed short chain alcohols into longer chain molecules. The process takes place at low temperatures, but requires additional enzyme (catalase) to prevent inactivation of the catalyst. This qualitative study introduces a model of a hybrid multicomponent nanomaterial that resembles the behavior of multienzymatic systems within confined spaces.

Introduction

Despite being increasingly considered as a biorenewable alternative to gasoline for transportation fuels, the use of ethanol in combustion engines remains limited to blends with petroleum based fuels (*1*, *2*). One of the main reasons for this limitation is the low vapor pressure of ethanol that arises from its ability to form hydrogen bonds. In addition, the low carbon to oxygen ratio of ethanol results in a low energy density, making the mileage per volume lower than that of gasoline (*3*). A potential solution to both of these problems is to eliminate the hydroxyl group and increase the carbon content of ethanol. This can be accomplished by deoxygenating and coupling individual molecules into an oligomer. This task has been performed using various approaches, most of them involving energy-intensive processes such as heating the alcohol at high

In Novel Materials for Catalysis and Fuels Processing; Bravo-Suárez, J., et al.;
ACS Symposium Series; American Chemical Society: Washington, DC, 2013.

temperatures in presence of suitable catalysts (*4–6*). However, it would be desirable to perform these conversions with as little thermal input as possible. To achieve this goal we designed a system that involves the use of two different catalytic species that perform a two step conversion of ethanol at low temperatures in a single pot. While deoxygenation is in principle a reduction, we considered an approach in which the alcohol is initially oxidized to an aldehyde and then oligomerized through a self-aldol condensation at low temperatures (eqs 1 and 2).

$$CH_3CH_2OH \xrightarrow{\text{Ox.}} CH_3CHO \qquad (1)$$

$$x\,CH_3CHO \xrightarrow{\text{Aldol}} CH_3(CH)_xCHO \qquad (2)$$

To perform these transformations at low temperature, we chose an enzyme, alcohol oxidase from *Pichia pastoris*, as the oxidation catalyst that would convert ethanol to acetaldehyde by reaction with oxygen (eq 1). The low temperature aldol condensation of acetaldehyde (eq 2), can be promoted by amines (*7*). One problem with this design is that amines can be oxidized by the enzyme (*8*). To avoid this, mesoporous silica nanoparticles (MSN) were functionalized with amines immobilized mainly in the interior of the pores, with the much larger enzyme attached to the external surface (Figure 1). This physical separation should prevent any mutual interference between both catalysts, allow them to act independently, yet enable sequential transformation of a substrate, thus behaving like a nanosized assembly line.

Experimental

Tetramethyl orthosilicate (98%), hydrochloric acid (37%), ethanol (99.5%), methanol (99.8%), 1-propanol (99.5%), 1-butanol (99.8%), acetaldehyde (99.5%), toluene (99.5%), alcohol oxidase from *Pichia pastoris* (1KU), catalase from bovine liver (3980 units/mg) were purchased from Sigma-Aldrich. 3-aminopropyl trimethoxysilane (97%), 3-glycidoxypropyl dimethyl methoxysilane (97%) were purchased from Gelest. Block copolymer Pluronic P104 was obtained from BASF. All reagents were used as received without further purification.

Catalyst Preparation

The MSN catalyst was prepared by co-condensation of 3-aminopropyl trimethoxysilane (2.1 mL) with tetramethyl orthosilicate (10.64 g) in presence of the templating agent nonionic block copolymer Pluronic P104 (7 g). The condensation was performed in an acidic medium (164 g H_2O and 109 g 4 M HCl) under constant stirring (400 rpm) for 24 h at 50 °C. The mixture was then

In Novel Materials for Catalysis and Fuels Processing; Bravo-Suárez, J., et al.;
ACS Symposium Series; American Chemical Society: Washington, DC, 2013.

set in a teflon-lined autoclave and heated at 120 °C for additional 24 h. The white solid obtained was filtered, washed with methanol, and dried in air at room temperature. The templating agent was then removed by Soxhlet extraction in ethanol for 24 h and the porous solid identified as AP-MSN was dried overnight under vacuum at room temperature.

To immobilize the enzyme, AP-MSN (1.0 g) was reacted with 3-glycidoxypropyl dimethyl methoxysilane linker (500 μL) by refluxing in anhydrous toluene (150 mL) for 3 h. The reaction product was filtered, washed with dry toluene, and dried overnight under vacuum at room temperature. The enzyme immobilization was achieved by mixing the linker-AP-MSN (20 mg) with a sucrose solution of alcohol oxidase from *Pichia pastoris* (50 μL, 100 units) in phosphate saline buffer (PBS, pH 7.4, 1.5 mL) at room temperature. The mixture was swirled at 75 rpm in an orbital shaker at room temperature for 6 h. For the catalase containing material, both enzymes (catalase and alcohol oxidase, 1.0 mg and 50 μL, respectively) were premixed in 0.5 mL PBS, pH 7.4, and a fresh suspension of linker-AP-MSN in 1.5 mL PBS was added. The mixture was then swirled at 75 rpm in an orbital shaker for 6 h at room temperature.

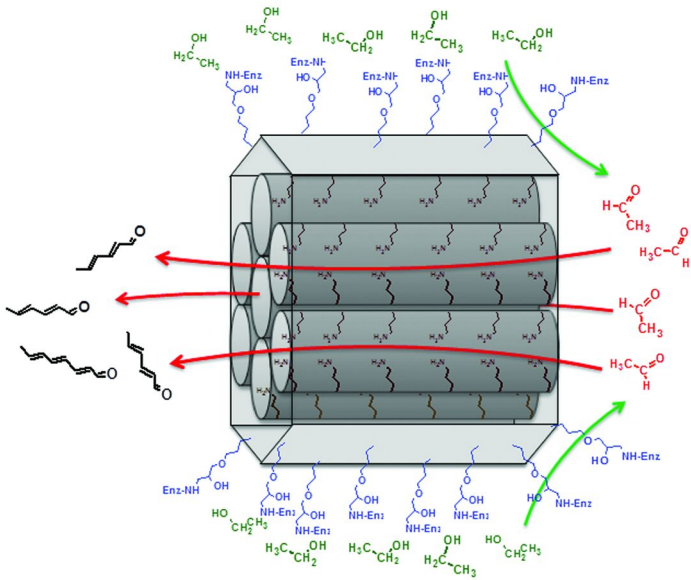

Figure 1. Design of the enzyme-organocatalyst material: an enzyme (Enz, blue.) is immobilized on the external surface of the nanoparticles to promote the oxidation of ethanol (green) to acetaldehyde (red), and an aldol catalyst (primary amine, brown) is located in the interior of the pores to oligomerize the acetaldehyde to compounds with longer carbon chains. (see color insert)

In Novel Materials for Catalysis and Fuels Processing; Bravo-Suárez, J., et al.;
ACS Symposium Series; American Chemical Society: Washington, DC, 2013.

Characterization

Surface analysis was performed by nitrogen physisorption isotherms in a Micromeritics Tristar surface analyzer. The surface areas were calculated by the Brunauer–Emmett–Teller (BET) method and the pore size distributions were calculated from the adsorption branch by the Barrett–Joyner–Halenda (BJH) method. Small angle powder X-ray diffraction patterns were obtained with a Rigaku Ultima IV diffractometer using Cu target at 40 kV and 44 mA. For transmission electron microscopy (TEM) imaging, an aliquot of the powder was sonicated in methanol. A single drop of this suspension was placed on a lacey carbon coated copper TEM grid and dried in air. The TEM examination was completed on a Tecnai G2 F20 electron microscope operated at 200 kV. Dynamic light scattering and ξ-potential measurements were performed in a Malvern Nanosizer ZS90 using suspensions of the materials with pH 7.4.

Solid-State NMR

^{13}C cross polarization magic angle spinning (CPMAS) solid-state NMR experiments were used to confirm the structures of the surface bound species. These experiments were preformed at 14.1 T on a Varian NMR System 600 spectrometer equipped with a 1.6-mm Fast MAS™ probe operated at 599.6 MHz (^{1}H) and 150.8 MHz (^{13}C). Experimental parameters are given in the figure caption using the following symbols: ν_R is the MAS rate, $\nu_{RF}(X)$ is the magnitude of radiofrequency magnetic field (RF) applied to X spins, τ_{CP} is the mixing time during cross polarization, τ_{RD} is the recycle delay, NS is the number of scans, and AT is the total acquisition time. The chemical shifts of ^{13}C and ^{1}H are reported using the δ scale and referenced to tetramethylsilane (TMS) at 0 ppm.

Catalytic Reactions

Self-aldol reaction was performed by stirring an aqueous suspension of AP-MSN or linker-AP-MSN (20.0 mg, 10.0 mL) and acetaldehyde (0.100 mL, 1.8 mmol) at 40 °C for 20 h. The reaction was monitored by extraction with 1.0 mL diethyl ether and analysis of the extract by gas chromatography with a mass spectrometry detector (GC–MS).

The sequential oxidation-self-aldol reaction was performed by adding ethanol (5 μL, 86 μmol) to a freshly prepared suspension of the enzyme-AP-MSN material in PBS (3.0 mL). Oxygen gas was bubbled into the suspension for 1 min, and the mixture was stirred at 40 °C for 20 h. Reaction products were monitored by extraction with 1.0 mL diethyl ether and GC–MS analysis.

Results and Discussion

Synthesis of AP-MSN and Catalysis of Self-Aldol Condensation

The co-condensation of organosilanes with orthosilicates in the presence of surfactants is a valuable technique for achieving homogeneous functionalization

In Novel Materials for Catalysis and Fuels Processing; Bravo-Suárez, J., et al.;
ACS Symposium Series; American Chemical Society: Washington, DC, 2013.

of mesoporous silicas. The interaction between the 3-aminopropyl group and the surfactant micelles during the synthesis of the material tends to favor its localization at the interface between the surfactant and the surface of silica (Figure 2a). This interface corresponds to the pore surface of the resulting materials (*9*, *10*). Powder X-ray diffraction of the material suggests a highly ordered 2D-hexagonal array of mesopores (Figure 2b), as confirmed by transmission electron microscopy (Figure 2c). Dynamic light scattering measurements were consistent with the sub-micron particle size observed by TEM (750 × 400 nm sized particles). Nitrogen physisorption analysis, following surfactant extraction, confirmed the material possessed a high surface area (575 m^2/g) and a narrow pore size distribution centered at 6.6 nm (Figure 2d). A positive ξ-potential of the material (+28.0 mV at pH 7.4) was consistent with the presence of the 3-aminopropyl functionality on the surface of the material.

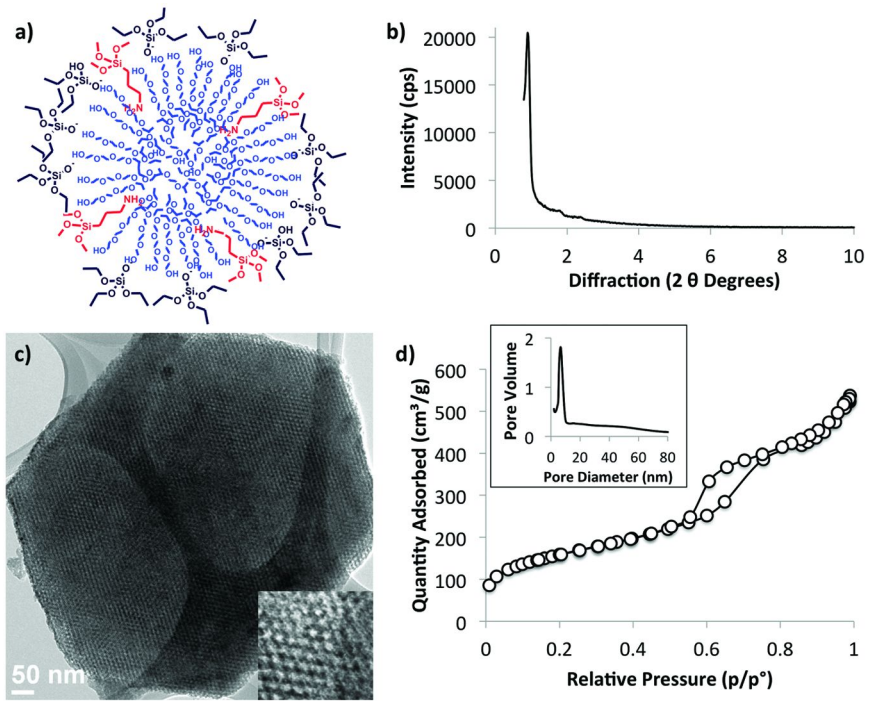

Figure 2. AP-MSN: a) Co-condensation of 3-aminopropyl groups at the interface between the growing silica polymer and the templating surfactant micelles, b) small angle powder X-ray diffraction pattern, c) transmission electron micrograph (insert: zoomed in detail of the micrograph showing the hexagonal pore order), and d) nitrogen physisorption isotherms (insert: pore size distribution in nanometers) of the material. (see color insert)

In Novel Materials for Catalysis and Fuels Processing; Bravo-Suárez, J., et al.;
ACS Symposium Series; American Chemical Society: Washington, DC, 2013.

The catalytic activity of AP-MSN for the self-aldol reaction was tested by addition of acetaldehyde to an aqueous suspension of AP-MSN. Within five minutes the white AP-MSN material started to gradually change color to a light yellow and eventually turned brown. This color change appears to result from the adsorption of hydroxylated oligomers on the surface of the the material through hydrogen bonding with surface silanols. GC–MS analysis of the ether extracts showed a mixture of products (Figure 3), the most abundant being the dimerization product 3-hydroxy-butanal (65% of the products observed). Increasing the amount of acetaldehyde lead to a more complex distribution of products than observed at low concentrations. A tenfold increase in acetaldehyde concentration altered the distribution of products towards higher molecular weights, with the trimer 2,4-hexadienal being the most abundant species (36% of the detected products), and the distinct formation of a tetramer (Figure 3c).

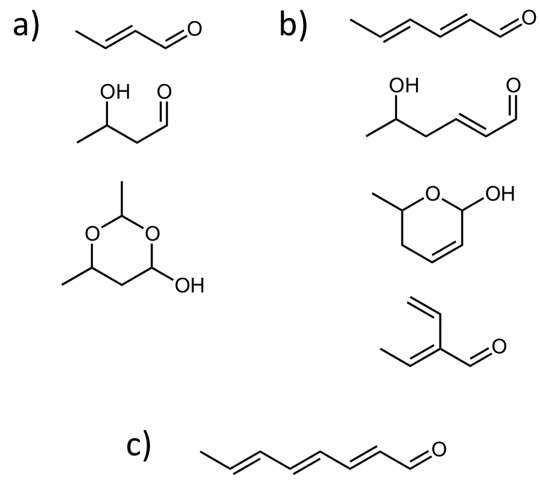

Figure 3. The most abundant products from the self-aldol reaction of acetaldehyde catalyzed by AP-MSN observed by GC–MS analysis of the ether extracts (20 h at 40 °C). Products are classified as a) dimers, b) trimers, and c) tetramer.

Incorporation of Enzyme and Catalysis for Sequential Conversion

AP-MSN was then grafted with the glycidoxypropyl silane linker and the presence of both groups was confirmed by solid-state NMR (Figure 4). The incorporation of the glycidoxypropyl group was expected to take place mainly at the most accessible external surface (*11*, *12*). This glycidoxypropyl modified AP-MSN suspended better in water and had a slightly more positive ξ-potential (+30.5 mV), consistent with the reduction of the number of silanol groups by the grafting procedure. This material was still capable of catalyzing the self-aldol reaction of acetaldehyde with a distribution of products similar to that of AP-MSN.

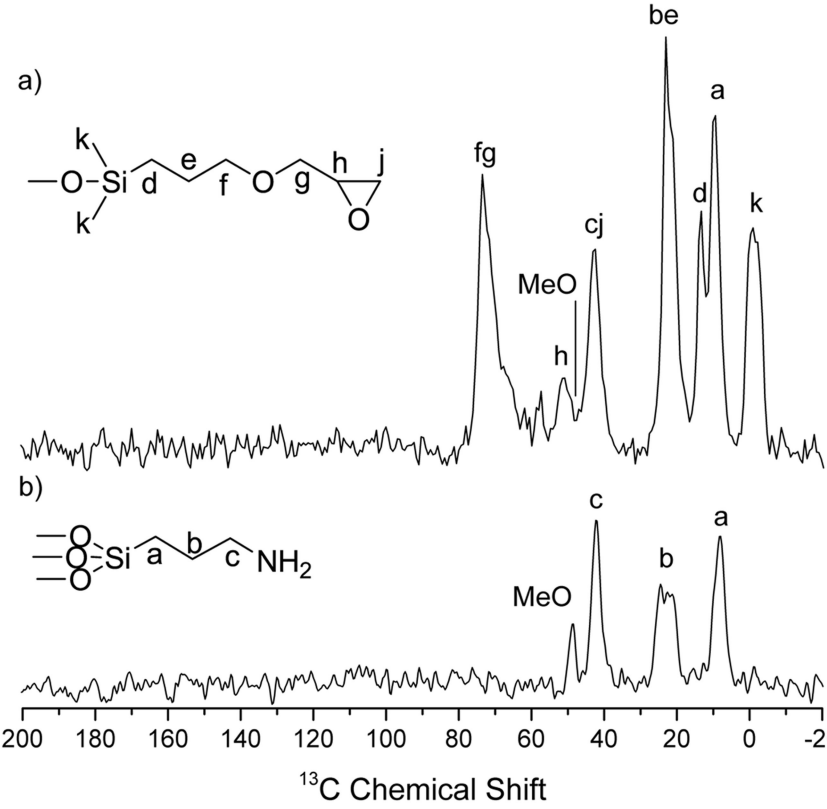

Figure 4. ^{13}C CPMAS NMR spectra of a) glycidoxypropyl-AP-MSN and b) AP-MSN. Spectrum a) was acquired using ν_R = 40 kHz, $\nu_{RF}(^{13}C)$ = 100 kHz, $\nu_{RF}(^{1}H)$ during CP = 60 kHz, $\nu_{RF}(^{1}H)$ during SPINAL-64 decoupling = 10 kHz, τ_{CP} = 1 ms, τ_{RD} = 3 s, NS = 12288, and AT = 10.3 h. Spectrum b) used ν_R = 40 kHz, $\nu_{RF}(^{13}C)$ = 60 kHz, $\nu_{RF}(^{1}H)$ during CP = 100 kHz, $\nu_{RF}(^{1}H)$ during SPINAL-64 decoupling = 11 kHz, τ_{CP} = 2 ms, τ_{RD} = 3 s, NS = 10240, and AT = 8.7 h.

Alcohol oxidase was immobilized on the material by covalently binding free amine groups of the enzyme with the glycidoxypropyl linker (eq 3) (*13*). The enzyme was added to a suspension of linker-AP-MSN and the mixture was shaken for 6 h at room temperature. This led to a red colored mixture, which became a pink solid after centrifugation and washing, indicative of the retention of the enzyme. The addition of ethanol to a suspension of the enzyme-AP-MSN nanocomposite produced an immediate color change to bright yellow, indicative of the irreversible inactivation of the enzyme. GC–MS analysis of ether extracts gave no indication of catalytic activity. To evaluate the possibility that the bound enzyme could be blocking the pores of the material, a sample was prepared by reacting linker-AP-MSN (100 mg) with bovine serum albumin (10 mg) as a model of the alcohol oxidase enzyme. Nitrogen physisorption analysis of the composite revealed that

In Novel Materials for Catalysis and Fuels Processing; Bravo-Suárez, J., et al.;
ACS Symposium Series; American Chemical Society: Washington, DC, 2013.

the binding of the protein significantly reduced the surface area of the material from the original 575 to 282 m^2/g, while the pore size decreased only moderately (from 6.6 to 5.6 nm). However, this reduction in porosity would not justify the lack of activity of the composite.

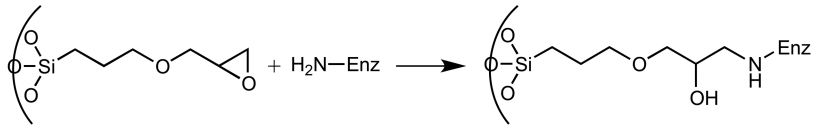

(3)

Hydrogen peroxide is a byproduct of the oxidation of alcohols catalyzed by alcohol oxidase, and this substance is a potent inhibitor of this enzyme (eq 4) (*14*). One way to circumvent this problem is to introduce into the reaction system a second enzyme (catalase) to facilitate the conversion of hydrogen peroxide to oxygen (eq 5) (*15*). The addition of catalase to the alcohol oxidase-AP-MSN suspension, followed by bubbling with oxygen and addition of ethanol, enabled the material to catalyze the tandem conversion of alcohol into acetaldehyde oligomers. No obvious signs of enzyme inactivation were observed during the first 20 h of the reaction. However, after 20 h at 40 °C the material failed to catalyze the conversion of additional ethanol, indicating the inactivation of the enzyme.

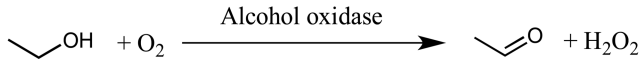

(4)

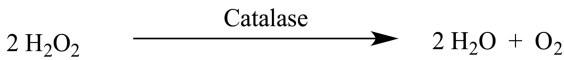

(5)

Surprisingly, contrary to the complex mixtures obtained from the AP-MSN catalyzed self-aldol reaction of acetaldehyde, the sequential oxidation-aldol reaction catalyzed by the enzyme-AP-MSN material gave a simple mixture consisting mainly of the linear trimer (2,4-hexadienal, 72% of the observed products), and two dimers (2-hydroxybutanal and 2-butenal, 10 and 18% of the detected products, respectively) (Figure 5). It should be stressed that the main product of the AP-MSN catalyzed self-aldol condensation was a dimer, whereas the tandem conversion catalyzed by the enzyme-AP-MSN material produced mainly a trimer. This suggests that the sequential reaction takes place in a more controlled fashion than the single step self-aldol reaction.

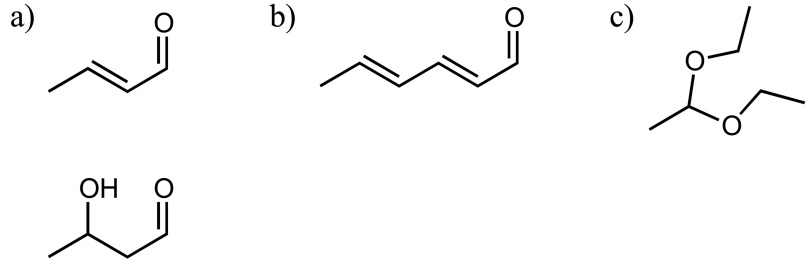

Figure 5. Products observed in the tandem oxidation-aldol conversion of ethanol catalyzed by the alcohol oxidase-AP-MSN nanocomposite: a) dimers, b) trimer, and c) acetal formed only upon addition of excess ethanol.

In contrast to the single step self-aldol reaction, a 10-fold increase in substrate did not have an effect on the product distribution, as the trimer (2,4-hexanedial) remained the main product of the sequential oxidation-aldol. However, increasing the amount of ethanol from 29 to 290 mM had two significant effects. First, it led to denaturing of the enzyme after only 1 h of reaction, as evidenced by the color change of the reaction media to a bright yellow and loss of activity. This change in color could not be reversed by bubbling additional oxygen. According to eq 4 addition of an excess of ethanol must have led to the production of high concentrations of hydrogen peroxide. If the concentration of this byproduct became too large, it could not be completely degraded by the limited amount of catalase available, and would therefore irreversibly deactivate alcohol oxidase (*14*, *15*). The second effect of the excess of ethanol was evidenced by the formation of an acetal as detected by GC–MS analysis (Figure 5c). This product was formed upon acetaldehyde trapping by unreacted ethanol (eq 6). This side-reaction prevented the already limited amount of acetaldehyde from undergoing further self-aldolization. Therefore the excess of alcohol inhibited both catalytic processes: the enzymatic oxidation and the self-aldol condensation.

$$CH_3CHO + 2\ CH_3CH_2OH \longrightarrow CH_3CH(OCH_2CH_3)_2 \qquad (6)$$

The product distribution observed in the sequential oxidation-aldol process in comparison to the one-step self-aldol catalyzed by AP-MSN was likely controlled by the limited availability of the intermediate acetaldehyde. The availability of acetaldehyde was regulated not only by the enzymatic activity, but also by the presence of excess ethanol that could capture the intermediate as an acetal. Therefore, optimization of the process is highly dependent on the rate of ethanol feeding. Low ethanol concentrations minimize formation of acetals (eq 6), and also slow the production of hydrogen peroxide by-product allowing for its efficient degradation by catalase (eqs 4 and 5).

Other alcohols were tested to evaluate the scope of application of this bifunctional catalyst. Alcohol oxidase is known to be a good substrate for short chain alcohols, with activity decreasing with increasing bulkiness of the organic group (*14*, *16*, *17*). Addition of propanol and butanol to suspensions of the enzyme-AP-MSN material in presence of catalase yielded the corresponding dimers with almost 100% selectivity (eqs 7 and 8). The crossed-aldol reaction between methanol and acetone was attempted but no aldol products were observed.

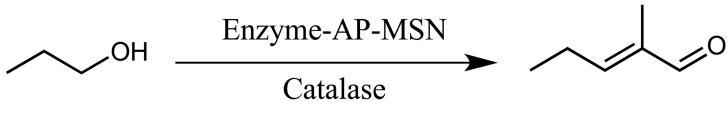

(7)

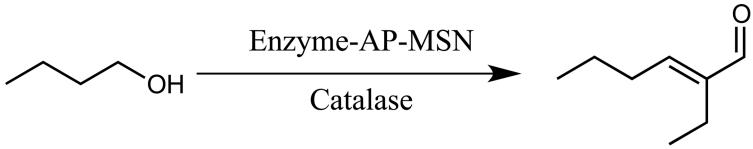

(8)

Conclusions

We developed a bifunctional heterogeneous catalyst comprised of an enzyme (alcohol oxidase) and an organocatalytic amine supported on high surface area mesoporous nanoparticles. This bicatalytic material is capable of promoting the sequential conversion of small chain alcohols into longer chain aldehydes with good selectivity. Site-separation of the two catalytic moieties within different domains of the nanoparticles prevented oxidation of the amine by the enzyme. Addition of catalase to the system degraded the by-product hydrogen peroxide, preventing inhibition of the alcohol oxidase enzyme. The reaction catalyzed by the multifunctional material displayed high selectivity for the product of trimerization, independent of the initial concentration of substrate alcohol. However, excess alcohol affected the stability of the enzyme due to accumulation of hydrogen peroxide. Further work is currently in progress to improve yields and enzyme stability. Fine tuning the amount of the aminopropyl active sites on the support, along with incorporation of an enzyme stabilizer, should provide improved conversion. This exploratory study demonstrates the enormous potential that the hybrid enzymatic-organocatalytic multifunctional nanodevices have for the transformation of small molecules into more complex and valuable products, despite the complexity and difficulties associated with the creation of such nanosized assembly lines.

Acknowledgments

This research was supported at the Ames Laboratory by the U.S. Department of Energy, Office of Basic Energy Sciences. Ames Laboratory is operated for the U.S. Department of Energy by Iowa State University under Contract No.

DE-AC02-07CH11358. The authors wish to thank BASF Co. for the generous donation of P104 triblock copolymer.

References

1. Abdel-Rahman, A. A.; Osman, M. M. *Int. J. Energy Res.* **1997**, *21*, 31–40.
2. Wallner, T.; Miers, S. A.; McConnell, S. *J. Eng. Gas Turbines Power* **2009**, *131*, 032802–9.
3. Jeuland, N.; Montagne, X.; Gautrot, X. *Oil Gas Sci. Technol.* **2004**, *59*, 559–570.
4. Oudejans, J. C.; Van Den Oosterkamp, P. F.; Van Bekkum, H. *Appl. Catal.* **1982**, *3*, 109–115.
5. Takahara, I.; Saito, M.; Inaba, M.; Murata, K. *Catal. Lett.* **2005**, *105*, 249–252.
6. Sun, J.; Zhu, K.; Gao, F.; Wang, C.; Liu, J.; Peden, C. H. F.; Wang, Y. *J. Am. Chem. Soc.* **2011**, *133*, 11096–11099.
7. Kandel, K.; Althaus, S. M.; Peeraphatdit, C.; Kobayashi, T.; Trewyn, B. G.; Pruski, M.; Slowing, I. I. *J. Catal.* **2012**, *291*, 63–68.
8. Fitzpatrick, P. F. *J. Labelled Compd. Radiopharm.* **2007**, *50*, 1016–1025.
9. Huh, S.; Wiench, J. W.; Yoo, J.-C.; Pruski, M.; Lin, V. S.-Y. *Chem. Mater.* **2003**, *15*, 4247–4256.
10. Yokoi, T.; Yoshitake, H.; Tatsumi, T. *Chem. Mater.* **2003**, *15*, 4536–4538.
11. Mal, N. K.; Fujiwara, M.; Tanaka, Y. *Nature* **2003**, *421*, 350–353.
12. De Juan, F.; Ruiz-Hitzky, E. *Adv. Mater.* **2000**, *12*, 430–432.
13. Haginaka, J. *J. Chromatogr., A* **2001**, *906*, 253–273.
14. Couderc, R.; Baratti, J. *Agric. Biol. Chem.* **1980**, *44*, 2279–2289.
15. Geissler, J.; Ghisla, S.; Kroneck, P. M. H. *Eur. J. Biochem.* **1986**, *160*, 93–100.
16. Sahm, H.; Schütte, H.; Kula, M.-R. In *Methods in Enzymology*; Willis, A. W., Ed.; Academic Press: 1982; Vol. 89, pp 424−428.
17. Menon, V.; Hsieh, C. T.; Fitzpatrick, P. F. *Bioorg. Chem.* **1995**, *23*, 42–53.

Chapter 12

Activity and Selectivity of Base Promoted Mono and Bimetallic Catalysts for Hydrogenolysis of Xylitol and Sorbitol

Xin Jin,[1,2] Bala Subramaniam,[1,2] and Raghunath V. Chaudhari[*,1,2]

[1]Center for Environmentally Beneficial Catalysis, University of Kansas, 1501 Wakarusa Dr., Lawrence, Kansas 66047, USA
[2]Department of Chemical and Petroleum Engineering, University of Kansas, Learned Hall 1530 W 15th St, Lawrence, Kansas 66045, USA
[*]E-mail: rvc1948@ku.edu

Hydrogenolysis of polyols (sorbitol and xylitol) was investigated using supported mono and bimetallic catalysts in aqueous medium. The role of different bimetallic formulations, supports, and solid acid and base promoters on catalytic activity and selectivity was studied in a batch slurry reactor. It was observed that the major products formed with Ru catalysts were C_2 and C_3 glycols and alcohols. The addition of a second metal such as Re promotes catalytic activity, whereas addition of solid base promoters enhance both activity and selectivity of liquid phase products. Based on the evaluation of different catalysts and studies with intermediate products as substrates, a reaction pathway and possible mechanism of hydrogenolysis are discussed.

Introduction

The production of transportation fuels and chemicals from biomass feedstocks requires efficient, cost-effective catalytic systems. During the past decade, the catalytic conversion of glycerol, a by-product from bio-diesel production, to various value-added chemicals such as 1,2-propanediol, 1,3-propanediol, ethylene glycol, and lactic acid has been extensively studied on Cu (*1*, *2*), Ni (*3*), Pt (*4*), Ru (*5*–*7*), Rh (*8*), and Ir (*9*, *10*) catalysts. In recent years, there has been a growing interest in converting other sugar derived polyols including xylitol,

In Novel Materials for Catalysis and Fuels Processing; Bravo-Suárez, J., et al.;
ACS Symposium Series; American Chemical Society: Washington, DC, 2013.

sorbitol, and mannitol to fuel-range molecules on metal-based catalysts (*11–13*). However, relatively limited work has been done on the synthesis of value added chemicals from xylitol (*14*) and sorbitol (*15*). Sohounloue and co-workers (*16*) found reverse aldolization of sorbitol as a key step in hydrogenolysis using supported Ru catalysts, while Montassier et al. (*17*) proposed that hydrogenolysis follows C–C and C–O bond breakage by a retro-Michael reaction. Zhao and co-workers (*15*) reported sorbitol hydrogenolysis over a Ru/carbon nanofiber catalyst with 68% conversion and 53% selectivity to glycols. Banu et al. (*18*) found that the presence of Ca^{2+} and Na^{+} in a Ni catalyst enhanced the selectivity of liquid products (glycols and alcohols). Sun and co-workers (*14*) studied hydrogenolysis of xylitol and found that retro-aldolization leads to the formation of smaller molecules such as 1,2-propanediol and ethylene glycol in the presence of a CaO promoter. The reaction network for the hydrogenolysis of xylitol and sorbitol involves more complex pathways compared to glycerol conversion due to the multiple C–C and C–O bond cleavage reactions that can occur on metal catalysts at elevated temperatures. Therefore, there is a need to better understand the hydrodeoxygenation of xylitol and sorbitol on Ru catalysts with respect to: (a) reaction pathways and the role of specific metals in determining the activity/selectivity behavior, and (b) the role of acidic and basic promoters. Here, we report experimental studies on the hydrogenolysis of xylitol and sorbitol over supported Ru, Rh, Pt, and Ir catalysts on activated carbon in the presence of various solid base promoters. Detailed results on the concentration-time profiles, activity and selectivity of mono and bimetallic Ru catalysts, and the stability of Ru catalysts are presented.

Experimental

Mono and bimetallic catalysts were prepared via a precipitation method and characterized previously (*7*). For the preparation of Ru based mono and bimetallic catalysts, 5.0 g of activated carbon (100 mesh, Sigma) was charged to 700 cm^3 of deionized water and the slurry was heated up to 368 K in a round-bottom flask with magnetic stirring for 2 h. Then, required amounts of $RuCl_3 \cdot xH_2O$ (99.98%, Sigma) and perrhenic acid (65 wt % in water, Sigma) solution were added to the slurry dropwise. The resultant slurry was stirred for another 3 h. A dilute $NH_3 \cdot H_2O$ solution (Fisher) was finally added to the system dropwise until a pH value of 10. After stirring for 3 h, the mixture was filtered and the solids were washed with 2000 cm^3 of deionized water at 363 K to remove chloride ions. The solid samples were then dried overnight in a vaccum oven at 393 K. The catalysts were activated at 573 K for 5 h in a tube furnace with flowing H_2 (99.95%, Linweld, 20 cm^3/min/g-catalyst) before testing for catalytic hydrogenolysis in a slurry reactor. The tube was first purged with N_2 (99.995%, Linweld, 20 cm^3/min/g-catalyst) at room temperature for 30 min, then heated at a rate of 5 K/min to 423 K. Then, the N_2 flow was switched off and H_2 was introduced to the system. Next, the sample was heated at a rate of 5 K/min to 573 K and activated for 5 h. Finally, the system was cooled to 423 K and then flushed with N_2 again. The samples were taken out of the tube furnace at room temperature and stored in a brown container.

In Novel Materials for Catalysis and Fuels Processing; Bravo-Suárez, J., et al.;
ACS Symposium Series; American Chemical Society: Washington, DC, 2013.

For Ru based catalysts, the metal contents employed are Ru(0.25–2.0 wt %)/C and Ru(1 wt %)Re(1 wt %)/C, as described previously (*7*). The supported Ru and RuRe catalysts were characterized by inductively coupled plasma (ICP) spectroscopy (JY-2000, HORIBA, Jobin Yvon Inc.) by digesting the samples in an autoclave with diluted aqueous hydrofluoric acid (47–51%, Fisher) and sulfuric acid (98%, Sigma) solutions. The measured specific metal contents for Ru(0.25 wt %)/C, Ru(0.5 wt %)/C, Ru(1 wt %)/C, and Ru(2.5 wt %)/C catalysts were 0.21, 0.49, 0.98, and 2.42 wt %, respectively. For the Ru(1 wt %)Re(1 wt %)/C catalyst, the metal compositions for Ru and Re were 0.97 and 1.08 wt %, respectively.

The same preparation procedure was followed for the synthesis of other metallic catalysts including Rh(1 wt %)/C, Pt(1 wt %)/C, and Ir(1 wt %)/C catalysts. $RhCl_3.xH_2O$ (99.9%, Sigma), $H_2PtCl_6.xH_2O$ (99.9%, Sigma), and $IrCl_3.xH_2O$ (99.9%, Sigma) were used as metal precursors. The measured specific metal compositions for Rh, Pt, and Ir were 1.04, 0.95, and 0.92 wt %, respectively.

Hydrogenolysis experiments were carried out in a high-pressure, high-temperature 300 cm^3 reactor supplied by Parr Instrument Co. In all batch tests, about 3.0 g of substrate [e.g., sorbitol (98%, sigma), xylitol (99%, sigma), glycerol (99.5%, sigma), or ethylene glycol (99.8%, sigma)] was first dissolved in 90 cm^3 of water solution. Approximately 0.4 g of solid catalyst [e.g., Ru(1 wt %)/C] was introduced to the reactor. If required, 0.4 g of solid promoters [e.g., MgO (99%, 325 mesh, Sigma), CeO_2 (99.9%, Fisher), or Hβ zeolite (CP811C-300, Zeolyst)] were then taken into the reactor before introducing the substrate aqueous solution. The reactor was sealed and purged thrice each with N_2 and followed H_2, respectively. The reactor was then heated up to desired temperature. During the reactor heating process, the stirring rate was set at <50 rpm to ensure reaction was restrained by mass transfer limitation. When the reactor reached the desired temperature, the stirring speed was increased to 1000 rpm to avoid external mass transfer limitations (*7*). Following a fixed batch-time reaction, the reactor was cooled down to room temperature. Then, the reactor was depressurized by releasing the gas-phase products to fill two external sampling loops for offline gas chromatography (GC) analysis (Shimadzu, Model GC-2014). In one sampling loop, C_2–C_5 alkanes were separated with an RT-QPLOT column (15 m long, inner diameter of ID = 0.53 mm) and analyzed via flame ionization detection (FID). In a second sampling loop, methane, ethane, CO, and CO_2 were separated with a 60/80 Carboxen 1000 packed column (4.57 m long, ID = 3.175 mm) and analyzed using a thermal conductivity detector (TCD) device. The liquid samples were analyzed using an HPLC (a Rezex ROA-Organic Acid H^+ column, 0.005 N aqueous H_2SO_4 as mobile phase and an RI detector). These analytical results were combined to obtain a quantitative assessment of each product in the gas and liquid phase and for calculation of conversion and selectivity.

Conversion (X) is defined as the ratio of moles of substrate converted to the moles of substrate charged initially. Selectivity (S) is defined as the moles of carbon in a specific product to the moles of carbon equivalent to converted substrate. Conversion rate (mol/g-atom/h) is defined as the amount of converted substrate (mol) per g-atom of metal per unit time. The conversion rate values were calculated at low conversion levels of polyols (X = 15–20%).

Results and Discussion

Catalyst Evaluation

A variety of monometallic catalysts consisting of Ru, Rh, Pt, and Ir were prepared and tested for sorbitol hydrogenolysis in presence of MgO as a solid basic promoter. In all the experiments, the carbon balance closure was found to be within a range of 85–95%. It is clearly seen from Figure 1 that Ru showed higher activity and selectivity for sorbitol hydrogenolysis compared to other metals. After 6 h of reaction, approximately 82% of sorbitol was converted with a total liquid products selectivity of about 82%. Furthermore, the Ru/C catalyst displayed slightly higher selectivity to C_3 products (1,2-propanediol, glycerol, and lactic acid) compared to the Pt/C catalyst, whereas the Rh/C showed relatively higher selectivity for isoerythritol and 1,2-butanediol.

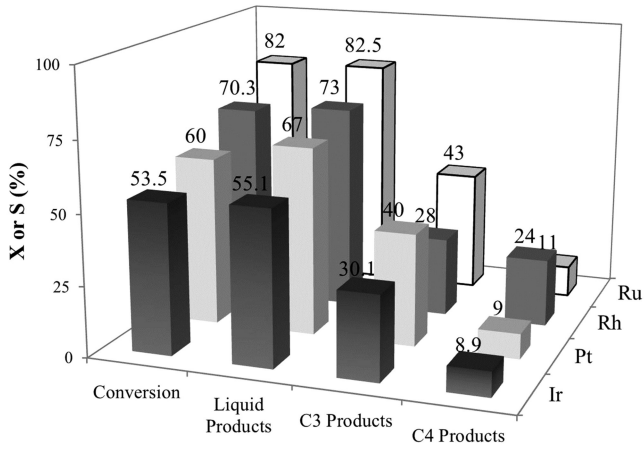

Figure 1. Conversion and liquid product carbon selectivities for sorbitol hydrogenolysis on noble metal/carbon + MgO admixture. Conditions: 503 K, P_{H2} of 7.6 MPa, 10 h. Liquid Products: methanol, ethanol, ethylene glycol, C_3, and C_4 products. C_3 products: propanediol, glycerol, lactic acid; C_4 products: isoerythritol, 1,2-butanediol.

Effect of Catalyst Composition

Sorbitol hydrogenolysis was studied over a monometallic Ru/C catalyst. As seen in Figure 2a, for sorbitol, a conversion rate of 214 mol/g-atom/h was observed for Ru loadings up to 1 wt %, which decreased by 10% at a higher Ru loading (2 wt %). The maximum conversion rate observed is greater than that reported (182 mol/g-atom/h) with a liquid base at the same temperature (*15*).

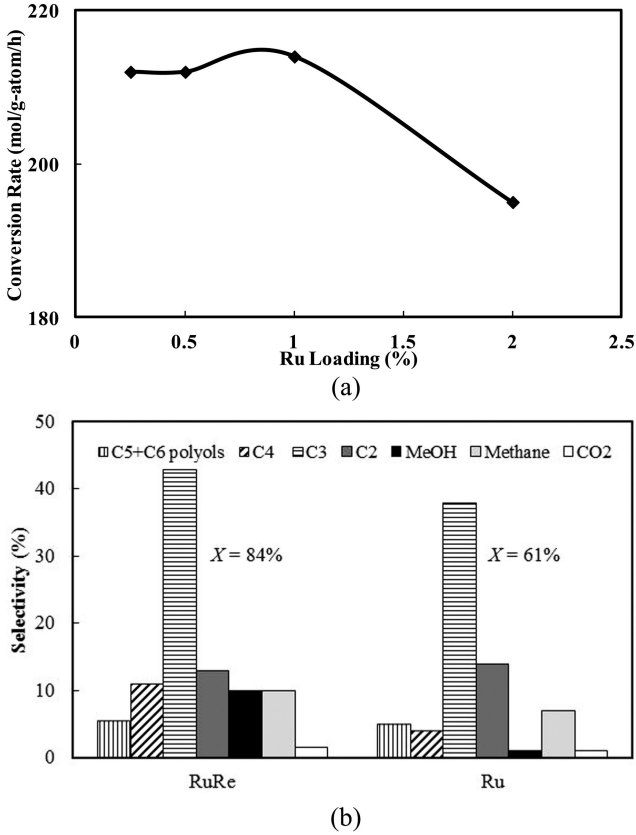

Figure 2. Conversion rate and selectivity for sorbitol hydrogenolysis. (a) Effect of Ru loading on initial activity of monometallic Ru/C catalyst. Conditions: 503 K, P_{H2} of 7.6 MPa, 0.5–1.0 h, sorbitol conversion of ~20%, and (b) The performance comparison between Ru(1 wt %) and Ru(1 wt %)Re(1 wt %) carbon supported catalysts. X = conversion, 503 K, H_2 pressure (P_{H2}), 7.6 MPa, 6 h, other conditions same as (a). MeOH: methanol; EtOH: ethanol; EG: ethylene glycol; C_3: propanediol, glycerol, lactic acid; C_4: isoerythritol, 1,2-butanediol; C_5+C_6 polyols: xylitol, 1,2,3-hexanetriol

Generally, it is believed that the hydrogenolysis of xylitol (*14*) and sorbitol (*16*) follows the retro-aldol mechanism, where dehydrogenation occurs first and produces unsaturated alcohols with olefinic bonds. The addition of Re increases the sorbitol conversion rate (256 mol/g-atom/h) over the Ru monometallic catalyst (Figure 2b). The presence of Re was also found to increase the selectivity of C_3 and C_4 diols.

In Novel Materials for Catalysis and Fuels Processing; Bravo-Suárez, J., et al.;
ACS Symposium Series; American Chemical Society: Washington, DC, 2013.

Concentration-Time Profiles

In order to establish the product distribution during hydrogenolysis of sorbitol and xylitol, several experiments were carried out using the Ru(1 wt %)Re(1 wt %)/C catalyst at 503 K and 7.6 MPa H_2 pressure. The results (Figure 3) showed that with sorbitol as the substrate, the selectivities of the major products [C_1 (methanol), C_2 (ethylene glycol), and C_3 (glycerol, 1,2-propanediol, and lactic acid)] display only slight changes with time except for 1,2-propanediol. From the structure of the sorbitol molecule, it is clear that C–C and C–O cleavage can occur at multiple locations during hydrogenolysis, producing C_5–C_6 polyols, triols, and diols in addition to lower aliphatic alcohols. The large number of products makes accurate analysis of C_5–C_6 products difficult. Similar challenges are associated with xylitol hydrogenolysis. At higher conversion levels, most of the C_5–C_6 intermediates are further hydrogenated and hence it was possible to obtain a more complete C balance.

Role of Acid and Base Promoters

The effects of acid and base promoters on the hydrogenolysis of sorbitol were also investigated. The results are shown in Figure 4 for conditions where complete sorbitol conversion is obtained. It was observed that a significant amount of gas phase alkanes (mainly methane) was formed with the addition of Hβ zeolite as a solid acid promoter, while the addition of a solid base (MgO or CeO_2) reduced the gas phase product selectivity from 25 to 11%. In previous reports, Kusserow et al. (*19*) and Montassier et al. (*17*) reported that unsaturated polyols (with similar structures as sugars) may undergo dehydration in acidic medium (Ru/C + a sulfate promoter) and result in the formation of furfurals (such as 5-hydroxymethylfurfural) instead of products from C_3–C_3 cleavage. Further, Huber and Dumesic (*20*) found that sorbitol undergoes hydrode-oxygenation at a higher temperature (523 K) over an acidic support with random C–C bond cleavage resulting in the formation of methane, ethane, and propane.

It is clear from the results in Figure 4 that acid and base promoters have a strong influence on product distribution. While the observed effects of acid promoters is consistent with previous reports (*11*), there is no specific data on the effect of solid base promoters for Ru catalyzed hydrogenolysis of sorbitol. The possible positions of C–C cleavage and hydrogenolysis reaction pathways in the presence of solid base promoters are not yet clearly understood. Several possible intermediate products were therefore tested as starting substrates to understand the effect of solid base promoters on the catalyst activity and product distribution (Figure 5). Specifically, a better understanding of the role of solid base in (a) C–O breakage and (b) methanation reactions, over bimetallic catalysts was sought. Based on the product distribution obtained from xylitol and sorbitol hydrogenolyses and proposed mechanisms from published literature (*5*, *6*), a detailed reaction pathway is proposed in Scheme 1.

According to Scheme 1, the conversion of sorbitol initiates with the base promoted dehydrogenation and C=O bond formation. Then, the unsaturated intermediate undergoes C–C cleavage via retro-aldolization. The possible C–C

cleavage positions include C_1–C_5, C_2–C_4, and C_3–C_3. The resulting small molecules undergo further hydrogenation, thus leading to glycerol, xylitol, and traces of erythritol in the final products. These intermediate polyols are further hydrodeoxygenated to 1,2-butanediol, 1,2-propanediol, ethylene glycol, and ethanol as the major products. As found in our previous report, glycerol can also undergo dehydrogenation and benzilic rearrangement to form lactic acid under our reaction conditions (*1*).

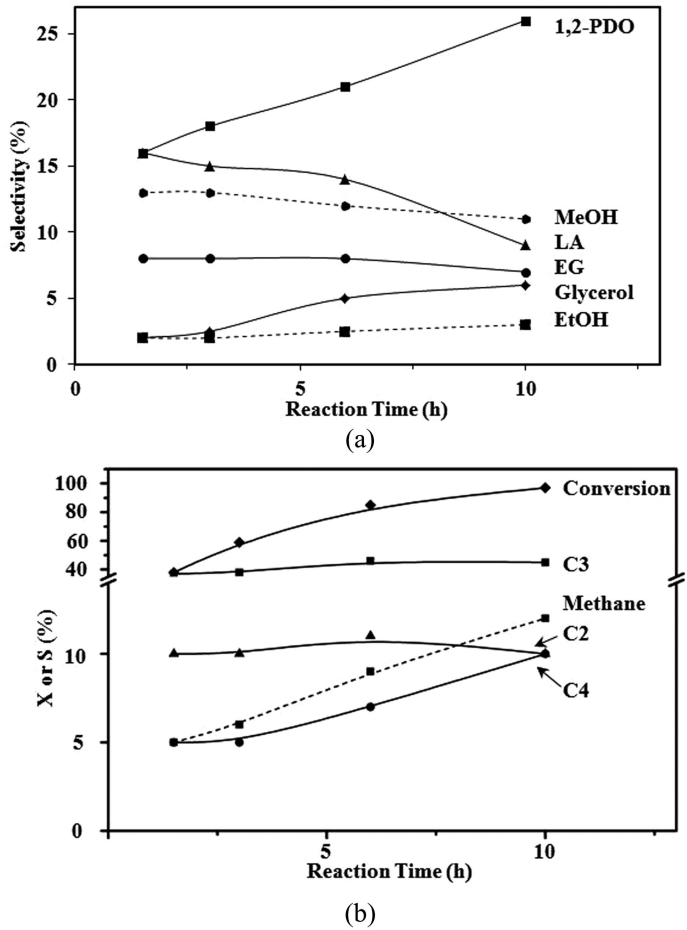

Figure 3. Product distribution during hydrogenolysis of sorbitol. (a) Selectivity of main liquid products, (b) total carbon balance. Conditions: Ru(1 wt %)Re(1 wt %)/C catalyst, MgO base promoter, 503 K, P_{H2} of 7.6 MPa. Carbon balance of 85–95%. Methanol (MeOH); C_2: ethanol (EtOH), ethylene glycol (EG); C_3: propanediol (PDO), glycerol, lactic acid (LA); C_4: isoerythritol, 1,2-butanediol.

In Novel Materials for Catalysis and Fuels Processing; Bravo-Suárez, J., et al.;
ACS Symposium Series; American Chemical Society: Washington, DC, 2013.

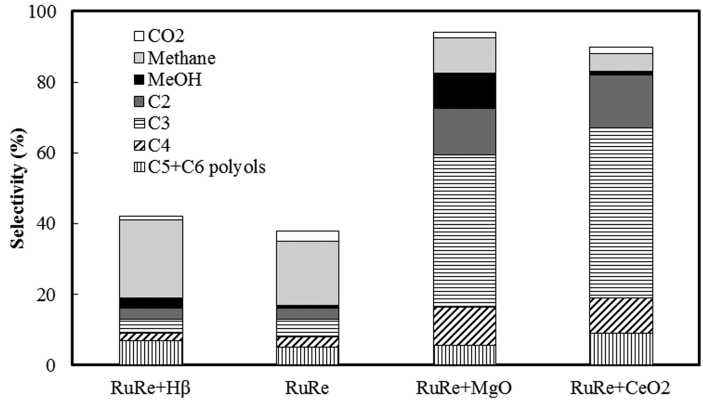

Figure 4. Effects of acid and solid base promoters in sorbitol hydrogenolysis. Conditions: Ru(1 wt %)Re(1 wt %)/C catalysts and solid promoters (if added), 503 K, 7.6 MPa (P_{H2}), 12 h, sorbitol conversion = 100%. Abbreviations as in Figure 2.

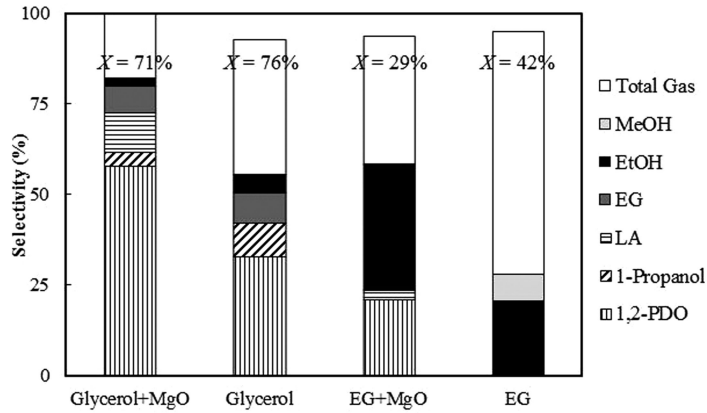

Figure 5. Product distribution of glycerol and ethylene glycol hydrogenolysis. Conditions: glycerol or ethylene glycol aqueous solution, Ru(1 wt %)Re(1 wt %)/C, MgO base promoter (if added), 503 K, P_{H2} of 7.6 MPa, 6 h. Total gas: methane, ethane; MeOH: methanol; EtOH: ethanol; EG: ethylene glycol; LA: lactic acid; PDO: propanediol.

In Novel Materials for Catalysis and Fuels Processing; Bravo-Suárez, J., et al.;
ACS Symposium Series; American Chemical Society: Washington, DC, 2013.

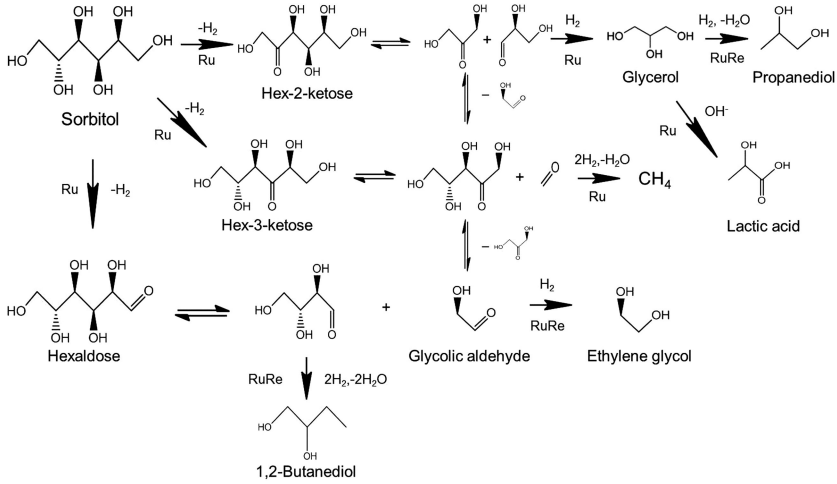

Scheme 1. Proposed reaction network for sorbitol hydrogenolysis.

From previous reports, it is noted that a liquid base such as NaOH enhances the conversion of polyols over Ru or Ni monometallic catalysts (*16*). In contrast, the addition of MgO as a solid base promoter does not enhance the activity of the RuRe bimetallic catalyst (Figure 5). This may be partially due to the addition of Re to Ru, which already promotes C–O cleavage. As mentioned above, the first step in sorbitol conversion in the presence of OH^- is assumed to be the dehydrogenation to form olefinic intermediates followed by rearrangement to form aldehydes or ketones. In our system, it was found that dehydration is also important in facilitating C–O bond cleavage followed by hydrogenation. The observation of 1,2-butanediol (approximately 10% selectivity) in the product mixture, not mentioned in the previous reports, seems to support our hypothesis.

The promoting effect of a base on C–O cleavage was reported previously for hydrogenolysis of glycerol and ethylene glycol (*4*). Our experiments (Figure 5) support two important conclusions: (a) C–C cleavage trend over Ru is different from that in the presence of OH^-; (b) C–C cleavage is restrained for lower carbon number polyols in the presence of MgO. Moreover, it is also found that the basic medium does not enhance the conversion of glycerol and ethylene glycol because it is clear that the addition of MgO slightly decreases the conversion of these substrates. As inferred from Figure 5, the selectivity of C_2–C_3 alcohols increases significantly in the presence of a base promoter (from 60 to 82% and from 30 to 60% for glycerol and ethylene glycol hydrogenolysis, respectively). In contrast, the methanation selectivity is restrained, from almost 40 to 18% and 70 to 50% during glycerol and ethylene glycol hydrogenolysis, respectively. These results are different from previous reports of Davada et al. (*21*) indicating that during aqueous phase reforming of polyols on Pt catalysts, the selectivity to H_2 decreases with increasing carbon number (from glycerol to sorbitol), but the selectivity to gaseous alkanes (methane, ethane, etc.) increases as carbon chain increases. In

In Novel Materials for Catalysis and Fuels Processing; Bravo-Suárez, J., et al.;
ACS Symposium Series; American Chemical Society: Washington, DC, 2013.

sharp contrast, our results clearly show that the reforming potential of ethylene glycol is more restrained than for glycerol in the presence of a base, producing ethanol as the major liquid product.

Furthermore, a number of publications previously assumed that glycerol undergoes retro-aldol reaction (*4*, *5*, *22*) leading to the formation of methanol and C_2 alcohols, but in our work it was found that the majority of the liquid products consist of 1,2-propanediol and lactic acid, with only less than 10% of C_1–C_2 alcohols, even in the presence of a base. This indicates that the solid base provides a favorable environment for the formation of aldehydes and ketones but not C–C cleavage. King et al. (*4*) found that alkali promoters with PtRe catalysts enhance glycerol conversion and also the fraction of carbon in liquid (C_2–C_3 alcohols) suggesting the suppression of reforming activity. The observed increases in the selectivities of liquid products from glycerol hydrogenolysis indicate that hydrogen is more efficiently utilized in a basic medium [as suggested from Scheme 2 (*23*)] for the formation of alcoholic products (e.g., propanediol) than in neutral and acidic environments. In summary, the role of the solid base promoter can be summarized as follows: (a) the base promoter activates polyols in retro-aldol condensation; (b) the base promoter affects the relative activities of the following three steps in the order: dehydration > reverse-aldolization >> methanation.

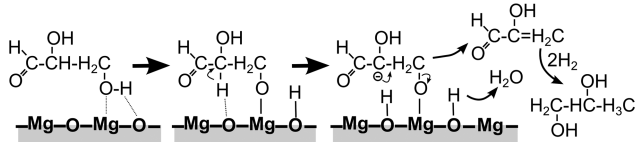

Scheme 2. Possible reaction pathway for dehydration of glyceraldehydes over a solid base.

Effect of Temperature

As presented in Scheme 1, conversion of sorbitol initiates with dehydrogenation and results in C_1–C_5, C_2–C_4, and C_3–C_3 as potential intermediate products. In order to understand the temperature effects on the C–C bond cleavage behavior of xylitol and sorbitol and resulting product distributions, several experiments were carried out at low conversion levels (~25%). As shown in Figure 6, low temperatures favor C_3 products compared to other products. At 483 K, the C_3 selectivity from xylitol and sorbitol is about 15% higher than the results at 503 and 518 K, while the C_1 and C_2 selectivity increases with increasing reaction temperatures. Therefore, it is plausible that at relatively low temperatures, C_3–C_3 cleavage is favored, whereas C_1–C_5 and subsequent C_2–C_3 cleavage dominate at high temperatures.

In Novel Materials for Catalysis and Fuels Processing; Bravo-Suárez, J., et al.;
ACS Symposium Series; American Chemical Society: Washington, DC, 2013.

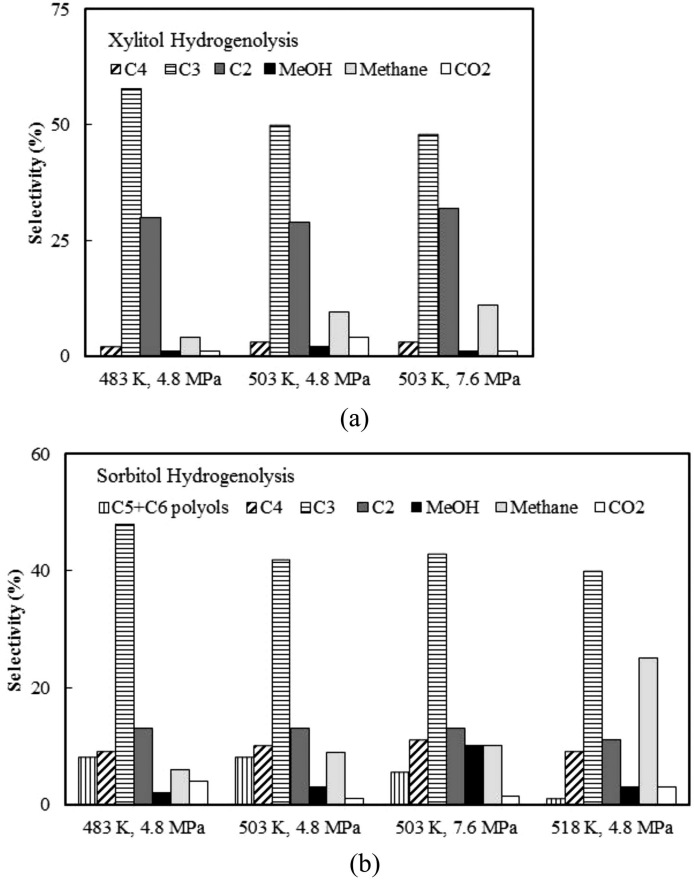

Figure 6. Product distribution of (a) xylitol and (b) sorbitol hydrogenolysis. Conditions: Ru(1 wt %)Re(1 wt %)/C, MgO base promoter, 0.5–1.5 h, xylitol and sorbitol conversion of ~25%. Abbreviations as in Figure 2.

It is important to recognize that C_3–C_3 bond breaking will result in glyceraldehyde or glycerate formation as intermediate products, which can be hydrogenated to glycerol (*5*) over the RuRe catalyst in the presence of hydrogen, while C_1–C_5 breakage [confirmed by the formation of traces of CO <1% in selectivity] probably leads to the formation of methanol and xylitol. Xylitol is found to easily undergo further C_2–C_3 cleavage under similar reaction conditions (Figure 6). Once C_3 or C_2 compounds are formed, the presence of Re enhances the C–O cleavage reactions, consistent with the reaction pathways in glycerol and ethylene glycol hydrogenolysis (*5*, *7*).

In Novel Materials for Catalysis and Fuels Processing; Bravo-Suárez, J., et al.;
ACS Symposium Series; American Chemical Society: Washington, DC, 2013.

The recyclability of the catalysts was also studied (at 483 K, H_2 pressure 7.6 MPa, and 1 h). The conversion rate of the fresh Ru(1 wt %)Re(1 wt %)/C+MgO catalyst was found as 256 mol/g-atom/h, whereas those of the first and second recycle were 213 and 210 mol/g-atom/h, respectively. The selectivity of C_3 products was 47.2, 46, and 46%, respectively. These results demonstrate that RuRe/C catalysts and MgO as a basic promoter are stable and recyclable under the reaction conditions.

Conclusion

The hydrogenolysis of xylitol and sorbitol in aqueous phase was studied on admixtures of carbon supported Ru, Rh, Pt, and Ir catalysts and a MgO base promoter. All catalysts were active for the formation of liquid products (methanol, ethanol, ethylene glycol, propanediol, glycerol, lactic acid, isoerythritol, and 1,2-butanediol) following an increasing order of activity of Ir/C < Pt/C < Rh/C < Ru/C. Furthermore, the addition of a second metal (Re) not only increased the activity of Ru catalysts but also enhanced the selectivity of C_2 and C_3 polyols. It is found that with a RuRe bimetallic catalyst and a solid base promoter (MgO), the selectivity of C_2 and C_3 products is as high as 72%. MgO and CeO_2, as solid base promoters, are found to favor hydrodeoxygenation reactions at a pH of 6.5–9 and a temperature range of 483–518 K in the presence of hydrogen. The presence of a solid base promoter facilitates dehydration of polyols and subsequent deoxygenation while restraining the methanation reaction. These results provide new insights into the reaction network for base-promoted hydrogenolysis of polyols that are useful for designing bimetallic catalysts that maximize the selectivity toward vauable liquid products.

Acknowledgments

X. J. acknowledges a graduate research funding from Center for Environmentally Beneficial Catalysis at the University of Kansas and a scholarship from China Scholarship Council. Partial support from United States Department of Agriculture (USDA/NIFA Award 2011-10006-30362) is gratefully acknowledged.

References

1. Roy, D.; Subramaniam, B.; Chaudhari, R.V. *ACS Catal.* **2011**, *1*, 548–551.
2. Yuan, Z. L.; Wang, L. N.; Wang, J. H.; Xia, S. X.; Chen, P.; Hou, Z. Y.; Zheng, X. M. *Appl. Catal., B* **2011**, *101*, 431–440.
3. Hosgun, H. L.; Yildiz, M.; Gercel, H. F. *Ind. Eng. Chem. Res.* **2012**, *51*, 3863–3869.
4. King, D. L.; Zhang, L. A.; Xia, G.; Karim, A. M.; Heldebrant, D. J.; Wang, X. Q.; Peterson, T.; Wang, Y. *Appl. Catal., B* **2010**, *99*, 206–213.
5. Ma, L.; He, D. H. *Top. Catal.* **2009**, *52*, 834–844.
6. Ma, L.; He, D. H. *Chin. J. Catal.* **2009**, *30*, 471–478.

7. Torres, A.; Roy, D.; Subramaniam, B.; Chaudhari, R. V. *Ind. Eng. Chem. Res.* **2010**, *49*, 10826–10835.
8. Shinmi, Y.; Koso, S.; Kubota, T.; Nakagawa, Y.; Tomishige, K. *Appl. Catal., B* **2010**, *94*, 318–326.
9. Nakagawa, Y.; Shinmi, Y.; Koso, S.; Tomishige, K. *J. Catal.* **2010**, *272*, 191–194.
10. Amada, Y.; Shinmi, Y.; Koso, S.; Kubota, T.; Nakagawa, Y.; Tomishige, K. *Appl. Catal., B* **2011**, *105*, 117–127.
11. Li, N.; Huber, G. W. *Abstr. Pap. Am. Chem. Soc.* **2009**, *238*.
12. Vispute, T. P.; Huber, G. W. *Green Chem.* **2009**, *11*, 1433–1445.
13. Li, N.; Tompsett, G. A.; Huber, G. W. *ChemSusChem* **2010**, *3*, 1154–1157.
14. Sun, J. Y.; Liu, H. C. *Green Chem.* **2011**, *13*, 135–142.
15. Zhao, L.; Zhou, J. H.; Sui, Z. J.; Zhou, X. G. *Chem. Eng. Sci.* **2010**, *65*, 30–35.
16. Sohounloue, D. K.; Montassier, C.; Barbier, J. *React. Kinet. Catal. Lett.* **1983**, *22*, 391–397.
17. Montassier, C.; Menezo, J. C.; Naja, J.; Granger, P.; Barbier, J.; Sarrazin, P.; Didillon, B. *J. Mol. Catal.* **1994**, *91*, 119–128.
18. Banu, M.; Sivasanker, S.; Sankaranarayanan, T. M.; Venuvanalingam, P. *Catal. Commun.* **2011**, *12*, 673–677.
19. Kusserow, B.; Schimpf, S.; Claus, P. *Adv. Synth. Catal.* **2003**, *345*, 289–299.
20. Huber, G. W.; Cortright, R. D.; Dumesic, J. A. *Angew. Chem., Int. Ed.* **2004**, *43*, 1549–1551.
21. Davda, R. R.; Shabaker, J. W.; Huber, G. W.; Cortright, R. D.; Dumesic, J. A. *Appl. Catal., B* **2005**, *56*, 171–186.
22. Maris, E. P.; Davis, R. J. *J. Catal.* **2007**, *249*, 328–337.
23. Di Cosimo, J. I.; Apesteguia, C. R.; Gines, M. J. L.; Iglesia, E. *J. Catal.* **2000**, *190*, 261–275.

Chapter 13

The Effect of Calcination Temperature on the Properties and Hydrodeoxygenation Activity of Ni_2P Catalysts Prepared Using Citric Acid

Victoria M. L. Whiffen and Kevin J. Smith*

Department of Chemical and Biological Engineering, University of British Columbia, 2360 East Mall, Vancouver, British Columbia V6T 1Z3, Canada
***E-mail: kjs@mail.ubc.ca**

The effect of calcination temperature on the preparation of unsupported high surface area Ni_2P catalysts, synthesized by adding citric acid (CA) to an aqueous solution of nickel nitrate and diammonium hydrogen phosphate, is reported. The addition of CA led to increased surface area, decreased particle size, and increased CO uptake of the reduced Ni_2P. However, increases in the Ni_2P-CA calcination temperature from 773 to 823 and to 973 K led to a deterioration in the catalyst properties. All Ni_2P catalysts deactivated following the hydrodeoxygenation (HDO) of 4-methylphenol (4-MP) at 623 K and 4.4 MPa. The deactivation was due to coking and was modeled by an exponential decay law. All Ni_2P catalysts had similar deactivation parameters, indicating the loss in activity was due to C deposition on similar sites. The Ni_2P-CA catalysts, with crystallite size in the range of 34–50 nm, had comparable initial TOFs, indicating that the HDO of 4-MP was structure insensitive over Ni_2P catalysts of this size.

Introduction

Pyrolysis oil derived from the fast pyrolysis of wood-waste is gaining attention as an alternative, renewable energy source. Compared with fossil fuels, pyrolysis oils generate far less green house gases, NO_x, and SO_x emissions (*1*). However, crude pyrolysis oils contain approximately 25 wt % moisture and 40–50 wt % O

In Novel Materials for Catalysis and Fuels Processing; Bravo-Suárez, J., et al.;
ACS Symposium Series; American Chemical Society: Washington, DC, 2013.

(*2–4*). The oxygen results in detrimental properties of the fuel such as instability, phase separation, high viscosity, low heating value, high acidity, and immiscibility with hydrocarbons (*4*, *5*). The presence of oxygen is the primary reason for the observed differences in the properties of pyrolysis oil compared to fossil fuels. Therefore, the oxygen in pyrolysis oils must be removed to be comparable and competitive with fossil fuels. Several studies have shown that metal phosphides are active for the hydrodeoxygenation (HDO) of pyrolysis oil model compounds (*6–8*), with more recent studies paying particular attention to Ni_2P (*9–13*).

Previous work by Whiffen et al. (*8*) has shown that an "optimum" calcination temperature exists for the preparation of unsupported high surface area MoP in the presence of citric acid (CA). A catalyst calcination temperature of 823 K maximized CO uptake, HDO conversion of 4-methylphenol, and hydrogenation (HYD) selectivity over this catalyst. In a similar way an "optimal" calcination temperature might also exist for the preparation of Ni_2P-CA.

In the present study, unsupported Ni_2P prepared using CA calcined at various temperatures, has been investigated and compared for the HDO of 4-methylphenol, a refractory model compound present in pyrolysis oils. The effect of calcination temperature on the reduced catalyst properties was investigated at temperatures of 773, 823, and 973 K. The chosen calcination temperatures were based on previous work by Whiffen et al. (*8*).

Experimental

Catalyst Preparation

Unsupported high surface area Ni_2P catalysts were synthesized using the traditional Ni phosphate temperature programmed reduction method and a P:Ni molar ratio of 1:1 (*16*). Aqueous solutions of nickel nitrate (99.9% $Ni(NO_3)_2.6H_2O$ Fisher Scientific) and diammonium hydrogen phosphate (99% $(NH_4)_2HPO_4$ Sigma-Aldrich) were prepared in de-ionized water (*8*, *9*, *14*, *15*). The CA (99.8% Fisher Scientific) was added to the salt solution to give a 2:1 CA:Ni molar ratio (*8*, *9*, *15*). Subsequently the precursor solutions were aged for 24 h in a covered beaker held at 363 K in a water-bath and dried in an oven at 397 K for 24 h. The dried samples were calcined by heating at 5 K min^{-1} to 773, 823, or 973 K in stagnant air and held for 5 h at the final temperature. Ni_2P prepared in the absence of CA was calcined to 773 K only. Approximately 0.7 g of the calcined catalyst precursors were ground to a powder (d_P < 53 μm) and converted to Ni_2P by temperature-programmed reduction (TPR) in UHP H_2 at a flow rate of 160 cm^3(STP) min^{-1} and a heating rate of 5 K min^{-1} to 573 K, followed by a heating rate of 1 K min^{-1} to 923 K. The final temperature was held for 2.5 h. The samples were then cooled to room temperature in a He flow and passivated in a flow of 1 mol % O_2/He for 3 h prior to removal from the quartz U-tube reactor for characterization purposes. Other catalysts used for activity measurements were transferred directly from the quartz U-tube used for reduction, under a He flow (25 cm^3(STP) min^{-1}) into ~15 cm^3 of decalin. They were then transferred to the reactor for activity measurements, without exposure to air (*8*). A P:Ni ratio of 2:1 for Ni_2P prepared with CA has shown better physical properties and

In Novel Materials for Catalysis and Fuels Processing; Bravo-Suárez, J., et al.;
ACS Symposium Series; American Chemical Society: Washington, DC, 2013.

higher activity for the HDS of 4,6-dimethyldibenzothiophene compared to Ni_2P prepared with a P:Ni ratio of 1:1 (*16*). However, in the present study a P:Ni ratio of 1:1 was used to reduce the production of PH_3 and to reduce P sublimation during preparation.

The reduced catalysts are identified as Ni_2P-CA-ttt K, where ttt is the precursor calcination temperature (K). The reduced catalysts prepared in the absence of CA are designated as Ni_2P-noCA.

Catalyst Characterization

Elemental C analysis was performed on the reduced and passivated Ni_2P catalysts and on the used Ni_2P samples (extracted following the 5 h HDO reaction) using a Perkin-Elmer 2400 Series II CHNS/O analyzer operated in the CHN mode. P analysis of selected samples was carried out using a colorimetric method, with direct comparison to a standard (*17*). Ni concentrations of select samples were determined by inductively coupled plasma atomic emission spectroscopy (ICP–AES).

Powder X-ray diffraction (XRD) patterns of the reduced and passivated Ni_2P catalysts were collected using a Bruker D8 Focus (LynxEye detector) with a Co Kα X-ray source of wavelength 1.79 Å.

Brunauer–Emmett–Teller (BET) surface areas of the reduced and passivated Ni_2P catalysts were determined from N_2 adsorption isotherms measured at 77 K using a Micromeritics Flowsorb II 2300. Samples were degassed in 30 mol % N_2/He at 15 cm^3(STP) min^{-1} for 16 h (*7*, *8*).

The CO uptake of the reduced Ni_2P catalysts was measured by pulsed chemisorption using a Micromeritics AutoChem II 2920 unit. The reduced Ni_2P samples were prepared from their calcined precursors by in situ reduction of approximately 0.1 g of sample in 9.5 mol % H_2/Ar (50 cm^3(STP) min^{-1}) while heating at 5 K min^{-1} to 573 K followed by a ramp of 1 K min^{-1} to 923 K with the final temperature held for 2.5 h (replicating the standard reduction procedure of the calcined Ni_2P precursors). The sample was then cooled in 50 cm^3(STP) min^{-1} He to room temperature prior to injecting pulses of CO (*7–9*).

Transmission electron microscopy (TEM) images of the reduced and passivated Ni_2P catalysts were obtained using a 120 kV Hitachi H7600 with a tungsten filament and a FEI Tecnai TEM operated at 200 kV with a LaB_6 filament. Log-normal particle size distributions were obtained by editing the images in Pixcavator 4.0 Image Analysis software and measuring the particle diameters and widths. Greater than 50 particles were measured for Ni_2P-CA catalysts whereas the Ni_2P-noCA particle size was based on >10 particles.

Catalyst Activity

The HDO reactions were carried out in a 300 cm^3 stirred-batch reactor operated in slurry mode with 0.36 g of reduced Ni_2P catalyst at 623 K and 4.4 MPa H_2 with 2.96 wt % of 4-methylphenol (4-MP) (99%, Sigma-Aldrich), used as a model reactant, in 100 cm^3 decalin (98%, Sigma-Aldrich). The concentration-time profiles were determined by withdrawing liquid samples

In Novel Materials for Catalysis and Fuels Processing; Bravo-Suárez, J., et al.;
ACS Symposium Series; American Chemical Society: Washington, DC, 2013.

from the reactor periodically and analyzing them using a 14-A Shimadzu gas chromatograph (GC) equipped with a flame ionization detector (FID) and an AT-5 25 m × 0.53 mm capillary column. The product distribution was confirmed by GC mass spectrometry (MS) analysis using a Shimadzu QP-2010S GC–MS and a Restek RTX5 30 m × 0.25 mm capillary column (*7–9*).

The reactant and product concentration data measured over time was used to determine the kinetic parameters of the HDO reaction over the Ni_2P catalysts. Because the catalysts were observed to deactivate, the kinetics of the decomposition of 4-methylphenol was assumed to follow the exponential decay law given in eq 1:

$$\text{Rate} = kC_a e^{-k_d C_{cat} t} \quad (1)$$

where t is the HDO reaction time (s), C_{cat} is the concentration of the catalyst in the reactor at ambient conditions (g_{Ni2P} cm^{-3}), C_a is the 4-methylphenol concentration at time t, k is the reaction rate constant (cm^3 min^{-1} g_{Ni2P}^{-1}), and k_d is the deactivation rate constant (cm^3 min^{-1} g_{Ni2P}^{-1}).

Results and Discussion

Catalyst Characterization

The properties of the reduced and passivated Ni_2P catalysts are summarized in Table 1. The Ni_2P prepared in the absence of CA (Ni_2P-noCA) was free of C. However, the catalysts prepared with CA contained a C:Ni-ratio of 0.6:1 for all calcination temperatures. Previous work by Whiffen et al. (*8*) reported that the calcination temperature used for the preparation of MoP-CA catalysts significantly affected their C content. The C:Mo ratio was high for MoP-CA-773 K at 2:1, whereas MoP-CA-973 K had a C:Mo of 0.5:1 (*8*). This implies that C is more easily removed from the Ni_2P-CA catalysts at calcination temperatures below 973 K compared with that of the MoP-CA catalysts. The Ni:P ratio of the Ni_2P-CA catalysts increased from 1:1 for the calcined Ni_2P-CA and noCA precursors to 2.3:1 for the reduced and passivated Ni_2P-CA catalysts and was 2.1:1 for the reduced and passivated Ni_2P-noCA catalyst. The increase in metal content was due to P losses during reduction of the Ni_2P calcined precursor, which led to PH_3 generation.

Table 1 also shows that the addition of CA to the catalyst precursors significantly increased the surface area of the reduced Ni_2P catalysts. Compared to Ni_2P-noCA calcined at 773 K, the surface area of the Ni_2P-CA-773 K increased by a factor of ~10 due to the formation of a metal citrate (*8*). As the calcination temperature of Ni_2P-CA catalysts increased from 773 to 973 K, the surface area decreased from 101 to 51 m^2 g_{cat}^{-1}. The decrease was caused by sintering of the Ni_2P-CA catalysts at higher calcination temperatures that led to agglomeration of the Ni_2P crystallites. Ni_2P prepared in the absence of CA had a crystallite size of 57 nm estimated by Scherrer's equation using the (210) plane of Ni_2P, whereas its particle size from TEM imaging was determined to be 259 nm. This again indicates significant agglomeration of the metal crystallites in the Ni_2P-noCA

In Novel Materials for Catalysis and Fuels Processing; Bravo-Suárez, J., et al.;
ACS Symposium Series; American Chemical Society: Washington, DC, 2013.

catalyst. Ni_2P-CA-773 K had a crystallite size of 34 nm compared to 42 nm for the Ni_2P-CA-823 K catalyst and 50 nm for the Ni_2P-CA-973 K catalyst. Ni_2P-noCA had a CO uptake of < 1 μmol g_{Ni2P}^{-1} compared to that of 20 μmol g_{Ni2P}^{-1} for the Ni_2P-CA-773 K catalyst. The CO uptake of Ni_2P-CA-773 K was also greater than both the Ni_2P-CA-823 K and the Ni_2P-CA-973 K catalysts that had CO uptakes of 9 and 10 μmol g_{Ni2P}^{-1}, respectively. These results further indicate that nearly complete C removal and particle sintering occurred at calcination temperatures above 773 K, leading to inferior Ni_2P-CA properties.

Table 1. Physical and chemical properties of Ni_2P prepared with and without CA

Ni_2P	*Ni:P Ratio*	*C:Ni Ratio*	*S_{BET} (m^2 g_{cat}^{-1})*	*d_{XRD} (hkl) (nm)*	*d_{TEM} (STDev) (nm)*	*CO Uptake (μmol g_{Ni2P}^{-1})*
CA-773 K	2.3	0.6	101	34 (210)	36 (11)	20
CA-823 K	2.3	0.6	75	42 (210)	54 (26)	10
CA-973 K	2.3	0.6	51	50 (210)	54 (15)	9
noCA	2.1	0	6	57 (210)	259 (44)	<1

The diffractograms of the Ni_2P catalysts can be seen in Figure 1. The XRD of the Ni_2P catalysts and used Ni_2P-CA-773 K showed the (210) reflection at 2θ = 47.6°, characteristic of Ni_2P (PDF#00-003-0953). Although the Ni_2P-CA catalysts contained C, reflections due to Ni_3C were not present in the XRD patterns. Additional, low intensity diffraction peaks for the Ni_2P-CA catalysts were displayed at 2θ = 44.8, 48.9, and 57.5°, characteristic of $Ni_{12}P_5$ (PDF#04-007-1003). The excess in Ni was also seen from the elemental analysis of the Ni:P ratio of the Ni_2P-CA catalysts in Table 1. This result suggests that CA addition to the Ni_2P catalysts leads to higher P loss (*9*). The presence of $Ni_{12}P_5$ was not reported in previous work by Wang and Smith (*16*) and Yang et al. (*18*) who reported phase pure Ni_2P prepared with a P:Ni ratio of 0.5:1–3:1 and a CA:Ni ratio of 1:1–3:1 (*16*); and a P:Ni ratio of 1:1 with Triton (polymer surfactant)/ethylene glycol (*18*). This difference may be due to minor differences in the thermal treatments of the samples and/or a consequence of the more sensitive XRD detector used in the present study.

TEM micrographs of the reduced and passivated Ni_2P catalysts and used Ni_2P-CA-773 K are presented in Figure 2. Separate 36–55 nm particles were clearly evident for the Ni_2P-CA catalysts (Figures 2a–c). Significant agglomeration was found to occur over Ni_2P-CA-823 K and Ni_2P-CA-973 K that had crystallites sizes of 42 and 50 nm but particle sizes of 54 nm each. Slight agglomeration was observed over Ni_2P-CA that had a crystallite size of 34 nm and a particle size of 36 nm. Ni_2P-noCA had an average particle size of 259 nm (Figure 2d). High resolution images of the Ni_2P-CA-773 K catalyst further confirmed the formation of Ni_2P with lattice d-spacings of 1.7 and 2.5 Å for the (300) and (200) plane of Ni_2P (Figure 2e).

In Novel Materials for Catalysis and Fuels Processing; Bravo-Suárez, J., et al.;
ACS Symposium Series; American Chemical Society: Washington, DC, 2013.

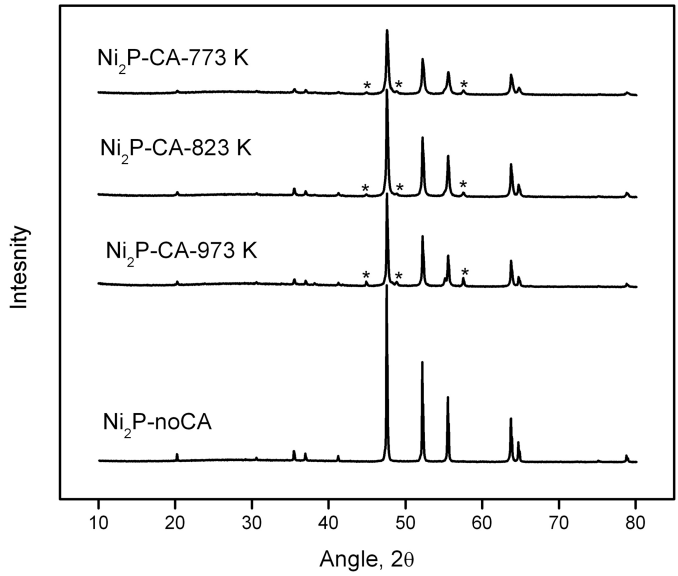

Figure 1. XRD diffractograms of reduced and passivated Ni_2P catalysts collected using a Co Kα X-ray source. $Ni_{12}P_5$ (*).

Catalyst Activity and Product Distribution

Figure 3 displays the natural logarithm (ln)-normal plot of the 4-methylphenol concentration versus time for the HDO reaction over the Ni_2P catalysts at 623 K and 4.4 MPa. This data accounts for the thermal reaction of 12% conversion of the initial 4-methylphenol concentration following the 5 h reaction. From Figure 3 it can be reported that the data does not follow a first order kinetic trend and that deactivation of all Ni_2P catalysts occurred during the HDO reaction. It was observed that CA addition did increase the conversion over the Ni_2P-CA-773 K catalyst compared to Ni_2P prepared without CA. Both Ni_2P-CA-823 K and Ni_2P-CA-973 K had similar activities indicating significant agglomeration of the Ni_2P-CA catalyst at a calcination temperature of 823 K. Previous work by Whiffen and Smith (*8*) found an "optimal" calcination temperature of 823 K for the preparation of MoP-CA as this led to the highest rate of hydrodeoxygenation of 4-methylphenol. Temperatures below 823 K led to residual C in MoP-CA that blocked the active sites, while temperatures above 823 K destroyed the Mo citrate structure and led to sintering of the catalyst particles (*8*). Overall, an "optimum" calcination temperature of 773 K existed for the preparation of Ni_2P-CA in the present study for the temperature range tested.

In Novel Materials for Catalysis and Fuels Processing; Bravo-Suárez, J., et al.;
ACS Symposium Series; American Chemical Society: Washington, DC, 2013.

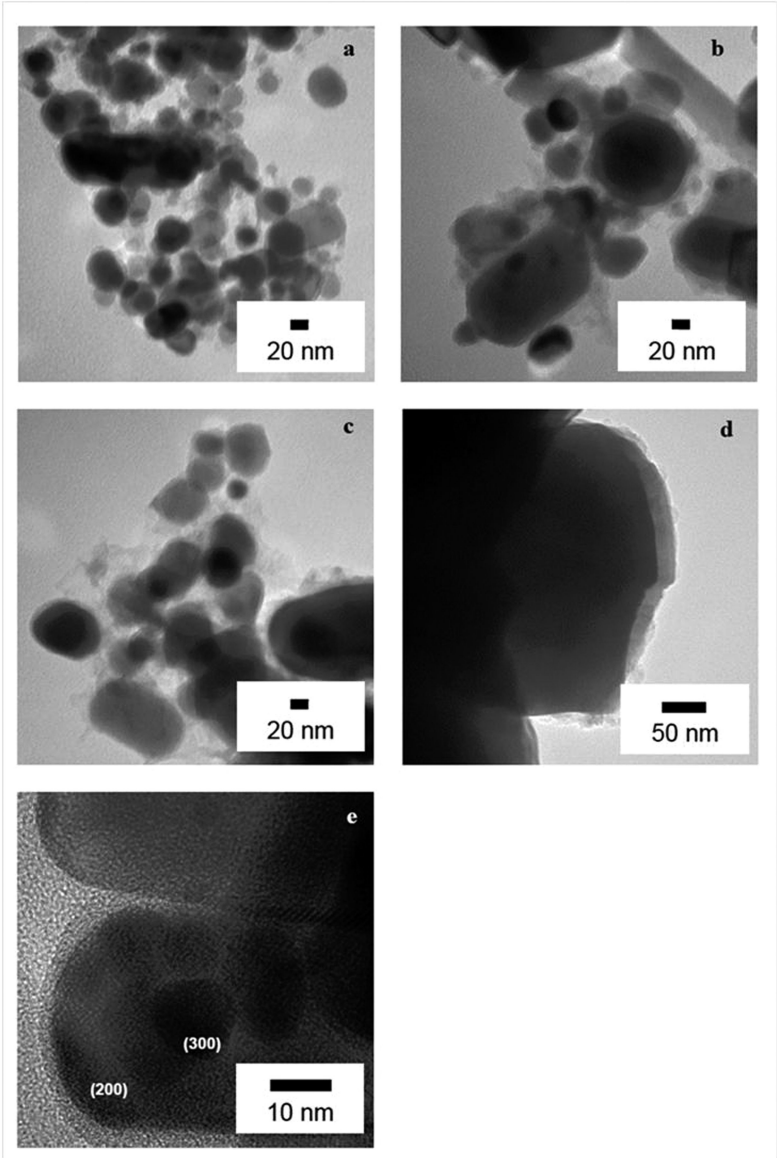

Figure 2. TEM images of reduced and passivated Ni_2P catalysts: (a) Ni_2P-CA-773 K; (b) Ni_2P-CA-823 K; (c) Ni_2P-CA-973 K; (d) Ni_2P-noCA; (e) lattice fringe d-spacing of Ni_2P-CA-773 K at 1.7 and 2.5 Å for the (300) and (200) plane of Ni_2P.

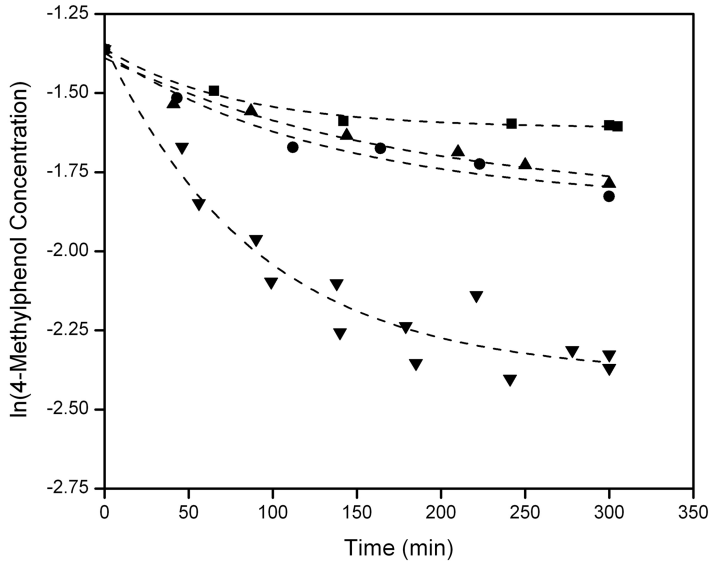

Figure 3. ln-normal plot of the 4-methylphenol concentration versus time for HDO reaction at 623 K and 4.4 MPa over Ni_2P catalysts. Ni_2P-CA-773 K (▾), Ni_2P-CA-823 K (▴), Ni_2P-CA-973 K (•), Ni_2P-noCA (▪), guideline shown for illustration (--).

Recent work by Li et al. (*11*), Zhao et al. (*12*), Bui et al. (*10*), and Cho et al. (*13*) observed minimal or no deactivation for the hydrodeoxygenation of pyrolysis oil model compounds over supported Ni_2P catalysts. These results are contrary to that of the present work; however, this may be a consequence of the presence of a catalyst support or different reactor configurations used in those studies. In the present work, the unsupported catalysts were tested over a range of conversions in batch mode, whereas in fixed-bed studies, the reactor typically operates at a single conversion determined by the chosen residence time. Coke precursors remain in the reactor and have the time to form coke in the batch mode, whereas this is less likely in a fixed-bed reactor.

In order to extract the reaction parameters, the exponential decay law given in eq 1 was applied to the Ni_2P concentration data. A plot of the Ni_2P rate versus time is given in Figure 4. The kinetic parameters (k and k_d) can be found in Table 2 along with the initial rates and turn over frequencies (TOFs) of the Ni_2P catalysts. All Ni_2P-CA catalysts had similar initial TOFs of 0.464 ± 0.006 s^{-1}, normalized by CO uptake, indicating structure insensitivity for the HDO of 4-methylphenol over the Ni_2P-CA catalysts (Figure 5). Structure insensitivity was also reported over MoP-CA catalysts for the HDO of 4-methylphenol (*8*). The present result is not surprising because of the relatively large crystallite dimensions (34–50 nm) of the Ni_2P-CA catalysts. The TOF of Ni_2P-noCA was not calculated due to the low CO uptake measured over this catalyst (< 1μmol g_{Ni2P}^{-1}).

In Novel Materials for Catalysis and Fuels Processing; Bravo-Suárez, J., et al.;
ACS Symposium Series; American Chemical Society: Washington, DC, 2013.

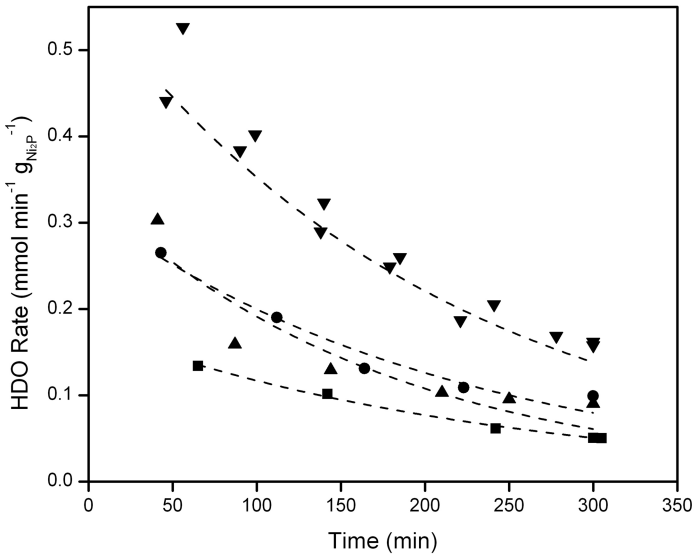

Figure 4. Hydrodeoxygenation rate versus time for the reaction at 623 K and 4.4 MPa over Ni_2P catalysts. Ni_2P-CA-773 K (▾), Ni_2P-CA-823 K (▴), Ni_2P-CA-973 K (•), Ni_2P-noCA (▪), exponential decay law model fit (--).

All the Ni_2P catalysts displayed deactivation and had a deactivation parameter in the range of 1.20 $cm^3\ min^{-1}\ g_{Ni2P}{}^{-1}$. This suggests that a similar mechanism of active site deactivation was present for all the Ni_2P catalysts. Previous work by Whiffen et al. (*9*) found that deactivation over Ni_2P catalysts was due to surface C deposition that led to decreased surface area, decreased CO uptake, and increased particle size. Significant C deposition was found over all the Ni_2P catalysts tested in this study, as reported in Table 2. It was observed that the amount of C deposited on the Ni_2P catalyst was correlated with the rate of reaction (k). It is suggested that the C deposition was due to the formation of isomerization product intermediates that polymerize and precipitate out of solution to form coke.

The hydrodeoxygenation of 4-methylphenol over Ni_2P proceeds through two pathways. The first pathway leads to the direct deoxygenation (DDO) product toluene. The second pathway involves the coupled ring saturation/rapid dehydration to produce 4-methylcyclohexene which is rapidly hydrogenated (HYD) to methylcyclohexane (*8*). Isomerization of 4-methylcyclohexene is also possible, however, isomerization products were not detected for the HDO of 4-methylphenol over Ni_2P catalysts. Therefore, it is proposed that the isomerization intermediates could be responsible for coke formation in this case.

In Novel Materials for Catalysis and Fuels Processing; Bravo-Suárez, J., et al.;
ACS Symposium Series; American Chemical Society: Washington, DC, 2013.

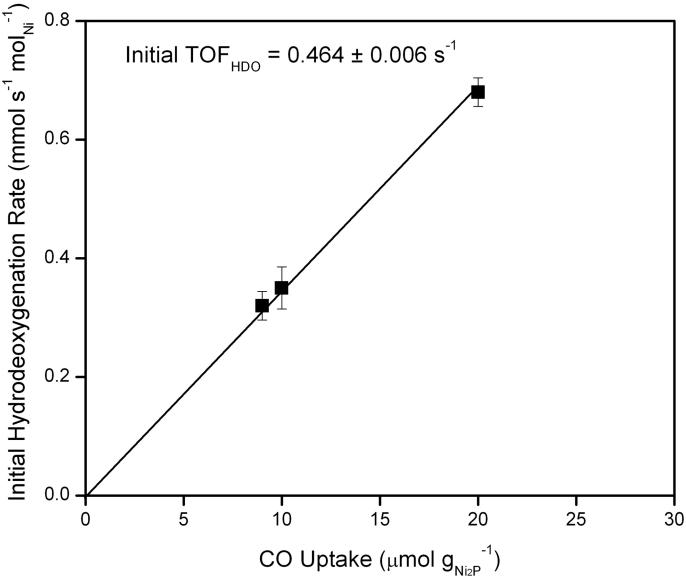

Figure 5. Initial rate of hydrodeoxygenation versus CO uptake over Ni_2P-CA catalysts.

The Ni_2P DDO (toluene) selectivity versus time is given in Figure 6a. The DDO selectivity versus time over the Ni_2P catalysts was found to decrease slightly with reaction time. Ni_2P-CA-823 K displayed the lowest selectivity towards DDO followed by Ni_2P-CA-773 K and Ni_2P-CA-973 K, whereas Ni_2P-noCA had the highest selectivity towards DDO. The Ni_2P HYD (methylcyclohexane) selectivity versus time is given in Figure 6b. The HYD selectivity versus time over the Ni_2P catalysts was found to increase with reaction time. Ni_2P-CA-823 K displayed the highest degree of HYD followed by Ni_2P-CA-773 K, Ni_2P-CA-973 K, and Ni_2P-noCA. This increase in HYD and decrease in DDO selectivity versus time suggests either the further HYD of toluene to methylcyclohexane as a function of reaction time or the deactivation of the DDO active site. With the exception of Ni_2P-CA-823 K, those catalysts displaying smaller particle sizes had a higher degree of hydrogenation. This variation in product selectivity with particle size may suggest structure sensitivity of the HYD and/or DDO routes over the Ni_2P catalysts, even though the initial TOF for 4-methylphenol consumption was not dependant on the particle size (Figure 5).

Table 2. Initial rate, initial TOF, reaction rate parameter, deactivation parameter, and C deposition following the 5 h reaction for the hydrodeoxygenation of 4-methylphenol over Ni_2P catalysts at 623 K and 4.4 MPa

Ni_2P	*Initial Rate* *(mmol min^{-1} g_{Ni2P} $^{-1}$)*	*Initial TOF* *(s^{-1})*	*k* *(cm^3 min^{-1} g_{Ni2P}^{-1})*	*k_d* *(cm^3 min^{-1} g_{Ni2P}^{-1})*	*C Deposition* *(wt %)*
CA-773 K	$0.55 \pm 1.7\times10^{-2}$	$0.449 \pm 1.8\times10^{-2}$	$2.15 \pm 9.0\times10^{-2}$	$1.20 \pm 4.9\times10^{-2}$	3.7
CA-823 K	$0.28 \pm 3.9\times10^{-2}$	$0.469 \pm 7.1\times10^{-2}$	$1.07 \pm 1.6\times10^{-1}$	$1.29 \pm 2.5\times10^{-2}$	2.6
CA-973 K	$0.26 \pm 2.0\times10^{-2}$	$0.470 \pm 3.7\times10^{-2}$	$1.01 \pm 6.8\times10^{-2}$	$1.16 \pm 9.2\times10^{-2}$	1.9
noCA	$0.18 \pm 8.2\times10^{-2}$	--	$0.70 \pm 2.3\times10^{-3}$	$1.17 \pm 5.0\times10^{-3}$	1.5

In Novel Materials for Catalysis and Fuels Processing; Bravo-Suárez, J., et al.;
ACS Symposium Series; American Chemical Society: Washington, DC, 2013.

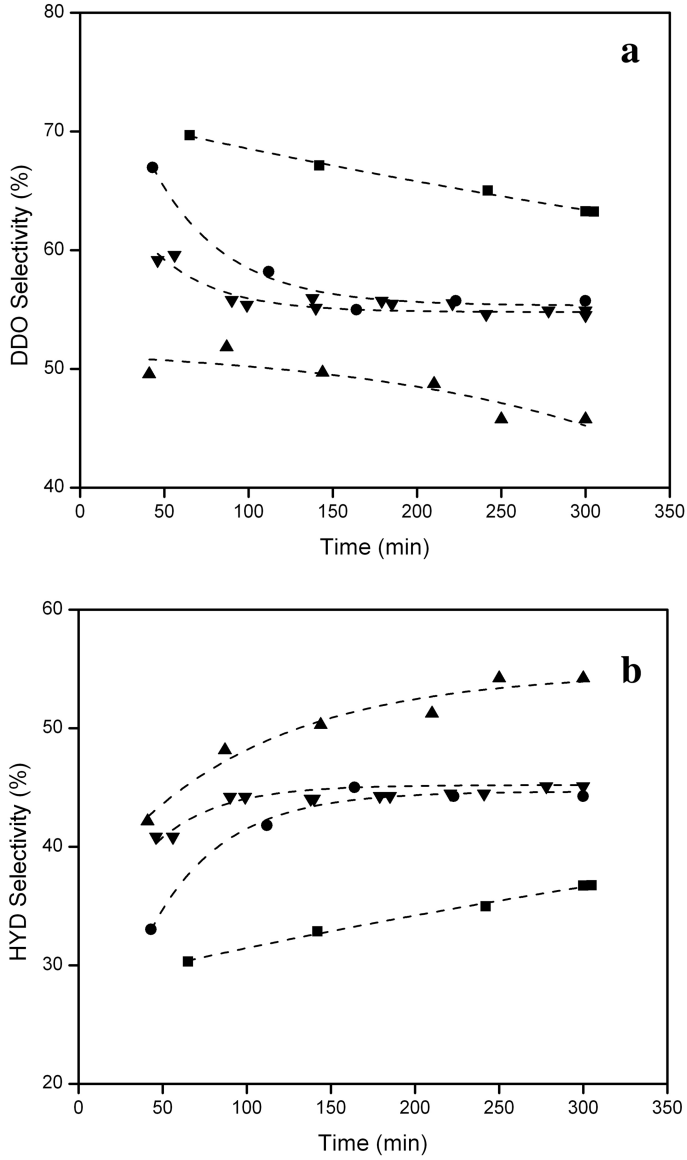

Figure 6. Direct deoxygenation (DDO) product selectivity of toluene (a) and hydrogenation (HYD) product selectivity of methylcyclohexane (b) versus time for the reaction at 623 K and 4.4 MPa over Ni_2P catalysts. Ni_2P-CA-773 K (▾), Ni_2P-CA-823 K (▴), Ni_2P-CA-973 K (•), Ni_2P-noCA (▪), shown for illustration (--).

In Novel Materials for Catalysis and Fuels Processing; Bravo-Suárez, J., et al.;
ACS Symposium Series; American Chemical Society: Washington, DC, 2013.

Previous work by Oyama et al. (*19*) found that the hydrodenitrogenation (HDN) of quinoline was structure sensitive over Ni_2P/SiO_2 catalysts. It was suggested that changes in the P levels on the surface of Ni_2P/SiO_2 disrupted a dual site involving an acid site and a basic site. In the present work, changes in P levels were observed between the Ni_2P catalysts prepared with and without CA. All Ni_2P-CA catalysts had the same P content. Previous work by Whiffen and Smith (*9*) suggested that differences observed in the HYD selectivity over Ni_2P-noCA and Ni_2P-CA-773 K was due to the production of $Ni_{12}P_5$ in Ni_2P-CA-773 K, resulting in a higher HYD selectivity compared to Ni_2P-noCA, which was free of $Ni_{12}P_5$. This was based on previous work by Wang et al. (*20*) who found that $Ni_{12}P_5/SiO_2$ has a higher C=C hydrogenation selectivity than Ni_2P/SiO_2 for the hydrogenation of cinnamaldehyde to hydrocinnamaldehyde.

Conclusions

The synthesis of unsupported high surface area Ni_2P-CA catalysts is reported. Calcination at 773 K led to nearly complete removal of C from the catalysts. Further calcination did not affect the C content of the catalysts, but led to sintering that reduced the catalysts surface area, CO uptake, and increased Ni_2P particle size. Unlike in the case of MoP, where an "optimum" calcination temperature of 823 K was observed (*8*), the present study found an "optimum" calcination temperature of 773 K for the preparation of Ni_2P-CA in the temperature range tested. This was due to nearly complete destruction of the Ni citrate in the calcined Ni_2P-CA precursor at 773 K that led to decreased C content. The Ni_2P catalysts deactivated during 4-methylphenol HDO due to C deposition on the catalyst surface. The deactivation parameter was found to be approximately equal over all Ni_2P catalysts, indicating a similar mechanism of deactivation. The initial TOFs of all Ni_2P-CA catalysts were comparable and independent of calcination temperature and particle size. This implies that the HDO of 4-methylphenol is structure insensitive for the Ni_2P crystallite sizes between 34−50 nm.

Acknowledgments

The authors would like to thank Bradford Ross from the Bioimaging Facility in the Department of Botany at the University of British Columbia for TEM measurements as well as acknowledge the financial support from the Natural Sciences and Engineering Research Council of Canada (NSERC).

References

1. Mohan, D.; Pittman, C. U.; Steele, P. H. *Energy Fuels* **2006**, *20*, 848–889.
2. Mercader, F. M.; Groeneveld, M. J.; Kersten, S. R. A.; Geantet, C.; Toussaint, G.; Way, N. W. J.; Schaverien, C. J.; Hogendoorn, K. J. A. *Energy Environ. Sci.* **2011**, *4*, 985–997.
3. Choudhary, T. V.; Phillips, C. B. *Appl. Catal., A* **2011**, *397*, 1–12.
4. Furimsky, E. *Appl. Catal., A* **2000**, *199*, 147–190.

5. Wildschut, J.; Mahfud, F. H.; Venderbosch, R. H.; Heeres, H. J. *Ind. Eng. Chem. Res.* **2009**, *48*, 10324–10334.
6. Bowker, R. H.; Smith, M. C.; Pease, M. L.; Slenkamp, K. M.; Kovarik, L.; Bussell, M. E. *ACS Catal.* **2011**, *1*, 917–922.
7. Whiffen, V. M. L.; Smith, K. *J. Energy Fuels* **2010**, *24*, 4728–4737.
8. Whiffen, V. M. L.; Smith, K. J.; Straus, S. K. *Appl. Catal., A* **2012**, *419-420*, 111–125.
9. Whiffen, V.; Smith, K. *J. Top. Catal.* **2012**, *55*, 981–990.
10. Bui, P.; Cecilia, J. A.; Oyama, S. T.; Takagaki, A.; Infantes-Molina, A.; Zhao, H.; Li, D.; Rodríguez-Castellón, E.; Jiménez López, A. *J. Catal.* **2012**, *294*, 184–198.
11. Li, K.; Wang, R.; Chen, J. *Energy Fuels* **2011**, *25*, 854–863.
12. Zhao, H. Y.; Li, D.; Bui, P.; Oyama, S. T. *Appl. Catal., A* **2011**, *391*, 305–310.
13. Cho, A.; Shin, J.; Takagaki, A.; Kikuchi, R.; Oyama, S. *Top. Catal.* **2012**, *55*, 969–980.
14. Stinner, C.; Prins, R.; Weber, T. *J. Catal.* **2000**, *191*, 438–444.
15. Wang, R.; Smith, K. *J. Appl. Catal., A* **2009**, *361*, 18–25.
16. Wang, R.; Smith, K. *J. Appl. Catal., A* **2010**, *380*, 149–164.
17. *Modern Organic Elemental Analysis*; Ma, T. S., Rittner, R. C., Eds.; Marcel Dekker, Inc.: New York, NY, 1979.
18. Yang, S.; Liang, C.; Prins, R. *J. Catal.* **2006**, *241*, 465–469.
19. Oyama, S. T.; Wang, X.; Lee, Y.; Bando, K.; Requejo, F. G. *J. Catal.* **2002**, *210*, 207–217.
20. Wang, H.; Shu, Y.; Zheng, M.; Zhang, T. *Catal. Lett.* **2008**, *124*, 219–225.

Chapter 14

Hydrocarbon Production from Carboxylic Acids via Catalytic Deoxygenation: Required Catalytic Properties

Zhong He and Xianqin Wang*

Department of Chemical, Biological and Pharmaceutical Engineering, New Jersey Institute of Technology, 323 MLK Boulevard, Newark, New Jersey 07102, USA
***E-mail: xianqin.wang@njit.edu**

Substitution of fossil-derived fuels by pyrolysis bio-oils is a potentially economic solution. However, the high acidity of pyrolysis bio-oils caused by carboxylic acids constitutes a big challenge to existing petroleum refining facilities. Catalysts are crucial for the successful deoxygenation of carboxylic acids to products that are less corrosive to reactors. This review addresses recent advances in the deoxygenation of carboxylic acids from pyrolysis bio-oils over many different types of catalysts, focusing on the required catalytic properties for partial or complete deoxygenation. Recent achievements suggest that deoxygenation of carboxylic acids can be fulfilled when the following catalytic properties are present: hydrogenation/hydrogenolysis sites such as metal sites or Brønsted acid sites to deliver hydrogen, acid sites for alcohol dehydration, and proper metal–oxygen bond strength in the oxide support for oxygen vacancy creation and regeneration. A synergic effect of these sites determines the final deoxygenation: partial or complete. Modification to the metal sites and acid sites can be achieved in a simple manner by proper promoter addition, which enables to tune the selectivity of the deoxygenation products to the desired ones.

In Novel Materials for Catalysis and Fuels Processing; Bravo-Suárez, J., et al.;
ACS Symposium Series; American Chemical Society: Washington, DC, 2013.

Introduction

Inexpensive crude oil has been dominant as a liquid fuel source since the 19th century. However, crude oil is derived from fossil fuel, which is nonrenewable and declining quickly in recent years. In this regard, plant biomass is gaining increasing attention due to wide and carbon-neutral sources during its utilization, and it is the only current sustainable source for producing liquid fuels (*1*). Thus, biomass has been considered as a high ranking solution to reduce CO_2 emissions and the dependence on fossil fuels (*1*).

Liquid fuels can be obtained by converting biomass via three primary paths including: aqueous sugar production by hydrolysis, bio-oil production by liquefaction and pyrolysis, and syngas formation by gasification followed by the Fischer–Tropsch process (*2*). Among these three major paths, bio-oil is a very promising alternative to crude oil for the production of liquid transportation fuels as bio-oil is derived from renewable biomass. Thus, there is a demonstrably growing interest in bio-oil as shown in Figure 1. Pyrolysis, especially fast pyrolysis, has been reported to be more economic than high pressure liquefaction in bio-oil production (*3*). In addition, fast pyrolysis bio-oil has many advantages, such as easy handling and transport, high-energy density, and low nitrogen and sulfur content as compared with petroleum products. Thus, it is not surprising to see that more recent studies have focused on bio-oil production by pyrolysis (*4–6*). In fact, bio-oils have been successfully tested in turbines, boilers, and engines (*7*).

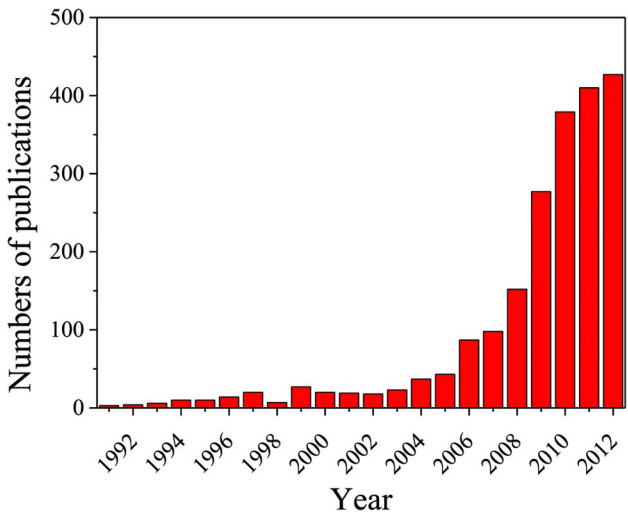

Figure 1. Number of publications on "bio-oil" by year, from 1991 to Dec. 2nd, 2012, according to Chemical Abstracts Service.

As crude oil contains high concentrations of sulfur and nitrogen, hydrodesulfurization (HDS) and hydrodenitrogenation (HDN) are required for the refining of crude oil to liquid transportation fuel. Bio-oil, on the other hand,

In Novel Materials for Catalysis and Fuels Processing; Bravo-Suárez, J., et al.;
ACS Symposium Series; American Chemical Society: Washington, DC, 2013.

has a lower concentration of sulfur and nitrogen, but with an obviously higher concentration of oxygen (up to 47 wt %) (*8*), causing instability, low heating value, and immiscibility with hydrocarbon fuels. Therefore, bio-oil must be deoxygenated prior to be suitable for use as liquid transportation fuels (Figure 2).

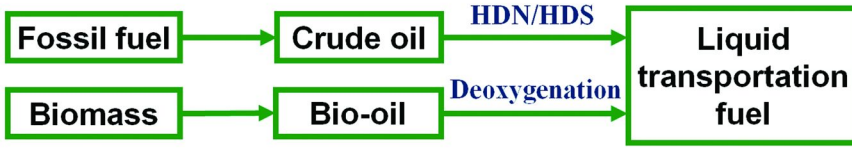

Figure 2. Strategies for the production of liquid transportation fuel from crude oil and bio-oil.

As pointed out in the literature (*8–10*), zeolite upgrading could not produce fuels with sufficient quality (high H/C and low O/C molar ratios). Therefore, a substantial amount of effort has been directed towards other deoxygenation processes to upgrade bio-oil such as hydrodeoxygenation (HDO). This process, which breaks C–O bonds selectively while maintaining C–C bonds, leads to the improvement in thermal stability, low acidity, heating values, and volatility of the treated bio-oil (*8–10*). The advantages of HDO are mainly twofold (*11*): high carbon efficiency and technology compatibility with the existing petroleum hydrotreating technology. However, the oxygen in the acidic groups should be partially or completely removed to lower the high acid number of bio-oil to avoid serious corrosion problems in standard refinery units (*12*). In addition, the acidic nature of bio-oil also constitutes a challenge for the equipment being used for its storage and transport (*10*). Thus, a better understanding of the catalytic process of deoxygenation of carboxylic acids is critical to drive the substitution of fossil-derived fuels by bio-oils. This work aims to address the recent advances in the deoxygenation of carboxylic acids from pyrolysis bio-oils over many different types of catalysts, focusing on the required catalytic properties for partial or complete deoxygenation.

Compounds To Be Upgraded in Bio-Oils

Pyrolysis bio-oil is a complex mixture of oxygenates with more than 300 different compounds identified so far (*7*). The properties of pyrolysis oils have been reviewed by Lu et al. (*13*). According to Bridgwater (*14*), bio-oil produced from pyrolysis contains mostly water (20–30 wt %), lignin fragments (15–30 wt %), aldehydes (10–20 wt %), carboxylic acids (10–15 wt %), carbohydrates (5–10 wt %), phenols (2–5 wt %), furfurals (1–4 wt %), alcohols (2–5 wt %), and ketones (1–5 wt %). With the exception of water, the other oxygenates in the bio-oils need to be upgraded in order to improve their quality. Among these oxygenates, carboxylic acids result in high acidity (with a pH value of 2–3 for bio-oil), corrosion, and further reactions that reduce the stability of bio-oil. Thus, the removal of carboxylic acids from bio-oil is an important step to improve its

In Novel Materials for Catalysis and Fuels Processing; Bravo-Suárez, J., et al.;
ACS Symposium Series; American Chemical Society: Washington, DC, 2013.

stability and minimize corrosion problems. The major compounds present in bio-oil carboxylic acids are presented in Figure 3 (*15*). Catalytic cracking is a widely used method to produce liquid hydrocarbons in the petroleum industry (*16*). However, this process suffers from serious coking formation and catalyst deactivation. Catalytic esterification is another commonly used technology to deal with carboxylic acids, but it has only a little effect on the removal of oxygen content in bio-oil (*17*). Compared with these two processes, deoxygenation with sacrificial hydrogen, also called HDO, is a more effective way to remove oxygen from carboxylic acids without serious coking formation (*18–23*).

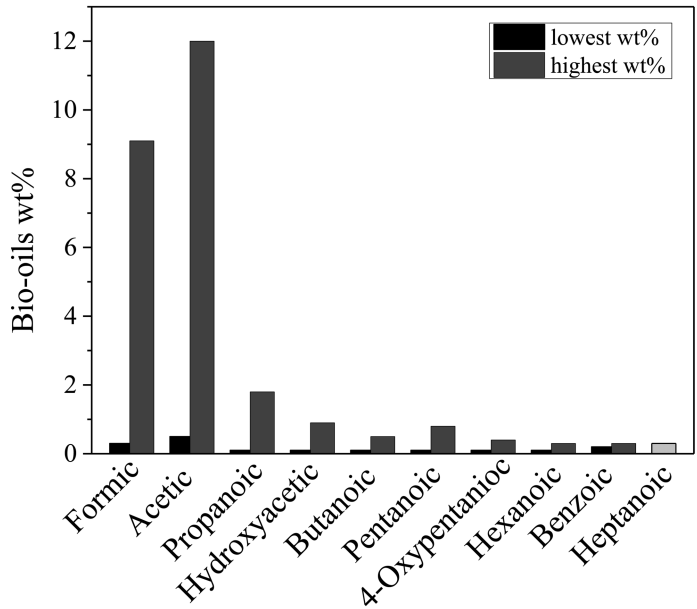

Figure 3. Acid compounds and percentage identified in bio-oils, data from reference (15).

Grange et al. (*24*) summarized the influence of temperature and H_2 consumption during the HDO reaction to investigate the reactivity of some model compounds over a commercial $CoMoS_x/\gamma\text{-}Al_2O_3$ hydrotreating catalyst as shown in Table 1. The carboxylic acids were found to be one of the most reactive components, with the hydrogenation of carboxylic acids occurring at temperatures below 300 °C over the $CoMoS_x/\gamma\text{-}Al_2O_3$ catalyst.

Table 1. Activation energy and temperatures of isoreactivity for HDO of different molecules or groups over a $CoMoS_x/\gamma\text{-}Al_2O_3$ catalyst. Reproduced with permission from reference (*24*). Copyright 1996 Elsevier.

	Activation energy (kcal/mol)	*Isoreactive temperatures[b] (°C)*	*Hydrogen consumption*
Ketone	12	203	$2H_2$/function[a]
Carboxylic acid	26	283	$3H_2$/function
Methoxy phenol	27	301	Up to $6H_2$/molecule
4-Methylphenol	33.6	340	Up to $4H_2$/molecule
2-Ethylphenol	35.8	367	Up to $4H_2$/molecule
Dibenzofuran	34.1	417	Up to $8H_2$/molecule

[a] function: functional group containing oxygen. [b] Isoreactive temperatures: the temperatures at which the conversion rates reach an identical value.

Mechanisms of Deoxygenation of Carboxylic Acids

Deoxygenation Reaction Pathways

Different catalysts even under the same reaction conditions can yield different products. The major reaction pathways are also different sometimes when the same catalyst is used under different reaction conditions. According to previous publications (*21*, *25–27*), three general routes are associated with the catalytic deoxygenation of carboxylic acids (Figure 4):

1) Ketonization by C–O bond cleavage to generate ketones, and further hydrogenation to produce alcohols;
2) Decomposition (decarboxylation and decarbonylation) of carboxylic acids by breaking C–C bonds to produce alkanes with one less carbon, CO, and/or CO_2;
3) HDO: Hydrogenolysis by C–O bond cleavage to produce aldehydes, followed by hydrogenation to form alcohols. These alcohols can be then dehydrated and hydrogenated to yield alkanes, or react with carboxylic acids to form esters.

In Novel Materials for Catalysis and Fuels Processing; Bravo-Suárez, J., et al.;
ACS Symposium Series; American Chemical Society: Washington, DC, 2013.

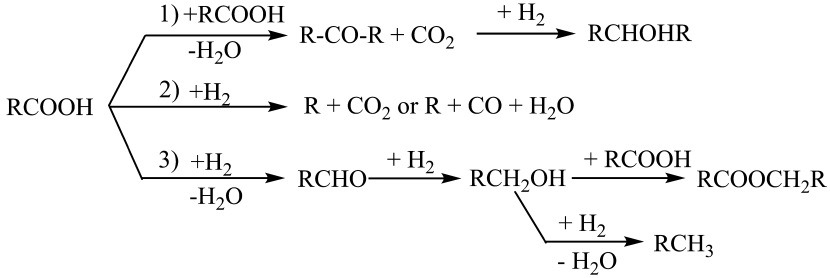

Figure 4. Main reaction pathways associated with HDO of carboxylic acids, R stands for alkyl groups.

Ketonization and Decomposition

Oxide catalysts are active in the ketonization of carboxylic acids (*28–31*). Gliński et al. (*28*) investigated 20 metal oxide catalysts (10 wt %) supported on SiO_2 in the ketonization of HOAc at 300–450 °C and atmospheric pressure in a continuous flow reactor. At 375 °C, the acetone yield is higher than 50% over the following oxides: MgO, CdO, CoO, Fe_2O_3, La_2O_3, CeO_2, and MnO_2. The loading of metal oxides has a positive effect on the yield of acetone, while Al_2O_3 is found to be the best support to generate a higher yield of acetone than other supports such as SiO_2 and TiO_2. A catalyst composed of 20 wt % MnO_2/γ–Al_2O_3 shows the highest yield of acetone, and was chosen for the ketonization of various aliphatic carboxylic acids, the results are presented in Table 2. The high yields of ketones from carboxylic acids of higher chain length can be obtained over the same catalyst but with a lower value against a higher chain length in carboxylic acids.

Table 2. Activity of 20 wt % MnO_2/γ-Al_2O_3 catalyst in the ketonization of various aliphatic carboxylic acids, LHSV=2 cm^3 g^{-1} h^{-1}. Reproduced with permission from reference (*28*) . Copyright 1995 Elsevier.

Acid	*Yield of ketone (%)*				
	275 °C	*300 °C*	*325 °C*	*350 °C*	*375 °C*
CH_3COOH	40	90	96	97	-
CH_3CH_2COOH	44	81	95	96	-
$CH_3(CH_2)_4COOH$	30	55	86	90	90[a]
$CH_3(CH_2)_5COOH$	23	50	78	89	90[a]

[a] Yield of ketone at total acid conversion

In Novel Materials for Catalysis and Fuels Processing; Bravo-Suárez, J., et al.;
ACS Symposium Series; American Chemical Society: Washington, DC, 2013.

Decomposition of carboxylic acid molecules on metal surfaces is rather straightforward: formic acid and acetic acid dissociate to form surface formate and acetate species, respectively (*31*). Surface carboxylate species have been detected on metal such as Cu, Fe, Pd, Pt, Ag, Ni, and Rh surfaces. Surface carboxylates have also been postulated as reaction intermediates on metal oxides such as MgO, CaO, Cr_2O_3, ZnO, TiO_2, Fe_2O_3, NiO, and SnO_2. However, Carboxylate ion, ketene, acyl carbonium ion, and parent molecular species had been reported on metal oxide surfaces, but only bimolecular interaction between either two adsorbed acetate ions or an adsorbed acyl carbonium ion and one adsorbed acetate ion would be responsible for ketonization of HOAc.

Hydrodeoxygenation Catalysts and Mechanisms

Table 3 shows an overview of the catalysts used for the deoxygenation of different model compounds of carboxylic acid feeds. Classic hydrotreating sulfided catalysts Ni(Co)–Mo/γ-Al_2O_3, Pt-based catalysts, Ru-based catalysts, and Cu-based catalysts have been studied for the deoxygenation of carboxylic acids. In these sulfided catalysts, it is generally believed that sulfur vacancies (coordinatively unsaturated sites), which are located at the edges of MoS_2 nanoclusters, are the active sites. In the case of metal supported catalysts, it is generally accepted that H_2 is adsorbed and activated on metal sites, while oxy-compounds can be adsorbed and activated on either metal sites or at the metal–support interface (exposed cations/oxygen vacancies) (*2*).

Acetic Acid

Acetic acid (HOAc) is the most abundant compound in cellulose-derived bio-oil (*37*), with a concentration up to 16.8 wt % in a beech wood bio-oil (*38*). Accordingly, it serves as a good model compound to investigate C–C bonds and C–O or C=O bonds activation in the deoxygenation of bio-oils.

Yang et al. (*27*) investigated the addition of Fe and Mo to the performance of a Ni/Al_2O_3 catalyst in the HOAc HDO at 4 MPa and 200–280 °C in a fixed bed reactor. Ni/Al_2O_3 favors ethyl acetate formation at low temperatures (200–240 °C), and C–C cleavage to form methane at high temperatures (260–280 °C), indicating that the reaction temperature has a great effect on the reaction pathways for the HOAc HDO. In addition, either Mo or Fe enhances the hydrogenation activity of the catalysts, improving the activity, especially when the reaction temperature is lower than 260 °C. Addition of different metal promoters result in changes of the catalyst acid properties, which can yield a different product distribution. For example, addition of Fe decreases the acidity, whereas Mo increases it. As a result, Fe promotes ethanol formation, whereas Mo enhances ethane generation. The results achieved by Yang et al. reveal the importance of metal sites that provide hydrogenation activity and the acid sites that correlate to the deoxygenation degree of HOAc. A catalyst with a higher hydrogenation activity favors higher conversion, whereas more acid sites enhance ethanol dehydration to ethylene followed by hydrogenation to the completely deoxygenated product ethane.

In Novel Materials for Catalysis and Fuels Processing; Bravo-Suárez, J., et al.;
ACS Symposium Series; American Chemical Society: Washington, DC, 2013.

Table 3. Performance of representative catalysts for the HDO of carboxylic acids.

Catalysts	*Loading (wt %)*	*Amount (g)*	*Feed*	*Acid concentration*	*Liquid flow rate (cm^3/h)*	*Gas flow rate (std cm^3/min)*	*Phase state*	*Setup*	*Conv. (%)*	*T (°C)*	*Total P (MPa)*	*Ref.*
$Ni/\gamma\text{-}Al_2O_3$	10								34.1			
$Ni–Fe/\gamma\text{-}Al_2O_3$	Ni:10, Fe:5	8 cm^3	HOAc[c]	4 wt % in heptane	12	H_2, 120	Vapor	Continuous	95.3	200	4.0	(*27*)
$Ni–Mo/\gamma\text{-}Al_2O_3$	Ni:10, Mo:5								97.7			
Pt/TiO_2	1	0.4	HOAc	8 wt % in heptane	6	H_2, 100	Vapor	Continuous	100	300	4.0	(*20*)
Pt/TiO_2	Pt:Ti=0.1[a]	0.2	HOAc	Saturated	0[e]	H_2, 90	Vapor	Continuous	100	425	0.12	(*36*)
$NiMoS_x/\gamma\text{-}Al_2O_3$	Commercial	Varied[b]	HOAc	99.7%	3	80% H_2 in N_2[b]	Vapor Liquid	Packed bed microreactor	60[g] 47[h]	450	0.1 2.07	(*32*)
Ru/C	5	0.2	HOAc	0.05 mol in 40 cm^3 water	-	-	Liquid	Batch	61	300	4.8	(*33*)
Pt/C									26			
Pd/C									3			
Ru/Al_2O_3									28			
Pt/Al_2O_3									10			
Pd/Al_2O_3									12			
Ru/C	5	0.2	HOAc	0.05 mol in 40 cm^3 *n*-heptane 0.05 mol in 40 cm^3 water	-	-	Liquid	Batch	30 19	200	4.8	(*33*)
Ru/C	1	6	HOAc	Aqueous 0.83 M	WHSV=1 h^{-1}	H_2, 80	Liquid	Continuous	76.5	190	6.4	(*21*)

Catalysts	*Loading (wt %)*	*Amount (g)*	*Feed*	*Acid concentration*	*Liquid flow rate (cm^3/h)*	*Gas flow rate (std cm^3/min)*	*Phase state*	*Setup*	*Conv. (%)*	*T (°C)*	*Total P (MPa)*	*Ref.*
Ru/C									93.5			
Ru/ZrO_2	1	6	PA[d] PA	Aqueous 0.83 M	WHSV=1 h^{-1}	H_2, 80	Liquid	Continuous	72.1	190	6.4	(*21*)
$Ru/\gamma\text{-}Al_2O_3$									47.9			
$Ru–MoO_x/ZrO_2$	Ru:1 Mo:Ru=0.2[a]	6	PA	Aqueous 0.83 M	WHSV=1 h^{-1}	H_2, 120	Liquid	Continuous	88.8	190	6.4	(*34*)
Cu/SiO_2	5								2.5			
Cu/CsPW	5								7			
$30wt\%HPW/SiO_2$	30	0.2	PA	2 % in H_2	0[f]	H_2, 10	Vapor	Continuous	5	250	0.1	(*35*)
0.5wt%Pd/CsPW	0.5								40			
0.5wt%Pt/CsPW	0.5								21			

[a] atomic ratios [b] Maintaining a constant residence time by varying catalyst weight (catalyst length of 0.025-0.18 m in a reactor with internal diameter of 7.62×10^{-4} m) [c] HOAc: acetic acid [d] PA: propionic acid [e] liquid was carried into system by H_2 at a saturation pressure of 25 mbar [f] liquid was introduced by H_2 at 47 °C, W/F=4 h g/mol [g] Extent of HDO: amount of hydrogen consumed/amount of hydrogen consumed for complete oxygen removal, conversion of vapor phase acetic acid [h] Conversion of liquid phase acetic acid

Pestman et al. (*36*) studied the HOAc HDO over the Pt/oxide systems, where a better activity and selectivity in comparison with single oxide alone were observed due to the hydrogenation ability of Pt (Pt/Fe_2O_3 had almost a 10 times higher activity than Fe_2O_3) (Figure 5). Figure 5 shows a volcano-shaped dependence of selectivity on metal–oxygen bond strength, where Fe_2O_3 with the medium strength gives the highest aldehyde selectivity. The authors further investigated Pt/TiO_2 in order to determine the specific function of each component of the catalysts (TiO_2 was chosen since it was unreducible to the metallic state under the conditions used). The results indicated that the overall activity increased with increasing oxide content, and no correlation was found between conversion and metal content. The reaction is suggested to proceed via a Mars–van Krevelen mechanism involving lattice oxygen from the support over Pt/TiO_2. The authors (*26*) confirmed these insights with iron oxide catalysts for the same reaction due to the medium strength of the metal–oxygen bond for this catalyst. These authors found that catalyst pretreatment and reaction conditions must be carefully controlled to partially maintain Fe in a metallic state, which is important for hydrogen activation and spillover. The selective HDO reaction to acetaldehyde takes place on the oxidic part of the catalyst also via a Mars–van Krevelen mechanism (Figure 6).

The required catalytic properties for HOAc HDO have also been studied over Pt supported on transition metal oxides in a fixed bed reactor at 300 °C and 4 MPa (*20*). The results indicated that, during HDO of acetic acid, Pt/TiO_2 was very selective towards ethane formation with production of traces of ethanol and ethyl acetate. Temperature-programmed desorption (TPD) experiments revealed that several conditions must be fulfilled to achieve high selectivity to ethane from acetic acid, including metal sites to activate and deliver hydrogen, moderate acidity for ethanol dehydration, and proper metal–oxygen bond strength in the oxide support for oxygen vacancy creation. The proposed detailed reaction pathways are presented in Figure 7. Here, it is proposed that HOAc adsorbs on the Pt–TiO_2 interface as η^1 species by the oxygen from the -OH group with the oxygen vacancies of TiO_2, while adjacent Pt dissociates H_2 to H that spills over to the interface where the catalytic reactions occur. The acid sites promote the dehydration of ethanol species to ethylene and allow for further hydrogenation to produce ethane as a completely deoxygenated product.

The reaction pathway of the gas-phase HOAc HDO was also studied in the presence of a sulfided $Ni–Mo/Al_2O_3$ catalyst in a packed bed microreactor at 200–450 °C and atmospheric pressure (*32*). The major observed reactions were decarbonylation, ketonization, and hydrogenation–esterification producing methane, acetone, acetaldehyde, ethanol, and ethyl acetate as shown in Figure 8.

Aqueous-phase HDO of HOAc was conducted by Wan et al. (*33*) over various supported noble metal catalysts (Ru, Pt, and Pd supported on both Al_2O_3 and carbon supports) at 300 °C and 4.8 MPa of hydrogen in a batch reactor for one hour. The detailed reaction conditions can be obtained in Table 3. The activity of HOAc conversion over the supported C catalysts followed the order: Ru > Pt > Pd, while the activity decreased over the supported Al_2O_3 catalysts with the sequence: Ru > Pd > Pt. The activity order did not follow the metal dispersion sequence when supported on either C or Al_2O_3. In addition, only some carbon supported catalysts

In Novel Materials for Catalysis and Fuels Processing; Bravo-Suárez, J., et al.;
ACS Symposium Series; American Chemical Society: Washington, DC, 2013.

were more active than their respective catalysts on Al_2O_3. These observations indicated the activity did not depend on metal sites alone. The major products were methane and CO_2, with their highest yield observed on the Ru/C catalyst due to its high activity for C–C bond cleavage (*39*). The proposed reaction network for the aqueous phase HDO of HOAc is shown in Figure 9. The presence of water could be beneficial for steam reforming of both HOAc and ethanol. The authors also investigated the effects of temperature at a H_2 pressure of 4.8 MPa, and the effects of H_2 partial pressure at 200 °C over Ru/C. Low temperatures (150 °C) favored the hydrogenation of acetyl species, leading to the high selectivity to ethanol. However, at high temperatures (300 °C), HOAc conversion increased from 5 to 60%. HOAc decomposition and ethanol reforming/hydrogenolysis were favored over hydrogenation of acetyl species, leading to high selectivities to CO_2 and methane. The highest ethane selectivity was found to be 15% at 200 °C. The conversion of HOAc and the selectivity of ethanol increased, while the selectivity of methane decreased with a higher hydrogen partial pressure. The selectivity of ethane and ethyl acetate was stable as a function of hydrogen partial pressure between 2–10 MPa.

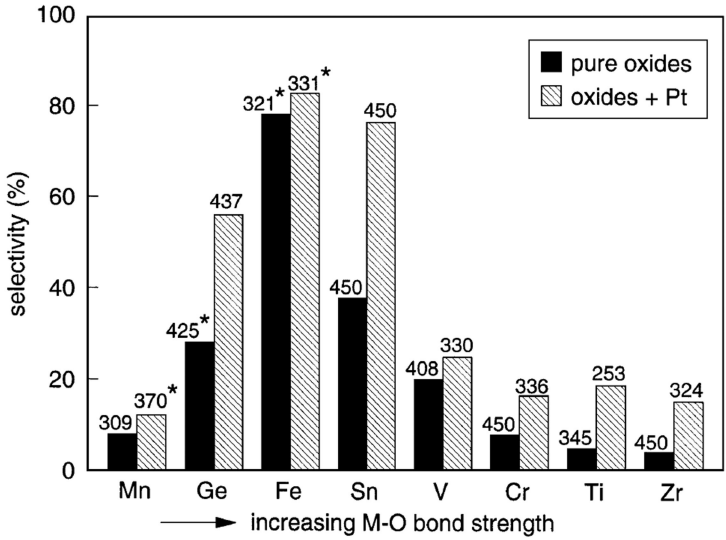

Figure 5. Maximum aldehyde selectivities of Pt/oxide systems as a function of metal–oxygen bond strength (not on scale). Above each bar is given the temperature (°C) at which this selectivity is reached. When the selectivity was obtained at decreasing temperature, this is marked with a star. Reproduced with permission from reference (36). Copyright 1997 Elsevier.

In Novel Materials for Catalysis and Fuels Processing; Bravo-Suárez, J., et al.;
ACS Symposium Series; American Chemical Society: Washington, DC, 2013.

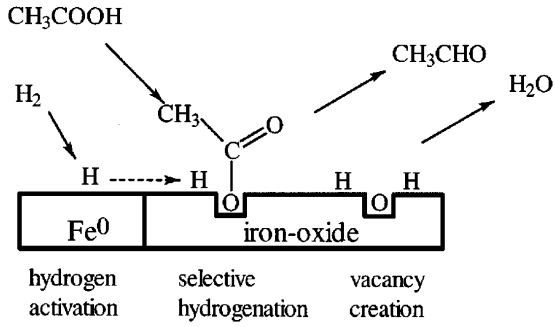

Figure 6. Reaction mechanism for the selective hydrodeoxygenation of HOAc to acetaldehyde over iron catalysts. Reproduced with permission from reference (26). Copyright 1998 Elsevier.

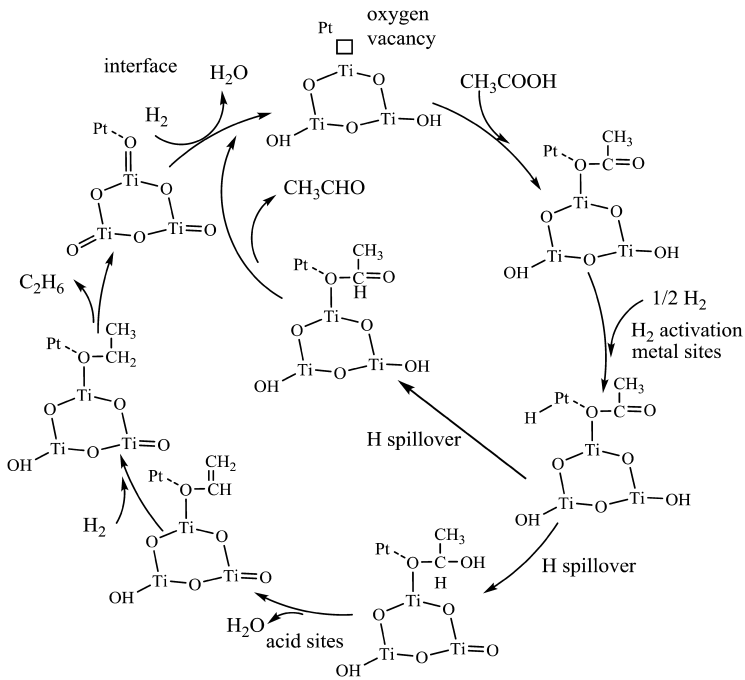

Figure 7. Schematic representation of the mechanism for the selective HDO of acetic acid to ethane over Pt/TiO2, with data from reference (20).

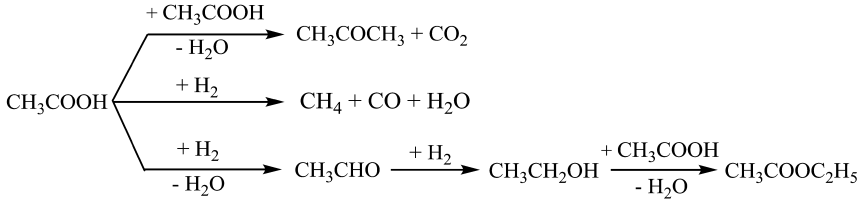

Figure 8. Reaction pathways of HDO of acetic acid over sulfided NiMo/Al_2O_3. Adapted with permission from reference (32). Copyright 2012 Elsevier

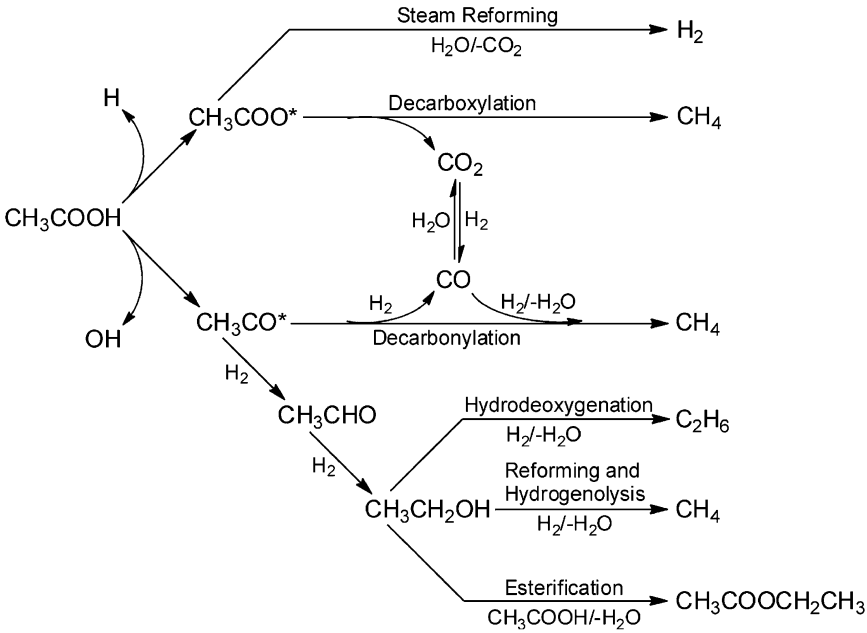

Figure 9. Proposed reaction network for aqueous phase HDO of acetic acid. Reproduced with permission from reference (33). Copyright 2012 ACS.

Propionic Acid

Aqueous-phase HDO of carboxylic acids (acetic acid, propionic acid (PA), butyric acid, and isobutyric acid) to alcohols or alkanes over Ru/C, Ru/ZrO_2, and Ru/Al_2O_3 catalysts were investigated at 300 °C and 6.4 MPa in a continuous-flow trickle-bed reactor by Chen et al. (*21*). These carboxylic acids were converted via two major routes as shown in Figure 10: (a) hydrogenolysis followed by hydrogenation to alcohol or dehydration–hydrogenation to alkane; and (b) decomposition (C–C bond cleavage) to form methane and an alkane with one less carbon. The C–C bond cleavage was improved at high temperature and on catalysts with high metal loadings, indicating the importance of metal sites for C–C bond cleavage. The acidic supports in combination with Ru metal favored the C=O hydrogenation, producing either an alcohol, or a completely deoxygenated alkane without carbon loss. This study (*21*) confirms that surface acidity and metal species are crucial for the deoxygenation of carboxylic acids.

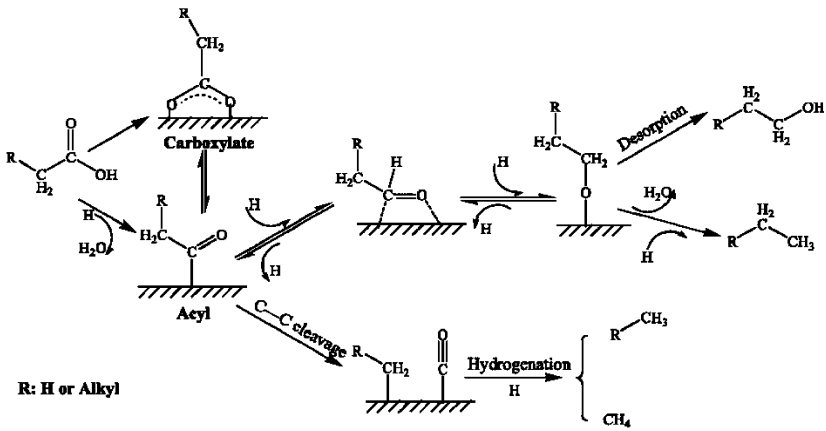

Figure 10. The surface reaction model for the deoxygenation of carboxylic acids over supported Ru catalysts. Reproduced with permission from reference (21). Copyright 2011 Elsevier.

Chen et al. (*34*) also studied the aqueous-phase HDO of PA at 6.4 MPa in the temperature range of 150–230 °C over Ru/ZrO_2 with or without MoOx promotion. Both C–C bond cleavage and C=O hydrogenation occurred over these two catalysts. The Ru/ZrO_2 catalyst favored the C–C bond cleavage reaction, producing more ethane and methane. On the other hand, $Ru–Mo/ZrO_2$ favored the C=O hydrogenation reaction but lowered the overall activity and C–C bond cleavage selectivity, resulting in higher selectivities to propanol and propane. The corresponding surface reaction model of C=O hydrogenation and C–C bond cleavage in propionic acid is presented in Figure 11. The formation of $Ru–MoO_x$ likely decreased the electron density around the Ru centers, which had a great impact on the C–C cleavage and C=O hydrogenation in the deoxygenation of carboxylic acids.

In Novel Materials for Catalysis and Fuels Processing; Bravo-Suárez, J., et al.;
ACS Symposium Series; American Chemical Society: Washington, DC, 2013.

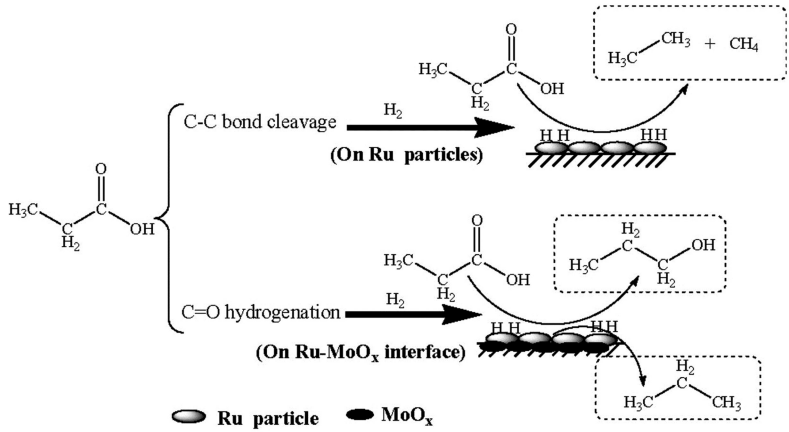

Figure 11. The surface reaction model for the HDO of propionic acid over ZrO_2 supported Ru and Ru–MoO_x catalysts. Reproduced with permission from reference (34). Copyright 2012 Elsevier.

The importance of metal sites to facilitate C=O hydrogenation to propanol in the HDO of PA was demonstrated by a turnover frequency (DFT) study over sulfided catalysts (*40*). For example, NiMoS was found to be more selective towards the formation of propanol from PA in comparison with MoS_2. This was because Ni addition lowers the activation energy of the rate-limiting step, which was believed to be the C–O bond cleavage.

The reaction pathways for the gas-phase deoxygenation of propionic acid over heteropolyacid and bifunctional metal-loaded heteropolyacid catalysts were studied in a fixed-bed reactor at 250–400 °C in H_2 or N_2 atmosphere (*35*). In one of the deoxygenation conversion routes, a Keggin-type heteropolyacid 30 wt % $H_3PW_{12}O_{40}$ (HPW) supported on SiO_2 and its bulk acidic salt $Cs_{2.5}H_{0.5}PW_{12}O_{40}$ (CsPW) favored ketonization reactions to yield 3-pentanone at 250 °C, and decarboxylation reactions to ethane at 400 °C in the presence of either H_2 or N_2 as shown in Table 4. These observations indicated the important role of acid sites for ketonization and decarbonylation reactions even with no H_2. In the presence of 0.5 wt % Pt or Pd on CsPW, decarbonylation and hydrogenation reactions were greatly enhanced at 250 °C, which led to the formation of ethane and 1-propanol, respectively; on the other hand, ethene dominates the products of decarbonylation at 400 °C. Metal-loaded CsPW catalysts showed the bifunctional properties including ketonization and decarbonylation/ hydrogenation at 250 °C, and decarbonylation to form ethene at the expense of ketonization at 400 °C. The 5 wt % Cu/CsPW catalyst also showed the dual function at both temperatures, which resulted in the formation of 3-pentanone, propanal, and 1-propanol at 250 °C, and ethane and ethene at 400 °C. In this catalyst, Cu was responsible for hydrogenation and decarbonylation in the presence of hydrogen. The turnover rate of propionic acid conversion followed the order: Pd > Pt > Cu. As these

In Novel Materials for Catalysis and Fuels Processing; Bravo-Suárez, J., et al.;
ACS Symposium Series; American Chemical Society: Washington, DC, 2013.

metals were active for the hydrogenation of the C=O bond and decarbonylation reactions, which involved the hydrogenolysis of C–O and C–C bonds under H_2 but not under N_2, the turnover rate indicated the reactivity order of these three metals using CsPW as the support.

Effects of Solvent/Co-Reactants

HOAc HDO was conducted by Wan et al. (*33*) over 5 wt % Ru/C at 200 °C and 4.8 MPa of hydrogen with water or *n*-heptane as a solvent. By replacing water with *n*-heptane as the solvent, the HOAc conversion (black bar) and selectivity of ethyl acetate (white bar) increased from 18 to 30% and from 1 to 60%, respectively. On the other hand, the selectivity of methane (gray bar), ethane (horizontally lined bar), and ethanol (diagonally lined bar) decreased. The results (Figure 12) indicated that both ethanol reforming/hydrogenolysis to produce methane and esterification reaction to form ethyl acetate were affected by water. In addition, the HDO activity of ethanol to ethane was higher with water as a solvent probably due the weaker competitive adsorption between water and HOAc in comparison with the adsorption between *n*-heptane and HOAc.

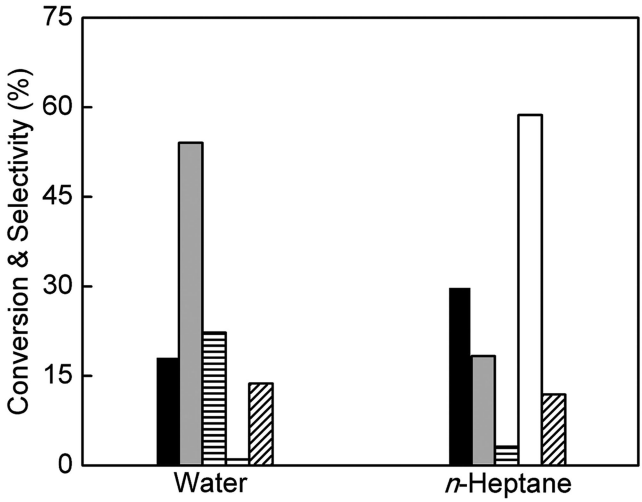

Figure 12. Solvent effects on acetic acid HDO. Reaction conditions: 0.2 g of Ru/C, 0.05 mol of HOAc, 40 cm³ of solvent, temperature of 200 °C, H_2 pressure of 48 bar, and batch reaction time of 1 h. Bar description: conversion (black) and selectivities to methane (gray), ethane (horizontal lines), ethyl acetate (white), and ethanol (diagonal lines). Reproduced with permission from reference (33). Copyright 2012 ACS.

In Novel Materials for Catalysis and Fuels Processing; Bravo-Suárez, J., et al.;
ACS Symposium Series; American Chemical Society: Washington, DC, 2013.

Table 4. The main reactions and products in the conversion of propionic acid in the absence and presence of hydrogen at 250 and 400 °C.

Catalyst	*Atmosphere*	*Products (250 °C)*	*Reactions (250 °C)*	*Products (400 °C)*	*Reactions (400 °C)*
CsPW	H_2 or N_2	3-pentanone	Ketonization	Ethane	Decarboxylation
30wt%HPW/SiO_2	H_2 or N_2				
0.5wt%Pd/CsPW	H_2	Ethene >> 1-propanol > 3-pentanone	Decarbonylation, hydrogenation, and ketonization	Ethene	Decarbonylation
0.5wt%Pt/CsPW	H_2				
5wt%Cu/CsPW	H_2	3-pentanone > propanal >> 1-propanol	Ketonization and hydrogenation	Ethane and ethene	Decarbonylation and decarboxylation

The solvent effects were also compared at 300 °C, where *n*-heptane was in a supercritical state. The HOAc conversion increased from 60 to nearly 100%, suggesting higher hydrogen availability in the supercritical phase promoted HOAc hydrogenation. The major products under such conditions were methane and CO_2, indicating that most of the HOAc underwent decomposition via either acetate or acetyl intermediates. High reaction temperatures did not improve ethane formation with the same solvent under different temperatures. At the identical reaction conditions with the mixed feed of *p*-cresol and HOAc, the conversion of HOAc decreased from 61 to 10%, indicating there existed stronger adsorption of *p*-cresol on the catalyst surface as compared with HOAc, which was the result of competitive adsorption. In contrast, the HDO of *p*-cresol was promoted by the presence of HOAc through the dehydration reaction (proton donation to 4-methylcyclohexene by HOAc), leading to high selectivity to methylcyclohexane.

Theoretical Calculations

Density functional theory (DFT) calculations were conducted for the conversions of HOAc over silica-supported 1.7 wt % Pt and Pt/Sn (1.7 wt % Pt and 0.82 wt % Sn (for $PtSn_{0.8}/SiO_2$) or 4.4 wt % Sn (for $PtSn_4/SiO_2$) catalysts at temperatures from 227 to 327 °C and 1 atm (*41*). The lowest energy transition states for C–O and C–C bond cleavage on $Pt_3Sn(111)$ were 25–60 kJ/mol higher compared with Pt(111), suggesting that C–O and C–C bond cleavage reactions were inhibited on $Pt_3Sn(111)$. On the other hand, energies of transition states for dehydrogenation–hydrogenation reactions increased by only 5–10 kJ/mol on $Pt_3Sn(111)$ compared with Pt(111). As a result, $PtSn/SiO_2$ catalysts were selective for conversion of HOAc to produce acetaldehyde and ethanol, while Pt/SiO_2 catalysts completely decomposed HOAc to CO, CH_4, and C_2H_6 as shown in Figure 13.

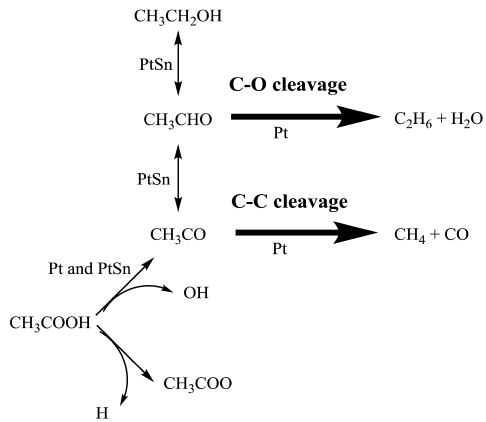

Figure 13. Reaction pathways over Pt and PtSn catalysts. Adapted with permission from reference (41). Copyright 2012 ACS.

In Novel Materials for Catalysis and Fuels Processing; Bravo-Suárez, J., et al.;
ACS Symposium Series; American Chemical Society: Washington, DC, 2013.

Non-local DFT calculations were used to explore some rules for design of HDO catalysts from HOAc to ethanol based on metal position in the periodic table (*42*). C–OH activation was found to be more favored on metals to the left in the periodic table, such as Re(0001), than on metals to the right. However, Re alone was not optimal since it also resulted in HOAc decomposition routes. However, Group VIII metals, such as Pd, showed lower activation barriers for hydrogenation and reduced HOAc decomposition, but they had poor activity for acetic acid C–O bond dissociation. An optimum catalyst was capable of preferentially activating the C–O bond without significantly enhancing β C–H bond activation of the carboxylic acid. A $Pd_{0.66}Re_{0.33}$ alloy, based on the DFT calculations, may be ideal for HOAc HDO to ethanol due to a nominal barrier for both C–OH bond breaking and C–H bond formation.

The activity of the aqueous-phase HDO of HOAc were measured over transition metal catalysts (Ru/C, Pt/C, Pd/C, Rh/C, Ir/Al_2O_3, Raney Ni, and Raney Cu catalysts) at temperatures of 110–290 °C and a total pressure of 5.17 MPa (*43*). The turnover frequencies (TOFs) of HOAc conversion decreased in the sequence: Ru > Rh ≈ Pt > Pd ≈ Ir > Ni > Cu. Ru/C also showed the highest selectivity of ethanol (~80%) at 160 °C. DFT calculations indicated that the different activity could be relevant to the intrinsic reactivity of the metals (except for Cu) for dissociating HOAc or acetate to acetyl (CH_3CO), which was likely to be rate-limiting instead of the subsequent hydrogenation of monoxy intermediates. A simple empirical correlation ($\Delta G^* = 0.73 \times \Delta G_{acetyl+OH} + 0.54$; $r^2=0.94$) was identified that may be used to estimate the free energy of the transition state for the rate-limiting step in HOAc conversion against the sum of free energies of acetyl and hydroxyl groups (Figure 14). These findings provided guidance for designing active and selective transition metal catalysts, particularly among those that bind acetyl and OH more strongly than Pt, Pd, and Cu, for the hydrogenation of organic acids and oxygenates in general.

The acetyl in HOAc conversion was found to be a key intermediate by Dumesic's group, where the overall rates of HOAc conversion over 5 wt % Cu/SiO_2 were determined by the hydrogenation of surface acetyl species at 297 °C and atmospheric pressure in a Pyrex down-flow reactor (*44*). It was found that the rate-determining step was applicable as well for the Pt/SiO_2 catalyst (*45*), where an equimolar mixture of CO and CH_4 was formed from HOAc over 6.92 wt % Pt/SiO_2 at 227–327 °C and atmospheric pressure in the same reactor setup.

Kinetic Models

A thorough review of kinetic studies of hydrodeoxygenation for several bio-oil model compounds has been published by Furimsky (*8*), whereas the kinetics of HDO of bio-oil was recently reviewed by Mortensen et al. (*9*). In the case of HDO of carboxylic acids in bio-oils, however, only sparse information on the kinetics is available. Herein, lumped kinetic expressions for the kinetics of HDO of some carboxylic acids isolated from the bio-oil are summarized, which were not discussed by Furimsky and Mortensen.

In Novel Materials for Catalysis and Fuels Processing; Bravo-Suárez, J., et al.;
ACS Symposium Series; American Chemical Society: Washington, DC, 2013.

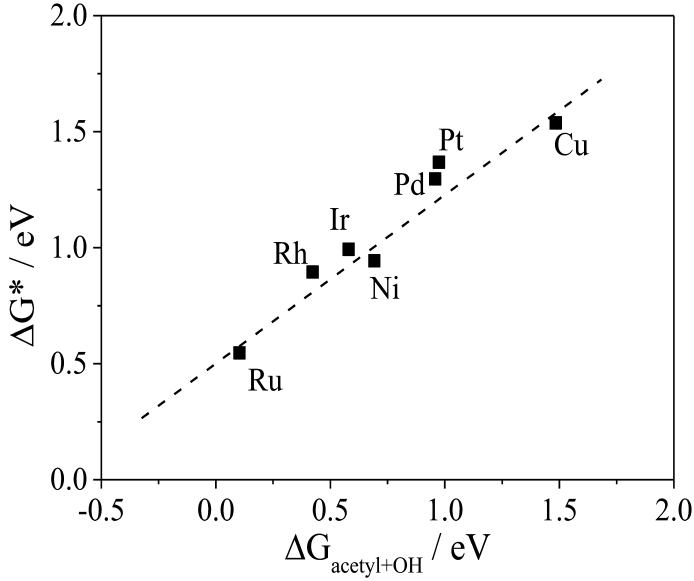

Figure 14. Free energies of the transition states of the rate-limiting step (ΔG) plotted against the sum of the free energies of acetyl and OH ($\Delta G_{acetyl+OH}$) adsorbed on the seven metals. The free energies are referenced to gas-phase HOAc. OH is fixed in the top site. Dashed line is the best linear fit of the data. Reproduced with permission from reference (43). Copyright 2010 Wiley.*

Rachmady et al. (*46*) established a kinetic model of HOAc HDO in the vapor phase at 150–300 °C, 13–93 kPa of hydrogen, and 0.9–6.6 kPa of HOAc over Pt supported on oxides (TiO_2, SiO_2, Al_2O_3, and Fe_2O_3) in a differential fixed-bed reactor (no solvent). The product selectivity was strongly dependent on the oxide supports and the reaction model correlated well with the data, which involved a Langmuir–Hinshelwood-type catalytic sequence. The model was based on the following assumptions:

1) Hydrogen and HOAc adsorbed dissociatively on one type of site existing on the metal surface in quasi-equilibrated processes (Equations 1–3).
2) HOAc adsorption on the support was also quasi-equilibrated (Equation 4).
3) Adsorbed hydrogen atoms and adsorbed acetate species were the predominant surface species on Pt.
4) Molecular HOAc was the only significant surface intermediate on the oxide surface sites (at low conversions).

The adsorbed acetic acid species involved a series of irreversible hydrogenation with the spillover hydrogen from Pt, producing aldehyde, ethanol and subsequently, ethane. Reversible steps are listed in Equations 6–8.

In Novel Materials for Catalysis and Fuels Processing; Bravo-Suárez, J., et al.;
ACS Symposium Series; American Chemical Society: Washington, DC, 2013.

$$H_{2(g)} + 2* \xrightarrow{K_{H_2}} 2H* \quad (1)$$

$$H* \xrightarrow{K_{sp}} H_{sp} \quad (2)$$

$$CH_3COOH_{(g)} + 2* \xrightarrow{K_{Ac}} CH_3COO* + H* \quad (3)$$

$$CH_3COOH_{(g)} + S \xrightarrow{K_A} CH_3COOH - S \quad (4)$$

$$CH_3COOH - S + H_{sp} \xrightarrow{k_1} CH_3COOH_2 - S \quad (5)$$

$$CH_3CHO - S \underset{k_{-3}}{\overset{k_3}{\rightleftharpoons}} CH_3CHO_{(g)} + S \quad (6)$$

$$CH_3CH_2OH - S \underset{k_{-6}}{\overset{k_6}{\rightleftharpoons}} CH_3CH_2OH_{(g)} + S \quad (7)$$

$$CH_3CH_3 - S \underset{k_{-9}}{\overset{k_9}{\rightleftharpoons}} CH_3CH_{3(g)} + S \quad (8)$$

Where * represents an active site on the Pt surface, and S is a site on the oxide surface. CH_3COO* and H* represent adsorbed acetate species and hydrogen atoms, respectively.

The resulting kinetic expression is shown below from the Equation 5 (rate-determining step):

$$r_{HOAc} = k_1' P_A P_{H_2}^{1/2} / [(K_2 P_{H_2}^{1/2} + K_3 P_A / P_{H_2}^{1/2})(1 + K_4 P_A)] \quad (9)$$

Where r_{HOAc} is the overall rate of formation of acetaldehyde, ethanol, and ethane; $k_1' = k_1 K_A K_{sp} K_{H2}^{1/2}$, $K_2 = K_{H2}^{1/2}$, $K_3 = K_{Ac}/K_{H2}^{1/2}$ and $K_4 = K_A$.

The expression fitted the data well, and there was an excellent agreement between the experimental and the predicted values for the apparent activation energies. Values for k'_1, K_2, K_3, and K_4 are listed in Table 5.

The Langmuir–Hinshelwood model also worked well for the same reaction system over a Fe/SiO_2 catalyst at 177–300 °C and 13–93 kPa of hydrogen (no solvent) as reported by the same authors (*47*). The rate-determining step is listed in Equation 10, where the addition of the first hydrogen atom to the adsorbed acetate species is rapid. The assumption, different from previous ones, was that surface acetate species (Ace) was the most abundant intermediate on the oxidic iron sites (at low conversions). The final product was ethanol instead of ethane over Fe/SiO_2. The reaction involved a metallic iron to activate hydrogen and oxidic iron to activate HOAc. The rate expression was slightly different from Equation 9 and is shown next:

$$CH_3CHO - S - OH + H* \xrightarrow{k_2} CH_3CHO - S + * + H_2O_{(g)} \quad (10)$$

$$r_{HOAc} = k\ P_A P_{H_2}^{3/2} / [(K_{H_2} P_{H_2} + K_{Ac} P_A)(1 + K_{Ace} K_A P_A)] \quad (11)$$

In Novel Materials for Catalysis and Fuels Processing; Bravo-Suárez, J., et al.;
ACS Symposium Series; American Chemical Society: Washington, DC, 2013.

Table 5. Optimized rate parameters in Equation 9 for Pt/TiO_2 catalysts. Reproduced with permission from reference (*46*). Copyright 2000 Elsevier.

Catalysts	k_1K_{sp} ($\mu mol/s \times gcat$)	K_{H2} ($atm^{-1} \times 10^{-5}$)	K_A (atm^{-1})	K_{Ac} ($atm^{-1} \times 10^{-7}$)
A. 0.69 wt % Pt/TiO_2 (HTR)[a]				
T=164°C	2.42	50.8	10.9	13.5
T=187°C	17.9	7.6	4.4	4.7
T=197°C	22.2	4.8	5.5	3.3
B. 2.01wt % Pt/TiO_2 (LTR)[b]				
T=149°C	8.16	17.4	4.3	8.9
T=172°C	26.6	6.1	3.3	4.2
T=192°C	627	0.7	0.4	0.9

[a] HTR: high temperature of reduction at 500 °C. [b] LTR: low temperature of reduction at 200 °C.

Here, K_{Ace} is the rate parameter of surface acetate species, and K_{Ac} is the rate parameter of HOAc.

The apparent reaction orders with respect to HOAc and hydrogen partial pressures for HOAc HDO over 4.1 wt % Fe/SiO_2 could be interpreted by a power rate law as shown in Table 6. The measurements were conducted at P_{H2}=93 kPa and P_{HOAc}=1.9 kPa, and the rate of reaction was expressed as $r_{HOAc}=k(P_{HOAc})^x(P_{H2})^y$. The apparent reaction order with respect to HOAc remained near zero while the reaction order with respect to hydrogen varied between 1 and 2. The changes of HOAc partial pressure did affect the product distribution significantly. However, the acetaldehyde and acetone were markedly affected by hydrogen partial pressure: acetaldehyde increased while acetone decreased with higher pressures of hydrogen.

Shin et al. (*48*) studied the effect of water to the HOAc HDO to ethanol at 230 °C under hydrogen pressure of 6890 kPa with a catalyst (RuO_2 powder) loading of 4 g/L in a batch reactor. The addition of water retarded the hydrogenation rates of HOAc probably due to the competitive adsorption between HOAc and water to the catalyst surface. However, water improved the yield of ethanol due to the hydrolysis of ethyl acetate. A variety of kinetic models were tested, and only a Langmuir rate expression gave the best fit to the experimental data as shown below.

$$\gamma = -\frac{dC_{ac}}{dt} = \frac{kK_{ac}K_hC_{ac}C_h}{(1 + K_hC_h + K_{ea}C_{ea} + K_{eo}C_{eo} + K_{ac}C_{ac} + K_wC_w)^2} \quad (12)$$

Where K_{ea}, K_{eo}, K_{ac}, K_h and K_w are the equilibrium adsorption constants on Ru for ethyl acetate, ethanol, HOAc, hydrogen, and water, respectively; C_{ea}, C_{eo}, C_{ac}, C_h, and C_w are the respective concentrations. $C_h=\alpha P_h$, where α is Henry's law constant.

In Novel Materials for Catalysis and Fuels Processing; Bravo-Suárez, J., et al.;
ACS Symposium Series; American Chemical Society: Washington, DC, 2013.

Table 6. Apparent reaction orders with respect to HOAc (*x*) and hydrogen (*y*) partial pressures for HOAc HDO over 4.1 wt % Fe/SiO_2. Adapted with permission from reference (*47*). Copyright 2002 Elsevier.

Temperature (°C)	*Reaction order*	
	x	*y*
257	0.08	1.1
273	0.06	1.4
295	0.09	1.7

By using regression analysis and parameter estimation, the order of magnitude of the adsorption equilibrium constant of water was the same as that of HOAc and ethanol, which confirmed the competitive adsorption between water and other reactants. It was also found that the esterification rate of ethanol and HOAc was enhanced at least three times by the presence of RuO_2. Based on the positive role of water on the yield of ethanol but a negative role on the reaction rate, the only way to achieve high selectivity and conversion would be to conduct the reaction with higher pressures and higher catalyst loading in the presence of water.

Aqueous-phase hydrogenation of PA over a 5 wt % Ru/C catalyst was carried out in a three-phase stirred batch reactor under the conditions of 70–150 °C, 3400–10300 kPa of hydrogen pressure, and 0.05–5 M aqueous acid solutions (*49*). In this case, a two-site Langmuir–Hinshelwood kinetic model with a single set of rate and adsorption constants fits the conversion kinetics of acid hydrogenation, which is expressed below. The model was based on the following assumptions:

1) The irreversible surface reaction of the adsorbed acid was assumed to be the rate-controlling step, all other steps were assumed rapid and close to equilibrium.
2) The adsorption of water was neglected.

$$-r_{\text{Acid}}\,(\text{kmol/kg of catalyst/s}) = k_{Acid}C_{Acid}P_{H_2} / [(1 + K_{Acid}C_{Acid} + K_{Alcohol}C_{Alcohol})(1 + \sqrt{K_{H_2}P_{H_2}})^2] \quad (13)$$

where $k_{Acid} = k_{sA}K_{Acid}K_{H2}C_{t1}(C_{t2})^2$ is a composite rate constant for each acid (m^3/kg of catalyst/MPa/s); k_{sA} is the surface reaction rate constant for each acid ((kg of catalyst)^2/kmol^2/s); K_{Acid} is the adsorption constant for the acid (m^3/kmol); $K_{Alcohol}$ is the adsorption constant for the alcohol product (m^3/kmol); K_{H2} is the adsorption constant for hydrogen (1/MPa); C_{t1} is the total catalyst site concentration for acid and alcohol adsorption (kmol/kg of catalyst); and C_{t2} is the total catalyst site concentration for hydrogen adsorption (kmol/kg of catalyst).

Overall, it has been found that a Langmuir–Hinshelwood kinetic model fits the experimental data well when the catalyst is selective to certain reaction pathways, such as HOAc HDO to acetaldehyde, ethanol, and ethane or PA HDO towards

In Novel Materials for Catalysis and Fuels Processing; Bravo-Suárez, J., et al.;
ACS Symposium Series; American Chemical Society: Washington, DC, 2013.

1-propanol without considering the effect of water. However, these models seem to apply only to the case when each carboxylic acid is studied independently at a low conversion. When more components are present, as in the case of bio-oil mixtures, more reactions will be involved and the model will need to be reconsidered. The kinetic model may work for other single carboxylic acids, however, at this stage it is unclear whether it will hold for mixed acids from bio-oils.

General Aspects

The catalytic HDO of carboxylic acids involve many active sites such as hydrogenation and hydrogenolysis sites, dehydration sites, and oxygen vacancies in the supports. These sites are typically present in metal supported on oxide catalysts, which are the most widely used and reported catalytic systems in the literature. Because of the multifunctional nature of these catalysts, it can be possible to tune the HDO product selectivity by modification of the metal–support interactions and surface acidity of the catalysts, by proper selection of active transition metals, supports, and addition of promoters.

The above mentioned insights for HDO of carboxylic acids in bio-oils can also be applicable to other acids with more carbons such as oleic acid (*50*) and fatty acids (*51*), which are obtained from vegetable oils and animal fats. The insights are also appropriate for HDO of other model compounds in bio-oils, such as guaiacol (*18*, *19*). In fact, the well-established dual-functional catalysts including metal sites and acidic sites have been reported to be responsible for HDO activity (*52–56*), where metal sites serve for hydrogenation, whereas acid sites are involved in hydrolysis and/or dehydration reactions. Such a dual-functional catalyst also has been reported to exhibit excellent HDO ability for other biomass-derivatives (*57*) to fuels and chemicals.

Based on literature reviews of the properties and reactivity of carboxylic acids from bio-oils, it can be concluded that carboxylic acids can be converted to other deoxygenated products that are less acidic and corrosive. Due to the different reactivity of the components in bio-oils, a two-stage hydrotreatment process was proposed by Elliott and Neuenschwander (*58*) in a down-flow trickle bed consisting of two fixed bed reactors at 21 MPa. The top one was operated below 300 °C, and the one below was in the temperature range of 300–400 °C. Delmon and co-workers also reported similar ideas (*24*). Because of the relatively high HDO reactivity of carboxylic acids, a reduction of the acid number in the bio-oil can be easily accomplished in the first reactor. More importantly, only hydrocarbon fuels can be produced from carboxylic acids, and the hydrophobic alkane can be removed if a proper catalyst is used in the first stage. Indeed, if the temperature is high enough in the first stage, carboxylic acids would be saturated. Therefore, no reactor corrosion will occur from carboxylic acids in the second stage. As the temperature in the second stage is higher than the first one, other reactions such as decomposition would be more favored due to higher C–C hydrogenolysis, resulting in the loss of carbon. In addition, integrated catalytic processing, which involves a two-step hydroprocessing (125 and 250 °C) and

In Novel Materials for Catalysis and Fuels Processing; Bravo-Suárez, J., et al.;
ACS Symposium Series; American Chemical Society: Washington, DC, 2013.

zeolite upgrading (Ru/C and zeolite catalysts), was also proposed to produce aromatic hydrocarbons and light olefins from pyrolysis oil in a more efficient and economical manner (*59*). Another important point to mention is that formic acid is one of the most abundant acids in bio-oils. This is relevant for HDO reactions because formic acid can be easily decomposed into hydrogen (and CO_2), which can then be used as a reductant for other higher carboxylic acids or compounds (*60*). From a material-design point of view, construction materials for the first stage reactor should have better corrosion-resistance properties.

One more thing to consider is the impact on the catalysts of water and sulfur present in the real pyrolysis oil. Bio-oils contain very high concentrations of water and they can contain concentrations of sulfur of more than hundreds of ppm depending on the source. Therefore, using a single model or a mixture of several compounds free of sulfur and under non-aqueous conditions fail to address the challenges during deoxygenation of real pyrolysis oil feedstocks. In this direction, many research efforts have been invested towards aqueous deoxygenation of model compounds recently (*21*, *34*, *52*, *53*, *61*, *62*). In very few cases the effect of H_2S effect on the catalyst performance has been investigated. However, these works were limited to sulfided Ni–Mo/γ-Al_2O_3 and/or Co–Mo/γ-Al_2O_3 catalysts (*63*, *64*). Simulating sulfur concentrations present in real pyrolysis oil when carrying out studies with single model compounds will be vital to evaluate the direct consequences of sulfur on the catalyst performance such as activity and stability.

Conclusions and Future Perspectives

The challenges arising from the energy crisis and greenhouse gas emissions have made energy from renewable resources especially from biomass very attractive in recent years. Substitution of fossil-derived fuels by pyrolysis bio-oils is a potential economic solution. However, the high acidity of pyrolysis bio-oils caused by carboxylic acids constitutes a big problem for using as feedstocks in existing petroleum refining facilities. Recently, there has been a lot of progress in the HDO of model carboxylic acids from pyrolysis bio-oils over different types of catalysts, including classic sulfided hydrotreating catalysts and metal supported catalysts. Some aspects of the chemistry and reaction mechanisms of carboxylic acids model compounds over these catalysts were presented in this review.

Recent achievements suggest that HDO of carboxylic acids can be fulfilled when the following catalytic properties are present: hydrogenation /hydrogenolysis sites such as metal sites or Brønsted acid sites to deliver hydrogen, acid sites for alcohol dehydration, and proper metal–oxygen bond strength in the oxide support for oxygen vacancy creation and regeneration. A synergic effect of these sites determines the final deoxygenated products: partial or complete deoxygenation. The modification of the metal and acid sites can be simply achieved by proper promoter addition, which enables the tuning of the selectivity of the deoxygenation products.

The future tasks concerning catalysts, feedstocks, and operations include:

In Novel Materials for Catalysis and Fuels Processing; Bravo-Suárez, J., et al.;
ACS Symposium Series; American Chemical Society: Washington, DC, 2013.

1) Lowering the cost of noble metal catalysts by reducing the amount of metals via promoters or new and more effective synthetic methods such as atomic layer deposition.
2) Addressing the challenges due to the presence of water and sulfur when using single and/or a mixture of model compounds of carboxylic acids.
3) Employing liquid-phase reactions instead of vapor-phase reactions in trickle-bed reactors.
4) Developing more complete kinetic models that include the effect of water and sulfur in the feedstock.
5) Improving the quality of pyrolysis bio-oils by finding new biomass resources or by genetic engineering.

Acknowledgments

The authors would like to thank the financial support from New Jersey Institute of Technology. The authors also would like to thank the useful and constructive suggestions and comments from the editors and reviewers to improve this work.

Nomenclature

HDO	Hydrodeoxygenation
HDS	Hydrodesulfurization
HDN	Hydrodenitrogenation
HOAc	Acetic acid
PA	Propionic acid
DFT	Density functional theory
TPD	Temperature-programmed desorption
CsPW	$Cs_{2.5}H_{0.5}PW_{12}O_{40}$
HPW	$H_3PW_{12}O_{40}$
TOF	Turnover frequency
PO	Pyrolysis oil

References

1. Huber, G. W.; Iborra, S.; Corma, A. *Chem. Rev.* **2006**, *106*, 4044–4098.
2. He, Z.; Wang, X. *Catal. Sustainable Energy* **2012**, *1*, 28–52.
3. Elliott, D. C.; Baker, E. G.; Beckman, D.; Solantausta, Y.; Tolenhiemo, V.; Gevert, S. B.; Hörnell, C.; Östman, A.; Kjellström, B. *Biomass* **1990**, *22*, 251–269.
4. Li, R.; Zhong, Z.; Jin, B.; Zheng, A. *Energy Fuels* **2012**, *26*, 2996–3002.
5. Demiral, İ.; Eryazıcı, A.; Şensöz, S. *Biomass Bioenergy* **2012**, *36*, 43–49.
6. Yoder, J.; Galinato, S.; Granatstein, D.; Garcia-Pérez, M. *Biomass Bioenergy* **2011**, *35*, 1851–1862.
7. Czernik, S.; Bridgwater, A. V. *Energy Fuels* **2004**, *18*, 590–598.
8. Furimsky, E. *Appl. Catal., A* **2000**, *199*, 147–190.

9. Mortensen, P. M.; Grunwaldt, J. D.; Jensen, P. A.; Knudsen, K. G.; Jensen, A. D. *Appl. Catal., A* **2011**, *407*, 1–19.
10. Zhang, Q.; Chang, J.; Wang, T.; Xu, Y. *Energy Convers. Manage.* **2007**, *48*, 87–92.
11. Brown, R. C., Ed. *Thermochemical Processing of Biomass: Conversion into Fuels, Chemicals and Power*; Wiley: Chippenham, Wiltshire, 2011.
12. Bu, Q.; Lei, H.; Zacher, A. H.; Wang, L.; Ren, S.; Liang, J.; Wei, Y.; Liu, Y.; Tang, J.; Zhang, Q.; Ruan, R. *Bioresour. Technol.* **2012**, *124*, 470–477.
13. Lu, Q.; Li, W.-Z.; Zhu, X.-F. *Energy Convers. Manage.* **2009**, *50*, 1376–1383.
14. Bridgwater, A. V.; Czernik, S.; Piskorz, J. The Status of Biomass Fast Pyrolysis. In *Fast Pyrolysis of Biomass: A Handbook*; Bridgwater, A. V., Ed.; CPL Press: Newbury, 2002; Vol. 2, pp 1−19.
15. Diebold, J. P. *A Review of the Chemical and Physical Mechanisms of the Storage Stability of Fast Pyrolysis Bio-oils*; Report No. NREL/SR-570-27613; National Renewable Energy Lab.: Golden, CO, U.S.A., 1999.
16. Hilten, R.; Speir, R.; Kastner, J.; Das, K. C. *J. Anal. Appl. Pyrolysis* **2010**, *88*, 30–38.
17. Wang, S.; Guo, Z.; Cai, Q.; Guo, L. *Biomass Bioenergy* **2012**, *45*, 138–143.
18. He, Z.; Wang, X. *Catal. Commun.* **2012**, submitted.
19. He, Z.; Wang, X. *Appl. Catal. B* **2012**, submitted.
20. He, Z.; Wang, X. *Appl. Catal. B* **2012**, submitted.
21. Chen, L.; Zhu, Y.; Zheng, H.; Zhang, C.; Zhang, B.; Li, Y. *J. Mol. Catal. A: Chem.* **2011**, *351*, 217–227.
22. Keane, M.; Larsson, R. *Catal. Lett.* **2009**, *129*, 93–103.
23. Afonso, J. C.; Schmal, M.; Cardoso, J. N. *Ind. Eng. Chem. Res.* **1992**, *31*, 1045–1050.
24. Grange, P.; Laurent, E.; Maggi, R.; Centeno, A.; Delmon, B. *Catal. Today* **1996**, *29*, 297–301.
25. Rachmady, W.; Vannice, M. A. *J. Catal.* **2002**, *207*, 317–330.
26. Pestman, R.; Koster, R. M.; Boellaard, E.; van der Kraan, A. M.; Ponec, V. *J. Catal.* **1998**, *174*, 142–152.
27. Yang, Y.-n.; Zhang, H.-k.; Lu, E.-j.; Zhang, C.-h.; Ren, J. *J. Mol. Catal. (China)* **2011**, *25*, 30–36.
28. Gliński, M.; Kijeński, J.; Jakubowski, A. *Appl. Catal., A* **1995**, *128*, 209–217.
29. Gaertner, C. A.; Serrano-Ruiz, J. C.; Braden, D. J.; Dumesic, J. A. *Ind. Eng. Chem. Res.* **2010**, *49*, 6027–6033.
30. Ignatchenko, A. V.; Kozliak, E. I. *ACS Catal.* **2012**, *2*, 1555–1562.
31. Rajadurai, S. *Catal. Rev.: Sci. Eng.* **1994**, *36*, 385–403.
32. Joshi, N.; Lawal, A. *Chem. Eng. Sci.* **2012**, *84*, 761–771.
33. Wan, H.; Chaudhari, R. V.; Subramaniam, B. *Energy Fuels* **2012**.
34. Chen, L.; Zhu, Y.; Zheng, H.; Zhang, C.; Li, Y. *Appl. Catal., A* **2012**, *411–412*, 95–104.
35. Alotaibi, M. A.; Kozhevnikova, E. F.; Kozhevnikov, I. V. *Appl. Catal., A* **2012**, *447–448*, 32–40.
36. Pestman, R.; Koster, R. M.; Pieterse, J. A. Z.; Ponec, V. *J. Catal.* **1997**, *168*, 255–264.

37. Milne, T.; Agblevor, F.; Davis, M.; Deutch, S.; Johnson, D. A Review of the Chemical Composition of Fast-Pyrolysis Oils. In *Developments in Thermochemical Conversion of Biomass*; Bridgwater, A. V., Boocock, D. G. B., Eds.; Blackie Academic and Professional: London, 1997; Vol. 1, pp 409−424.
38. Demirbas, A. *Fuel Process. Technol.* **2007**, *88*, 591–597.
39. Maris, E. P.; Davis, R. J. *J. Catal.* **2007**, *249*, 328–337.
40. Dupont, C.; Lemeur, R.; Daudin, A.; Raybaud, P. *J. Catal.* **2011**, *279*, 276–286.
41. Alcala, R.; Shabaker, J. W.; Huber, G. W.; Sanchez-Castillo, M. A.; Dumesic, J. A. *J. Phys. Chem. B* **2004**, *109*, 2074–2085.
42. Pallassana, V.; Neurock, M. *J. Catal.* **2002**, *209*, 289–305.
43. Olcay, H.; Xu, L.; Xu, Y.; Huber, G. W. *ChemCatChem* **2010**, *2*, 1420–1424.
44. Santiago, M. A. N.; Sánchez-Castillo, M. A.; Cortright, R. D.; Dumesic, J. A. *J. Catal.* **2000**, *193*, 16–28.
45. Gursahani, K. I.; Alcalá, R.; Cortright, R. D.; Dumesic, J. A. *Appl. Catal., A* **2001**, *222*, 369–392.
46. Rachmady, W.; Vannice, M. A. *J. Catal.* **2000**, *192*, 322–334.
47. Rachmady, W.; Vannice, M. A. *J. Catal.* **2002**, *208*, 158–169.
48. Shin, Y.-S.; Lee, C.-K. *J. Chin. Chem. Soc.* **1985**, *32*, 29–34.
49. Chen, Y.; Miller, D. J.; Jackson, J. E. *Ind. Eng. Chem. Res.* **2007**, *46*, 3334–3340.
50. Madsen, A. T.; Ahmed, E. H.; Christensen, C. H.; Fehrmann, R.; Riisager, A. *Fuel* **2011**, *90*, 3433–3438.
51. Santillan-Jimenez, E.; Morgan, T.; Lacny, J.; Mohapatra, S.; Crocker, M. *Fuel* **2013**, *103*, 1010–1017.
52. Zhao, C.; He, J.; Lemonidou, A. A.; Li, X.; Lercher, J. A. *J. Catal.* **2011**, *280*, 8–16.
53. Wawrzetz, A.; Peng, B.; Hrabar, A.; Jentys, A.; Lemonidou, A. A.; Lercher, J. A. *J. Catal.* **2010**, *269*, 411–420.
54. Zhu, X.; Lobban, L. L.; Mallinson, R. G.; Resasco, D. E. *J. Catal.* **2011**, *281*, 21–29.
55. Lee, C. R.; Yoon, J. S.; Suh, Y.-W.; Choi, J.-W.; Ha, J.-M.; Suh, D. J.; Park, Y.-K. *Catal. Commun.* **2012**, *17*, 54–58.
56. Basaran, D.; Genest, A.; Rösch, N. *J. Catal.* **2012**, *287*, 210–213.
57. Serrano-Ruiz, J. C.; West, R. M.; Dumesic, J. A. *Annu. Rev. Chem. Biomol.* **2010**, *1*, 79–100.
58. Bridgwater, A. V., Boocock, D. G. B., Eds. *Liquid fuels by low-severity hydrotreating of biocrude*; Blackie Academic & Professional: London, 1996.
59. Vispute, T. P.; Zhang, H.; Sanna, A.; Xiao, R.; Huber, G. W. *Science* **2010**, *330*, 1222–1227.
60. Xiong, W.-M.; Fu, Y.; Zeng, F.-X.; Guo, Q.-X. *Fuel Process. Technol.* **2011**, *92*, 1599–1605.
61. Ryu, J.; Kim, S. M.; Choi, J.-W.; Ha, J.-M.; Ahn, D. J.; Suh, D. J.; Suh, Y.-W. *Catal. Commun.* **2012**, *29*, 40–47.
62. Li, N.; Huber, G. W. *J. Catal.* **2010**, *270*, 48–59.

In Novel Materials for Catalysis and Fuels Processing; Bravo-Suárez, J., et al.;
ACS Symposium Series; American Chemical Society: Washington, DC, 2013.

63. Bunch, A. Y.; Wang, X.; Ozkan, U. S. *J. Mol. Catal. A: Chem.* **2007**, *270*, 264–272.
64. Şenol, O. İ.; Viljava, T. R.; Krause, A. O. I. *Appl. Catal., A* **2007**, *326*, 236–244.

Editors' Biographies

Juan J. Bravo-Suárez

Juan J. Bravo-Suárez earned his Ph.D. in Chemical Engineering in 2004 from Industrial University of Santander (Colombia) in collaboration with Virginia Polytechnic Institute and State University under the supervision of Prof. E. A. Páez-Mozo and Prof. S. T. Oyama. From 2004–2008, he was a postdoctoral researcher at the National Institute of Advanced Industrial Science and Technology, AIST (Japan). In Japan, he was awarded the prestigious JSPS Postdoctoral Fellowship for Foreign Researchers. During 2008–2009, he did a postdoctoral stay at LBNL/UC-Berkeley. Since 2009, he has been a research associate at the University of Kansas–Center for Environmentally Beneficial Catalysis (CEBC). His main interests include the spectroscopic and kinetics assisted design of catalysts for the synthesis of fuels and chemicals from bio-derived and alternative feedstocks. He is (co)author of 22 peer reviewed manuscripts and four patent applications. He has been a member of the American Chemical Society since 2006 and serves in the scientific advisory committee of Revista Ion (Colombia).

Michelle K. Kidder

Michelle K. Kidder is a Senior Staff member within the Chemical Sciences Division at Oak Ridge National Laboratory. Dr. Kidder received her B.S. in Chemistry at the State University of New York at Brockport and finished her Ph.D. in Chemistry at South Dakota State University, where she developed fluorescent naphthalimide dye sensors for the selective detection of transition metal cations in non-aqueous environments. She followed her education with a postdoctoral candidacy at ORNL. Her research interest focuses on the challenges faced in basic and applied areas of energy production and storage, such as structure-reactivity relationships that control the kinetics, mechanisms and product selectivity for the thermochemical and catalytic transformations of oxygen-containing, biomass-related molecules under pyrolytic conditions and at solid metal oxide interfaces. She has served as Newsletter Editor for the ACS Division of Energy and Fuels (2008-present; formerly FUEL division) as well as Secretary (2011-present). Dr. Kidder co-organized the symposium on Novel Materials for Catalysis and Fuels Processing at the 243rd and 245th ACS National Meeting.

In Novel Materials for Catalysis and Fuels Processing; Bravo-Suárez, J., et al.;
ACS Symposium Series; American Chemical Society: Washington, DC, 2013.

Viviane Schwartz

Viviane Schwartz, Research Scientist at the Center for Nanophase Materials Science at Oak Ridge National Laboratory, completed her Ph.D. in Chemical Engineering at Virginia Polytechnic Institute and State University with Prof. Ted Oyama in 2000 on the application of transition metal carbides and nitrides as hydroprocessing catalysts. Her research encompasses a series of activities with the ultimate goal of creating and sharing innovative solutions for nanomaterials in the catalysis science. Her research has contributed important new insights into carbon-based catalytic materials for oxidation chemistry and sulfur clean-up; study of selective catalysts for ethanol production; study of highly active and selective gold nano-catalysts for CO oxidation of value for automotive fuel cell applications; and utilization of synchrotron techniques as a tool for unraveling the structure of nanomaterials. She has mentored four postdoctoral fellows and a number of graduate-student users from the CNMS User Program, and she has over 40 publications in refereed journals, being cited more than 600 times.

In Novel Materials for Catalysis and Fuels Processing; Bravo-Suárez, J., et al.;
ACS Symposium Series; American Chemical Society: Washington, DC, 2013.

Subject Index

In Novel Materials for Catalysis and Fuels Processing; Bravo-Suárez, J., et al.;
ACS Symposium Series; American Chemical Society: Washington, DC, 2013.

F

G

H

In Novel Materials for Catalysis and Fuels Processing; Bravo-Suárez, J., et al.;
ACS Symposium Series; American Chemical Society: Washington, DC, 2013.

L

M

In Novel Materials for Catalysis and Fuels Processing; Bravo-Suárez, J., et al.;
ACS Symposium Series; American Chemical Society: Washington, DC, 2013.

N

O

P

R

In Novel Materials for Catalysis and Fuels Processing; Bravo-Suárez, J., et al.;
ACS Symposium Series; American Chemical Society: Washington, DC, 2013.

S

In Novel Materials for Catalysis and Fuels Processing; Bravo-Suárez, J., et al.;
ACS Symposium Series; American Chemical Society: Washington, DC, 2013.

T

U

V

In Novel Materials for Catalysis and Fuels Processing; Bravo-Suárez, J., et al.;
ACS Symposium Series; American Chemical Society: Washington, DC, 2013.

Z

In Novel Materials for Catalysis and Fuels Processing; Bravo-Suárez, J., et al.;
ACS Symposium Series; American Chemical Society: Washington, DC, 2013.